HIGH LET, PASSIVE SPACE RADIATION DOSIMETRY AND SPECTROMETRY

NASA JSC Grant No. NAG9-235

FINAL REPORT

Submitted to NASA Lyndon B. Johnson Space Center
Houston, Texas

March 1995

by

E.V. Benton, A.L. Frank, E.R. Benton, R.P. Keegan
L.A. Frigo, D. Sanner and V. Rowe

Department of Physics
University of San Francisco
2130 Fulton Street
San Francisco, CA 94117-1080

USF-TR-82

TABLE OF CONTENTS

OMIT
TO P.20

HIGH LET, PASSIVE SPACE RADIATION DOSIMETRY AND SPECTROMETRY

I. Introduction

The development of high LET, passive space radiation dosimetry and spectrometry is needed for the purpose of accurate determination of equivalent doses and assessment of health risks to astronauts on long duration missions such as aboard the space station or on planetary missions.

During the past six years, under NASA Grant No. NAG9-235, several research and application projects for spaceflight dosimetry have been pursued. The projects include ground-based studies, flight dosimetry and flight experiments. Detector calibrations and particle fragmentation studies have been made with detectors and materials irradiated with accelerated particle beams. Dosimeter arrays were flown on spacecraft for the purpose of increasing accuracy of measurement through testing and intercomparison of dosimeters exposed to space radiations and to measure depth dose distributions under thin shielding ($0.0026/cm^2$) outside of spacecraft. Spaceflight dosimeters also allow us to test the use of refined techniques to increase accuracy of equivalent dose measurement by including short-range (10-80 μm) particle tracks (produced by secondary particles) in LET spectra measurements.

Experimental radiation measurements have been intercompared (passive versus active methods) and also compared with predictions based on environmental models. Studies of radiation levels in

spacecraft have also been made through collection and collation of experimental data.

II. Projects

A number of projects were included, as follows:

1. Intercomparisons of Cosmic Ray Equivalent Dose and LET Spectra Measurements between STS Missions and between Astronauts

Dosimeter measurement intercomparisons under spaceflight conditions provide basic tests of accuracy and reliability and yield the orbital dependence of dose, equivalent dose and LET spectra. Plastic nuclear track detector (PNTD) measurements of LET spectra from crew passive dosimeters (CPDs) worn by the seven astronauts on the STS-35 mission (Appendix A) have been intercompared. Maximum deviations of ± 20% from the mean were found for the LET flux spectra between 5 and 150 keV/μm, and the curve slopes are very similar. The deviations increased for dose rate spectra and equivalent dose rate spectra due to preferential weighting of these values by the high LET tails of the spectra where statistical accuracy declines. The shielding differences of CPDs worn by astronauts during the mission may account for much of the variation.

Comparison of LET spectra measurements have also been made with PNTDs from area passive dosimeters (APDs) flown on ten different STS missions under similar shielding (Appendix B). The results show that integral flux, dose rate and equivalent dose rate values follow a general increase with respect to increasing orbital inclination and altitude but that there are large variations from a simple relationship. This is to be expected since it has been

shown that Shuttle attitude variations, combined with the anisotropic particle flux at the SAA, can result in differences of a factor of 2 in dose rate inside the Shuttle (Badhwar et al., 1995). Solar cycle and shielding differences also result in variations in radiation dose between STS missions.

Spaceflight dosimeters from the STS missions are also being used in development of a method for increasing LET spectra measurement accuracy by extending LET measurements to particle tracks of ranges 10-80 μm. Refinements in processing and measurement techniques for the flight PNTDs have yielded increased detection efficiencies for the short tracks when LET spectra determined by using the standard and refined methods were intercompared.

2. Increased LET Spectra Measurement Accuracy with ATAS

The measurement accuracy of LET spectra is being increased through extended use of the Automated Track Analysis System (ATAS). At present, this system has been developed to perform a standardized method of measuring LET spectra from PNTDs exposed on spaceflights. The ATAS system parameters have been optimized for a PNTD standardized processing condition which detects particle tracks down to a minimum LET value of ~5 keV/μm. The system employs a fully automated scan of CR-39 PNTDs for particle track detection, then interactive modes for track classification and measurement. The measured track parameters are converted to LET spectra with developed software and the proper response functions. All the LET spectra in this progress report have been measured by

this method.

The above procedure is not optimized for short-range (<80 μm) particle tracks and some of these tracks are not detected. A method of PNTD processing and readout (Method B) is being developed for increased detection efficiency of the short range particle tracks. Reduced processing preserves short tracks which are degraded and lost by the standard method. A disadvantage is that track enlargement does not progress very far. Small tracks must be detected and the relevant parameters measured. The result is that the smaller-sized tracks (for lower LET particles) are inefficiently measured and the minimum LET cutoff must be set much higher than in the standard method. The optimum LET spectrum is derived by combining measurements of the standard and "B" methods.

An example is given in Fig. 1 for the LET spectrum measured from PNTDs contained in the USF APD flown on STS-57. The standard and combined LET spectra are compared showing a large increase in the combined spectrum in the high LET region. On the STS-57 high altitude (473 km) low inclination (28.5°) orbit, the geomagnetic threshold cuts off lower energy GCRs which might contribute to the high LET region. Particle tracks in this region are mainly due to short-range secondaries produced by the high fluxes of trapped protons. Thus the addition of Method B processing to the measurements makes a large difference in the high LET region.

3. Space Radiation Measurements for Intercomparisons of Passive (PNTD, TLD, TRND, Emulsion) and Active (TEPC, RME-III) Dosimeters

Intercomparisons of dosimeter measurements by different

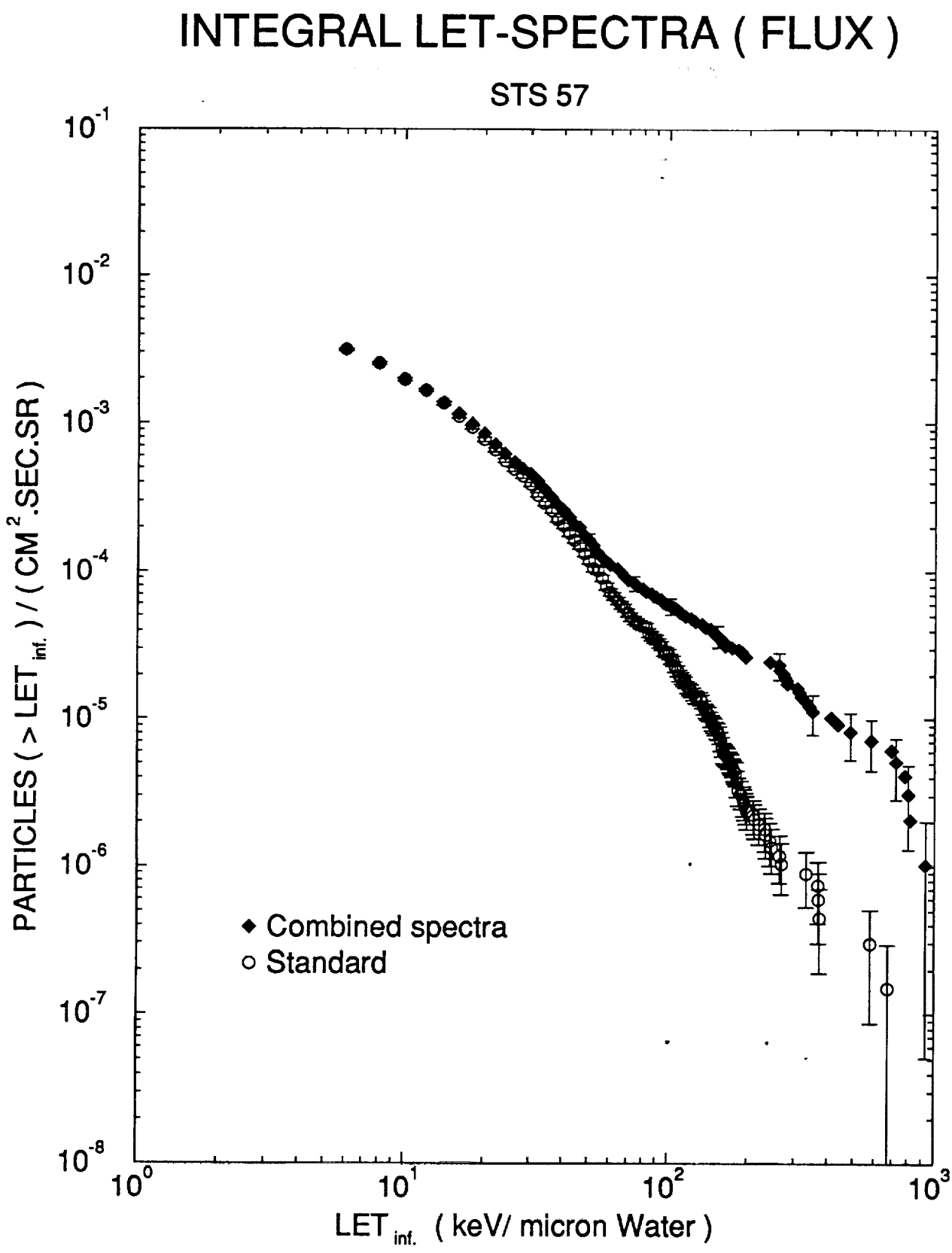

Fig. 1. Comparison of the standard and combined integral LET spectra on the STS-57 APD.

laboratories are being conducted for increased accuracy of measured dose, equivalent dose and LET spectra. Of primary interest are intercomparisons between passive PNTDs and the active TEPC microdosimeter.

a) Intercomparison of USF/Russian passive dosimeter measurements. Two APDs were prepared for the STS-57 mission which contain both Russian and USF passive dosimeters. Included are TLDs, PNTDs, nuclear emulsions, and thermal/resonance neutron detectors (TRNDs). Total absorbed doses from the USF TLDs, LET spectra from the USF PNTDs and low energy neutron fluence and dose equivalent from the USF TRNDs have been measured. The data have been included in a paper covering a range of NASA and Russian instruments (Badhwar et al, 1994) [Appendix C-1]. A more complete description of the experiment and measurements carried out by USF on the STS-57 mission is given in Appendix C-2.

b) Intercomparisons of equivalent dose on the RME-III missions. Several STS missions (42, 45, 53, 56, 51) flew the RME-III active instrument for dosimetry. The RME APD is included for comparisons of active and passive measurements. Each of these APDs carries 10 CR-39 PNTD stacks positioned at 7 angular orientations. The total solid angle is therefore covered in increments by the PNTDs, which are directional in response when used individually. The APDs also contain TLDs from both USF and JSC at the four sides. At the present time the TLDs have been read out for all flights. The PNTDs have

been read out for STS-42 and the remaining PNTD measurements are pending. The absorbed dose rates measured with TLDs are given in Table 1 and the corresponding STS flight parameters are given in Table 2. The results for STS-42 are given in Appendix D.

4. Interaction of Cosmic Ray Particles with Nuclei in Matter

When cosmic rays penetrate spacecraft materials a fraction will interact with target nuclei within the materials. If the cosmic ray is a multi-charged particle, a probability exists for its fragmentation with the resulting production of lower Z projectile secondaries. A probability also exists for secondary production from the target nucleus. These are typically of lower energies with shorter ranges and can be elastic or, if the target nucleus is multi-charged, inelastic.

The propagation of radiation through matter depends on the interaction cross sections of the relevant projectile and target nuclei, on secondary particle multiplicities and the energy and angular distributions. Transport calculations are complex and require extensive testing against experimental measurements for verifications of results. Ground-based studies of secondary particle production and cross sections with simplified shielding geometries are essential for the improvement of predictive calculations of spacecraft radiation.

A number of collaborative studies in this area have been undertaken. Papers include measurements of cross sections and secondary multiplicities in emulsions, using accelerated heavy ions

TABLE 1. Absorbed Doses Measured with TLDs in the RME APDs

STS Mission	Absorbed Dose Rates (mrad d^{-1}) FRONT	LEFT	BACK	RIGHT	AVERAGE
42	10.0 ±0.7	----	11.0 ±0.7	10.4 ±0.7	10.5 ±0.5
45	9.31±0.68	9.49±0.66	9.44±0.73	9.84±0.68	9.53±0.46
53	16.9 ±1.0	16.4 ±1.0	17.1 ±1.1	16.8 ±1.0	16.8 ±0.7
56*	23.8 ±0.8	24.7 ±0.9	26.6 ±1.0	24.5 ±0.9	25.0 ±0.6
51	7.98±0.24	8.13±0.24	8.22±0.24	8.08±0.24	8.10±0.16

*It is suspected that these TLDs received a spurious dose in transit.

TABLE 2. Flight Parameters for RME APD Missions

STS Mission	Launch Date	Duration (d)	Altitude (km)	Inclination (°)
42	01-22-92	8.052	302	57
45	03-24-92	8.924	296	57
53	12-02-92	7.306	389/378	57
56	04-08-93	9.256	296	57
51	09-12-93	9.842	296	28.5

of various energies, by Dudkin et al. (1990 [Appendix E]), Dudkin et al. (1991 [Appendix F]), Dudkin et al. (1993 [Appendix G]) and Dudkin et al (1994 [Appendix H]). Fragmentation cross sections of ^{16}O between 0.9 and 200 GeV/nucleon, for a variety of target nuclei, have been measured by Hirzebruch et al. (1992 [Appendix I]).

Measurements have also been made and compared with transport calculations for the penetration of Fe beams through multi-layered slabs. LET spectra were measured behind slabs of Pb-Al and Pb-$(CH_2)_X$ for 518 MeV/n Fe beams. A paper from this project (Shinn et al, 1994) is given in Appendix J. More recently, irradiations were

made with Fe beams of 200 and 505 MeV/n and Ar beams of 522 MeV/n. Slabs of Al and polyethylene from 2-10 g/cm^2 were used. The PNTDs from these experiments await available time for processing and readout.

5. Radiation Measurements after Long Duration Space Exposures

Long duration space exposures offer opportunities to measure with high accuracy those portions of the radiation field for which statistical accuracy is poor after space missions of a few days (the norm for Shuttle flights). The EURECA satellite was in orbit for eleven months and offered a nearly unique opportunity to do LEO dosimetry under conditions of high statistical accuracy. The dosimeters flown on this mission included a Trackoscope which holds 14 PNTD stacks for directional differentiation of incident radiation. Also included were a thick stack of TLDs and PNTDs for depth dependence measurements and low energy neutron detectors (TRNDs). Of particular interest is the ability to measure short-range (<80 μm) particle LET spectra in the LET range of ≥150 keV/μm on the PNTDs. To date, the TLDs on EURECA have been read out. A recent paper on TLD measurements is included in Appendix K.

Preliminary measurements of LET spectra have been made with PNTDs. Figure 2 shows directional effects on LET spectra using orthogonal and opposing-face PNTD stacks from the Trackoscope. A factor of 6 difference in integral particle flux was measured (max./min.) for LET ≥ 5 keV μm^{-1}.

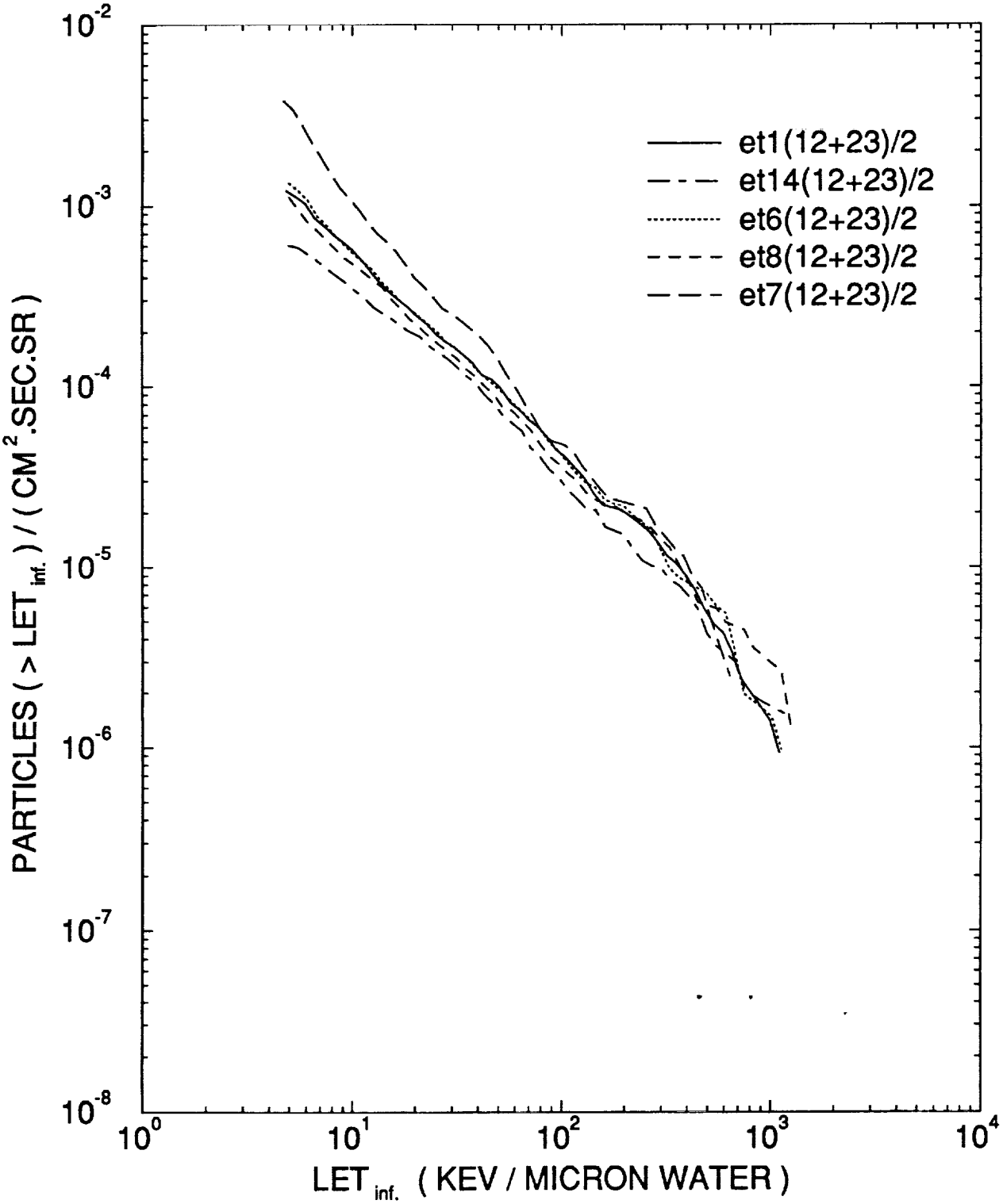

Fig. 2. Integral LET flux spectra from the EURECA Trackoscope. Spectra et1 and et14 are from opposing face PNTD stacks, as are et6 and et8. Spectra et1, -6, -7, -8 and -14 stacks are orthogonal in spatial orientation and show the effects of directionality of radiation in the EURECA satellite.

6. Ground Based Dosimeter Calibrations

Accuracy of spaceflight dosimeter measurements depends on calibrations of dosimeters and materials. Irradiations by accelerated ion beams are necessary for basic calibrations which cannot be performed in the complex space radiation environment. Several exposures have taken place, as follows:

a) CR-39 PNTD material was exposed at the LBL BEVALAC, before the shut-down, to Fe ions (250-600 MeV/n), Au ions (1 GeV/n) and Ar ions (522 MeV/n). The exposed PNTDs are being used for basic calibrations of the material. The use of degraders and wedges during the irradiations yields a wide range of particle LETs. Material sensitivity as a function of particle LET is measured. Recent calibrations of Batch 21 USF-3 CR-39 PNTDs, for two processing conditions are shown in Fig. 3.

b) Recent exposures of CR-39 PNTD material have been made at the TIARA Cyclotron of JAERI, Takasaki, Japan (10 MeV protons; 50 MeV ^{4}He ions) and at the RIKEN Ring Cyclotron in Japan (135 MeV/n ^{14}N ions). The major purpose of these irradiations is to study intrinsic sensitivity variations over PNTD surfaces at low LET values. This study could lead to improved LET response curves for the PNTDs in the low LET (5-25 keV/μm) region.

c) CR-39 is also being exposed at the new heavy ion acclerator at GSI in Germany. Stack exposures are being made at a series of angles to investigate sensitivity as a function

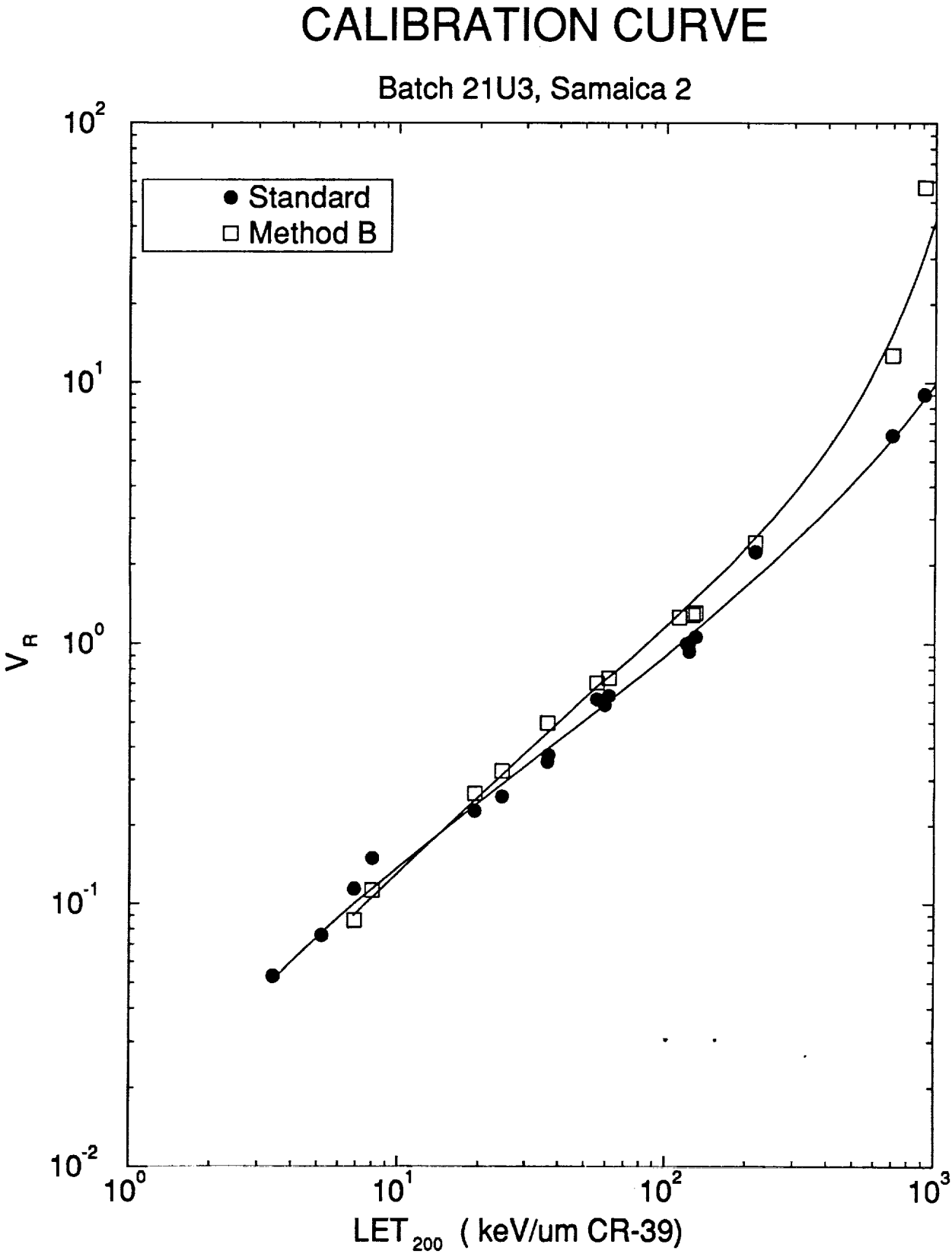

Fig. 3. A comparison of PNTD calibration curves for the Standard and Method B processing conditions. Method B was developed to enhance PNTD sensitivity for short range (8-80 μm) particle tracks.

of particle dip angle for improvement of the response calibration. Ions obtained to date are 80 MeV/n C, 420 MeV/n Ne, 128 and 789 MeV/n Ar, 722 MeV/n Fe, 300 MeV/n Ni and 1156 MeV/n Au. These irradiations will be continued.

7. Neutron Detector Calibrations

The neutron fluxes on spacecraft are an important source of equivalent dose which is poorly known because of difficulties of measurement in the presence of large ionizing particle fluxes. Passive neutron detectors are used by us to determine fluxes in the high energy (>1 MeV), resonance (0.2 eV - 1 MeV) and thermal (<0.2 eV) range and these detectors have been calibrated with proton beams. Passive neutron detectors which are currently used in spaceflight measurements include high energy neutron detectors employing fission foils (FFNDs) and thermal/resonance neutron detectors (TRNDs) which contain ^{6}LiF. Both detector types have some response both to neutrons and protons. In the case of the FFNDs, fission is induced with similar cross sections by protons and neutrons with energy >25 MeV. High energy proton beams can therefore be used to calibrate the detectors. The original calibrations of FFNDs were performed using the lower energy neutrons available from a neutron generator (≤16 MeV). The calibration factor changes for nucleon energies extending into the GeV range.

Irradiations of FFNDs have been made with protons of 80 and 154 MeV at the Harvard Cyclotron Laboratory (HCL) and at 1.8 and 4.9 GeV at the LBL BEVALAC. Detection efficiencies (tracks/proton)

have been measured at these energies. The results are given in Appendix L.

In the case of the TRNDs, the response is dominated by the $^{6}Li(n,\alpha)T$ reaction where the cross section peaks at thermal neutron energy. The question of whether or not the large proton fluxes in space have a significant effect on response through (p,α) reactions has been addressed. Proton calibrations of the detector have been made at 80 MeV and 154 MeV and the measured efficiencies have been compared with space flight data to evaluate space proton effects. The results of this study are given in Appendix M. It has been found that space protons contribute a very small fraction of the short-range secondary α particles counted on the neutron detectors from LEO missions (<4%, with an average contribution of approximately 1%).

8. Radiation Measurements on Soviet/Russian Spacecraft

The NASA Shuttle radiation measurements have been supplemented with several radiation experiments performed on Russian space missions. These missions include Cosmos 782, 939, 1129, 1887 and 2044 and also Photon-8, Bion-10 and Mir Space Station deployment. The orbits of the spacecraft were different from those of the Shuttle and the measurements served to extend the NASA data. Also, dosimeters were flown outside the spacecraft, under very low shielding, on some missions. This is difficult to arrange on the Shuttle. In addition, dosimeters were often flown together with those of other nations for comparison.

Measurements of LET spectra, absorbed doses and neutron fluxes

and dose equivalents have been made and comparisons with environmental models and between missions performed. Recent papers include a study of LET spectra from Cosmos flights (Akopova et al., 1990 [Appendix N]), depth dose under low shielding on Cosmos 1887 (Akatov et al., 1990 [Appendix O]), measurements of LET and neutron spectra on Cosmos 2044 (Dudkin et al., 1992a [Appendix P], 1992b [Appendix Q] and 1992c [Appendix R]; Marenny et al., 1992 [Appendix S]), a study of neutron fluences and spectra on a number of flights (Dudkin et al., 1990 [Appendix T]) and space effects on plant seeds (Anikeeva et al., 1990 [Appendix U]). Readout of some of the dosimeters flown on the later flights are pending due to time constraints. The details of the work performed at USF for a recent flight project (Cosmos 2044) are spelled out in USF Technical Report No. 76 (Frank et al., 1990 [Appendix V]).

9. Space Radiation Measurements Under Thin Shielding

The depth dose profiles under thin shielding in space are important in projecting astronaut doses during EVA and providing data for testing of environmental model calcuations. Electronic effects, particularly in regard to solar cell degradation, are also dependent on depth dose under thin shielding. A number of radiation experiments have been conducted by this laboratory on the outside of orbital spacecraft under thin shielding (15 μm-thick Kapton plastic windows). These include Russian Cosmos flights 1887 and 2044, a period on the Mir Space Station and on the Shuttle (STS-46) in which the measurements have been completed. In addition, similar measurements from dosimeters flown on the Russian

Photon-8 and Bion-10 mission are pending. The depth dose profiles under thin shielding have not been often measured during space missions and the USF data represents a significant part of the total.

Comparisons of measurements with environmental model calculations have been made for some of the missions. Figure 4 shows measurements and calculations of depth dose for Cosmos 2044 (AE8 and AP8 models used). The low energy electrons are seen to dominate absorbed dose down to depths >2 g/cm^2. The model deviates from the measurements by more than a factor of 5 at small depths (Fig. 4) and also deviates at the larger depths. Figure 5 shows four measured depth dose profiles and calculations corresponding to one of the missions (Mir Space Station). For the Mir orbit the calculations are much lower than the measurements. These studies show that improvements are needed in the environmental trapped electron models. The measurements should be extended to a variety of inclinations and altitudes to provide a comprehensive test for modeling.

10. Space Radiation Studies

An understanding of the complex space radiation environment requires a range of studies including measurements over the exposure variables (altitude, inclination, shielding, solar cycle), corresponding modeling of the radiation and development of transport codes, and the collection, collation and analysis of data. Several collaborative studies have been published, including a review of space radiation dosimetry on U.S. and Soviet manned

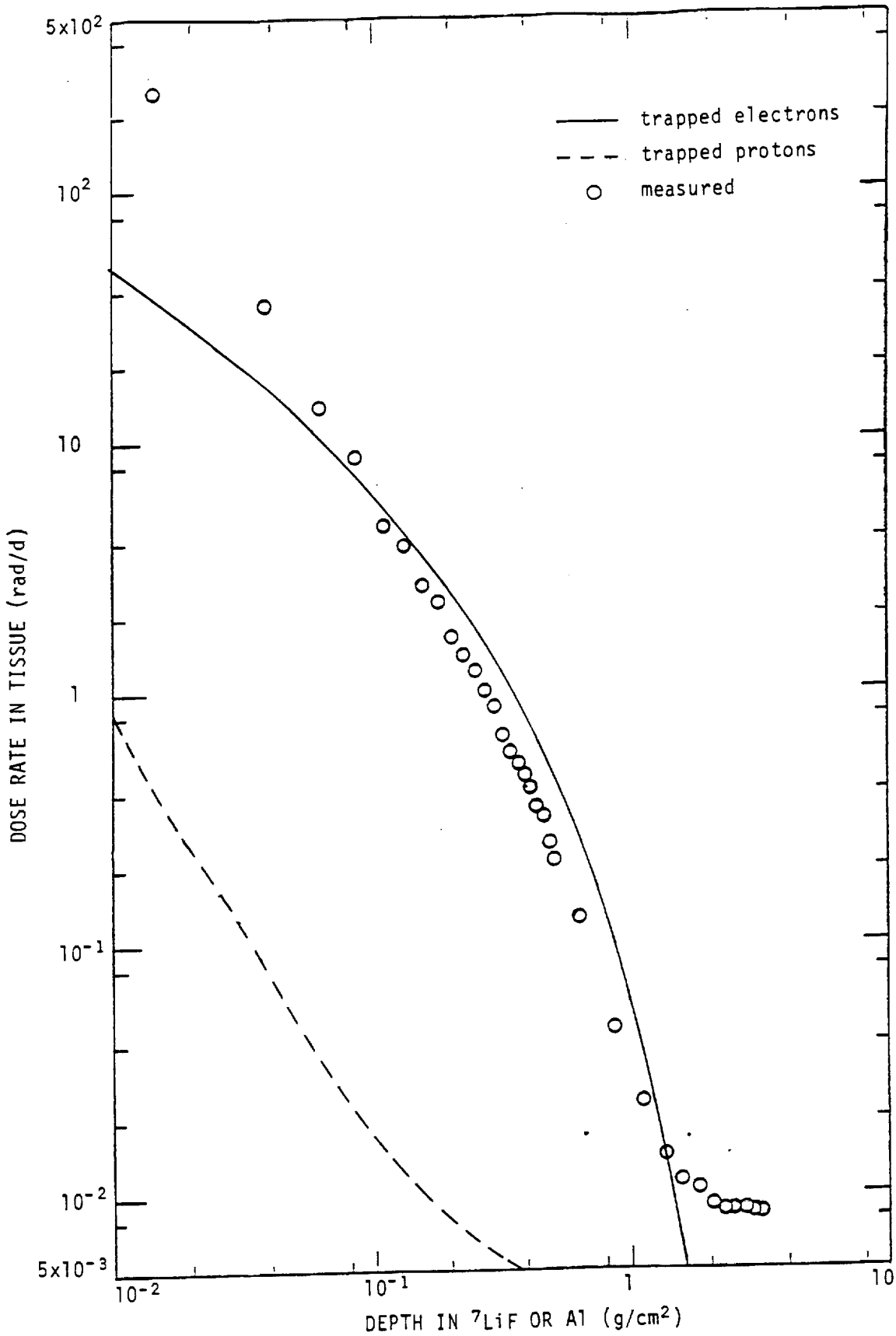

Fig. 4. Comparison of the average TLD dose rates in Plate No. B9-4 with the calculated depth dose rates of trapped electrons and protons for tissue behind aluminum plane shields /Watts, 1990/. The calculations were for the Cosmos 2044 orbit at solar maximum.

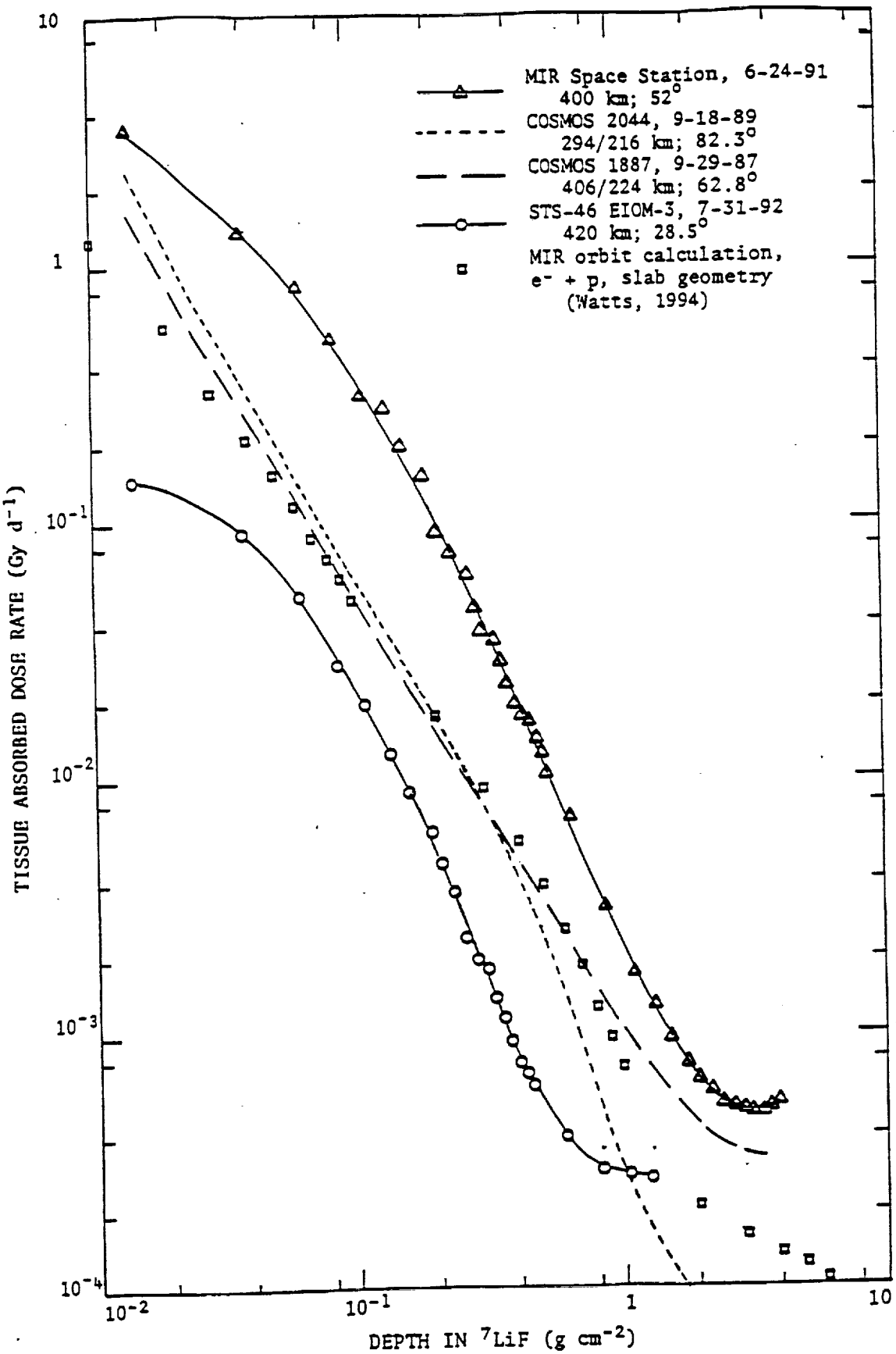

Fig. 5. TLD depth-dose rates measured in low shielding environment on the MIR space station (measured and calculated), Cosmos biosatellites Nos.1887 and 2044, and STS-46.

missions (Benton and Parnell, 1988 [Appendix W]), radiation shielding estimates for manned Mars space flights (Dudkin et al., 1992 [Appendix X]), a comparison of measured LET spectra to models (Wiegel et al., 1992 [Appendix Y]), galactic cosmic ray abundances and spectra behind defined shielding (Heinrich et al., 1994 [Appendix Z]) and development of a model for space radiation effects on the central nervous system-neuritogenesis (Vazquez et al., 1994 [Appendix AA]).

APPENDIX A

LET SPECTRA MEASUREMENTS FROM THE STS-35 CPDs

LET spectra derived from ATAS track parameter measurements for CPDs flown with the astronauts on STS-35 are plotted in Figures 1, 2 and 3. Figure 1 shows the total particle flux spectra for $LET_{\infty} \cdot H_2O \geq 5$ keV/μm. The spread between the seven individual spectra is typical of past manual measurements of sets of CPDs. This difference is probably due to the cumulative net shielding variations experienced by the CPDs as the astronauts carrying them went about their activities on the Space Shuttle. The STS-35 mission was launched on Dec. 2, 1990, at 28.5° inclination and 352 km altitude. This is somewhat higher than the nominal 300-km flights and the orbit intersects more of the high intensity trapped proton region in the South Atlantic Anomaly (SAA). However, in comparing with APD spectra measured on earlier lower altitude missions (STS-26, -29, -30, -32) the flux spectra are all roughly comparable. This may be due to the fact that the STS-35 mission took place close to solar maximum (Feb. 1990), or perhaps to shielding differences.

The corresponding dose and dose equivalent spectra for this mission are shown in Figures 2 and 3. The effect of statistical fluctuations at the higher LET values, where track densities are small, is very noticeable. This results in an increased spread within the dose rate and dose equivalent rate spectra, as compared to the flux spectra. The contribution to dose and dose equivalent per measured track is much greater in the high LET region and the differences, though numerically small, are heavily weighted in the integral spectra. The optimum measurement and characterization of the high LET tails of the spectra represent an important part of the research into PNTD response.

Table 1 gives the integral flux, dose rate, dose equivalent rate and mission dose equivalent for the seven astronauts. Flux is

2.87 ± 0.34 x 10^{-4} particles/$cm^2 \cdot s \cdot sr$, dose rate is 0.755 ± 0.060 mrad/d and dose equivalent rate is 5.41 ± 0.67 mrem/d (for $LET_\infty \cdot H_2O$ >5 keV/μm) for the CPDs. These numbers are in the range expected for low altitude, low inclination orbits.

TABLE A1. PNTD Measurements for the Crew Passive Dosimeters on STS-35

CPD	Flux ($cm^{-2}s^{-1}sr^{-1}$)	Absorbed Dose Rate (mrad d^{-1})	Dose Equiv. Rate (mrem d^{-1})	Total Dose Equiv. (mrem)
3501	3.00 e-04	0.832	6.11	54.9
3502	2.92 e-04	0.761	5.29	47.6
3503	2.91 e-04	0.705	4.82	43.3
3504	2.54 e-04	0.743	6.01	54.0
3505	2.28 e-04	0.685	5.20	46.8
3506	3.06 e-04	0.839	6.03	54.2
3507	3.42 e-04	0.718	4.39	39.5

(for $LET_\infty \cdot H_2O$ >5 keV μm^{-1})

The accuracy of the measurements is affected by counting statistics, track parameter measurement errors, stability and homogeneity of response of the PNTDs. Calibrations indicate σ of approximately ± 10%.

FIGURE CAPTIONS

Fig. A1. LET total flux spectra for seven CPDs on the STS-35 mission.

Fig. A2. LET dose rate spectra for seven CPDs on the STS-35 mission.

Fig. A3. LET dose equivalent rate spectra for seven CPDs on the STS-35 mission.

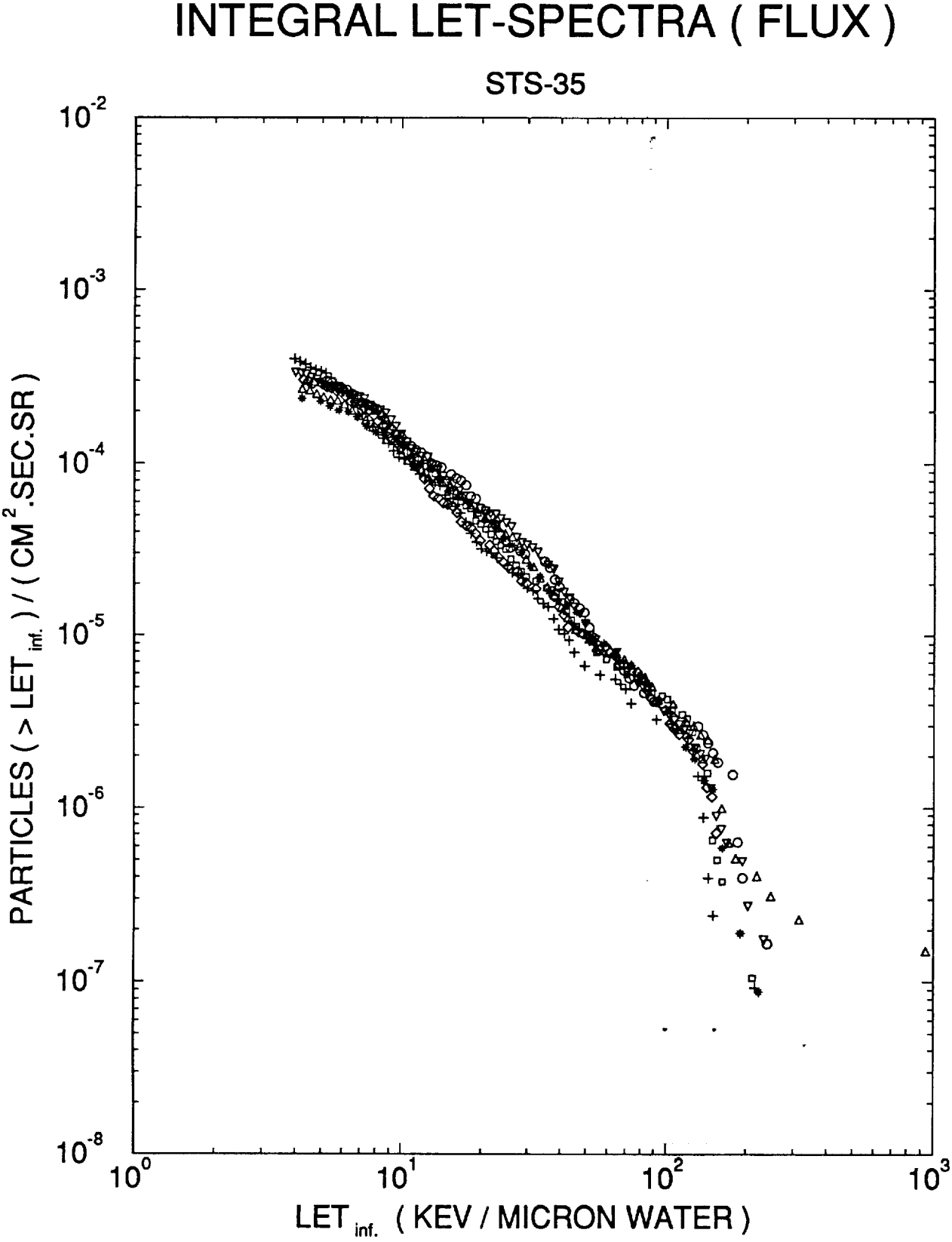
INTEGRAL LET-SPECTRA (FLUX)
STS-35
PARTICLES (> LET inf.) / (CM 2 .SEC.SR)
LET inf. (KEV / MICRON WATER)
10-2
10-3
10-4
10-5
10-6
10-7
10-8
100
101
102
103

FIGURE A1

DOSE RATE SPECTRA

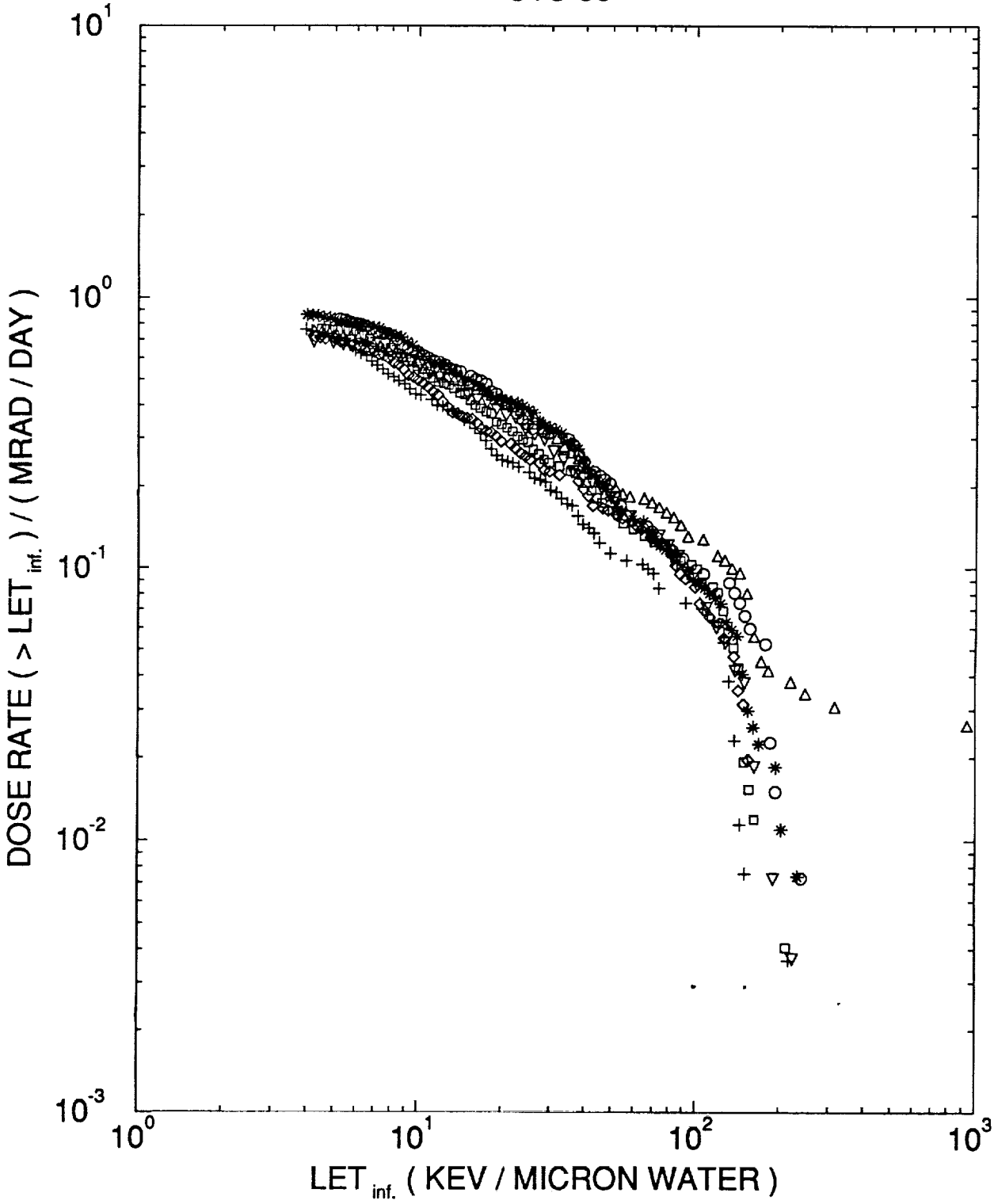

FIGURE A2

DOSE EQUIVALENT RATE SPECTRA

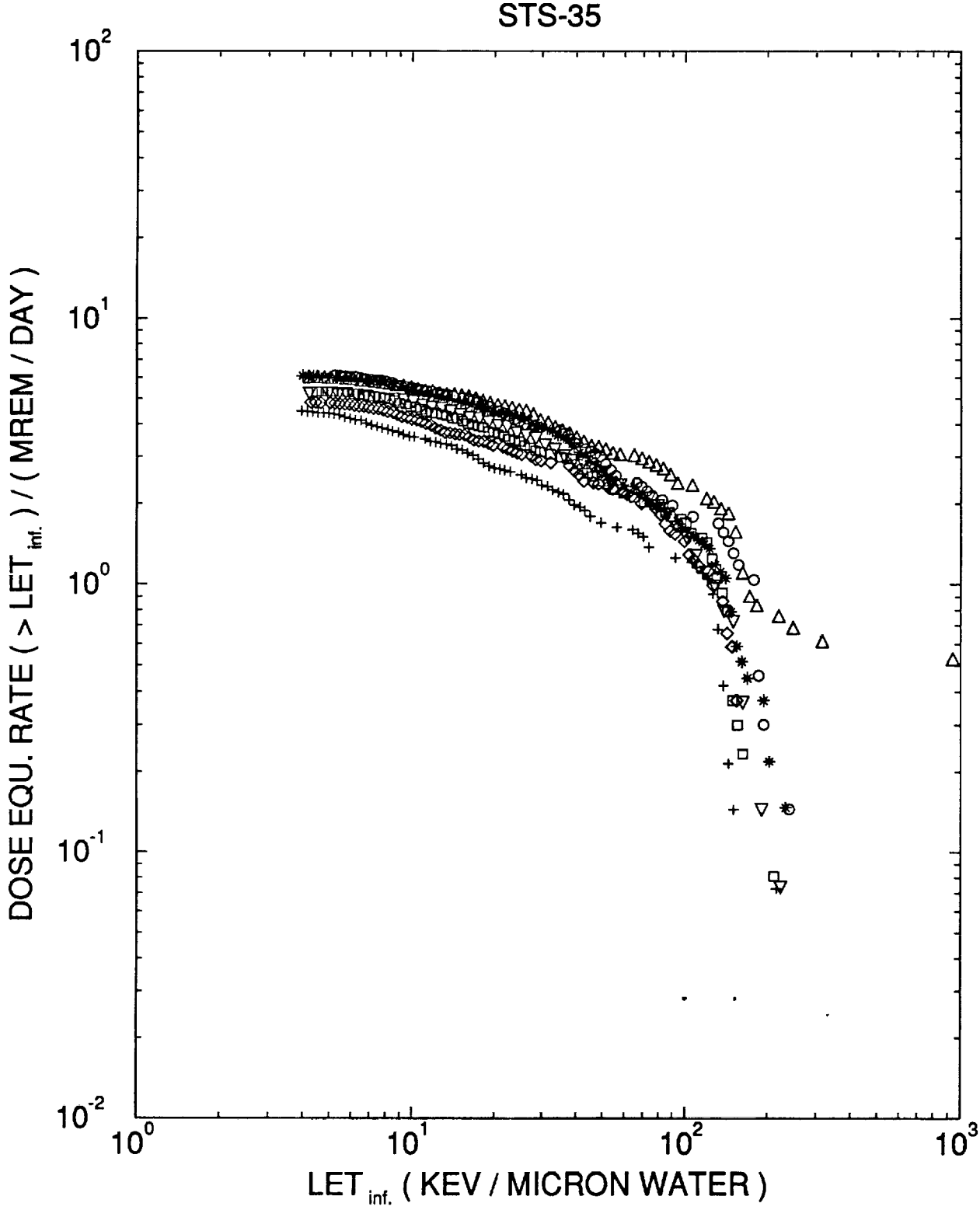

FIGURE A3

APPENDIX B

SUMMARY OF LET SPECTRA AND DOSE MEASUREMENTS ON TEN STS MISSIONS

Introduction

The dosimetry performed on STS flights includes Area Passive Dosimeters (APDs) and Crew Passive Dosimeters (CPDs). Each dosimeter type contains plastic nuclear track detectors (PNTDs) for the measurement of LET spectra of heavy particles ($LET_{\infty} \cdot H_2O \geq 5$ keV/μm). For purposes of mission intercomparisons, or of comparisons with model calculations or other measurements, the APDs yield more consistent results. The PNTD stacks are directional in response. The APDs contain three orthogonal stacks to average over solid angle. The CPDs, which are carried by astronauts in a breast pocket, depend on the movement of the crew about the Shuttle to average over solid angles. Also the APDs have been mounted in the same locker location and orientation for all recent missions. For this reason a selection of APD PNTDs have been read out to provide LET data for missions with different flight parameters.

Flight Dosimetry

The APD dosimetry results reported here are for the STS-37, -39, -40, -41, -42, -43, -44, -45, -48 and -50 missions. The APDs were located in Locker MF71C in the Shuttle crew compartment, except for STS-42 in which results were derived from a portion of the RME APD. Each of the three orthogonal PNTD stacks consisted of a CR-39 doublet (two sheets of film with dimensions of 4.5 cm x 3.0 cm x 0.06 cm) separated by an 8 μm-thick film of polycarbonate plastic.

After return of the flight dosimeters, the CR-39 PNTDs were processed by the standard method to delineate latent particle tracks. The readout of the PNTDs requires a scanning procedure to locate tracks in the surfaces of the CR-39 followed by measurement of individual track parameters. Particle LET is calculated from the lengths of the major and minor axes of elliptical track

openings, depths of material etched from the CR-39 surfaces and calibration curves of PNTD sensitivity versus particle LET. The calibration curves are constructed from a series of measurements with accelerated particles of known LET.

Automated Readout of PNTDs

Readout of PNTDs is carried out on the automated scanning and measurement SAMAICA systems at The University of San Francisco. SAMAICA is an acronym for Scanning and Measuring with Automated Image Contour Analysis and is a product of ELBEK GmbH in Siegen, Germany. The system performs a fully automated scan of CR-39 PNTDs for track detection and then incorporates interactive modes for track classification and measurement. The classification involves an examination of the four surfaces of an assembled CR-39 doublet by the system operator to determine whether the particle was long range (creating four colinear tracks at the surfaces) or short range (creating 2 or 3 colinear tracks). In all cases the particle was required to create a track pair at the adjacent (#2, #3) surfaces of the doublet.

After classification the tracks on surface #3 of the doublet were measured. (The system software makes an initial fit of an ellipse to the track opening, then allows the operator to manually adjust the fit.) The measurement data were then reduced to integral and differential LET spectra with standard analysis software developed at USF. Data from the three orthogonal (x, y, z) stacks were combined into average LET spectra.

Measurements

Integral LET flux spectra for the ten missions listed above are shown in Figures 1 to 10. Shown are curves for long range (>1200 μm) and short range tracks (80 to 1200 μm) with a total curve shown in each case for both flux components added together. Long range particles are likely to be galactic cosmic rays and projectile secondaries, while short range particles are probably stopping primary particles plus secondaries from target nuclei. At the highest Shuttle altitudes the short range particles are dominated by the contribution from trapped particles in the Earth's magnetic field, mainly protons. The lower LET detector threshold

in each case is approximately 5 keV/μm. Relevant information for each flight concerning flux, dose-rate, dose-equivalent rate and total dose is given in Tables 1-10. The dose equivalent rate is determined by weighting particle LET fluxes by Quality Factors from ICRU 19 (1971).

Discussion

As can be seen from the integral flux plots, the contribution to total flux from short range tracks is, as expected, greater than that for long range tracks, for all altitudes and inclinations. At high altitudes the contribution is dominated by trapped protons. The short registration range of protons in CR-39 (~1000 μm) ensures that most of this contribution (stopping primary and secondary protons) are classified as short range. At lower altitudes, and especially at higher inclinations, the galactic cosmic rays (which produce the long range tracks) become more important. However, most of the GCRs have LETs <5 keV/μm, the sensitivity limit of CR-39. Their contributions to the LET spectra come through nuclear reactions and the production of target secondary particles, which are classified as short range. Even at very low altitude and high inclination orbits, the CR-39 detects a large fraction of short range particles.

When the flux spectra are converted to dose rates a different picture emerges. The long range particles tend to be higher in LET than short range particles and they become relatively more important. The contribution of long range particles to total dose is given by the long range dose ratio defined as (long range dose)/(total dose) and is given in Table 11 for each flight. As can be seen from this table, the long range dose ratio seems to increase with inclination, with the ratio being greatest for relatively low altitude (approx. 290 km), high inclination (57°) orbits. However, the ratio for STS-48 was 0.207 which is due to the fact that this flight had an altitude of 565 km and therefore cut across Earth's inner radiation belt at the South Atlantic Anomaly, hence registering a greater percentage of short range particles. Since the lowest and highest altitudes for a given

inclination of 57° in this report were for flights STS-39 and STS-48, the effect of changing the orbital altitude can clearly be seen, with ratios of 0.578 and 0.207 respectively. The dose ratio for the 28° inclination orbit is variable but decreases with orbital altitude. In general the dose ratio is much lower for 28° orbits for two reasons: the magnetic field cutoff for GCRs extends to higher particle energies and the Shuttle spends a greater fraction of orbital time within the SAA.

Figure 11 is a plot of dose equivalent rate against altitude and inclination, therefore enabling a general inter-comparison of dose equivalents to be made. The dose equivalent rate tends to increase with both altitude and inclination. There are significant variations within this relationship, however. For instance, the STS-44 dose equivalent appears higher than would be expected while that for STS-37 is less. It is interesting to note that the crew average total dose rates for these missions, as measured with TLDs by Johnson Spaceflight Center personnel, are 0.294 mGy d^{-1} on STS-37 and 0.094 mGy d^{-1} for STS-44. These dose rates are much as expected from the orbital parameters. This demonstrates that the high LET portion of cosmic radiation (>5 keV/μm) is much more variable than total dose, which is dominated by more penetrating low LET radiation. The differences can arise from effective shielding variations between missions (different Shuttle contents or different orientations with respect to the directions of maximum incoming radiation). The dose rate of particles >5 keV/μm is only 5.6% of total crew dose rate for STS-37 and 29% of total for STS-44. These dose rate fractions are near the extreme lower and upper boundaries which have been measured with PNTDs on Shuttle missions.

TABLES

Tables 1-11: Data concerning dose ratios, altitudes and inclinations for each of the flights indicated below (see Figure Captions).

FIGURE CAPTIONS

Figure 1: Integral LET flux spectra for the STS-37 APDs.
Figure 2: Integral LET flux spectra for the STS-39 APDs.
Figure 3: Integral LET flux spectra for the STS-40 APDs.
Figure 4: Integral LET flux spectra for the STS-41 APDs.
Figure 5: Integral LET flux spectra for the STS-42 APDs.
Figure 6: Integral LET flux spectra for the STS-43 APDs.
Figure 7: Integral LET flux spectra for the STS-44 APDs.
Figure 8: Integral LET flux spectra for the STS-45 APDs.
Figure 9: Integral LET flux spectra for the STS-48 APDs
Figure 10: Integral LET flux spectra for the STS-50 APDs
Figure 11: Plot of dose equivalent rate against altitude and inclination for all flights presented in this report.

Table 1: STS 37 APD DOSE TABLE

For LET$\geq 5KeV/\mu m$

	FLUX ($cm^{-2}s^{-1}sr^{-1}$)	DOSE RATE ($mrad\ day^{-1}$)	DOSE EQUIV. RATE ($mrem\ day^{-1}$)	TOTAL DOSE EQUIV. ($mrem$)
TOTAL	1.004×10^{-3}	2.534	14.310	85.631
LR	4.943×10^{-5}	0.165	1.297	7.761
SR	9.548×10^{-4}	2.374	13.012	77.864

Table 2: STS 39 APD DOSE TABLE

For LET$\geq 5KeV/\mu m$

	FLUX ($cm^{-2}s^{-1}sr^{-1}$)	DOSE RATE ($mrad\ day^{-1}$)	DOSE EQUIV. RATE ($mrem\ day^{-1}$)	TOTAL DOSE EQUIV. ($mrem$)
TOTAL	6.267×10^{-4}	1.853	14.039	116.62
LR	1.869×10^{-4}	0.670	6.872	57.086
SR	4.582×10^{-4}	1.183	7.166	59.528

Table 3: STS 40 APD DOSE TABLE

For LET$\geq 5 KeV/\mu m$

	FLUX ($cm^{-2}s^{-1}sr^{-1}$)	DOSE RATE ($mrad\ day^{-1}$)	DOSE EQUIV. RATE ($mrem\ day^{-1}$)	TOTAL DOSE EQUIV. ($mrem$)
TOTAL	2.611×10^{-4}	0.687	5.095	46.332
LR	8.139×10^{-5}	0.233	1.916	17.424
SR	1.797×10^{-4}	0.454	3.178	28.900

Table 4: STS 41 APD DOSE TABLE

For LET$\geq 5 KeV/\mu m$

	FLUX ($cm^{-2}s^{-1}sr^{-1}$)	DOSE RATE ($mrad\ day^{-1}$)	DOSE EQUIV. RATE ($mrem\ day^{-1}$)	TOTAL DOSE EQUIV. ($mrem$)
TOTAL	1.148×10^{-3}	2.914	15.671	64.047
LR	4.090×10^{-5}	0.156	1.621	6.625
SR	1.107×10^{-3}	2.758	14.051	57.426

Table 5: **STS 42 APD DOSE TABLE**

For LET$\geq 5 KeV/\mu m$

	FLUX $(cm^{-2}s^{-1}sr^{-1})$	**DOSE RATE** $(mrad\ day^{-1})$	**DOSE EQUIV. RATE** $(mrem\ day^{-1})$	**TOTAL DOSE EQUIV.** $(mrem)$
TOTAL	7.859×10^{-4}	2.005	14.587	117.45
LR	3.890×10^{-4}	0.961	7.820	62.970
SR	4.043×10^{-4}	1.044	6.767	54.490

Table 6: **STS 43 APD DOSE TABLE**

For LET$\geq 5 KeV/\mu m$

	FLUX $(cm^{-2}s^{-1}sr^{-1})$	**DOSE RATE** $(mrad\ day^{-1})$	**DOSE EQUIV. RATE** $(mrem\ day^{-1})$	**TOTAL DOSE EQUIV.** $(mrem)$
TOTAL	8.061×10^{-4}	2.135	12.942	115.050
LR	3.220×10^{-4}	0.549	2.882	25.620
SR	4.840×10^{-4}	1.586	10.060	89.433

Table 7: STS 44 APD DOSE TABLE

For LET$\geq 5 KeV/\mu m$

	FLUX ($cm^{-2}s^{-1}sr^{-1}$)	DOSE RATE ($mrad\ day^{-1}$)	DOSE EQUIV. RATE ($mrem\ day^{-1}$)	TOTAL DOSE EQUIV. ($mrem$)
TOTAL	1.675×10^{-3}	5.559	36.490	253.64
LR	8.894×10^{-5}	0.345	2.740	19.046
SR	1.586×10^{-3}	5.214	33.752	234.61

Table 8: STS 45 APD DOSE TABLE

For LET$\geq 5 KeV/\mu m$

	FLUX ($cm^{-2}s^{-1}sr^{-1}$)	DOSE RATE ($mrad\ day^{-1}$)	DOSE EQUIV. RATE ($mrem\ day^{-1}$)	TOTAL DOSE EQUIV. ($mrem$)
TOTAL	7.587×10^{-4}	2.271	16.051	143.239
LR	2.939×10^{-4}	0.940	8.096	72.249
SR	4.647×10^{-4}	1.331	7.954	70.981

Table 9: **STS 48 APD DOSE TABLE**

For LET$\geq 5 KeV/\mu m$

	FLUX $(cm^{-2}s^{-1}sr^{-1})$	**DOSE RATE** $(mrad\ day^{-1})$	**DOSE EQUIV. RATE** $(mrem\ day^{-1})$	**TOTAL DOSE EQUIV.** $(mrem)$
TOTAL	5.708×10^{-3}	14.122	75.024	401.53
LR	2.003×10^{-3}	3.749	17.587	94.12
SR	3.705×10^{-3}	10.375	57.438	307.41

Table 10: **STS 50 APD DOSE TABLE**

For LET$\geq 5 KeV/\mu m$

	FLUX $(cm^{-2}s^{-1}sr^{-1})$	**DOSE RATE** $(mrad\ day^{-1})$	**DOSE EQUIV. RATE** $(mrem\ day^{-1})$	**TOTAL DOSE EQUIV.** $(mrem)$
TOTAL	6.944×10^{-4}	2.578	20.723	286.25
LR	1.403×10^{-4}	0.441	4.694	64.838
SR	5.635×10^{-4}	2.138	16.029	221.41

Table 11: LONG RANGE DOSE EQUIV. RATIO FOR EACH STS FLIGHT

STS NO.	ALTITUDE (km)	INCLINATION ($degrees$)	LONG RANGE DOSE EQUIV. RATIO
37	450	28.5	9.06×10^{-2}
44	361	28.5	7.51×10^{-2}
43	296	28.5	2.23×10^{-1}
50	296	28.45	2.27×10^{-1}
41	291	28.5	1.03×10^{-1}
40	296	39.0	3.76×10^{-1}
48	565	57.0	2.34×10^{-1}
42	302	57.0	5.36×10^{-1}
45	296	57.0	5.04×10^{-1}
39	263	57.0	4.90×10^{-1}

INTEGRAL LET-SPECTRA (FLUX)

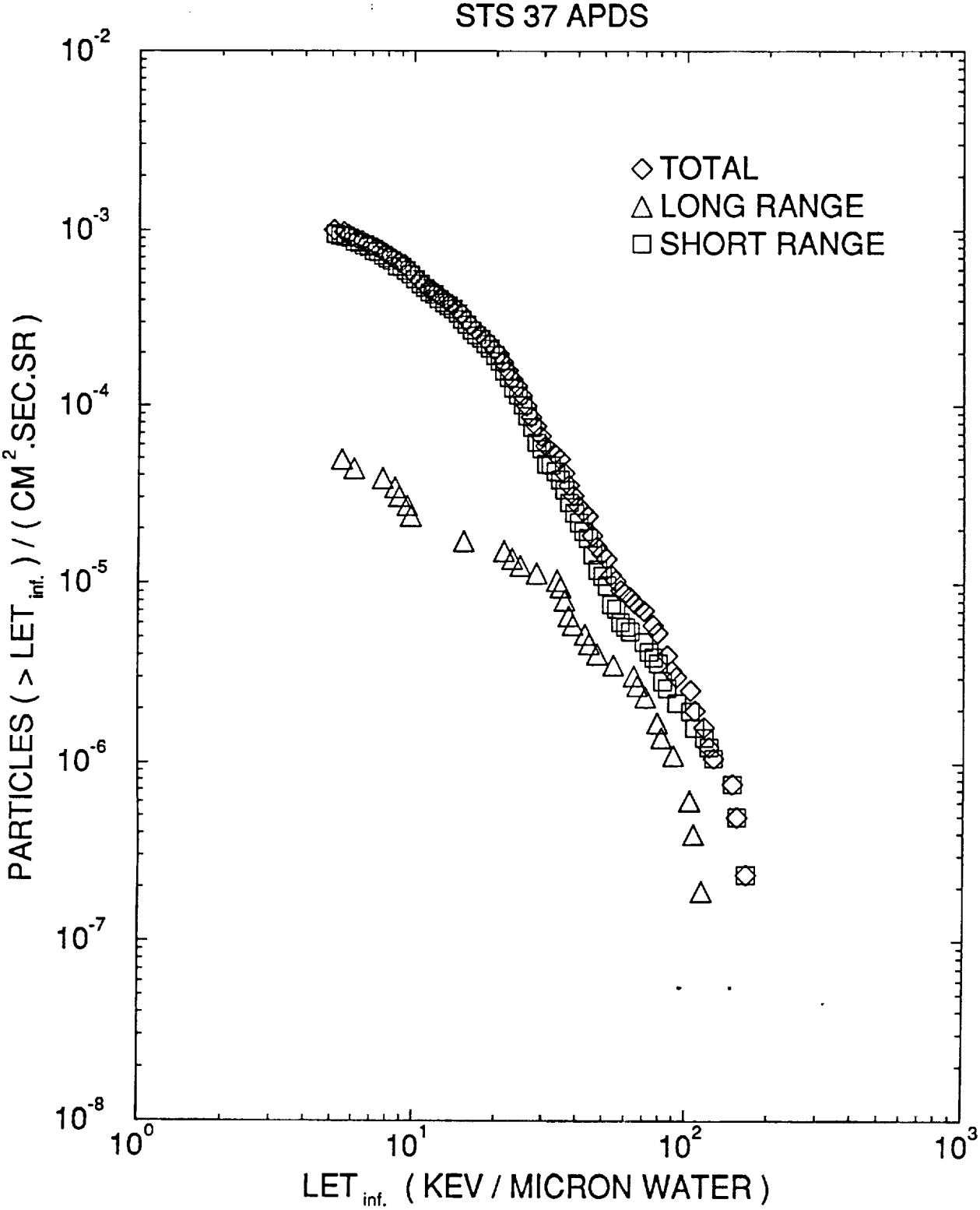

FIGURE B1

INTEGRAL LET-SPECTRA (FLUX)

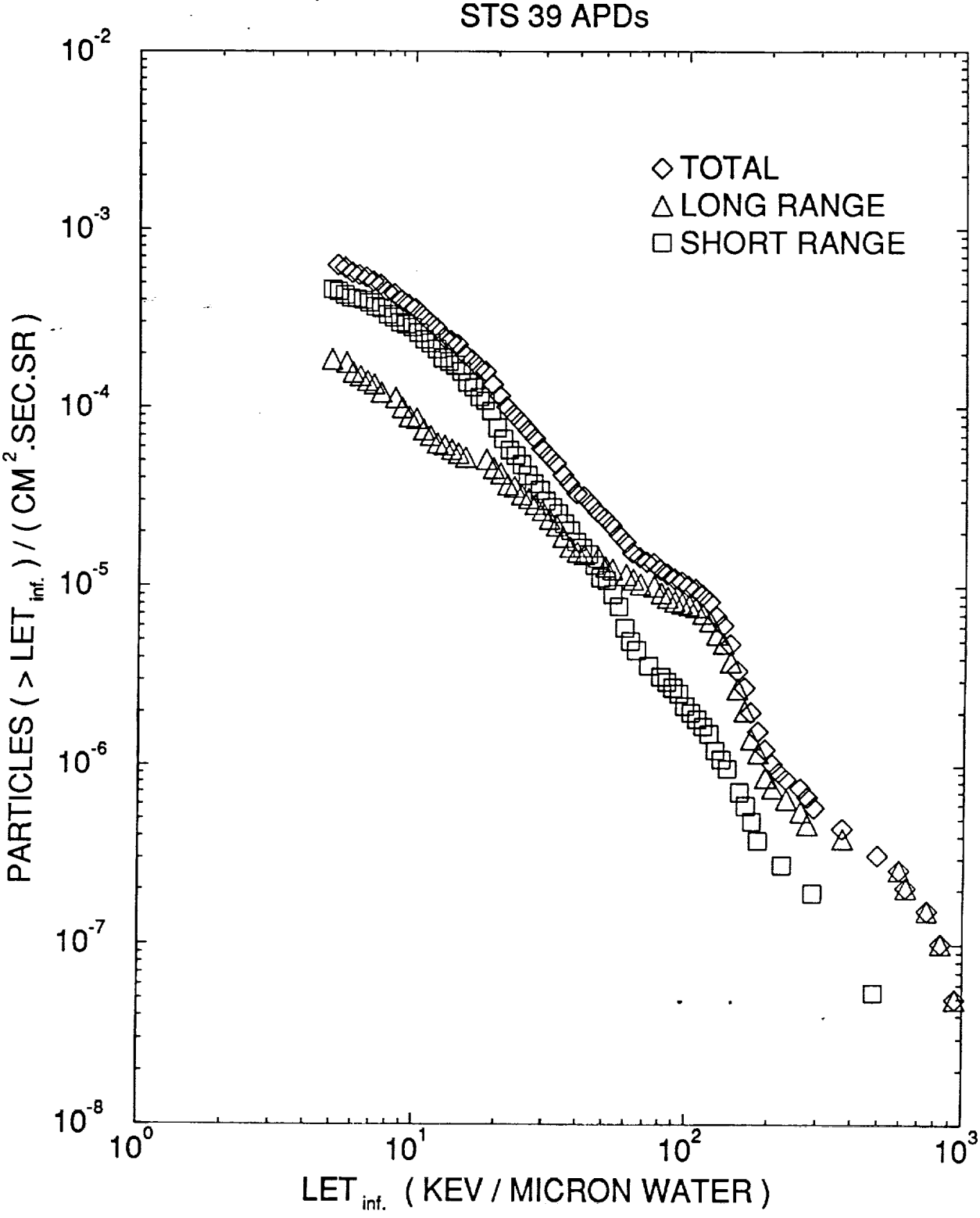

FIGURE B2

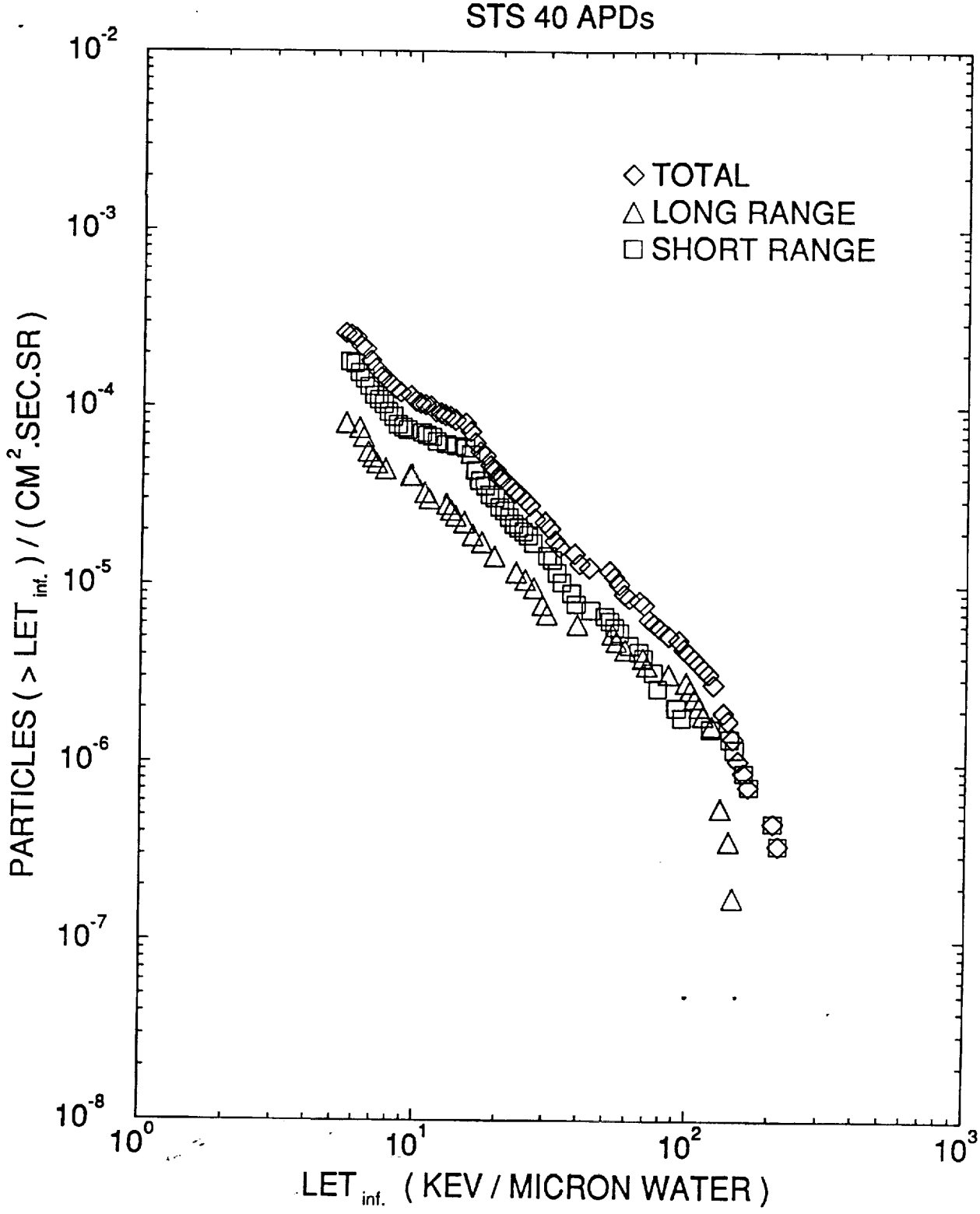
INTEGRAL LET-SPECTRA (FLUX)
STS 40 APDs
◇ TOTAL
△ LONG RANGE
□ SHORT RANGE
PARTICLES (> LET inf.) / (CM 2 .SEC.SR)
LET inf. (KEV / MICRON WATER)
10-2
10-3
10-4
10-5
10-6
10-7
10-8
100
101
102
103

FIGURE B3

INTEGRAL LET-SPECTRA (FLUX)

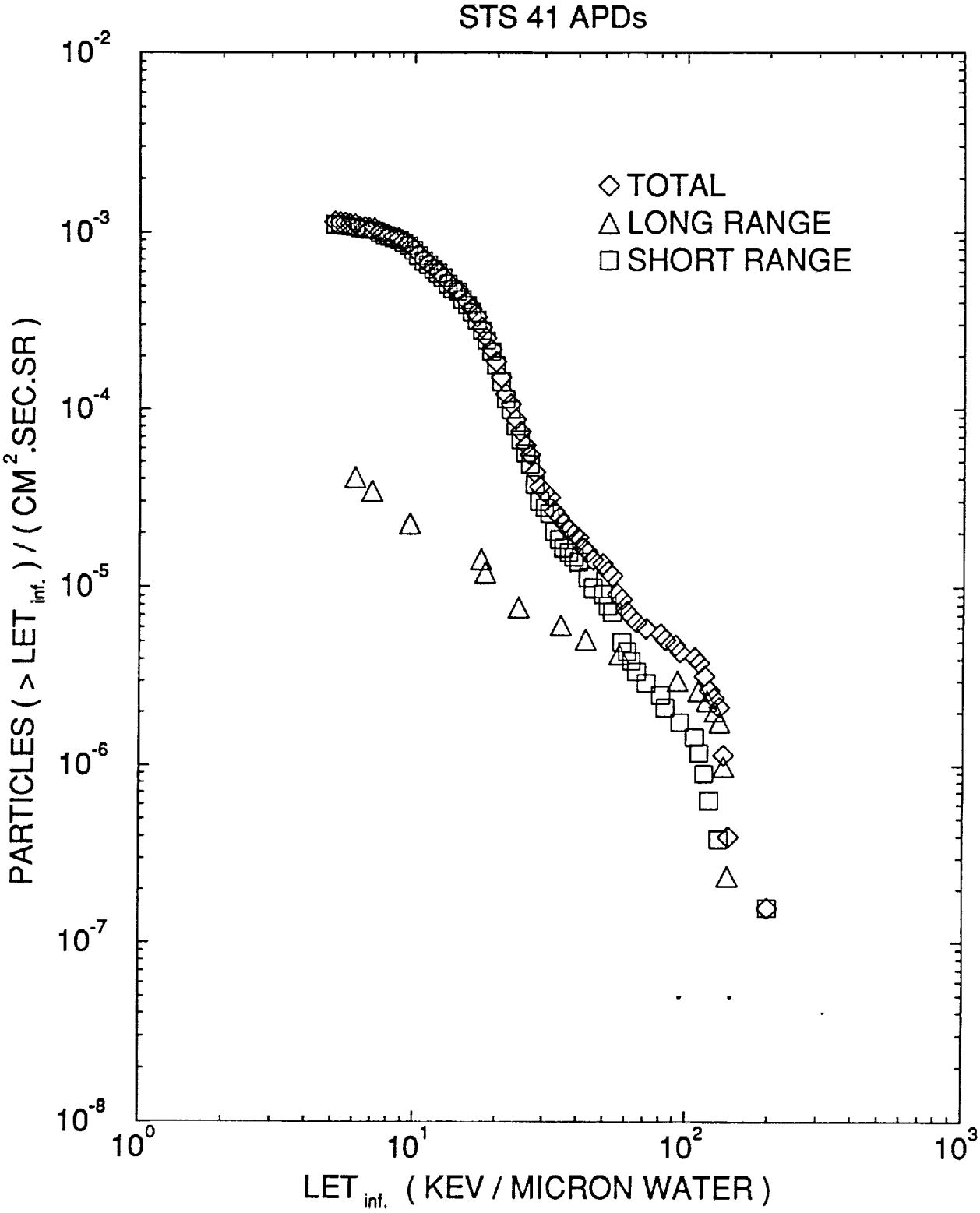

FIGURE B4

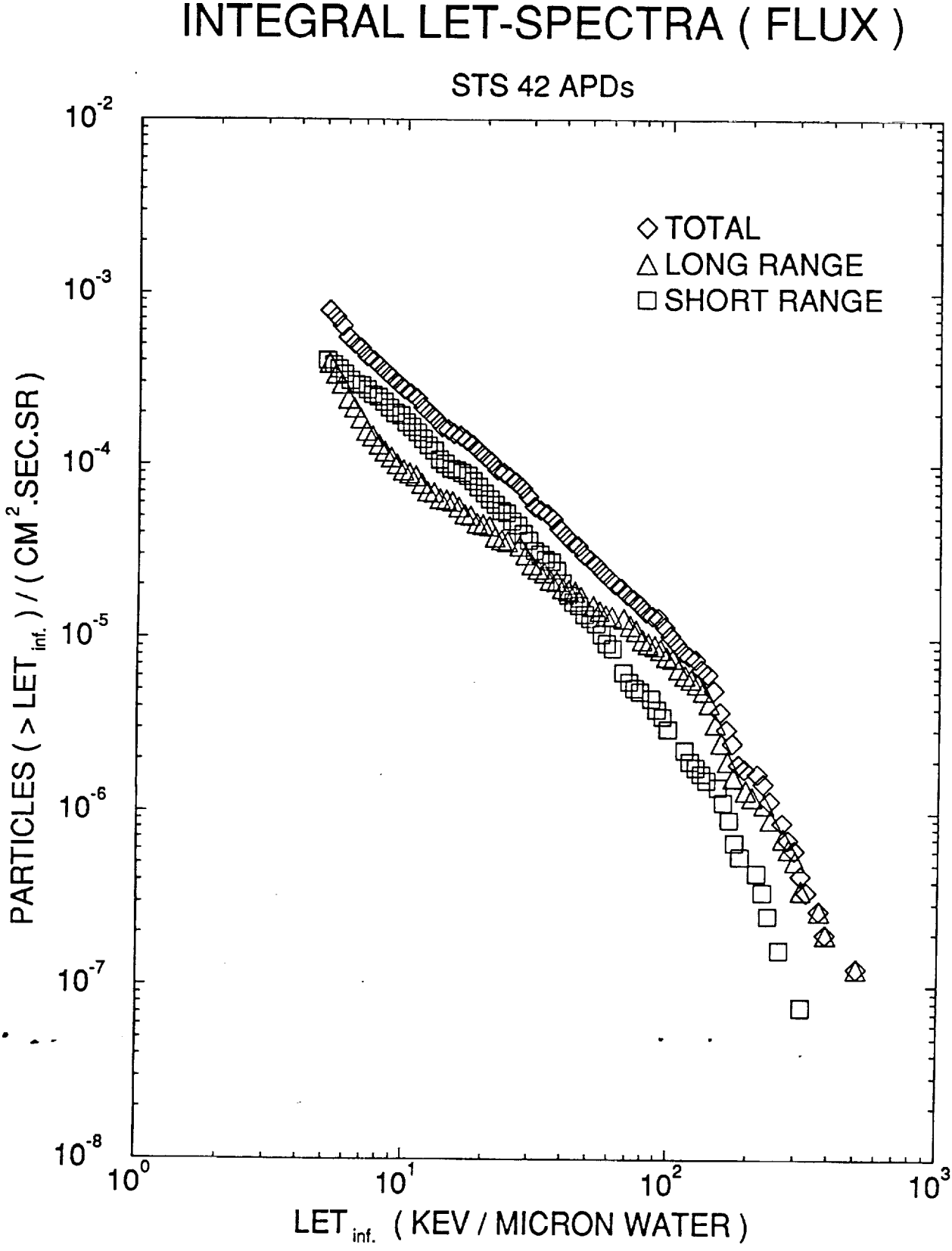
INTEGRAL LET-SPECTRA (FLUX)
STS 42 APDs
◇ TOTAL
△ LONG RANGE
□ SHORT RANGE
PARTICLES (> LET inf.) / (CM 2 .SEC.SR)
LET inf. (KEV / MICRON WATER)
10-2
10-3
10-4
10-5
10-6
10-7
10-8
100
101
102
103

FIGURE B5

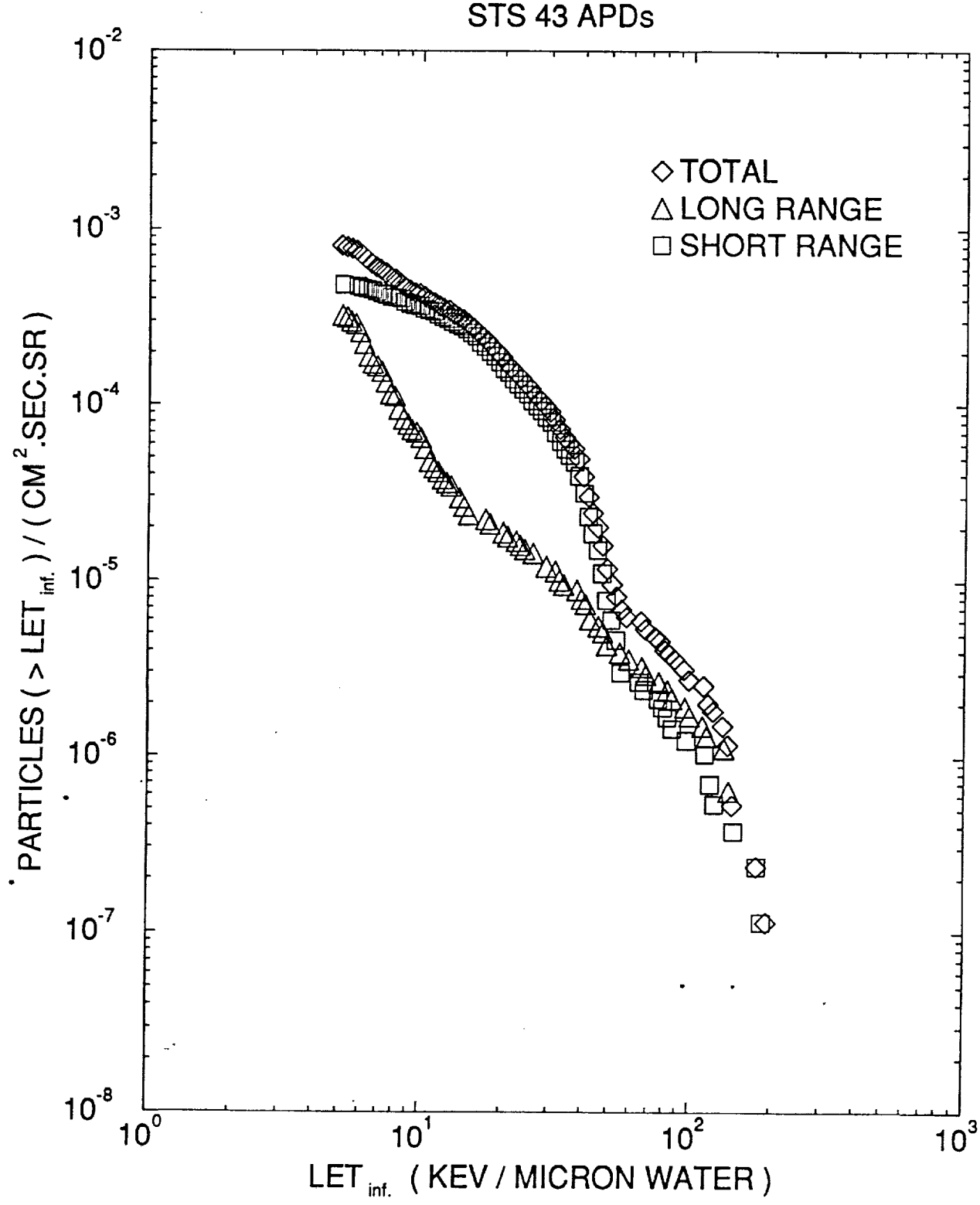
INTEGRAL LET-SPECTRA (FLUX)
STS 43 APDs
TOTAL
LONG RANGE
SHORT RANGE
PARTICLES (> LET inf.) / (CM 2 .SEC.SR)
LET inf. (KEV / MICRON WATER)
10-2
10-3
10-4
10-5
10-6
10-7
10-8
100
101
102
103

FIGURE B6

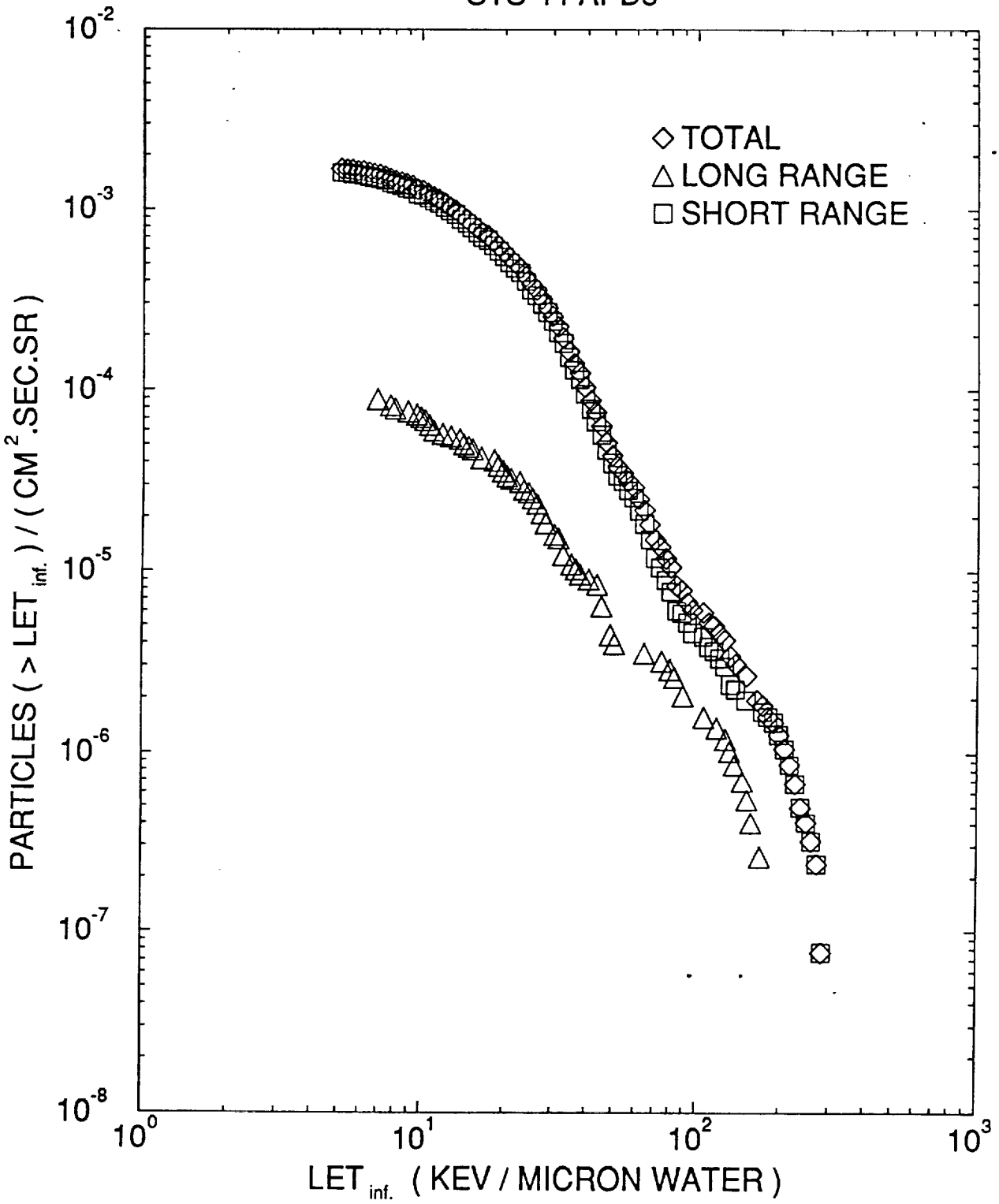
INTEGRAL LET-SPECTRA (FLUX)
STS 44 APDs
◇ TOTAL
△ LONG RANGE
□ SHORT RANGE
PARTICLES (> LET inf.) / (CM 2 .SEC.SR)
LET inf. (KEV / MICRON WATER)
10-2
10-3
10-4
10-5
10-6
10-7
10-8
100
101
102
103

FIGURE B7

INTEGRAL LET-SPECTRA (FLUX)

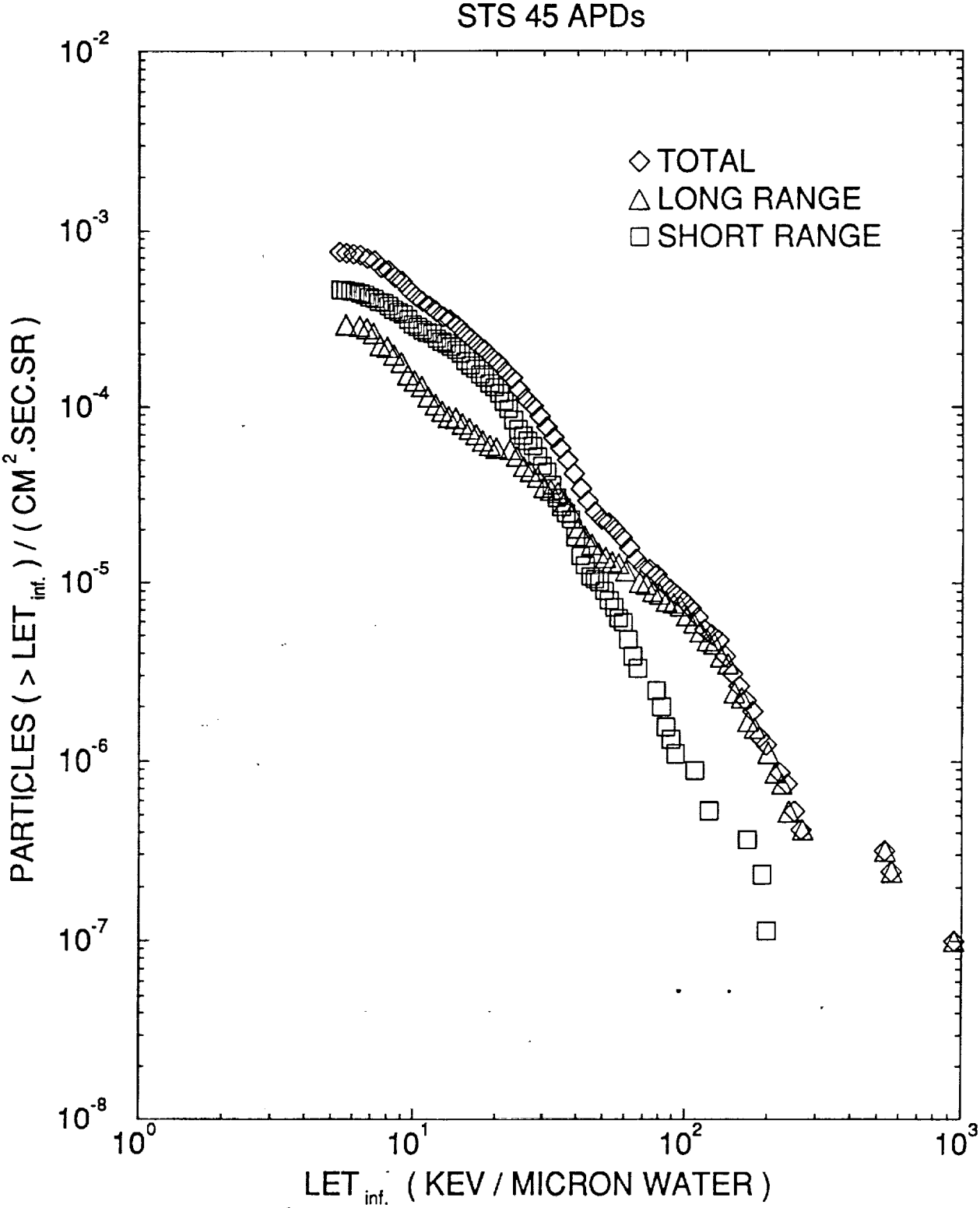

FIGURE B8

INTEGRAL LET-SPECTRA (FLUX)

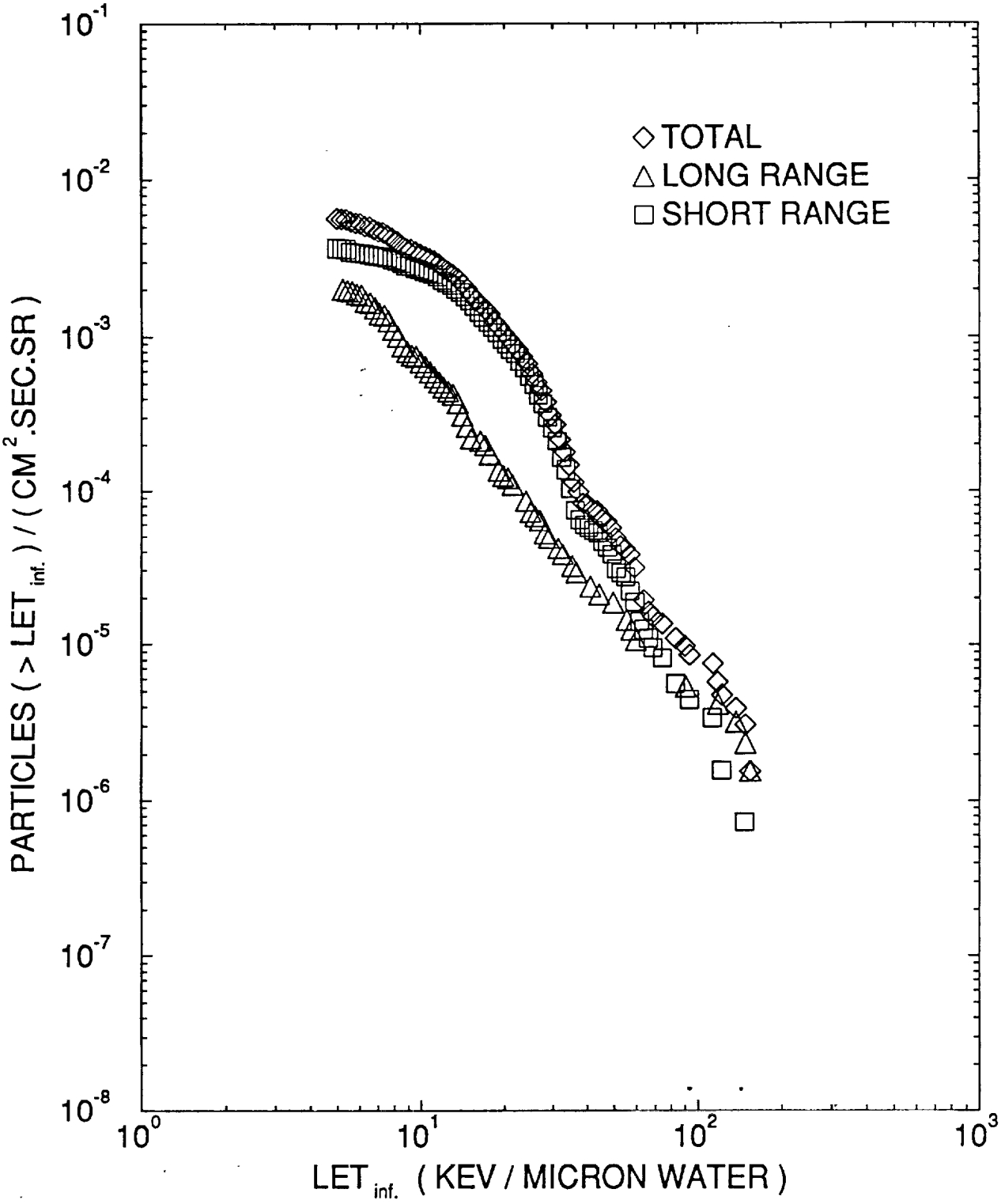

FIGURE B9

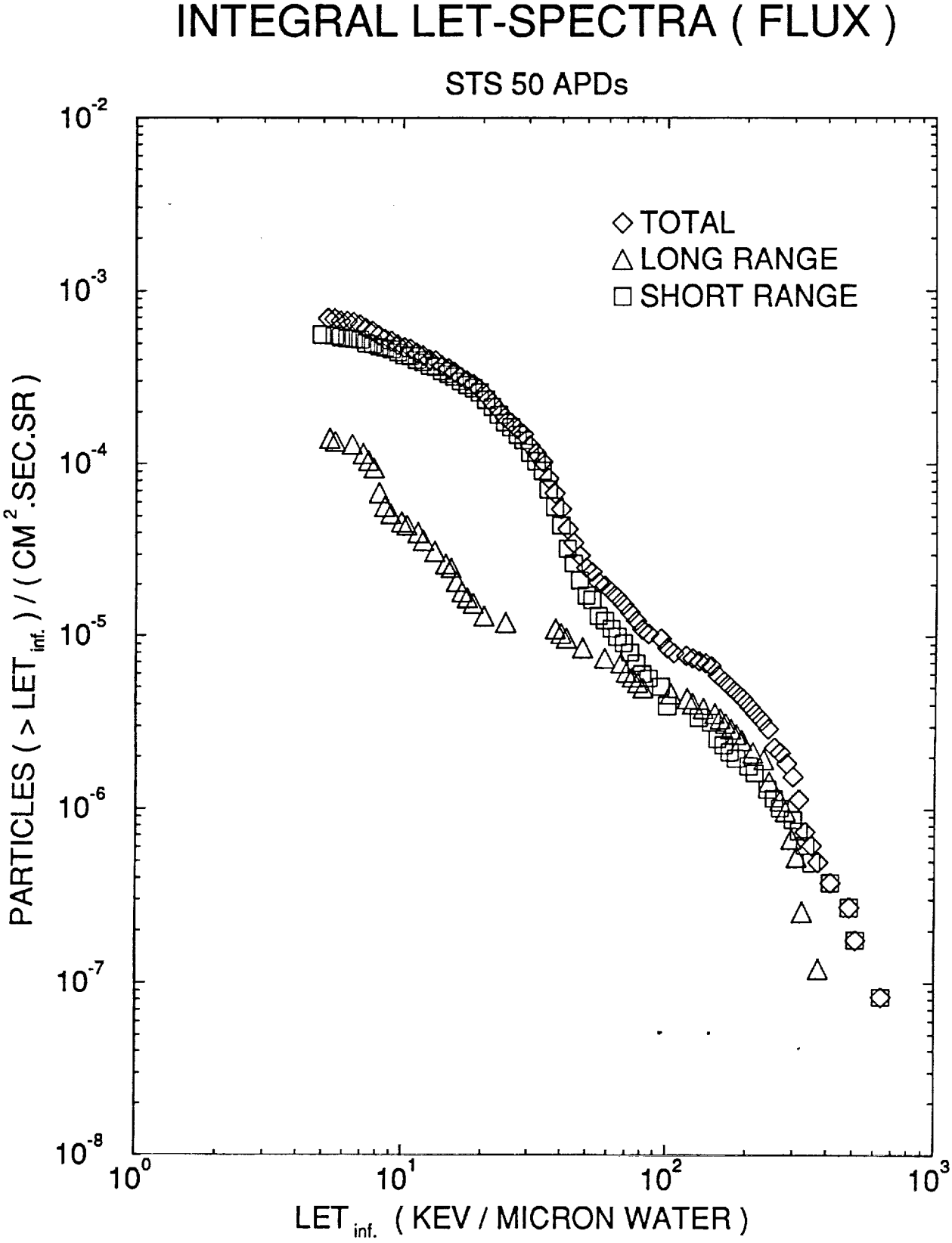
INTEGRAL LET-SPECTRA (FLUX)
STS 50 APDs
◇ TOTAL
△ LONG RANGE
□ SHORT RANGE
PARTICLES (> LET inf.) / (CM 2 .SEC.SR)
LET inf. (KEV / MICRON WATER)
10-2
10-3
10-4
10-5
10-6
10-7
10-8
100
101
102
103

FIGURE B10

DOSE EQUIVALENT RATE PLOT FOR STS FLIGHTS 37,39,40,41,42,43,44,45,48 AND 50

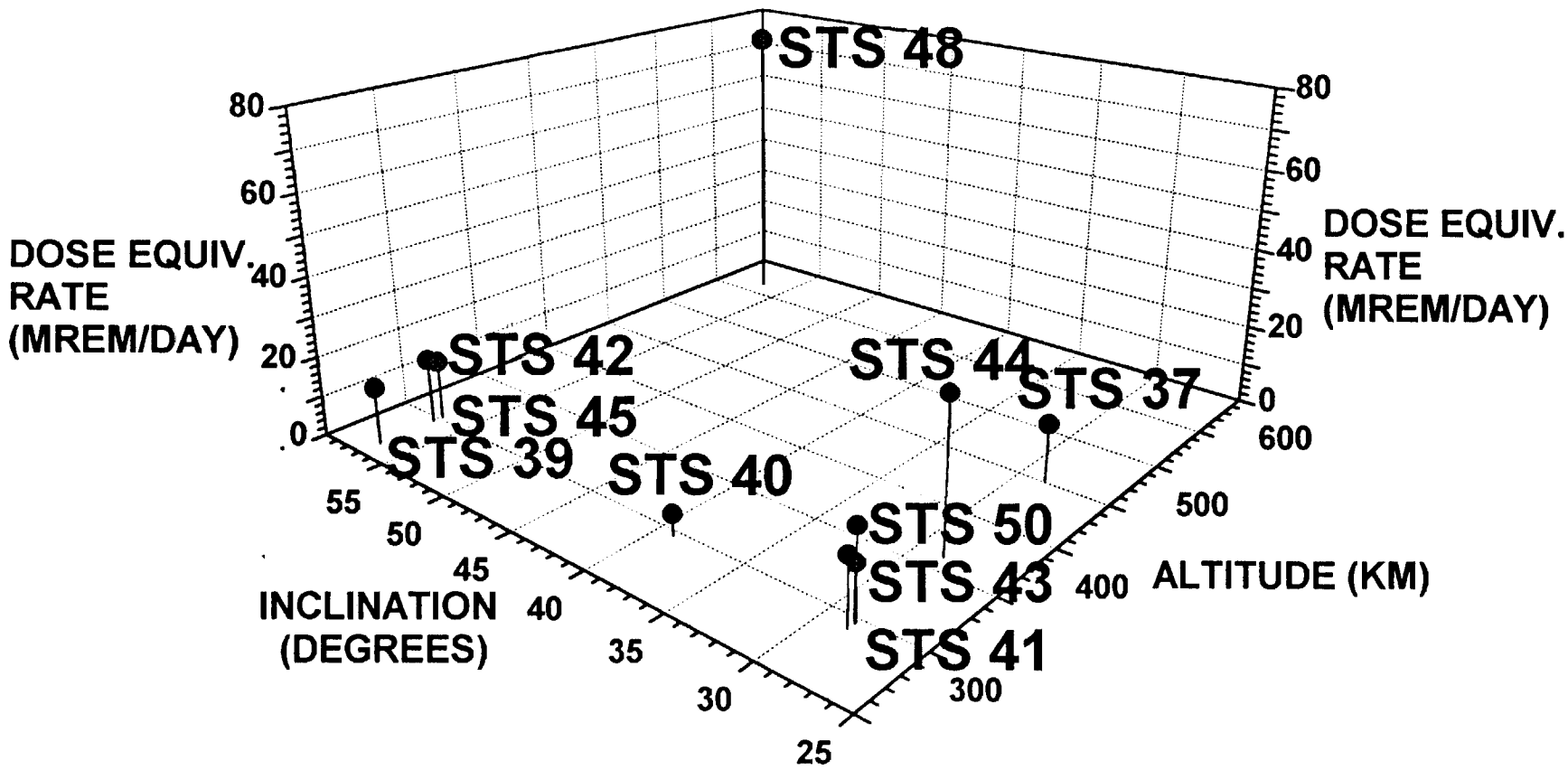

FIGURE B11

APPENDIX C-1

N95-25914

A Study of the Radiation Environment On Board the Space Shuttle Flight STS-57

53-72
44627
p. 24

G.D. Badhwar, W. Atwell*, E.V. Benton+, A.L. Frank+ and R.P. Keegan+

NASA Johnson Space Center, Houston, Texas 77058

Rockwell, Space Systems Division, Houston, Texas 77058

Department of Physics, University of San Francisco, San Francisco, CA 94117-1080

and

V.E. Dudkin, O.N. Karpov, Yu. V. Potapov, A.B. Akopova

Research Center for Spacecraft Radiation Safety

Shchukinskaya Str. 40, Moscow 123182, Russia

and

N.V. Magradze, L.V. Melkumyan, and Sh. B. Rshtuni

Yerevan Physics Institute, Yerevan 375036, Armenia

Abstract

A joint NASA-Russian study of the radiation environment inside a SPACEHAB 2 locker on Space Shuttle flight STS-57 was conducted. The Shuttle flew in a nearly circular orbit of 28.5° inclination and 462 km altitude. The locker carried a charged particle spectrometer, a tissue equivalent proportional counter (TEPC), and two area passive detectors consisting of combined NASA plastic nuclear track detectors (PNTDs) and thermoluminescent detectors (TLDs), and Russian nuclear emulsions, PNTDs and TLDs. All the detector systems were shielded by the same Shuttle mass distribution. This makes possible a direct comparison of the various dose measurement techniques. In addition, measurements of the neutron energy spectrum were made using the proton recoil technique.

The results show good agreement between the integral LET spectrum of the combined galactic and trapped particles using the tissue equivalent proportional counter and track detectors between about 15 keV/μm and 200 keV/μm. The LET spectrum determined from nuclear emulsions was systematically lower by about 50%, possibly due to emulsion fading. The results show that the TEPC measured an absorbed dose 20% higher than TLDs, due primarily to an increased TEPC response to neutrons and a low sensitivity of TLDs to high LET particles under normal processing techniques. There is a significant flux of high energy neutrons that is currently not taken into consideration in dose equivalent calculations. The results of the analysis of the spectrometer data will be reported separately.

Introduction

The complex radiation environment in low-Earth orbits has received considerable attention for the past three decades. Detailed knowledge of this environment under varied spacecraft shielding geometry is necessary for minimizing risk due to radiation exposure. The radiation exposure received by crew members in space flights has primarily been studied using passive thermoluminescent detectors (TLDs). Although some measurements of the linear energy transfer spectrum have been made using plastic nuclear track detectors (PNTDs) and nuclear emulsions, they have rarely been used in assessing crew exposures. Active ionization chambers have flown on the Skylab mission (Parnell et al., 1986) and are currently used on the Mir orbital station. Although ionization chambers provide dose rate data, they do not provide the LET spectrum which is the key to obtaining effective dose equivalent. High energy ($\geq$ 0.5 MeV) neutron measurements have received virtually no attention in the US space program. Active tissue equivalent proportional counters have been flown on a limited number of Shuttle flights. The Radiation Monitor Equipment (RME) is a three channel detector that provides absorbed dose, and a rough estimate of dose equivalent as a function of mission elapsed time (Golightly et al., 1994). Badhwar et al. (1992, 1994a) have flown, first, a 15-channel and more recently, a 512-channel tissue equivalent counter in a number of Shuttle flights. Nguyen et al. (1989) flew a dose and dose-equivalent meter on the Mir station, and now a new instrument that provides the LET spectrum is onboard the Mir station. These measurements indicate that estimates of radiation exposure using passive TLDs are low compared to those measured using active

detectors. The PNTDs do not respond to radiation below about 5 keV/μm, a region that can contribute nearly 60-70% of the absorbed dose. These detectors are not fully efficient till about 10-15 keV/μm. The nuclear track detectors, because of their simplicity, have been routinely flown on virtually all Shuttle flights. However, a direct comparison of these measurements with active detectors has not been possible, because invariably the active and passive detectors were flown under different Shuttle mass shielding. This current experiment was designed to remedy these problems.

This paper describes the results of absorbed dose, dose equivalent, LET spectrum, and neutron energy spectrum inside a Shuttle locker.

Experimental Details

The flight experiment consisted of four separate detector systems: (i) a charged particle directional spectrometer (CPDS), (ii) a tissue equivalent proportional counter (TEPC), (iii) two area passive detectors with combined NASA and Russian complements. All four of these detectors were housed inside a SPACEHAB 2 locker. The SPACEHAB 2 itself was in the payload bay of the Space Shuttle. Thus all of the detectors saw nearly identical mass shielding distribution.

Figure 1 is a schematic of the particle spectrometer. It consists of two 1 mm thick lithium drifted silicon detectors, A1 and A2, that define the basic telescope geometry. At the top

of each of these detectors are 16 x 16 strip detectors to determine the x,y coordinates of those particles that formed the coincidence A1A2. Each of these silicon position-sensitive detectors (PSDs) is 300 μm thick. This basic telescope was followed by six 5 mm thick lithium drifted silicon detectors, B1 to B6, followed by a 1 mm thick A3, PSD 3, and 1 cm thick sapphire Cerenkov detector viewed head-on by a photomultiplier tube. The area-solid product of the A1A2 coincidence is 6.2 cm2 sr for an isotropic incidence flux. For A1A2 coincidences, the voltage output of every detector is pulse-height analyzed using 4096 channel analog-to-digital converters.

The tissue equivalent proportional counter (Figure 2) consists of a cylindrical detector 1.78 cm long and 1.78 cm in diameter simulating a ~ 2 μm-diameter site that is bounded by tissue-equivalent plastic. The detector uses low pressure gas and operates around -750 volts. The detector signal is processed by a very low-noise preamplifier and two amplifiers that differ in gain by a factor of 50. The pulse height of the voltage output from each amplifier is analyzed in a 256-channel analog-to-digital converter. The root mean square of the electronic system noise is approximately 130 electrons at room temperature. The lower level discriminator is set around 0.2 keV/μm. The instrument covers a lineal energy range, y, from about 0.2 to 1250 keV/μm. The energy resolution of the electronics is 0.1 keV/μm below 20 keV/μm and 5 keV/μm above 20 keV/μm. The full lineal energy spectrum is recorded every minute. In addition, absorbed dose is computed by the instrument and recorded either every 2 or 20 s depending upon the dose rate.

The proportional counter was calibrated in terms of lineal energy by exposing it to fission neutrons and ^{137}Cs sources. The detector calibration was verified post flight by using 80 and 170 MeV protons at the University of Loma Linda, California, proton accelerator.

The NASA portions of the area passive detectors contained TLD-700, CR-39, TLD-600 with CR-39 and Gd foils to measure thermal and epi-thermal neutrons. The Russian portions contained TLD-600, CR-39, and Soviet Bya- and BR-type nuclear photo-emulsions.

The STS-57 flight was launched in to 28.5° x 462 km nearly circular orbit on June 21, 1993 for a period of 9.986 days. The TEPC and CPDS were turned on after attaining orbit and turned off prior to re-entry.

Data Analysis

The methods of analysis of data from these detectors is unique to each detector system. These methods are discussed separately in previous publications. The analysis of the spectrometer data followed the procedure described in Badhwar et al. (1994b), is not yet completed, and will be reported separately. Figure 3 shows the A1 counting rate and A1A2 coincidence rate as a function of mission elapsed time. The large spikes are the Shuttle passes through the South Atlantic Anomaly (SAA). A1 and A2 are thin planar detectors and count particles coming from any direction. The coincidence rate A1A2

restricts the opening to particles within a cone of 45° full angle. Because of the anisotropic nature of trapped particle flux and the viewing angle, the A1A2 count rate shows a different time profile than the omni-directional detector A1. Particles that form the A1A2 coincidence provide a measure of the average energy loss per particle. This can be determined separately for trapped and galactic particle portions of the Shuttle orbit. Thus individual A1 or A2 count rate can appropriately be scaled to dose rates in silicon.

Figure 3 plots the TEPC measured dose rate as a function of the mission elapsed time. This information has been used to separate the data into categories of trapped (SAA) and galactic cosmic rays (GCR). The method of analysing TEPC data has been described in detail (Badhwar et al., 1994a).

The analysis of the NASA TLDs and CR-39 followed well established techniques that are described in a number of publications from Benton et al. (1983a,b, 1988, 1991) and Csige et al. (1991). The techniques for determining the LET spectrum from nuclear emulsions are described by Akopova et al., (1985, 1987, 1990). The differentail fast-neutron energy spectrum was measured using the recoil proton energy spectrum generated as a result of the elastic scattring of neutrons from unbounded hydrogen in the emulsions. Measurements were made only of proton tracks whose ends were located within the volume of the emulsion. Due to a significant visual inefficeincy of the short path-length recoil protons ($E_n \leq 1$ MeV) and proton contaminatiion from $^{14}N(n,p)$ reaction with emulsion nitrogen, neutron fluxes with $E_n < 1$ MeV were not measured. More detailed

description of this technique can be found in Dudkin et al. (1990). We refer the reader to these publications for more details.

Results

Dose Measurements

The dose rate measured using the tissue equivalent proportional counter was 1109.7 μGy/day, with GCR particles contributing 71.3 μGy/day and trapped particles contributing 1038.4 μGy/day. The TLDs mounted on the front surface of the APD box measured 929±28 and 936±28 μGy and those mounted on the back surface measured 920±28 and 909±27 μGy. The average dose rate using TLDs was 925.3 μGy/day. The dose rate measured by TEPC is 20% higher than this rate. The reason for this difference is that the TEPC responds to neutrons whereas the TLDs do not under normal processing. Also, TLDs are less sensitive to high LET particles.

Neutron Spectrum

The fast-neutron spectrum was calculated using the measured recoil proton energy spectrum generated as a result of the elastic (n,p) scattering of neutrons from the hydrogen in the emulsion. Figure 4 shows the derived spectrum in ~ 1-15 MeV range. Integrating this spectrum gives an absorbed dose rate of 20 μGy/day and dose equivalent

rate of 174 μSv/day. This dose equivalent is a factor of nearly 3 higher that in STS-55 (6 μGy/day and 53 μSv/day) derived using the same technique (Dudkin et al., 1994) and factor 4 to 8 higher than in high inclination COSMOS flights that missed the SAA (Dudkin et al., 1990). The STS-57 flight was in a higher 462 km altitude orbit compared to STS-55 (28.5° x 290 km). These results suggest that a large fraction of the neutrons are produced in the Shuttle shielding by the interactions of trapped protons and GCR. This is quite consistent with observations of Keith et al. (1992) that indicated that at Dloc 2 location in the Shuttle mid-deck nearly 80% of the neutrons below 15 MeV were due to secondaries and 20% were due to atmospheric albedo. Based on a number of thermal and epi-thermal neutron measurements (< 1 MeV) under the same shielding, Benton et al. (1988) have estimated their dose equivalent contribution of less than 1 MeV neutrons to be about 22 μSv/day. Thus we have about a 200 μSv/day contribution to dose equivalent from thermal to about 15 MeV. Model calculations (Armstrong and Colburn, 1992, Keith et al., 1992) suggest that this energy region provides only about one-half of the total dose equivalent. Thus the dose equivalent contributions from neutrons could approach nearly 400 μSv/day on this flight, which is higher than the dose contributed by the GCR particles. It is important to note that the depth-dose equivalent of neutrons in body tissue is markedly different than that of protons. At organ levels then, neutrons could provide a much higher dose equivalent than GCR particles at the STS-57 (or higher) altitudes.

Linear Energy Transfer Spectra

Figure 5 is the integral LET spectrum of the combined trapped and galactic particles. The spectrum measured by the CR-39 PNTDs, incorporating a technique that enhances the efficiency of very high LET events, is shown for comparison. THE PNTD measurements fall somewhat above TEPC at high LETs (by approximately a factor of 2), then gradually merge with TEPC data at about 15-50 keV/μm and fall below at low LETs. This difference may be due in part to the short range secondaries produced in the two detectors. The lining of the TEPC sensitive volume is tissue-equivalent, while the CR-39 PNTD is $O_7C_{12}H_{18}$. The CR-39 therfore has a higher density of heavier nuclei and lower density of hydrogen, as compared to TEPC liner. Secondary particle spectra produced by primaries interacting with nuclei in the two media will therfore be different. A greater fluence of high LET secondaries would be expected in the CR-39 while a greater fluence of light, proton recoil (low LET) secondaries would be expected in the TEPC, in qualitative agreement. In addition, the CR-39 loses efficiency below ~ 15 keV/μm which explains the fall-off below TEPC measurements in the low LET region. The solid circles are data obtained using the nuclear emulsion technique. The shape of this spectrum above ~ 10 keV/μm is nearly the same as the TEPC spectrum, but it is systematically lower in flux by about a factor of 2.3. The charged particle flux at this altitude is dominated by the anisotropic trapped particles. The area-solid angle product however has been calculated using the assumption of an isotropic flux. This can lead to a systematic increase in the calculated flux. Nuclear emulsions from this flight could not be immediately returned to Moscow. The delay could have lead to fading and hence a lower efficiency. A combination of these two effects is the probable cause of the lower flux. The average quality factors

using the ICRP-60 definition, were 1.86 for the whole flight, 3.08 for galactic cosmic rays and 1.78 for trapped particles. Thus GCR particles contribute 220 μSv/day, which is nearly equal to the contribution from neutrons with energies between thermal and ~ 15 MeV.

Thus, under moderate shielding thicknesses the neutron contribution to dose and dose equivalent cannot be ignored. This is roughly 20% of the charged particle skin dose equivalent and about twice what was observed using Bonner spheres and gold activation foil techniques in earlier Shuttle flights, including the highest altitude flight to date, the STS-31 Hubble mission (Keith et al., 1992). However, for these measurements the Bonner spheres were mounted in one of the least shielded locations (Dloc 2) in the mid-deck. Skin doses recieved by astronauts are more typical of a higher shielding than this location. Clearly, additional neutron measurements are essential to quantify the neutron dose contribution for long duration flights.

Figure 6 and 7 show the integral LET spectra of trapped and GCR particles separately. The solid lines are model calculations based on the AP-8 Min (Sawyer and Vette, 1976) and the GCR model of Badhwar and O'Neill (1994). It was shown earlier that the absorbed dose calculated using the AP-8 Min model is a factor of 1.8 higher than the measured absorbed dose. Thus the AP-8 model calculated spectrum was normalized by this factor. There is reasonable agreement in the shape of the measured and model spectra in the intermediate LET range about 15 to 100 keV/μm, however, this is not the case at

both low and high LET ends. The particle spectrometer has confirmed the presence of less than 6 MeV secondary electrons. These electrons would be seen by the proportional counter but not by the CR-39 or nuclear emulsion. These electrons are not taken in to account in the model either. The GCR radiation transport calculations were done using the recently modified HZETRN code (Cucinotta, 1993,1994). There is very good agreement between the model calculations and observations, except at very high LETs.

Conclusions

A joint NASA-Russian experiment was flown on the SPACEHAB 2 mission in 28.5° x 462 km orbit. This altitude is very close to that of the planned International Space Station Alpha, which will be in a 51.8° inclination orbit and will thus see more galactic cosmic radiation flux than in this flight. The results have shown that: (i) there is good agreement between the TEPC and PNTD measured LET spectra from about 15 keV/μm to 200 keV/μm, (ii) the shape of the nuclear emulsion deduced spectrum is the same as that determined from these two techniques, (iii) the total absorbed dose measured using TEPC is 20% higher than the total dose measured using TLDs, (iv) there is a substantial flux of high energy neutrons that contribute at least as much dose equivalent as the galactic particles, and more likely nearly twice as much, and (v) these neutrons are essentially all secondaries generated by the interactions of trapped and galactic particles with spacecraft shielding. This implies that there is a significant secondary proton component also. This neutron contribution must be taken into account for crew risk assessment, particularly for long duration missions at higher than 400 km altitudes.

Acknowledgments

This experiment was started with remarkable support and encouragement of Mr. Timothy White, Assistant to the Director of Space and Life Sciences, Johnson Space Center, Houston, Texas and built and flight certified in near record time of one year. Mr. Dennis

Grounds and Dr. Dane Russo provided excellent support and encouragement. Mr. Terry Byers and Ken Kaufman provided excellent flight integration support. We appreciate the excellent programming support of Mr. Omar Baltaji and Fadi Riman, and mechanical engineering support of Mr. Robert Dunn, all of Lockheed. Dr. Thomas Conroy, Battelle Pacific Northwest Laboratory, Richland, WA, provided electronic engineering support. Frank Gibbons and Terry Byers were instrumental and getting the position sensitive detectors to work. We are grateful for the hard work of all these individuals. We are also grateful to Luis Frigo and El-Sayed Awad for important contributions with regard to the PNTD data. The University of San Francisco portion of the work was supported by NASA grants Nos. NAG9-235 and NAGW-4154.

References

Akopova, A.B., Dudkin V.E., Kovalev E.E., Magradze N.V., and Potapov Yu. V. (1987) Linear energy transfer spectra of cosmic radiation aboard Cosmos-1129 artificial; satellite. *Radiat. Prot. Dosim.* **18**, 153-156.

Akopova, A.B., Magrade N.V., Dudkin V.E., Kovalev E.E., Potapov Yu. V., Benton E.V., Frank A.L., Benton E.R., Parnell T.A. and Watts J.W. Jr. (1990) Linear energy transfer (LET) spectra of cosmic radiation in low Earth orbit. *Nucl. Tracks Radiat. Meas.* **17**, 93-97.

Akopova, A.B., Vikhrov A.I., Dudkin V.E., Magradze N.V., Moiseenko A.A., Muradyan A.H., Ovnanyan K.M. and Potapov Yu. V. (1985) Measuring the linear energy transfer spectra of cosmic radiation aboard the Cosmos-1129 satellite. *Kosm. Issled XXIII*, 479-481.

Armstrong, T.W., and Colborn B.L. (1992) Predictions of induced radioactivity for spacecraft in low Earth orbit, *Nucl. Tracks Radiat. Meas.*, 20, 101-130.

Badhwar, G.D., Konradi A., Hardy A., and Braby L.A (1992) Active dosimetric measurements on Shuttle flights, *Nucl. Tracks Radiat. Meas. 20*, 13-20.

Badhwar, G.D., Cucinotta F.A., Braby L.A., and Konradi A., Measurements on the Shuttle of the LET spectra of galactic cosmic radiation and comparison with radiation transport model, *Radia. Res.* **139**, 344-351.

Badhwar, G.D., Patel J.U., Cucinotta F.A., and Wilson J.W. (1994) Measurements of the secondary particle energy spectra in the space Shuttle, *Radiat. Meas.* (to be published).

Badhwar, G.D., and O'Neill P.M. (1993), Time lag of twenty two year solar modulation. In Proceedings of the *23rd International Cosmic Ray Conference*, **3**, 535-539, Calgary.

Benton, E.V. (1983) Dosimetric radiation measurements in space. *Nucl. Tracks Radiat. Meas. 7*, 1-11.

Benton, E.V. and Henke R.P. (1983) Radiation exposures during space flight and their measurements. *Adv. Space Res.* **3**, 171-185.

Benton, E.V. and Parnell, T.A. (1988) Space radiation dosimetry on U.S. and Soviet Manned missions, in NATO ASI Series A, Life Sciences, **154**, *Terrestrail Space Radiation and its Biological Effects*, P.D. McCormack, C.E. Swenburg and H. Bucker, eds. Plenum Press (1988), pp729-794.

Benton, E.V., Frank, A.L., Benton, E.R., Csige, I., Parnell, T.A., and Watts, J.W. Jr. (1991), Radiation exposure of LDEF: Intial results, Proceedings of *LDEF: 69 Months in Space*, Kissimmee, Florida, June 2-8, 1991.

Csige, I., Benton, E.V., Frank, A.L., Figo, L.A., Benton, E.R., Parneel, T.A., and Watts, J.W. Jr. (1991), Charged particle LET spectra measurements aboard LDEF, Proceedings of *LDEF: 69 Months in Space*, Kissimmee, Florida, June 3-8, 1991

Cucinotta, F.A (1993) Calculations of cosmic ray helium transport in shielding materials, TP 3354, NASA, Washington, DC, also private communication September 1994.

Dudkin, V.E., Potapov Yu. V., Akova A.B., Melkumyan L.V., E.V. Benton, and Frank A.L. (1990) Differential neutron energy spectra measured on spacecraft in low earth orbit. *Nucl. Tracks Radiat. Meas.* **17**, 87-91.

Dudkin, V.E., Karpov O.N., Potapov Yu. V., Akopova A.B., Magradze N.V., Melkumyan L.V., and Rshtuni Sh. B. (1994) Study of the radiation environment on board STS-55 and STS-57 by passive detectors method, In Proceedings of *12th International Conference on Nuclear Tracks in Solids*, Dubna, Russia, August 24-28.

Golightly, M.J., Hardy K., and Quam W. (1994) Radiation dosimetry measurements during U.S. Space Shuttle missions with the RME-III, *Radiat. Meas.* **23**, 25-42.

Keith, J.E., Badhwar G.D., and Lingstrom D.J (1992) Neutron spectrum and dose-equivalent in shuttle flights during solar maximum, *Nucl. Tracks Radiat. Meas.* **20**, 41-48.

Nguyen, V.D., Bouisset P., Parmentier N., et al. (1989) Real time quality factor and dose equivalent meter "CIRCE" and its use on board the Soviet orbital station MIR. In Humans in Earth Orbit and Planetary Exploration Missions, *Int. Acad. Astronaut. 8th Symp.* Tashkent, Uzbekistan, U.S.S.R

Parnell, T.A., Watts J.W. Jr., Fishman G.J., Benton E.V., Frank A.L., and Greogory J.C. (1986) The measured radiation environment within Spacelab 1 and 2 and comparisons with predictions, *Adv. Space Res.*, **6**, 125-137.

Sawyer, D.M. and Vette J.I. (1976) AP-8 trapped proton environment for solar maximum and minimum. Report NSSDC/WDC-A-R&S 76-06, NASA, Goddard Space Flight Center, Greenbelt, Maryland

Figure Captions

Figure 1: A schematic diagram of the charged particle telescope

Figure 2: A schematic diagram of the tissue equivalent proportional counter

Figure 3: Plots of the TEPC measured dose rate, A1 single and A1A2 coincidence rate as a function of the mission elapsed time.

Figure 4: Plot of the neutron energy spectrum measured using proton recoil technique.

Figure 5: Plot of the integral linear energy transfer spectrum using TEPC, CR-39, and nuclear emulsions.

Figure 6: Plot of the trapped particle integral LET spectrum and comparison with model calculations.

Figure 7: Plot of the GCR integral LET spectrum and comparison with model calculations.

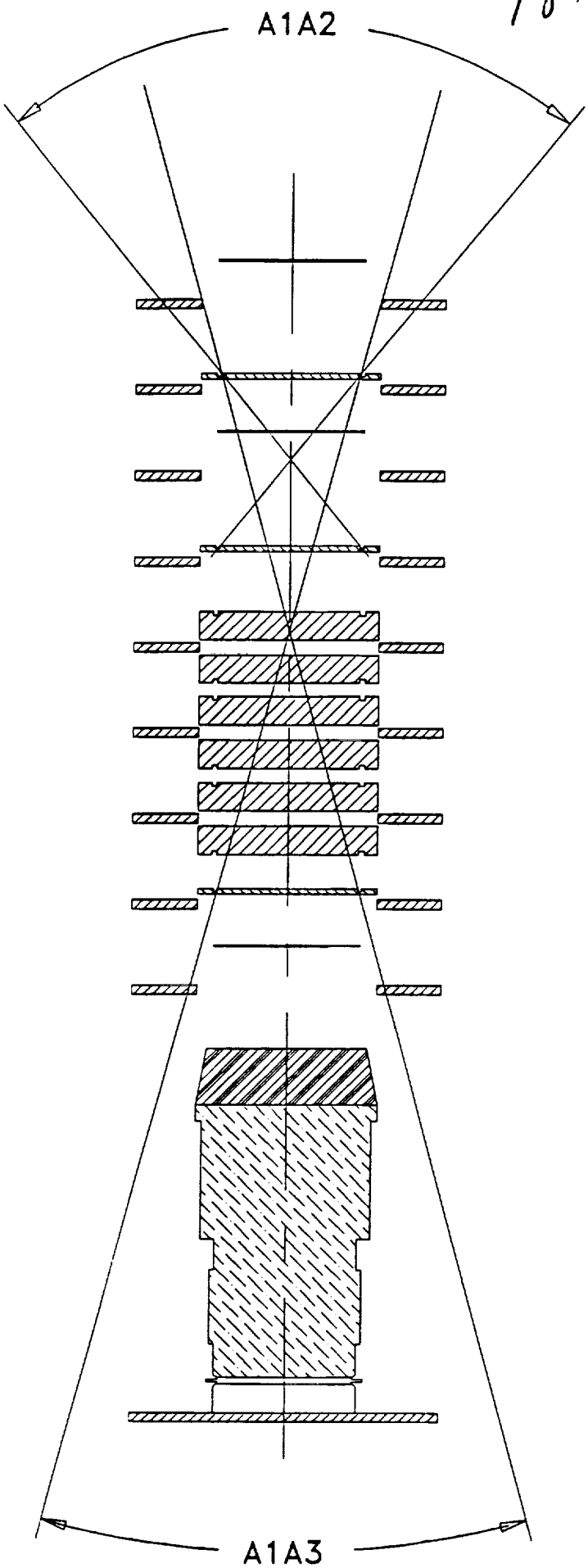

PSD 1 [25x25x0.003mm]

A1 [ø25x1mm]

PSD 2 [25x25x0.003mm]

A2 [ø25x1mm]

B1 [ø25x5mm]
B2 [ø25x5mm]
B3 [ø25x5mm]
B4 [ø25x5mm]
B5 [ø25x5mm]
B6 [ø25x5mm]

A3 [ø25x1mm]

PSD 3 [25x25x0.003mm]

CERENKOV

C DET

Fig 1

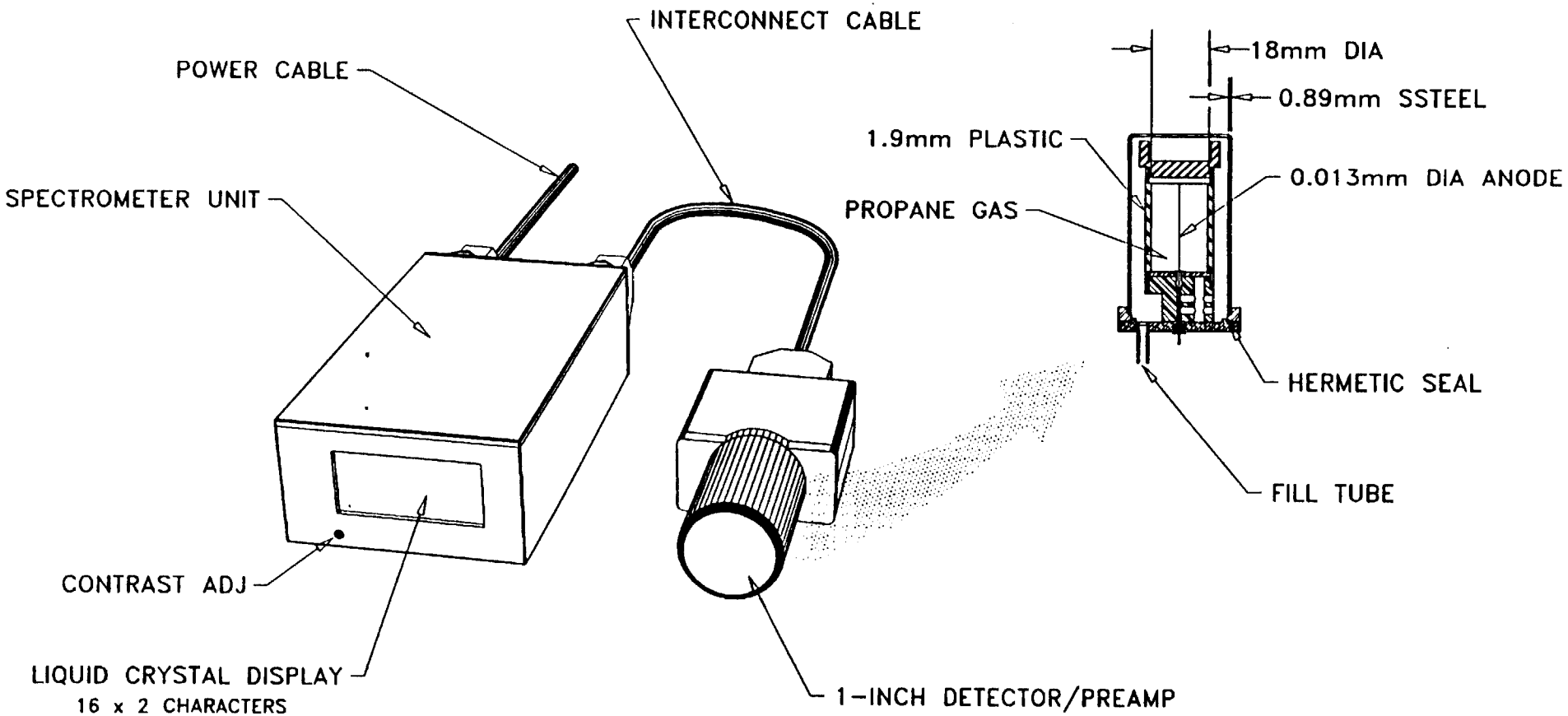
INTERCONNECT CABLE
POWER CABLE
SPECTROMETER UNIT
CONTRAST ADJ
LIQUID CRYSTAL DISPLAY
16 x 2 CHARACTERS
1-INCH DETECTOR/PREAMP
18mm DIA
0.89mm SSTEEL
1.9mm PLASTIC
0.013mm DIA ANODE
PROPANE GAS
HERMETIC SEAL
FILL TUBE

FIG. 2

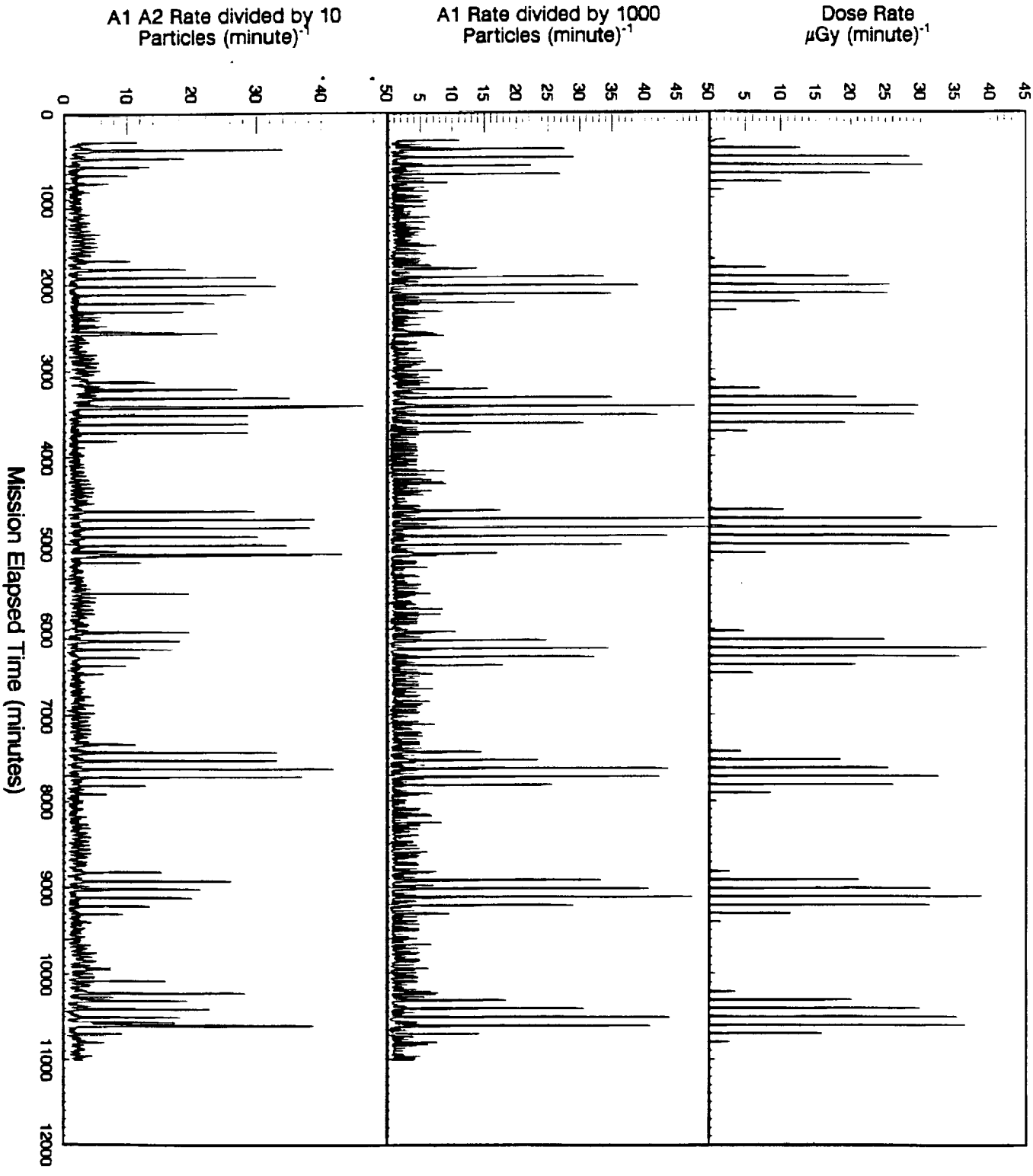
A1 A2 Rate divided by 10
Particles (minute)-1
A1 Rate divided by 1000
Particles (minute)-1
Dose Rate
μGy (minute)-1
0
10
20
30
40
50
5
10
15
20
25
30
35
40
45
0
1000
2000
3000
4000
5000
6000
7000
8000
9000
10000
11000
12000
Mission Elapsed Time (minutes)

Fig. 3

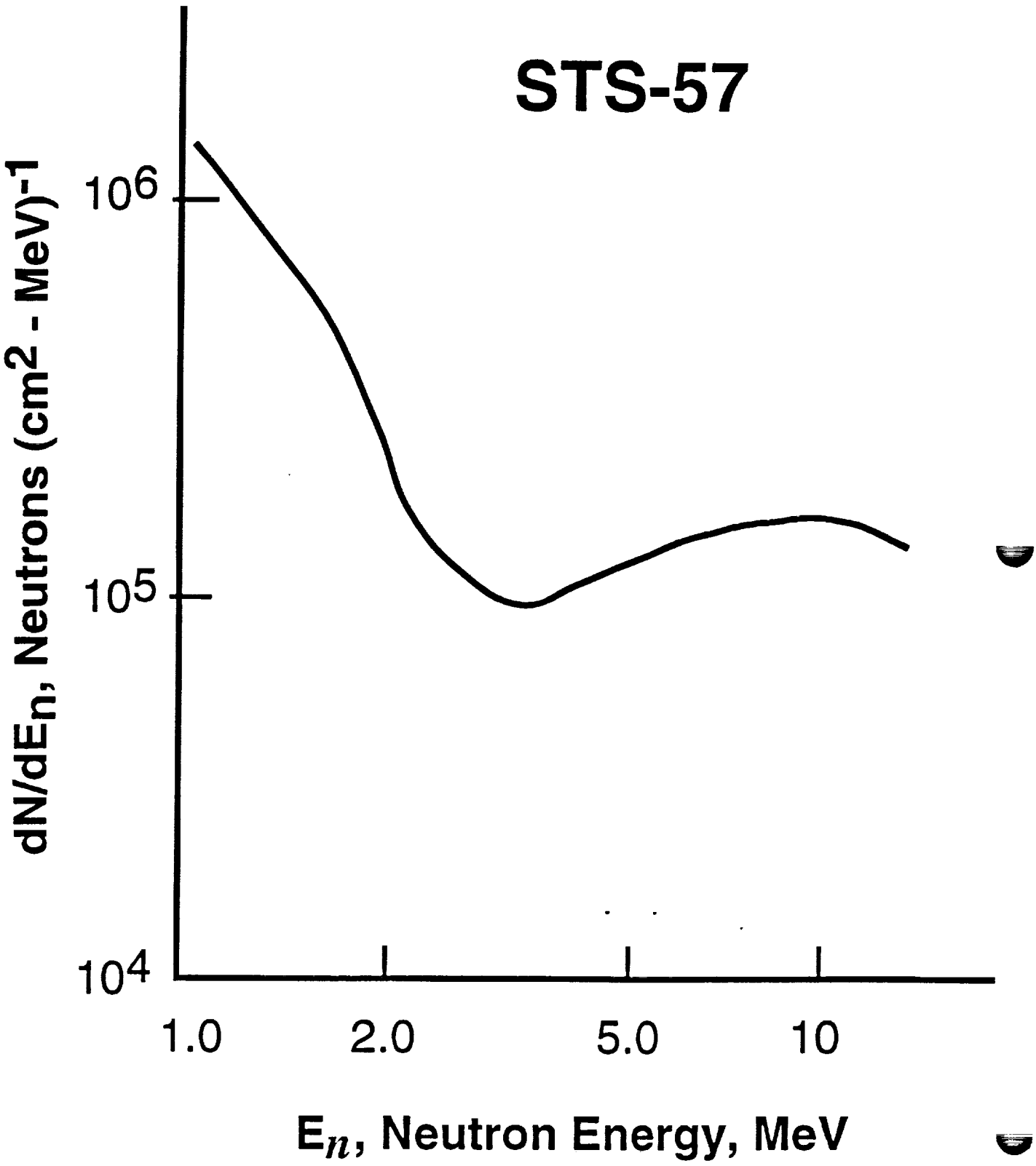
STS-57
dN/dEn, Neutrons (cm2 - MeV)-1
10^6
10^5
10^4
1.0
2.0
5.0
10
En, Neutron Energy, MeV

FIG. 4

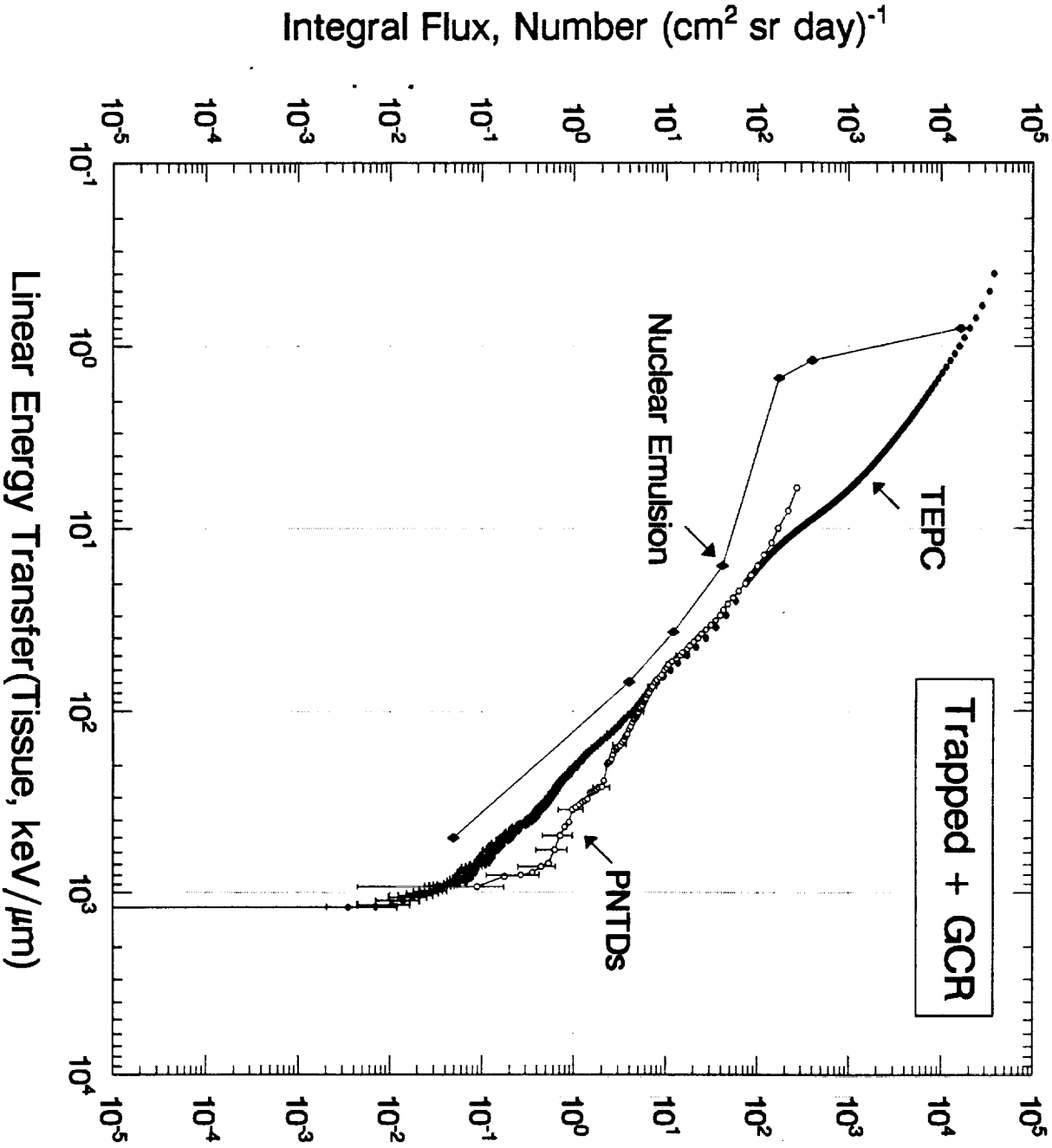
Integral Flux, Number (cm^2 sr day)$^{-1}$
Linear Energy Transfer(Tissue, keV/μm)
Nuclear Emulsion
TEPC
PNTDs
Trapped + GCR

Fig. 5

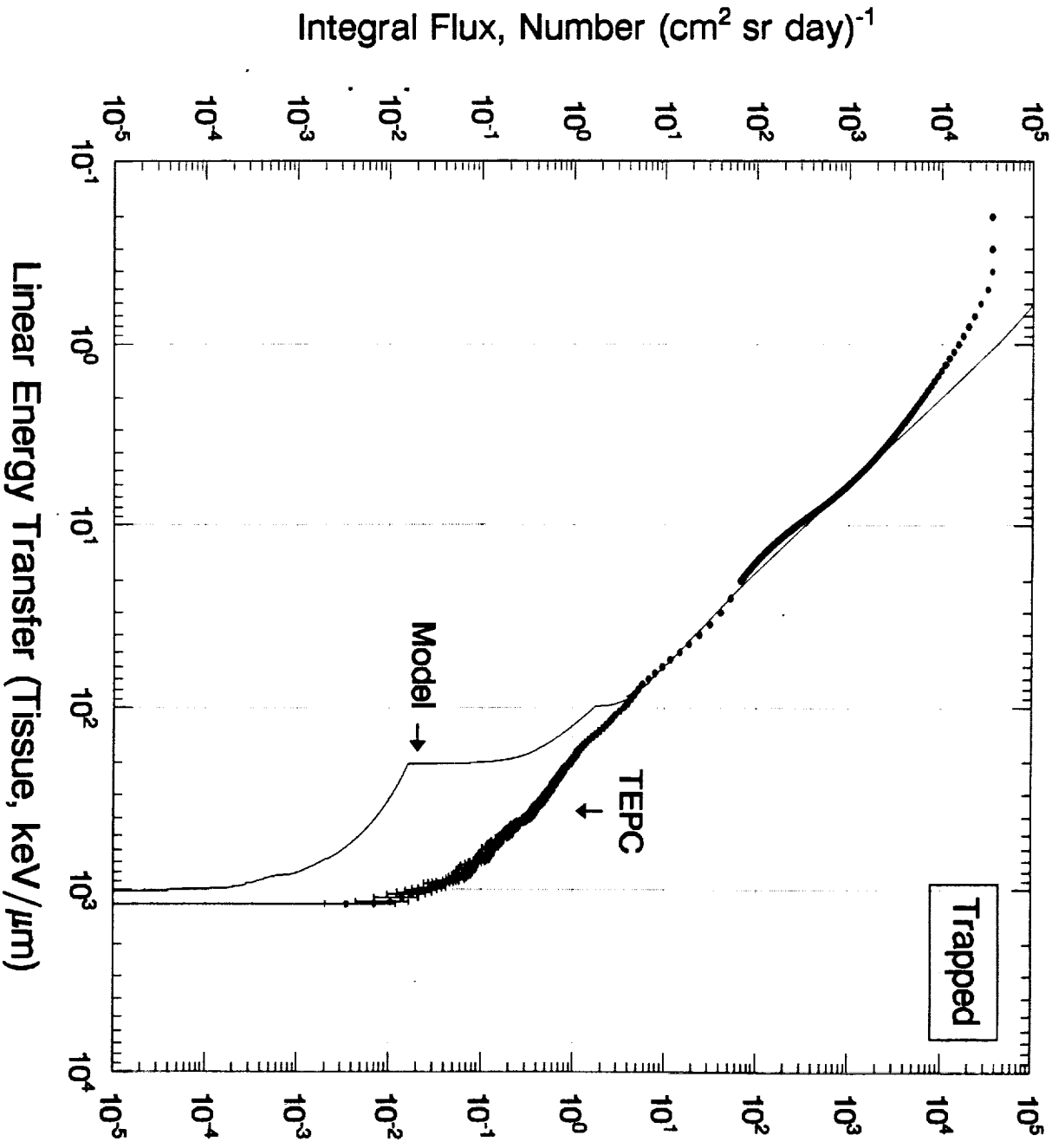
Integral Flux, Number (cm^2 sr day)$^{-1}$
Linear Energy Transfer (Tissue, keV/μm)
Model
TEPC
Trapped
10^{-5}
10^{-4}
10^{-3}
10^{-2}
10^{-1}
10^{0}
10^{1}
10^{2}
10^{3}
10^{4}
10^{5}

Fig. 6

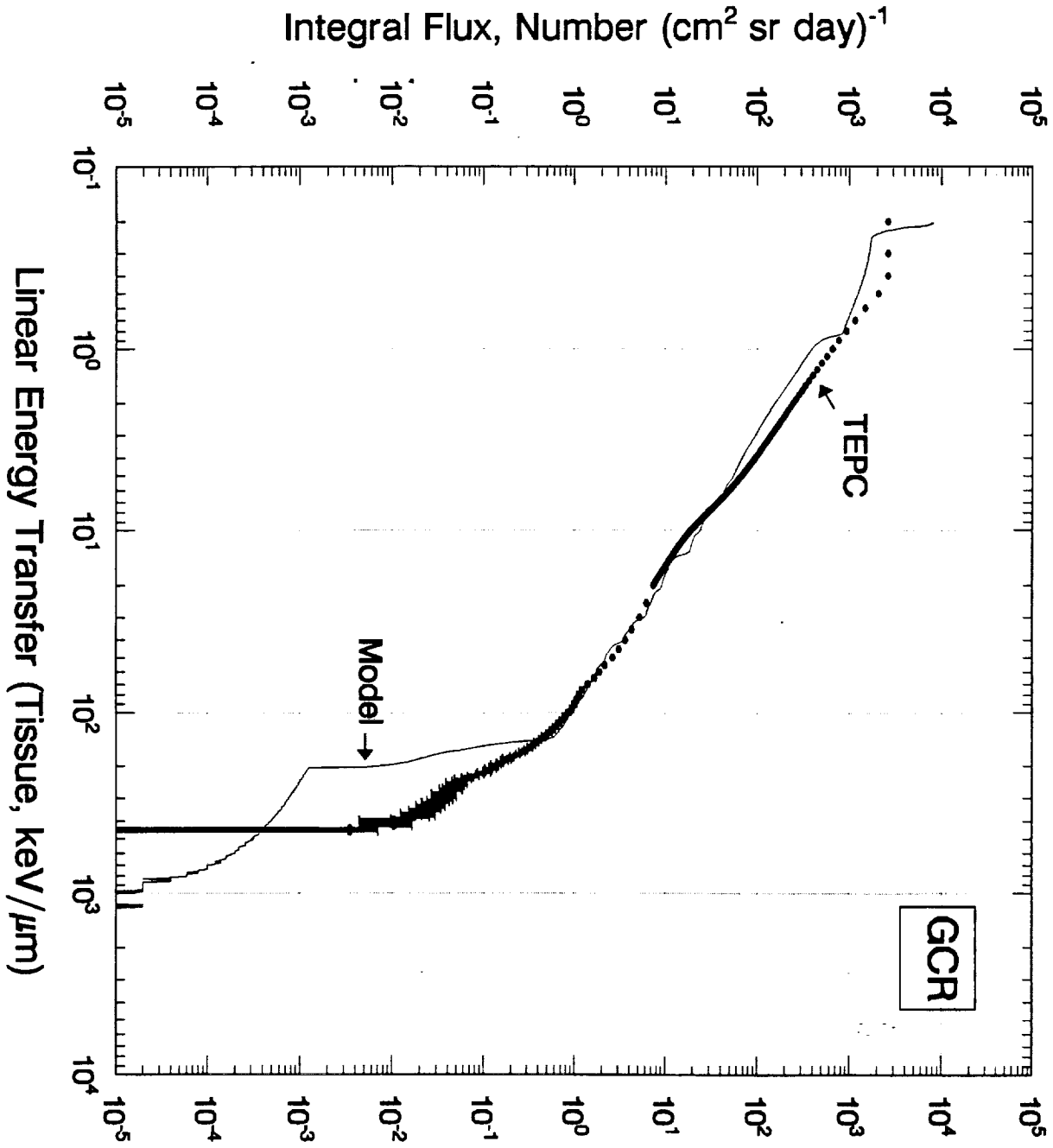
Integral Flux, Number (cm^2 sr day)$^{-1}$
Linear Energy Transfer (Tissue, keV/μm)
Model
TEPC
GCR

Fig. 7

APPENDIX C-2

USF/Russian Dosimetry on STS-57

Two APDs were flown in the CPDS/TEPC locker on the Space Shuttle during the STS-57 mission. Due to placement, the shielding and radiation environment of the APDs were nearly the same and the dosimeters distributed in the two boxes can be considered equally exposed. The dosimeter types included plastic nuclear track detectors (PNTDs), TLDs, nuclear emulsions and thermal/resonance neutron detectors (TRNDs). The USF dosimeters included PNTDs, TLDs and TRNDs, while the Russian dosimeters included PNTDs, TLDs and nuclear emulsions. The contents of the two APDs (Serial Nos. 5716 and 5717) are shown in Figures 1-7.

The major purpose of this experiment was to conduct an international comparison of passive dosimetry methods in space. The results can also be compared to other dosimetry present on STS-57 and, since the shielding vectors of the containment locker are known, this will present an opportunity for comparisons with model calculations of radiation.

The STS-57 mission orbit had an altitude of 473 km and an inclination of 28.5°. The duration was 9.990 days. At this orbit the radiation was dominated by trapped protons and their secondary particles, with most of the dose being accumulated during Shuttle passages through the South Atlantic Anomaly (SAA).

The measured TLD absorbed doses are given in Table 1. Calibrations were made with a standard ^{137}Cs source. Unfortunately, the Ground Control background TLDs became separated from the flight units during the return shipment but the background should have been a small correction. The average dose measured was 9.24 mGy. Other TLD doses measured in the Shuttle varied from 4.00 to 8.52 mGy, or somewhat less (Cash, 1993).

The low energy neutron fluences and dose equivalents, measured with the TRNDs, are given in Table 2. The measurements are averages from the front- and back-mounted TRNDs. The low energy neutrons contributed a very small fraction to total flight dose

equivalent, which was more than 1000 times less than that measured with TLDs. For STS-57, in the CPDS locker, this component of dose equivalent was negligible.

The LET spectrum measured with PNTDs is compared with that measured with the TEPC in Fig. 8. It is seen that the PNTD spectrum is higher at high LETs (above 80 keV μm^{-1}) and lower at low LETs (below 20 keV μm^{-1}). The higher high LET flux represents an improvement in PNTD response obtained with a new method of processing and readout. The spectrum represents a combination of the new (Method B) and standard techniques.

The reason for the greater PNTD flux at high LETs (compared with TEPC) is not clear, but one possibility is in the respective elemental compositions of CR-39 PNTDs and of the tissue-equivalent lining and gas of the TEPC sensitive volume. The CR-39 composition is $O_7C_{12}H_{18}$ while that of TEPC is close to H_2O. The particles forming high LET tracks on STS-57 were mainly short range (only a few μm) and were therefore secondaries created within the CR-39 by interactions between incident primary protons and target nuclei. A somewhat different secondary particle spectrum would be expected in TEPC. The TEPC had a higher partial density of H and correspondingly less of the heavier elements. When the energetic protons interact with the nuclei in the two detectors, there will be a higher probability for producing lower LET proton secondaries (elastically scattered H) in the TEPC and a higher probability for higher LET secondaries (from elastic and inelastic interactions with C and O) in the PNTDs.

In the LET region below 20 keV μm^{-1} there is a possibility of loss of sensitivity due to the small track sizes and inhomogeneity of the detector surfaces. This may also account for a part of the decline of the PNTD spectrum below TEPC.

The integral flux, dose rate and dose equivalent rate for LET >5 keV μm^{-1} are given in Table 3.

In order to determine the real dose and dose equivalent for STS-57, the TLD absorbed dose must be corrected for reduced sensitivity to high LET particles. The average efficiency for

measurement of the absorbed dose in the LET spectrum can be found from

$$\epsilon = \sum_{5\ \mathrm{keV}/\mu\mathrm{m}}^{\mathrm{LET}_{max}} \epsilon(\mathrm{LET})\ D(\mathrm{LET})/D$$

where ϵ(LET) is the efficiency curve as a function of LET (Fig. 9) and D(LET) is the differential dose spectrum. The equation gives $\epsilon = 0.60 \pm 0.05$ for STS-57. It should be noted that the LET spectrum in CR-39 plastic was not the same as that in TLD-700 because of a difference in the short range secondary particles generated in the two media. However, this will not have contributed substantial errors into the determinations of absorbed dose in this paper. The low LET component of absorbed dose is therefore

$$D_L = D_{TLD} - 0.60\ D_{PNTD}$$

and

$$D_H = D_{PNTD}$$
$$D_T = D_L + D_H$$

where D_L and D_H are the low- and high-LET absorbed doses, respectively, and D_T is the total absorbed dose. The dose equivalent is given by

$$H_T = D_L + H_{PNTD}$$

and

$$\overline{QF} = H_T/D_T.$$

From the above

$D_{TLD} = 924 \pm 18$ mrad
$D_L = 855 \pm 20$ mrad LET <5 keV μm^{-1}
$D_H = 114 \pm 8$ mrad LET ≥5 keV μm^{-1}
$D_T = 969 \pm 20$ mrad
$H_T = 1910 \pm 80$ mrem
$QF = 1.97 \pm 0.11$

These quantities can be compared with the measurements

These quantities can be compared with the measurements reported by Badhwar et al. (1994). The TEPC measured totals of 1109 mrad and 2063 mrem for QF = 1.86. The TEPC absorbed dose and dose equivalent were therefore 14% and 78%, respectively, higher than our combined TLD/PNTD measurements, giving a slightly lower QF. The TEPC was placed in the same locker with the APDs, with very similar shielding. The difference may be due to factors such as measurement efficiencies of neutrons or other particles.

TABLE 1. TLD Absorbed Doses in STS-57 APDs

APD Serial No.	Location	Absorbed Dose (mGy)	Dose Rate (mGy d^{-1})
5716	Front	9.29 ± 0.28	0.930
	Back	9.20 ± 0.28	0.921
5717	Front	9.36 ± 0.28	0.937
	Back	9.09 ± 0.27	0.910
Average		9.24 ± 0.12	0.925

TABLE 2. Low Energy Neutron Fluence and Equivalent Dose from the STS-57 APD TRNDs

Energy Range	Neutron Fluence (cm^{-2})	Equivalent Dose mrem
<0.2 eV	$8.6 \pm 5.0 \times 10_3$	0.009 ± 0.005
0.2 eV--1 MeV	$1.5 \pm 0.7 \times 10_5$	0.74 ± 0.35

TABLE 3. Results of PNTD Measurements from the APD on STS-57

Flux ($cm^{-2}s^{-1}sr^{-1}$)	Absorbed Dose Rate (mrad d^{1})	Dose Equiv. Rate (mrem d^{-1})	Total Dose Equiv. (mrem)
3.22e-03	11.44	105.1	1050

REFERENCES

Badhwar G.D., Atwell W., Benton E.V., Frank A.L., Keegan R.P., Dudkin V.E., Karpov O.N., Potapov Yu.V., Akapova A.B., Magradze N.V., Melkumyan L.V. and Rshtuni Sh.B. (1994). A study of the radiation environment on board the Space Shuttle flight STS-57. Rad. Meas. (in press).

Cash B. (1993). Mission STS-57 dosimetry report. NASA Lyndon B. Johnson Space Center Internal Report.

Area Passive Dosimeter (APD) - Side View

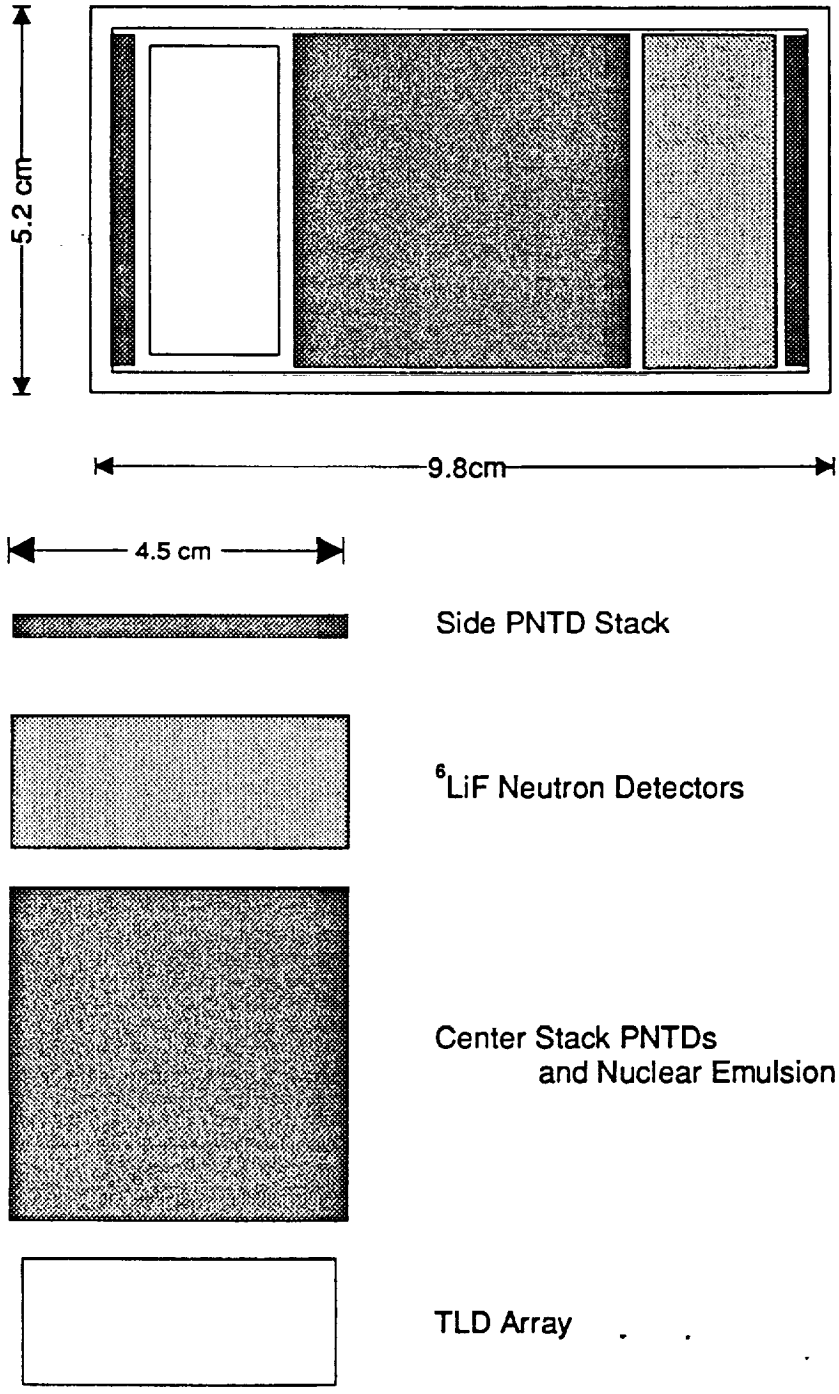

Figure 1: Side view of the APD box and its contents.

Area Passive Dosimeter (APD) - Top View

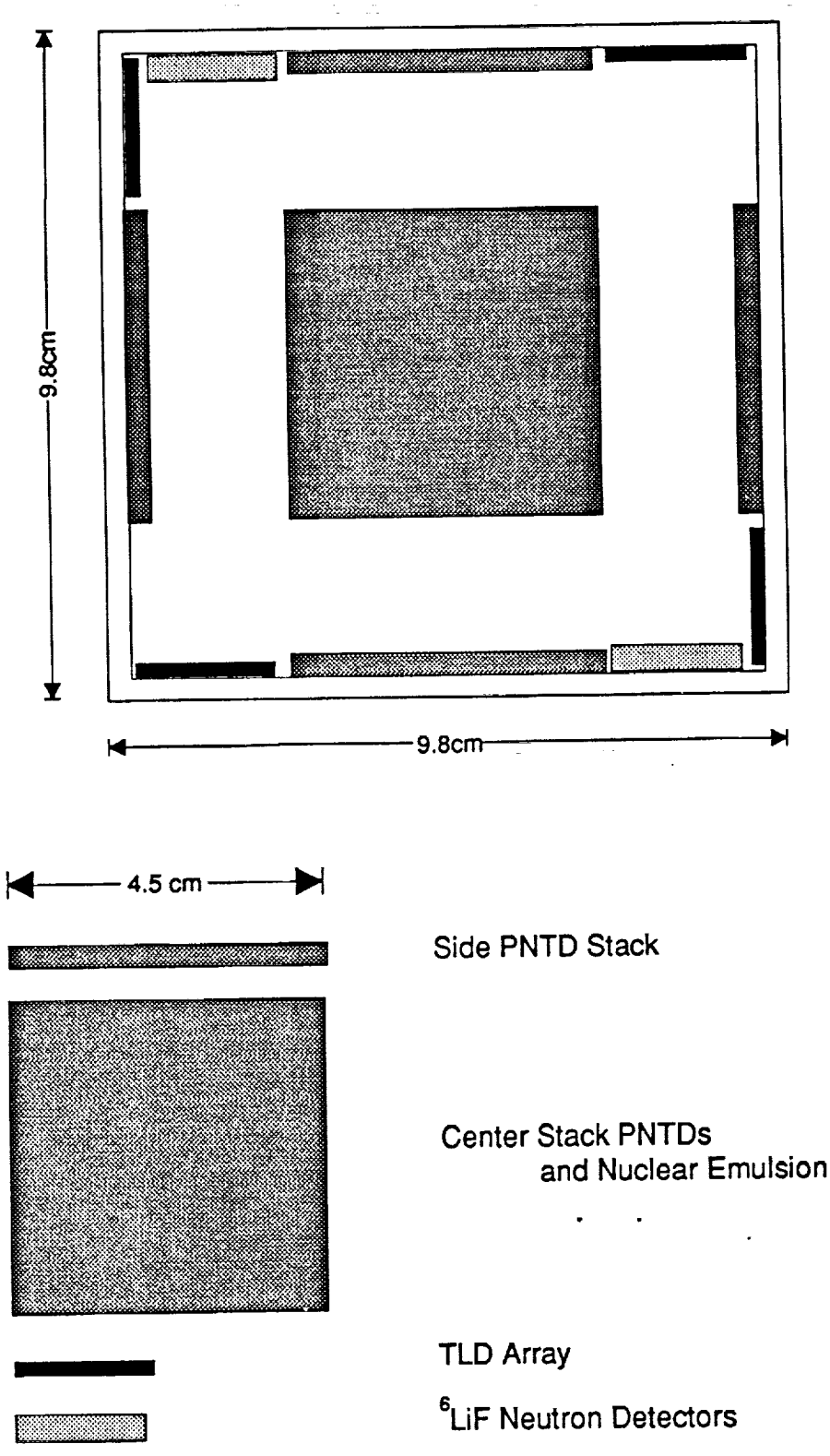

Figure 2: Top view of the APD box and its contents.

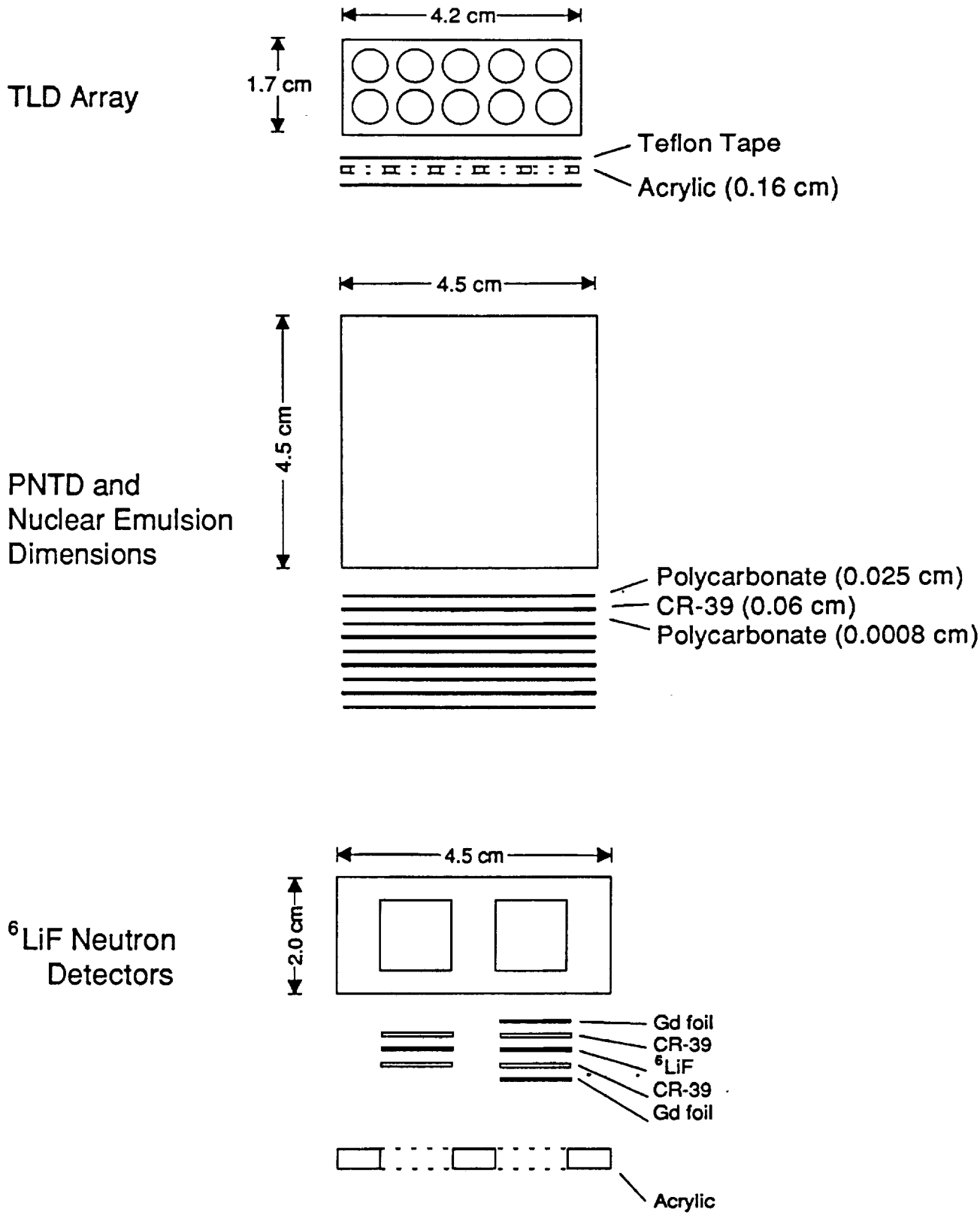

Figure 3: Dimensions of the TLD Array, PNTD center stack and TRND.

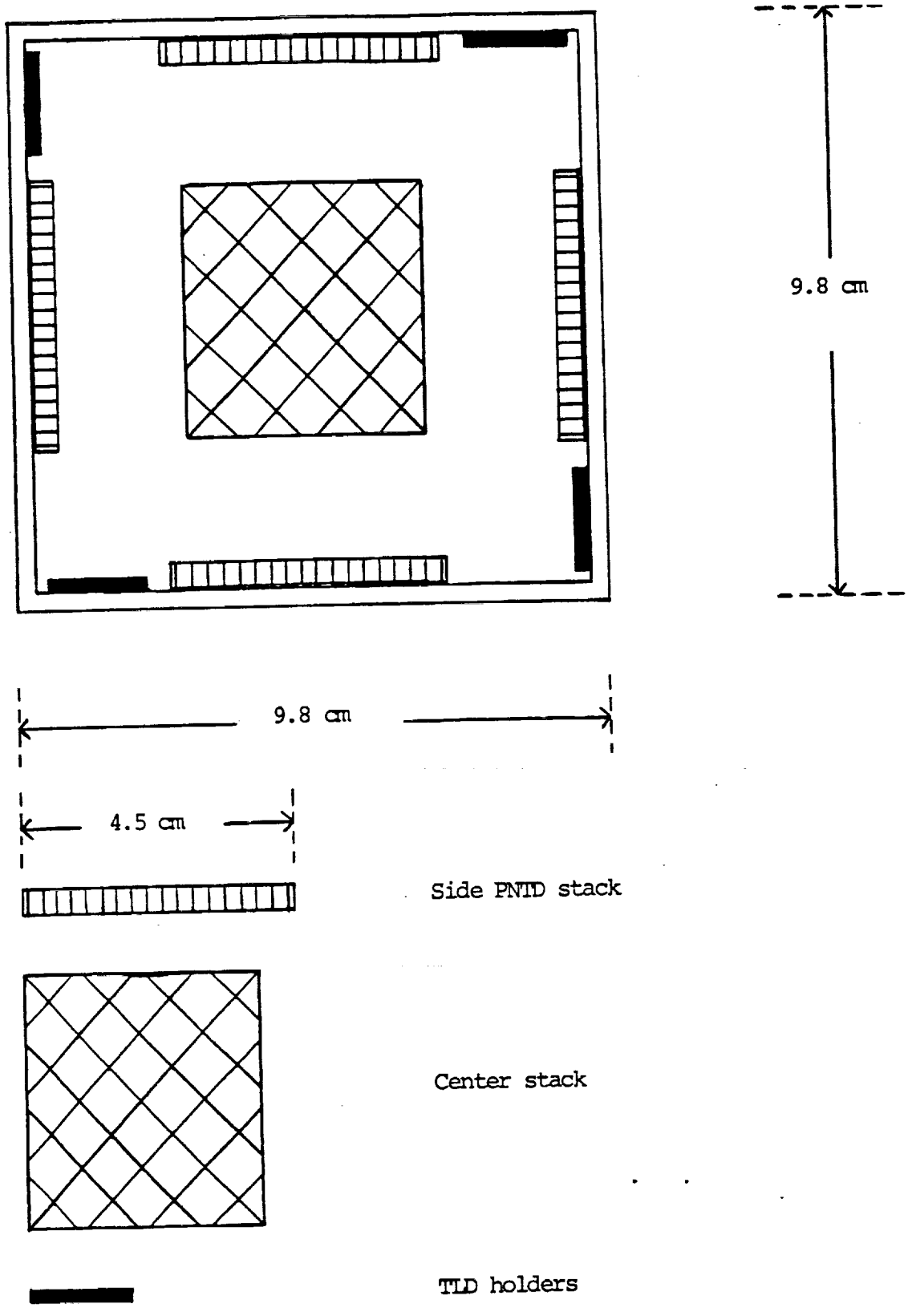

Fig. 4. Top view of APD #5717

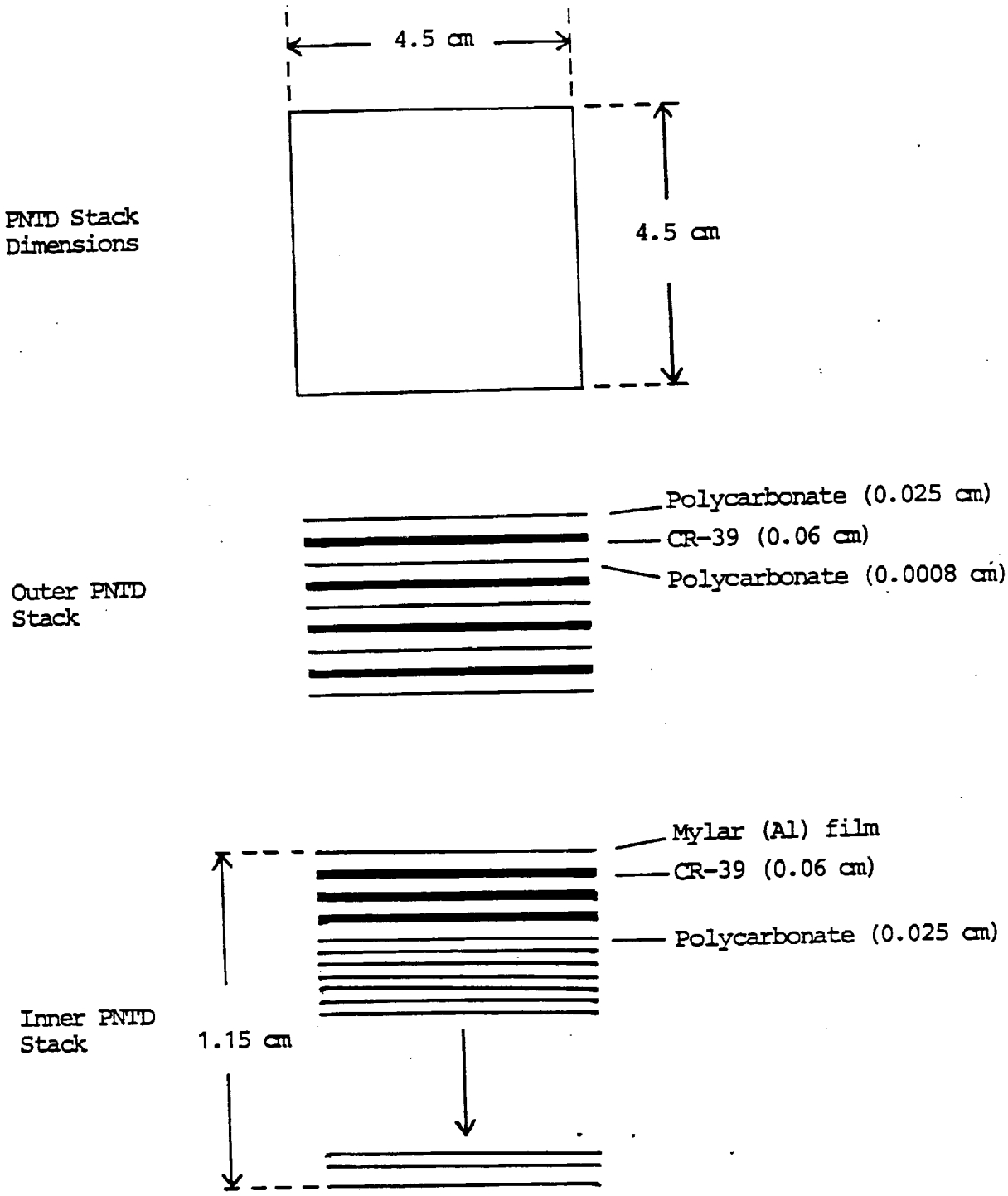

Fig. 5. Sketches of PNTD stack components and dimensions, APD #5717

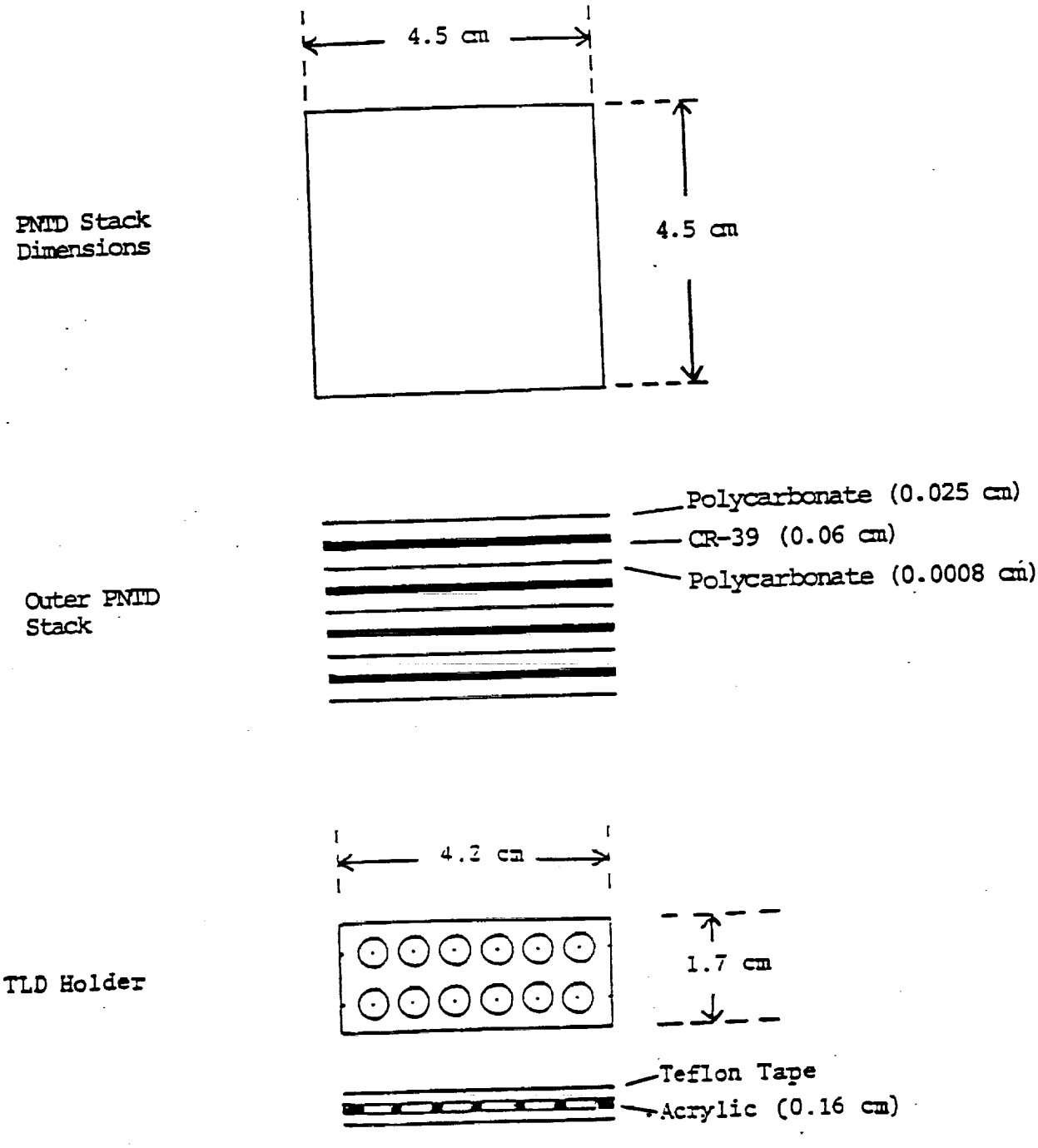

Fig. 6. Dimensions and components of the outer PNTD stacks and the TLD holder - PNTD #5717

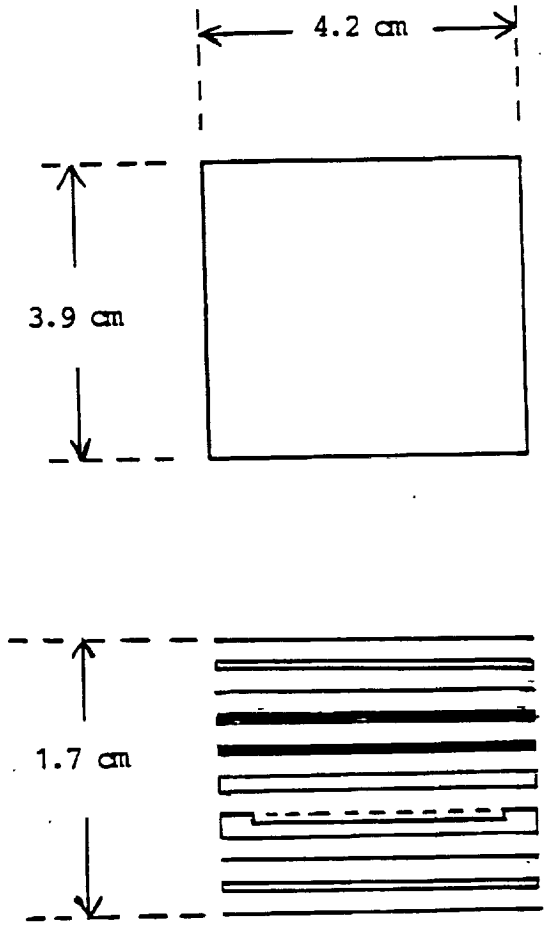

Fig. 7. Dimensions and components of the Center PNTD and TLD stacks - APD #5717

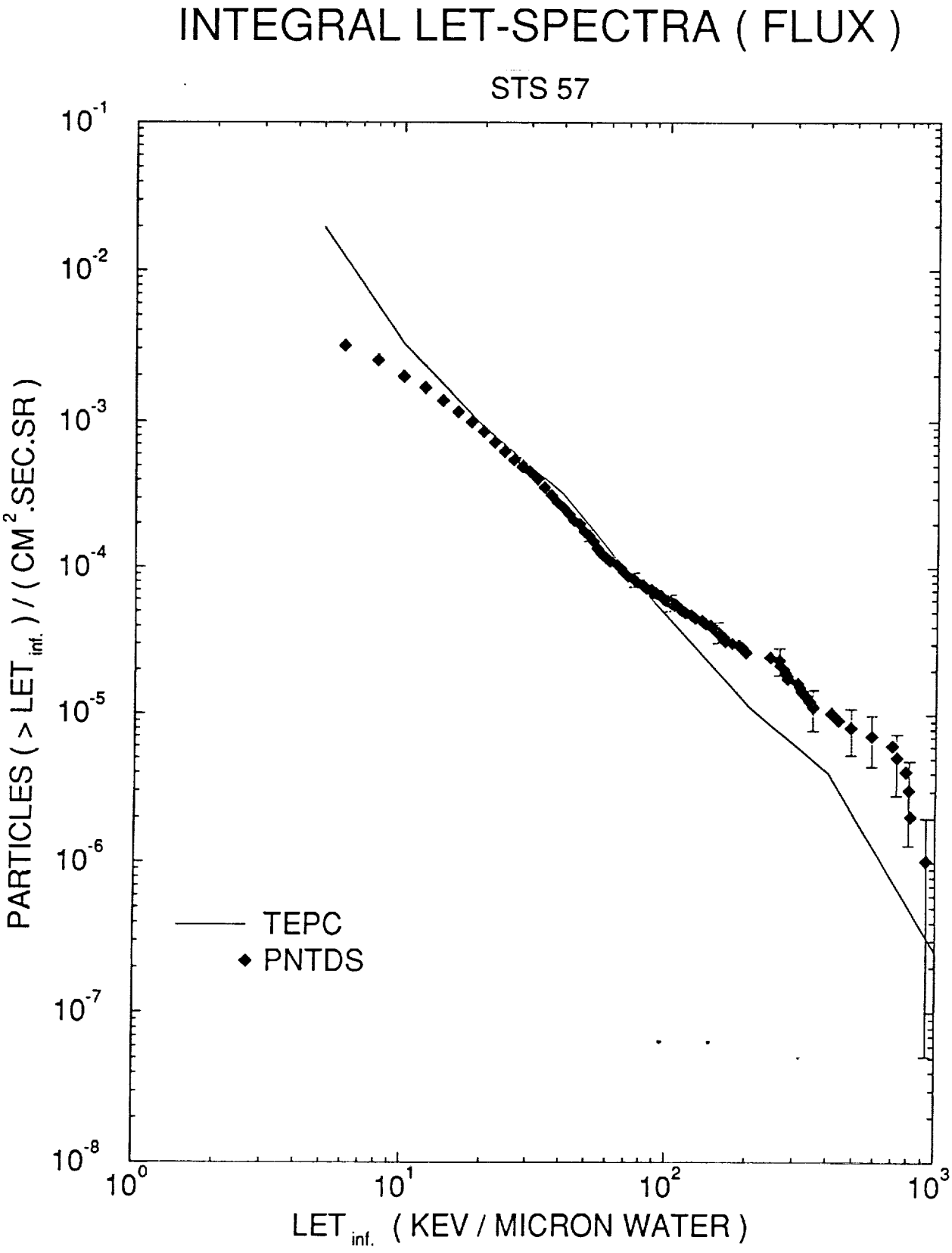

Fig. 8. Comparison of integral LET spectra measured by PNTDs and the TEPC microdosimeter on STS-57

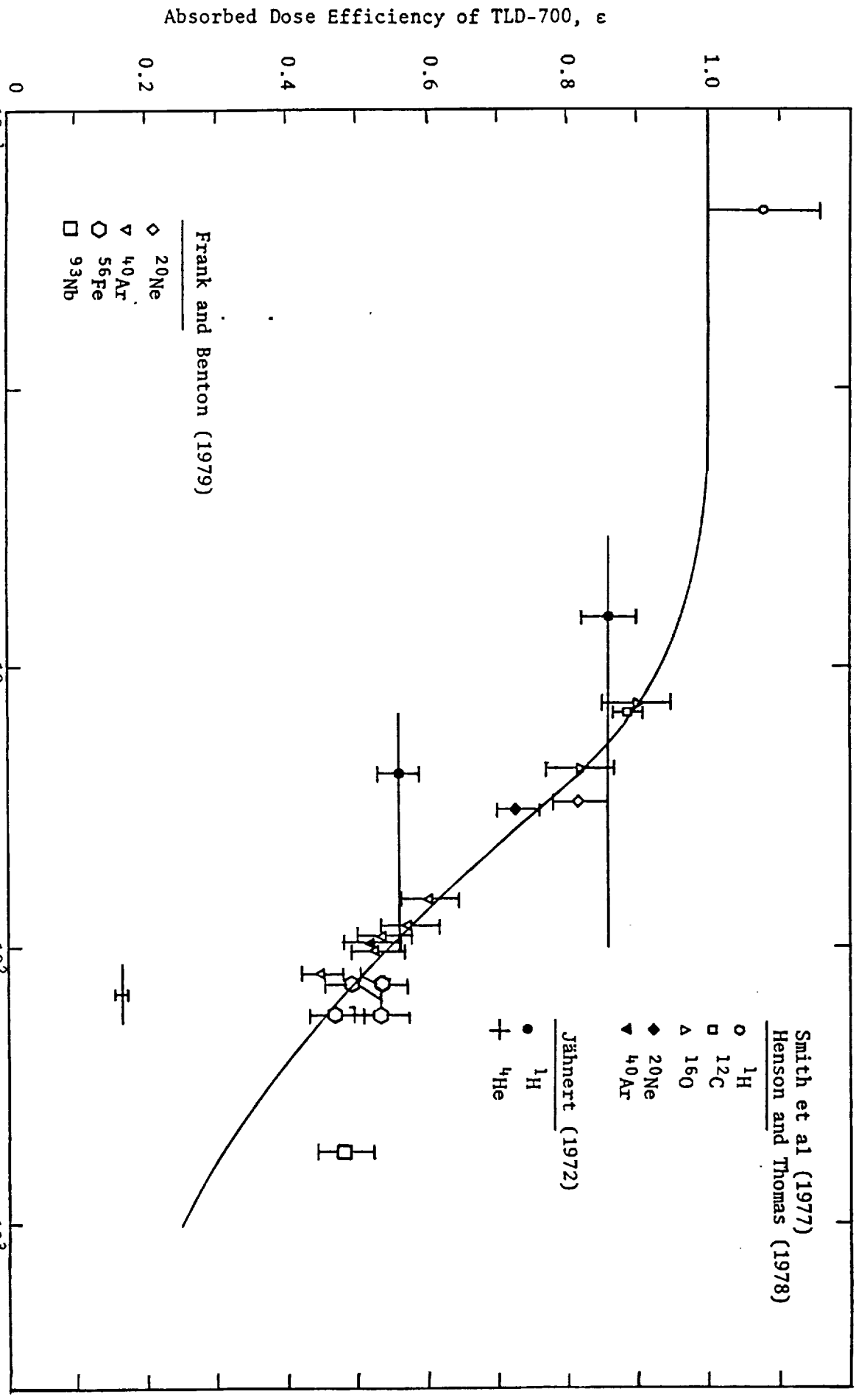

Fig. 9. Efficiency of measurement of absorbed dose as a function of LET for accelerated heavy ions on TLD-700 chips.

APPENDIX D

DOSIMETRY ON STS-42 WITH THE RME APD

Introduction

Beginning with the STS-42 mission, this laboratory began participating in instrument comparison studies in which space radiation was measured contiguously by passive and active methods. The active instrument was the RME-III microdosimeter. This instrument measures 4-channel LET spectra and employs a tissue-equivalent proportional counter. It is sensitive to the full LET range of ionizing radiation present.

Our Area Passive Dosimeter, the RME APD, contained arrays of PNTDs and TLDs. The PNTDs measure LET spectra ($LET_{\infty} \cdot H_2O \geq 5$ keV μm^{-1}), while the TLDs measure total absorbed dose. The object of this experiment is to compare the active and passive measurements on the basis of LET spectra, total absorbed dose and dose equivalent.

The STS-42 mission was launched on January 22, 1992, with a flight duration of 8.052 days. The orbit had an inclination of 57°and an altitude of 302 km. The Shuttle in this orbit is expected to encounter radiation levels dominated by GCRs with a lesser contribution from trapped protons in the lower region of the SAA.

Experiment

The RME APD consisted of an acrylic box (9.8 x 9.8 x 5.2 cm in outer dimensions) containing ten stacks of PNTDs which were oriented in seven directional angles and also four sets of TLDs which were positioned at the sides of the box. There were also four sets of TLDs from Johnson Space Center at the sides of the box. The RME APD is sketched in Figures 1 and 2.

The placement and angular orientation of the PNTD stacks is intended to compensate for the angular sensitivity of these detectors, which have maximum response to particles incident normal to the surface. The response is characterized by a cutoff angle of incidence, δ_c(LET). The solid angle of acceptance decreases with decreasing LET and goes to zero below ~5 keV μm^{-1}. In the RME APD

six stacks are adjacent to the box walls while the remaining four are perpendicular to the axes of the box corners.

After the return of the APD the TLDs were read out with a Harshaw Model 4000 reader. The PNTDs were processed to delineate the latent tracks and then read out with a semi-automated digitizer system. This consists of locating the tracks on the surfaces, rejecting background features and measuring the major and minor axes of the elliptical track openings. Tracks were accepted in two categories, for "Short Range" and "Long Range" particles. The short range particles left track pairs on the adjacent surfaces of a CR-39 doublet. A long range particle also left tracks at both of the outer surfaces of the doublet, showing that it had penetrated at least 1200 μm of CR-39 material.

The TLD signals were converted to absorbed doses by the use of ^{137}Cs standard source calibrations. The PNTD track parameter files were converted to LET spectra using calibrations performed with accelerated ion beams of various LETs. Doses and dose equivalents for high LET particles ($\geq$5 keV μm^{-1}) were then found from the LET spectra.

Measurements

The TLD measurements are given in Table 1. Some of the individual TLD measurements were lost due to a reader malfunction but there was sufficient data to yield a good average for the APD box.

The PNTD measurements of seven categories of LET flux spectra are shown in Figure 3. The seven categories represent the different angular alignments of PNTDs present in the APD box. The X, Y and Z directions are represented by averages of pairs of PNTD stacks (at opposite sides of the box). The remaining four are single stacks. There is approximately a factor of 2 between minimum and maximum values of integral flux with the X direction being the highest. The spread in values represent differences in directional shielding and averaged incident directional fluxes. The Shuttle did not maintain a particular orientation with respect to the Earth so the directions of maximum intensity of incident

radiation varied. In the high LET region (>200 keV/μm) there is a large spread in the measurements but the statistical accuracy is poor (only a few tracks were found).

The flux, dose rate and dose equivalent rate spectra for three APD configurations are given in Figures 4, 5 and 6. The RME APD includes all ten of the PNTD stacks. The USF APD includes six of the stacks (+x, -x, +y, -y, +z, -z). The Basic APD includes only three of the stacks (+x, +y, +z) and is the simple orthogonal configuration flown on most Shuttle flights as part of the mission dosimetry effort. The integral quantities for these curves are given in Table 2. Similar data for the seven directions are given in Table 3. The three APD configurations have differences up to 17% in flux, 16% in dose rate and 18% in dose equivalent rate, with the Basic APDs being highest.

Discussion

The comparison of the three data sets revealed a significant advantage in using PNTD stacks oriented in seven directions, rather than three directions, to measure the averaged 4π radiation fluxes in space. There was also a smaller difference between six-stack and three-stack measurements in three directions (7%) which may have been due to attenuation through the APD box or to improved sampling of the radiation, using larger detector areas.

The TLDs do not measure high LET absorbed dose with 100% efficiency. For the orbit of STS-42, the average efficiency of dose from particles with LET >5 keV/μm is about 50%. Total dose rate is therefore

$$D_T = (D_{TLD} - D_{PNTD}) + 2\ D_{PNTD}$$

or

$$D_T = D_{TLD} + D_{PNTD}$$

It is of interest to compare total dose rate (11.5 mrad/d) with PNTD dose rate (0.983 x 2 = 1.97 mrad/d). This demonstrates that more than 80% of the dose is due to radiation with $LET_\infty \cdot H_2O$ <5 keV/μm, mainly from higher energy protons (E_p >10 MeV). The doses measured on STS-42 can be given as follows:

D_{TLD} = 10.5 mrad d^{-1}

D for $LET_{\infty} \cdot H_2O$ <5 keV μm^{-1} = 9.52 mrad d^{-1}

D for $LET_{\infty} \cdot H_2O$ >5 keV μm^{-1} = 1.97 mrad d^{-1}

D_T = 11.5 mrad d^{-1}

Dose equivalent rate for $LET_{\infty} \cdot H_2O$ >5 keV μm^{-1} = 8.15 mrem d^{-1}

Total dose equivalent rate = 17.7 mrem d^{-1}

Average Quality Factor = 1.54

APPENDIX E

Multiplicities of Secondaries in Interactions of 1.8 GeV/Nucleon ^{56}Fe Nuclei with Photoemulsion and the Cascade Evaporation Model

by

V.E. Dudkin, E.E. Kovalev, N.A. Nefedov
V.A. Antonchik, S.D. Bogdanov, V.I. Ostroumov
H.J. Crawford and E.V. Benton

Nuclear Physics A509 (1990) 783–799
North-Holland

MULTIPLICITIES OF SECONDARIES IN INTERACTIONS OF 1.8 GeV/NUCLEON ^{56}Fe NUCLEI WITH PHOTOEMULSION AND THE CASCADE EVAPORATION MODEL

V.E. DUDKIN, E.E. KOVALEV and N.A. NEFEDOV

Institute of Biomedical Problems of the Ministry of Public Health of the USSR, Moscow, USSR

V.A. ANTONCHIK, S.D. BOGDANOV and V.I. OSTROUMOV

Leningrad Polytechnical Institute, Leningrad, USSR

H.J. CRAWFORD

University of California Space Sciences Laboratory, Berkeley, CA 94720, USA

E.V. BENTON

Physics Department, University of San Francisco, San Francisco, CA 94117, USA

Received 19 June 1989
(Revised 16 October 1989)

Abstract: A nuclear photographic emulsion method was used to study the charge-state, ionization, and angular characteristics of secondaries produced in inelastic interactions of ^{56}Fe nuclei at 1.8 GeV/nucleon with H, CNO, and AgBr nuclei. The data obtained are compared with the results of calculations made in terms of the Dubna version of the cascade evaporation model (DCM). The DCM has been shown to satisfactorily describe most of the interaction characteristics for two nuclei in the studied reactions. At the same time, quantitative differences are observed in some cases.

E NUCLEAR REACTIONS Multiplicities, interactions of high energy nuclei, photoemulsions, cascade evaporation model.

1. Introduction

Nuclear collisions at high energies keep arousing considerable interest because of the search for feasible manifestations of unusual properties of nuclear matter under conditions of high pressure and high temperatures. The great number of proposed theoretical approaches to describing the inelastic interaction of two nuclei [1]) make it obviously necessary to carry out a detailed quantitative comparison of experimental data on nucleus-nucleus interactions with the predictions of various models.

The present work compares the experimental data on the charge-state, ionization, and angular characteristics of the secondaries produced in the collisions of ^{56}Fe nuclei with hydrogen, light (CNO) and heavy (AgBr) components of photographic

91.

emulsion with the calculation results obtained in terms of the Dubna version of the cascade model (DCM).

2. Experiment and model

The experimental data has been obtained by studying a NIKFI BR-2 emulsion chamber irradiated by 1.9 GeV/nucleon Fe ions at the Lawrence Berkeley Laboratory BEVALAC. Interactions were sought by double (fast and slow) scanning of tracks. At a 112.77 m length, 1478 events were recorded from which a 7.63 ± 0.21 cm mean free path was inferred. The range-energy dependence was used [2]) to find the mean energy of the collision-initiating nuclei which proved to be 1.8 GeV/nucleon.

The energy and specie of the secondaries were inferred from the measured track lengths and from ionization loss. The ionization parameters (I) were taken to be the grain density per unit track length at $I < 9 I_0$ (where I_0 is the minimum ionization of a singly-charged particle) and the number of ocular scale intervals closed by grain conglomerates on unit track length (at $I > 4 I_0$) [3]). The charged particles which stopped in emulsion were identified using the relation between the specific ionization loss and the residual range. The ionization loss variation on a visible range length was determined for the particles ejected from the chamber.

The charges of the fragments of projectile nuclei were found by three methods, namely, by measuring the grain density, the lacunarity and the δ-electron number density. In this way, the energy of the initiating nucleus and the ejection angles and charges of all secondaries were found for each of the processed interactions.

In accordance with the emulsion terminology, all secondaries in stars were classified into black (b) particles with energy $E_p \leq 26$ MeV; gray (g) particles with $26 < E_p \leq 400$ MeV; stream (s) particles with $E_p > 400$ MeV; heavily ionizing (h) particles from target break-up; and fragments of projectile nuclei [4]). It should be noted also that the relativistic single-charged particles whose emission angle is below $5°$ ($\theta < 5°$) were treated as singly-charged fragments of a projectile nucleus and were not regarded as s-particles. The total charge of non-interacting fragments of the projectile nucleus $Q = \sum_i n_i Z_i$ was determined in each interaction [n_i is the number of fragments with charge Z_i (at $\theta < 5°$); the summation is with respect to all such fragments in an event]. In accordance with the classification adopted in cosmic-ray physics, the charge spectrum of the fragments was broken into the following groups: group L ($3 \leq Z \leq 5$), group M ($6 \leq Z \leq 9$), group H ($10 \leq Z \leq 19$), and group vH ($20 \leq Z \leq 26$). Also, the singly- and doubly-charged fragments (p and α, respectively) were discriminated.

The measurements were made from 558 inelastic interactions of iron nuclei with emulsion nuclei. Out of these, 314 interactions were selected without any discrimination. Also selected were 244 stars (processed to increase the ensemble of events in the hydrogen and light nuclei of emulsion) consisting of fewer than 11 particle fragments emanating from target nuclei ($n_h \leq 10$). The criteria developed in ref. [5])

were used to classify the events into three groups according to the target-nucleus specie, namely, the ^{56}Fe interactions with hydrogen (H) and with light (CNO) and heavy (AgBr) nuclei in emulsion which included 107, 228 and 162 events, respectively.

The calculations were made in terms of the DCM [6-8]) allowing for the meson production processes, for the Lorentz compression, for the Pauli exclusion principle, and for the effect of nucleon matter density variations as a cascade develops. The process of removing the excitation of nuclear residues after completing the fast stage was described in terms of a statistical model [9]). The calculational statistics were obtained by Monte Carlo interactions for the H, C, N, O, Ag and Br targets, which were summed up afterwards with the weights corresponding to the calculated cross sections for inelastic nucleus-nucleus interactions and to the elemental composition of emulsion. In all, 4767 events were simulated.

3. Interaction cross sections

The experimental probabilities for iron nuclei to interact with hydrogen and with light and heavy nuclei in the emulsion were (16.6 ± 0.8)%, (35.6 ± 1.7)% and (47.8 ± 2.6)%, respectively. The effective cross sections for disintegration of nuclei with similar masses may be approximately assumed to be proportional to their geometric dimensions, thereby making it possible to calculate the interaction cross sections for each of the elements separately if the elemental composition of the emulsion and the measured mean free path of iron nuclei in the emulsion are known (see table 1). Table 1 presents also the effective cross sections calculated in terms of the DCM and by the Bradt-Peters formula [10]):

$$\sigma_{in} = \pi r_0^2 [A_1^{1/3} + A_2^{1/3} - B(A_1^{-1/3} + A_2^{-1/3})]^2 , \quad (1)$$

TABLE 1

Comparison of the measured inelastic cross sections (in barns) with those calculated using DCM and formula (1) for 1.8 GeV/nucleon ^{56}Fe incident on photoemulsion nuclei

Target	Experiment	Calculation DCM	Calculation formula (1)
H	0.74 ± 0.07	0.75 ± 0.02	0.77 ± 0.02
C	1.75 ± 0.11	1.82 ± 0.05	1.67 ± 0.04
N	1.80 ± 0.12	1.93 ± 0.07	1.76 ± 0.04
O	1.86 ± 0.13	2.04 ± 0.08	1.83 ± 0.04
Br	3.09 ± 0.26	3.17 ± 0.10	3.26 ± 0.08
Ag	3.30 ± 0.28	3.53 ± 0.14	3.65 ± 0.08
CNO	1.80 ± 0.12	1.93 ± 0.07	1.74 ± 0.04
AgBr	3.24 ± 0.27	3.35 ± 0.11	3.46 ± 0.08

where A_1 and A_2 are masses of projectile nucleus and of target-nucleus, respectively; $r_0 = 1.32$ fm; $B = 0.85$.

It can be seen that the presented experimental and DCM-calculated cross sections are in agreement within statistical errors. The results are also close to the data obtained elsewhere. For example, the cross sections for inelastic interactions of ^{56}Fe nuclei with hydrogen, carbon, and silver at a similar energy presented in ref. [11]) are 0.68 ± 0.04, 1.56 ± 0.05 and 3.34 ± 0.08 b, respectively; in ref. [9]), the cross section for pFe collisions at 2.8 GeV was found to be 0.69 ± 0.03 b.

The results of calculating the cross sections for nucleus-nucleus collisions by the formula (1) which approximates the well-known data on relativistic projectile nuclei of lower masses [12]) proved to agree satisfactorily with the cross sections obtained in the present experiment. This fact makes it possible to extend the application scope of (1) to the projectile masses $A_1 = 56$.

4. Fragmentation of projectile nucleus

Table 2 presents the cross sections for fragmentation of iron nuclei on the various emulsion components. It is seen that the fragmentation cross section depends strongly on the target-nucleus specie. In ref. [13]), where the 2.1 GeV/nucleon ^{12}C and ^{16}O fragmentation was studied, the cross section for production of a projectile-nucleus fragment, σ^{f}_{PT}, was presented as

$$\sigma^{f}_{PT} = \gamma_T \gamma^{f}_{P}, \tag{2}$$

where γ_T is a target factor (defined by the properties of a given target-nucleus and with the dimension of cross section), and γ^{f}_{P} is the factor describing fragmentation of projectile P into fragment f. On the above-mentioned assumptions, the ratio of the fragment yields of identical groups for different target nuclei is defined solely by the ratio $\gamma_{T_1}/\gamma_{T_2}$ (where γ_{T_1} and γ_{T_2} are factors of the first and second targets) and does not depend on the fragment type. Studying the cross sections for production of fragments with $Z = 18$–24 in the interactions of iron nuclei of the same energy with various targets [11]) has yielded the target factors of 1.4 ± 0.1, 1.9 ± 0.09, and

TABLE 2

Fragmentation cross sections (barns) for 1.8 GeV/nucleon ^{56}Fe interacting with different types of photoemulsion nuclei

Target	Type of fragment					
	p ($Z = 1$)	α ($Z = 2$)	L ($3 \leq Z \leq 5$)	M ($6 \leq Z \leq 9$)	H ($10 \leq Z \leq 19$)	vH ($20 \leq Z \leq 26$)
H	2.22 ± 0.14	1.03 ± 0.10	0.10 ± 0.02	0.10 ± 0.02	0.33 ± 0.04	0.34 ± 0.04
CNO	7.02 ± 0.57	3.38 ± 0.31	0.36 ± 0.06	0.38 ± 0.06	0.50 ± 0.08	0.49 ± 0.06
AgBr	10.70 ± 0.72	4.54 ± 0.49	0.62 ± 0.08	0.29 ± 0.09	0.32 ± 0.13	0.91 ± 0.18

2.94 ± 0.14 for the Fe+H, Fe+C, and Fe+Ag collisions, respectively. The γ_H/γ_C and γ_C/γ_{Ag} values are then, 0.73 ± 0.06 and 0.65 ± 0.06 and appear to be close to the values 0.84 ± 0.08 and 0.69 ± 0.06 obtained in our experiment for the respective range of fragment charges ($Z = 18$-24).

To allow for the transformation of the charge state of cosmic rays as they traverse matter, it is necessary to know, to within as high an accuracy as possible, the mean production multiplicities of fragments (the fragmentation parameters, P_{ij}) which are defined to be the mean numbers of fragments of type j produced in disintegration of a projectile nucleus of type i. Table 3 presents the fragmentation parameters for the collisions of iron nuclei with emulsion nuclei (em) and with its components. Fig. 1 shows the distribution of the number of secondary fragments in an interaction event for the Fe+em disintegrations.

The inelastic nuclear collisions in an emulsion are usually studied using the criterion of discrimination of "central" interactions which means that any charged fragments of a projectile nucleus must be absent in a star. In our experiment, the events of this type amounted to less than 2%. At the same time, the number of singly-charged fragments in an interaction event may reach 12, while the numbers of doubly-charged fragments and the fragments with charges exceeding three may be 6 and 3, respectively, thereby indicating a very strong feasible excitation of the projectile-nucleus residue after the first interaction stage.

An increase in the target-nucleus mass results in a decreased fraction of disintegrations with multicharge fragments ($Z \geq 3$). The values of $P_{Fe,Z\geq 3}$ are 1.17 ± 0.04, 0.96 ± 0.04, and 0.76 ± 0.04 for the H, CNO, and AgBr targets, respectively. Also, it should be noted that a noticeable number of events with two and more $Z \geq 4$ particles

TABLE 3

Comparison of experimental fragmentation parameters to the results calculated using fireball phenomenology (shown in parentheses) for 1.8 GeV/nucleon ^{56}Fe interacting with different types of photoemulsion nuclei

Type of fragment	Type of interaction			
	Fe+H	Fe+CNO	Fe+AgBr	Fe+em
p	3.00 ± 0.19	3.90 ± 0.18 (2.96)	3.2 ± 0.2 (1.43)	3.4 ± 0.1 (2.35)
α	1.39 ± 0.14	1.88 ± 0.11 (1.02)	1.4 ± 0.2 (0.75)	1.6 ± 0.1 (0.81)
L	0.14 ± 0.03	0.20 ± 0.03 (0.12)	0.19 ± 0.04 (0.14)	0.12 ± 0.05 (0.13)
M	0.13 ± 0.04	0.21 ± 0.03 (0.12)	0.09 ± 0.03 (0.12)	0.10 ± 0.03 (0.10)
H	0.44 ± 0.05	0.28 ± 0.04 (0.46)	0.10 ± 0.04 (0.42)	0.20 ± 0.03 (0.40)
vH	0.46 ± 0.05	0.27 ± 0.03 (0.30)	0.28 ± 0.05 (0.12)	0.29 ± 0.03 (0.23)

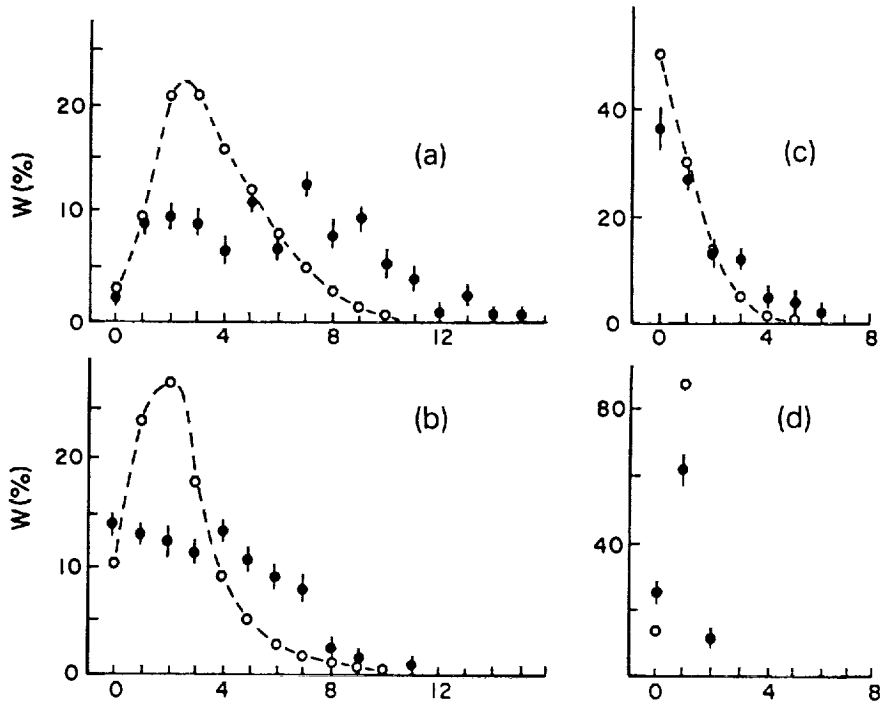

Fig. 1. Relative probabilities for a definite number of the ^{56}Fe fragments with charges $Z \geq 1$ (a), $Z = 1$ (b), $Z = 2$ (c) and $Z \geq 3$ (d) to occur in collision with emulsion nuclei at a 1.8 GeV/nucleon projectile energy. The full dots are experimental data; the open dots are calculated results of the model [17]).

ejected at small angles ($\theta \leq 2°$) were observed in the ^{56}Fe + H collisions. The occurrence frequency of such stars was (12 ± 3)%.

The results obtained for fragmentation of iron nuclei on hydrogen may be explained by examining the data on production of heavy fragments of a target nucleus in the "mirror" p + Fe collision at the same energies of incident proton. According to ref. [14]), the probability for the $Z \geq 4$ fragments to be ejected at $E_p = 2$ GeV from heavy nuclei of an emulsion is (4 ± 1)%. The presence of two and more multicharged particles belonging to a projectile nucleus in the Fe + H collisions may, then, be interpreted to be indicative of the process of Fe target-nucleus fragmentation in a "mirror" reaction. In this sense, a multicharged particle of the highest charge may be defined to be a residue nucleus, while the remaining such particles are regarded as fragments.

The validity of the above assumption is corroborated by the fact that the charged-particle multiplicity in the Fe + H events with a single multicharged fragment and with two such fragments was 7.82 ± 0.39 and 11.61 ± 0.76, respectively. The same dependence was also observed in the case of the initiating protons [15]); namely, the multicharged fragment ejection probability increases with the disintegration degree of a target nucleus. The total multiplicity of singly- and doubly-charged particles, which characterizes the Fe nucleus excitation degree, also increases when going over from the disintegrations with a single multicharged particle to the stars with two such particles (from 4.1 ± 0.3 to 5.9 ± 0.7, respectively).

Thus, studying the disintegrations with two and more multicharged particles may yield unique information for examining the nuclear fragmentation process. In this case, hydrogen is expedient to use as targets because the occurrence probability of stars with two large fragments in the Fe+H collisions is three times as high as in the Fe+CNO collisions and almost five times as high as in the Fe+AgBr collisions.

A sufficiently simple possibility of detecting a residue nucleus is one of the advantages of studying the Fe+H events compared with the "mirror" events. As a result of studying the properties of the residue products of disintegrations at $Z = 23$-27, Rudstam [16]) proposed a formula to describe the yield of residue nuclei. The mean charge $\langle Z \rangle$ of residue nuclei may be expressed as $\langle Z \rangle = Z_p - 1/k$, where k is a fitting parameter which is 1.13 [ref. [9])] at $E_0 = 2$ GeV. In our case the mean charge of residue nucleus in the Fe+H collisions was 17.7 ± 0.6, which is close to 18.3 the value given by the Rudstam formula. The strong dependence of parameter k on the mass of the interaction partner (the mean charge of residue nucleus in the Fe+CNO and Fe+AgBr collisions was 12.2 ± 0.5 and 9.8 ± 0.8 charge units, respectively) and the nonexponential distribution of fragment yields with increased fragment charges prevent the Rudstam formula from being used in the case of the Fe+CNO and Fe+AgBr interactions.

Using the fireball-model phenomenology [17]), we calculated the fragmentation parameters for interactions of iron nuclei with emulsion nuclei at 1.8 GeV/nucleon. In the fireball model, the fragment mass and charge are defined by the number of nucleons lost by a projectile nucleus during the fast interaction stage (N_{int}) and in the course of subsequent "cooling" (N_{ev}) of a produced excited residue nucleus. In this case we get

$$A_{fr} = A_p - (N_{int} + N_{ev}), \qquad Z_{fr} = Z_p - (Z_{int} + Z_{ev}),$$

where A_p, Z_p and A_{fr}, Z_{fr} are, respectively, the mass numbers and the charges of a projectile nucleus and of a produced fragment.

The number of knocked-out nucleons was inferred from the collision geometry on assumption that the nuclei are spheres with well-expressed boundaries and that all the projectile-nucleus nucleons appearing in the region of overlapping with the target nucleus suffer interactions and are emitted from the nucleus. The excitation energy of the residue nucleus was determined, according to ref. [18]), by the formula

$$E_{ex} = \alpha \Delta S, \tag{3}$$

where α is the surface-energy coefficient taken to be 0.95 MeV/fm^2; ΔS is the difference between the surface area of a produced residue-nucleus when a cylinder meets a sphere and the surface area of a sphere containing the same number of nucleons. We note that both the projectile Fe and the heavier target nuclei have matter distributions characterized by an exponential fall-off with increasing radius, not a hard-sphere edge as used here. This will make the spectrum of transferred energies softer than the one we have used in this work. We find that, typically, we require a harder transfer spectrum to match the data, however.

The evaporation of an excited nucleus was calculated using the scheme [9]) with the level-density parameter $a = \frac{1}{20}A$. The calculated fragmentation parameters are presented in parentheses in table 3. The statistical errors in the values do not exceed 3%. From table 3 it follows that the given model gives systematically overestimated values of the highly-charged fragment multiplicities and gives underestimated values of the yields of singly- and doubly-charged fragments. We are of the opinion that this circumstance has arisen from the low excitation energy ascribed to the residue nucleus, which is particularly evident from comparing between the experimental and calculated distributions of the number of fragments in an individual disintegration event (see fig. 1). The calculated mean energy of residue projectile-nucleus excitation in interactions with emulsion nuclei proved to be ~50 MeV, i.e., approximately 5 times as low as the energy necessary for the experimental α-particle and proton multiplicities to be accounted for. At the same time, it should be noted that the model reproduces correctly the trend in the variations of the residue projectile-nucleus charge with increasing the target mass. For example, the calculated $\langle Z \rangle$ values are 14.7 for Fe+CNO and 12.5 for Fe+AgBr interactions, whereas the experimental $\langle Z \rangle$ values for the events in the same targets are 12.2 ± 0.5 and 9.8 ± 0.8, respectively.

The angular distributions of the fragment particles can conveniently be characterized by mean emission angles $\langle \theta \rangle$ (see table 4). From the experimental data it follows that $\langle \theta \rangle$ decreases with increasing fragment mass and that there is a trend in the mean emission angle of composite particles to increase with target-nucleus mass. The increase is due mainly to a higher fraction of particles emitted at anomalously large angles. In the events with light nuclei, for example, (8.4 ± 0.2)% of relativistic α-particles are emitted at angles exceeding 5°, while (11.4 ± 2.4)% of such particles are observed in the Fe+AgBr interactions. In the latter case, 2% of all the doubly-charged particles are emitted at angles exceeding 10°. Obviously, the ejection of such fragments can hardly be explained by the stripping mechanism because this mechanism implies that the momentum transferred to a relativistic α-particle must exceed 1800 MeV/c.

TABLE 4

Mean emission angles (degrees) of fragments for 1.8 GeV/nucleon ^{56}Fe interacting with hydrogen, light and heavy nuclei, and with all nuclei of emulsion

Target	Type of fragment					
	p ($Z = 1$)	α ($Z = 2$)	L ($3 \leq Z \leq 5$)	M ($6 \leq Z \leq 9$)	H ($10 \leq Z \leq 19$)	vH ($20 \leq Z \leq 26$)
H	2.63 ± 0.07	1.94 ± 0.10	1.31 ± 0.17	1.37 ± 0.18	1.16 ± 0.12	1.03 ± 0.08
CNO	2.78 ± 0.04	2.50 ± 0.08	2.00 ± 0.15	1.44 ± 0.13	1.16 ± 0.08	1.10 ± 0.07
AgBr	2.52 ± 0.05	2.58 ± 0.12	2.24 ± 0.28	1.87 ± 0.39	1.01 ± 0.19	
em	2.63 ± 0.03	2.44 ± 0.07	2.00 ± 0.10	1.63 ± 0.11	1.08 ± 0.08	1.04 ± 0.08

A similar rise in the fraction of relativistic fragments emitted at large angles was observed as the impact parameter of interacting nuclei decreases. The fraction of the fragment α-particles whose emission angle exceeds 5° was $(12 \pm 2)\%$ and $(17 \pm 3)\%$ for the Fe+CNO and Fe+AgBr collisions, respectively, in the disintegrations corresponding approximately to the complete overlapping of one of the interacting nuclei (with $Q \leq 19$ for CNO and $Q \leq 15$ for AgBr target, where Q is the total charge of relativistic fragments) and was $(4 \pm 1)\%$ and $(6 \pm 1)\%$ for more peripheral nuclei ($Q > 19$ and $Q > 15$).

The occurrence of particles of the above types in the system composed of the remaining projectile nuclei cannot be explained in terms of a simple "abrasion-ablasion" model [19]) used to account for fragmentation of relativistic nuclei and necessitates other mechanisms of nucleus-nucleus interactions.

A new class of models currently under development is the multi-fragmentation model. This approach seeks to distinguish between sequential break-up of ever smaller systems and simultaneous break-up of a larger system into many small pieces. Randrup [20]) has recently reviewed some of these approaches in an attempt to understand the time development of the fragmentation process. Such approaches may well help to explain the large number of events observed to have multiple complex fragments in the final state here.

5. Mean multiplicities of secondaries

Table 5 presents the mean multiplicities of the b-, g-, h- and s-particles produced in the collisions of ^{56}Fe nuclei with nuclei of different masses and compares the experimental and calculated (in parentheses) values for a singled-out class of

TABLE 5

Comparison of experimental mean multiplicities to those calculated using DCM (shown in parentheses) for different types of 1.8 GeV/nucleon ^{56}Fe interactions

Type of interaction	Fe+H	Fe+CNO	Fe+AgBr	Fe+AgBr ($n_h \geq 28$)	Fe+em
$\langle n_b \rangle$	0.12 ± 0.03	1.77 ± 0.10	6.63 ± 0.33	9.37 ± 0.56	4.07 ± 0.23
	(0.011 ± 0.003)	(1.57 ± 0.03)	(6.54 ± 0.11)	(9.14 ± 0.22)	(3.68 ± 0.08)
$\langle n_g \rangle$	0.26 ± 0.04	2.87 ± 0.14	13.66 ± 0.96	27.33 ± 1.34	8.23 ± 0.60
	(0.35 ± 0.01)	(3.93 ± 0.05)	(15.3 ± 0.3)	(31.8 ± 0.5)	(8.77 ± 0.24)
$\langle n_h \rangle$	0.38 ± 0.05	4.64 ± 0.13	20.29 ± 1.13	36.7 ± 1.30	12.30 ± 0.76
	(0.36 ± 0.01)	(5.49 ± 0.04)	(21.9 ± 0.5)	(40.9 ± 0.5)	(12.45 ± 0.38)
$\langle n_s \rangle$	2.50 ± 0.17	8.12 ± 0.50	14.01 ± 0.98	25.57 ± 1.33	10.53 ± 0.68
	(2.36 ± 0.05)	(9.53 ± 0.18)	(15.7 ± 0.4)	(31.8 ± 0.5)	(11.28 ± 0.32)
$\langle Q \rangle$	24.33 ± 0.15	20.05 ± 0.35	15.84 ± 0.69	8.06 ± 0.71	18.83 ± 0.43
	(24.74 ± 0.05)	(20.66 ± 0.13)	(18.05 ± 0.26)	(10.09 ± 0.28)	(19.03 ± 0.18)
$\langle n_- \rangle$	3.00 ± 0.19	3.9 ± 0.18	3.30 ± 0.20	4.35 ± 0.34	3.46 ± 0.18
	(4.85 ± 0.05)	(9.03 ± 0.07)	(4.88 ± 0.07)	(7.00 ± 0.10)	(6.44 ± 0.06)

interactions at small impact parameters ($n_h \geq 28$) and for the emulsion as a whole (Fe+em).

The increase of the multiplicity of various types of particles with rising target-nucleus mass can be explained by the power-law dependence $n \sim A^{\alpha}$, where $\alpha = 0.34 \pm 0.04$ for s-particles, 0.82 ± 0.06 for g-particles, and 0.68 ± 0.06 for b-particles. These values are very close to the values obtained experimentally with a ^{14}N beam of the same velocity [21]) (the respective values are 0.35 ± 0.03, 0.88 ± 0.05 and 0.77 ± 0.04). The agreement seems, however, to be accidental because the approximation was made in two works with respect to only three (in the case of s-particles) and two (in the case of g- and b-particles) experimental points. It may be claimed, nevertheless, that the character of the dependence of mean multiplicities of secondaries is almost independent (at least for $A_p = 14$–56) of the type of a projectile nucleus.

As the projectile mass increases, the g- and s-particle multiplicity increases too, while the number of low-energy particles (b-particles) remains in practice the same, or even decreases. For comparison, it should be indicated that the mean multiplicity of the b-, g-, and s-particles in the ^{14}N+AgBr interactions was found in ref. [21]) to be 7.25 ± 0.27, 8.51 ± 0.46, and 10.35 ± 0.40, respectively. In our case, the respective values for the ^{56}Fe+AgBr collisions proved to be 6.36 ± 0.33, 13.66 ± 0.96, and 14.01 ± 0.98, respectively. This means that the energy spectrum of protons from target nuclei gets harder with increasing projectile mass, which was indicated earlier ref. [22]). In this connection, it should be noted that a replacement of projectile nucleus (of ^{14}N by ^{56}Fe) gives rise to a substantial increase in the occurrence frequency of large ($n_h \geq 28$) disintegrations, namely, from $(16 \pm 2)\%$ to $(33 \pm 5)\%$.

Comparison between the experimental and the DCM-calculated mean multiplicities (see table 5) has shown that the given model can satisfactorily reproduce the mean yields of various types of particles. It should also be noted that the mean multiplicities in the calculated iron nucleus-hydrogen interactions are in better agreement with experimental data compared with the Fe+CNO and Fe+AgBr events. The calculated total charge of noninteracting fragments of a projectile nucleus (Q) is somewhat in excess of its experimental value. The difference arises mainly from the difference in the multiplicities of n_s stripping protons of projectile nucleus. Both experimental and calculated (not presented here) distributions of the numbers of definite types of particles are of a falling form typical of relativistic nucleus-nucleus interactions [23]) and prove to be in satisfactory agreement with each other. Some quantitative differences are observed in the multiplicity distributions of the "gray" and relativistic s-particles. For example, the fraction of disintegrations with $n_g \geq 5$ is $(23 \pm 4)\%$ in the calculated ensemble of the Fe+CNO interactions, whereas the experimental value is $(14 \pm 3)\%$. In the Fe+AgBr interactions, the calculated and experimental relative occurrence probabilities of events with $n_h \geq 28$ proved to be 0.38 ± 0.03 and 0.33 ± 0.05, respectively, while the fraction of events with $n_s \geq 40$ was $(11 \pm 2)\%$ and $(2.5 \pm 1)\%$. Similar overestimation of the relative contribution of

the interactions with strong disintegrations of colliding nuclei is also observed in the case of the "central" ($n_h \geq 28$) interactions for which the DCM-calculated values of $\langle n_s \rangle$, $\langle n_h \rangle$ and $\langle n_g \rangle$ are much in excess of their experimental values (see table 5).

6. Correlations of multiplicities

One of the effective methods for verifying the adequacy of a model describing nuclear interactions is to obtain the correlations among secondaries in a star. The g-particle multiplicity in a disintegration and the charge of noninteracting fragments of a projectile (Q), which characterize the degree of overlapping of two nuclei in a collision, were selected to be arguments (see figs. 2-5). The figures present the experimental data on the ^{56}Fe interactions with light and heavy nuclei of an emulsion,

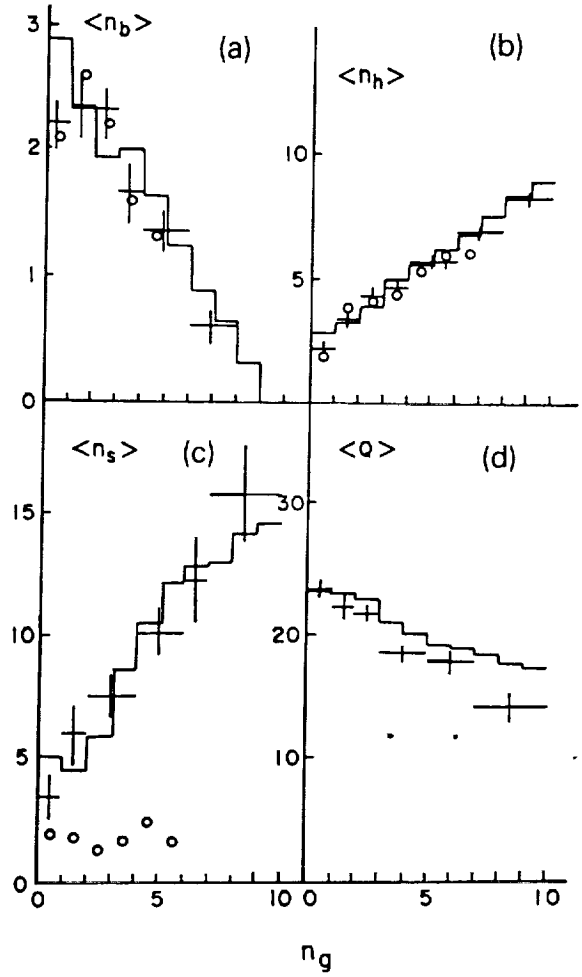

Fig. 2. Correlation functions versus n_g in nuclear interactions with CNO emulsion nuclei: (a) $\langle n_b \rangle$; (b) $\langle n_h \rangle$; (c) $\langle n_s \rangle$ and (d) $\langle Q \rangle$. The open dots are experimental data for projectile-proton at energy E_0 = 3.6 GeV/nucleon. The crosses are experimental data with error bars for ^{56}Fe at E_0 = 1.8 GeV/nucleon. The histograms are the DCM calculation results for ^{56}Fe at E_0 = 1.7 GeV/nucleon.

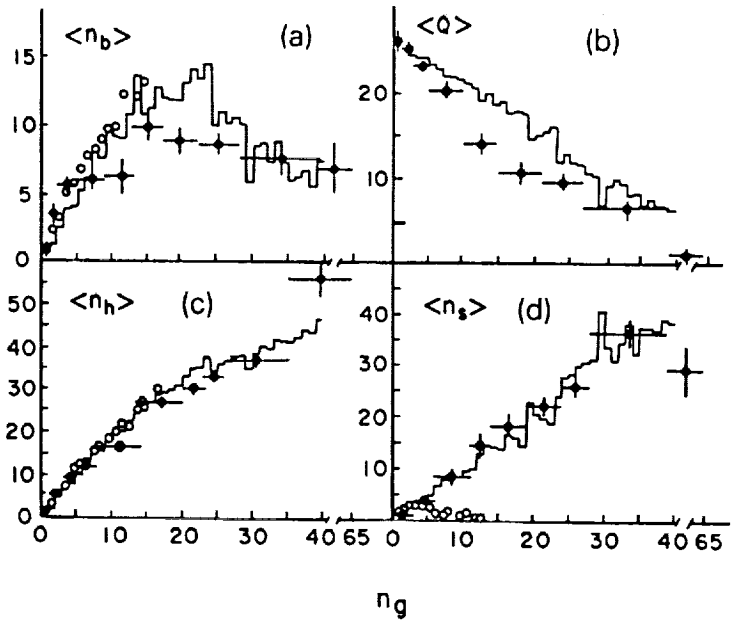

Fig. 3. Correlation functions versus n_g in nuclear interactions with AgBr emulsion nuclei: (a) $\langle n_b \rangle$; (b) $\langle Q \rangle$; (c) $\langle n_h \rangle$ and (d) $\langle n_s \rangle$. The open dots are experimental data for projectile-proton collisions at $E_0 = 3.6$ GeV [ref. [24]]. The full dots are experimental data for ^{56}Fe at $E_0 = 1.8$ GeV/nucleon. The histograms are the DCM calculation results for ^{56}Fe at $E_0 = 1.7$ GeV/nucleon.

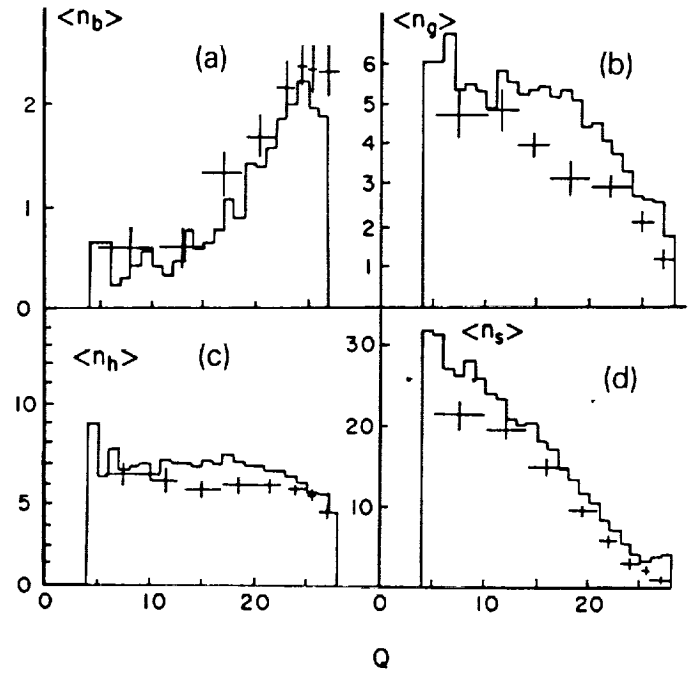

Fig. 4. Correlation functions versus Q in Fe+CNO interactions: (a) $\langle n_b \rangle$; (b) $\langle n_g \rangle$; (c) $\langle n_h \rangle$ and (d) $\langle n_s \rangle$. The dots are experimental data. The histograms are the DCM calculation results.

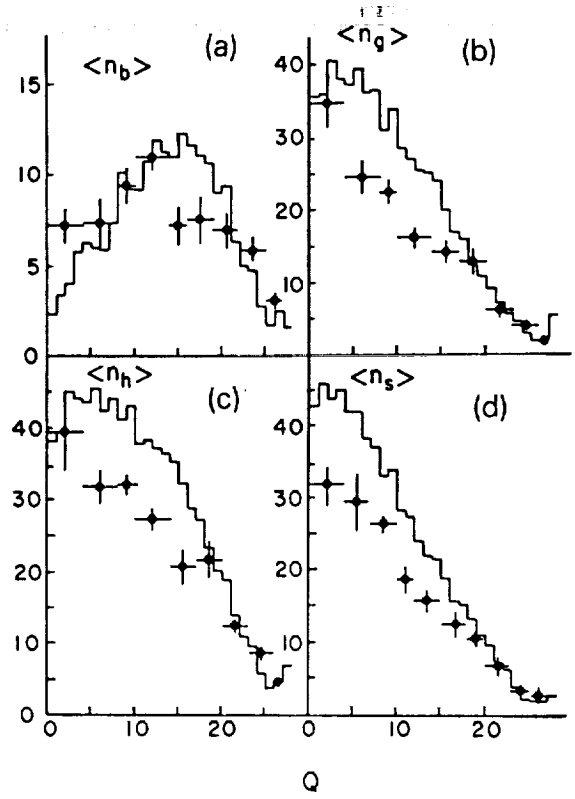

Fig. 5. Correlation functions versus Q in Fe + AgBr interactions: (a) $\langle n_b \rangle$; (b) $\langle n_g \rangle$; (c) $\langle n_h \rangle$ and (d) $\langle n_s \rangle$. The dots are experimental data. The histograms are the DCM calculation results.

the DCM calculation results, and the proton-nucleus interaction data [24]). The correlations of the $\langle n_g \rangle(Q)$ and $\langle Q \rangle(n_g)$ type make it possible to see the relationship between the arguments; namely, at small impact parameters the value of $\langle n_g \rangle$ (the number of target-nucleus protons knocked out during the fast interaction stage) is high, while the value of Q is at its minimum; as the impact parameter increases, the $\langle n_g \rangle$ value decreases, while the value of Q rises accordingly. The $\langle Q \rangle$ value can be used also to estimate the mean number of the projectile-nucleus protons involved in the fast reaction stage, namely, $n_{in} = 26 - \langle Q \rangle$. From the data of table 5 it may be obtained that the mean ratio of the numbers of protons involved in the fast reaction stage for the CNO, Fe and AgBr nuclei is $(0.48 \pm 0.06) : 1 : (1.34 \pm 0.16)$, i.e. 0.5 and 1.34 recoil protons are knocked out on the average from light and heavy target-nuclei, respectively, per single interacting nucleon of a projectile nucleus. The above ratio is close to the $Z_p^{2/3}$ dependence. Examination of the correlations $\langle Q \rangle(n_g)$ and $\langle n_g \rangle(Q)$ has shown, however, that in the case of peripheral nuclear collisions the ratio n_g/n_{in} of projectile is close to unity in the interactions with both light and heavy nuclei. In case of central collisions (small values of Q), the values of the n_g/n_{in} ratio are very different for different emulsion components and reach 0.22 ± 0.05 for the Fe + CNO collisions and 1.6 ± 0.2 for the Fe + AgBr collisions. The observed dependence of the ratios of interacting protons under nuclear collisions seems to us to

be associated with the rising importance of the secondary nucleon-nucleon interactions in the central nuclear collisions subject to finiteness of proton number in each of the colliding nuclei.

Having been normalized by a single interacting proton of a projectile nucleus, the multiplicity of relativistic s-particles appears to be 1.4 ± 0.1 and is the same for the target nuclei with very different masses (H, CNO, AgBr) and for a sampling of central events with $n_h \geq 28$. The correlation function $\langle n_s \rangle(Q)$ (figs. 4d and 5d) may also be presented as a straight line, $\langle n_s \rangle = 1.4 \times (26 - Q)$ in case of both light and heavy nuclei of an emulsion. This dependence of $\langle n_s \rangle$ on Q agrees with the model of independent interactions and is indicative of the decisive role of the first interaction of nucleons. The dependences $\langle n_s \rangle(n_g)$ for both components of emulsion are nearly linear with positive coefficients depending on target-nucleus mass and are absolutely at variance with the proton-nucleus interaction data; that is, the mean multiplicity of s-particles in the p+CNO interactions is in practice independent of the number of "gray" particles (figs. 2c and 3d), while the correlation function $\langle n_s \rangle(n_g)$ in the p+AgBr interactions exhibits even a trend to decrease.

Visual correlation between the fast and slow stages of the reaction of inelastic interaction of two nuclei may be obtained by examining a correlation of the $\langle n_h \rangle(n_g)$ form (figs. 1a and 3a). The form of this dependence in the case of heavy nuclei shows that it is approximately linear at a small g-particle number which can be related to the low degree of cascading in target nucleus, i.e., the emission of each g-particle makes, on the average, the same contribution to the excitation energy.

The same correlation in the p+AgBr interactions exhibits a stronger dependence (figs. 1a and 3a), thereby indicating that the g-particles in nucleon-nucleus collisions excite the target-nucleus more effectively. The small n_g values in nucleus-nucleus interactions correspond to high impact parameters when the colliding nuclei touch each other but slightly, so the g-particles are protons knocked out from the extreme periphery of a heavy nucleus. The same number of "gray" rays in the proton-produced star correspond to low impact parameters, to more intensive cascading, and, hence, to higher excitations of target-nucleus. At high n_g values (above 15), i.e. in the region attainable only in nucleus-nucleus interactions, the mean multiplicity $\langle n_h \rangle$ not only is independent of the number of "gray" rays in a star, but also exhibits a trend to decrease. Two factors are notable among the reasons for the above described $\langle n_h \rangle(n_g)$ behaviour. The first factor is the above-mentioned "finiteness" of a target-nucleus. If a target-nucleus loses 20-25 protons during the fast reaction stage (the inflexion zone of the correlation function $\langle n_h \rangle(n_g)$, see fig. 3a), a "lack" of nucleons is observed in the target-nucleus residue during the second, "slow", stage. The second factor consists of the high excitation energies of the residue nuclei of targets which may give rise to an explosion-like process of secondary particle emission, thereby resulting in their acquiring an energy exceeding the energy boundary of the "black" rays. The effect of the two factors appears to be most visual in the case of the correlation function $\langle n_h \rangle(n_g)$ under interactions of iron nuclei with light nuclei of an emulsion. Here, an increase of the number of "gray" rays in a

star leads in practice to the complete disappearance of b-particles in a disintegration (fig. 2a). The character of the dependences $\langle n_b \rangle(Q)$ (figs. 4a and 5a) is the same as the behaviour of the correlation function $\langle n_b \rangle(n_g)$ (figs. 2a and 3a), so they are most probably defined by identical factors.

From figs. 2–5 it is seen that the DCM can rather well reproduce the behaviour of the experimental correlations. Some differences are observed in the Q-dependences (figs. 4 and 5). The following trend can be noted in this case: the DCM reproduces quite properly the experimental data at high values of the total charge of the projectile-nucleus fragments ($Q > 18$), which correspond to peripheral interactions. In the case of central interactions, the DCM overestimates the mean multiplicities of secondaries. On the other hand, the form of the $\langle Q \rangle(n_g)$-type inverse correlations shows that the model predicts higher values of $\langle Q \rangle$ under a significant destruction of target-nucleus compared with experimental data. It should also be noted that the differences between experimental and calculated values manifest themselves more pronouncedly in the Fe + AgBr interactions compared with the Fe + CNO reactions.

Since the Q-values summarize the stripping fragments of a projectile nucleus with $Z = 1$, which differ only in angle, they may include the produced particles whose model-predicted mean multiplicity is fairly high (see table 5). Obviously, if this excessive meson production could have been suppressed in the model, the agreement between the experimental and calculated mean s-particle multiplicities would have been much improved and, in addition, a better agreement between the $\langle n_s \rangle(n_g)$ and $\langle Q \rangle(n_g)$ correlation functions would have been attained. The inclusion of the πN and NN resonances [25]) in the calculations may substantially diminish the cascade branching and, accordingly, the secondary-particle multiplicity would decrease. The inclusion of the above resonances is particularly important in the case of collisions of heavy nuclei. The disagreement between the experimental and calculated dependences $\langle n_i \rangle(Q)$ may also arise from using the statistical evaporation theory, which seems to be ineffective at small impact parameters of nuclei, to describe the characteristics of particles emitted from the projectile nucleus. It should also be noted that the given version of the model disregards the distortions of projectile trajectories by Coulomb forces and neglects the momentum transfers to interacting nuclei, as a whole, in a collision; i.e., the model fails to allow for the effects which become noticeable under collisions of heavy nuclei. The allowance for the above-mentioned factors may result in a decreased probability of interactions at small impact parameters; i.e., in a lower occurrence frequency of many-ray stars; besides, it will decrease the Q-value and improve, in this way, the degree of agreement between the calculated and experimental data.

7. Conclusions

The following conclusions may be drawn from the results of the present work and from the subsequent analysis.

(i) The experimental cross sections for inelastic interactions of 1.8 GeV/nucleon iron nuclei with photographic emulsion nuclei may be described in terms of the Bradt-Peters geometric model and prove to agree satisfactorily with the DCM-calculated cross sections.

(ii) The fragmentation parameters of iron nuclei depend strongly on partner-nucleus mass. In this case the fraction of disintegrations with multicharged fragments ($Z \geq 3$) decreases with increasing the target-nucleus mass. Emission of two or more $Z \geq 4$ fragments was observed in $(12 \pm 3)\%$ of the Fe + H interactions.

(iii) The charge distribution of residue nuclei in the Fe + H collisions may be described by the Rudstam formula which, however, appears to be inapplicable to the Fe + CNO and Fe + AgBr interactions.

(iv) Theoretical calculations obtained in terms of the model described by Gosset *et al.* [18]) disagree with experimental data. The excitation energy ascribed by the calculations to the residual nucleus leads to disagreement with the experimental multiplicity of "evaporation" particles.

(v) The angular distributions of projectile fragments comprise particles with anomalously large emission angles. The fraction of such particles increases with target-nucleus mass.

(vi) The dependences of the mean b-particle multiplicity, or Q, are of different forms for target-nuclei of different masses. The effect of the "finiteness" of a heavy target nucleus, which is not observed in nucleon-nucleus interactions, manifests itself in the Fe + AgBr interactions.

(vii) The analysis of the correlation functions of particle multiplicities in a disintegration has shown that the simple superposition model for nucleon-nucleus interactions is inapplicable to the nucleus-nucleus interactions. The model assumes a linear dependence between the number of secondaries and the number of interacting projectile nucleons. This type of dependence is observed only in the case of s-particles, but does not take place in the case of b- and g-particles.

(viii) The DCM describes qualitatively all the experimental data examined. A quantitative agreement is observed with the results for Fe + H reactions and in the case of peripheral Fe + CNO and Fe + AgBr interactions. To get a better description of central collisions at small impact parameters, the model must be further refined.

The University of San Francisco work was partially supported by NASA-Ames Research Center Grant No. NCC2-521 and NASA-Johnson Space Center, Houston, Grant No. NAG9-235.

References

1) R. Stock, Nucl. Phys. **A434** (1985) 537
2) W. Gelbrath and W.C. Williams, High energy and nuclei physics data handbook (Chilton, 1963)

3) V.A. Antonchik, V.A. Bakaev, S.D. Bogdanov, A.I. Vikhrov, V.E. Dudkin, V.V. Iroshnikov and N.A. Nefedov, Yad. Fiz. (Sov. J. Nucl. Phys.) **35** (1982) 1103
4) B.P. Bannik *et al.*, J. of Phys. **G14** (1988) 949
5) V.A. Antonchik *et al.*, Yad. Fiz. (Sov. J. Nucl. Phys.) **28** (1978) 435
6) K.K. Gudima and V.D. Toneev, Yad. Fiz. (Sov. J. Nucl. Phys.) **27** (1978) 658
7) K.K. Gudima, H. Iwe and V.D. Toneev, J. of Phys. **G2** (1979) 237
8) K.K. Gudima and V.D. Toneev, Nucl. Phys. **A400** (1983) 173c
9) V.S. Barashenkov and V.D. Toneev, Interaction of high-energy particles and atomic nuclei with nuclei (Atomizdat, Moscow, 1972)
10) H.L. Bradt and B. Peters, Phys. Rev. **77** (1950) 54
11) G.D. Westfall, L.W. Wilson, P. J. Lindstrom, H.J. Crawford, D.E. Greiner and H.H. Heckman, Phys. Rev. **C19** (1979) 1309
12) A.H. Viniczkiy *et al.*, Joint Institute of Nuclear Research Preprint, Dubna, P1-80-473, 1980
13) P.J. Lindstrom, D.E. Greiner, H.H. Heckman, B. Cork and F.S. Bieser, Lawrence Berkeley Laboratory Report No LBL-3650 (1975)
14) O.V. Logkin and N.A. Perfilov, Nuclear chemistry (Nauka, Moscow, 1965)
15) O.V. Logkin, Zh. Exsp. Teor. Fiz. (Sov. J. Exp. Theor. Phys.) **33** (1957) 354
16) G.Z. Rudstam, Z. Naturforsch. **27a** (1966) 1027
17) G.D. Westfall, J. Gosset, P.J. Johansen, A.M. Poskanzer, W.G. Meyer, H.H. Gutbrod, A. Sandoval and R. Stock, Phys. Rev. Lett. **37** (1976) 1202
18) J. Gosset, H.H. Gutbrod, W.G. Meyer, A.M. Poskanzer, A. Sandoval, R. Stock and G.D. Westfall, Phys. Rev. **C16** (1977) 629
19) M. Bleszynski and C. Sander, Nucl. Phys. **A326** (1979) 525
20) J. Randrup, Nucl. Phys. **A495** (1989) 245c
21) G.M. Chernov *et al.*, Nucl. Phys. **A280** (1977) 478. [Also: G.M. Chernov *et al.*, Dokl. Izbec. Akad. Nauk. **2** (1977) 20 (in Russian)]
22) V.A. Antonchik, V.A. Bakaev, S.D. Bogdanov, A.I. Vikhrov, V.E. Dudkin, N.A. Nefedov, V.I. Ostroumov and Yu.V. Potapov, Yad. Fiz. (Sov. J. Nucl. Phys.) **33** (1981) 1057
23) V.A. Antonchik *et al.*, Yad. Fiz. (Sov. J. Nucl. Phys.) **33** (1981) 3; 1057
24) M.I. Adamovich *et al.*, High Energy Physics Institute of Kazach Academy of Sciences Preprint, Alma-Ata, No 81-11, 1981
25) V.S. Barashenkov *et al.*, Joint Institute of Nuclear Research Preprint, Dubna, P2-83-117 (1983)

57-72
41631
N95-25918

APPENDIX F

Target Fragments in Collisions of 1.8 GeV/Nucleon ^{56}Fe Nuclei with Photoemulsion Nuclei, and the Cascade-Evaporation Model

by

V.E. Dudkin, E.E. Kovalev, N.A. Nefedov
V.A. Antonchik, S.D. Bogdanov, V.I. Ostroumov
E.V. Benton and H.J. Crawford

Nuclear Physics A530 (1991) 759–769
North-Holland

TARGET FRAGMENTS IN COLLISIONS OF 1.8 GeV/NUCLEON ^{56}Fe NUCLEI WITH PHOTOEMULSION NUCLEI, AND THE CASCADE-EVAPORATION MODEL

V.E. DUDKIN, E.E. KOVALEV and N.A. NEFEDOV

Institute of Biomedical Problems of the Ministry of Public Health of the USSR, Moscow, 123007, USSR

V.A. ANTONCHIK, S.D. BOGDANOV and V.I. OSTROUMOV

Leningrad Polytechnical Institute, Leningrad, USSR

E.V. BENTON

University of San Francisco, San Francisco, CA 94117, USA*

H.J. CRAWFORD

Space Science Laboratory, University of California, Berkeley, CA 94720, USA

Received 9 April 1990
(Revised 11 January 1991)

Abstract: Nuclear photographic emulsion is used to study the dependence of the characteristics of target-nucleus fragments on the masses and impact parameters of interacting nuclei. The data obtained are compared in all details with the calculation results made in terms of the Dubna version of the cascade-evaporation model (DCM).

E NUCLEAR REACTIONS Target-nucleus, photoemulsion method, cascade-evaporation model, fragmentation, relativistic nuclear collisions.

1. Introduction

Successful acceleration of relativistic heavy-ion beams up to iron has provided researchers with auspicious possibilities for studying the features of high-energy nuclear interactions. In this connection, any information on non-relativistic secondaries (the upper boundary of their energy spectrum is ususally taken to be 400 MeV/nucleon), whose characteristics are defined mainly by processes in the target nuclei [1]), proves to be of great importance when constructing and verifying any models which would be adequate to explain experimental data.

* Supported in part by NASA-Ames Research Center Grant No. NCC2-521 and by NASA-Johnson Space Center, Houston, Grant No. NAG9-235.

The characteristics of non-relativistic secondaries in reactions of relativistic nuclei p, ^{12}C, ^{16}O, and ^{22}Ne were studied in detail in previous works [2-4]), where comprehensive comparison with calculation results obtained in terms of the cascade-evaporation model was used to conclude that the given model is qualitatively applicable to describing the characteristics of singly-charged particles emitted from emulsion nuclei. It is of interest, therefore, to study the characteristics of target-nucleus fragments in the collisions initiated by a much heavier projectile nucleus.

2. Experiment

The present work continues the studies of collisions of 1.8 GeV/nucleon ^{56}Fe nuclei with emulsion nuclei [5-8]). The experimental conditions, the search methods and the initial processing of the events were described earlier [8]). The secondaries with energies below 400 MeV/nucleon were charge- and energy-separated by the same techniques as in refs. [2-4]). All singly-charged particles were assumed to be protons, while all doubly-charged particles were regarded as α-particles.

The experimental statistics amounted to 558 events. In conformity with Dudkin *et al.* [8]), the studied events were classified into interactions of Fe nuclei with the light (CNO) and heavy (AgBr) nuclei of photoemulsion. A class of interactions was also singled out in which the number of h particles, i.e. particles with energies below 400 MeV/nucleon, exceeded 27. The given events occur as a result of almost complete breakup of target nuclei.

The calculations were made in terms of the Dubna version of the cascade model (DCM) [9-11]). The calculation statistics amounted to 4767 events. All the model-calculated interactions were recorded on magnetic media and were then processed using the same criteria as those applied to the real events.

3. Analysis

Following refs. [2-4]), the energy range of secondaries was divided in our analysis into two sub-ranges: fast particles ($30 < E_p < 400$ MeV, $40 < E_\alpha < 1600$ MeV) and slow particles ($E_p \leq 30$ MeV, $E_\alpha \leq 40$ MeV).

Tables 1 and 2 present the mean values of multiplicities $\langle n \rangle$, emission angles $\langle \Theta \rangle$, energies $\langle E \rangle$, transverse $\langle p_\perp \rangle$ and longitudinal $\langle p_\parallel \rangle$ momenta (or "forward/backward" (f/b) ratio) obtained in our experiment for protons and α-particles with energies below 400 MeV/nucleon. The DCM calculation results are presented in brackets.

Figs. 1 and 2 show the experimental and calculated energy spectra of protons and α-particles from the Fe+CNO and Fe+AgBr interactions, and from the collisions accompanied by almost complete breakup of a heavy target nucleus ($n_h \geq 28$).

From table 1 it is seen that the mean multiplicity of fast protons ($E > 30$ MeV) increases with increasing target-nucleus mass or with decreasing impact parameters

TABLE 1

Characteristics of 30–400 MeV protons and 10–400 MeV/n α-particles produced in interactions of Fe nuclei ($E_0 = 1.8$ GeV/nucleon) with photoemulsion nuclei (DCM results shown in parentheses)

Interaction type	Secondary-particle species	$\langle n \rangle$	$\langle \Theta \rangle$ (degree)	$\langle E \rangle$ (MeV)	$\langle P_\perp \rangle$ (MeV/c)	$\langle P_\parallel \rangle$ (MeV/c)
Fe+CNO	p	2.46 ± 0.13 (3.58 ± 0.04)	48 ± 1 (54.3 ± 0.4)	198 ± 5 (166 ± 2)	359 ± 8 (352 ± 3)	394 ± 14 (314 ± 5)
Fe+AgBr	p	11.4 ± 0.3 (13.9 ± 0.1)	52.8 ± 1 (58.9 ± 0.9)	179 ± 3 (161 ± 1)	355 ± 5 (359 ± 1)	345 ± 9 (258 ± 4)
Fe+AgBr ($n_h \geq 28$)	p	23.8 ± 0.9 (28.8 ± 0.4)	54 ± 1 (59.0 ± 0.4)	176 ± 4 (162 ± 1)	364 ± 7 (359 ± 2)	338 ± 12 (246 ± 4)
Fe+AgBr	α	0.5 ± 0.1 (0.8 ± 0.1)	58 ± 4 (50 ± 1)	172 ± 24 (273 ± 11)	708 ± 42 (840 ± 20)	373 ± 60 (860 ± 25)
Fe+AgBr ($n_h \geq 28$)	α	1.1 ± 0.2 (1.7 ± 0.1)	60 ± 5 (45 ± 1)	186 ± 30 (312 ± 16)	793 ± 74 (885 ± 28)	408 ± 80 (969 ± 35)

TABLE 2

The characteristics of slow protons ($E_p \leq 30$ MeV) and α-particles ($E_\alpha \leq 40$ MeV) produced in the interactions of 1.8 GeV/nucleon Fe nuclei with photoemulsion nuclei

Interaction type	Secondary-particle energy (MeV)	$\langle n \rangle$ particle/interaction	$\langle \Theta \rangle$ (degree)	$\langle E \rangle$ (MeV)	$\langle P_- \rangle$ (MeV/c)	$\bar{n}/\bar{n}$ [a]
Fe+CNO	$E_p \leq 30$	1.66 ± 0.10 (1.45 ± 0.03)	84 ± 2 (83 ± 1)	9.1 ± 0.4 (13.9 ± 0.1)	91 ± 3 (114 ± 2)	1.3 ± 0.2 (1.35 ± 0.04)
Fe+AgBr		5.1 ± 0.2 (6.6 ± 0.1)	86 ± 1 (81.9 ± 0.3)	11.8 ± 0.3 (14.6 ± 0.1)	113 ± 2 (125 ± 1)	1.2 ± 0.1 (1.51 ± 0.04)
Fe+AgBr ($n_h \geq 28$)		7.8 ± 0.5 (9.7 ± 0.2)	86 ± 1 (79.1 ± 0.6)	13.3 ± 0.5 (15.8 ± 0.2)	120 ± 3 (130 ± 1)	1.41 ± 0.10 (1.68 ± 0.07)
Fe+CNO	$E_\alpha \leq 40$	0.18 ± 0.03 (0.24 ± 0.02)	79 ± 6 (84 ± 1)	17.2 ± 1.2 (14.5 ± 0.6)	264 ± 19 (244 ± 4)	2.2 ± 0.5 (1.30 ± 0.06)
Fe+AgBr		1.1 ± 0.1 (0.4 ± 0.1)	85 ± 3 (85 ± 1)	17.4 ± 0.8 (20.2 ± 0.2)	272 ± 10 (288 ± 2)	1.3 ± 0.2 (1.49 ± 0.07)
Fe+AgBr ($n_h \geq 28$)		1.4 ± 0.2 (0.40 ± 0.04)	95 ± 6 (70 ± 1)	20.1 ± 1.2 (18.8 ± 0.3)	286 ± 18 (263 ± 5)	1.0 ± 0.2 (2.91 ± 0.06)

[a]) The ratio of particle emissions to the forward and backward hemispheres.

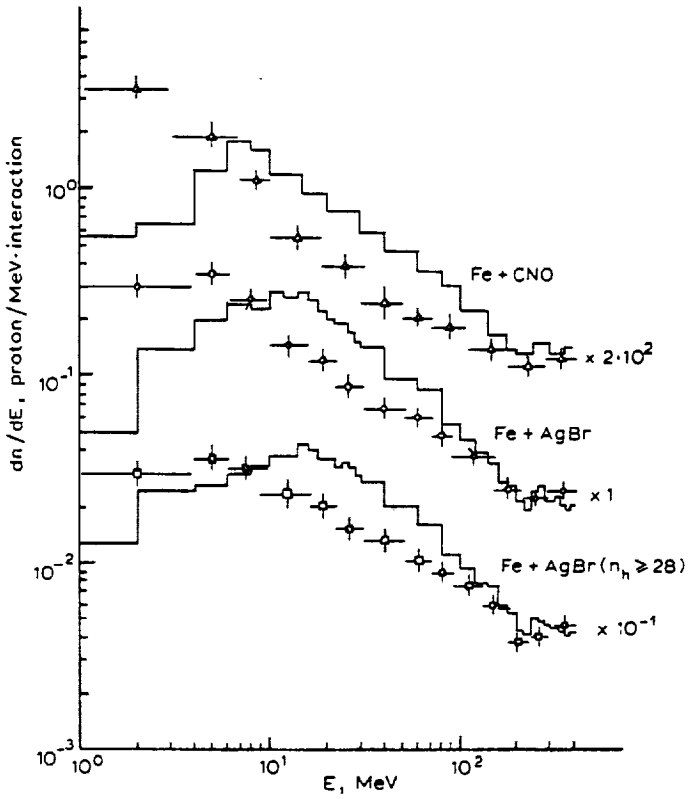

Fig. 1. The $E_p \leq 400$ MeV proton energy spectra. Triangles are for Fe+CNO interactions, circles are for Fe+AgBr interactions, and squares are for Fe+AgBr ($n_h \geq 28$) interactions. The histograms are the DCM calculation results for these interactions. All data are given in absolute units.

(under transition to the $n_h \geq 28$ events). The DCM does describe the increase, but the experimental values prove to be overestimated systematically by 20-30%. At the same time, the calculated mean values of the energies and longitudinal momenta of fast protons prove to be below their experimental values. The experimental and calculated mean transverse momenta are in fairly good agreement with each other. However, the experimental values of mean emission angles of fast protons prove to be below their calculated values (see table 1), reflecting the above-mentioned $p_{\parallel}$ difference.

From the fast-proton energy spectra displayed in fig. 1 it follows that the main difference between the calculated and experimental distributions occurs in the energy range below 100 MeV. It should be noted that the distributions are presented in absolute units without any normalization. At higher proton energies, the calculated and experimental spectra are in fairly good agreement with each other.

Fig. 3 shows the longitudinal and transverse momentum distributions of fast protons produced in the Fe+AgBr interactions. It is seen that the calculated and

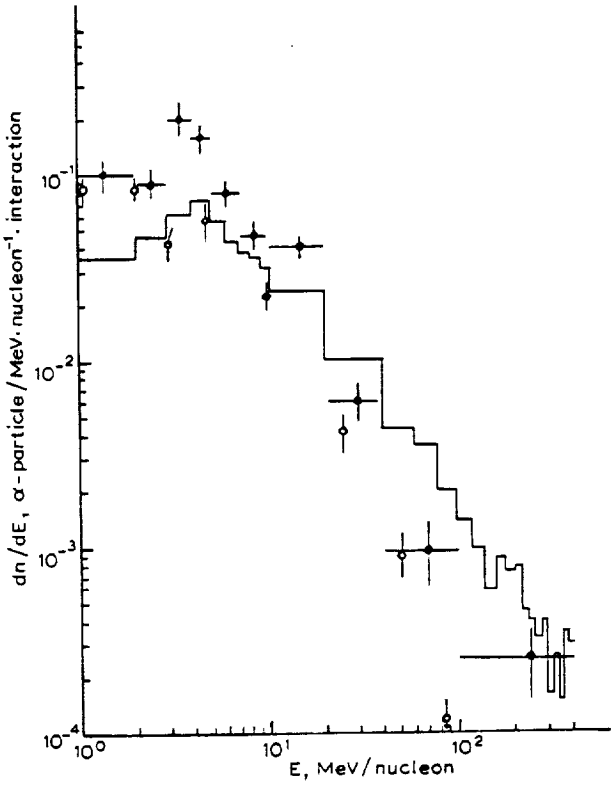

Fig. 2. The $E_\alpha \leq 400$ MeV/nucleon α-particle energy spectrum for Fe+AgBr interactions. The points: experiment; the histogram: DCM calculation results.

experimental distributions are in quantitative agreement with each other at the longitudinal and transverse momenta above 400 MeV/c. At lower values of $p_\parallel$ and $p_\perp$, the "model" spectra are 20–30% in excess of the experimental spectra. We are of the opinion that such a systematic overestimation is accounted for by the fact that the calculated 30–100 MeV proton yield is in excess of its experimental value (see fig. 1). Indeed, the momenta of the 30–100 MeV protons are 240–450 MeV/c, so the $p_\parallel$ and $p_\perp$ momentum distributions can get distorted at values below 450 MeV/c. The calculation overestimated 30–100 MeV proton multiplicity in all three interaction classes singled out above, (FE+CNO, Fe+AgBr, and Fe+AgBr ($n_h \geq 28$)), gives rise not only to an increase in the total multiplicity of the 30–400 MeV particles, but also to a systematic underestimation of the mean energies and longitudinal momenta of fast protons and to higher values of the mean emission angle (see table 1). Despite the quantitative disagreement, the DCM gives a correct qualitative description of the increase in $\langle\Theta\rangle$ of $E_p > 30$ MeV protons and the decrease in $\langle E\rangle$ and $\langle p_\parallel\rangle$ of the same protons when going from Fe+CNO to Fe+AgBr and to Fe+AgBr ($n_h \geq 28$) interactions.

113 A

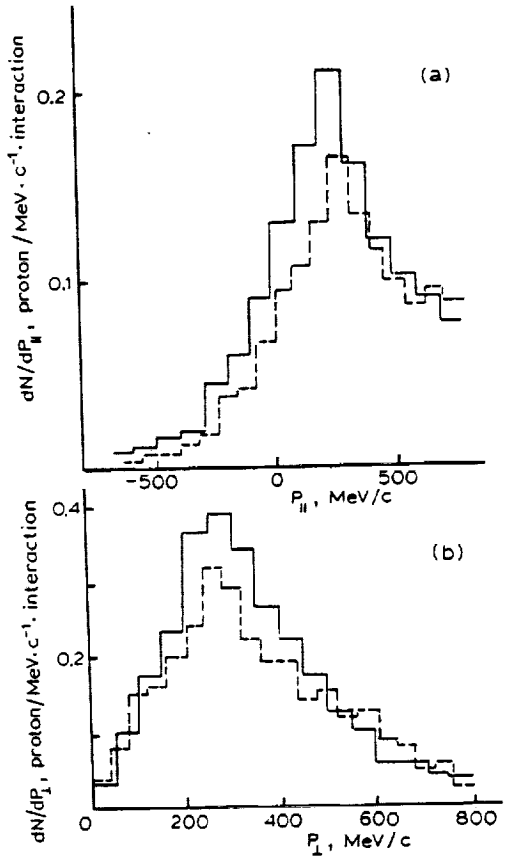

Fig. 3. The longitudinal (lab) (a) and transverse (b) momentum distributions of 30–400 MeV protons in the Fe+AgBr interactions. The dashed and solid-line histograms are the experimental and DCM calculation results, respectively.

Discrepancies between the experimental and calculated characteristics of fast α-particles are much larger than for protons. From the energy distributions displayed in fig. 2, it follows that the calculated yields of α-particles with energy more than 80 MeV (20 MeV/nucleon) are much in excess of the experimental values (see table 1). A substantial preference of the model-simulated α-particles for emission in the forward hemisphere (lower values of $\langle\Theta\rangle$) is also worth noting. The above-mentioned differences in mean characteristics and in the energy spectra suggest that the model does not describe the emission of fast doubly-charged particles satisfactorily.

Let us now examine the degree of agreement between experimental and DCM-calculated characteristics of slow singly- and doubly-charged fragments of a target nucleus. From comparing the data presented in table 2 it is seen that the calculated mean proton multiplicity for the Fe+AgBr collisions has been overestimated, and the mean α-particle value underestimated. The calculated mean proton and α-

particle energies are somewhat in excess of the experimental values for the interactions with both light and heavy emulsion components. The energy spectra of protons and α-particles in the Fe+CNO, Fe+AgBr, and Fe+AgBr ($n_h \geq 28$) interactions (see figs. 1 and 2) and proton energy spectra ($E_p \leq 30$ MeV), for emission angles $\Theta \leq 90°$ and $\Theta > 90°$ (see fig. 4a, b), indicate a small number of the "subbarrier" fragments of a target nucleus ($E_p < 4$ MeV) in model-simulated interactions compared with experimental data. The given differences in the forms of the experimental and calculated spectra are observed in both forward and backward hemispheres (see fig. 4a, b).

The calculated transverse momenta are higher than their experimental values not only in the "mean" interactions but also in the subset of Fe+AgBr ($n_h \geq 28$) (see table 2), thereby indicating that the model temperature of the excited residual target-nucleus is, on the average, higher than its experimental value. A higher excitation of target nucleus leads to a higher number of evaporated protons and to a lower multiplicity of low-energy α-particles (the relative probability for doubly-charged particles to be emitted decreases sharply at high excitation energies in the evaporation model). This assertion was verified by comparing the measured and

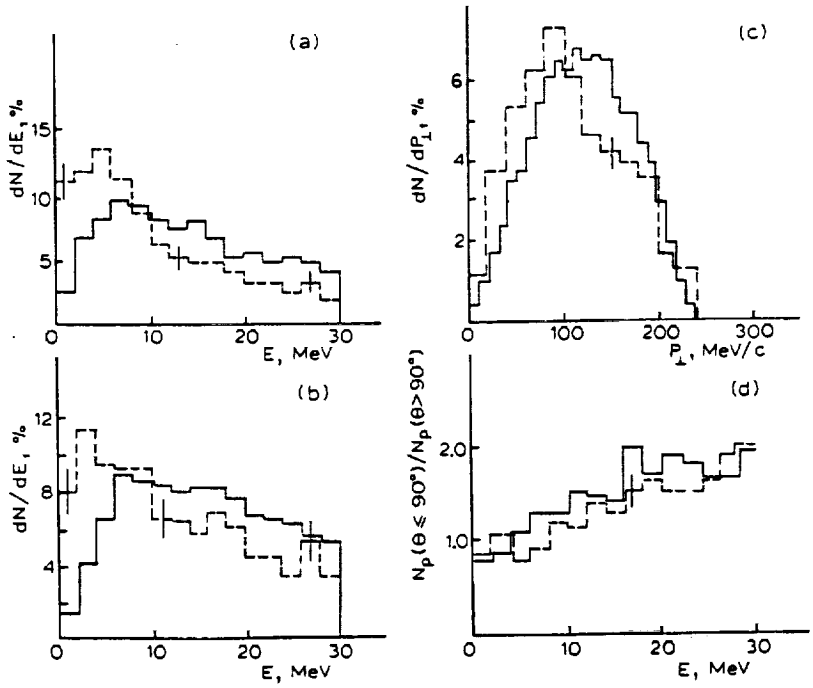

Fig. 4. The characteristics of $E_p \leq 30$ MeV protons in the Fe+AgBr interactions: the energy spectra at forward (a) and backward (b) hemispheres; the transverse-momentum distribution (c), and the "forward-to-backward" ratio energy dependence (d), the dashed and solid-line histograms are the experimental and DCM calculation results, respectively.

calculated transverse-momentum ($p_\perp$) distributions of the $E \leq 30$ MeV protons in AgBr interactions (see fig. 4c). It is seen that the calculated and experimental distributions are shifted with respect to each other but display the same form. The "effective" temperature of the particle-emitting system may be estimated assuming that the singly-charged particle distribution of each of the 3-momentum components corresponds to a gaussian distribution with parameter $\sigma = \sqrt{2/\pi}\langle P_\perp \rangle$ and that the "effective" temperature is: $T_0 = \sigma^2/m$. The estimate inferred in such a manner from experimental data is $T_0 \sim 7$ MeV, whereas the model-calculated "effective" temperature proves to be about 10 MeV.

Examination of the angular distributions (not presented here) and of the mean emission angles of low energy protons and α-particles (see table 2) has shown that the experimental distributions exhibit a smaller forward asymmetry compared with the model. The calculated f/b ratios for all interactions (1.51 ± 0.14) and for the "central" interactions at $n_h \geq 28$ (1.68 ± 0.07) are markedly in excess of their experimental values, 1.2 ± 0.1 and 1.4 ± 0.1, respectively. The disagreement is preserved also in the f/b energy dependence (fig. 4d), although the character of its behavior (an increase of anisotropy with increasing energy) is represented correctly by the model.

Thus, the consistent comparison between the experimental and DCM-calculated characteristics of fast and slow fragments of a target nucleus has shown that higher numbers of both nucleons and complex particles are emitted from target-nuclei during the first (fast) interaction stage in the DCM-simulated events compared with experimental data. As a result, at the end of the cascade, the "model" residual target nuclei have a higher "effective" temperature T_0 and a higher longitudinal velocity $\beta_\parallel$. The resultant anomalously-high T and $\beta_\parallel$ give rise to an increased mean energy of the particles emitted from residual nuclei. Therefore, the number of the $E \leq 5$ MeV particles in the model interactions (even with light nuclei) is significantly decreased.

The effect of the projectile mass on the low-energy particle characteristics ($E_p \leq 30$ MeV, $E_\alpha \leq 40$ MeV) was studied in the present work by comparing the results obtained with the earlier experimental data [2,4,12]). With this purpose, following Antonchik *et al.* [12]), we plotted the distributions of longitudinal velocity $\beta_\parallel$ of emitted particles (see fig. 5) and approximated the plots by the gaussian distributions:

$$\frac{dN}{d\beta_\parallel} \sim \exp\left[-\frac{(\beta_\parallel - \langle\beta_\parallel\rangle)^2}{\beta_0^2}\right] \quad (1)$$

where β_0 is the characteristic velocity of the particles emitted from an excited nucleon system; $\langle\beta_\parallel\rangle$ is the mean longitudinal velocity of the system.

In this case [12]), the "effective" temperature T_0 of the particle-emitting system is $T_0 = \frac{1}{2}m\beta_0^2$, where m is an emitted particle mass.

The longitudinal velocity distributions of the $E \leq 30$ MeV proton and of the $E \leq 40$ MeV α-particles, shown in fig. 5 are quite properly approximated by gaussian distributions [1]) in agreement with the assumption that residual target-nuclei can be

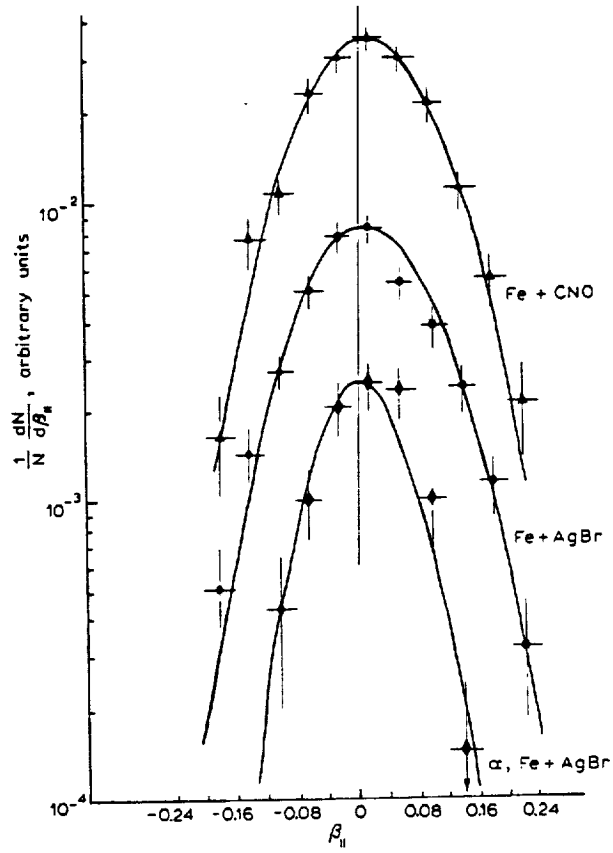

Fig. 5. The longitudinal (lab) velocity ($\beta_\parallel$) distributions for $E_p \leq 30$ MeV secondary protons in the Fe+CNO (triangles) and Fe+AgBr (circles) interactions, and for $E_\alpha \leq 40$ MeV α-particles in the Fe+AgBr (diamonds) interactions. The curves are the approximations by gaussian distributions.

represented as a distribution of excited nucleon systems moving longitudinally at velocity $\langle\beta_\parallel\rangle$ and emitting particles isotropically.

Table 3 presents the $\langle\beta_\parallel\rangle$ and $\langle\beta_0\rangle$ values inferred from experimental and model-calculated (in parentheses) data and shows also the results obtained elsewhere. The set of data presented in table 3 indicates that the mean longitudinal velocity of the system is rather low and varies within the $0.005 < \langle\beta_\parallel\rangle < 0.02$ range, irrespective of the projectile mass. At the same time, a systematically-higher velocity of the residue of light target-nuclei is observed.

Analysis of the values of β_0 presented in table 3 shows that β_0 remains in practice constant at a level of 0.10–0.12 as energy increases or the target nucleus changes and when the impact parameter in the collisions with heavy (AgBr) nuclei (transition to $n_h \geq 28$ collisions) decreases, thereby indicating that the "effective" temperature T_0, which characterizes the excitation energy of the target nucleus per nucleon [12]),

114/A

TABLE 3

Characteristics of the excited nucleon system emitting slow particles (DCM results shown in parentheses)

Interaction type	Projectile energy [GeV/nucleon]	Secondary particle	$\langle\beta_{\parallel}\rangle$	$\langle\beta_0\rangle$	Ref.
Fe+CNO	1.8	Protons $E_p \leq 30$ MeV	0.016 ± 0.005 (0.003 ± 0.002)	0.110 ± 0.010 (0.137 ± 0.003)	this work
Fe+AgBr	1.8		0.011 ± 0.003 (0.019 ± 0.002)	0.118 ± 0.004 (0.150 ± 0.002)	this work
Fe+AgBr ($n \geq 28$)	1.8		0.013 ± 0.004 (0.025 ± 0.003)	0.121 ± 0.007 (0.156 ± 0.003)	this work
Ne+CNO	3.6		0.011 ± 0.007	0.110 ± 0.010	[4]
Ne+AgBr	3.6		0.005 ± 0.003	0.125 ± 0.005	[4]
p+CNO	3.6		0.007 ± 0.008	0.120 ± 0.010	[2]
p+AgBr	3.6		0.003 ± 0.003	0.103 ± 0.004	[2]
Fe+AgBr	1.8	α-particles $E_\alpha \leq 40$ MeV	0.007 ± 0.004 (0.013 ± 0.002)	0.08 ± 0.01 (0.07 ± 0.01)	this work
Ne+AgBr	3.6		0.009 ± 0.003	0.08 ± 0.02	[4]
p+AgBr	3.6		0.013 ± 0.005	0.08 ± 0.03	[2]
He+AgBr	2.1	$R < 4$ mm	0.016 ± 0.004	0.117 ± 0.002	
O+AgBr	2.1	$E_p < 31$ MeV	0.015 ± 0.004	0.115 ± 0.002	[12]
Ar+AgBr	2.1		0.012 ± 0.002	0.117 ± 0.002	

is also constant. The value of T_0 for low-energy protons was estimated to be 5–7 MeV for all of the experimental data presented in table 3. The DCM calculations lead (as mentioned above) to a higher "effective" temperature and to a higher longitudinal velocity of the emitted low-energy particles.

4. Conclusions

The main results of the present work may be summarized as follows:

(1) The energy, momenta, and angle characteristics of singly- and doubly-charged fragments of target nuclei have been obtained for interactions of 1.8 GeV/nucleon ^{56}Fe nuclei with light and heavy nuclei in emulsions; the dependencies of these characteristics on target mass have been studied.

(2) The consistent comparison with the DCM calculation results has shown that the DCM describes the differential energy spectra of protons with energy $E >$ 100 MeV but does not describe the emission of fast complex particles. The high model-simulated excitation energies, which exceed their experimental values, distort the energy spectra of low-energy particles.

(3) The increase of projectile nucleus mass from proton to iron in the relativistic energy range (1.8–3.6 GeV/nucleon) does not significantly affect the characteristics of an excited nucleon system which emits slow particles. This is consistent with the concept of factorization.

The authors are indebted to Dr. K.K. Gudima for kindly providing the DCM calculation results.

References

1) V.S. Barashenkov and V.D. Toneev, Interaction of high-energy particles and atomic nuclei with nuclei Atomizdat, Moscow (1972)
2) V.A. Antonchik *et al.*, Yad. Fiz. (Sov. J. Nucl. Phys.) **40**, no. 3(9) (1984) 752
3) Cosice-Leningrad, collaboration, Yad. Fiz. (Sov. J. Nucl. Phys.) **28** (1978) 435
4) V.A. Antonchik *et al.*, Yad. Fiz. (Sov. J. Nucl. Phys.) **46**, no. 5(11) (1987) 1344
5) V.A. Antonchik *et al.*, Yad. Fiz. (Sov. J. Nucl. Phys.) **35**, no. 5(11) (1982) 1103
6) V.A. Antonchik *et al.*, Yad. Fiz. (Sov. J. Nucl. Phys.) **42**, no. 6(12) (1985) 1289
7) V.A. Antonchik *et al.*, Yad. Fiz. (Sov. J. Nucl. Phys.) **44**, no. 6(12) (1986) 1508
8) V.E. Dudkin, E.E. Kovalev, N.A. Nefedov, V.A. Antonchik, S.D. Bogdanov, V.I. Ostroumov, H.J. Crawford and E.V. Benton, Nucl. Phys. **A509** (1990) 783
9) K.K. Gudima and V.D. Toneev, Yad. Fiz. (Sov. J. Nucl. Phys.) **27** (1978) 658
10) K.K. Gudima, H. Iwe and V.D. Toneev, J. Phys. **G2** (1979) 237
11) K.K. Gudima and V.D. Toneev, Nucl. Phys. **A400** (1983) 173
12) H.H. Heckman *et al.*, Phys. Rev. **C17** (1978) 1651

114 C

APPENDIX G

Dependence of the Multiplicities of Secondary Particles on the Impact Parameter in Collisions of High-Energy Neon and Iron Nuclei with Photoemulsion Nuclei

by

V.E. Dudkin, E.E. Kovalev, N.A. Nefedov
V.A. Antonchik, S.D. Bogdanov, V.F. Kosmach, A.Yu. Likhachev
E.V. Benton and H.J. Crawford

Nuclear Physics A551 (1993) 723–733
North-Holland

NUCLEAR
PHYSICS A

Dependence of the multiplicities of secondary particles on the impact parameter in collisions of high-energy neon and iron nuclei with photoemulsion nuclei

V.E. Dudkin, E.E. Kovalev and N.A. Nefedov
Research Test Center for Radiation Safety of Space Flights of the Ministry of Public Health of Russia, Moscow 123182, Russian Federation

V.A. Antonchik, S.D. Bogdanov, V.F. Kosmach and A.Yu. Likhachev
St. Petersburg State Technical University, St. Petersburg, Russian Federation

E.V. Benton
Department of Physics, University of San Francisco, San Francisco, CA 94117-1080, USA

H.J. Crawford
Space Science Laboratory, University of California, Berkeley, CA 94720, USA

Received 8 January 1992
(Revised 6 July 1992)

Abstract: A method is proposed for finding the dependence of mean multiplicities of secondaries on the nucleus-collision impact parameter from the data on the total interaction ensemble. The impact parameter has been shown to completely define the mean characteristics of an individual interaction event. A difference has been found between experimental results and the data calculated in terms of the cascade-evaporation model at impact-parameter values below 3 fm.

1. Introduction

The characteristics of secondaries produced in an interaction between two nuclei are defined as a first approximation by the energy of the projectile nucleus, the masses of the colliding nuclei, and the impact parameter of the collision. As a rule, the energy of the projectile nucleus and the masses of the colliding partners are known, whereas the impact parameter is difficult to determine for a particular interaction. The collision centrality can be estimated from the characteristics of the projectile-nucleus spectator fragments produced by a given collision, just as was done in the experiment [1]) by detecting charged secondaries of pseudo-rapidities $\eta > 1.3$ generated in relativistic oxygen-ion interactions with various targets. In experiments which measure all charged secondaries, however, the study of the dependence of interaction characteristics on impact parameter has been qualitative

Correspondence to: Professor E.V. Benton, Physics Research Laboratory, Ignatian Heights, San Francisco, CA 94117-1080, USA.

and dealt mainly with two extreme situations, namely, the extremely peripheral and central collisions [2-6]).

The present work is aimed at (a) testing the methods of determining the collision impact parameter; (b) finding the dependence of the mean multiplicities of secondaries on the impact parameter; and (c) studying the impact-parameter dependence as a function of the masses and energies of interacting nuclei and of the secondary species.

2. Initial data and method

The analyzed experimental ensembles are composed of 497 inelastic interactions of Fe nuclei (1.8 GeV/nucleon) and 236 interactions of Ne nuclei (3.6 GeV/nucleon) with photoemulsion nuclei [7-9]). The target nucleus (H, CNO or AgBr), the individual charges of all particles, and the polar (θ) and azimuthal (ψ) angles of the latter were found for each of the interactions. To classify interactions according to the type of target nucleus, we used the results of refs. [10,11]) where the characteristic features of collisions on each group of photoemulsion nuclei were studied using nuclear emulsions with different concentrations of light components (of H, C and O nuclei). Energy was determined for secondaries with energies below 400 MeV/nucleon. All singly charged particles were treated as protons, and all doubly charged particles as α-particles. Following Antonchik *et al.* and Krasnov *et al.* [4,5]), all secondaries were classified into "black" particles (b-particles, $E \leq 26$ MeV/nucleon), "grey" particles (g-particles, $26 < E \leq 400$ MeV/nucleon) and "shower" particles (s-particles, $E > 400$ MeV/nucleon), except the projectile fragments.

Each of the interactions was characterized by the particle number of a particular species (n_b, n_g, n_s), by the total number of all charged particles (n_{ch}) produced in an interaction, and by the total charge of the non-interacting fragments of a projectile nucleus (Q). Targets in the emulsion experiments were identified by criteria developed in Dudkin *et al.* [7,8]), and did not bias the multiplicity analysis.

The experimental results were compared with the cascade-evaporation model using two calculated ensembles of the interactions on H, CNO, Br, Ag nuclei: the first ensemble was produced by 1.8 GeV/nucleon ^{56}Fe nuclei - 4767 events were calculated with the DCM version of the model [12]), and the second ensemble was produced by 3.6 GeV/nucleon ^{22}Ne nuclei - 4976 events with the CEM version [13]). In both cases all the events were summed with weights corresponding to the observed cross sections and to the emulsion composition.

We use the experimental integral distributions which define the probability for producing interactions with the number of rays of type i equalling or exceeding a certain number n_i:

$$W_{(\geq n_i)} = \sum_{k_i \geq n_i} W_{(k_i)} = W_{(n_i)} + W_{(n_i+1)} + W_{(n_i+2)} + \cdots , \qquad (1)$$

where $W_{(n_i)}$ is the experimental estimate of the probability of disintegration with the number of rays n_i to occur, which equals the ratio of the number of stars with n_i to the total number of stars in an ensemble. The subscript i indicates the type of ray (b-, g-, s-particles) or the total charge Q of non-interacting fragments.

In terms of the geometrical approach to nucleus-nucleus collisions, it was postulated that as the degree of overlap of two nuclei increases (the impact parameter decreases), the multiplicity of secondaries increases in strictly monotonic fashion [14]. The highest impact parameter (b_i) in a nucleus-nucleus interaction which gives rise to disintegration with the number of rays of type i equalling or exceeding n_i will, then, be

$$b_i = \sqrt{\sigma/\pi}\sqrt{W_{(\geq n_i)}}, \tag{2}$$

where σ is the total inelastic cross section (cm^2); b_i is the impact parameter (cm); the subscript i indicates that the impact parameter is estimated from the integral star distribution of the particles of type i. Note that the disintegrations with n_i particles will correspond to the collisions whose impact parameters belong to the range:

$$\Delta b_i = \sqrt{\sigma/\pi}(\sqrt{W_{(\geq n_i-1)}} - \sqrt{W_{(\geq n_i)}}). \tag{3}$$

Having postulated a strictly monotonic decrease in the number of non-interacting protons of a projectile nucleus (Q) with decreasing impact parameter, after similar reasoning we obtain

$$b_Q = \sqrt{\sigma/\pi}\sqrt{1 - W_{(\geq Q)}}. \tag{4}$$

Thus, using the interaction ensemble data and the above formulae, we may transform the integral distributions $W_{(\geq n_i)}$ to obtain the dependence of the number of particles of type i in an individual disintegration on the impact parameter $n_i(b_i)$, and to find the range of the impact parameters of nucleus-nucleus interactions which give rise to interactions with a definite number (n_i) of secondaries. Also, the experimental correlations of multiplicities of type $\langle n_j\rangle(n_i)$ and $\langle n_j\rangle(Q)$ inferred from the same ensemble of events may be used together with the relations between n_i and b_i [eqs. (2)-(4)] to obtain the dependence of the mean multiplicity of particles of type j on impact parameter [$\langle n_j\rangle(b_i)$ and $\langle n_j\rangle(Q)$]. The above-mentioned transformation procedure is shown schematically in fig. 1.

Let us assume a total ensemble of events in which the number of all charged particles and g-particles is recorded for each of the events. The data on the ensemble can then be used to obtain the integral distribution of the number of all charged particles (n_{ch}) in the event (fig. 1a) and to obtain the correlation dependence $\langle n_g\rangle(n_{ch})$ of the mean number of g-particles in the disintegration on n_{ch} (fig. 1b). Eq. (3) is used to find the range of the impact parameters corresponding to the interactions with a particular n_{ch} value. For example, the events with $n_{ch} = 4$ at $\langle n_g\rangle = 0.75 \pm 0.09$ belong to the variation range from $W_{(\geq 5)} = 0.09$ to $W_{(\geq 4)} = 0.25$ and, according to eq. (3), correspond to the impact parameters ranging from $0.3\sqrt{\sigma/\pi}$ to $0.5\sqrt{\sigma/\pi}$.

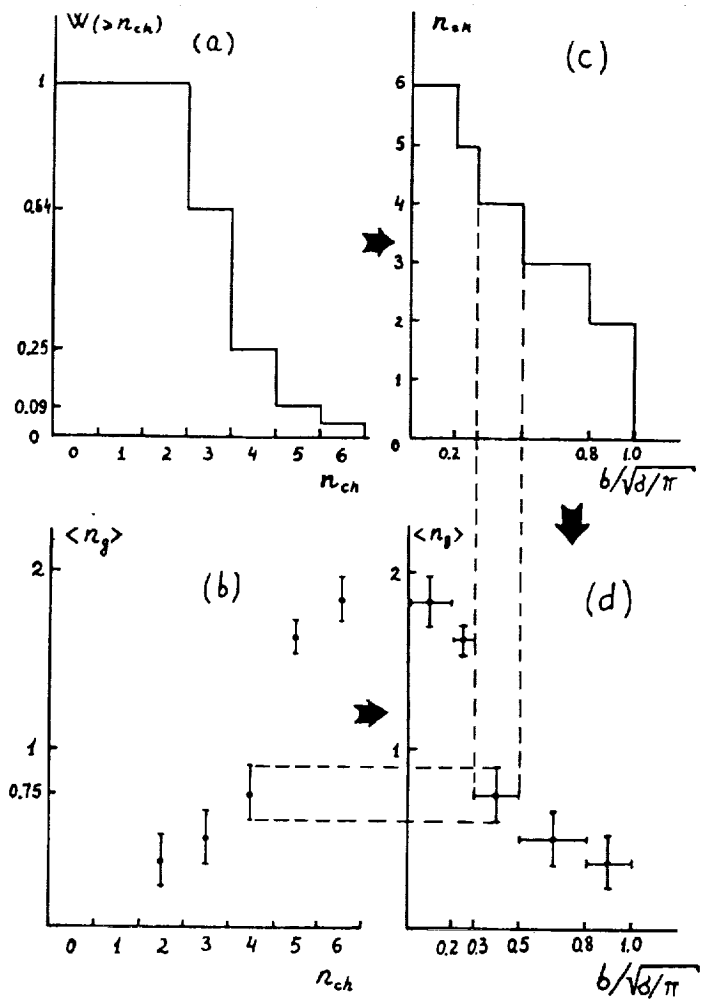

Fig. 1. A scheme for estimating impact parameter: (a) the integral distribution of the total number of charged particles in a disintegration; (b) the correlation dependence of the mean number of g-particles in a disintegration on the total number of charged particles involved; (c) the dependence of the mean multiplicity of all charged particles in a disintegration on the impact parameter; (d) the dependence of the mean g-particle multiplicity on the impact parameter.

Thus, in terms of our geometrical concepts, the mean g-particle multiplicity for the $0.3\sqrt{\sigma/\pi} - 0.5\sqrt{\sigma/\pi}$ interval will be 0.75 ± 0.09.

The scheme shown in fig. 1 illustrates the use of an ensemble of events when only the numbers n_{ch} and n_g were recorded. In the case where additional information has been obtained (i.e. the numbers n_λ, Q, etc.), the impact-parameter dependence of mean particle multiplicity may be found by different techniques (from different correlations of $\langle n_j \rangle$ with other n_i and Q).

3. Results and discussion

The above formulae and the CEM-calculated ensembles of interactions of 3.6 GeV/nucleon ^{22}Ne nuclei with H nuclei (617 events), CNO nuclei (1629 events),

and Ag, Br nuclei (2730 events) were used to obtain the dependencies of the number of all charged particles (n_{ch}) per event and of the mean multiplicity of these particles in a star ($\langle n_{ch} \rangle$) on the impact parameter (fig. 2a). Fig. 2b shows similar dependence of the multiplicity and the mean multiplicity of g-particles in a disintegration. The techniques treated in this work were checked for consistency by using the impact parameter prescribed in the CEM calculations for a particular event and by obtaining the "direct" dependencies of the mean multiplicities $\langle n_{ch} \rangle$ and $\langle n_g \rangle$ on the impact parameter. From fig. 2 it is seen that the dependencies on the Monte Carlo sample

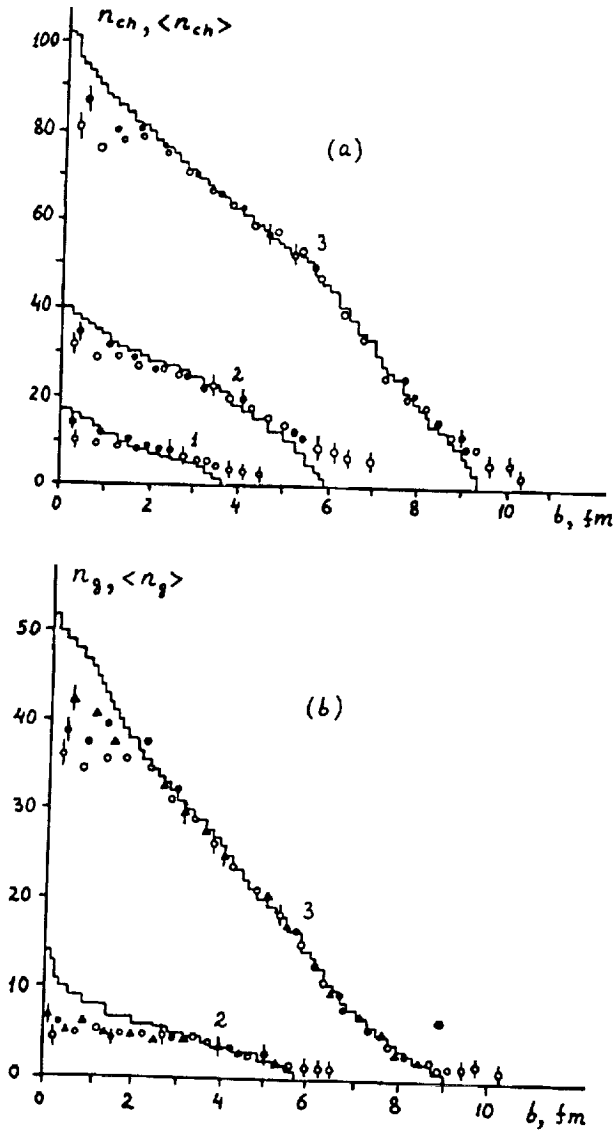

Fig. 2. The impact-parameter dependencies of the number and of the mean multiplicity of all charged particles (a) and of g-particles (b) in calculated interactions of 3.6 GeV/nucleon ^{22}Ne nuclei with hydrogen nuclei (1), with CNO nuclei (2) and with AgBr nuclei (3). The histograms are the dependencies $n_{ch}(b_i)$ and $n_g(b_i)$ inferred from the n_{ch} and n_g multiplicity distributions. The filled-in circles and triangles are the dependencies $\langle n_i \rangle (b_i)$ inferred from correlations with n_s and with n_{ch}, respectively. The open circles are the results of the straightforward verification by CEM calculations.

$\langle n_{ch}\rangle(b)$ and $\langle n_g\rangle(b)$ obtained by different techniques, including the direct methods, coincide with each other in remarkable agreement. The agreement is observed for all three reactions which differ substantially in the masses of interacting nuclei, in the variation range of the mean particle multiplicity, and in the variation range of the impact parameter in a disintegration. [The analysis of the dependence of particle number on b has shown that the functions $n_i(b_i)$ have significant dispersion, so only the dependencies of mean multiplicities inferred from correlations should be treated.]

The results obtained indicate that the impact parameter defines unambiguously the mean characteristics of a nucleus-nucleus interaction event. Therefore, given five dependencies of the types $\langle n_b\rangle$, $\langle n_g\rangle$, $\langle n_s\rangle$, $\langle n_{ch}\rangle$ and $\langle Q\rangle$ on impact parameter, one can readily obtain twenty correlation dependencies of the types $\langle n_i\rangle(n_j)$ which are frequently analyzed in theoretical and experimental studies of nucleus-nucleus interactions.

The experimental dependencies of the mean multiplicities of particles produced during the first (fast) stage of nucleus-nucleus interaction on impact parameter and those calculated in terms of two modifications of the cascade-evaporation model [12,13]) are compared in figs. 3 and 4 and table 1.

From the data obtained (fig. 3a, c and table 1) it follows that the mean total charge of the non-interacting fragments of a projectile nucleus (whose velocities are close to the projectile velocity and whose transverse momenta are lower than 230 MeV/c nucleon) depends on the impact parameter and, obviously, on the masses of colliding nuclei. A nearly linear dependence $\langle Q\rangle(b)$ with a positive coefficient depending on projectile-nucleus mass is obtained in the collisions of relativistic nuclei with light (CNO) and heavy (AgBr) nuclei in most of the impact-parameter ranges. The coefficient proved to be 1.4 charge unit/fm in the case of ^{22}Ne, and almost 2.5 times as high (3.4 charge unit/fm) in the case of ^{56}Fe. In central collisions (at low values of b) the coefficient decreases with decreasing b. The effect is enhanced by increasing the mass of the colliding nuclei.

Both cascade-evaporation model versions describe qualitatively the trend in the experimental correlation dependencies but show a systematic excess over experimental data for a range of small b.

The mean multiplicity of s-particles (the produced pions with energy $E > 60$ MeV, and the interacting protons with energy $E > 400$ MeV and transverse momentum $P > 230$ MeV/c) increases with decreasing impact parameter of collision (see fig. 3b, d) in all the interaction types examined. Note the similar absolute values of the impact-parameter dependencies of the s-particle multiplicities for different beams and energies.

The data of table 1 indicate that the multiplicity n_s increases with target-nucleus mass. In the case of interactions at the impact parameters ranging from 2 to 4 fm, for example, the experimental value of $\langle n_s\rangle$ is 8.9 ± 1.2 for the ^{22}Ne + CNO collisions and $\langle n_s\rangle = 30 \pm 4$ for the ^{22}Ne + AgBr collisions.

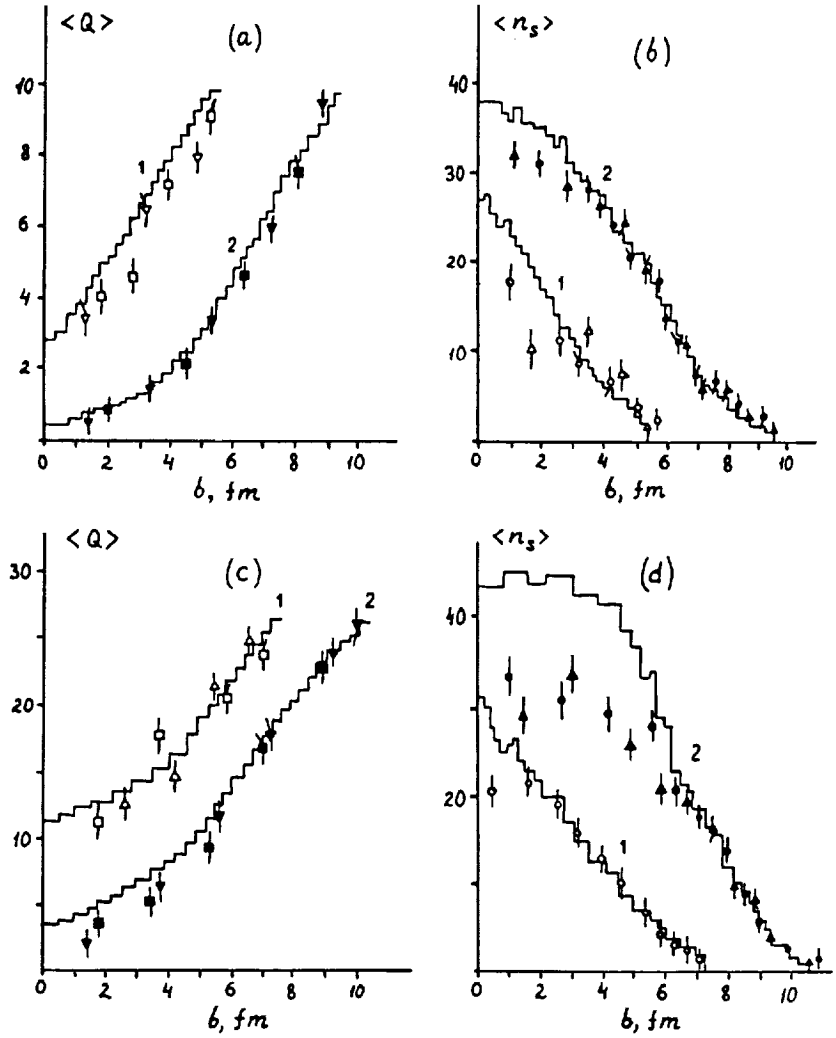

Fig. 3. The impact-parameter dependencies of the mean total charge (Q) of projectile-nucleus fragments (a, c) and of the mean s-particle multiplicity (b, d) in the interactions of 3.6 GeV/nucleon ^{22}Ne nuclei (a, b) and 1.8 GeV/nucleon ^{56}Fe nuclei (c, d) with CNO nuclei (1) (open circles) and with AgBr nuclei (2) (filled-in circles). The experimental dependencies are inferred from correlations with Q (circles), with n_s (squares), with n_g (triangles) and with n_{ch} (inverted triangles). The histograms are the dependencies calculated in terms of CEM (a, b) and DCM (c, d).

The examination of the impact-parameter dependencies of the mean multiplicities of g-particles (the 26-400 MeV knocked-out from target nuclei), $\langle n_g \rangle(b)$ (fig. 4a, c), has shown that the form of $\langle n_g \rangle(b)$ is substantially affected by the target-nucleus mass. In the case of interactions with CNO nuclei, $\langle n_g \rangle$ proves in practice to be nearly independent of impact parameter at $b = 0$–3 fm; afterwards, the multiplicity decreases slightly with increasing b. The variation of the projectile-nucleus mass by a factor of more than 2 (when going from ^{22}Ne to ^{56}Fe) does not result in any pronounced changes of the character or numerical values of the given correlation.

In the case of collisions with heavy nuclei, on the contrary, the target-nucleus mass affects substantially the g-particle multiplicity. In this case, a nearly linear

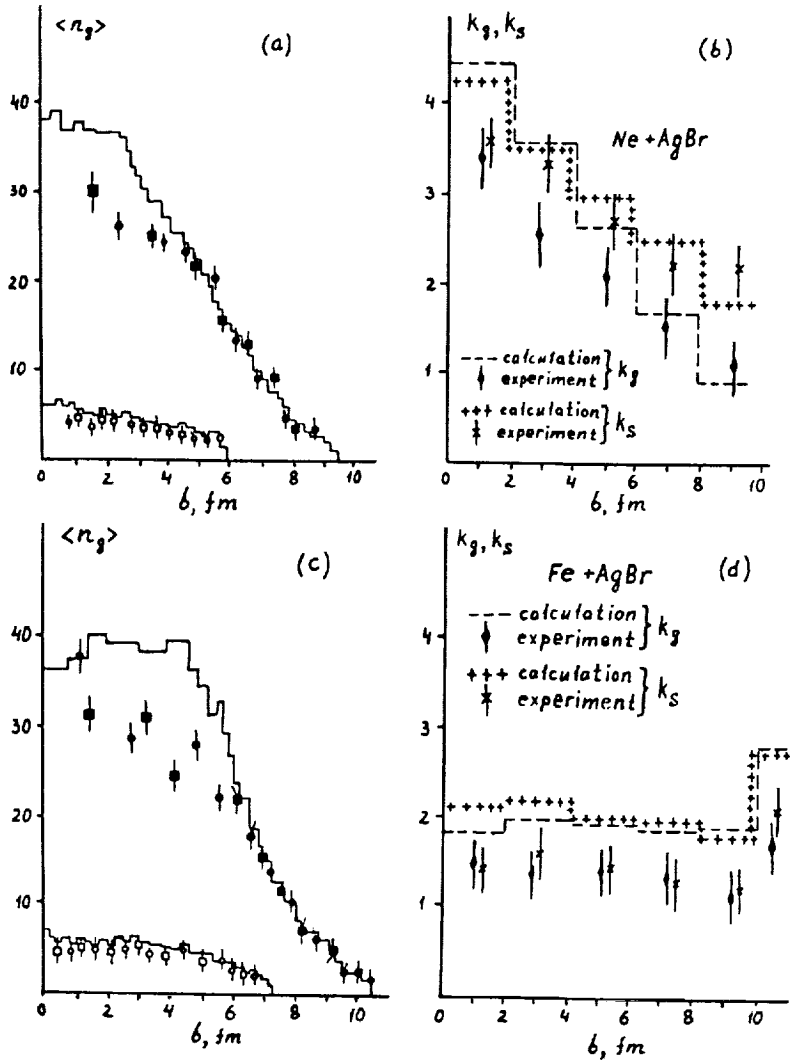

Fig. 4. The impact-parameter dependencies of the mean g-particle multiplicity (a, c) and of the specific multiplicities of s- and g-particles (b, d) in the interactions of 3.6 GeV/nucleon ^{22}Ne nuclei (a, b) and 1.8 GeV/nucleon ^{56}Fe nuclei (c, d) with CNO nuclei (open circles), and with AgBr nuclei (filled-in circles). The experimental dependencies are inferred from correlations with Q (circles), and with n_s (squares). The k_s and k_g dependencies are for AgBr target. The histograms are the dependencies calculated in terms of CEM (a, b) and DCM (c, d).

dependence $\langle n_g \rangle(b)$ is observed at a high negative coefficient amounting to 4 g-particles/fm.

The comparison between the experimental and model-calculated dependencies $\langle n_g \rangle(b)$ and $\langle n_s \rangle(b)$ has shown that the models can quantitatively represent the peripheral collisions only. At low values of impact parameters ($b < 5$ fm for ^{22}Ne + AgBr and $b < 6$ fm for ^{56}Fe + AgBr collisions), the calculation results are systematically in excess of the experimental data.

For the purposes of further analysis, it is expedient to present the s- and g-particle multiplicities per single interacting proton of a projectile nucleus:

$$k_s = \frac{\langle n_s \rangle}{Z - \langle Q \rangle}, \qquad k_g = \frac{\langle n_g \rangle}{Z - \langle Q \rangle}, \tag{5}$$

where Z is the charge of the projectile nucleus.

TABLE 1

Mean values of g- and s-particle multiplicities and of Q as functions of impact parameter in ^{56}Fe and ^{22}Ne collisions with light and heavy photoemulsion nuclei. Shown in parentheses are the cascade-evaporation model calculation results

Reaction type	Type of secondary	Range of impact parameter (fm)						
		0-2	2-4	4-6	6-8	8-10	10-12	0-12
Fe ± AgBr	$\langle n_g \rangle$	34 ± 3	28 ± 2	24 ± 1	14.1 ± 0.8	3.3 ± 0.2	1.6 ± 0.2	12.9 ± 1.1
		(39.22)	(38.63)	(29.43)	(14.23)	(4.41)	(1.87)	(15.32)
	$\langle n_s \rangle$	33 ± 3	33 ± 3	24 ± 2	13 ± 1	3.5 ± 0.3	1.9 ± 0.2	12.9 ± 1.0
		(44.4)	(42.87)	(29.05)	(13.82)	(4.13)	(1.81)	(15.71)
	$\langle Q \rangle$	3.2 ± 0.4	5.1 ± 0.8	9.4 ± 1.1	15.8 ± 0.9	23.0 ± 0.3	25.1 ± 0.2	16.1 ± 0.8
		(5.09)	(6.02)	(10.94)	(18.72)	(23.64)	(25.36)	(18.05)
Fe ± CNO	$\langle n_g \rangle$	4.5 ± 0.8	4.3 ± 0.7	3.1 ± 0.6	1.8 ± 0.4			2.87 ± 0.14
		(5.43)	(5.09)	(3.82)	(2.71)			(3.93)
	$\langle n_s \rangle$	21.1 ± 1.3	14.5 ± 0.9	6.7 ± 0.8	2.4 ± 0.4			8.12 ± 0.50
		(24.9)	(15.23)	(7.44)	(3.95)			(9.52)
	$\langle Q \rangle$	10.1 ± 1.4	17.8 ± 1.1	21.8 ± 0.6	24.0 ± 0.5			20.0 ± 0.4
		(13.36)	(16.72)	(21.32)	(23.95)			(20.66)
Ne ± AgBr	$\langle n_g \rangle$	33 ± 4	22 ± 4	14 ± 3	6.5 ± 0.8	0.7 ± 0.2		10.9 ± 0.8
		(39.56)	(29.31)	(16.83)	(5.32)	(0.996)		(12.15)
	$\langle n_s \rangle$	35 ± 4	30 ± 4	18 ± 3	9.5 ± 0.9	1.3 ± 0.3		14 ± 1
		(37.86)	(29.31)	(18.93)	(7.79)	(2.23)		(13.82)
	$\langle Q \rangle$	0.3 ± 0.2	1.4 ± 0.2	3.3 ± 0.3	5.7 ± 0.8	9.4 ± 0.4		5.0 ± 0.3
		(1.18)	(1.70)	(3.53)	(6.81)	(8.70)		(5.43)
Ne ± CNO	$\langle n_g \rangle$	3.7 ± 0.7	2.6 ± 0.4	1.7 ± 0.3				2.3 ± 0.2
		(5.23)	(3.97)	(1.7)				(2.97)
	$\langle n_s \rangle$	19 ± 3	8.9 ± 1.2	3.9 ± 0.4				7.8 ± 0.7
		(20.5)	(11.1)	(3.21)				(8.33)
	$\langle Q \rangle$	3.3 ± 0.5	6.4 ± 0.8	8.0 ± 0.8				6.8 ± 0.3
		(3.89)	(5.89)	(8.29)				(6.85)

The resultant impact-parameter dependencies of the multiplicities in the case of the interactions of ^{22}Ne and ^{56}Fe nuclei with heavy photoemulsion nuclei (fig. 4b, d) exhibit very different trends. The specific multiplicities decrease systematically with increasing impact parameter in the case of ^{22}Ne + AgBr interactions, whereas any noticeable correlation between k_s, k_g and b is absent in the case of ^{56}Fe + AgBr interactions.

The difference in the absolute values of k_s for ^{22}Ne and ^{56}Fe projectiles is readily explained by a greater fraction of charged pions, $\langle n_\pi \rangle = k_s - 1$, per single interacting proton of a projectile nucleus when changing from 1.8 GeV/nucleon (^{56}Fe) interactions to the 3.6 GeV/nucleon (^{22}Ne) interactions. Such an explanation is corroborated by the similar variations of k_s in the interactions with light (CNO) nuclei (see table 1).

The k_g value defines, first of all, the ratio of the masses of interacting nuclei. If the target-nucleus mass exceeds the projectile mass, the specific g-particle multiplicity

will exceed unity, and vice versa (see table 1). Any increase in the collision energy enhances the cascading because the latter involves both the produced particles and the singly interacting nucleons. The increase of k_s and k_g with decreasing impact parameter in the case of ^{22}Ne + AgBr, and the absence of any definite dependence in the case of ^{56}Fe + AgBr, seem to us to indicate a substantial effect of the produced particles on the cascading, especially in the central and nearly central interactions. The cascade-type models represent quite adequately the experimental dependencies $k_s(b)$ and $k_g(b)$, thereby indicating that the nucleus-nucleus interaction can be described in terms of these models. At the same time, the quantitative differences between the calculated and experimental data rise systematically with an increasing interacting nucleon number in an individual collision. For example, the model can well describe the ^{22}Ne collisions with light photoemulsion nuclei [except the range $b = 0$–2 fm; the interval of differences increases up to $b = 0$–4 fm in the case of ^{22}Ne + AgBr collisions and reaches 0–6 fm in the case of ^{56}Fe + AgBr interactions].

4. Conclusions

The main results of the present work can be summarized as follows:

(1) The impact parameter of a collision has been shown to unambiguously define the mean multiplicities of secondaries in the interaction;

(2) The techniques for finding the impact-parameter dependence of mean particle multiplicity from the data on the total ensemble of interactions have been proposed and tested;

(3) The projectile-nucleus energy, the masses of the colliding nuclei, and the species of the examined secondaries have been found to substantially affect the impact-parameter dependencies of the mean and specific multiplicities of the secondaries.

(4) The experimental results have been compared with the data calculated in terms of the cascade-evaporation model. The particular impact-parameter values at which the theoretical data differ from the experimental results have been found.

E.V. Benton would like to acknowledge partial support by NASA under grant number NAG9-235.

References

1) R. Albrecht *et al.*, Z. Phys. **C38** (1988) 3
2) S.D. Bogdanov and V.I. Ostroumov, Izv. Akad. Nauk SSSR, Ser. Fiz. **40** (1976) 965
3) V.A. Antonchik, V.A. Bakaev and V.I. Ostroumov, Yad. Fiz. (Sov. J. Nucl. Phys.) **33** (1981) 737
4) V.A. Antonchik *et al.*, JINR Preprint, Dubna, P1-83-577 (1983)
5) S.A. Krasnov *et al.*, JINR Rapid Communications, Dubna, 16-86 (1986) 11
6) S.A. Krasnov *et al.*, JINR Preprint, Dubna, P1-89-213 (1989)
7) V.E. Dudkin, E.E. Kovalev, N.A. Nefedov, V.A. Antonchik, S.D. Bogdanov, V.I. Ostroumov, H.J. Crawford and E.V. Benton, Nucl. Phys. **A509** (1990) 783

8) V.E. Dudkin, E.E. Kovalev, N.A. Nefedov, V.A. Antonchik, S.D. Bogdanov, V.I. Ostroumov, E.V. Benton and H.J. Crawford, Nucl. Phys. **A530** (1991) 759
9) G.S. Shabratova *et al.*, Acta Phys. Slovaca **28** (1978) 132
10) Cosiče-Leningrad collaboration, Yad. Fiz. (Sov. J. Nucl. Phys.) **29** (1979) 117
11) V.A. Antonchik *et al.*, Yad. Fiz. (Sov. J. Nucl. Phys.) **46** (1987) 1344
12) K.K. Gudima and V.D. Toneev, Nucl. Phys. **A400** (1983) 173
13) V.S. Barashenkov *et al.*, JINR Preprint, Dubna, E2-83-117 (1983)
14) M. Demoulins *et al.*, Phys. Lett. **B241** (1990) 476

APPENDIX H

Multiplicities of Secondaries in Nuclear Interactions, Induced by ^{20}Ne, ^{40}Ar and ^{56}Fe Nuclei at 0.1-0.5 GeV/Nucleon

by

V.E. Dudkin, E.E. Kovalev, N.A. Nefedov, V.A. Antonchik
S.D. Bogdanov, V.F. Kosmach, A.Yu. Likhachev, J. Hassan
E.V. Benton and H.J. Crawford

Nuclear Physics A568 (1994) 906–916
North-Holland

NUCLEAR
PHYSICS A

Multiplicities of secondaries in nuclear interactions, induced by ^{20}Ne, ^{40}Ar and ^{56}Fe nuclei at 0.1–0.5 GeV/nucleon

V.E. Dudkin, E.E. Kovalev, N.A. Nefedov

Research Test Center for Radiation Safety of Space Flights of the Ministry of Public Health of Russia, 123182 Moscow, Russian Federation

V.A. Antonchik, S.D. Bogdanov, V.F. Kosmach, A.Yu. Likhachev, J. Hassan

St. Petersburg State Technical University, St. Petersburg, Russian Federation

E.V. Benton [1]

Physics Department, University of San Francisco, San Francisco, CA 94117-1080, USA

H.J. Crawford

University of California Space Sciences Laboratory, Berkeley CA 94720, USA

Received 26 October 1992
(Revised 23 June 1993)

Abstract

Multiplicities of various species of charged secondaries produced in inelastic interactions of ^{20}Ne, ^{40}Ar and ^{56}Fe nuclei with emulsion nuclei at 0.1–0.5 GeV/nucleon have been measured. The data obtained are compared with the results for interactions of higher energy nuclei with emulsion nuclei. The dependences of the nucleus–nucleus interaction parameters on masses and energies of colliding nuclei are examined.

Key words: NUCLEAR REACTIONS Em(^{20}Ne, X), $E = 0.28$ GeV/nucleon; Em(^{40}Ar, X), $E = 0.27$ GeV/nucleon; Em(^{56}Fe, X), $E = 0.48$ GeV/nucleon; measured σ_{in}, mean multiplicities $\langle n_i \rangle$ of charged secondaries in reactions with hydrogen, light (C, N, O) and heavy (Ag, Br) target nuclei. Examined the relationship $\langle n_i \rangle$ (E, A_p, A_t).

[1] USF portion of the work partially supported by NASA Grant No. NAG9-235, NASA-Johnson Space Center, Houston.

SSDI 0375-9474(93)E0433-9

1. Introduction

Photoemulsion measurements of secondary-particle multiplicities in nuclei-induced interactions below 1 GeV/nucleon have had a revival of interest among researchers recently [1]. Copious data have been obtained on interactions of nuclei of relativistic and ultra-relativistic velocities [2–5], so the necessity has arisen for deriving comparative data measured by identical techniques, but at lower projectile velocities.

The present work provides new experimental data on interactions of Ne, Ar and Fe nuclei at lower energies with emulsion nuclei and analyzes the effect of projectile velocity on the basic characteristics of a nucleus–nucleus interaction event.

2. Experimental design

Photoemulsion (Em) chambers assembled of Russian-manufactured nuclear emulsion BR-2 layers were irradiated by 0.39 GeV/nucleon ^{20}Ne, 0.48 GeV/nucleon ^{40}Ar, and 0.583 GeV/nucleon ^{56}Fe nuclei at the BEVALAC accelerator of the University of California, Berkeley. The layers were developed and marked at the High Energy Laboratory of JINR (Dubna). The interactions were sought by double inspection of tracks at a 60×15 magnification. The average ranges of stopping ions were 61.75 ± 0.06 mm for 0.39 GeV/nucleon ^{20}Ne ions, 53.11 ± 0.05 mm for 0.48 GeV/nucleon ^{40}Ar ions, and 45.45 ± 0.04 mm for 0.583 GeV/nucleon ^{56}Fe ions. These ranges can be approximated by the range–energy dependence for multiply charged ions [6,7], thereby permitting the energies of projectile nuclei to be determined at the points of their interactions with photoemulsion nuclei. The error in finding the energy of a split-inducing nucleus did not exceed 1%. Accuracy in the finding of the projectile energy in the interaction point is due to the very small spread of the BEVALAC beam energy. Determined from the stopping ion range distributions, experimental stragglings were (0.95 ± 0.06)%, (0.96 ± 0.05)% and (0.42 ± 0.02)% for ^{20}Ne, ^{40}Ar and ^{56}Fe ions, respectively. These stragglings proved to be more than theoretical values: 0.26%, 0.16% and 0.14% calculated according to Barkas et al. [8] for the ions mentioned above. At the same time, the results obtained showed the possibility of accurately defining the projectile energy in the interaction point by measuring the particle path in emulsion before collision and using the range–energy dependence for heavy ions. The ranges of nuclei of different energies and charges calculated by these techniques [6–9] were also used to identify secondaries.

The total statistics of the recorded events were 436 (^{20}Ne + Em, $E_0 = 0.1$–0.39 GeV/nucleon (the mean value of projectile energy $\langle E_0 \rangle = 220 \pm 20$ MeV/nucleon)), 396 (^{40}Ar + Em, $E_0 = 0.1$–0.48 GeV/nucleon ($\langle E_0 \rangle = 270 \pm 20$ MeV/

Table 1
Experimental statistics of events used for present analysis

Projectile	$\langle E_0 \rangle$ (MeV/nucleon)	Target	Number of events
^{20}Ne	220 ± 20	H	37
		CNO	96
		AgBr	163
^{40}Ar	270 ± 20	H	23
		CNO	63
		AgBr	116
^{56}Fe	480 ± 20	H	71
		CNO	218
		AgBr	322

nucleon)), and 1005 (^{56}Fe + Em, $E_0 = 0.1$–0.58 GeV/nucleon ($\langle E_0 \rangle = 480 \pm 20$ MeV/nucleon)), while the mean free paths for interaction were 11.99 ± 0.58 cm, 10.07 ± 0.57 cm and 8.19 ± 0.26 cm, respectively. A number of events (1, 109) were selected randomly from the overall statistics of the detected collisions and were then processed by the standard techniques [2,3]. The species of target-nuclei were found and the energies and changes of all secondaries were determined. The statistics used for our analysis are presented in Table 1.

3. Interaction cross sections

The experimental interaction paths of Ne, Ar and Fe nuclei, the numbers of interactions with a selected species of target nuclei, and concentrations of individual nuclei in emulsion [10] were used to find the cross sections for inelastic

Table 2
Total inelastic cross sections (mb)

Projectile		Target					
ion	energy (GeV/nucleon)	H	C	N	O	Br	Ag
Ne	0.22	330 ± 60	930 ± 100	990 ± 110	1040 ± 110	2060 ± 170	2380 ± 190
	3.6 [a]	360 ± 70	960 ± 110	1030 ± 120	1090 ± 130	2260 ± 210	2650 ± 240
Ar	0.27	360 ± 80	1070 ± 140	1130 ± 150	1190 ± 150	2590 ± 240	2930 ± 280
	1.1 [b]	510 ± 90	1190 ± 150	1260 ± 150	1330 ± 150	3020 ± 270	3480 ± 290
Fe	0.48	450 ± 60	1540 ± 110	1580 ± 120	1630 ± 130	2820 ± 300	3230 ± 340
	1.8 [c]	740 ± 70	1750 ± 110	1800 ± 120	1860 ± 130	3090 ± 260	3300 ± 280

[a] See ref. [11].
[b] See ref. [3].
[c] See ref. [2].

interactions with particular emulsion nuclei (see Table 2). Table 2 also presents the experimental data [2,3,11] obtained at higher energies. From the comparison it is seen that, as the projectile energy increases from a few hundred MeV/nucleon to a few GeV/nucleon, the cross sections also increase; that is in agreement with the data of the experiment by Webber et al. [12] and Chen et al. [13]. In the early experiments with < 1 GeV/nucleon nuclei, the nuclear interaction cross sections for $p + A$ collisions were noted to increase with increasing projectile mass more rapidly than in A–A reactions. In our experiment the difference in the increases is less perceptible. The approximation of the cross sections for non-relativistic and relativistic interactions by the Bradt–Peters formula:

$$\sigma = \pi R_0^2 \left[A_p^{1/3} + A_t^{1/3} - \beta_0 \left(A_p^{-1/3} + A_t^{-1/3} \right) \right]^2, \tag{1}$$

using the least squares method, has yielded $R_0 = 1.27 \pm 0.03$ fm, $\beta_0 = 1.14 \pm 0.11$; $\chi^2/k = 0.8$, and $R_0 = 1.28 \pm 0.01$ fm, $\beta_0 = 0.75 \pm 0.05$; $\chi^2/k = 1.81$, for energies of 0.1–0.5 GeV/nucleon and above 1.0 GeV/nucleon, respectively. In the case of relativistic interactions, the factors R_0 and β_0 proved to be close to those presented in ref. [14] which summarized the data on the interactions of nuclei with energies above 1 GeV/nucleon ($R_0 = 1.32 \pm 0.01$ fm and $\beta_0 = 0.85 \pm 0.03$). It should be noted that at both $E_0 \geqslant 1$ GeV/nucleon and $E_0 = 0.1$–0.5 GeV/nucleon, the R_0 value, which characterizes the radii of interacting nuclei, remains constant. The only variable is the overlap parameter β_0 which rises with decreasing projectile energy. This means that the interacting nuclei become more transparent at $E_0 = 0.1$–0.5 GeV/nucleon. Such a variation in β_0 (at a constant R_0 value) is not a trivial result and seems to us to necessitate further experimental studies [15].

4. Multiplicities of secondaries

The experiments discriminate between slow target fragments (b-particles, with $E_p \leqslant 26$ MeV), fast fragments of a target nucleus (g-particles, with $26 < E_p < 400$ MeV), "shower" particles (s-particles, with $E_p > 400$ MeV and $E_\pi > 60$ MeV, which are interacting projectile protons and produced π-mesons), s′-particles (which are relativistic singly charged fragments of a projectile nucleus with $E_p < 26$ MeV in the system of the projectile and which are excluded from the number of s-particles), g′-particles (which are projectile fragments with $Z = 2$), and b′-particles (which are projectile fragments with $Z \geqslant 3$). In addition, the total charge Q of the non-interacting projectile fragments was found.

Fig. 1 shows the laboratory relative-rapidity distribution Y/Y_0 ($Y = \frac{1}{2}\ln[(E + P_\parallel)/(E - P_\parallel)]$; Y_0 is the projectile rapidity) of the examined particles for interactions of argon nuclei with light and heavy nuclei at non-relativistic and relativistic velocities of a projectile. The statistics presented in Antonchik et al. [3], where the

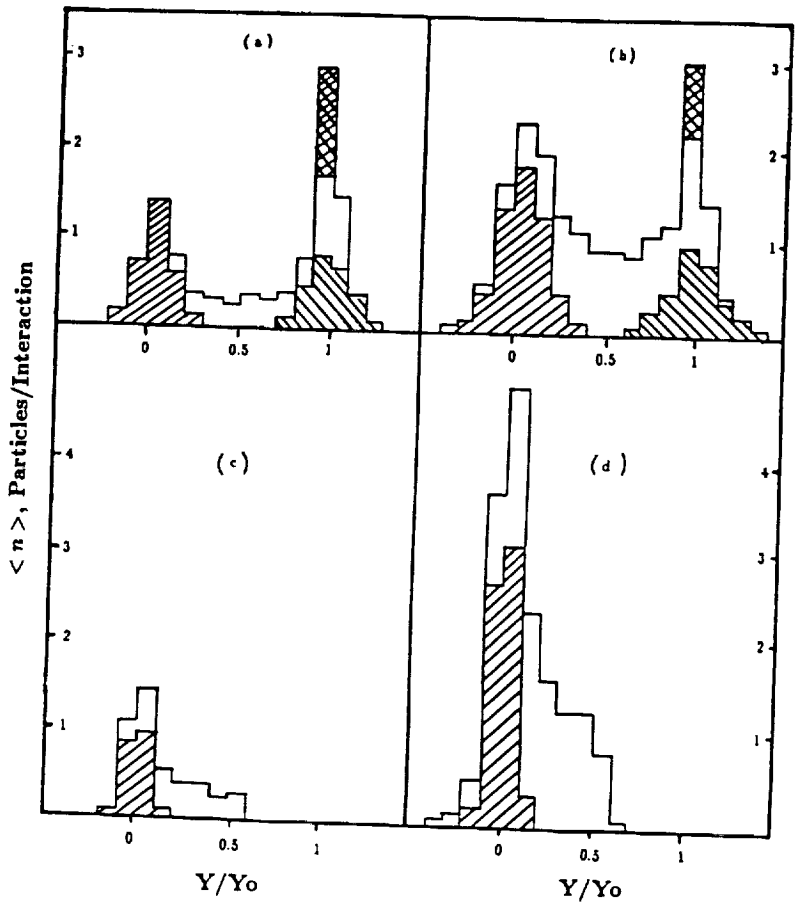

Fig. 1. Relative-rapidity (Y/Y_0) distributions (Y_0 is the projectile rapidity) for (a) the interactions ^{40}Ar + C, N, O and (b) ^{40}Ar + Ag, Br at energy 0.27 GeV/nucleon, and for (c) interactions ^{40}Ar + C, N, O and (d) ^{40}Ar + Ag, Br at a 1.1 GeV/nucleon projectile energy. The non-shaded area indicates g- and s-particles; right-inclined hatches represent b-particles; left-inclined hatches are for (s′ + g′)-particles; and the doubly shaded area is for multiply charged ($Z \geq 3$) fragments. For projectile energy 1.1 GeV/nucleon (c, d), only distributions corresponding to b- and g-particles are shown.

energies of secondaries were found for the b- and g-particles only, were for the case of relativistic nuclear interactions. The distributions presented in Figs. 1a, b exhibit two pronounced peaks due mainly to the b- and (s′ + g′)-particles, i.e. the particles emitted from an excited residual target nucleus (b-particles, $Y/Y_0 \simeq 0$) and from a projectile residue (s′- and g′-particles, $Y/Y_0 \simeq 1$). An additional contribution to the peak at $Y/Y_0 \simeq 1$ is from the projectile fragments (b′-particles) which may be treated as residues of a given nucleus on completing the slow stage. The non-shaded area (g-particles at $Y/Y_0 < 0.5$ and s-particles at $Y/Y_0 > 0.5$) is mainly located within the 0.1–0.9 relative-rapidity range and fills the gap between two peaks. From Fig. 1 it follows that, as regards the kinematic parameters, the b- and g-particles may be attributed to the target nucleus, and the b′-, g′-, s′- and s-particles to the projectile nucleus, although the correlation of the g- and

Table 3
Mean multiplicities of secondaries in non-relativistic interactions

Reaction type	$\langle n_b \rangle$	$\langle n_g \rangle$	$\langle n_s \rangle$	$\langle n_{s'} \rangle$	$\langle n_{g'} \rangle$	$\langle Q \rangle$	$\langle n_{in} \rangle$
Ne + H	0.14 ± 0.06	0.59 ± 0.08	0.54 ± 0.12	1.43 ± 0.20	1.03 ± 0.17	9.73 ± 0.12	0.5 ± 0.2
Ne + CHO	2.89 ± 0.12	1.54 ± 0.15	1.67 ± 0.16	1.69 ± 0.13	1.45 ± 0.13	8.35 ± 0.17	3.3 ± 0.4
Ne + AgBr	5.31 ± 0.42	3.54 ± 0.32	2.08 ± 0.17	1.53 ± 0.10	1.02 ± 0.08	7.50 ± 0.22	5.0 ± 0.5
Ne + Em	3.88 ± 0.25	2.52 ± 0.19	1.75 ± 0.11	1.57 ± 0.08	1.16 ± 0.07	8.06 ± 0.14	3.9 ± 0.3
Ar + H	0.61 ± 0.10	0.17 ± 0.08	0.26 ± 0.09	1.00 ± 0.21	0.35 ± 0.13	17.74 ± 0.11	0.6 ± 0.2
Ar + CNO	2.94 ± 0.17	1.16 ± 0.15	1.67 ± 0.23	2.33 ± 0.19	1.38 ± 0.15	16.65 ± 0.21	3.0 ± 0.4
Ar + AgBr	5.87 ± 0.48	4.38 ± 0.51	3.57 ± 0.34	2.78 ± 0.16	1.47 ± 0.12	14.25 ± 0.41	8.3 ± 0.9
Ar + Em	4.36 ± 0.31	2.90 ± 0.32	2.60 ± 0.22	2.44 ± 0.11	1.32 ± 0.09	15.40 ± 0.26	5.8 ± 0.5
Fe + H	0.36 ± 0.07	0.62 ± 0.16	1.06 ± 0.23	1.94 ± 0.28	1.02 ± 0.18	25.62 ± 0.35	0.8 ± 0.7
Fe + CNO	2.43 ± 0.14	2.26 ± 0.17	3.04 ± 0.24	3.46 ± 0.21	1.92 ± 0.12	22.18 ± 0.29	8.2 ± 0.6
Fe + AgBr	7.98 ± 0.38	8.17 ± 0.69	5.79 ± 0.47	3.38 ± 0.21	1.77 ± 0.12	19.55 ± 0.59	13.9 ± 1.2
Fe + Em	5.11 ± 0.27	5.18 ± 0.31	4.26 ± 0.34	3.24 ± 0.20	1.74 ± 0.11	21.19 ± 0.32	10.4 ± 0.7

s-particles with the respective nuclei is less stringent when compared with the case of b- and (s′ + g′)-particles.

Table 3 presents the mean multiplicities of the above-mentioned particles and shows the estimates of the number of the projectile nucleons involved in an interaction:

$$\langle n_{in} \rangle = A_p - \frac{A_p}{Z_p} \langle Q \rangle, \tag{2}$$

where A_p and Z_p are the projectile mass and charge numbers, respectively.

From Table 3 it follows that the non-relativistic nucleus–nucleus collisions exhibit some of the features found when studying the > 1 GeV/nucleon nuclear interactions [2,4,16,17], namely:

(1) the mean number of the interacting projectile nucleons $\langle n_{in} \rangle$ increases with target-nucleus mass;

(2) the singly-to-doubly charged projectile fragment ratio $\langle n_{s'}/n_{g'} \rangle$ is defined mainly by the projectile species and depends very little on the target mass;

(3) the specific multiplicities of the charged secondaries of all species, $\langle n_i \rangle / \langle n_{in} \rangle$, where subscript i is the type of secondary, prove to be below the respective mean multiplicities for the interactions of protons of the same velocities with emulsion nuclei;

(4) as the masses of interacting nuclei increase, the multiplicities of all particle species are observed to rise.

Thus, the analysis of the data has shown that the projectile energy decrease from 3.6 to 0.3 GeV/nucleon does not result in any variation of the qualitative behavioral features of the multiplicities of secondaries.

We used the data of Table 3, as well as the experimental results for 3.6 GeV/nucleon protons, carbon and oxygen [16], 3.2 GeV/nucleon ^{22}Ne [4], 1.1 GeV/nucleon ^{40}Ar [3], and 1.8 GeV/nucleon ^{56}Fe [2] beams, to study the mean multiplicities of the identified species of secondaries as a function of the masses and energies of colliding nuclei on the assumption that, on average, ^{14}N and ^{94}Nb are the light and heavy emulsion nuclei, respectively [17]. The dependence on the nuclear masses and energies was taken to be

$$\langle n_i \rangle = \alpha_0 A_p^{\alpha_p} A_t^{\alpha_t} E_0^{\alpha_E}, \tag{3}$$

where A_p and A_t are the mass numbers of projectile and target, respectively; E_0 is the projectile kinetic energy in GeV/nucleon. Parametrization of the above type is used frequently to study nucleus–nucleus interactions. The factor α_0 and power exponents α_p, α_t and α_E were determined by the nonlinear least squares method for the case of different precision measurements [18]. The zero approximation was selected from the linear approximation (by taking the logarithm in the right part of

Table 4
Coefficients of approximation of the dependence (3), obtained by least squares method

Particle type	α_0	α_p	α_t	α_E	χ^2_{23}
$\langle n_b \rangle$	0.28 ± 0.04	0.03 ± 0.03	0.68 ± 0.02	-0.12 ± 0.02	216
$\langle n_{s'} + n_{g'} \rangle$	0.32 ± 0.04	0.58 ± 0.04	0.07 ± 0.03	-0.07 ± 0.02	261
$\langle n_g \rangle$	0.037 ± 0.008	0.51 ± 0.05	0.81 ± 0.03	0.34 ± 0.03	114
$\langle n_s \rangle$	0.21 ± 0.04	0.52 ± 0.05	0.39 ± 0.02	0.70 ± 0.03	79
$\langle Q \rangle$	0.49 ± 0.02	0.97 ± 0.02	-0.06 ± 0.01	-0.033 ± 0.004	149
$\langle n \rangle$	1.38 ± 0.13	0.34 ± 0.03	0.38 ± 0.03	0.27 ± 0.02	185

Eq. (3)). The approximation was calculated (stoppage of the program) if the decrease in value of the residual sum of the squares in the kth step was smaller than 1%.

The errors (covariational matrix) of the sought factor and exponents were determined by means of linear approximation using the matrix of derivatives at the point of the $(k-1)$th approximation. The relative error of the initial data (of the multiplicities of different-species particles) was some 5–10%. In the case of the 27 experimental points which we have described by parametrization (3) (four unknowns), the relative error in the unknowns proved to be reduced, on average, by a factor of two to three, depending on the particular values of the matrix of derivatives at the point of the $(k-1)$th approximation.

The values obtained for the unknowns in parametrization (3), to be used to describe the dependence of the mean multiplicities of different-species particles, are presented in Table 4 which also shows values of the normalized sum of squares χ^2_{23} together with the values of the approximation coefficients for the mean multiplicity of all charged particles in an interaction $\langle n \rangle$.

We examine some of the dependences obtained. The b-particle multiplicity is characterized by an extremely weak dependence on A_p. As a nucleus–nucleus collision energy increases, the decrease of the mean multiplicity of b-particles becomes perceptible (the α_E value is negative). In the case of "evaporation" particles from a projectile residue $\langle n_{s'} + n_{g'} \rangle$ we again observe that any dependence on the mass of a collision partner nucleus in practice is absent and that the α_E value is negative. It seems to us that the similarity (to within experimental errors) among all the approximation coefficients for $\langle n_b \rangle$ and $\langle n_{s'} + n_{g'} \rangle$ (allowing the substitution of A_p for A_t) is indicative of identical mechanisms of the generation of these particular particle species (see also Fig. 1). The multiplicity of the g-particles, which are mostly target protons having interacted with some of the projectile nucleons, depends strongly on the target mass. The $\langle n_g \rangle / \langle n_b \rangle$ ratio characterizing the energy spectrum of target-emitted secondaries rises with an increase in both the projectile size, $\sim A_p^{0.48}$, and the target size $\sim A_t^{0.13}$. The energy dependence of the g-particle multiplicity in nucleus–nucleus interactions ($\alpha_E = 0.34 \pm 0.03$) has proved to be much weaker than in proton–nucleus interactions

($\alpha_E = 0.70$ [17]), contrary to the consequences of the simple superposition models which assume that the nucleus–nucleus interactions can be treated as a non-coherent sum of nucleon–nucleus, or even nucleon–nucleon, collisions. On the contrary, the multiplicity of s-particles (the generated pions included) exhibits an E_0-dependence close to that observed in the proton–nucleus interactions ($\alpha_E = 0.70 \pm 0.03$ and $\alpha_E = 0.70$, respectively). From Table 4 it follows that the mean total charge of non-interacting projectile fragments (this value characterizes a projectile residue after the rapid stage) decreases with increase in the partner-nucleus mass [2] and/or with increasing interaction energy: $\alpha_t < 0$, $\alpha_E < 0$. We are of the opinion that the dependence $\langle Q \rangle (E_0)$ observed at the 0.3–3.6 GeV/nucleon range may reflect the energy dependence of the nucleon–nucleon interaction cross section in this particular energy range. At ~ 0.3 GeV/nucleon the nucleon–nucleon interaction cross sections run through their minimum, so the interacting nuclei prove to be most transparent.

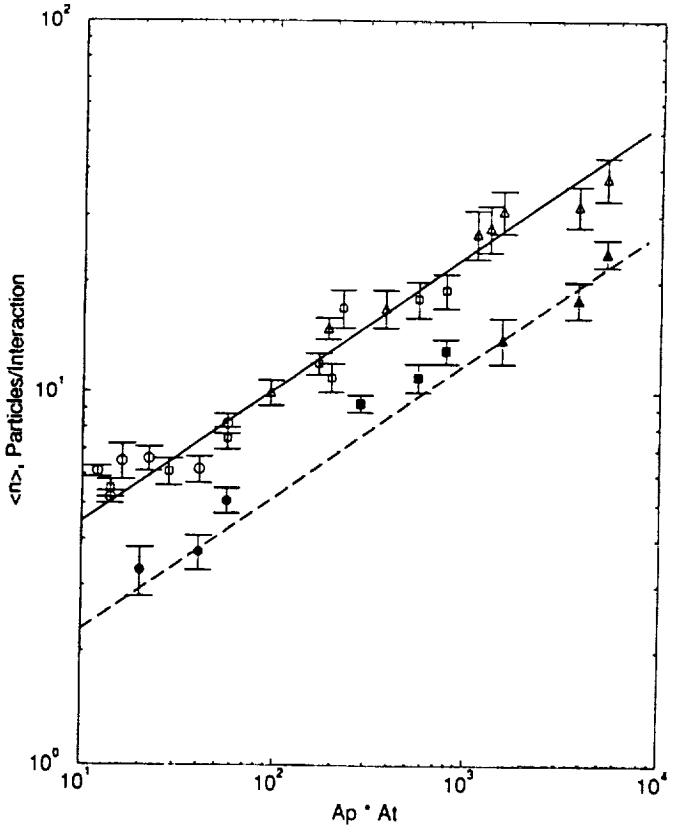

Fig. 2. The mean total multiplicity of all charged particles in an interaction versus the product of mass numbers of colliding nuclei and projectile energy. The symbols: ●, ○ = interactions with hydrogen; ■, □ = interactions with C, N, O, and ▲, △ = interactions with Ag, Br. The filled-in symbols (●, ■, ▲) and open symbols (○, □, △) correspond to projectile energies 0.1–0.5 GeV/nucleon and 1.8–3.6 GeV/nucleon, respectively. The solid and dashed lines are Eq. (3) approximations for energies 3.6 and 0.3 GeV/nucleon, respectively, and $\alpha_p = \alpha_t = 0.36$.

It is of great interest to examine the feasibility of describing the dependences of the total multiplicity of all charged particles in an interaction $\langle n \rangle = \langle n_b + n_g + n_s + n_{s'} + n_{g'} + n_{b'} \rangle$ on energies and masses of colliding nuclei. From Table 4 it is seen that the power-law exponents α_p and α_t of the dependences equal 0.38 ± 0.03 and 0.34 ± 0.03, respectively, i.e. exponents are the same to within the experimental errors. In its turn, the result obtained permits the mean multiplicity of all charged particles in interactions $A_p + A_t$ and $A_t + A_p$ to be regarded as identical, i.e. the effect of the mass of a colliding nucleus is of the same character, irrespective of whether the nucleus is a projectile or a target.

Since the total multiplicity $\langle n \rangle$ includes not only the recoil nucleus and evaporation particles (the particles already in nuclei), but also the newly generated mesons, the result obtained cannot be regarded as trivial, although the high χ^2_{23} value is indicative of poor applicability of the simple power-law model to describing the interaction of two nuclei.

Fig. 2 illustrates the feasibility of examining the dependence of the total multiplicity of secondaries on only two, rather than three (A_p, A_t and E) parameters, namely, on the product of the masses of colliding nuclei ($A_p \times A_t$) and on the projectile energy. The values of the total multiplicities (except those obtained in this work) have been borrowed from refs. [2–4,10,14,15,19,20]. The lines in Fig. 2 represent $\alpha_p = \alpha_t = 0.36$ at $E_0 = 0.30$ and 3.6 GeV/nucleon. The dependence (Eq. (3)) describes the data quite well.

5. Conclusions

Analyzing the available experimental and calculated data has shown that:

(1) a decrease of a projectile energy from a few GeV/nucleon to hundreds of MeV/nucleon gives rise to a 10–15% decrease in the total nuclear interaction cross section and, hence, to an increased mean-free path of projectile nuclei;

(2) in the non-relativistic energy range, the interactions involve a smaller degree of destruction of colliding nuclei;

(3) the multiplicity of the particles (b, s′, g′) emitted during the slow interaction stage is defined unambiguously by the mass of the parent nucleus, and also depends little on the mass and energy of partner nuclei;

(4) the 3.6–0.3 GeV/nucleon variation of a projectile energy fails to alter the form of secondary-particle multiplicity dependence on the masses of interacting nuclei.

The authors are indebted to the personnel of the Berkeley BEVALAC and of the JINR High Energy Laboratory for enabling the photoemulsions to be studied; we are also grateful to laboratory workers who shared with us the burden of searching for events.

References

[1] B. Jakobsson et al., Nucl. Phys. A509 (1990) 195
[2] V.E. Dudkin, E.E. Kovalev, N.A. Nefedov, V.A. Antonchik, S.D. Bogdanov, V.I. Ostroumov, H.J. Crawford and E.V. Benton, Nucl. Phys. A509 (1990) 783
[3] V.A. Antonchik et al., Yad. Fiz. (Sov. J. Nucl. Phys.) 51 (1990) 765
[4] A-ABGDDEKLMRTU-B Collaboration, Yad. Fiz. (Sov. J. Nucl. Phys.) 45 (1987) 123
[5] G. Singh et al., Phys. Rev. Lett. 61 (1988) 1073
[6] W. Galbraith et al., High energy and nuclear physics data handbook (Chilton, Didcot, UK, 1963)
[7] H.H. Heckman et al., Phys. Rev. C117 (1960) 544
[8] W.H. Barkas et al., Phys. Rev. 98 (1955) 605
[9] V.E. Dudkin, E.E. Kovalev, N.A. Nefedov, V.A. Antonchik, S.D. Bogdanov, V.I. Ostroumov, E.V. Benton and H.J. Crawford, Nucl. Phys. A530 (1991) 759
[10] VLGKLMT Collaboration, Joint Institute of Nuclear Research report JINR R1-8313 (Dubna, 1974)
[11] A.V. Belousov, Summary of thesis for Candidate's Degree (Leningrad, 1984)
[12] W.R. Webber et al., Phys. Rev. C41 (1990) 520
[13] C.-X. Chen et al., Proc. XXII Int. cosmic ray conf. (ICRC), Vol. 2, Dublin, 1991 (Leeds Univ. Press, Leeds, UK, 1992) p. 296
[14] All-union state standard, GOST 25645.212-85 (Standardizdat, Moscow, 1986)
[15] Hoang, Cork and H.J. Crawford, Z. Phys. C29 (1985) 611
[16] V.A. Antonchik et al., Yad. Fiz. (Sov. J. Nucl. Phys.) 39 (1984) 1228
[17] V.S. Barashenkov and V.D. Toneev, Interactions of high energy particles and atomic nuclei with nuclei (Atomizdat, Moscow, 1972)
[18] V.N. Grishin et al., Mathematical processing and interpretation of physics experiments (Moscow State University Editorial Board, Moscow, 1988)
[19] DELTW Collaboration, Nucl. Phys. A208 (1973) 626
[20] K.G. Gulamov et al., Dokl. Akad. Nauk UzSSR 2 (1977) 20

APPENDIX I

Fragmentation Cross Sections of ^{16}O Between 0.9 and 200 GeV/Nucleon

by

S.E. Hirzebruch, W. Heinrich, K.D. Tolstov, A.D. Kovalenko and E.V. Benton

Fragmentation cross sections of ^{16}O between 0.9 and 200 GeV/nucleon

S. E. Hirzebruch,[1] W. Heinrich,[1] K. D. Tolstov,[2] A. D. Kovalenko,[2] and E. V. Benton[3]
[1]*University of Siegen, Department of Physics, Adolf-Reichweinstr. 2, 5900 Siegen, Germany*
[2]*Laboratory of High Energies, Joint Institute for Nuclear Research, Dubna, Russia*
[3]*University of San Francisco, Department of Physics, San Francisco, California 94177* *
(Received 10 April 1992)

Inclusive cross sections for high energy interactions at 0.9, 2.3, 3.6, and 13.5 GeV/nucleon of ^{16}O with C, CR-39 ($C_{12}H_{18}O_7$), CH_2, Al, Cu, Ag, and Pb targets were measured. The total charge-changing cross sections and partial charge-changing cross sections for the production of fragments with charge $Z=6$ and $Z=7$ are compared to previous experiments at 60 and 200 GeV/nucleon. The contributions of Coulomb dissociation to the total cross sections are calculated. Using factorization rules the partial electromagnetic cross sections are separated from the nuclear components. Energy dependence of both components are investigated and discussed.

PACS number(s): 25.75.+r

I. INTRODUCTION

A. General

Depending on the impact parameter between the colliding nuclei, the type of reaction differs. For an impact parameter smaller than the sum of the projectile's and target's radii, the interaction is dominated by the strong force. For impact parameters which are too large for an overlap of target and projectile nuclei, the interaction is purely electromagnetic. For high projectile energies and strong electromagnetic fields (i.e., high-Z targets), the probability increases that this interaction leads to a fragmentation of the projectile or target nucleus. This effect, which is called electromagnetic dissociation (ED), has become the subject of systematic studies over the last years. Several groups report experimental results for the measurement of ED for different projectile [1–13] and target [14–17] fragmentation reactions. Recently, Olson *et al.* [18] reported direct observation of the giant dipole resonance of ^{16}O via electromagnetic dissociation.

During the last years, we have been measuring fragmentation cross sections for high-energy heavy-ion reactions. In this paper we present our results for ^{16}O projectiles at beam energies of 0.9 GeV/nucleon for H, CH_2, C, and Pb targets and at 2.3, 3.6, and 13.5 GeV/nucleon for H, CH_2, CR-39, C, Al, Cu, Ag, and Pb targets. Cross sections for the hydrogen target were calculated with the subtraction method using the CH_2/C data. We performed the 13.5-GeV/nucleon (14.5-GeV/c momentum) experiment at the Alternating Gradient Synchrotron (AGS) facility at Brookhaven National Laboratory (BNL). The 0.9-, 2.3-, and 3.6-GeV/nucleon experiments were carried out at the Synchrophasotron in Dubna (Russia).

In combination with the earlier published data for ^{16}O at 60 and 200 GeV/nucleon [9], we are now able to analyze the energy dependence of nuclear and electromagnetic cross sections in the energy range from 1 to 200 GeV/nucleon. Our interest is focused onto the following points: (a) The process of electromagnetic dissociation contributes significantly to the total charge-changing cross sections for heavy targets within the investigated energy range. With the complete set of our ^{16}O data, we are able to determine the energy dependence of the ED contribution of different targets to the total charge-changing cross sections. (b) Cross sections for the hydrogen target are important input data for astrophysical calculations which describe the propagation of cosmic-ray nuclei through interstellar space. The energy dependence of hydrogen partial cross sections, which we have observed beyond 1 GeV/nucleon [19,20], can be analyzed in more detail. (c) The validity of factorization rules for partial elemental cross sections for the heavier targets is tested.

B. Experimental setup

We used stacks of CR-39 ($C_{12}H_{18}O_7$) plastic nuclear track detectors, which were mounted up and downstream of the target. One stack consists typically of five sheets of CR-39. The CR-39 used was produced by American Acrylics and has a unique charge resolution. The detection threshold lies near the energy loss for relativistic boron ($Z=5$) ions. The detectors were etched in 6n NaOH at 70 °C for 36 or 48 h. After this procedure etch cones of relativistic nuclei with charges $Z=5$–8 could be detected. Using the advanced Siegen automatic measuring system, we scanned all detector surfaces, which contained typically 70 000 tracks each (1.4×10^6 objects for 1 target and energy). Further detailed information about the experimental setup and the automatic measuring system can be found in [21,22]. Since etch cones for particles with charge 5 were detected with a reduced efficiency, we could only determine partial cross sections for charges 6 and 7.

C. Nuclear and ED total cross sections

The total nuclear cross section is generally parametrized by overlap formulas, which have the form

*USF portion of this work partially supported by NASA Grant No. NAG9-235, Johnson Space Center, Houston, TX.

$$\sigma_{\text{nuc}}^{\text{tot}}(P,T)=\pi(R_T+R_P-\delta_{PT})^2 , \quad (1)$$

where R_T and R_P are the radii of target and projectile nucleus and δ_{PT} takes into account the drop of the nuclear density in the nucleus sphere. Since none of common cross-section formulas [23–26,38] take the ED effect into account (most of them are not even energy dependent), all of them give constant cross-section values for energies greater than 2 GeV/nucleon. This is expected to be correct for the nuclear component of the cross section because of the concept of limiting fragmentation.

For a theoretical description of the ED effect, Bertulani and Baur [27–29] have derived spectra of virtual photons, which are equivalent to the electromagnetic pulse a projectile suffers while passing a target nucleus (or vice versa). The intensity of the photon-number spectra dN/dE_γ is approximately proportional to $Z_T^2 \ln\gamma/E_\gamma$, where Z_T is the target charge, γ is the Lorentz factor of the projectile in the laboratory frame, and E_γ is the energy of an absorbed photon. The nucleus absorbs the photon by giant resonances, by the quasideuteron effect [30], or by resonances which lie in higher-photon-energy regimes (e.g., Δ resonances). The deexcitation of these excited modes can easily lead to the emission of protons or alpha particles or may even cause a severe destruction of the nucleus [10]. For high energies the relativistic contracted field of the target seen by the passing projectile is nearly a plane wave which contains all photon multipolarities with the same strength. In this case the total charge-changing ED cross section can be calculated by

$$\sigma_{\text{em}}^{\text{tot}}=\int n(E_\gamma)\sigma_\gamma(E_\gamma)dE_\gamma , \quad (2)$$

where $n(E_\gamma)$ is the virtual-photon spectrum and $\sigma_\gamma(E_\gamma)$ is the photonuclear charge-changing cross section for ^{16}O, respectively. This is equivalent to the method used by Weizsäcker [31] and Williams [32].

For smaller projectile energies, the strengths of the different multipolarities differ very much, especially in the photon-energy region of the ^{16}O giant resonance. For that reason electrical dipole ($E1$) absorption has to be distinguished from the electrical quadrupole ($E2$) absorption process. The total charge-changing ED cross section can then be calculated by evaluating (3):

$$\sigma_{\text{em}}^{\text{tot}}=\int [n_{E1}(E_\gamma)\sigma_{\gamma E1}(E_\gamma) + n_{E2}(E_\gamma)\sigma_{\gamma E2}(E_\gamma)]dE_\gamma . \quad (3)$$

Since photonuclear cross sections measured with real photon beams contain all absorption modes, separation of the $E1$ and $E2$ contributions has to be performed using several assumptions. In previous calculations of Norbury [33–35], $E2$ contributions were obtained using a Lorentzian distribution as an approximation of the quadrupole excitation cross section in combination with sum rules and empirical formulas for the position of the resonances. This method may be adequate for heavy nuclei. However, for light nuclei such as ^{16}O, for which the $E2$ photon cross section is fragmented in energy, this procedure is possibly incorrect.

In a recent theoretical paper by Fleischhauer and Scheid [36], (γ,n) and (γ,p) $E2$ cross sections for ^{16}O were calculated. In order to determine the charge-changing ED cross section, we use their cross sections $\sigma_{\gamma E2p}$ to calculate $\sigma_{\gamma E2}$. In addition to the (γ,p) process, the (γ,α) process plays an important role in the $E2$ absorption process. We use experimental data compiled by Fuller [37] to determine the contribution of the α channel to $\sigma_{\gamma E2}$ and estimate $\sigma_{\gamma E2\alpha}$ by multiplying the given experimental (γ,α) cross sections by the ratio of the relevant sum-rule values σ_0 in the photon-energy interval from 9 to 29 MeV [37]:

$$\sigma_{\gamma E2\alpha}=\sigma_{\text{expt}}(\gamma,\alpha)\frac{\sigma_0(E2)}{\sigma_0(E1)+\sigma_0(E2)} =\sigma_{\text{expt}}(\gamma,\alpha)0.176 . \quad (4)$$

The charge-changing $E2$ cross section is then calculated with help of (5):

$$\sigma_{\gamma E2}=\sigma_{\gamma E2p}+\sigma_{\text{expt}}(\gamma,\alpha)0.176 . \quad (5)$$

$\sigma_{\gamma E1}$ is obtained by subtracting $\sigma_{\gamma E2}$ from the experimental cross section $\sigma_{\gamma\text{expt}}$:

$$\sigma_{\gamma E1}=\sigma_{\gamma\text{expt}}-\sigma_{\gamma E2} . \quad (6)$$

The total charge-changing ED cross sections were calculated inserting (5) and (6) into (3) and using the virtual-photon spectra derived from Bertulani and Baur [27]. This method is effectively equivalent to using $n=0.978n_{E1}+0.022n_{E2}$ for the virtual-photon spectra in the whole γ-energy regime of the giant resonance. This effective weighting differs from the weighting of $n=0.96n_{E1}+0.04n_{E2}$, which we have used in [9]. The consequences of the different weighting, however, have a negligible influence on the calculated ED cross sections at CERN energies. At lower energies the calculated ED cross sections are about 3% smaller (Pb target, 2.3 GeV) than those using the method described in [9]. More details about the photonuclear data used can be found in [9].

The only adjustable parameter in our calculation of the total charge-changing ED cross section is b_{min}, which is the minimum impact parameter giving the maximum range of the strong force. For our calculations we used the overlap formula of Lindstrom *et al.* [23], which gives total nuclear cross sections σ_L. This parametrization is a fit to the data obtained with ^{12}C and ^{16}O projectiles at low Bevalac energies and is in good agreement with different experimental data, which we have compiled in [9]. We calculate the minimum impact parameter setting $b_{\text{min}}=(\sigma_L/\pi)^{0.5}$.

To determine the error of our calculation, we consider contributions by the error of the measured photonuclear cross section, the different weighting of the photon spectra, and the selection of b_{min}: (i) The error of the photonuclear data is estimated to be about 6% (after averaging where possible over several experimentalists data) [9]. (ii) Considering the weighting of different multipolarities, we assume an error of 50% for the calculated $E2$ cross section. This leads to a contribution to the total error of $\sigma_{\text{em}}^{\text{tot}}$ of about 4% for 2.3 GeV/nucleon and decreases to 1% at 200 GeV/nucleon. (iii) The influence of b_{min} on

TABLE I. Measured cross sections for ^{16}O projectiles. All cross sections are given in mb.

Target	Total charge-changing cross section	Partial cross section $\Delta Z=1$	Partial cross section $\Delta Z=2$
	0.9 GeV/nucleon		
H	302.6±22.7	67.5±4.8	67.3±5.7
CH_2	500.3±9.6	81.5±1.9	88.3±2.0
C	895.8±35.1	109.3±3.9	130.4±4.7
Pb	3426.0±204.7	277.8±15.1	301.9±15.8
	2.3 GeV/nucleon		
H	307.3±29.4	54.8±4.8	61.0±5.7
CH_2	497.9±17.7	70.5±2.9	81.2±3.4
CR-39	626.2±21.6	81.7±3.0	90.6±3.4
C	871.1±24.7	101.5±3.9	121.1±4.7
Al	1293.3±32.2	121.8±5.0	142.5±5.8
Cu	1955.2±51.9	162.7±8.2	181.5±9.0
Ag	2498.0±83.6	204.3±10.6	216.1±11.3
Pb	3479.4±142.9	320.8±17.4	299.6±18.0
	3.6 GeV/nucleon		
H	286.9±27.9	52.2±4.6	63.4±5.7
CH_2	481.8±16.8	69.2±2.8	82.6±3.5
CR-39	618.3±17.8	81.9±2.8	89.2±3.3
C	863.8±23.9	102.7±3.6	120.5±4.3
Al	1250.3±32.2	125.5±4.7	147.7±5.4
Cu	1941.8±51.9	171.7±9.7	188.4±9.2
Ag	2524.2±70.5	228.1±10.2	203.7±10.3
Pb	3545.8±179.0	389.2±17.1	302.2±19.9
	13.5 GeV/nucleon		
H	284.9±20.0	46.5±4.8	56.3±5.1
CH_2	491.0±12.2	67.7±3.0	75.5±3.2
CR-39	627.9±13.0	80.0±2.6	86.0±2.8
C	895.0±15.3	109.4±3.7	113.4±3.9
Al	1309.0±27.2	143.9±5.1	140.5±5.5
Cu	2042.0±54.0	219.2±9.0	193.9±9.0
Ag	2693.0±66.2	311.5±11.4	225.9±10.2
Pb	3936.0±76.0	588.7±22.3	334.4±17.8

the error of σ_{em}^{tot} is estimated by comparing predictions of empirical cross-section formulas. In addition to the formula of Lindstrom *et al.* [23], we use the parametrizations of Westfall *et al.* [24] and Benesh, Cook, and Vary [38]. Differences in b_{min} reach a maximum for the lead target. We use $\Delta b_{min}/b_{min}=5.7\%$, which is deduced from half the difference of b_{min} determined after Westfall *et al.* [24] and Lindstrom *et al.* [23] for the lead target. The compiled data of [9], which are best described by the formula of Lindstrom *et al.*, lie within the range of this error. The error to σ_{em}^{tot} inferred by the uncertainty of b_{min} is about 4.8% for the lower-energy data (0.9 GeV) and 1% for CERN energy data.

Assuming independence of the error sources, we obtain a total error of σ_{em}^{tot} of 10.3%, 7.6%, 7.5%, 6.6%, 6.2%, and 6.1% for the 0.9-, 2.3-, 3.6-, 13.5-, 60-, and 200-GeV/nucleon data, respectively. A further error source is multiple-photon excitation. Llope and Braun-Munziger [39] have shown that the contribution of multiple-photon excitation for ^{28}Si interacting with a Pb target accounts about 1% to the total ED cross section, almost independent of projectile energy. For the ^{16}O projectile, this effect should be even smaller than for ^{28}Si. According to the calculations of Llope and Braun-Munziger for ^{16}O and ^{238}U target [39], higher-order excitation contributes only 0.83% to the total ED cross section at 100 GeV/nucleon. An effect of this strength can be neglected in our case since the other errors discussed are considerably larger. For other projectile, target, and energy combinations, however, the contribution of multiple-photon excitation can be more significant [39,40].

II. RESULTS

The obtained experimental total and partial cross sections for charges 6 and 7 for the 0.9-, 2.3-, 3.6-, and 13.5-GeV/nucleon experiments are listed in Table I. The cross sections for the hydrogen target were calculated using the cross sections for CH_2 and C targets.

A. Total charge-changing cross sections

The calculated total charge-changing ED cross sections are given in Table II. The determined total ED cross sections were subtracted from the measured total ones to derive the pure nuclear component. In Fig. 1 we show measured total cross sections (solid squares), calculated ED cross sections (solid triangles), and difference cross sections (open squares) for Pb, Ag, and Cu targets. The horizontal lines give the average value of the difference cross section for the five energies (six for the lead target). The nuclear fragmentation cross sections obviously are constant at high energies. This means that the method we use succeeded in estimating the energy dependence of the ED contribution to the total reaction cross section.

The difference cross sections for the light targets H, C, and Al where the ED contribution is small are shown in Fig. 2. For these targets the total charge-changing cross sections are also constant in the whole energy regime from 2.3 to 200 GeV/nucleon.

The averaged nuclear cross sections for the five heavier targets and all energies are compared with results which

TABLE II. Calculated total ED cross sections for ^{16}O. All cross sections are given in mb.

Target	Kinetic energy (GeV/nucleon) 2.3	3.6	13.5	60	200
C	2.0±0.1	2.4±0.2	4.5±0.3	8.3±0.5	12.0±0.7
Al	7.8±0.6	9.7±0.7	19.0±1.3	36.1±2.2	53.6±3.3
Cu	32.7±2.5	41.6±3.1	84.9±5.6	166.8±10.3	251.7±15.4
Ag	76.0±5.8	98.5±7.4	207.4±13.7	416.6±25.8	636.6±38.8
Pb	194.4±14.8	259.4±19.5	573.0±37.8	1184.7±73.5	1841.2±112.3

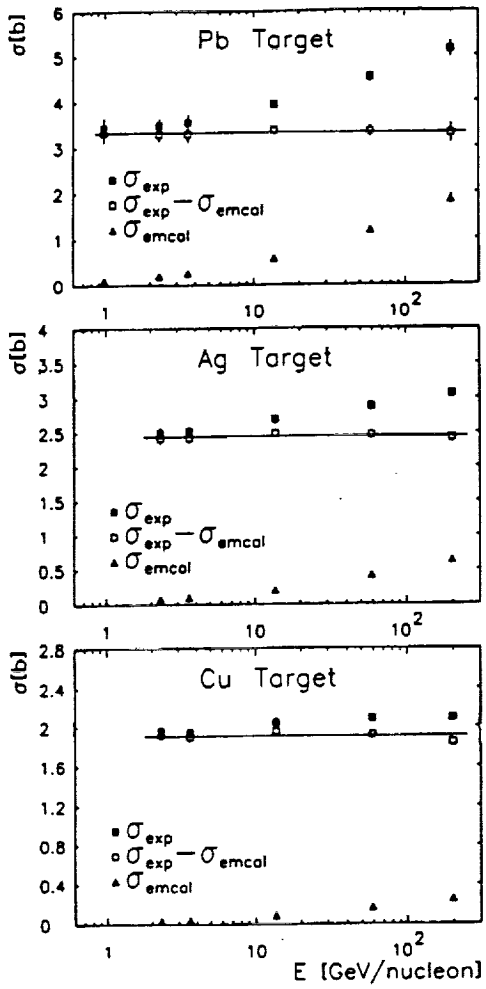

FIG. 1. Energy dependence of ^{16}O charge-changing cross-section data for Pb (top), Ag (middle), and Cu (bottom) targets. The solid squares show the measured reaction cross sections, while the solid triangles represent the calculated charge-changing electromagnetic cross sections. The difference cross sections, which include errors from measured and calculated cross sections, are given by the open squares. The horizontal line represents the average value of difference cross sections for all energies.

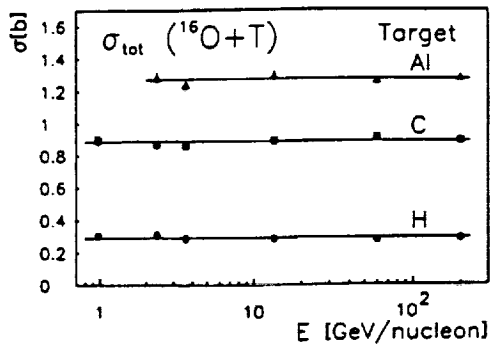

FIG. 2. Energy dependence of ^{16}O cross-section data for the light targets H (results are calculated from C and CH_2 targets), C, and Al after subtraction of the ED component. The horizontal line represents the average value of our cross-section data for all energies.

are obtained from empirical formulas. The empirical estimations of Westfall *et al.* [24] and Binns *et al.* [26] give total charge-changing cross sections as measured in our experiment. The formulas of Lindstrom *et al.* [23], Benesh, Cook, and Vary [38], and Kox *et al.* [25] give the total nuclear reaction cross sections. In order to compare our data with the results of these formulas, we have to estimate the contribution of the σ ($Z=8\rightarrow 8$) neutron-emission channel. This contribution is obtained by using the data of Olson *et al.* [41] from a similar experiment (^{16}O projectile fragmentation at 2.1 GeV/nucleon), which allows the calculation of this contribution with the help of factorization rules. As can be seen in Table III, the measured cross sections agree with the total charge- and mass-changing cross sections derived from different formulas. Only the value for the lead target is overestimated by some formulas. (All formulas are energy independent above 2 GeV/nucleon and do not take into account the ED contribution.)

B. Partial charge-changing cross sections

Partial nuclear cross sections can be described by the factorization rule expressed as

TABLE III. Total nuclear cross sections in comparison to results of different cross section formulas. The first column gives the averaged value of the nuclear cross sections for our experiments at five energies. The next two columns include charge-changing cross sections derived from empirical formulas. In the fourth column, the average total cross sections including the neutron-emission channel are given. The contribution of this channel was estimated using data of Olson *et al.* [41]. These cross sections are compared with the results of four empirical formulas. All cross sections are given in mb.

Target	Average $\Delta Z>0$	Ref. [24] $\Delta Z>0$	Ref. [26] $\Delta Z>0$	Average +Ref. [41] $\Delta A>0$	Ref. [24] $\Delta A>0$	Ref. [23] $\Delta A>0$	Ref. [38] $\Delta A>0$	Ref. [25] $\Delta A>0$
C	883.4±9.7	906.6	999.2	927.2±9.8	924.0	898.3	987.5	999.3
Al	1271.5±11.9	1259.3	1314.4	1326.8±12.1	1314.2	1290.2	1394.6	1438.5
Cu	1908.5±21.1	1853.6	1811.3	1972.5±21.2	1979.5	1861.9	2054.3	2125.0
Ag	2444.6±31.0	2383.5	2234.0	2515.8±31.2	2577.7	2367.9	2629.1	2699.1
Pb	3313.9±69.7	3311.7	2949.2	3393.0±69.8	3632.9	3249.0	3620.1	3649.2

TABLE IV. Calculated γ_{PT} and ε_{PT} for ^{16}O. For definitions, see text.

Target		Kinetic energy (GeV/nucleon) 2.3	3.6	13.5	60	200
C	γ_{PT}	1.000	1.000	1.000	1.000	1.000
	ε_{PT}	1.000	1.000	1.000	1.000	1.000
Al	γ_{PT}	1.216	1.200	1.204	1.179	1.200
	ε_{PT}	3.980	4.071	4.237	4.372	4.444
Cu	γ_{PT}	1.487	1.485	1.482	1.455	1.439
	ε_{PT}	16.604	17.414	18.944	20.192	20.905
Ag	γ_{PT}	1.669	1.678	1.671	1.648	1.652
	ε_{PT}	38.553	41.213	46.301	50.437	52.871
Pb	γ_{PT}	1.944	1.953	1.943	1.919	1.925
	ε_{PT}	98.660	108.548	127.893	143.427	152.925

$$\sigma_{\text{nuc}}(P,T,F)=\gamma_{PT}\gamma_P^F , \tag{7}$$

where $\sigma_{\text{nuc}}(P,T,F)$ is the nuclear fragmentation cross section for the projectile P incident upon the target T producing the fragment F. The factor γ_P^F depends only on the species of projectile and fragment, while γ_{PT} depends only on the species of projectile and target [41].

We found that in a similar way it is also possible to determine partial electromagnetic cross sections [10]. The photon spectra for different targets at constant beam energies do not change significantly in shape, but only in intensity. Therefore the relative probabilities for the production of different projectile fragments in interactions with different targets should be independent of the target. We introduce a factor ε_P^F, which is proportional to the probability to produce a fragment F by ED in a collision of projectile P with an arbitrary target. At a given energy, the absolute value of the partial ED cross section into a given channel is expected to scale with the intensities of the photon spectra associated with each target. We use the target factors γ_{PT} and ε_{PT}, defined separately for each energy as

$$\gamma_{PT}:=\sqrt{\sigma_{\text{nuc}}(P,T)/\sigma_{\text{nuc}}(P,T=C)} \tag{8}$$

and

$$\varepsilon_{PT}:=\sigma_{\text{emc}}^{\text{tot}}(P,T)/\sigma_{\text{emc}}^{\text{tot}}(P,T=C) , \tag{9}$$

where $\sigma_{\text{nuc}}(P,T)$ is the total nuclear cross section for the target T obtained by subtracting the calculated total charge-changing ED cross sections $\sigma_{\text{emc}}^{\text{tot}}(P,T)$ from the measured data. The scaling on the C target is arbitrary, and so scaling to a different target does not lead to any difference in the separated cross sections.

The partial ED cross section is written as

$$\sigma_{\text{em}}(P,T,F)=\varepsilon_{PT}\varepsilon_P^F . \tag{10}$$

For the measured partial cross sections $\sigma_{\text{meas}}(P,T,F)$, we can write

$$\sigma_{\text{meas}}(P,T,F)=\gamma_{PT}\gamma_P^F+\varepsilon_{PT}\varepsilon_P^F . \tag{11}$$

The fragment factors γ_P^F and ε_P^F are evaluated for all energies and fragments by minimizing the expression

$$\sum_T \frac{[\gamma_{PT}\gamma_P^F+\varepsilon_{PT}\varepsilon_P^F-\sigma_{\text{meas}}(P,T,F)]^2}{[\Delta\sigma_{\text{meas}}(P,T,F)]^2}\longrightarrow \text{minimum} , \tag{12}$$

where $\Delta\sigma_{\text{meas}}(P,T,F)$ is the error of the measured partial cross section $\sigma_{\text{meas}}(P,T,F)$.

Nuclear and electromagnetic target factors determined by this procedure are given in Table IV for all five energies. The fragment factors determined by our fit procedure are shown in Table V. Using (7) and (10), the pure nuclear and pure electromagnetic components were determined. In Fig. 3 the partial charge-changing nuclear cross sections $\Delta Z=1$ and 2 are shown together with data of Olson *et al.* at 2.1 GeV/nucleon [41]. In general, our partial nuclear cross sections are constant in the whole energy range and agree with the data of Olson *et al.* It should be noted that all cross sections belong to one fixed energy scale with one fragment factor and its error. For that reason all cross sections for a certain energy but different targets are smaller or bigger than the average for all energies (for example, the 13.5-GeV/nucleon data for $\Delta Z=1$ are significantly larger than the average).

Figure 4 shows the energy dependence of the partial electromagnetic cross sections for the lead target. The cross section $\sigma(Z=8\rightarrow Z\leq 5)$ was calculated by sub-

TABLE V. γ_P^F and ε_P^F as determined from fit procedures. All data are in mb.

	Kinetic energy (GeV/nucleon) 2.3	3.6	13.5	60	200
$\gamma_P^F(Z=7)$	97.50±2.79	99.02±2.65	107.76±2.76	105.01±2.99	105.94±3.96
$\varepsilon_P^F(Z=7)$	1.24±0.17	1.70±0.15	2.94±0.16	5.44±0.21	6.75±0.27
$\gamma_P^F(Z=6)$	116.89±3.25	119.72±3.06	113.72±2.86	122.28±3.16	124.75±4.26
$\varepsilon_P^F(Z=6)$	0.66±0.19	0.45±0.18	0.88±0.14	1.62±0.20	1.98±0.26

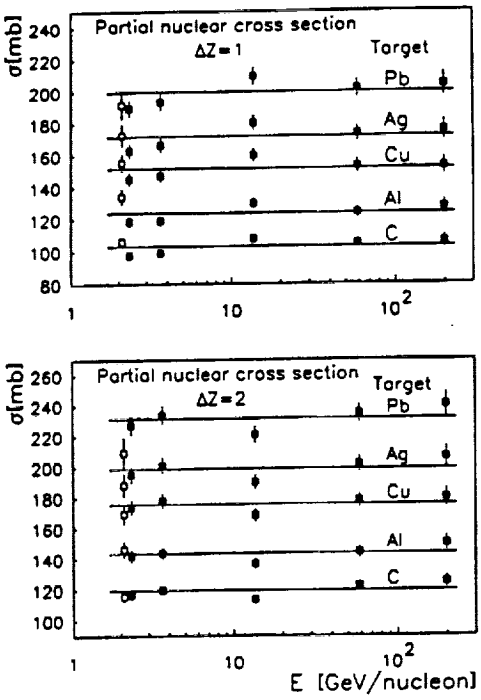

FIG. 3. Partial nuclear cross sections $\Delta Z=1$ (top) and $\Delta Z=2$ (bottom) for the reaction of ^{16}O with targets C, Al, Cu, Ag, and Pb determined from our experiments (solid squares) based on factorization rules. The data include cross sections from [41] at 2.1 GeV/nucleon (open squares). The horizontal line represents the average value of our cross-section data for all energies.

tracting the two partial ED cross sections from the calculated total one. The relative abundance of the ED partial cross sections to the total ED cross sections derived from the data for all targets is shown in Fig. 5. From both figures it can be seen that the partial cross sections for $\Delta Z=1$ and 2 are the dominant electromagnetic interac-

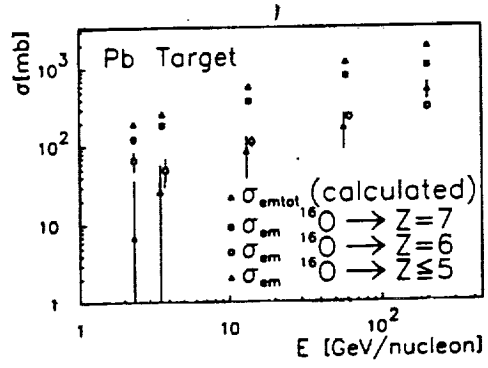

FIG. 4. Partial electromagnetic cross sections for the reaction of ^{16}O with a Pb target. The open triangles give the calculated total charge-changing cross sections. The solid and open squares represent the cross sections for $\Delta Z=1$ and 2, respectively. The solid triangles give the cross section for $\Delta Z\geq 3$, which was calculated by subtracting the $\Delta Z=1$ and 2 contributions from the calculated total ED cross section. Some of the partial cross sections have a small offset in energy for better comparability of the error bars.

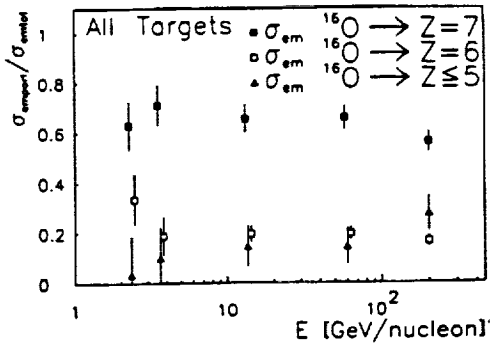

FIG. 5. Relative contributions of partial electromagnetic cross sections for ^{16}O to the total charge-changing electromagnetic cross section. The plot includes results of all targets since the given quotient for one energy only scales with the constant factor ε_p^F. Some of the partial cross sections have a small offset in energy for better comparability of the error bars.

tion channels. These interactions are induced by proton or alpha emission from the giant resonance of the ^{16}O projectile. With higher energies the virtual-photon spectra become harder and the excitation of a delta resonance becomes more likely. The excitation of a delta resonance within the projectile nucleus can lead to an intranuclear cascade and can cause a more complete destruction of the projectile nucleus. That is the reason why the $\Delta Z\geq 3$ channel exceeds the $\Delta Z=2$ channel at 200 GeV/nucleon. This fact was also observed for ^{32}S data at 200 GeV/nucleon [10].

C. Cross sections for light targets

The cross sections of the three light targets CH_2, CR-39, and C were used for the determination of the hydrogen-target cross sections. The energy dependence of the total charge-changing cross sections together with cross-section data of Webber, Kish, and Schrier [42,43] are shown in Fig. 6. It turns out that the data of Webber, Kish, and Schrier match our data at 2 GeV/nucleon

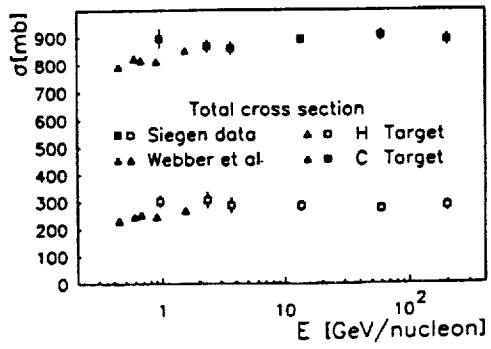

FIG. 6. Total charge-changing cross sections for ^{16}O for H and C targets. The squares (open for the H target, solid for the C target) represent our data, while the triangles give the data measured by Webber, Kish, and Schrier [42,43] (open triangle for the H target, solid triangle for the C target).

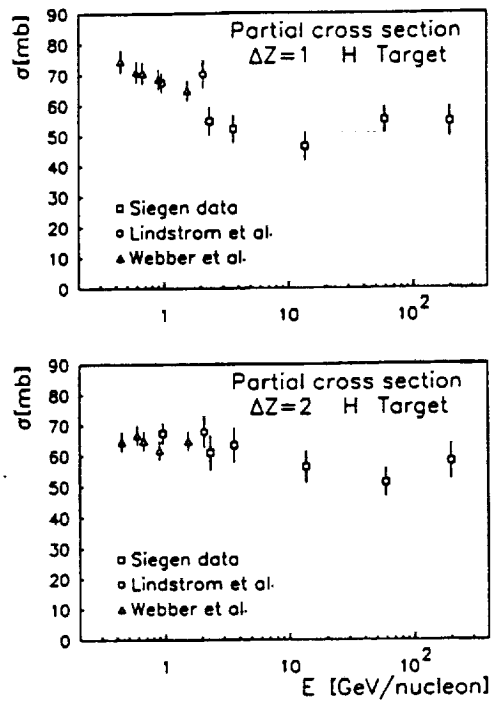

FIG. 7. Energy dependence of partial cross sections for $\Delta Z=1$ (top) and $\Delta Z=2$ (bottom) reaction of ^{16}O with hydrogen. Data from Webber, Kish, and Schrier [42,43] (open triangles) and Lindstrom *et al.* [23] (open circles) are also included.

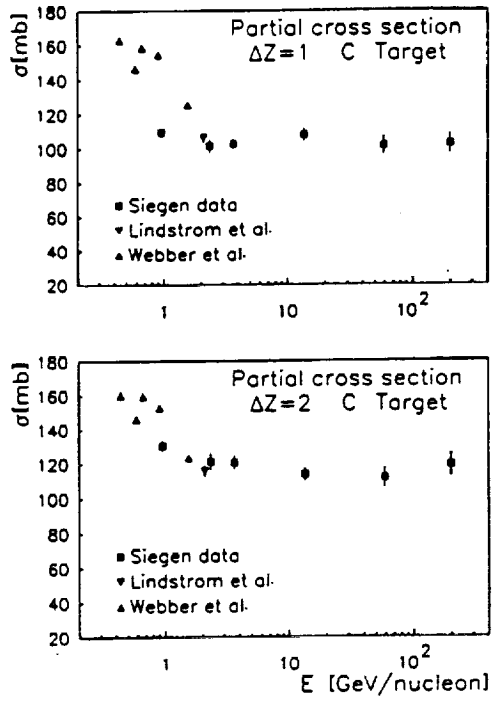

FIG. 8. Energy dependence of partial cross sections $\Delta Z=1$ (top) and $\Delta Z=2$ (bottom) for reaction of ^{16}O with carbon. Data from Webber, Kish, and Schrier [42,43] (triangles) and Lindstrom *et al.* [23] (inverted triangles) are also included.

quite well, whereas at 1 GeV/nucleon their cross sections are about 10% smaller. Figure 7 gives the partial cross section for hydrogen. It shows a decrease of the cross section for $\Delta Z=1$ between 1 and 13.5 GeV/nucleon. For $\Delta Z=2$ the observed decrease is less strong. A decrease of these partial cross sections of this strength cannot be reproduced completely with intranuclear cascade calculations [44]. Further detailed studies of this effect are necessary.

Our partial cross sections for the carbon target in comparison to other data are shown in Fig. 8. The partial cross sections for $\Delta Z=1$ and 2 are constant between 2 and 200 GeV/nucleon. In contradiction to the data of Webber, Kish, and Schrier, we only observe a slight decrease from 1 to 2 GeV/nucleon. Our data point at 2.3 GeV/nucleon is consistent with the data point of Lindstrom *et al.* at 2.1 GeV/nucleon [23]. A surprising point is that for low energies the two partial cross sections $\Delta Z=1$ and 2 for the C target of Webber, Kish, and Schrier [43] show nearly no odd/even effect which is present at higher energies.

The fact that the partial hydrogen target cross sections are smaller at energies of some GeV/nucleon than expected implies a change of parameters for astrophysical models for propagation of cosmic-ray heavy ions from the sources to the Earth. These calculations relate measured nuclear abundances near the Earth to source compositions. The thickness of penetrated matter and the probabilities of the nuclei escaping our Galaxy are obtained in these calculations. A reduced partial fragmentation cross section $\Delta Z=1$ (^{16}O→N), which must be put into these calculations to reproduce the experimental data, e.g., for the measured N/O ratio, affects the escape probabilities [45].

III. CONCLUSION

Fragmentation cross sections for ^{16}O were measured for a set of targets in the energy range from 0.9 to 200 GeV/nucleon. The rise of the total charge-changing cross sections with energy, especially for heavy targets caused by the ED effect, was observed. The contribution of the ED process was calculated using virtual-photon spectra and photonuclear data. Subtracting this ED contribution from the measured total cross sections, we obtained the pure nuclear component of the cross sections. The total nuclear cross sections for all targets show no energy dependence, as is expected by the concept of limiting fragmentation. Fit procedures enabled us to separate nuclear and ED components also for the partial cross sections. The partial nuclear cross sections for heavier targets are almost energy independent and agree quite well with other data. The partial ED cross sections show that with high energies (> 100 GeV/nucleon) the ED process cannot lead to the emission of nucleons and α particles only, but can result in a much more complete destruction of the projectile nucleus. The data for the H target may influence the output of astrophysical model calculations.

ACKNOWLEDGMENTS

We are thankful to the staffs of Brookhaven and Dubna laboratories. This work was funded by the German Federal Ministry for Research and Technology (BMFT) under Contract No. 06 SI 146.

1/46

[1] H. H. Heckman and P. J. Lindstrom, Phys. Rev. Lett. **37**, 56 (1976).
[2] D. L. Olson, B. L. Berman, D. E. Greiner, H. H. Heckman, P. J. Lindstrom, G. D. Westfall, and H. J. Crawford, Phys. Rev. C **24**, 1529 (1981).
[3] N. Ardito *et al.*, Europhys. Lett. **6**, 131 (1988).
[4] P. B. Price, R. Guoxiao, and W. T. Williams, Phys. Rev. Lett. **61**, 2193 (1989).
[5] G. Singh, K. Sengupta, and P. L. Jain, Phys. Rev. C **41**, 999 (1990).
[6] J. Barette *et al.*, Phys. Rev. C **41**, 1512 (1990).
[7] G. Baroni *et al.*, Nucl. Phys. **A531**, 691 (1991).
[8] S. Y. Bahk *et al.*, Phys. Rev. C **43**, 1410 (1991).
[9] C. Brechtmann and W. Heinrich, Z. Phys. A **330**, 407 (1988).
[10] C. Brechtmann and W. Heinrich, Z. Phys. A **331**, 463 (1988).
[11] C. Brechtmann and W. Heinrich, Phys. Rev. C **39**, 2222 (1989).
[12] W. Heinrich and C. Brechtmann, Mod. Phys. Lett. A **4**, 1879 (1989).
[13] W. Heinrich, C. Brechtmann, S. E. Hirzebruch, E. Winkel, K. D. Tolstov, and A. D. Kovalenko, in *Relativistic Nuclear Physics and Quantum Chromodynamics*, edited by A. M. Baldin, V. V. Burov, and L. P. Kaptari (World Scientific, Singapore, 1991), p. 509.
[14] J. C. Hill, F. K. Wohn, J. A. Winger, and A. R. Smith, Phys. Rev. Lett. **60**, 999 (1988).
[15] J. C. Hill, F. K. Wohn, J. A. Winger, M. Khayat, K. Leininger, and A. R. Smith, Phys. Rev. C **38**, 1722 (1988).
[16] J. C. Hill, F. K. Wohn, J. A. Winger, M. Khayat, M. T. Mercier, and A. R. Smith, Phys. Rev. C **39**, 524 (1989).
[17] J. C. Hill, F. K. Wohn, and D. D. Schwellenbach, Phys. Lett. B **273**, 371 (1991).
[18] D. L. Olson, M. Baumgartner, D. E. Greiner, P. J. Lindstrom, T. J. M. Symons, R. Wada, M. L. Webb, B. L. Berman, H. J. Crawford, and J. M. Engelage, Phys. Rev. C **44**, 1862 (1991).
[19] W. Heinrich, C. Brechtmann, S. E. Hirzebruch, E. Winkel, and G. Rusch, in Proceedings of the 21st International Cosmic Ray Conference, Adelaide, 1990 (unpublished), Vol. 3, p. 436.
[20] S. E. Hirzebruch, W. Heinrich, K. D. Tolstov, and A. D. Kovalenko, in Proceedings of the 22nd International Cosmic Ray Conference, Dublin, 1991 (unpublished), Vol. 2, p. 280.
[21] C. Brechtmann and W. Heinrich, Nucl. Instrum. Methods B **29**, 675 (1988).
[22] W. Trakowski, B. Schöfer, J. Dreute, S. Sonntag, C. Brechtmann, J. Beer, H. Drechsel, and W. Heinrich, Nucl. Instrum. Methods **225**, 92 (1984).
[23] P. J. Lindstrom, D. E. Greiner, H. H. Heckman, B. Cork, and F. S. Bieser, in Proceedings of the 14th ICRC, Munich, 1975 (unpublished), p. 2315.
[24] G. D. Westfall, L. W. Wilson, P. J. Lindstrom, H. J. Crawford, D. E. Greiner, and H. H. Heckman, Phys. Rev. C **19**, 1309 (1979).
[25] S. Kox *et al.*, Phys. Rev. C **35**, 1687 (1987).
[26] W. R. Binns, T. L. Garrard, M. H. Israel, M. P. Kertzmann, J. Klarmann, E. C. Stone, and C. J. Waddington, Phys. Rev. C **36**, 1870 (1987).
[27] C. A. Bertulani and G. Baur, Nucl. Phys. **A442**, 739 (1985).
[28] C. A. Bertulani and G. Baur, Nucl. Phys. **A458**, 725 (1986).
[29] G. Baur and C. A. Bertulani, Phys. Rev. C **34**, 1654 (1986).
[30] J. S. Levinger, Phys. Rev. **84**, 43 (1951).
[31] C. F. Weizsäcker, Z. Phys. **88**, 612 (1934).
[32] E. J. Williams, Phys. Rev. **45**, 729 (1934).
[33] J. W. Norbury, Phys. Rev. C **41**, 372 (1990).
[34] J. W. Norbury, Phys. Rev. C **42**, 711 (1990).
[35] J. W. Norbury, Phys. Rev. C **42**, 2259 (1990).
[36] R. Fleischhauer and W. Scheid, Nucl. Phys. **A510**, 817 (1990).
[37] E. G. Fuller, Phys. Rep. **127**, 185 (1985).
[38] C. J. Benesh, B. C. Cook, and J. P. Vary, Phys. Rev. C **40**, 1198 (1989).
[39] W. J. Llope and P. Braun-Munziger, Phys. Rev. C **41**, 2644 (1990).
[40] W. J. Llope and P. Braun-Munziger, Phys. Rev. C **45**, 799 (1992).
[41] D. L. Olson, B. L. Berman, D. E. Greiner, H. H. Heckman, P. J. Lindstrom, and H. J. Crawford, Phys. Rev. C **28**, 1602 (1983).
[42] W. R. Webber, J. C. Kish, and D. A. Schrier, Phys. Rev. C **41**, 520 (1990).
[43] W. R. Webber, J. C. Kish, and D. A. Schrier, Phys. Rev. C **41**, 533 (1990).
[44] P. Kozma (private communication).
[45] J. P. Meyer, in Proceedings of the 19th International Cosmic Ray Conference, La Jolla, 1985 (unpublished), Vol. 9, p. 141.

APPENDIX J

HZE Beam Transport in Multilayered Materials

by

J.L. Shinn, J.W. Wilson, F.F. Badavi, E.V. Benton
I. Csige, A.L. Frank and E.R. Benton

Pergamon

Radiation Measurements, Vol. 23, No. 1, pp. 57–64, 1994
Elsevier Science Ltd
Printed in Great Britain

1350-4487(93)E0016-F

HZE BEAM TRANSPORT IN MULTILAYERED MATERIALS

J. L. SHINN,* J. W. WILSON,* F. F. BADAVI,† E. V. BENTON,‡ I. CSIGE,§ A. L. FRANK‡ and E. R. BENTON‡

*NASA Langley Research Center, Hampton, VA 23681, U.S.A.; †Christopher Newport University, Newport News, VA 23601, U.S.A.; ‡University of San Francisco, San Francisco, CA 94117, U.S.A.; and §Institute of Nuclear Research, ATOMKI, H-4001 Debrecen, Hungary

(*Received* 26 *July* 1993; *in revised form* 7 *September* 1993)

Abstract—A nonperturbative analytic solution of the high charge and energy (HZE) Green's function is used to implement a computer code for laboratory ion beam transport in multiple-layered materials. The code is established to operate on the Langley nuclear fragmentation model used in space engineering applications. Computational procedures are established to generate linear energy transfer (LET) distributions for a specified ion beam and target for comparison with experimental measurement. Comparison with ^{56}Fe ion with Pb–Al and Pb–$(CH_2)_x$ targets shows reasonable agreement.

1. INTRODUCTION

GREEN's functions were identified as the likely means of generating efficient HZE shielding codes for space engineering which are capable of being validated in laboratory experiments (Wilson *et al.*, 1989). A derivation of the Green's function as a perturbation series gave promise for development of a laboratory-validated engineering code (Wilson *et al.*, 1990) but computational inefficiency provided a major obstacle to code development (Wilson and Badavi, 1992). More recently, nonperturbative approximations to HZE Green's functions have shown promise in providing an efficient validated engineering code (Wilson *et al.*, 1993a, c). Previous work has found a solution to HZE transport in a homogeneous medium using nonperturbative methods (Wilson and Badavi, 1992; Wilson *et al.*, 1993b, c). In the present report, we derive solutions for inhomogeneous multilayered media. The resulting computer code is used to derive LET spectra behind multilayered targets for ion beams with $Z \leqslant 28$ corresponding to the major components of the galactic cosmic ray spectrum. The results of the computation are compared with ^{56}Fe accelerator beam experiments with Pb–Al and Pb–$(CH_2)_x$ shield configurations.

2. GREEN'S FUNCTION FOR A SINGLE MEDIUM

We restrict our attention to the multiple charged ions for which the Boltzmann equation may be reduced (Wilson, 1977a) to:

$$\left[\frac{\partial}{\partial x} - \frac{\partial}{\partial E}\bar{S}_j(E) + \sigma_j\right]\phi_j(x, E) = \sum_k \sigma_{jk}\phi_k(x, E), \quad (1)$$

where $\phi_j(x, E)$ is the ion flux at x with energy E (MeV/amu), $\bar{S}_j(E)$ is the change in E per unit distance, σ_j the total macroscopic reaction cross section and σ_{jk} the macroscopic cross section for collision of ion type k to produce an ion of type j. The solution to equation (1) is to be found subject to the boundary condition:

$$\phi_j(0, E) = f_j(E), \quad (2)$$

which for laboratory beams has only one value of j for which $f_j(E)$ is not zero and that $f_j(E)$ is described by a mean energy E_0 and energy spread σ such that:

$$f_j(E) = \frac{1}{\sqrt{2\pi}\sigma}\exp[-(E - E_0)^2/2\sigma^2]. \quad (3)$$

The usual method of solution is to proceed solving equation (1) as a perturbation series (Wilson 19[illegible] b; Wilson *et al.*, 1990). In practice, the computational requirements limit the usefulness of the technique for deep penetration (Wilson and Badavi, 1992).

The Green's function is introduced as a solution of:

$$\left[\frac{\partial}{\partial x} - \frac{\partial}{\partial E}\bar{S}_j(E) + \sigma_j\right]G_{jm}(x, E, E_0) = \sum_k \sigma_{jk}G_{km}(x, E, E_0), \quad (4)$$

subject to the boundary condition

$$G_{jm}(0, E, E_0) = \delta_{jm}\,\delta(E - E_0). \quad (5)$$

The solution to equation (1) is given by superposition as

$$\phi_j(x, E) = \sum_k \int G_{jk}(x, E, E')f_k(E')\,dE'. \quad (6)$$

148 A.

If $G_{jk}(x, E, E')$ is known as a transcendental function, the evaluation of equation (6) may be accomplished by simple integration techniques, and the associated errors in numerically solving equation (1) are avoided (Wilson *et al.*, 1991).

The above equations can be simplified by transforming the energy into the residual range as:

$$r_j = \int_0^E \mathrm{d}E'/\bar{S}_j(E'), \tag{7}$$

and defining new field functions as:

$$\psi_j(x, r_j) = \bar{S}_j(E)\phi_j(x, E) \tag{8}$$

$$\mathcal{G}_{jm}(x, r_j, r'_m) = \bar{S}_j(E)G_{jm}(x, E, E') \tag{9}$$

$$\hat{f}_j(r_j) = \bar{S}_j(E)f_j(E) \tag{10}$$

and equation (4) becomes:

$$\left[\frac{\partial}{\partial x} - \frac{\partial}{\partial r_j} + \sigma_j\right]\mathcal{G}_{jm}(x, r_j, r'_m) = \sum_k \frac{v_j}{v_k}\sigma_{jk}\mathcal{G}_{km}(x, r_k, r'_m), \tag{11}$$

where v_j is the range scale factor as $v_j r_j = v_m r_m$ and is taken as $v_j = Z_j^2/A_j$ and the boundary condition is now:

$$\mathcal{G}_{jm}(0, r_j, r'_m) = \delta_{jm}\,\delta(r_j - r'_m) \tag{12}$$

and with solution to the ion fields given by

$$\psi_j(x, r_j) = \sum_m \int_0^\infty \mathcal{G}_{jm}(x, r_j, r'_m)\hat{f}_m(r'_m)\,\mathrm{d}r'_m. \tag{13}$$

The solution to equation (11) is written as a perturbation series:

$$\mathcal{G}_{jm}(x, r_j, r'_m) = \sum_i \mathcal{G}^{(i)}_{jm}(x, r_j, r'_m) \tag{14}$$

where

$$\mathcal{G}^{(0)}_{jm}(x, r_j, r'_m) = g(j)\,\delta_{jm}\,\delta(x + r_j - r'_m) \tag{15}$$

and

$$\mathcal{G}^{(1)}_{jm}(x, r_j, r'_m) \approx \frac{v_j\sigma_{jm}g(j, m)}{x(v_m - v_j)} \tag{16}$$

where $\mathcal{G}^{(1)}_{jm}(x, r_j, r'_m)$ is zero unless

$$\frac{v_j}{v_m}(r_j + x) \leqslant r'_m \leqslant \frac{v_j}{v_m}r_j + x \tag{17}$$

for $v_m > v_j$. If $v_j > v_m$, as can happen in neutron removal, the negative of equation (16) is used and the upper and lower limits of equation (17) are switched. The higher terms are approximated as:

$$\mathcal{G}^{(i)}_{jm}(x, r_j, r'_m) \approx \sum_{k_1 k_2 \cdots k_{i-1}} \times \frac{v_j\sigma_{jk_1}\sigma_{k_1k_2}\cdots\sigma_{k_{i-1}m}g(j, k_1, k_2, \ldots, k_{i-1}, m)}{x(v_m - v_j)}. \tag{18}$$

In the above, the g-function of n-arguments is found recursively by:

$$g(j) = \mathrm{e}^{-\sigma_j x} \tag{19}$$

and

$$g(j_1, j_2 \cdots j_n, j_{n+1}) = \frac{g(j_1, j_2 \cdots j_{n-1}, j_n) - g(j_1, j_2 \cdots j_{n-1}, j_{n+1})}{\sigma_{j_{n+1}} + \sigma_{j_n}}. \tag{20}$$

Note that the $\mathcal{G}^{(i)}_{jm}(x, r_j, r'_m)$ are purely dependent on x for $i > 0$ which we represent as $\mathcal{G}^{(i)}_{jm}(x)$ (Wilson and Badavi, 1992). In terms of the above, the solution to equation (1) becomes (Wilson and Badavi, 1992)

$$\psi_j(x, r_j) = \mathrm{e}^{-\sigma_j x}\hat{f}_j(r_j + x) + \sum_{m,i}\mathcal{G}^{(i)}_{jm}(x)[\hat{F}_m(r'_{ml}) - \hat{F}_m(r'_{mu})]. \tag{21}$$

In equation (21), r'_{mu} and r'_{ml} are given by the upper and lower limits of the inequality (17). The symbol $\hat{F}_m(r'_m)$ refers to the integral spectrum:

$$\hat{F}_m(r'_m) = \int_{r'_m}^\infty \hat{f}_m(r)\,\mathrm{d}r. \tag{22}$$

We note that:

$$\hat{F}_m(r'_m) \equiv F_m(E') \tag{23}$$

with

$$F_m(E') = \int_{E'}^\infty f_m(E)\,\mathrm{d}E \tag{24}$$

and

$$r'_m = \int_0^E \mathrm{d}E/\bar{S}_m(E). \tag{25}$$

We now introduce nonperturbative terms for the summation in equation (21).

First, we recall that the g-function of n-arguments was generated by the perturbation solution of the transport equation neglecting ionization energy loss (Wilson *et al.*, 1989) given by:

$$\left[\frac{\partial}{\partial x} + \sigma_j\right]g_{jm}(x) = \sum_k \sigma_{jk}g_{km}(x) \tag{26}$$

subject to the boundary condition:

$$g_{jm}(0) = \delta_{jm} \tag{27}$$

for which the solution is

$$g_{jm}(x) = \delta_{jm}g(m) + \sigma_{jm}g(j, m) + \cdots \tag{28}$$

It is also true that:

$$g_{jm}(x) = \sum_k g_{jk}(x - y)g_{km}(y) \tag{29}$$

for any positive values of x and y. Equation (29) may

be used to propagate the function $g_{jm}(x)$ over the solution space, after which:

$$\mathcal{G}_{jm}(x, r_j, r'_m) \approx e^{-\sigma_j x}\delta_{jm}\delta(x + r_j - r'_m) + v_j[g_{jm}(x) - e^{-\sigma_j x}\delta_{jm}]/x(v_m - v_j). \quad (30)$$

The approximate solution of equation (1) is then given by

$$\psi_j(x, r_j) = e^{-\sigma_j x}\delta(r_j + x) + \sum_m \frac{v_j[g_{jm}(x) - e^{-\sigma_j x}\delta_{jm}]}{x(v_m - v_j)}[\hat{F}_m(r'_{mu}) - \hat{F}_m(r'_{ml})] \quad (31)$$

which is a relatively simple quantity (Wilson *et al.*, 1993a).

3. GREEN'S FUNCTION IN A SHIELDED MEDIUM

The major simplification in the Green's function method results from the fact that the scaled spectral distribution of secondary ions to a first approximation depends only on the depth of penetration as seen in equations (16), (18) and (30). Our first approach to a multilayered Green's function will rely on this observation and assume its validity for multilayered shields.

Consider a domain labeled as 1 which is shielded by a second domain labeled as 2; the number of type j ions at depth x in 1 due to type m ions incident on domain 2 of thickness y is:

$$g_{12jm}(x, y) = \sum_k g_{1jk}(x)g_{2km}(y). \quad (32)$$

The leading term in equation (32) is the penetrating primaries as:

$$g_{12jm}(x, y) = e^{-\sigma_{1j}x - \sigma_{2j}y}\delta_{jm} + [g_{12jm}(x, y) - e^{-\sigma_{1j}x - \sigma_{2j}y}\delta_{jm}], \quad (33)$$

where all higher order terms are in the bracket of equation (33).

The first term of the scaled Green's function is then:

$$\mathcal{G}^{(0)}_{12jm}(x, y, r_j, r'_m) = e^{-\sigma_{1j}x - \sigma_{2j}y}\delta_{jm} \times \delta[x + r_j - (r'_m - \rho y)], \quad (34)$$

where ρ is the range factor for the two media:

$$\rho = R_{1j}(E)/R_{2j}(E). \quad (35)$$

The ratio is shown for protons in Fig. 1. We take a single value for ρ corresponding to 600 MeV/amu. The secondary contribution is similarly found by noting that equation (17) becomes:

$$\frac{v_j}{v_m}(r_j + x + \rho y) \leqslant r'_m \leqslant \frac{v_j}{v_m}r_j + x + \rho y, \quad (36)$$

from which the average spectrum is evaluated. The full approximate Green's function is then:

$$\mathcal{G}_{12jm}(x, y, r_j, r'_m) \approx e^{-\sigma_{1j}x - \sigma_{2j}y}\delta_{jm} \times \delta(x + \rho y + r_j - r'_m) + v_j[g_{12jm}(x, y) - e^{-\sigma_{1j}x - \sigma_{2j}y}\delta_{jm}]/(x + \rho y)(v_m - v_j). \quad (37)$$

Equation (37) is our first approximation to the Green's function in a shielded medium (two layers) and is easily modified to multiple layers (see Appendix). We now consider the first spectral modification.

It is easy to show that the first collision term has the properties:

$$\mathcal{G}^{(1)}_{12jm}(x, y, r_j, r'_m) = \frac{v_j\sigma_{1jm}e^{-\sigma_{1m}x - \sigma_{2m}y}}{|v_m - v_j|} \quad \text{for } r'_m = r'_{mu}$$
$$= \frac{v_j\sigma_{2jm}e^{-\sigma_{1j}x - \sigma_{2j}y}}{|v_m - v_j|} \quad \text{for } r'_m = r'_{ml}. \quad (38)$$

We use these properties to correct the average spectrum as:

$$\mathcal{G}^{(1)}_{12jm}(x, y, r_j, r'_m) = \frac{v_j g^{(1)}_{12jm}(x, y)}{|v_m - v_j|(x + \rho y)} + b_{jm}(x, y)(r'_m - \bar{r}_m), \quad (39)$$

where $g^{(1)}_{12jm}(x, y)$ is the first collision term of equation (37) and

$$\bar{r}'_m = (r'_{mu} + r'_{ml})/2 \quad (40)$$

is the midpoint of $\bar{r}'_m$ between its limits given by equation (36). The b_{jm} term of equation (39) has the property that:

$$\int_{r'_{ml}}^{r'_{mu}} b_{jm}(x, y)(r' - \bar{r}'_m)\,dr' = 0, \quad (41)$$

ensuring that the first term of equation (39) is indeed the average spectrum as required. The spectral slope parameter is found to be:

$$b_{jm}(x, y) = v_j v_m(\sigma_{1jm}e^{-\sigma_{1m}x - \sigma_{2m}y} - \sigma_{2jm} \times e^{-\sigma_{1j}x - \sigma_{2j}y})/[(x + \rho y)(v_m - v_j)|v_m - v_j|]. \quad (42)$$

A similarly simple spectral correction could be made to the higher order terms. The spectral correction given in equation (42) is included in the present Green's function code.

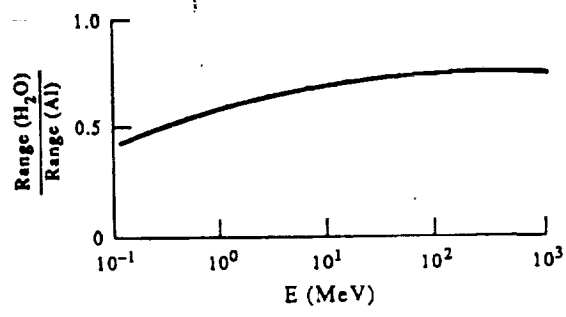

FIG. 1. Ratio of range in water to range in aluminum for proton beams.

4. LET SPECTRA FOR LABORATORY BEAMS

We use the boundary condition appropriate for laboratory beams given by equation (3). The cumulative spectrum is given by:

$$F_j(E) = \frac{1}{2}\left[1 - erf\left(\frac{E - E_0}{\sqrt{2}\sigma}\right)\right]. \quad (43)$$

The cumulative energy moment needed to evaluate the spectral correction is:

$$\bar{E}_j(E) = \frac{1}{2}E_0\left[1 - erf\left(\frac{E - E_0}{\sqrt{2}\sigma}\right)\right] + \frac{\sigma}{\sqrt{2\pi}}\exp\left[-\frac{(E - E_0)^2}{2\sigma^2}\right]. \quad (44)$$

The average energy on any subinterval (E_1, E_2) is then:

$$\bar{E} = [\bar{E}_j(E_1) - \bar{E}_j(E_2)]/[F_j(E_1) - F_j(E_2)]. \quad (45)$$

The beam generated flux is:

$$\psi_j(x, y, r_j) = e^{-\sigma_{1j}x - \sigma_{2j}y}\hat{f}_j(r_j + x + \rho y) + \sum_{m,i}\mathscr{G}^{(i)}_{jm}(x, y)[\hat{F}_m(r'_{mu}) - \hat{F}_m(r'_{ml})] + \sum_m b^{(1)}_{jm}(x, y)[r'_m(\bar{E}) - \bar{r}'_m] \times [\hat{F}_m(r'_{mu}) - \hat{F}_m(r'_{ml})], \quad (46)$$

where $\bar{E}$ is evaluated using equation (45) with E_1, and E_2 as the lower and upper limits associated with r'_{ml} and r'_{mu}.

A series of evaluations for a lead scattering foil (2.24 g/cm^2) in front of a water target is shown in Fig. 2. The lead scattering foil is usually part of the accelerator beam line so that the fragments from the

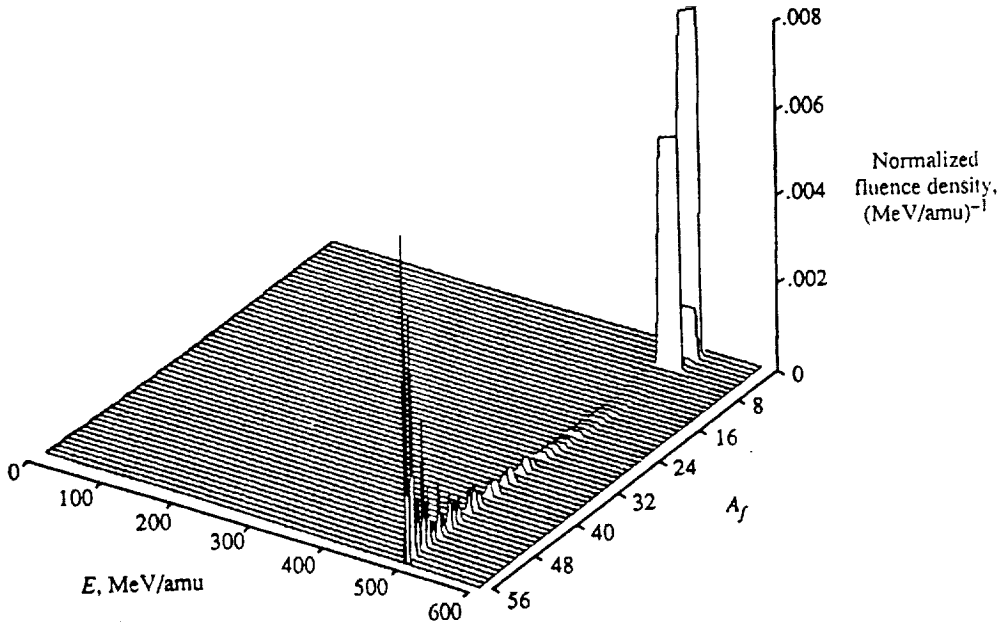

(a)

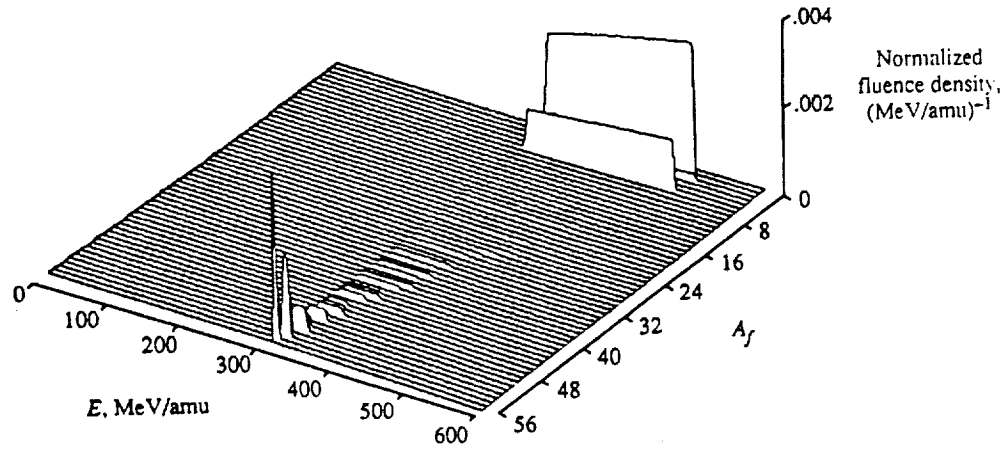

(b)

FIG. 2 (a) and (b).

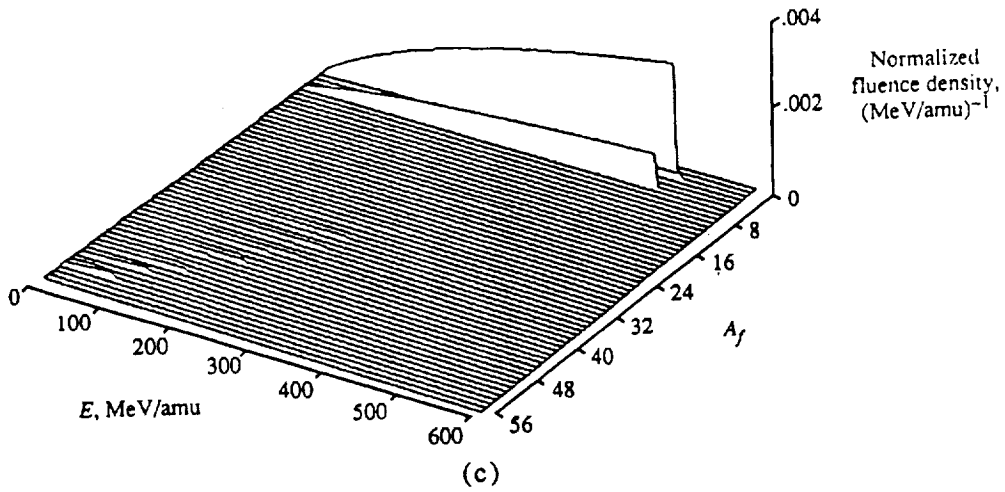

(c)

Fig. 2. Differential fluence for 525 MeV/amu ^{56}Fe beam with a 2.5 MeV/amu standard deviation after passing through a 2.24 g/cm^2 lead scattering foil and a water target. (a) 0 cm H_2O; (b) 5 cm H_2O; (c) 10 cm H_2O.

lead target are seen as contamination. Clearly, these fragments must be modeled to properly interpret the attenuation of the beam in the water target in actual experiments.

5. NUCLEAR DATA BASE

The nuclear absorption cross sections are fits to quantum mechanical calculations developed at the Langley Research Center over the past 20 years (Wilson, 1973, 1974; Wilson and Costner, 1975; Wilson and Townsend, 1981; Townsend and Wilson, 1986) and are considered reliable to about 10%. The nuclear fragmentation cross sections for most nuclei on hydrogen targets are taken from Silberberg *et al.* (1983) and are augmented for light fragment production with the Bertini model (Bertini, 1969). It was noted that early versions of these cross sections failed to conserve mass and charge (Wilson *et al.*, 1974) and still exhibit mass loss for $10 \leqslant Z \leqslant 22$ by as much as 30%. This is displayed in Fig. 3 where σ_{abs} is compared to $\Sigma A_i \sigma_{ip}/A_p$, where A_i is fragment mass, σ_{ip} is the fragmentation cross section for projectile p and A_p is the projectile mass. The breakup of light nuclei ($A \leqslant 4$) is taken from the quantum calculations of Cucinotta *et al.* (1993). The fragmentation of the remaining nuclei ($A_p > 4$) is evaluated from the latest versions of the NUCFRAG model (Wilson *et al.* 1987a, b). Since the public release version of NUCFRAG (HZEFRG1, Townsend *et al.*, 1993), a de-excitation scheme for mass two and mass three fragments and a coulomb trajectory calculation have been added for more realistic cross sections at low energy (Wilson *et al.*, 1993a). The elemental fragmentation cross sections are displayed in Fig. 4 at several energies. The reduced light fragment production at low energy results from coulomb trajectory corrections. This is the same data base used in the most recent energy dependent engineering code HZETRN (Shinn *et al.*, 1992).

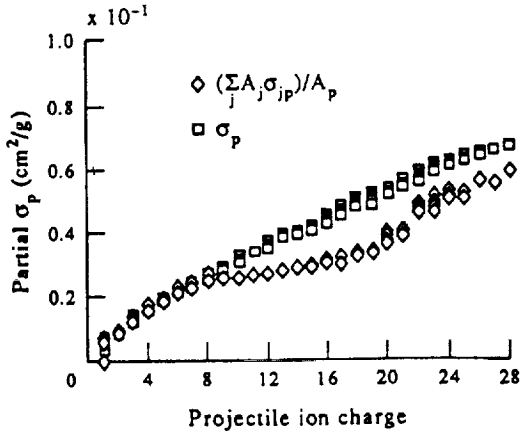

FIG. 3. The absorption cross section in hydrogen targets and mass averaged production cross sections at 600 MeV/amu for various projectiles.

The transport codes usually represent a reduced set of isotopes. In the past, we usually represented each charge group with an associated mass taken as the nearest mass on the stability curve for the given fragment charge. The most recent version of HZETRN uses an isobaric flux representation with the nearest charge on the stability curve and the distance to the nearest isobar was calculated

$$D = (A_i - A_l)^2 + 4(Z_i - Z_l)^2, \qquad (47)$$

where A_i, Z_i represent the fragment and A_l, Z_l represent the listed isobar mass used in the calculation and nearest charge to the stability curve. The present calculation uses an 80-isotope representation and the nearest isotope in the list is found using equation (47).

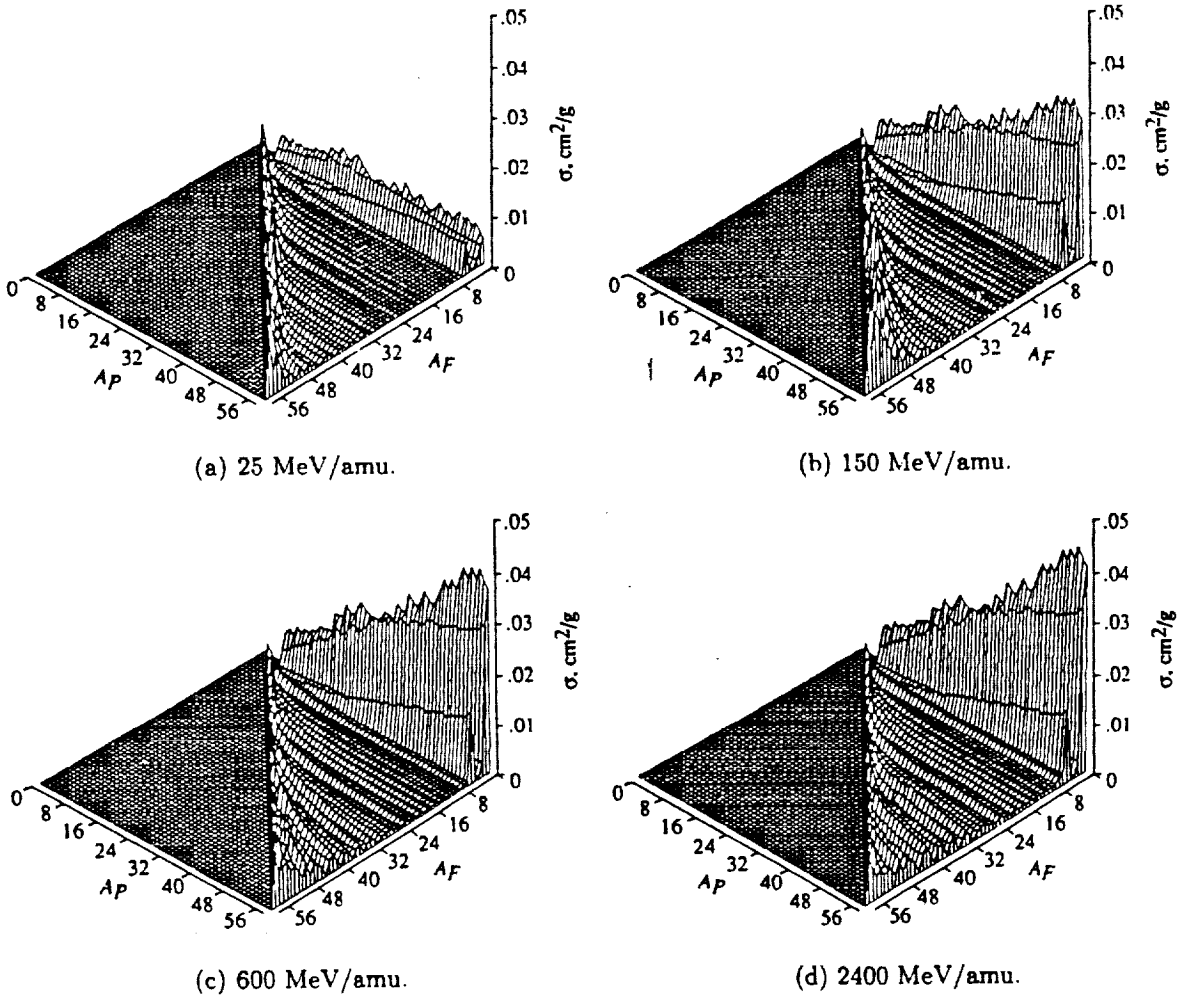

(a) 25 MeV/amu. (b) 150 MeV/amu.

(c) 600 MeV/amu. (d) 2400 MeV/amu.

FIG. 4. The fragment production cross section in H_2O targets including coulomb corrections.

6. EXPERIMENTAL METHODS AND COMPARISON

The ^{56}Fe nuclei were accelerated to 600 MeV/amu at the Lawrence Berkeley Laboratory Bevalac facility and passed through a series of beam transport elements, triggering devices and a 2.24 g/cm² lead foil prior to exiting the beam pipe and impacting the target. Two targets of 2 g/cm² Al and 4.6 g/cm² of polyethylene $(CH_2)_x$ were used to evaluate their transport properties. The beam energy is inferred to be 557 MeV/amu when only the lead foil and target are considered for transport analysis. The transported beam exciting the target was measured using CR-39 plastic foils (Benton *et al.*, 1986). The beam intensity was measured by a monitoring foil in front of the target. The detectors and targets are run in good geometry so that acceptance corrections are not required.

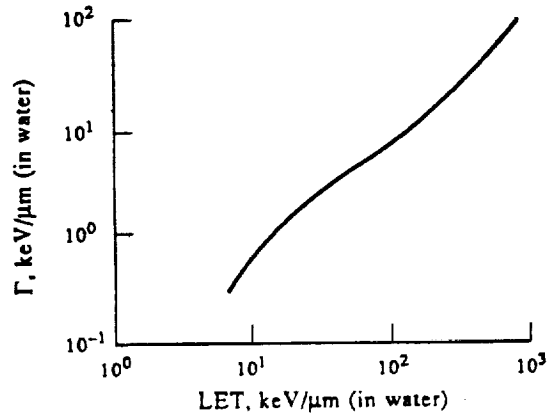

FIG. 5. Measured CR-39 response parameter (Benton *et al.*, 1986).

The detector response is assumed to be approximately Gaussian with an LET dependent width Γ shown in Fig. 5. A correction for non-Gaussian contributions is taken as:

$$R(L, L_0) = 0.8 \frac{1}{\sqrt{2\pi\sigma_0^2}} e^{-(L-L_0)^2/2\sigma_0^2} + 0.2 \frac{1}{\sqrt{2\pi\sigma_1^2}} e^{-(L-L_0)^2/2\sigma_1^2}, \quad (48)$$

where $\sigma_0 = 0.4247\Gamma$ and σ_1 (taken as $2.4\sigma_0$) is fit to the

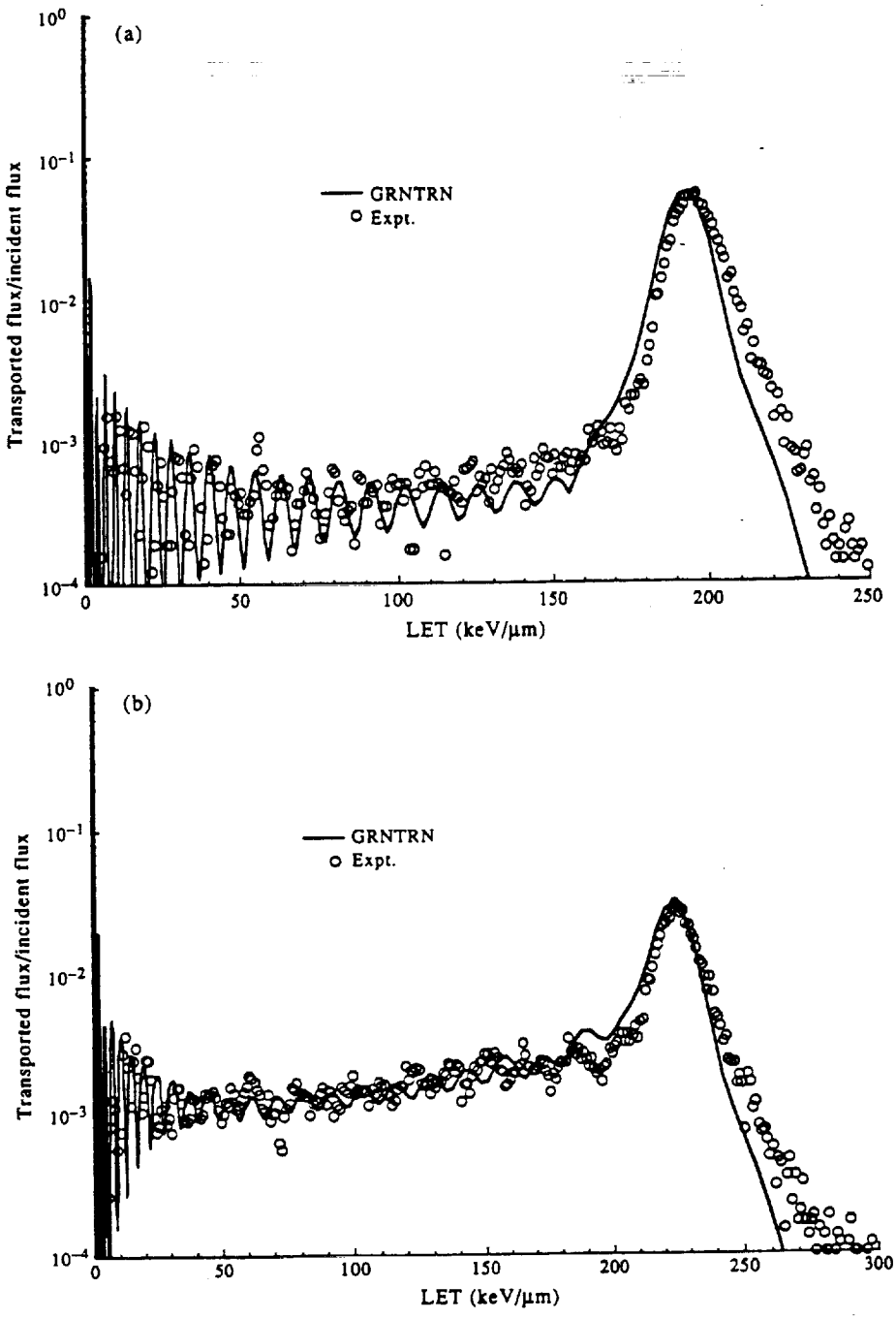

FIG. 6. Transport experiments for a lead-shield multilayer combination for 557 MeV/amu iron beams. (a) 2.24 g/cm^2 Pb + 2 g/cm^2 Al; (b) 2.24 g/cm^2 Pb + 4.6 g/cm^2 $(CH_2)_x$.

high LET side of the primary ion peak. The response function of equation (48) is used to compare the theory to the experiment.

The distribution of ions produced in passing a 557 MeV/amu ^{56}Fe beam through a 2.24 g/cm^2 of lead and the two target materials (separately) was mapped into detector response using equation (48). The comparison with experimental measurements is shown in Fig. 6. While the calculated result for polyethylene is in good agreement with the experimental data (Fig. 6(b)), the calculated aluminum curve (Fig. 6(a)) suggests that the aluminum fragmentation cross sections may be 20–30% low.

Acknowledgements—One of us (EVB) would like to thank both Dr Walter Schlimmerling of NASA Headquarters for suggesting our involvement in the fragmentation work and Dr Jack Miller of UC-LBL and his group for sharing their Bevalac beam time and for their help during the irradiations.

USF portion of the work supported partially by NASA grant NAG9-235.

REFERENCES

Benton E. V., Ogura K., Frank A. L., Atallah T. and Rowe V. (1986) Response of different types of CR-39 to energetic ions, *Nucl. Tracks Radiat. Meas.* **12,** 79–82.

Bertini H. W. (1969) Intranuclear-cascade calculation of the secondary nucleon spectrum from nucleon–nucleus interactions in the energy range 340 to 2900 MeV and comparisons with experiments. *Phys. Rev.* **188,** 1711–1730.

Cucinotta F. A., Townsend L. W. and Wilson J. W. (1983) Description of alpha–nucleus interaction cross sections for cosmic ray shielding studies. NASA TP-3285.

Shinn J. L., John S., Tripathi R. K., Wilson J. W., Townsend L. W. and Norbury J. W. (1992) Fully energy-dependent HZETRN (a galactic cosmic-ray transport code). NASA TP-3243.

Silberberg R., Tsao C. H. and Letaw J. R. (1983) Improvement of calculations of cross sections and cosmic ray propagation. In *Composition and Origin of Cosmic Rays* (ed. Shapiro M. M.), pp. 321–336. D. Reidel Publ.

Townsend L. W. and Wilson J. W. (1986) Energy-dependent parameterization of heavy-ion absorption cross sections. *Radiat. Res.* **106,** 283–287.

Townsend L. W., Wilson J. W., Tripathi R. K., Norbury J. W., Badavi F. F. and Khan F. (1993) HZEFRG1: An energy-dependent semiempirical nuclear fragmentation model, NASA TP-3310.

Wilson J. W. (1973) Intermediate energy nucleon–deuteron elastic scattering. *Nucl. Phys.* **B66,** 221–224.

Wilson J. W. (1974) Multiple scattering of heavy ions, Glauber theory, and optical model. *Phys. Lett.* **B52,** 149–152.

Wilson J. W. (1977a) Analysis of the theory of high-energy ion transport. NASA TN D-8381.

Wilson J. W. (1977b) Depth–dose relations for heavy ion beams. *Virginia J. Sci.* **28,** 136–138.

Wilson J. W. and Badavi F. F. (1992) New directions in heavy ion shielding. *Proc. Topical Meeting on New Horizons in Radiation Protection and Shielding.* Am. Nuc. Soc. pp. 205–211.

Wilson J. W., Badavi F. F., Costen R. C. and Shinn J. L. (1993a) Nonperturbative methods in HZE transport. NASA TP-3363.

Wilson J. W., Chun S. Y., Badavi F. F. and John S. (1993b) Coulomb effects in low-energy nuclear fragmentation. NASA TP-3352.

Wilson J. W., Costen R. C., Shinn J. L. and Badavi F. F. (1993c) Green's function methods in heavy ion shielding. NASA TP-3311.

Wilson J. W. and Costner C. M. (1975) Nucleon and heavy ion total and absorption cross sections for selected nuclei. NASA TN D-8107.

Wilson J. W., Lamkin S. L., Farhat H., Ganapol B. D. and Townsend L. W. (1989) A hierarchy of transport approximations for high energy heavy (HZE) ions. NASA TM-4118.

Wilson J. W. and Townsend L. W. (1981) An optical model for composite nuclear scattering. *Can. J. Phys.* **59,** 1569–1576.

Wilson J. W., Townsend L. W. and Badavi F. F. (1987a) Galactic HZE propagation through the earth's atmosphere. *Radiat Res.* **109,** 173–183.

Wilson J. W., Townsend L. W. and Badavi F. F. (1987b) A semiempirical nuclear fragmentation model. *Nucl. Inst. Meth. Phys. Res.* **B18,** 225–231.

Wilson J. W., Townsend L. W., Bidasaria H. B., Schimmerling W., Wong M. and Howard J. (1984) ^{20}Ne depth–dose relations in water. *Health Phys.* **46,** 1101–1111.

Wilson J. W., Townsend L. W., Lamkin S. L. and Ganapol B. D. (1990) A closed form solution to HZE propagation. *Radiat. Res.* **122,** 233–228.

Wilson J. W., Townsend L. W., Schimmerling W., Khandelwal G. S., Khan F., Nealy J. E., Cucinotta F. A., Simonsen L. C., Shinn J. L. and Norbury J. W. (1991) Transport methods and interactions for space radiations. NASA RP-1257.

APPENDIX

The preceding formalism is extended to a three-layer configuration as follows. The solution to equation (26) in a three-layered medium is:

$$g_{123jm}(x, y, z) = \sum_{kl} g_{1jk}(x) g_{2kl}(y) g_{3lm}(z). \tag{A1}$$

The leading term is the penetrating primaries, and equation (A1) may be written as:

$$g_{123jm}(x, y, z) = e^{-\sigma_{1j}x - \sigma_{2j}y - \sigma_{3j}z}\delta_{jm} + [g_{123jm}(x, y, z) - e^{-\sigma_{1j}x - \sigma_{2j}y - \sigma_{3j}z}\delta_{jm}]. \tag{A2}$$

The scaled Green's function is then:

$$\mathcal{G}_{123jm}(x, y, z, r_j, r'_m) \approx -e^{-\sigma_{1j}x - \sigma_{2j}y - \sigma_{3j}z}\delta_{jm} \times \delta(x + \rho_2 y + \rho_3 z + r_j - r'_m) + v_j[g_{123jm}(x, y, z) - e^{-\sigma_{1j}x - \sigma_{2j}y - \sigma_{3j}z}\delta_{jm}]/(x + \rho_2 y + \rho_3 z)(v_m - v_j), \tag{A3}$$

where $\rho_2 = R_{1j}(E)/R_{2j}(E)$ and $\rho_3 = R_{1j}(E)/R_{3j}(E)$. The range condition of equation (17) becomes:

$$\frac{v_j}{v_m}(r_j + x + \rho_2 y + \rho_3 z) \leqslant r'_m \leqslant \frac{v_j}{v_m} r_j + x + \rho_2 + \rho_3 z. \tag{A4}$$

The spectral corrections are similarly derived.

APPENDIX K

Preliminary Results of Radiation Measurements on EURECA

by

E.V. Benton and A.L. Frank

Proc. Third Post-Retrieval LDEF Symposium, Williamsburg VA, Nov. 8-12, 1993.

PRELIMINARY RESULTS OF RADIATION MEASUREMENTS ON EURECA*

E.V. Benton and A.L. Frank
Physics Research Laboratory
University of San Francisco
San Francisco, CA 94117-1080, U.S.A.

ABSTRACT

The eleven-month duration of the EURECA mission allows long-term radiation effects to be studied similarly to those of the Long Duration Exposure Facility (LDEF). Basic data can be generated for projections to crew doses and electronic and computer reliability on spacecraft missions. A radiation experiment has been designed for EURECA which uses passive integrating detectors to measure average radiation levels. The components include a Trackoscope, which employs fourteen plastic nuclear track detector (PNTD) stacks to measure the angular dependence of high LET (≥6 keV/μm) radiation. Also included are TLDs for total absorbed doses, thermal/resonance neutron detectors (TRNDs) for low energy neutron fluences and a thick PNTD stack for depth dependence measurements. LET spectra are derived from the PNTD measurements.

Preliminary TLD results from seven levels within the detector array show that integrated doses inside the flight canister varied from 18.8±0.6 cGy to 38.9±1.2 cGy. The TLDs oriented toward the least shielded direction averaged 53% higher in dose than those oriented away from the least shielded direction (minimum shielding toward the least shielded direction varied from 1.13 to 7.9 g/cm^2, Al equivalent). The maximum dose rate on EURECA (1.16 mGy/day) was 37% of the maximum measured on LDEF and dose rates at all depths were less than measured on LDEF. The shielding external to the flight canister covered a greater solid angle about the canister than in the LDEF experiments.

INTRODUCTION

The EURECA mission provided the opportunity for measurements of the space radiation environment in low earth orbit (LEO) over an extended period (11 months). Compared with the LDEF mission, the time period was 16% as long, but the number of orbits was sufficient to obtain an excellent average over the LEO radiation

*Work partially supported by NASA Grant No. NAG9-235, NASA-Johnson Space Center, Houston, TX

field. In orientation EURECA was in stable alignment with the sun, rather than Earth, which complicates the shielding distribution about the experiments. However, calculations based on environmental radiation models can be made by averaging over shielding for comparisons with the measurements.

A selection of passive integrating radiation detectors has been flown on the EURECA mission in a sealed aluminum canister. This experiment is similar to the A0015 and P0006 experiments which were flown on LDEF. The EURECA experiment included plastic nuclear track detectors (PNTDs), TLDs and thermal/resonance neutron detectors (TRNDs) to measure total absorbed doses, high LET particle fluences, directionality and shielding depth dependence of the space radiation. A silicon wafer in contact with PNTDs was also included for measurement of the high LET fluences of secondary particles originating in the silicon. The secondary radiation may contribute substantially to electronic microcircuit failures in space.

The radiation detectors in this experiment allow a number of measurements to be made. At present only the TLDs have been read out. Absorbed doses as functions of shielding thickness (due to the Al canister and the composition of the detectors only) are given. The remaining measurements will be reported at a later date.

EXPERIMENT

The EURECA satellite was launched with the STS-46 mission at 8:57 a.m. CDT on July 31, 1992 and returned with the STS-57 mission at 7:52 a.m. CDT on July 1, 1993, for a total duration in space of 335 days. The orbit was 426 km in altitude with an inclination of 28.5°. The flight canister was mounted within the Exobiology Radiation Assembly (discussed below) with open space through an aperture to one side of the canister.

The complement of detectors included in the experiment were a TLD plate, nearest the top of the canister, followed by the Trackoscope and the thick detector stack. The layout is shown in Fig. 1. The TLD plate was acrylic, with 16 holes for placement of TLDs; 4 around the center of the plate and 3 at each side.

The Trackoscope base was a truncated cube of acrylic with 14 faces (7 parallel pairs with 6-cm separations). PNTD stacks of 2.86 cm diameter and 0.45 cm thickness were attached to the faces. This arrangement compensates for the directional response of the PNTDs.

The thick detector stack contains layers of TLDs, PNTDs and aluminum, interspersed, and also a silicon wafer, held in place within a polyethylene sheet, and a TRND layer. The thick stack allows a measurement of shielding dependence of absorbed dose and heavy particle LET spectra. A comparison of the LET spectrum

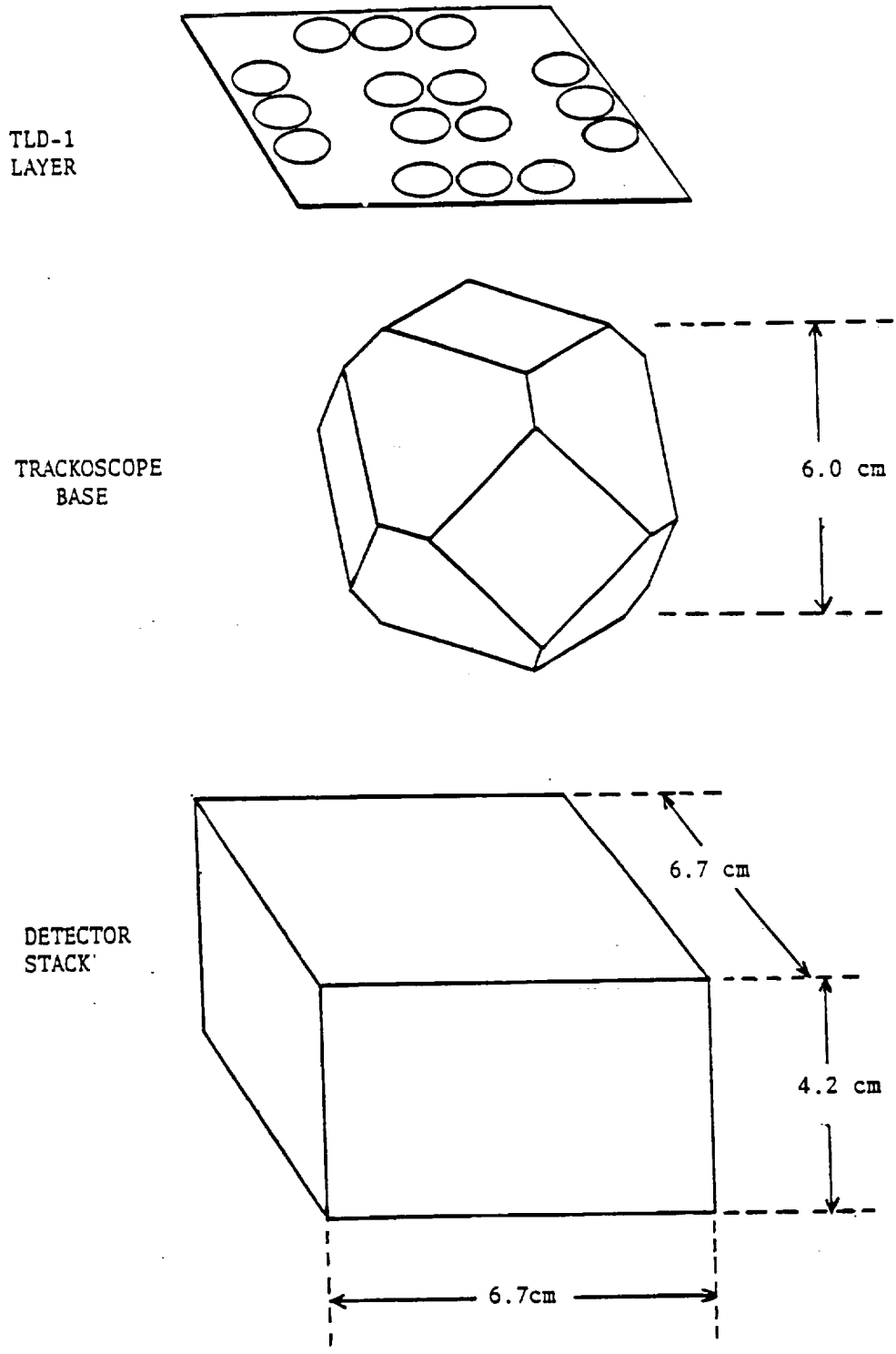

Fig.1 Detector components for EURECA radiation experiment. The Trackoscope base is a truncated cube with 7 pairs of parallel faces. PNTD sub-stacks (2.86 cm diam. x 0.25 cm thick) were placed on each of the 14 faces. The detector stack contained 6 additional TLD layers at various depths.

adjacent to the Si wafer with that in the near vicinity will yield information about secondary particle production within the wafer. The low energy neutron fluence, to be measured with the TRNDs, is of interest from the standpoint of dosimetry and as a test for the radiation modeling codes. The contents of the detector array are given in Table 1.

There were seven TLD plates included in the detector array with 16 TLD-700 chips (0.635 x 0.635 x 0.089) in each. After the mission, the TLDs were read out, with controls and ^{137}Cs γ-ray calibration chips, in a Harshaw Model 4000 reader. A pre-readout annealing cycle was used (120°C for 10 sec) to eliminate the low temperature LiF glow peak from the response. A low temperature fading study has shown that this eliminates the need for a fading correction for the EURECA time period. The flight and calibration TLDs were recalibrated together afterward to improve response accuracy.

MEASUREMENTS

The 16 TLD doses in each plate have been averaged into 5 groups: center, left, back, right, front. The measurements are given in Table 2 and Fig. 2. The direction of maximum intensity of radiation is seen to be diagonally through the right side and top of the canister. The minimum and maximum doses are 18.8 and 38.9 cGy.

DISCUSSION

The direction of maximum radiation intensity in the flight canister should correspond to the direction of minimum external shielding. The positions of the Biostack flight canisters, one of which was occupied by the detectors, is shown in Fig. 3 relative to the Exobiology Radiation Assembly. It can be seen that one side of the canister is unshielded to space. Also the top of the canister is set back from the side of the assembly so that the top has a significant solid angle open to space. It is also probable that the top of the canister receives a significant fraction of dose through the side of the assembly. This corresponds well to the expected external shielding as projected from the dose distribution.

An accurate solid angle distribution of external shielding about the detector canister will allow the dose measurements to be compared with calculations based on environmental radiation models. A comparison with dose rates measured on LDEF (Frank et al., 1992) is given in Fig. 4. For equivalent shielding, the EURECA dose rates are less than those at all LDEF locations. This is qualitatively consistent with the difference in the external shielding. The LDEF flight canisters (P0006 and A0015) were open to space over an approximately 2π solid angle, while the open solid angle on EURECA was much smaller. Also the different altitudes of

EURECA and LDEF contributed to higher LDEF doses. EURECA was launched from STS-46 with a Shuttle altitude of 426 km. LDEF was launched from STS-41C with the Shuttle at an altitude of 478 km. The LDEF altitude decayed, but a higher average trapped proton flux can be expected for this mission. At greater shielding depths the differences are smaller and the EURECA dose rates may be approximately equal to those at the LDEF leading edge.

REFERENCES

Frank A.L., Benton E.V., Armstrong T.W. and Colborn B.L. (1992) Absorbed dose measurements and predictions on LDEF. Second Post-Retrieval LDEF Symposium, San Diego, CA, June 1992. NASA Conference Publication 3194, Part 1, Washington DC, pp. 163-170.

TABLE 1. EURECA DETECTOR ASSEMBLY

Material	Layers	Layer Thickness (cm)	Label
TLD (Acrylic)	1	0.165	TLD #1
Trackoscope		6.92	ET-1 -- ET-14
Lexan	1	0.025	
TLD (Acrylic)	1	0.165	TLD #2
CR-39 (+PC)*	4	0.060	EUR-1 -- EUR-4
Al	1	0.159	
TLD (Acrylic)	1	0.165	TLD #3
CR-39 (+PC)	4	0.060	EUR-5 -- EUR-8
Al	1	0.159	
TLD (Acrylic)	1	0.165	TLD #4
CR-39 (+PC)	4	0.060	EUR-9 -- EUR-12
Al	1	0.318	
TLD (Acrylic)	1	0.165	TLD #5
CR-39 (+PC)	4	0.060	EUR-13 -- EUR-16
Al	1	0.318	
TLD (Acrylic)	1	0.165	TLD #6
CR-39 (+PC)	4	0.060	EUR-17 -- EUR-20
Si/Polyethylene	1	0.015	
CR-39	1	0.060	EUR-21
Al	1	0.159	
TLD (Acrylic)	1	0.165	TLD #7
^{6}LiF/CR-39 (Acrylic)	1	0.350	EUR-TRND
Lexan	1	0.025	

*8μm-thick polycarbonate film was placed between adjacent layers of CR-39

TABLE 2

TLD Absorbed Doses Measured on EURECA

Absorbed Dose (cGy)

TLD PLATE	Center	Front	Left	Back	Right	Shielding Thickness Al Equiv. (g/cm^2)
1	30.9±0.9	33.9±1.0	28.8±0.9	32.8±1.0	38.9±1.2	0.92
2	22.3±0.7	24.6±0.7	19.7±0.6	25.8±0.8	32.9±1.0	8.30
3	23.2±0.7	24.7±0.7	20.1±0.6	25.4±0.8	31.3±0.9	9.36
4	22.2±0.7	25.2±0.8	20.7±0.6	23.7±0.7	29.7±0.9	10.4
5	22.9±0.7	24.1±0.7	20.1±0.6	24.5±0.7	28.6±0.9	11.9
6	21.1±0.6	22.3±0.7	18.8±0.6	22.8±0.7	29.0±0.9	13.4
7	21.7±0.7	24.1±0.7	19.4±0.6	22.8±0.7	29.6±0.9	14.9

The uncertainty given is standard deviation, σ.

The shielding given is the averaged vertical shielding to the top of the detector array and includes the top of the flight canister. Shielding external to the canister is not given.

Minimum shielding of the side TLDs through the sides of the canister was 1.13 g/cm^2, Al equivalent.

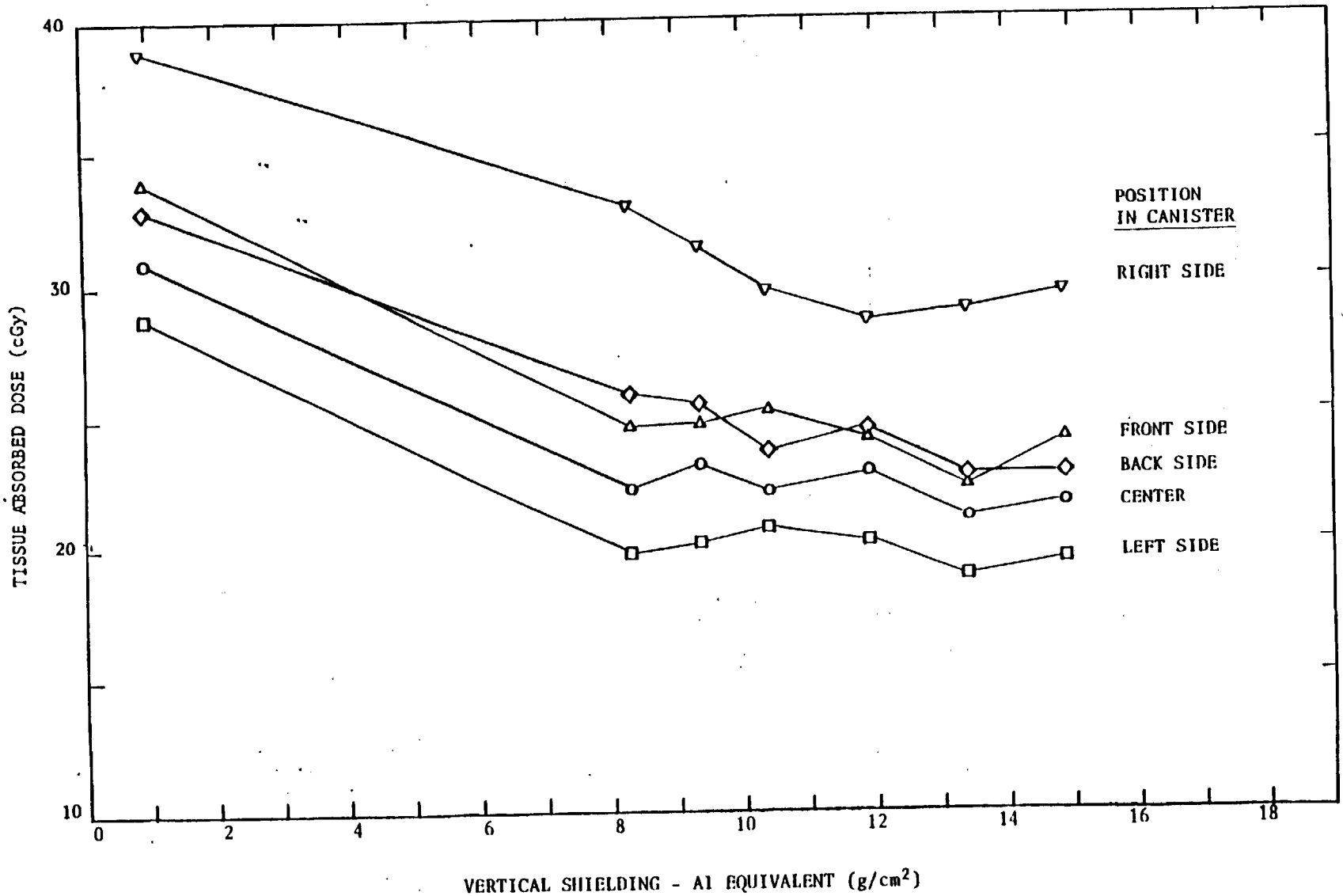

Fig. 2. TLD-700 dose as a function of shielding thickness of the LDEF A0015 canister and contents. Shielding is measured vertically to the top of the canister. Minimum external shielding is to the right side of the canister.

EURECA
EXOBIOLOGY RADIATION ASSEMBLY

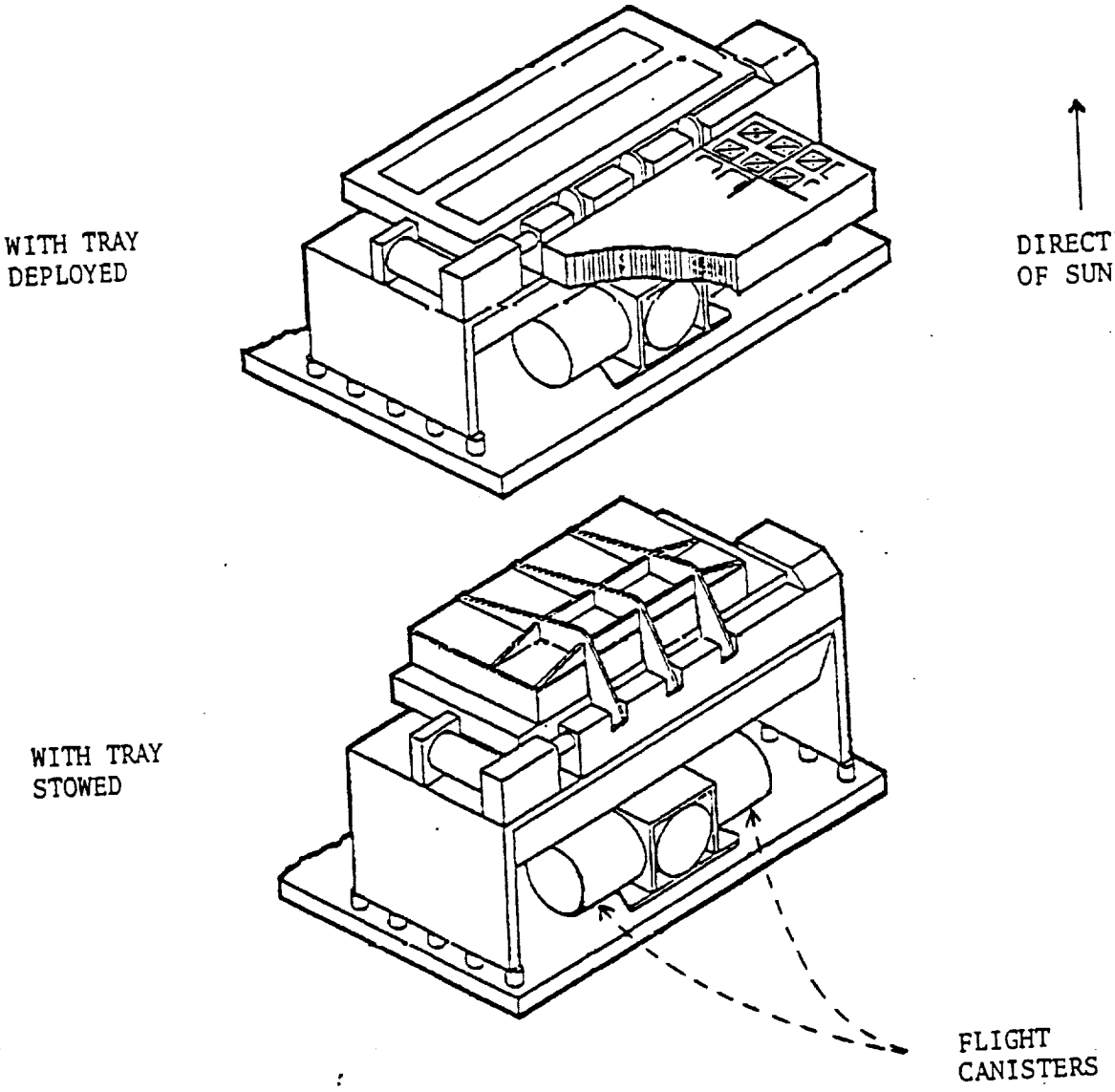

Fig. 3. The positions of flight canisters relative to the exobiology radiation assembly on the EURECA satellite

165

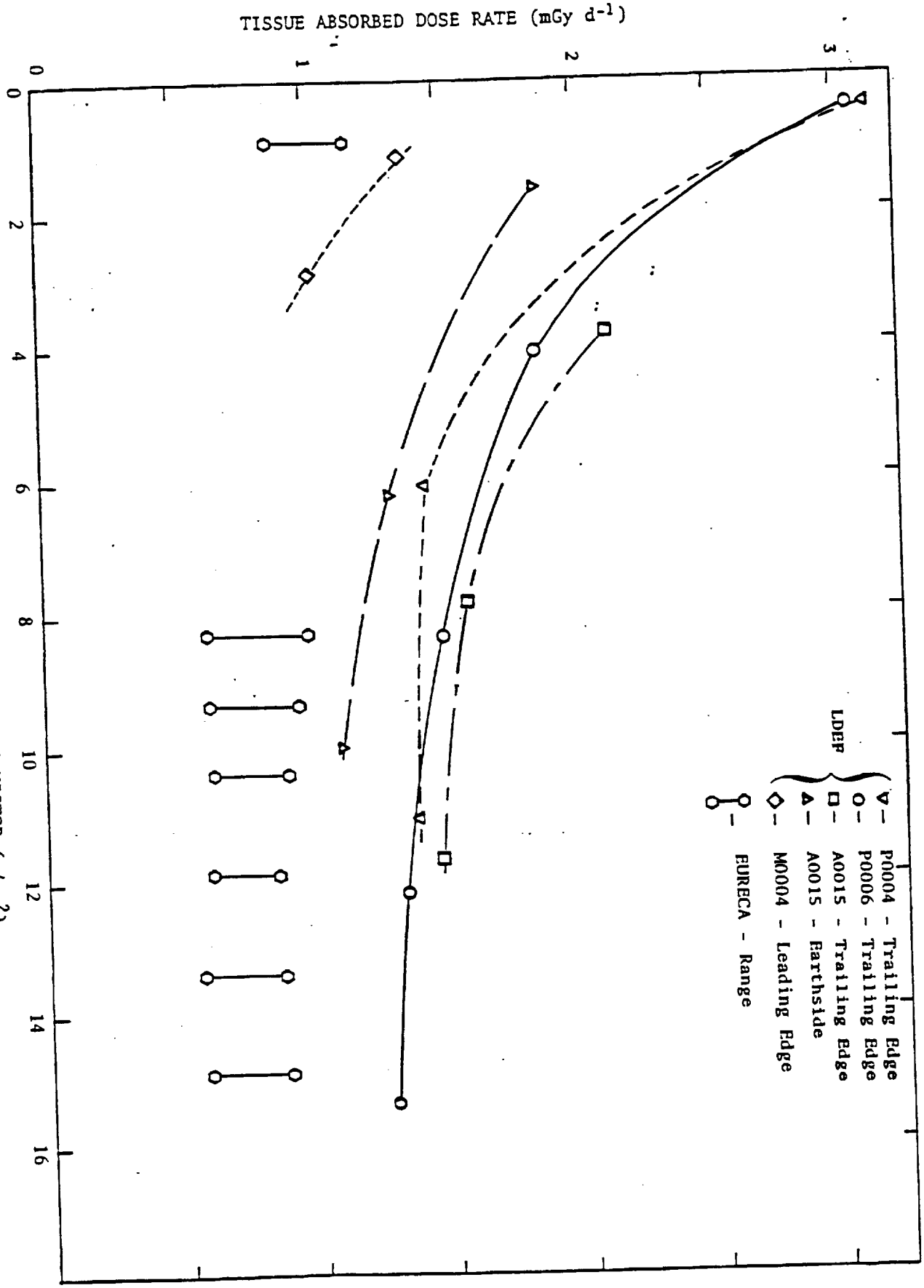

Fig. 4. Comparison of LDEF and EURECA TLD-700 dose rates as functions of shielding from the flight canisters and their contents (also thermal blankets on LDEF).

APPENDIX L

Fission Foil Detector Calibrations with High Energy Protons

by

A.L. Frank and E.V. Benton

APPENDIX L

FISSION FOIL DETECTOR CALIBRATIONS WITH HIGH ENERGY PROTONS

A.L. Frank and E.V. Benton
Department of Physics, University of San Francisco
San Francisco, CA 94117-1080

Introduction

Fission foil detectors (FFDs) are passive devices composed of heavy metal foils in contact with muscovite mica films. The heavy metal nuclei have significant cross sections for fission when irradiated with neutrons and protons. Each isotope is characterized by threshold energies for the fission reactions and particular energy-dependent cross sections. In the FFDs, fission fragments produced by the reactions are emitted from the foils and create latent particle tracks in the adjacent mica films. When the films are processed surface tracks are formed which can be optically counted. The track densities are indications of the fluences and spectra of neutrons and/or protons.

FFDs have previously been used for spaceflight measurements (Benton et al., 1982-1983; Benton et al., 1978; Benton et al., 1981; Frank et al., 1990; Dudkin et al., 1992). In cases where the proton contribution to track densities can be subtracted out, the FFDs can be used as high energy (>1 MeV) neutron dosimeters. These detectors have been calibrated with neutrons of energies up to ~15 MeV and found to have efficiencies $\epsilon = 1.16 \times 10^{-5}$ tracks/neutron barn (Pretre et al., 1968), where "thick" foils are used (the thickness of the foils exceeds the ranges of the fission fragments produced so that maximum efficiency is achieved). There have been no calibrations performed with nucleons of higher energies or with FFDs having threshold energies above 15 MeV. In the past, detection efficiencies have been calculated using the low energy neutron calibration and published fission cross sections for neutrons and protons. The problem is that the addition of a large kinetic energy to the (n,nucleus) or (p,nucleus) reaction could increase the energies and ranges of emitted fission fragments and increase the detector sensitivity as compared with lower energy

neutron calibrations.

High energy calibrations are the only method of resolving the uncertainties in detector efficiencies. At high energies, either proton or neutron calibrations are sufficient since the cross section data, plotted in Figure 1 (Lomanov et al., 1979; Wollenberg and Smith, 1969; Stehn et al., 1965), show that the proton and neutron fission cross sections are approximately equal.

Experiment

High energy proton beams have been utilized at the Lawrence Berkeley Laboratory BEVALAC and at Harvard Cyclotron Laboratory (HCL). Beam energies were 1.8 and 4.9 GeV at the BEVALAC and 80 and 140 MeV at HCL. All irradiated FFDs were assembled with thick foils. During the irradiations the proton beams were incident normal to one surface of the detectors. The two mica films therefore measure the tracks of fission fragments emitted backward (opposite to the proton direction) and forward (in the direction of the protons), respectively (Figure 2).

For the BEVALAC irradiations, the proton doses were monitored by arrays of TLDs (TLD-700) held in acrylic plates. The plates were aligned with the FFDs during the irradiations. At HCL, their calibrated ion chambers were used to determine the doses. In each case the proton fluence is found from

$$F_p = \text{Dose(rad)}/[1.602 \times 10^{-8} \times \frac{dE}{dX}\ (\text{MeV}\cdot\text{cm}^2\cdot\text{g}^{-1})]$$

After the irradiations, the mica films were etched in 50% HF for 1 hr at 21°C to reveal the fission fragment tracks. They had been etched for 3 hr prior to the irradiations to enlarge the latent fossil tracks. Average track densities were measured by scanning several strips across each film under an optical mocroscope at 200X or 430X, depending on track densities. Backgrounds were counted on reverse sides of the films.

Track densities from aged ^{238}U foils are reduced due to oxidation. This was compensated for by dividing the measured track densities by 0.7, so that the results are consistent with new, unoxidized foils. The background due to spontaneous fissions in the ^{238}U foils were measured by storage of assembled FFDs.

Measurements

The measured detector efficiencies are given in Table 1. The track densities on the two mica films (backward and forward) have been averaged for each fission foil, as would be done in space measurements. In all cases the track density in the forward (beam) direction was greater than in the backward direction, showing that beam energies have a distinct effect on fission fragment ranges. The ratios of backward-to-forward track densities with better statistics varied from 0.45 (1.8 GeV protons on ^{181}Ta) to 0.85 (140 MeV protons on Pb) but the data are too sparse to determine variations as functions of beam energy or atomic number of the foil.

The standard deviations (σ) for the 1.8 and 4.9 GeV measurements are in the range of 7 to 15%. This is mainly due to uncertainties in proton fluences caused by gradients across the detectors during the irradiations. The track counting statistics were about 2-4%. The beam was uniform across the detectors at HCL, resulting in smaller σs in the 80 and 140 MeV measurements.

The efficiency measurements are plotted in Figure 3 along with some calculated neutron efficiencies for ^{238}U and ^{232}Th at lower energies. The cross section curves (Figure 1) have been used as guides in filling in the efficiency curves over a wide energy range. The ^{232}Th measurement at 4.9 GeV does not fit in with other measurements or with projections from the cross sections. The reason for this could not be determined.

Conclusions

A beginning has been made to the calibration of fission foil detectors to high energy nucleons. Measured sensitivities above 1 GeV (tracks/nucleon) are higher by factors of approximately 2-3 than those which would be calculated using published fission cross sections and the efficiency equation derived from low energy neutron calibrations. The calibrations will be improved by measurements at a greater number of energies. The energy range of interest in space applications extends to 100 GeV (Armstrong and Colborn, 1990) so the published fission cross section curves will

continue to be useful in supplementing measurements.

REFERENCES

Armstrong T.W. and B.L. Colborn (1990), Scoping estimates of the LDEF satellite induced radioactivity. SAIC, Report No. SAIC-90/1462.

Benton E.V., R.M. Cassou, A.L. Frank, R.P. Henke and D.D. Peterson (1978), Space radiation on board Cosmos 936--U.S. portion of experiment K206, in: Final Reports of U.S. Plant and Radiation Experiments Flown on the Soviet Satellite Cosmos 936 (S.N. Rosenzweig and K.A. Souza, eds.). NASA TM 78526.

Benton E.V., R.P. Henke, A.L. Frank, C.S. Johnson, R.M. Cassou, M.T. Tran and E. Etter (1981), Space radiation dosimetry aboard Cosmos 1129--U.S. portion of experiment K309, in: Final Reports of U.S. Plant and Radiation Experiments Flown on the Soviet Satellite Cosmos 1129 (M.R. Heinrich and K.A. Souza, eds.) NASA TM 81288.

Benton E.V., R.P. Henke, A.L. Frank, R.M. Cassou, C.S. Johnson and M.T. Tran (1982-1983). Final Dosimetry Reports for STS-3, STS-4, STS-5, STS-6, TR-54, -56, -57, -58, University of San Francisco Physics Research Laboratory.

Dudkin V.E., Yu.V. Potapov, A.B. Akopova, L.V. Melkumyan, Sh.B. Rshtuni, E.V. Benton and A.L. Frank (1992), Neutron fluences and energy spectra in the Cosmos-2044 Biosatellite orbit, Nucl. Tracks Radiat. Meas. 20(1), 139-141.

Frank A.L., E.V. Benton, E.R. Benton, V.E. Dudkin and A.M. Marenny (1990), Radiation experiments on Cosmos 2044: K-7-41, Parts A,B,C,D,E, TR-76, University of San Francisco Physics Research Lab.

Lomanov M.F., G.G. Shimchuk and R.M. Yakovlev (1979), Solid state detectors of fission fragments for the REM dose measurement of mixed proton and neutron radiation. Hlth. Phys. 37, 677-686.

Pretre S., E. Tochilin and N. Goldstein (1968), Solid state detectors of fission fragments for the REM-dose measurement of mixed proton and neutron radiation. Hlth. Phys. 37, 677-686.

Stehn J.R., M.D. Goldberg, R. Wiener-Chasmon, S.F. Mughabghab, B.A. Magurno and V.M. May (1965), Neutron Cross Sections Vol.III, BNL 325.

Wollenberg H.A. and A.R. Smith (1969), Energy and flux determinations of high-energy nucleons, UCRL-19364.

171 C-3

ACKNOWLEDGEMENTS

We thank Dr. A Koehler of Harvard Cyclotron Laboratory for assistance in making these irradiations. The University of San Francisco work was supported by NASA Grants No. NAG9-235, Johnson Space Center, Houston, Texas, and NAG8-168, Marshall Spaceflight Center, Huntsville, Alabama.

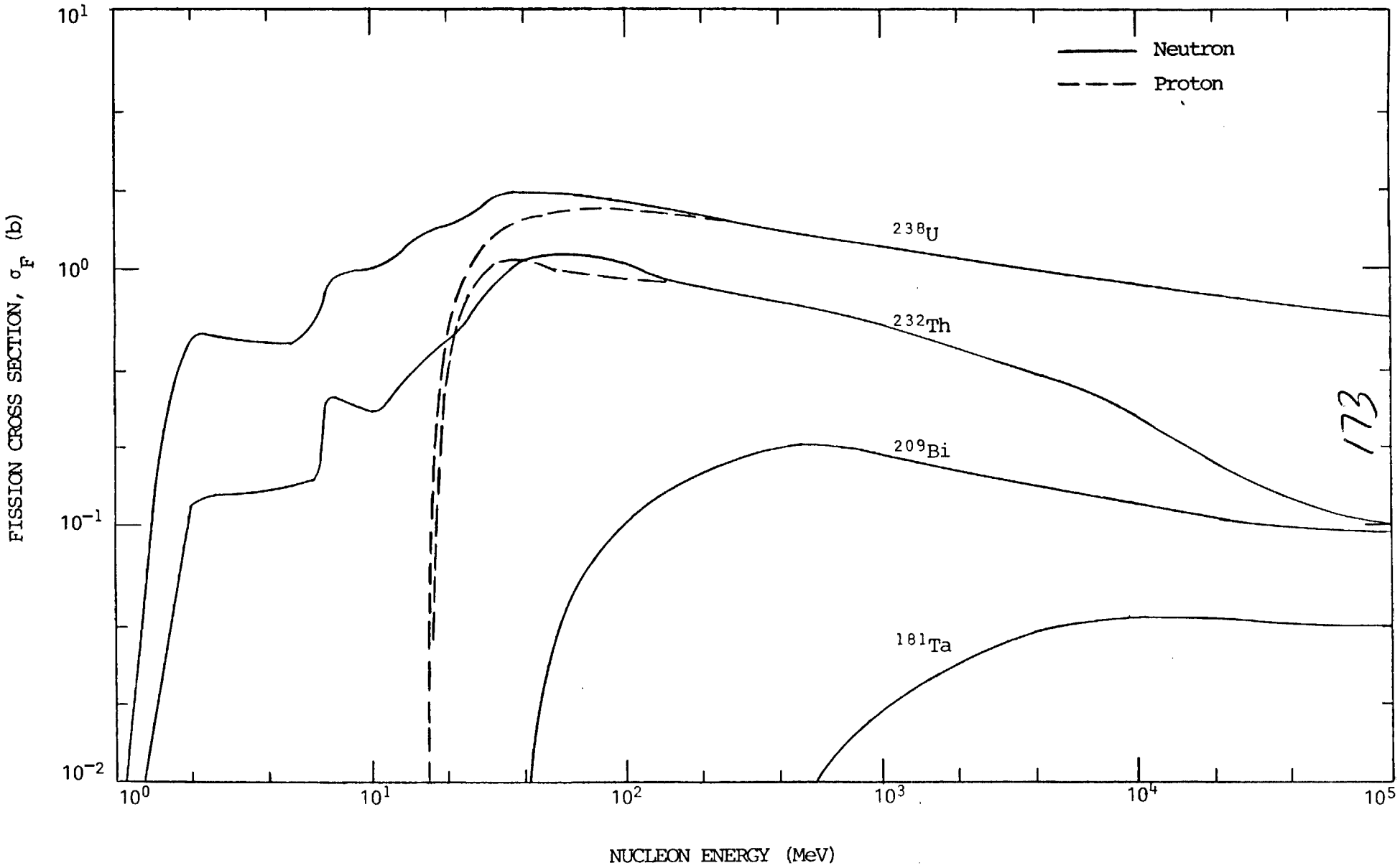

Fig. 1. Fission cross sections for neutrons and protons incident on heavy metal foils

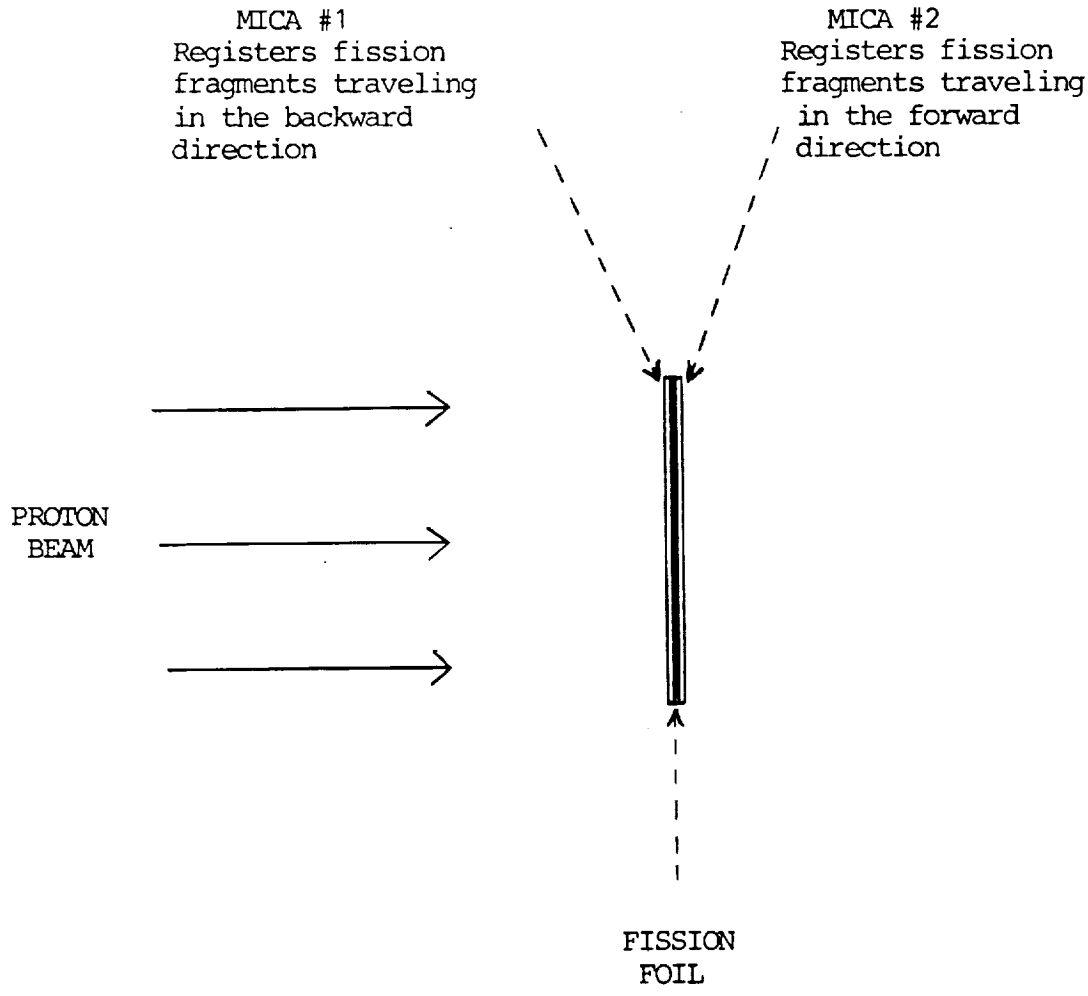

Fig. 2. Sketch of the experiment

Table 1. MEASURED SENSITIVITIES OF FISSION FOIL DETECTORS

Fission Foil	14 MeV Neutrons* (tracks/n)	80 MeV Protons (tracks/p)	140 MeV Protons	1.8 GeV Protons (tracks/p)	4.9 GeV Protons (tracks/p)
^{181}Ta	0	0	---	$9.8\pm0.9\times10^{-7}$	$1.59\pm0.15\times10^{-6}$
^{209}Bi	0	$6.21\pm0.25\times10^{-7}$	$1.43\pm0.05\times10^{-6}$	$2.65\pm0.32\times10^{-6}$	$2.60\pm0.18\times10^{-6}$
^{232}Th	4.76×10^{-6}	$1.32\pm0.05\times10^{-5}$	$1.14\pm0.04\times10^{-5}$	$6.5\pm0.8\times10^{-6}$	$1.46\pm0.22\times10^{-5}$
^{232}U	1.43×10^{-5}	$1.63\pm0.06\times10^{-5}$	$2.00\pm0.07\times10^{-5}$	---	$1.66\pm0.19\times10^{-5}$
Pb(nat)	0	$2.46\pm0.12\times10^{-7}$	$6.17\pm0.28\times10^{-7}$	---	$3.47\pm0.47\times10^{-6}$

*Calculated from cross sections and calibrated efficiency for neutrons

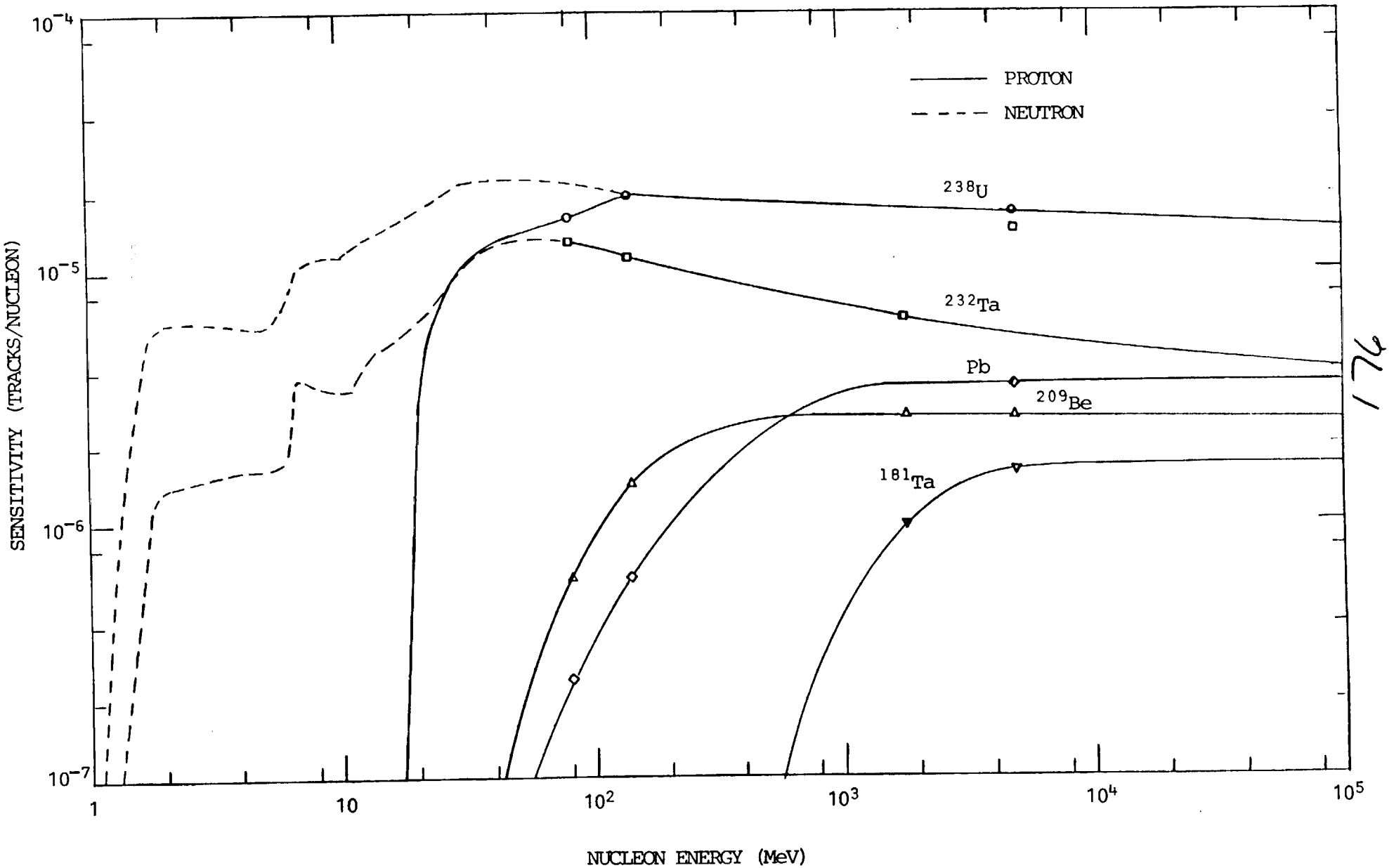

Fig. 3. Sensitivities of fission foil detectors to neutrons and protons

APPENDIX M

Proton Calibration of Low Energy Neutron Detectors Containing ^{6}LiF

by

A.L. Frank and E.V. Benton

APPENDIX M

PROTON CALIBRATION OF LOW ENERGY NEUTRON DETECTORS CONTAINING ^{6}LiF

A.L. Frank and E.V. Benton
Department of Physics, University of San Francisco
San Francisco, CA 94117-1080

Introduction

Neutron detectors composed of layers of ^{6}LiF placed between films of plastic nuclear track detectors (PNTDs) have been used on numerous space missions to measure thermal and resonance neutron fluences. The detectors have typically been mounted in pairs, with one of the pair covered by Gd or Cd foil to absorb out the thermal neutron component. The neutrons are detected through the ^{6}Li(n,α)T reaction which has a high cross section at thermal energies (950 b) and declines with increasing neutron energy ($\sigma = 150.2/\sqrt{E_n}$). The ^{6}LiF layer becomes a radiator foil for the PNTD films. The emitted α-particle track densities are counted in the PNTDs and are converted to neutron fluences through detector calibrations and response calculations.

The accuracy of these neutron measurements has recently been questioned by Keith et al. (1992). The reason has to do with the high fluences of energetic protons incident on the spaceflight detectors during the measurements. There are reactions other than neutron absorption by ^{6}Li which can produce α-particle emissions, such as ^{6}Li(p,α), ^{7}Li(p,α) and ^{19}F(p,α). They believe it possible that a large fraction of the α-particle tracks counted on these detectors are induced by protons rather than neutrons. If true, the measured neutron fluences would be overestimated and the large deviations in the ratios of proton and neutron fluences present in the spacecraft, plus proton spectrum fluctuations, would result in inaccuracies of uncertain magnitudes.

The purpose of the present calibrations is to measure the proton response of the detectors with accelerated beams having energies within the region of maximum intensities in the trapped

proton spectrum encountered in near-Earth orbit. This response is compared with the responses of the spaceflight detectors when related to proton exposures. All of the spaceflight neutron measurements have been accompanied by TLD absorbed dose measurements in close proximity within the spacecraft. For purposes of comparison, the spaceflight TLD doses are assumed to be proton doses.

Experiment

Detectors were assembled from layered arrays of ^{6}LiF and ^{7}LiF TLDs (TLD-600 and TLD-700) with films of CR-39 PNTDs on both sides. The individual TLDs are 0.635 cm square and 0.089 cm thick. The ^{7}LiF detectors were included to reveal the effect of the ^{6}Li isotope in determining response to protons. The detector components were covered with dense cardboard sheet during the irradiations.

Detectors were mounted in pairs (one of each type) side-by-side for the irradiations. The proton beams were incident at 45° angles to the surface of the PNTD and LiF layers. Proton beam energies of 80 and 153.6 MeV were obtained at the Harvard Cyclotron Laboratory. The detectors exposed to 80 MeV protons were given 15.1 rads, while those exposed to 153.6 MeV were given 9.88 rads. These doses correspond to 1.085×10^{8} and 1.129×10^{8} protons/cm^{2}, respectively. A third pair of detectors traveled with the others for background purposes.

After return of the detectors, the CR-39 films were removed and processed by standard techniques to delineate the latent tracks and provide good visual discrimination between short, stopping α-particle tracks and other tracks present in the surfaces. The etchant used was 6.25N NaOH at 70° and the etching time was 4 hr. The films were scanned and the track densities counted at 200x under an optical microscope. Spaceflight detectors are read out using the same methods.

Measurements

The measured track densities per rad are given in Table A-I-1. The error limits given are calculated from the standard deviations

based on counting statistics plus a 10% uncertainty due to track classification. The added uncertainty derives from the nature of the track size distribution. On spaceflight detectors, the track counting is relatively easy because the targeted tracks, short, stopping α-particle tracks from the $^{6}Li(n,\alpha)$ reaction, are relatively distinct from other tracks present with few border-line events. The proton-irradiated detectors contained a more undifferentiated track size distribution. This made track classification more difficult and may have caused added track density variations of up to ± 10%, after background subtractions.

The track densities found for ^{6}LiF are greater than for ^{7}LiF at 80 MeV, but less than at 153.6 MeV. However, the uncertainties in the measurements may account for the differences. The track densities at 153.6 MeV are greater than at 80 MeV when calculated per rad but are about the same when calculated per incident proton.

Included in Table A-I-1 are the results of calculating track densities per TLD rad for 17 spacecraft measurements. The spaceflight track densities used were those measured for the resonance neutrons. Because of the way thermal neutron track densities are found from the pair of flight detectors (subtraction of the Gd-covered-detector track densities from uncovered-detector track densities) all of the tracks produced by space protons would be included with the resonance neutron component. There were large variations in the spaceflight measurements of track density per TLD rad, with a trend to very low values for high altitude flights. At high altitudes high doses of lower energy protons are encountered in the SAA. The data suggest that these protons are relatively inefficient at producing secondary neutrons through interactions with the spacecraft material.

In comparing spaceflight track densities with those measured for protons it is seen that there is approximately a factor of 100 between them. This implies that the proton-induced fraction of track densities attributed to resonance neutrons in spacecraft measurements averages about 1% and would not be expected to exceed 4% on any mission.

Conclusions

Based on a simulation of spaceflight protons by 80 and 153.6 MeV accelerated protons, the average overestimate of measured resonance neutron fluences during LEO missions is about 1%. Since the accuracy given for these spaceflight measurements is about a factor of 2, the proton contribution is not significant. Track densities of short-range, stopping α particles, measured with ^{6}LiF and ^{7}LiF radiator foils were not significantly different, implying that the p,α cross-sections of the radiator foil isotopes are comparable at these proton energies.

Reference

J.E. Keith, G.D. Badhwar and D. J. Lindstrom (1992) Neutron spectrum and dose-equivalent in Shuttle flights during solar maximum. Nucl. Tracks Radiat. Meas. 20(1), 41-48.

Acknowlegement

We thank Dr. A. Koehler of Harvard Cyclotron Laboratory for making these measurements possible.

TABLE A-I-1. Track Densities of Stopping α-Particles Induced by Protons

Proton Energy (MeV)	Radiator Layer	Track Density (cm^{-2} rad^{-1})	(Tracks/Proton)
80	^{6}LiF	9.3±1.8	1.29±0.25 x 10^{-6}
80	^{7}LiF	6.8±1.3	9.5 ± 1.8 x 10^{-7}
153.6	^{6}LiF	11.0±2.1	9.7 ± 1.9 x 10^{-7}
153.6	^{7}LiF	15.4±2.1	1.36±0.19 x 10^{-6}
Spaceflight	^{6}LiF	1060±670*	

APPENDIX N

Linear Energy Transfer (LET) Spectra of Cosmic Radiation in Low Earth Orbit

by

A.B. Akopova, N.V. Magradze, V.E. Dudkin, E.E. Kovalev,
Yu.V. Potapov, E.V. Benton, A.L. Frank, E.R. Benton
T.A. Parnell and J.W. Watts, Jr.

Nucl. Tracks Radiat. Meas., Vol. 17, No. 2, pp. 93–97, 1990
Int. J. Radiat. Appl. Instrum., Part D
Printed in Great Britain

0735-245X/90 $3.00 + .00
Pergamon Press plc

LINEAR ENERGY TRANSFER (LET) SPECTRA OF COSMIC RADIATION IN LOW EARTH ORBIT

A. B. AKOPOVA,* N. V. MAGRADZE,* V. E. DUDKIN,† E. E. KOVALEV,† YU. V. POTAPOV,† E. V. BENTON,‡ A. L. FRANK,‡ E. R. BENTON,‡ T. A. PARNELL‖ and J. W. WATTS JR‖

*Yerevan Institute of Physics, Yerevan, U.S.S.R.; †Institute of Biomedical Problems of the Ministry of Public Health of the U.S.S.R., Moscow 123007, U.S.S.R.; ‡University of San Francisco,§ CA 94117, U.S.A. and ‖NASA Marshall Spaceflight Center, Huntsville, AL 35812, U.S.A.

(*Received* 30 *May* 1989)

Abstract—Integral linear energy transfer (LET) spectra of cosmic radiation (CR) particles were measured on five Cosmos series spacecraft in low Earth orbit (LEO). Particular emphasis is placed on results of the Cosmos 1887 biosatellite which carried a set of joint U.S.S.R.–U.S.A. radiation experiments involving passive detectors that included thermoluminescent detectors (TLDs), plastic nuclear track detectors (PNTDs), fission foils, nuclear photo-emulsions, etc. which were located both inside and outside the spacecraft. Measured LET spectra are compared with those theoretically calculated. Results show that there is some dependence of LET spectra on orbital parameters. The results are used to estimate the CR quality factor (QF) for the Cosmos 1887 mission.

INTRODUCTION

THE INTEGRAL linear energy transfer (LET) spectra are important for characterizing cosmic radiation (CR) because they can be used to estimate the absorbed and equivalent particle dose and to evaluate the respective quality factors. Earlier, the integral LET distributions were measured in the following works: Petrov *et al.* (1975), Benton (1983, 1986), and Akopova *et al.* (1985, 1986, 1987, 1988). As a rule, these investigations used passive detectors (plates, emulsions) which permitted measurements in a restricted LET interval. In some investigations (e.g. Akopova *et al.*, 1987, 1988; Heinrich, 1977; Heinrich and Baer, 1984), the LET distributions were calculated as a function of shielding. In all of these theoretical studies, only the galactic cosmic ray particles were regarded as sources of cosmic radiation.

This paper presents the results of a recent experimental and calculational study carried out by the authors. Particular attention was paid to comparing results obtained by various experimental techniques, and to finding the laws which govern the dependence of the forms of the integral LET distributions on orbital parameters. Measurements were taken in free space (behind very thin shielding), and inside the spacecraft where the mean thickness of the shielding of detectors reached tens of g cm^{-2}. The contribution of trapped protons and electrons is also taken into account in the theoretical calculations.

EXPERIMENTAL TECHNIQUES

The use of LET spectral data is necessary for appraising the radiation environment inside spacecraft. Previous measurements were made on board Cosmos 782, 936, and 1129 using an electron spectrometer, nuclear emulsions, and plastic detectors. These results have been presented by Benton (1986) together with dosimetric measurements and LET spectra obtained on board some of the U.S. Shuttle flights.

The current work presents the results obtained on board five Cosmos-type satellites using two types of detectors, namely, nuclear photo-emulsions (NPE) and solid state nuclear track detectors (SSNTDs). The NPE assemblies containing 200 μm thick BR- and BYa-type emulsions wrapped with light-tight paper and aluminized Lavsan were placed either in instrument modules outside the spacecraft or inside the spacecraft. After exposure and recovery, each layer of emulsion assembly was treated by the selective-development technique which makes it possible to control the NPE layer threshold sensitivity in a broad interval of LET (see Akopova *et al.*, 1983). The emulsion threshold sensitivity control is based on the introduction of Br^- ions into an exposed emulsion layer by diffusion. The Br^- ions emanated from BR-type layers (emitters) glued to either of the surfaces of the exposed layer that had been irradiated beforehand with blue–violet light. The Br^- ion generation and diffusion from the emitters to the exposed

§USF work partially supported by NASA–Ames Research Center Grant No. NCC2-521, NASA–MSFC Grant No. NAG8-071 and NASA–ISC Grant No. NAG9-235.

layers gives rise to a negative bromine barrier around the latent image centers, thereby increasing the induction periods of developing centers. The ability of the centers to be developed depends, then, upon the ratio of the height of the barrier restricting the arrival of electrons at the centers to the depth of the potential well in which the electrons are captured. Thus, controlling the NPE threshold sensitivity is based on different degrees of dispersion of the latent image centers produced by particles with different LET values. The threshold sensitivity of the exposed layer permits only those particle tracks to be developed for which the LET is at least equal to some threshold LET value. Therefore, the technique of finding the planar fluence of the particles with LET $\geq$ LET$_{thresh}$ does not require the track parameters to be measured but is reduced to counting the number of the tracks traversing a particular section of an NPE surface. Calibration of the technique was achieved by exposing NPEs to particle beams of well-defined LETs.

We used BYa-type emulsion which permits the integral LET spectra to be measured within an interval from 12 to $\sim 10^4$ MeV cm^{-1} of biological tissue (water), with the lower limit (~ 12 MeV cm^{-1}) being defined by the effective sensitivity of the BYa-type emulsion. To obtain a complete LET distribution, we sometimes used the relativistic BR-type emulsion, thereby making it possible (to within a large microscope scanning error) to find the planar fluence of cosmic radiation particles at small LET values (the LET of relativistic protons in tissue is $\simeq 2.0$ MeV cm^{-1}. The error in counting these tracks at LET$_{thresh} \simeq 2.0$ MeV cm^{-1} increases (i) due to a high track exposure of the detectors (the satellite flights lasted, as a rule, for more than 10 days) and (ii) because the operator can easily overlook tracks of relativistic protons (low grain densities).

The second technique for finding the LET distributions is based on the use of SSNTDs of the CR-39, CN, and polycarbonate type, whose effective LET thresholds of track detection are 40, 1000, and 2250 MeV cm^{-1} in water, respectively. CN and Lexan were used in earlier measurements (the ASTP, Skylab, and Apollo 17 missions). During later flights, including the 24 initial flights of the U.S. Shuttle, use was made of SSNTDs of the CR-39, polycarbonate, and polystyrene types which were subjected after the flights to the standard NaOH etching with 6.25 N at 70°C. Preliminary scanning showed that the density

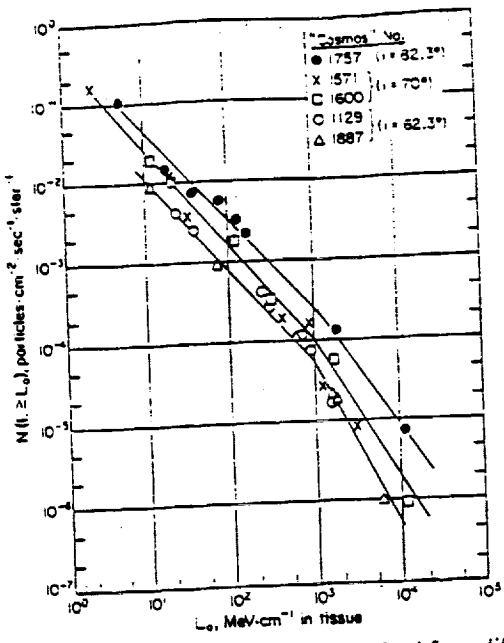

FIG. 1. The experimental LET spectra obtained from different satellites of the Cosmos series at $\delta \leq 1.0$ g cm^{-2} by the NPE method.

of the tracks detected in polycarbonate and polystyrene was very low compared with that of CR-39. The method for using SSNTD to find the LET spectra is described in detail by Henke and Benton (1974).

RESULTS AND DISCUSSION

In Fig. 1 are shown the results of LET spectra measurements by the NPE method. The NPE assemblies were placed in external instrument modules on spacecraft with different orbital parameters (see Table 1). For these external assemblies, the shielding thickness may be considered not to exceed ~ 1.0 g cm^{-1}. The shielding of the detectors by the satellite bodies and by the Earth and the geometry of the exposures were approximately the same for all of the flights.

The integral LET spectra shown in Fig. 1 have been obtained mainly with the BYa-type emulsions, so the distribution ranged from 12 to 1.5×10^4 MeV cm^{-1} of tissue. From Fig. 1 it is seen that the values of the integral spectrum at the lower LET values were

Table 1. The flight parameters of the satellites on which the NPE assemblies were exposed

Cosmos series satellite	Exposure time	Apogee/ perigee (km)	Orbital inclination	Solar activity period
1129	Sep. 25–Oct. 10, 1979	406/226	62.8°	max
1571	Jun. 11–Jun. 26, 1984	420/355	70°	min
1600	Sep. 27–Oct. 10, 1984	420/354	70°	min
1757	Jun. 11–Jun. 19, 1986	252/189	92.3°	min
1887	Sep. 29–Oct. 12, 1987	406/224	62.8°	min

obtained using the relativistic BR-type emulsion on board Cosmos 1571 and 1757 only. In order to make the presentation of data clear, the experimental points have been unified by a solid line of the approximate form $\alpha \cdot L^{-\beta}$, where L is LET in tissue; α and β are constants.

The following preliminary conclusions may be drawn from the curves presented in Fig. 1:

(1) experimental values of the integral LET distributions are very close to each other for the satellites with similar orbital parameters (Cosmos 1129 and 1887, Cosmos 1571 and 1600);

(2) effects of solar activity are insignificant (the values of the spectra obtained from Cosmos 1129 and 1887 are alike);

(3) slopes of the integral spectra obtained from satellites differing in orbit inclination, i, are similar to each other (the spectral index β of all three spectra for the LET ranging from 10 to 10^3 MeV cm^{-1} of tissue is the same within deviations of $\pm 15\%$);

(4) values of the LET spectra seem to rise with increasing orbit inclination at $i \geq 60°$;

(5) the integral LET spectrum obtained from Cosmos 1757 is higher than all the other spectra despite the fact that the particular orbit was 1.5 times lower in altitude than the other orbits.

A preliminary conclusion may be drawn from comparing these results with the results of Benton (1983): in the case of highly inclined orbits ($i > 60°$) the absolute flux values of the LET spectra and, hence, of the absorbed and equivalent doses, depend more strongly on the orbit inclination (i) than on altitude (h), whereas in the case of low inclination orbits ($i < 60°$) their flux values depend more strongly on altitude than on orbit inclination. Further measurements in high inclination orbits are needed for verification.

The observation can be understood by considering how the various contributions to LET vary with orbital altitude and inclination. Above 60° inclination at low altitudes galactic cosmic rays dominate the LET. The GCR is not strongly modulated by altitude at the altitudes considered, but is modulated by the rigidity cut-off, which is a function of geomagnetic latitude. For lower inclination orbits, trapped particles are more important. Trapped particles are strongly modulated with altitude, but not so strongly modulated with inclination.

Figures 2 and 3 present the integral LET spectra obtained from Cosmos 1887 by the NPE and SSNTD methods. The respective values for the external assemblies are shown in Fig. 2, while the data obtained inside the satellite are presented in Fig. 3. The two figures also show the calculated results obtained by the method described in Akopova *et al.* (1987) behind shielding thickness $\delta = 1.0$ g cm^{-2} (Fig. 2) and $\delta = 1.0$, 10.0, and 20.0 g cm^{-2} (Fig. 3). The calculations were made for the Cosmos 1887 orbit parameters. The number of histories is 10^4.

A method for calculating the integral LET spectrum of galactic cosmic ray particles is described in Akopova *et al.* (1987). Our work is the first to include both the galactic cosmic ray particles and the radiation belt protons in the region of the South Atlantic Anomaly (SAA). The LET distributions from the protons were determined from the energy spectra of radiation belt protons calculated using the Sawyer

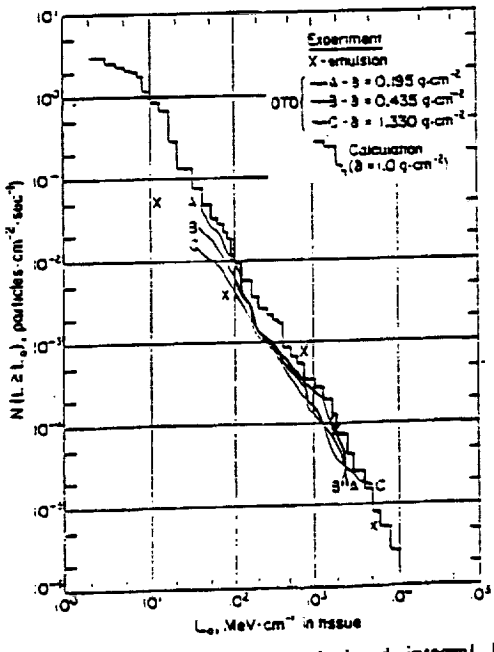

FIG. 2. The experimental and calculated integral LET spectra obtained from Cosmos 1887 (outside the satellite).

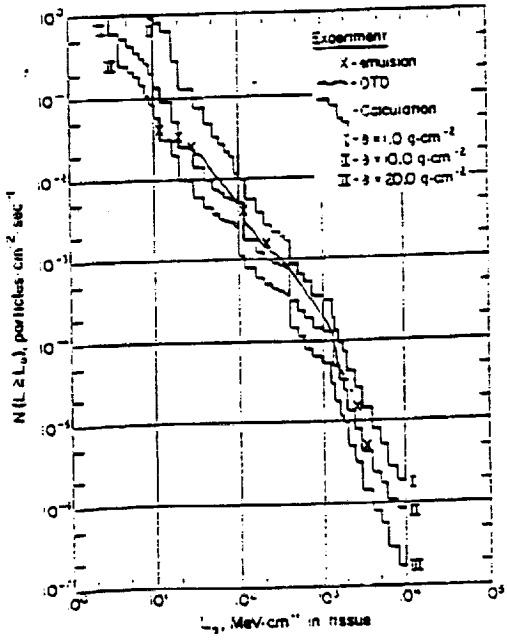

FIG. 3. The experimental and calculated integral LET spectra obtained from Cosmos 1887 (inside the satellite).

and Vette (1976) AP8MIN trapped proton environment. Figures 2 and 3 present the total calculated LET distributions (the histograms).

The following preliminary conclusions may be drawn from analyzing the curves presented in Figs 2 and 3.

(1) the experimental results obtained by the NPE and SSNTD methods are similar in the region where the LET spectra overlap. thereby indicating that both methods may be used in studies of this type. The best agreement between the experiments was obtained from measurements made inside the spacecraft (Fig. 3);

(2) the experimental and calculated data are also in satisfactory agreement with each other. The fact that the experimental and calculated curves shown in Fig. 3 are about the same at $\delta = 10.0\ g\ cm^{-2}$ seems to imply that the mean thickness of the shielding of the detectors was close to $\sim 10.0\ g\ cm^{-2}$;

(3) it should be noted that the calculated and experimental data disagree at small shielding thicknesses ($\delta \leqslant 1.0\ g\ cm^{-2}$) especially for the lower LET values (Fig. 2). As shown by a relevant analysis, 85–95% of the spectrum at the LET values from ~ 10 to 100 MeV cm^{-1} of tissue is due to the radiation belt protons (on assumption of the isotropic proton distribution in the SAA). The trapped proton calculations therefore seem to be less consistent with the experiment than the GCR calculations. However, the experimental points are scanty in the given LET range, a fact that should be taken into account in further studies;

(4) the results of calculating the integral LET spectra from galactic cosmic ray particles behind shielding from 0 to $50\ g\ cm^{-2}$ were previously done by Heinrich (1977) and Heinrich and Baer (1984), where the following two main conclusions were reached, namely, (i) the spectral slopes change at $\sim 10^3$ MeV cm^{-1} for all shielding thicknesses and (ii) the spectral slope angle is independent of shielding thickness for LET $> 10^3$ MeV cm^{-1} and depends upon the latter (increases with thickness) for LET $\leqslant 10^3$ MeV cm^{-1}. Our studies have confirmed the first conclusion completely. Our calculations have shown that the slope angles of the LET spectra are alike in the range of LET $\geq 10^3$ MeV cm^{-1} where the value of the spectrum is defined solely by the galactic cosmic ray particles (mainly, by Fe nuclei). The contribution of radiation belt protons to the total integral LET distribution decreases with increasing shielding thickness. The opposing dependencies lead to the near-independence of the slope angle of the total GCR and proton distributions on shielding for shielding thicknesses up to at least $20\ g\ cm^{-2}$, for LET $\leq 10^3$ MeV cm^{-1}.

We have used our experimental and calculated LET distribution data to estimate the mean quality factor (QF) in the Cosmos 1887 orbit behind shieldings of 1.0 and $10\ g\ cm^{-2}$. This applies to particles having LET in tissue from 2.0 to 10^4 MeV cm^{-1}. We used the AE8MIN environment (Teague and Vette, 1972) to calculate the doses from the radiation belt electrons in the Cosmos 1887 orbit behind a $1.0\ g\ cm^{-2}$ shielding. In the case of a $10.0\ g\ cm^{-2}$ shielding, the electrons were neglected because of their small contribution to the total dose. We have found their QF to be 1.3 ± 0.2 and 1.7 ± 0.2 at 1.0 and $10.0\ g\ cm^{-2}$, respectively. These values are in good agreement with the calculated and experimental data published elsewhere (Kovalev *et al.*, 1979; Curtis *et al.*, 1986).

In future studies, particular attention should be paid to detection of spectra at small LET values. In addition, knowing the distribution of the spacecraft shielding is extremely important, as this information will allow a more correct comparison between the calculated and experimental data.

REFERENCES

Akopova A. B., Dudkin V. E., Karpov O. N., Melkumyan L. V., Potapov Yu. V. and Rshtuni Sh. B. (1986) Determination of cosmic radiation characteristics aboard Salyut-7 orbital station. *Nucl. Tracks Radiat. Meas.* 12, 489–491.

Akopova A. B., Dudkin V. E., Karpov O. N., Melkumyan L. V., Potapov Yu. V. and Rshtuni Sh. B. (1988) Determination of cosmic radiation characteristics on board Salyut-7 orbital station. *Kosm. Issled.* XXVI, 162–165.

Akopova A. B., Dudkin V. E., Kovalev E. E., Magradze N. V. and Potapov Yu. V. (1987) Linear energy transfer spectra of cosmic radiation aboard Cosmos-1129 artificial satellite. *Radiat. Prot. Dosim.* 18, 153–156.

Akopova A. B., Magradze N. V., Moiseenko A. A., Muradyan S. H. and Ovnanyan K. M. (1983) Method of selective development of thick-layer nuclear emulsions. Preprint EFI-671 (61)-83 of the Yerevan Physical Institute, Yerevan, U.S.S.R.

Akopova A. B., Vikhrov A. I., Dudkin V. E., Magradze N. V., Moiseenko A. A., Muradyan A. H., Ovnanyan K. M. and Potapov Yu. V. (1985) Measuring the linear energy transfer spectra of cosmic radiation aboard the Cosmos-1129 satellite. *Kosm. Issled.* XXIII, 479–481.

Benton E. V. (1983) Dosimetric radiation measurements in space. *Nucl. Tracks Radiat. Meas.* 7, 1.

Benton E. V. (1986) Summary of radiation dosimetry results on U.S. and Soviet manned spacecraft. XXVI COSPAR Meeting, Toulouse, June/July, 1986. COSPAR Paper VII, p. 7.

Curtis S. P., Atwell W., Beever R. and Hardy A. (1986) Radiation environments and absorbed dose estimations on manned space missions. *Adv. Space Res.* 6, 269–274.

Heinrich W. (1977) Calculation of LET-spectra of heavy cosmic ray nuclei at various absorbed depths. *Radiat. Effects* 33, 143–148.

Heinrich W. and Baer J. (1984) The radiation situation in space and its modification by geomagnetic field and shieldings. *Adv. Space Res.* 4, 133–142.

Henke R. P. and Benton E. V. (1974) Heavy cosmic ray measurement on Apollo 16 and 17 missions. Results of the HZE Dosimeter Experiment. University of San Francisco, CA 94117. Technical Report No. 34.

Kovalev E. E., Bryskin V. N., Vinogradov Yu. A., Dudkin V. E., Kozlova S. B., Marenny A. M., Markelov V. V., Nefedov N. A., Potapov Yu. V., Redko V. I. and Hovanskaya A. I. (1979) Measuring the linear energy transfer spectra of cosmic radiation on board Cosmos-782 satellite. *Kosm. Issled.* XVII, 634–636.

Petrov V. M., Akatov Yu. A., Kozlova S. B., Markelov V. V., Redko V. I., Smirenny L. N., Khorsev A. V. and Chernych I. V. (1975) The study of the radiation environment in near-Earth space. *Space Res.* 13, 129.

Sawyer D. M. and Vette J. T. (1976) AP-8 trapped proton environment for solar maximum and solar minimum. NSSDS/WDS-A-R and S-76-06. National Space Science Data Center, NASA/Goddard Space Center, Greenbelt, MD.

Teague M. J. and Vette J. T. (1972) The inner ion electron model AE-5. NSSDS 72-10. National Space Science Data Center, NASA/Goddard Space Center, Greenbelt, MD, September 1972.

APPENDIX O

Depth Distribution of Absorbed Dose on the External Surface of the Cosmos 1887 Biosatellite

by

Yu.A. Akatov, V.E. Dudkin, E.E. Kovalev, E.V. Benton, A.L. Frank
J.W. Watts, Jr. and T.A. Parnell

Nucl. Tracks Radiat. Meas., Vol. 17, No. 2, pp. 105–107, 1990
Int. J. Radiat. Appl. Instrum., Part D
Printed in Great Britain

0735-245X/90 $3.00 + .00
Pergamon Press plc

DEPTH DISTRIBUTION OF ABSORBED DOSE ON THE EXTERNAL SURFACE OF COSMOS 1887 BIOSATELLITE

YU. A. AKATOV,* V. E. DUDKIN,* E. E. KOVALEV,* E. V. BENTON,† A. L. FRANK,†
J. W. WATTS JR§ and T. A. PARNELL§

*Institute of Biomedical Problems of the Ministry of Public Health of the U.S.S.R., Moscow 123007, U.S.S.R.; †University of San Francisco,‡ CA 94117–1080, U.S.A. and §NASA Marshall Spaceflight Center, Huntsville, AL 35812, U.S.A.

(*Received* 30 *May* 1989)

Abstract—Significant absorbed dose levels exceeding 1.0 Gy day^{-1} have been measured on the external surface of the Cosmos 1887 biosatellite as functions of depth in stacks of thin thermoluminescent detectors (TLDs) of U.S.S.R. and U.S.A. manufacture. The dose was found to decrease rapidly with increasing absorber thickness, thereby indicating the presence of intensive fluxes of low-energy particles. Comparison between the U.S.S.R. and U.S.A. results and calculations based on the Vette Model environment are in satisfactory agreement. The major contribution to the dose under thin shielding thickness is shown to be from electrons. The fraction of the dose due to protons and heavier charged particles increases with shielding thickness.

INTRODUCTION

THE DEPTH distribution of absorbed dose in matter is an important characteristic of the radiation environment. It is of particular interest to examine the absorbed dose values which apply to the surface layers of materials placed outside spacecraft.

Experiments measuring absorbed doses under very thin shielding have been made on board the Soviet recoverable satellites since the late seventies using integral-type solid-state detectors. In the Cosmos 936 (1977) and 1129 (1979) biosatellite experiments, thermoluminescence detectors (TLD) of 1.0 g cm^{-2} thickness covered by 0.001–1.0 g cm^{-2} thick opaque materials were mounted on the external surfaces of the satellites (Akatov *et al.*, 1981; Benton, 1983). These experiments have shown that absorbed doses measured outside the satellites are as much as 50–1000 times higher than the absorbed doses measured with similar detectors inside the satellites. The doses increase rapidly with decreasing shielding, thereby indicating that the dominant contribution to the surface dose is from the low-energy component of ionizing radiation.

The measurements were continued on board Cosmos 1514 biosatellite (1983) and other recoverable satellites (1984–1986) using thinner (up to 20 μm) TLDs (Akatov *et al.*, 1985, 1988; Szabo *et al.*, 1986, 1987). In these measurements, the absorbed dose in 0.005–0.03 g cm^{-2} thick detectors covered with 0.001–0.002 g cm^{-2} thick foils was found to be 2–10 Gy day^{-1}. The doses varied as a function of the exposure conditions, namely, orbital parameters, solar activity and shielding by satellite structures. However, the character of the depth distribution of doses remained the same, with the dose decreasing rapidly in the 0.005–0.1 g cm^{-2} thickness interval, then decreasing more slowly.

This paper presents the results of the K-6-25 joint Soviet–American dosimetric experiment on board the Cosmos 1887 biosatellite, as well as the results of theoretical calculations for the Cosmos 1887 orbit (altitude of 406 km apogee and 224 km perigee; inclination of 62.8°). The flight lasted from 29 September to 12 October 1987.

EXPERIMENTAL TECHNIQUES

The American ^{7}LiF detectors (Harshaw TLD-700) of two thicknesses (0.00914 and 0.0889 cm) and the Soviet-manufactured 0.8 cm diameter thermoluminescent glass detector of 0.012 and 0.1 cm thicknesses were used in the experiments. The detectors were stacked in vertical cylindrical channels of a metallic container. Two four-channel containers were used in which the ^{7}LiF detectors were stacked in three channels, and the glass detector in one channel. The containers had a diameter of 5 cm and a height of 2 cm (see Fig. 1). The maximum depths of the detector stacks were 3.4 g cm^{-2} for ^{7}LiF and 3.8 g cm^{-2} for glass. The container surfaces facing free space were covered with a Kapton film 0.002 g cm^{-2} thick, metallized on both sides to protect the detectors against direct sunlight and against

‡USF work partially supported by NASA–Ames Research Center Grant No. NCC2-521 and NASA–JSC Grant No. NAG9-235.

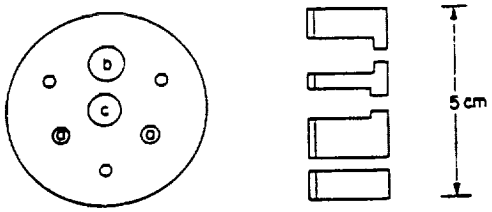

FIG. 1. Drawing, half actual size, of TLD stack container (Al) for Cosmos 1887 experiment. The U.S. detectors of 0.32 cm × 0.32 cm were in hole (a), U.S. detectors of 0.64 cm × 0.64 cm were in hole (b) and Soviet detectors of 0.8 cm diameter were in hole (c).

heating. The optical density of the metallized film surfaces is 3.

The detector containers were mounted in a special device covered with a lid for protection during re-entry. The device with the lid open was fastened under a fairing on the external surface of the satellite before launch. (When in orbit, the fairing is jettisoned; on re-entry, the lid is closed. In this manner the detectors are open to nearly free space while in orbit, and are heat-shielded during the satellite launching and recovery periods.)

After the flight, the detectors were processed at the laboratories in the U.S.S.R. and the U.S.A. by similar methods. The ^{7}LiF detectors were measured using the HARSHAW Model 4000 TLD Reader, and the glass detectors using the NHZ-203 instrument. The detectors were calibrated separately in the U.S.S.R. and the U.S.A. using ^{137}Cs γ-rays.

RESULTS AND DISCUSSION

In Fig. 2 are shown the measured and calculated values of absorbed dose as a function of shielding thickness for the Cosmos 1887 experiment. The dose levels in the least protected upper detectors (~ 0.002 g cm^{-2}) were 1.2–2.5 Gy day^{-1} and decreased by a factor of $\sim 10^3$ at a 1 g cm^{-2} depth. This confirms the earlier observations indicating the occurrence of substantial low-energy particle fluxes in free space.

The character of the depth distribution of the dose inferred from the American- and Soviet-made detectors has proved to be the same despite some differences in the absolute dose values. The main difference is observed in the uppermost detectors where the dose in the American detectors is about twice as high as the Soviet detector dose. This may be due to the difference in the detector thickness (0.024 g cm^{-2} for ^{7}LiF (U.S.A.) and 0.31 g cm^{-2} for TL glass (U.S.S.R.), since the averaged specific value of dose in a thicker detector will be lower if the dose falls significantly across the thickness of the detector. At greater depths, the discrepancy in the readings decreases and is in the range of 20–40%. Some of the variations may arise from differences in detector arrangement; for instance, the American detectors were not packed closely in the cylindrical assembly

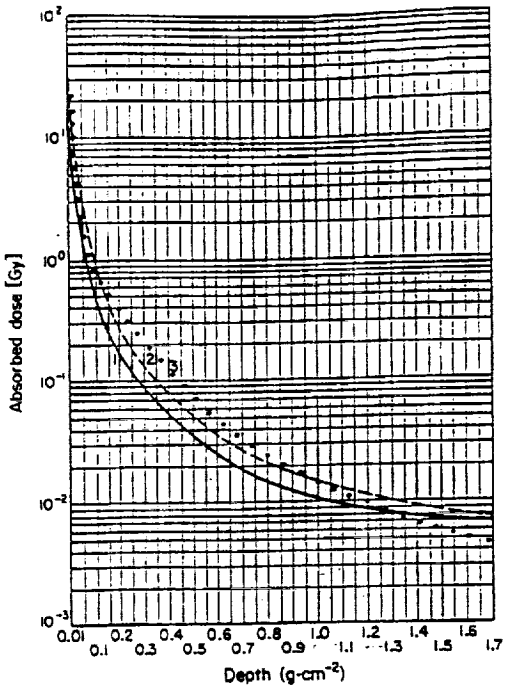

FIG. 2. Depth distribution of absorbed tissue dose on the external surface of Cosmos 1887 biosatellite. The dose measurement error is ~10%. Curve 1: data of the Soviet-made glass TLD. Curve 2: data of the American-made ^{7}LiF TLD. Curve 3: calculated data.

channels. Also, there may be small differences in detector-calibration procedures.

The depth distributions of doses were calculated considering the contribution from trapped electrons and protons and galactic cosmic rays (GCR). The flight occurred near solar minimum so no solar flare proton contribution was considered. Trapped radiation belt fluxes were calculated using the Vette AE8-MIN electron and AP8-MIN proton model environments (Teague *et al.*, 1976; Sawyer and Vette, 1976). According to this data, most of the electron flux lies within a 0.05–4.5 MeV energy range, while the proton flux covers a 0.1–450 MeV range. The dose at small shielding thicknesses is due to the proton and electron ionizing energy loss, whereas the electron bremsstrahlung makes a significant contribution to the dose for thicknesses in the range above 2 g cm^{-2}.

The methods used to calculate the GCR spectra and, hence, the doses in low Earth orbit are the same as described in Dudkin *et al.* (1986). The calculations allowed for the deformation of the GCR particle spectrum in the Earth's magnetic field and for the secondary radiation generated in inelastic interactions of particles in the shielding. The absorbed doses from both the trapped and the GCR particles were calculated for the case of isotropic incidence of a broad particle beam onto an Al planar shield and for solar minimum conditions.

The calculation results have shown that the doses under low shield thicknesses (< 1 g cm^{-2}) are due

Table 1. Component composition of cosmic ray dose (%) under various shield thicknesses on Cosmos 1887

Shield thickness ($g\ cm^{-2}$) / Particle species	0.1	0.5	1.0	1.5	2.0	5.0
e	99.2	95.6	79	42.8	13.7	2.2
p	0.6	2.7	11.8	30	42.5	34.0
GCR	0.2	1.7	9.2	27.2	43.8	63.8

mainly to ionization loss of radiation belt electrons. The fraction of dose due to radiation belt and GCR protons and to electron bremsstahlung increases with shield thickness. Comparisons between the calculated and experimental data shown in Fig. 2 indicate that they are in good agreement. The calculated data used to analyze the doses from the different radiation types outside the biosatellite are presented in Table 1.

As noted in Szabo *et al.* (1987), the average dose rate outside satellites depends substantially on orbital parameters. The character of the dependence of the dose on shielding thickness varies also and is very difficult to describe with a unified expression applying to different spacecraft orbits. We are of the opinion that further studies should be aimed at examining the depth distribution of the absorbed dose for different orbital parameters and different solar activity periods. In so doing, particular attention should be paid to the experimental geometry and to careful calibration of detectors, especially in the interval of high doses of about 10–1000 Gy where linearity of the dose characteristics is observed to vary in some types of detectors.

Acknowledgements—The authors would like to thank Drs O. N. Karpov and Yu. V. Potapov for their help with the dose calculations.

REFERENCES

Akatov Yu. A., Arkhangelsky V. V., Kovalev E. E., Spurný F. and Votochková I. (1988) Absorbed dose measurements on the external surface of Cosmos satellites with glass thermoluminescent detectors. *Adv. Space Res.* 9(10), 237–241.

Akatov Yu. A., Arkhangelsky V. V. and Spurný F. (1985) Attenuation of cosmic ray doses by small protective thicknesses. *XVIII Meet. Intercosmos Working Groups Space Med. Biol.*, Gagra, U.S.S.R., May 1985, p. 253.

Akatov Yu. A., Vichrov A., Dudkin V., Marenny A., Sakovitch V., Spurný F., Turek K. and Hashegan D. (1981) The results of radiation-physical experiments on the Cosmos-1129 satellite. *XIV Meet. Intercosmos Working Groups Space Med. Biol.*, Varna, Bulgaria, May 1981, p. 72.

Benton E. V. (1983) Dosimetric radiation measurements in space. *Nucl. Tracks Radiat. Meas.* 7, 1–11.

Dudkin V. E., Kovalev E. E., Petrov V. M., Just L. and Kudela K. (1986) Some medical aspects of cosmic ray exposure in orbital flights. Paper VII. 8 at COSPAR XXVI Meeting, Toulouse, France, 30 June–7 July 1986.

Sawyer D. M. and Vette J. T. (1976) AP-8 trapped proton environment for solar maximum and solar minimum. National Space Science Data Center Report No. 76-06. Greenbelt, Maryland, December 1976.

Szabó P. P., Fehér I. and Akatov Yu. A. (1987) The application of ultrathin TLD discs for space dosimetry. *XIV Reg. Congr. IRPA Yugosl.–Austr.–Hung. Radiat. Prot. Meet.* Current Problems and Concerns in the Field of Radiation Protection, Kupari, Dubrovnik 6, Yugoslavia, 29 September–2 October 1987.

Szabó P. P., Fehér I., Akatov Yu. A. and Lancsaries Gy. (1986) Dose distribution measurements of cosmic radiation in $CaSO_4$:Dy-teflon rods. *Radiat. Prot. Dosim.* 17, 211.

Teague M. J., Chan K. W. and Vette J. T. (1976) AE6: a model environment for trapped electrons for solar maximum. NSSDC/WDC-A-RS 76-01. National Space Science Data Center, Greenbelt, Maryland.

APPENDIX P

Neutron Fluences and Energy Spectra in the Cosmos-2044 Biosatellite Orbit

by

V.E. Dudkin, Yu.V. Potapov, A.B. Akopova, L.V. Melkumyan
Sh.B. Rshtuni, E.V. Benton and A.L. Frank

Nucl. Tracks Radiat. Meas., Vol. 20, No. 1, pp. 139–141, 1992
Int. J. Radiat. Appl. Instrum., Part D
Printed in Great Britain

0735-245X/92 $5.00 + .00
Pergamon Press plc

NEUTRON FLUENCES AND ENERGY SPECTRA IN THE COSMOS-2044 BIOSATELLITE ORBIT

V. E. DUDKIN,* YU. V. POTAPOV,* A. B. AKOPOVA,† L. V. MELKUMYAN,† SH. B. RSHTUNI,† E. V. BENTON‡ and A. L. FRANK‡

*Research Center of Spacecraft Radiation Safety, Ministry of Health, Moscow 123182, U.S.S.R.; †Yerevan Physical Institute, Yerevan, Armenia and ‡Physics Department, University of San Francisco, San Francisco, CA 94117–1080, U.S.A.

(*Received* 21 *February* 1991; *in revised form* 7 *May* 1991)

Abstract—Joint Soviet–American measurements of the neutron component of space radiation (SR) were carried out during the flight of the Soviet biosatellite Cosmos-2044. Neutron flux densities and differential energy spectra were measured inside and on the external surface of the spacecraft. Three energy intervals were employed: thermal ($E_n \leq 0.2$ eV), resonance (0.2 eV $< E_n < 1.0$ MeV) and fast ($E_n \geq 1.0$ MeV) neutrons. The first two groups were measured with U.S. ^{6}LiF detectors, while fast neutrons were recorded both by U.S. fission foils and Soviet nuclear emulsions. Estimations were made of the contributions to absorbed and equivalent doses from each neutron energy interval and a correlation was presented between fast neutron fluxes, measured outside the satellite, and the phase of solar activity (SA). Average dose equivalent rates of 0.018 and 0.14 mrem d^{-1} were measured for thermal and resonance neutrons, respectively, outside the spacecraft. The corresponding values for fast neutrons were 3.3 (U.S.) and 1.8 (U.S.S.R.) mrem d^{-1}. Inside the spacecraft, a value of 3.5 mrem d^{-1} was found.

INTRODUCTION

THE PRESENT measurements are a continuation of previous investigations begun on board the biosatellite Cosmos-1887 which showed the necessity of further development within the S.U.–U.S. joint research program. The flight of Cosmos-2044 had two major features which distinguished it from other satellite flights. Firstly, its orbit was near to polar, and secondly, the experiment was carried out on the eve of the phase of maximal solar activity.

In our previous works (Akopova *et al.*, 1988; Dudkin *et al.*, 1990) we presented the results of neutron measurements in near-Earth orbits performed in recent years. Estimations of fast-neutron fluences at the end of the 1970s were made from nuclear emulsion data having insufficient statistical accuracy. Hence, the error in determination of fluence values reached ±50% and more. In recent years, the value of the statistical error in these investigations has been reduced to ±25%. Experimental data on fast neutrons have enabled us to evaluate the correlation of the neutron fluxes of $E_n \geq 1.0$ MeV with the SA-phase in order to verify the hypothesis that the neutrons recorded outside the spacecraft are mainly albedo neutrons and correlate with the fluxes of the GCR particles, i.e. with the SA-phase.

METHODS

The investigation of the SR neutron component was carried out both inside and on the external surface of the Cosmos-2044 biosatellite which had the following flight parameters: apogee = 294 km, perigee = 216 km, inclination ≃ 82°, flight time = 14 days (15–29 September 1989). The satellite was not oriented. Thermal and resonance neutrons were measured with the U.S. ^{6}LiF detectors through the ^{6}Li$(n,\alpha)T$ reaction. The fluences of α particles emitted from ^{6}LiF film surfaces were recorded in plastic detectors (CR-39). Separation of thermal from resonance neutrons was made using Gd-foils which shielded the detectors. Rough estimation of fast neutrons was made with the help of the U.S. thorium (Th) foils, where the tracks of fission fragments produced by Th were recorded in mica detectors. Since disintegrations can be caused by both fast neutrons and protons, the estimation of neutron fluences by this method is complicated.

The differential fast-neutron energy spectra were measured using the recoil proton energy spectrum generated as a result of the elastic scattering of neutrons from unbounded hydrogen in the emulsion. Measurements were made only of proton tracks whose ends were located within the volume of the emulsion. Allowance should be made for the fact that, due to a significant visual error during

‡USF portion of the work partially supported by NASA Grant Nos NCC2-521 (NASA–Ames Research Center) and NAG9-235 (NASA–Johnson Space Center).

Table 1. Experimental measurements of thermal neutrons on board Cosmos-2044

Detector	F_1	F_2	GC
Neutron fluence, neutr. cm^{-2}	$(2.56 \pm 0.16) \times 10^5$	$(2.23 \pm 0.16) \times 10^5$	$(0.15 \pm 0.05) \times 10^5$
Dose equiv. rate, mrem day^{-1}	0.019 ± 0.002	0.017 ± 0.002	—

Table 2. Experimental measurements of resonance neutrons on board Cosmos-2044

Detector	F_1	F_2	GC
Neutron fluence, neutr. cm^{-2}	$(0.99 \pm 1.16) \times 10^5$	$(6.8 \pm 1.3) \times 10^5$	$(4.29 \pm 0.46) \times 10^5$
Dose equiv. rate, mrem day^{-1}	0.036 ± 0.041	0.25 ± 0.04	0.15 ± 0.02

determination of the short path-length recoil protons ($E_p \leq 1.0$ MeV) and proton contamination from $^{14}N(n,p)$ reaction with emulsion nitrogen, neutron fluxes with $E_n < 1.0$ MeV were not measured in this experiment.

More detailed descriptions of measurements of neutron fluxes and spectra using fission foils and nuclear emulsion were given in Akopova *et al.* (1988) and Dudkin *et al.* (1990).

RESULTS AND DISCUSSION

Tables 1–3 present the results of measurements of thermal (Table 1), resonance (Table 2), and fast (Table 3) neutron fluxes in various locations on board Cosmos-2044. The data also include the equivalent dose estimations for each group of neutrons.

As is seen from Table 3, there is some disagreement between the U.S. and Soviet fluence values measured on the external surface of the spacecraft (about a factor of two). It may be accounted for by the fact that errors shown in the tables are exclusively statistical. The magnitude of the absolute error is significantly greater due to the ambiguity of the values of fast neutron and proton fluxes and their spectral forms and this must be borne in mind when TH fission foils are used. The estimated error is within a factor of 3.

In Table 2 there is a large difference between resonance neutron measurements from the two outside detectors (F_1 and F_2). The ground control detector (GC) gave a fluence value which was a significant fraction of that from F_2 and larger than that from F_1. The reason for the variation is not known but it is larger than statistical uncertainties would account for.

Figure 1 presents experimental differential neutron spectra measured in the flight of Cosmos-2044 with nuclear photoemulsions. These spectra are in the range from 1.0 to 10–15 MeV with a maximum, as a rule, in the 2–5 MeV neutron energy range. Neutron fluxes inside the satellite are approximately twice as high as on the external surface, i.e. somewhat greater than the values obtained in our previous investigations (Dudkin *et al.*, 1990).

According to the current concepts, the neutrons detected in near-Earth orbits originate mainly from two sources: the albedo neutrons produced in the interaction of galactic cosmic rays (GCR) with the Earth's atmosphere, and the secondary neutrons produced in the spacecraft hull and structure (local neutrons). The form of the local neutron spectra is similar to the form of the spectra produced in nuclear reactions.

The analysis of Dudkin *et al.* (1990) did not reveal any definite dependence of the neutron flux density on altitude or orbital inclination to the plane of the equator. In the present work we made the first attempt to analyse dependence of the fast neutron flux density on the phase of solar activity. If the albedo neutrons do originate mainly from the GCR particles, then neutron fluxes, especially those measured outside the satellite where the contribution of local neutrons is small, must correlate with the phase of solar activity; i.e. in the period of minimum SA, they must be more numerous than in the period of maximum solar activity, in proportion to the ratios of the GCR particle fluxes in a given orbit. Figure 2 illustrates this assumption, showing values of the fast neutron flux densities (the experimental points) measured on flights of various satellites within the

Table 3. Experimental measurements of fast neutrons on board Cosmos-2044

Detector	F_1 (U.S.A.)	Outside F_2 (U.S.A.)	Avg. for assemblies Nos 1, 3, 5 (U.S.S.R.)	Inside Avg. for assemblies Nos 2, 4 (U.S.S.R.)
Neutron fluence, neutr. cm^{-2}	$(8.1 \pm 1.1) \times 10^5$	$(7.0 \pm 1.1) \times 10^5$	4.0×10^5	7.74×10^5
Dose equiv. rate, mrem day^{-1}	3.5 ± 0.5	3.0 ± 0.5	1.80	3.50

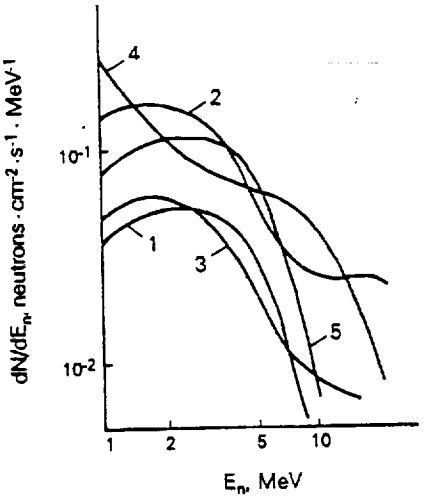

FIG. 1. Differential neutron energy spectra measured outside and inside the Soviet biosatellite Cosmos-2044. (1) Assembly No. 1 (outside); (2) assembly No. 2 (inside); (3) assembly No. 3 (outside); (4) assembly No. 4 (inside); (5) assembly No. 5 (outside).

past five years with inclination $i = 70$–$90°$ and $h = 200$–400 km. Curve 1 is a calculated dependence curve (Lingenfelter, 1963) of the albedo neutron flux on the SA-phase for the same orbits. Curve 2 shows a relative time dependence of the GCR particle flux. This curve is constructed on the basis of our calculations of the GCR particle fluxes in high-latitude orbits, taking into account the geomagnetic cutoff. As is seen in this figure, our assumption about correlation of the albedo neutrons with measured neutron fluxes and with the dependence of these values on SA-phase (in correlation with the GCR particle fluxes) found strong confirmation.

It appears that in future studies special attention should be given to neutron energy regions where measurements have not yet been made, or have been made with rough accuracy—less than 1.0 MeV and higher than 15 MeV.

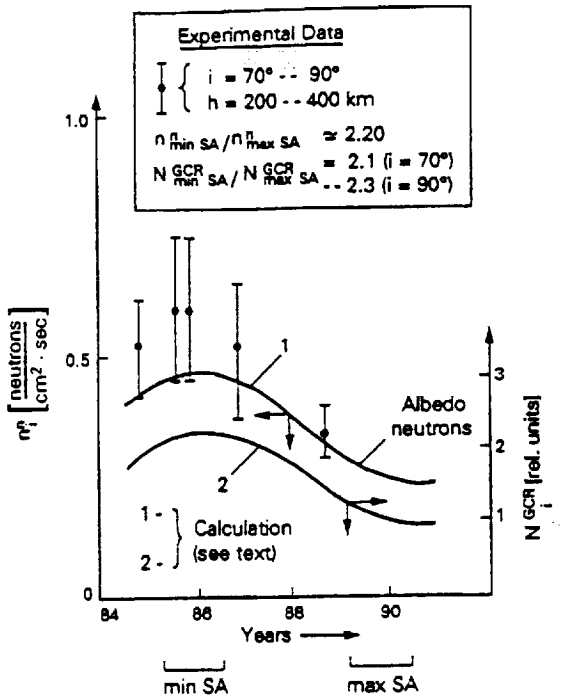

FIG. 2. The correlation of fast-neutron fluxes with solar activity (SA) phase in near-Earth orbits. Curve 1: calculated dependence of albedo neutron flux on SA cycle (Lingenfelter, 1963). Curve 2: calculated relative time dependence of GCR particle flux (this paper).

REFERENCES

Akopova A. B., Dudkin V. E., Melkumyan L. V., Potapov Yu. V. and Rshtuni Sh. B. (1988) Neutron energetic spectra in near-Earth orbits. Report, all-Union conference on cosmic rays, *Proc. Acad. Sci. Kaz. SSR*, part 2, pp. 42–44. Alma-Ata.

Dudkin V. E., Potapov Yu. V., Akopova A. B., Melkumyan L. V., Benton E. V. and Frank A. L. (1990) Differential neutron energy spectra measured on spacecraft in low Earth orbit. *Nucl. Tracks Radiat. Meas.* 17, 87–91.

Lingenfelter R. E. (1963) The cosmic ray neutron leakage flux. *J. geophys. Res.* 68, 5633.

APPENDIX Q

Experimental and Calculated LET Distributions in the Cosmos-2044 Biosatellite Orbit

by

V.E. Dudkin, O.N. Karpov, Yu.V. Potapov, A.B. Akopova, N.V. Magradze, A.A. Moiseenko, E.V. Benton, A.L. Frank and J.W. Watts, Jr.

Nucl. Tracks Radiat. Meas., Vol. 20, No. 1, pp. 143–147, 1992
Int. J. Radiat. Appl. Instrum., Part D
Printed in Great Britain

0735-245X/92 $5.00 + .00
Pergamon Press plc

EXPERIMENTAL AND CALCULATED LET DISTRIBUTIONS IN THE COSMOS-2044 BIOSATELLITE ORBIT

V. E. DUDKIN,* O. N. KARPOV,* YU. V. POTAPOV,* A. B. AKOPOVA,† N. V. MAGRADZE,† A. A. MOISEENKO,† E. V. BENTON,‡ A. L. FRANK‡ and J. W. WATTS JR§

*Research Center of Space Craft Radiation Safety, Ministry of Public Health, Moscow 123182, U.S.S.R.; †Yerevan Institute of Physics, Yerevan, U.S.S.R.; ‡University of San Francisco, San Francisco, CA 94117, U.S.A. and §NASA Marshall Spaceflight Center, Huntsville, AL 35812, U.S.A.

(*Received* 21 *February* 1991; *in revised form* 7 *May* 1991)

Abstract—During the flight of the Cosmos-2044 biosatellite, joint U.S.S.R.–U.S.A. investigations of different characteristics of cosmic radiation (CR) in the near-Earth environment were carried out. The U.S. dielectric track detectors CR-39 and Soviet BYa- and BR-type nuclear photo-emulsions were used as detectors. The present work shows some results of experimental measurements of linear energy transfer (LET) spectra of CR particles obtained with the use of these detectors, which were placed both inside and outside the satellite. The LET spectra measurement with plastic detectors is composed of two parts: the measurement of galactic cosmic rays (GCR) particles, and of short-range particles. The contributions of these components to the total LET distribution at various thicknesses of the shielding were analyzed and the results of these studies are presented. Calculated LET spectra in the Cosmos-2044 orbit were compared with experimental data. On the basis of experimental and calculated values of the LET spectra, absorbed and equivalent CR doses were calculated. In the shielding range of 1–1.5 g cm^{-2}, outside the spacecraft, the photo-emulsions yielded 10.3 mrad d^{-1} and 27.5 mrem d^{-1} (LET $\geq$2 MeV cm^{-1}) while the CR-39 yielded averages of 1.43 mrad d^{-1} and 13.4 mrem d^{-1} (LET $\geq$40 MeV cm^{-1}). Inside the spacecraft ($\geq$10 g cm^{-2}) the photo-emulsions yielded 8.9 mrad d^{-1} and 14.5 mrem d^{-1}.

INTRODUCTION

THE EXPERIMENTAL studies which were begun on board Cosmos-1887 (Akopova *et al.*, 1990) showed the necessity of extending investigations of the near-Earth space environment using passive detectors. The present experiments had two characteristic properties: the orbit of Cosmos-2044 was near to polar (inclination $i \simeq 82°$), and the flight period almost coincided with the maximum of solar activity (SA).

In our previous work (Akopova *et al.*, 1990) we analyzed the experimental LET distributions which were available at that time and showed some orbital dependence. It was noted that some orbits were not amply studied. Also, it was necessary to verify the conclusion that absolute values of LET distributions, and, consequently, absorbed and equivalent doses, are more strongly dependent on orbit inclination (i) than on altitude, for $H = 200$–400 km above the Earth, in the case of highly inclined ($i \geq 60°$) orbits.

As is apparent from the above, the main purpose of the present investigation was to obtain experimental data about LET distributions of the CR particles in a nearly polar orbit of the satellite in close to maximum SA-phase, using various passive detectors. Comparisons of experimental data for LET distributions at different shielding thicknesses are also discussed.

EXPERIMENTAL TECHNIQUE

The flight parameters of the satellite were as follows: inclination (i) $\simeq 82°$, apogee altitude = 294 km, perigee = 216 km, duration = 14 days from 15 to 29 September 1989; i.e. the flight was in the period close to the solar maximum.

The assemblies of passive detectors (plastic detectors CR-39 and BYa and BR-type nuclear photo-emulsions) were placed on the lid and the bottom of a special container with scientific equipment (outside assemblies), and inside the satellite (nuclear photo-emulsions).

After exposure and recovery, the layers of nuclear emulsions were treated by the selective-development technique (Akopova *et al.*, 1983) to ensure quenching of the accompanying background and threshold sensitivity control in a broad interval of LET. It is then possible to develop only those particle tracks for which the LET is not below threshold.

‡USF portion of the work partially supported by NASA Grant Nos NCC2-521 (NASA–Ames Research Center) and NAG9-235 (NASA–Johnson Space Center).

In the experiment, BYa-type photo-emulsions were used to measure LET spectra within an interval from 12 to 3.5×10^3 MeV cm^{-1} in biological tissue with the lower limit being defined by the effective sensitivity of BYa-type emulsions. In several cases in this experiment we have succeeded in obtaining the planar fluence of the particles with LET $\simeq 2.0$ MeV cm^{-1} in tissue, using the relativistic BR-type emulsion, thereby making it possible to evaluate the doses from CR particles practically within the whole LET interval.

The CR-39 detectors have higher effective LET thresholds of track detection (~ 40 MeV cm^{-1} in tissue). In the present experiment, their assemblies were located, as a rule, next to nuclear emulsions to provide more accurate comparison of measurements made with the two types of detectors, with due account taken of the difference in LET intervals of the particles which are registered by these detectors.

Two integral LET spectra were measured in each location of the CR-39—the spectrum generated by the GCR particles which are not stopped in the detector, and the spectrum formed by short-range particles. Since the CR-39 registers particles with LET ≥ 40 MeV cm^{-1} in tissue (corresponding to the protons with energy less than ~ 12 MeV, alpha particles with energy less than ~ 65 MeV nucleon^{-1}, and particles heavier than carbon with any energy) and the satellite had an almost polar orbit, a great number of low-energy particles were stopped and registered in the detectors.

Besides the above-mentioned detectors, other investigators measured the LET spectra on board Cosmos-2044 using plastic track detectors (Beaujean *et al.*, 1990) and detectors based on AgCl (Baican *et al.*, 1990).

In this work, together with experimental studies, LET spectra for the Cosmos-2044 orbit were calculated according to two different programs developed in the U.S.S.R. and the U.S.A. The U.S. program takes into consideration the contribution to the total LET distribution of the GCR particles (protons and alpha particles only), protons of the internal radiation belt of the Earth, and the contribution from the anomalous component with the charge $Z = 1$. The program takes into account the close-to-maximum SA phase during which the flight took place, geomagnetic cut-off, and screening of particles by the Earth. However, it disregards geomagnetic disturbances. A similar program was developed in the U.S.S.R., but it included only the contribution of GCR particles from hydrogen to nickel.

To compare experimental data with calculations, LET distributions from the GCR particles with $Z > 3$ were calculated following the U.S.S.R. code, and added to the corresponding LET distributions resulting from the U.S. program. All experimental and calculated LET distributions were normalized for 2π geometry.

Table 1. Fluxes of CR particles with LET >40 MeV cm^{-1} in tissue behind small shieldings ($\delta < 2.0$ g cm^{-2}) on board the biosatellite Cosmos-2044

Particles cm^2 s sr $\times 10^{-4}$			δ
N_{ST}	N_{GCR}	N_Σ	g cm^{-2}
10.23	5.60	15.83	0.0935
25.18	2.11	27.29	0.164
12.83	2.02	14.85	0.239
10.92	1.82	12.74	0.250
5.58	1.72	7.30	0.397
2.27	2.20	4.47	1.49
1.53	1.52	3.05	1.95

N_Σ = total flux; N_{GCR} = flux of GCR particles; N_{ST} = flux of particles producing short-length tracks.

RESULTS AND DISCUSSION

Experimental data concerning the integral LET distributions on the external surface of Cosmos-2044 were obtained with two assemblies of detectors: the U.S. detectors F-1 and F-2, behind shielding thicknesses $\delta = 0.164$, 0.239, 0.397, 1.47 and 1.95 g cm^{-2} (assembly F-1) and $\delta = 0.0935$, 0.250, 1.49 and 1.97 g cm^{-2} (assembly F-2), and the Soviet detectors, $\delta = 1.2$ and 1.9 g cm^{-2}. Inside the satellite, LET spectra were measured with the Soviet detectors.

Since the orbit of the satellite was near to polar, it was assumed that the number of low-energy particles with various charges was great and this would cause a difference in fluxes of particles registered on the external surface of the satellite even behind shieldings slightly differing in thickness. This premise can be confirmed by the data in Table 1 which exhibit the values of fluxes of particles measured with the U.S. detectors behind small shielding with $\delta < 2$ g cm^{-2} at LET >40 MeV cm^{-1} in tissue on board Cosmos 2044. Shielding with thickness under 1.5 g cm^{-2} is made of plastic; at $\delta > 1.5$ g cm^{-2} shielding is composed of 0.59 g cm^{-2} stainless steel, 0.120 g cm^{-2} is

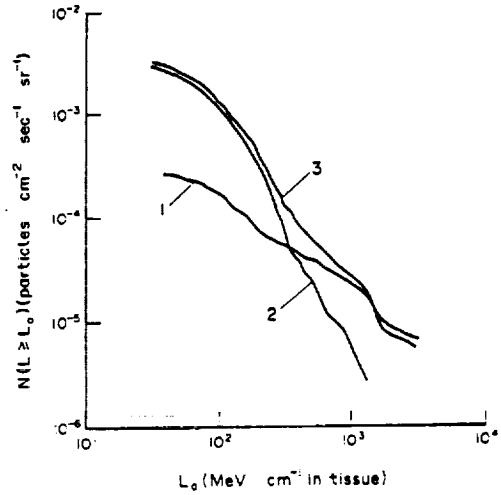

FIG. 1. Integral LET spectrum measured on board Cosmos-2044 with CR-39 track detectors behind $\delta = 0.164$ g cm^{-2}.

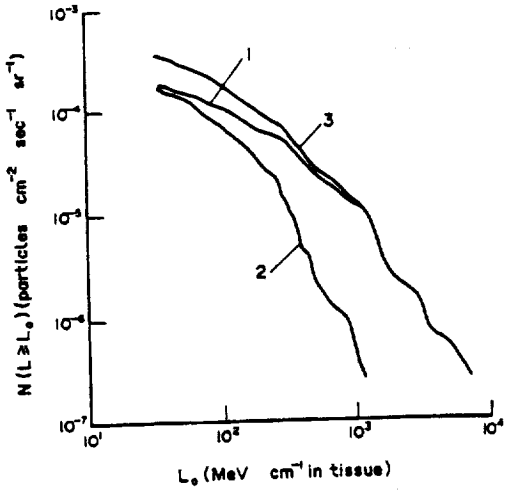

FIG. 2. Integral LET spectrum measured on board Cosmos-2044 with CR-39 track detectors behind $\delta = 1.95$ g cm^{-2}.

nuclear emulsion and the rest is plastic. Flux values corresponding to the smallest thicknesses in the F-1 and F-2 containers (0.164 and 0.0935 g cm^{-2}) show that there was a significant difference in orientation or external shielding between the two.

Moreover, this hypothesis is clearly verified by the data presented in Figs 1 and 2. Figure 1 shows LET distributions measured with CR-39 on the external surface of the satellite behind shielding with $\delta = 0.164$ g cm^{-2}; Fig. 2 shows the analogous distributions at $\delta = 1.95$ g cm^{-2}. In these figures, curves 1 denote LET spectra formed by the GCR particles; curves 2, the LET spectra of low-energy, short-range particles; and curves 3, their total. Comparing the curves from Figs 1 and 2 and analyzing similar LET distributions measured in this experiment behind other shieldings and at $L_0 > 40$ MeV cm^{-1}, it becomes evident that at $\delta < 1.0$ g cm^{-2} the main contributors

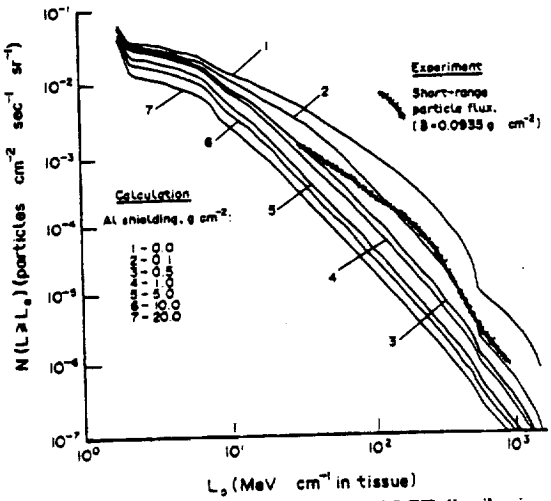

FIG. 3. Comparison of calculated integral LET distributions from trapped protons and GCRs of $Z < 3$ (curves 1–7) with the experimental LET spectrum produced by short-range particles in the flight of Cosmos-2044.

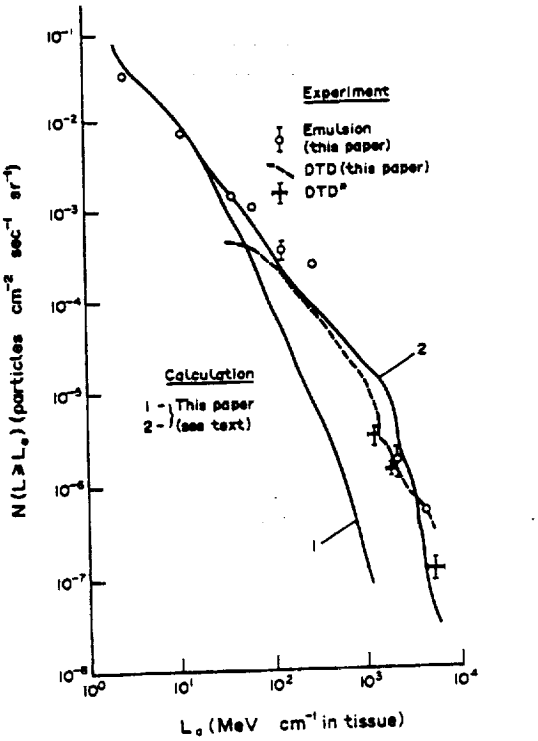

FIG. 4. Comparison of calculated and experimental LET distributions in investigations on board Cosmos-2044 behind small shielding ($\delta = 1.0$–1.5 g cm^{-2})—external assemblies. [*(DTD): Beaujean *et al.*, 1990.]

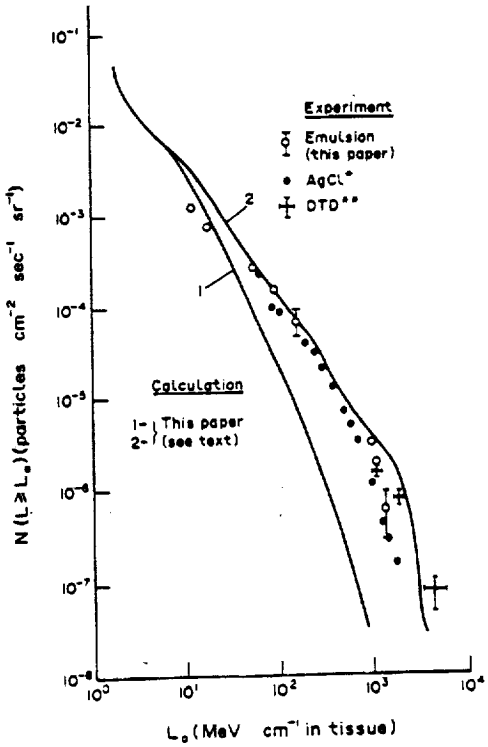

FIG. 5. Comparison of calculated and experimental LET distributions in investigations on board Cosmos-2044 (behind shielding of $\delta > 10$ g cm^{-2})—internal assemblies. [*(AgCl): Baican *et al.*, 1990; **(DTD): Beaujean *et al.*, 1990.]

to the LET spectra are the short-range particles (under $L_0 = 200$–300 MeV cm^{-1}), and with an increase of L_0 this role passes to the GCR particles. At $\delta > 1.0$ g cm^{-2}, in practically the whole LET range of particles registered with CR-39, the bulk of the contribution belongs to the GCR particles.

Figures 3–5 demonstrate results of comparison of the experimental and calculated data. Comparison of LET distributions, calculated according to the U.S. code (without accounting for the contribution of the GCR particles with $Z > 3$) and the experimental LET spectrum, produced by low-energy particles with a residual path $< 1200\ \mu$m in CR-39 plastic (Fig. 3) with shielding $\delta \simeq 0.1$ g cm^{-2}, revealed a satisfactory agreement in the range of L_0 from 100 to 1000 MeV cm^{-1}. At $L_0 < 100$ MeV cm^{-1} the calculated curve surpasses the experimental one by approximately a factor of two, which may possibly be explained by the contribution to the total distribution from fast particles which have a residual path $> 1200\ \mu$m in the plastic detector.

Figures 4 and 5 show the comparison of experimental and calculated data with respect to LET distributions on the external surface of the satellite ($\delta \simeq 1.0$–1.5 g cm^{-2}) (Fig. 4) and inside it ($\delta > 10.0$ g cm^{-2}) (Fig. 5). The figures also include, for comparison, data obtained by other investigators during the flight of the satellite. Calculated curves in Figs 4 and 5 were constructed following the above-mentioned techniques (curve 1: the U.S. code, curve 2: the sum of curve 1 and the LET distribution contributed by GCR particles with $Z > 3$, calculated by the Soviet program). Explanations of the experimental data are given in the corresponding figures. Results of experimental measurements made with different detectors (nuclear emulsions, plastic detectors, AgCl detectors) should be noted as to their satisfactory conformity with total calculated integral LET distributions. Differences in calculated and experimental data values at $L_0 \gtrsim 10^3$ MeV cm^{-1}, apart from experimental errors, can also be explained by rather great statistical errors in calculations by the Monte Carlo method.

LET spectra from the present experiment were compared with results of our previous investigations of LET spectra (Akopova *et al.*, 1990) for various inclinations of the orbit (i) from 60 to 83°. The Soviet satellite Cosmos-1757, as well as Cosmos-2044, had an inclination $i = 82°$. However, in the first case, the magnitude of the values of LET spectra flux was two- to three-fold higher compared with the present data. In our opinion, there are three factors which may be involved in this phenomenon. Firstly, Cosmos-1757 was in orbit in the period of deep SA-minimum when fluxes of the GCR particles in these orbits increase 1.5–2.0 times compared with the SA-maximum, when Cosmos-2044 was launched. Secondly, the shielding of detectors used for LET distribution measurements presented in Fig. 4 ($\delta = 1.0$–1.5 g cm^{-2}) was almost an order of magnitude greater than in the experiment on board Cosmos-1757 ($\delta = 0.1$–0.2 g cm^{-2}). This conclusion is also confirmed by measurements which were made in this experiment with plastic detectors behind various shieldings (Table 1). Indeed, the difference in fluxes behind $\delta = 0.164$ g cm^{-2} and $\delta = 1.95$ g cm^{-2} is almost equal to an order of magnitude. This difference is observed over the whole interval of LET which was registered by the plastic detectors. And, thirdly, in our work (Akopova *et al.*, 1990) we took into account the fact that Cosmos-1757 was oriented and detectors were located on the external surface of the satellite in the spot where, to quote Akopova *et al.* (1989), the normalizing geometric factor, allowing for the spatial angle at which a CR particle penetrates a detector, was 4.1 against 6.28 in the flight of Cosmos-2044. Each of these three factors affected an increase of the fluence of particles in the experiment on board Cosmos-1757 compared with Cosmos-2044.

The data contained in the integral LET spectra were used to estimate the radiation environment inside and outside the biological satellite. Values of absorbed and equivalent doses were calculated using

Table 2. Values of absorbed and equivalent doses obtained from experimental data and calculated values of LET spectra on board Cosmos-2044

		Outside ($\delta = 1.0$–1.5 g cm^{-2})		Inside ($\delta \geq 10$ g cm^2)	
	Doses / Data	D, mrad day^{-1}	H, mrem day^{-1}	D, mrad day^{-1}	H, mrem day^{-1}
1	2	3	4	5	6
LET ≥ 2.0 [MeV cm^{-1}]	Calculation	9.30 ($\delta = 1.0$)	23.6 ($\delta = 1.0$)	4.40 ($\delta = 20.0$)	9.14 ($\delta = 20.0$)
	Experiment (NPE)*	10.30 ($\delta = 1.2$)	27.5 ($\delta = 1.2$)	8.9 ($\delta = 10.0$)	14.5 ($\delta = 10.0$)
LET ≥ 40.0 [MeV cm^{-1}]	Calculation	1.38 ($\delta = 1.0$)	16.8 ($\delta = 1.0$)	—	—
	Experiment (CR-39)	1.32 ($\delta = 1.47$)	12.8 ($\delta = 1.47$)	—	—
		1.53 ($\delta = 1.49$)	13.9 ($\delta = 1.49$)	—	—

*NPE: nuclear photo-emulsion method.

Table 3. Calculated components of total absorbed dose (mrad day^{-1}) in the orbit of Cosmos-2044

No.	Sources	h, km	(δ, g cm^{-2}) 1.0	1.5	2.0	10	20
1.	Electrons of RBE*	200	52.6	10.7	1.25	0.12	—
		300	72.0	20.0	1.73	0.17	—
2.	Protons of RBE*	200	0.06	0.05	0.04	—	—
		300	3.71	3.20	2.94	1.11	0.52
3.	GCR	200	6.64	6.58	6.52	5.28	4.19
		300	6.71	6.65	6.58	5.34	4.29
4.	2 + 3	200	6.70	6.63	6.62	5.30	4.20
		300	10.4	9.8	9.4	6.45	4.8
5.	1 + 4	200	59.6	17.3	7.8	5.4	4.2
		300	82.4	30.0	11.2	6.6	4.8

*RBE: radiation belts of Earth.

total flux curves (curves 3) in Figs 4 and 5 (Table 2, line 1). The table lists the values of doses obtained from the experimental data (nuclear emulsions) covering the whole interval of LET (Table 2, line 2), as compared with the plastic detector interval of $L_0 \geq 40$ MeV cm^{-1} in tissue (Table 2, calculation: line 3; experiment: line 4).

The dose values in Table 2 do not include the contribution of electrons which, as it was shown in Akatov *et al.* (1990), at small shieldings can reach 70–90% of a total dose. In view of this, the dose values for maximal SA would be: $D(\delta = 1.0) = 69.3$ mrad day^{-1} and $H(\delta = 1.0) = 83.6$ mrem day^{-1} and $D(\delta = 1.2) = 27.8$ mrad day^{-1} and $H(\delta = 1.2) = 48.0$ mrem day^{-1}. Contribution of electrons at $\delta > 10$ g cm^{-2} is negligibly small. The dose values calculated for positions inside the satellite are approximate due to the absence of information about mass distribution in the shielding which screened these detectors.

The techniques described in Akatov *et al.* (1990), were used to calculate dose values for the orbit of Cosmos-2044. Results of these calculations, presented in Table 3, are in satisfactory agreement with the experimental data in Table 2.

CONCLUSIONS

(1) In orbits with a large angle of inclination, a strong dependence of the CR particle fluence on the shielding thickness is observed in a range from 0.1 to 2.0 g cm^{-2}. This has been confirmed by previous investigations.

(2) For similar satellite orbits, the magnitude of total fluence is a function of the measurement period, i.e. on SA-phase.

(3) The LET spectra measured by different methods (nuclear emulsions, plastic detectors, AgCl detectors) are in satisfactory agreement within overlapping intervals of registration.

(4) Calculated estimations in an undisturbed magnetic field allow a satisfactory prediction of the results of experiments.

Future investigations should be aimed at quantification of total fluence of all particles including relativistic protons.

It is also necessary to give more detailed study to LET spectra with a sufficiently high experimental statistical accuracy in the area of very low (< 10 MeV cm^{-1}) and very high ($> 5 \times 10^3$ MeV cm^{-1}) LET values.

REFERENCES

Akatov Yu. A., Dudkin V. E., Kovalev E. E., Benton E. V., Frank A. L., Watts J. W. Jr and Parnell T. A. (1990) Depth distribution of absorbed dose on the external surface of Cosmos-1887 biosatellite. *Nucl. Tracks Radiat. Meas.* 17, 105–107.

Akopova A. B., Ambartsumian A. G., Dudkin V. E., Melkumian L. V., Potapov Yu. V. and Rshtuni Sh. B. (1989) Study of spectral characteristics of light nuclei on Cosmos-1571. *Space Invest.* XXVII (2), 318–321.

Akopova A. B., Magradze N. V., Dudkin V. E., Kovalev E. E., Potapov Yu. V., Benton E. V., Frank A. L., Benton E. R., Parnell T. A. and Watts J. W. Jr (1990) Linear Energy Transfer (LET) spectra of cosmic radiation in low Earth orbit. *Nucl. Tracks Radiat. Meas.* 17, 93–97.

Akopova A. B., Magradze N. V., Moiseenko A. A., Muradian S. H. and Ovanian K. M. (1983) Selective development of nuclear emulsions with thick layers. Preprint ErFI-661, 661–83, Yerevan.

Baican B., Schopper E., Wendnagel Th., Schott J. U. and Hailmann C. (1990) The life science experiment 'Seeds' on the Biocosmos satellite 9; Physical part. Abstracts of report on *15th Int. Conf. Particle Tracks in Solids*, Marburg, Germany, September 1990.

Beaujean R., Kopp J. and Enge W. (1990) Measurements of high-LET spectra on Biocosmos-9. *Contr. 15th Int. Conf. Particle Tracks in Solids*, Marburg, Germany, September 1990. IFKKI 90/4, pp. 5–8.

APPENDIX R

Cosmic Ray LET Spectra and Doses on Board the Cosmos-2044 Biosatellite

by

V.E. Dudkin, E.E. Kovalev, Yu.V. Potapov, E.V. Benton, A.L. Frank
E.R. Benton, J.W. Watts, Jr., T.A. Parnell, E. Schopper,
B. Baican, G. Reitz. H. Bücker, R. Facius,
R. Beaujean and C. Heilmann

Nucl. Tracks Radiat. Meas., Vol. 20, No. 1, pp. 149–155, 1992
Int. J. Radiat. Appl. Instrum., Part D
Printed in Great Britain

0735-245X/92 $5.00 + .00
Pergamon Press plc

COSMIC RAY LET SPECTRA AND DOSES ON BOARD COSMOS-2044 BIOSATELLITE

V. E. DUDKIN,* E. E. KOVALEV,* YU. V. POTAPOV,* E. V. BENTON,† A. L. FRANK,† E. R. BENTON,† J. W. WATTS JR.,‡ T. A. PARNELL,‡ E. SCHOPPER,§ B. BAICAN,§ G. REITZ,‖ H. BÜCKER,‖ R. FACIUS,‖ R. BEAUJEAN¶ and C. HEILMANN**

*Research Center for Space Flight Radiation Safety, Ministry of Public Health, Moscow 123182, U.S.S.R.; †University of San Francisco, San Francisco, CA 94117, U.S.A.; ‡NASA–Marshall Spaceflight Center, Huntsville, AL 35812, U.S.A.; §Institute for Nuclear Physics, Frankfurt am Main, Germany; ‖DLR Institute for Aerospace Medicine, Köln, Germany; ¶University of Kiel, Kiel, Germany; **Centre de Recherches Nucléaires, Strasbourg, France

(*Received* 23 *June* 1991; *in revised form* 3 *July* 1991)

Abstract—Results of the experiments on board Cosmos-2044 (Biosatellite 9) are presented. Various nuclear track detectors (NTD) (dielectric, AgCl-based, nuclear emulsions) were used to obtain the LET spectra inside and outside the satellite. The spectra from the different NTDs have proved to be in general agreement. The results of LET spectra calculations using two different models are also presented. The resultant LET distributions are used to calculate the absorbed and equivalent doses and the orbit-averaged quality factors (QF) of the cosmic rays (CR). Absorbed dose rates inside ($\sim 20\ g\ cm^{-2}$ shielding) and outside ($1\ g\ cm^{-2}$) the spacecraft, omitting electrons, were found to be 4.8 and 8.6 mrad d^{-1}, respectively, while the corresponding equivalent doses were 8.8 and 19.7 mrem d^{-1}. The effects of the flight parameters on the total fluence of, and on the dose from, the CR particles are analyzed. Integral dose distributions of the detected particles are also determined. The LET values which separate absorbed and equivalent doses into 50% intervals are estimated. The CR-39 dielectric NTD is shown to detect 20–30% of the absorbed dose and 60–70% of the equivalent dose in the Cosmos-2044 orbit. The influence of solar activity phase on the magnitude of CR flux is discussed.

1. INTRODUCTION

THE RADIATION environment in near-Earth space needs to be shown in order to estimate the radiation risk for any planned manned space mission. The need for this knowledge becomes even more necessary in the case of long-term missions.

Cosmic ray dosimetry is faced with certain difficulties due to the complicated composition of radiation fields in near-Earth space, the diversity of the factors affecting the qualitative and quantitative compositions of the fields, and some characteristic features inherent to space flights. Copious relevant information has been accumulated within the last decades, including the total absorbed dose, the dose rates, the particle LET spectra, and the particle flux densities. The information relates mainly to low-inclined orbits (inclination $i \leqslant 70°$) with altitudes not exceeding ~ 450 km.

Recently, the absorbed and equivalent doses have been estimated using not only dosimeters, but also NTDs which make it possible to measure the integral LET spectra of cosmic ray particles in low orbits. Measurements of that type were made earlier (Benton, 1983, 1986; Benton and Henke, 1983; Akopova *et al.*, 1985, 1986, 1987, 1988, 1990a) for various satellite orbit parameters and thicknesses of detector shieldings during different solar activity (SA) periods. Some works should also be noted (Benton, 1986; Akopova *et al.*, 1985, 1986, 1987, 1988, 1990a; Heinrich, 1977; Heinrich and Baer, 1984; Heinrich *et al.*, 1989) where the LET distributions were calculated for different satellite parameters. These calculations treated only the galactic cosmic ray (GCR) particle component of the radiation field.

The characteristic features of the Cosmos-2044 flight were as follows: the flight took place during solar maximum and the orbit was near-polar ($i = \sim 82°$). Various NTDs (dielectric plastics, AgCl single-crystals and nuclear emulsions of different types), mounted inside and outside the satellite, were used to measure the CR particle LET spectra within a broad range. The present work compares the results of the measurements taken inside and outside (under low shielding thicknesses) the Cosmos-2044 satellite. The resultant LET spectra are used to calculate the total absorbed and equivalent doses and the LET distributions of the doses.

The following four basic factors affect the magnitude of the charged-particle flux measured in

†USF portion of the work partially supported by NASA Grant Nos NCC2-521 (NASA–Ames Research Center) and NAG9-235 (NASA–Johnson Space Center).

space: (a) solar modulation, i.e. the dependence of particle flux on SA period; (b) geomagnetic cut-off threshold (the GCR flux increases with satellite orbit inclination); (c) the detector shielding thickness; and (d) the satellite flight altitude (the trapped proton flux increases steeply with orbital altitude). The degree of the effect of these factors on the measured LET distributions will also be discussed below.

Work by Akopova *et al.* (1990b) and Dudkin *et al.* (1992) presents the Biosatellite-9 preliminary experimental data including the results obtained by Soviet experts using nuclear emulsions (Akopova *et al.*, 1990b) and the results of the joint Soviet–American researchers (Dudkin *et al.*, 1992). These are compared with the relevant calculated results.

2. EXPERIMENTAL DESIGN

In conformity with the scientific program for Biosatellite 9 (Cosmos-2044), the solid-state nuclear track detectors (SSNTDs), i.e. nuclear emulsions, AgCl-based detectors, and dielectric detectors, were placed in specially designed containers and exposed inside and outside the satellite during 14 days of flight near the Earth (at 294 km apogee, 216 km perigee, orbit inclination $i = 82.3°$) under quiet geomagnetic conditions. The participants in the experiment are the ESA, represented by Frankfurt University, Germany (the AgCl detectors), Kiel University, Germany (the dielectric detectors with different thresholds of particle LET detection), the Centre de Recherches Nucléaires, Strasbourg, France (nuclear emulsions), and the Research Center of Spacecraft Radiation Safety, Moscow, U.S.S.R. (nuclear emulsions of various types). Plastic nuclear track detectors were contributed by the University of San Francisco, U.S.A. The AgCl detectors were mounted only inside the satellite, and the American-made dielectric detectors only outside the satellite, while the German-made dielectric detectors and the French- and Soviet-made nuclear emulsions were mounted both inside and outside the satellite.

The SSNTDs used in the experiment are characterized by effective particle LET thresholds above which the particles could be detected (L_{thresh}: see Table 1).

Various types of nuclear emulsions were used to detect the CR particles throughout their LET range. Emulsion stacks containing 200-μm-thick BR- and BYa-type emulsions wrapped with light-tight paper and aluminized Lavsan were placed in instrument modules either outside or inside the satellite. After exposure and recovery, each layer of the emulsion stack was treated by the selective development technique which makes it possible to control the emulsion layer threshold sensitivity in a broad interval of LET (Akopova *et al.*, 1983). The emulsion threshold sensitivity control is based on the introduction of Br^- ions into an exposed emulsion layer by diffusion. The Br^- ions were emitted from BR-type layers (emitters) glued to either of the surfaces of an exposed layer that had been irradiated beforehand with blue–violet light. The Br^- ion generation and diffusion from the emitters to the exposed layers gives rise to a negative bromine barrier around the latent image centers, thereby increasing the induction periods of developing centers. The ability of the centers to be developed depends, then, upon the ratio of the height of the barrier restricting the arrival of electrons at the centers to the depth of the potential well in which the electrons are captured. Thus, the emulsion threshold sensitivity control is based on different degrees of dispersion of the latent image centers produced by particles with different LET values. The threshold sensitivity of the exposed layer permits only those particle tracks to be developed for which the LET is at least equal to some threshold LET value. Therefore, the technique of finding the planar fluence of the particles with $LET \geqslant LET_{thresh}$ does not require the track parameters to be measured but is reduced to counting the number of the tracks traversing a particular section of an emulsion surface. Calibration of the technique was achieved by exposing emulsions to particle beams of well-defined LETs.

We used BYa-type emulsion which permits the integral LET spectra to be measured within an interval from 12 to $\sim 10^4$ MeV cm^{-1} of biological tissue (water), with the lower limit (12 MeV cm^{-1}) being defined by the effective sensitivity of the BYa-type emulsion. To obtain a complete LET distribution, we sometimes used the relativistic BR-type emulsion, thereby making it possible (to within a large microscope scanning error) to find the planar fluence of CR particles at small LET values (the LET of relativistic protons in tissue is ~ 2.0 MeV cm^{-1}). Scanning error with BR-type emulsion increases (a) due to a high track exposure of the detectors (the satellite flights lasted, as a rule, for more than 10 days); and (b) because the operator can easily overlook tracks of relativistic protons (low grain densities).

This method has the drawback of emulsion shrinkage after the layers have been fixed and developed, which may lead to distortion. The necessity for a

Table 1. Effective thresholds (L_{thresh}) of particle detection by the Cosmos-2044 NTDs

Detector	Dielectric detectors				Single crystal	Nuclear emulsion		
Detector type	CR-39	CN_k	CN_D	Lexan	AgCl	BR-2	BYa-2	Ilford K2
Country	U.S.A.	Germany			Germany	U.S.S.R.	U.S.S.R.	France
		Kiel	Kiel	Kiel	Frankfurt			
L_{thresh}, MeV cm^{-1}, in tissue	~40	1200	1800	5800	60	2.0	12.0	>10

~60% ambient humidity to be maintained is also a drawback of the method.

The method for finding the LET distributions with dielectric detectors of CR-39, CN, and Lexan types, whose effective thresholds of particle LET detection are presented in Table 1, has been tested earlier during various spacecraft flights. After being etched under appropriate time–temperature conditions, the Kiel detectors were scanned to find the LET spectra by counting the particle track densities per surface and correcting for flight duration and for the effective solid angles for registration of particles incident on the detectors. The particle numbers were then plotted at the respective LET thresholds for each of the detectors.

The American-made CR-39 plastic NTDs, of ~600 μm thickness each, were etched in the standard manner for 7 days in a 6.25 N NaOH solution at 50°C. The bulk etch B (i.e. the total thickness removed from each surface) was measured in all the layers. For readout, pairs of detectors were segregated according to their orientations during the flight. Each two adjacent inner surfaces were scanned with an optical microscope, thereby making it possible to group the particles into short-range (SR) tracks, when the matching tracks appear on two inner surfaces only, and the long-range GCR tracks, when the matching tracks appear on all four surfaces of the pairs of detectors. The SR particles included the SR secondaries from target nuclei within the plastic, the stopping primary GCR particles, and the trapped RB particles. All protons were classified as SR particles because of their short registration paths in CR-39. The GCR particles include the primary CR particles and the long-range secondaries which are mainly projectile fragments of primary GCRs. Etching of the CR-39 produces conical tracks at the particle entrance and exit points. The intersections of the cones with the CR-39 surfaces are elliptical in shape. The lengths of the major and minor axes of the ellipses were measured on the detector surfaces. The axial lengths and the values of B in the specimens, together with the calibration of particle LET response in CR-39, were then used to find the total LET distributions.

The AgCl single-crystal layers coated with a Cd grease on a glass underlayer were used to obtain the LET spectra inside the satellite. For particle detection by AgCl crystals, high-power yellow–green light sources are used to preserve the latent track image before development (German-made lithium batteries were used on the satellite). The 140-μm-thick AgCl single crystals were mounted inside specially designed containers where biological objects were also placed. Such a detector was used earlier in spaceborne experiments, mainly in radiobiological experiments (for example, on Cosmos-1887). The detectors could record particles with LET above 10 MeV g^{-1} cm^{-2}. During the spaceflight, the latent image centers produced by the particles with low LET values disappear due to the fading which occurs continually within the detector volume, so the effective detection threshold for particle LET gets shifted towards higher LET values (~60 MeV cm^{-1} of tissue in the given experiment). The detectors are used to find the LET spectra of CR particles in the LET range above the threshold.

In the present work, the experiments were supplemented with calculations of the LET spectra in the Cosmos-2044 orbit using two independent programs designed in the U.S.A. and in the U.S.S.R. The American program allows for the contributions of GCR particles (protons and He nuclei only), of the inner RB protons, and of the $Z = 1$ anomalous component to the integral LET distributions. Allowance is also made for geomagnetic cut-off and for the screening of particles by the Earth without, however, any geomagnetic disturbance. A similar program designed in the U.S.S.R. was used to calculate the contribution from the $Z \geqslant 3$ GCR particles only. More details can be found in Dudkin *et al.* (1992).

3. RESULTS AND DISCUSSION

Figures 1 and 2 show the integral LET spectra outside (Fig. 1) and inside (Fig. 2) Cosmos-2044. The spectra have been obtained with different NTDs. In all cases, the planar particle fluence, i.e. the number of tracks traversing the detector surface, was measured.

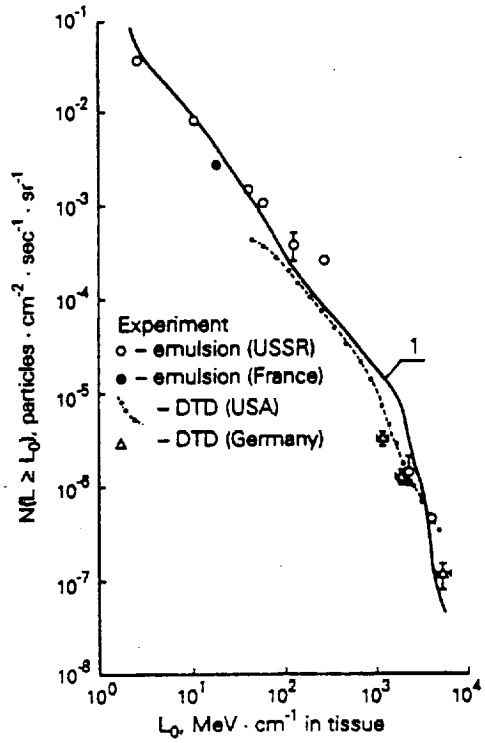

FIG. 1. Comparison between the calculated (curve 1—for 1 g cm^{-2}) and experimental integral LET distributions of CR particles obtained on Cosmos-2044 (stacks outside the satellite); DTD denotes plastic dielectric track detectors.

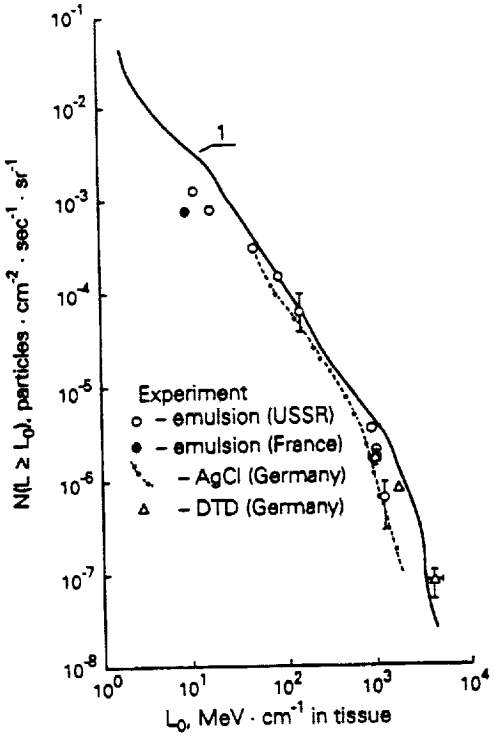

FIG. 2. Comparison between the calculated (curve 1—for 20 g cm^{-2}) and experimental LET distributions of CR particles obtained on Cosmos-2044 (stacks inside the satellite); DTD denotes plastic dielectric track detectors.

It should be noted that the measurement results obtained at different research centers with different detectors have proved to be in satisfactory agreement. Certain differences in the integral spectra obtained outside the satellite (Fig. 1) can be accounted for by the difference in the detector shielding thicknesses. Because of a near-polar inclination of the satellite orbit, the contribution of SR particles to the total flux must depend substantially on the detector shielding thickness, even in the case of small thicknesses ($\delta < 2$ g cm^{-2}). The American-made dielectric detector data show that the SR particle flux density under a shielding $\delta = 0.2$ g cm^{-2} is almost an order of magnitude higher than that of $\delta \sim 2.0$ g cm^{-2} (Dudkin *et al.*, 1992).

For comparison, Figs 1 and 2 also present the calculated integral LET distributions of CR particles on the Cosmos-2044 orbit during solar maximum. The calculations were made at $\delta = 1.0$ g cm^{-2} (Fig. 1) and $\delta = 20$ g cm^{-2} (Fig. 2) using the two available models for calculating the LET spectra. The figures show the total LET spectra of CR particles (curve 1). Each of the distributions consists of an LET spectrum defined by the light CR components (the GCR protons, the He nuclei and the RB protons) as calculated by the American program, and includes the LET distribution of the $Z > 3$ CR particles (GCR particles) calculated by the Soviet program. A good agreement is seen between the experimental and theoretical data in the two figures.

It should be noted that the simultaneous usage of different techniques for measuring the LET spectra has proved to be very fruitful because, firstly, a broader range of LET values can be covered and, secondly, the reliability of the measurement results in the intervals of overlapped measurements are improved.

The LET distributions obtained were used to calculate the absorbed and equivalent doses inside and outside the satellite. To facilitate the calculations, the LET spectra were approximated by piecewise continuous functions:

$$N(L \geq L_0) = \alpha \times L_0^{-\beta}, \qquad (1)$$

where α and β are constants.

The integral LET spectra of CR particles measured in different low-Earth orbits and outside the magnetosphere exhibit a characteristic knee at $L \sim 1350$ MeV cm^{-1}. The knee, i.e. a decrease of the exponent β in (1), can be accounted for by the fact that the GCR Fe nuclei are detected at $L \cong 1350$ MeV cm^{-1} and higher, and that the flux of Fe nuclei decreases with increasing L very rapidly in comparison with the range $L < 1350$ MeV cm^{-1}, where all CR particles from protons to Fe nuclei contribute to the total flux.

The same pattern was recorded on Cosmos-2044; from Figs 1 and 2 it is seen that the characteristic knees in the LET distributions at $L > 10^3$ MeV cm^{-1} are observed. When calculating the doses for these spectra, therefore, we approximated the resultant integral LET spectra by expressions of type (1) in two L ranges, $2.0 \leq L_0 \leq 1350$ MeV cm^{-1} and $1350 < L_0 < 5 \times 10^4$ MeV cm^{-1}.

To find the effect of the spread of the experimental points in the LET spectra on the absorbed and equivalent doses, we applied the approximation functions of type (1) to each of the spectra shown in Figs 1 and 2 in such a manner that all the experimental and calculated values of $N(L \geq L_0)$ would be below (the first case, "Maximum" version) and above (the second case, "Minimum" version) the approximation functions. Table 2 presents the resultant values of the

Table 2. The values of the approximation constants α and β

			Detectors mounted			
			Outside the satellite		Inside the satellite	
Version	LET range, in tissue	constant:	α	β	α	β
Maximum	$2 \leq L \leq 1350$ MeV cm^{-1}		0.2088	1.3800	0.1425	1.4540
	$1350 < L < 5 \times 10^4$ MeV cm^{-1}		1.052×10^3	2.5626	1.00×10^6	3.641
Minimum	$2 \leq L \leq 1350$ MeV cm^{-1}		0.2370	1.5645	0.1836	1.8197
	$1350 < L < 5 \times 10^4$ MeV cm^{-1}		2.850×10^6	3.826	5.03×10^{16}	7.39

Table 3. Calculated values of the absorbed (D) and equivalent (H) doses in the Cosmos-2044 orbit

Version \ Dose	Detectors mounted			
	Outside the satellite ($1\ g\ cm^{-2}$)		Inside the satellite ($20\ g\ cm^{-2}$)	
	D, $\frac{mrad}{day}$	H, $\frac{mrem}{day}$	D, $\frac{mrad}{day}$	H, $\frac{mrem}{day}$
Maximum	9.7	25.9	5.6	12.5
Minimum	7.6	13.6	4.0	5.1
Mean doses	8.6 ± 1.4	19.7 ± 6.2	4.8 ± 0.8	8.8 ± 3.7

constants α and β. Table 3 presents the doses calculated throughout the L range in two versions and also gives the mean values of the doses.

The QFs averaged over the LET spectra on the given orbit are 2.3 outside and 1.8 inside the satellite. It should be noted that the values of the doses and QFs obtained outside the satellite do not allow for the contribution to the total dose from the RB electrons which, according to Akatov *et al.* (1990), may constitute 70–90% of the total dose under shielding of less than $\sim 1.5\ g\ cm^{-2}$ (even during solar minimum and at an orbital inclination of 60°). With the electron component included, the doses during solar maximum at 82° inclination and 250 km altitude will increase to $D(\delta = 1.0) = 69.3\ mrad\ day^{-1}$ and $H(\delta = 1.0) = 83.6\ mrem\ day^{-1}$. The averaged QF on such an orbit under shielding $\delta = 1.0\ g\ cm^{-2}$ will fall to QF = 1.2, in agreement with Akatov *et al.* (1990).

The equivalent doses were calculated using our approximation of the dependences of QF on LET $\equiv L_\infty$ in tissue, the values of which are tabulated in ICRP-26 (1977):

$$\left.\begin{aligned} &QF = 1 \\ &\quad \text{at } L \leqslant 35\ MeV\ cm^{-1} \\ &QF = 2.857 \times 10^{-2} \times L \\ &\quad \text{at } 3.5 < L \leqslant 70\ MeV\ cm^{-1} \\ &QF = 6.830 \times 10^{-2} \times L^{0.7950} \\ &\quad \text{at } 70 < L \leqslant 530\ MeV\ cm^{-1} \\ &QF = 2.625 \times 10^{-1} \times L^{0.5803} \\ &\quad \text{at } 530 < L \leqslant 1750\ MeV\ cm^{-1} \\ &QF = 20 \\ &\quad \text{at } L > 1750\ MeV\ cm^{-1}. \end{aligned}\right\} \quad (2)$$

The disagreement between the approximated data and the recommended QF values is not greater than ±5% throughout the L range. It should also be noted that the CR doses were calculated in some studies (Silberberg *et al.*, 1984; Letaw *et al.*, 1986, 1987; Letaw and Clearwater, 1986) using other functions to approximate the dependence $QF = f(L)$:

$$QF = \begin{cases} 1 & \text{at } L \leqslant 35\ MeV\ cm^{-1} \\ 0.072 \times L^{0.74} & \text{at } 35 < L < 2000\ MeV\ cm^{-1} \\ 20 & \text{at } L \geqslant 2000\ MeV\ cm^{-1}. \end{cases} \quad (3)$$

An analysis has shown that the equations (3) underestimate the recommended QF values by up to 20–30% at $35 < L < 2000\ MeV\ cm^{-1}$. It is noteworthy that the absorbed doses calculated in the versions "Maximum" and "Minimum" (see Table 3) differ from each other by not more than ~30% for the LET spectra measured both inside and outside the satellite. At the same time, the equivalent doses differ from each other by a factor of 2.0–2.5 for the same LET distributions. It should be emphasized that this corresponds to the largest spreads found between the different measurements.

Figure 3 presents our calculated integral LET distributions of the absorbed and equivalent doses outside and inside the satellite. The approximation functions in the version "Maximum" were used as the input data. From Fig. 3 it is seen that the general trend of the LET dependence is the same outside and inside the satellite with the dependence being "shifted" towards smaller LET values (towards higher particle energies) inside the satellite, as would be expected in principle.

Nearly 50% of the total equivalent dose is from the particles whose LET exceeds 400 MeV cm^{-1}, whereas ~50% of the absorbed dose is from the particles with LET below 10 MeV cm^{-1}. Knowing, for example, that dielectric detectors such as CR-39 measure particles with LET ≥ 40 MeV cm^{-1} in tissue, we can note from Fig. 3 that, in this instance, the detected

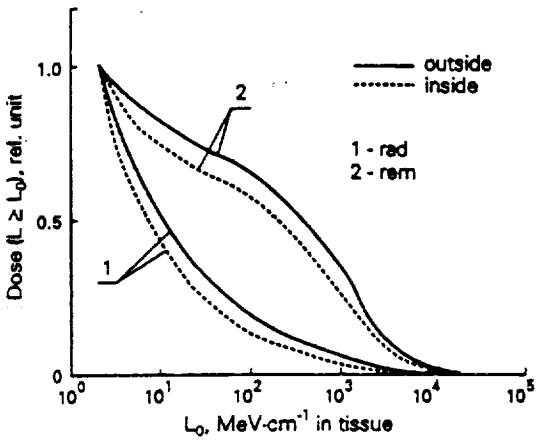

FIG. 3. The dose-LET distributions obtained on Cosmos-2044. The outside curves are for 1 g cm^{-2} shielding; inside curves are for 20 g cm^{-2}.

absorbed dose can be as small as 20–30% of the total, while the equivalent dose is 60–70% of the total. This fact has been corroborated by the data of Dudkin *et al.* (1992) where absorbed and equivalent doses which were measured with CR-39 outside Cosmos-2044 are presented. According to Fig. 3, the absorbed dose (1.32–1.53 mrad day^{-1}) under an ~ 1.5 g cm^{-2} shielding is 23% of the total dose, thereby yielding ~ 6.2 mrad day^{-1} when the total dose is estimated for the full LET range, in agreement with the mean value of (8.6 ± 1.4) mrad day^{-1} from Table 3 at ~ 1.0 g cm^{-2}. Similarly, according to Fig. 3, the value of (12.8–13.9) mrem day^{-1} must constitute $\sim 72\%$ of the total dose. Simple calculations yield 18.5 mrem day^{-1}, also in good agreement with the data of Table 3 for outside the satellite.

The greatest differences in the values of the LET spectra measured by different techniques occur in the tails of the spectra. The differences may be accounted for by a low statistical accuracy of the results for rare events (particles with high LET values) and by marginal detection of the fluence of CR particles with LETs near the detector thresholds. Particular attention should be paid in the future to the correct determination of the total fluence (at the lowest ionization values) and of the fluence at $L > 10^3$ MeV cm^{-1}.

As noted above, the Cosmos-2044 flight was distinguished by the following factors: the flight took place during solar maximum on a near-polar orbit with an apogee of close to 300 km. The effect of the orbital parameters on the different sources of radiation in the Earth's environment (GCR particles and RB protons and electrons) varies. The GCR particle flux changes little with orbital altitude, but decreases with increasing solar activity (due to the screening effect of solar wind on the GCR flux) and increases with orbital inclination (due to a decrease in the geomagnetic cut-off threshold). The RB proton contribution decreases with increasing solar activity and with decreasing orbital altitude (at ~ 200–300 km the orbit passes under the zone of the most intense fluxes of the Brazilian anomaly) and increases with decreasing i, for $i > \sim 35°$ (due to a longer residence of the satellite in the region of the Brazilian anomaly). The RB electron fluxes increase with solar activity, whereas the contribution of precipitating electrons in the Earth's near-polar zone increases with decreasing altitude and increasing inclination.

The above-mentioned relationships have been confirmed experimentally by comparing doses measured with American-made thermoluminescent dosimeters on two satellites (Cosmos-2044 and -1887) (Frank *et al.*, 1990; Benton *et al.*, 1988). Cosmos-1887 flew at a higher altitude and a smaller inclination during solar minimum.

As noted above, the Cosmos-2044 flight is distinguished by its coincidence with the maximum of Solar Cycle 22. According to some predictions [see the review ISSN 0208-1849 (1990)] the Cycle 22 maximum should have exceeded all the previous cycles in solar activity. If so, we would expect a pronounced decrease in the GCR particle flux and in the RB proton flux in low orbits. This was not observed, however.

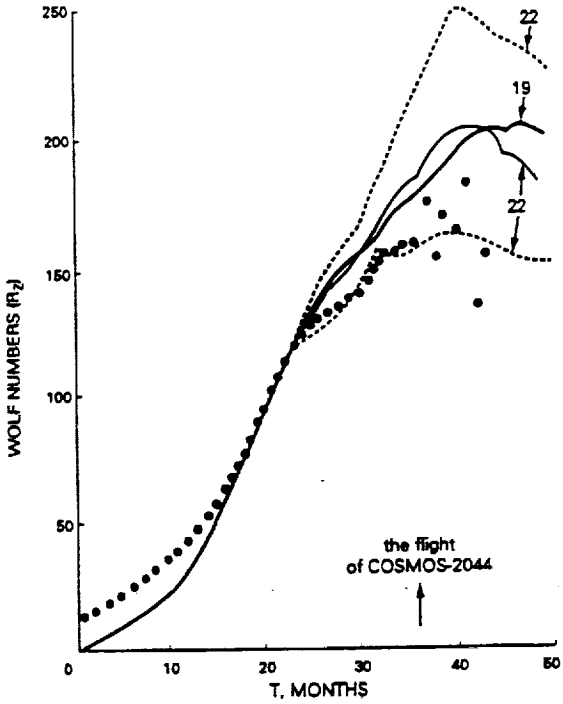

FIG. 4. Wolf numbers versus time during Solar Cycle 22.

The Wolf numbers (R_z), recorded continually at various ground-based observatories, are known to be a significant criterion for estimating solar activity. Figure 4, borrowed from ISSN 0208-1849 (1990), presents the Wolf number data up to March 1990. September 1986 is taken to be the onset of Cycle 22; the Cycle 19 data are presented for comparison (Cycle 19 was the most intense of the last five decades). The thick solid line represents the R_z values during Cycle 19 (smoothed mean-monthly R_z values); the dashed lines represent a 90% confidence interval; the dots are observation data (smoothed R_z values up to August 1989 and observed values up to March 1990).

From Fig. 4 it is seen that, up to the present, a maximum of extreme intensity has not been attained in Cycle 22. At most, the R_z values will approach the values observed during Cycle 19, but will not exceed them. Thus, despite the violent rise of solar activity during its initial phases, Cycle 22 can be considered to be fairly moderate, with the highest values of R_z reaching 150–170, which are close to the levels during Cycles 18 and 19.

Considering the fact that Cosmos-2044 flew in September 1989 and that the delay between solar activity and GCR particle modulation is about half a year, we may say that solar activity during the Cosmos-2044 flight was moderate and comparable with the levels during the previous solar cycle. Our results are consistent with this conclusion.

208

4. CONCLUSIONS

(i) The experimental studies of integral LET distributions carried out on board Cosmos-2044 by experts from different countries using various detectors have demonstrated that the results obtained are in satisfactory agreement in the overlapping LET ranges. A satisfactory agreement was also obtained between the experimental data and the LET spectrum calculations obtained with two different calculation models.

(ii) The absorbed and equivalent doses inside and outside the satellite have been calculated using the measured LET distributions as input data. This approach has been demonstrated to yield good results for calculating the absorbed dose and to be applicable for estimating the equivalent dose. For improved results, it is necessary to increase the accuracy of flux measurements in the tails of the LET spectra and, particularly, to measure the fluence of all charged heavy CR particles by multiple methods.

(iii) The integral dose LET distributions calculated for Cosmos-2044 show that ~50% of the absorbed dose is from the particles with LET below 10 MeV cm^{-1}, while ~50% of the equivalent dose is from the particles with LET above 400 MeV cm^{-1}. The CR-39 detector, with a LET threshold for particle detection at ~40 MeV cm^{-1}, may detect as little as 20–30% of the absorbed dose and 60–70% of the equivalent dose in a Cosmos-2044 type of orbit.

(iv) The Cosmos-2044 flight is distinguished by a near-polar orbit and by its coincidence with solar maximum. The orbit tends to increase the detected particle fluence, in comparison with the usual lower inclination orbits, due to a decrease in the geomagnetic cutoff threshold. The coincidence with solar maximum, on the other hand, results in a general decrease in fluences of both GCR particles and RB protons. These factors, along with a rather low orbital altitude, explain the variations in radiation exposure as compared with earlier spaceflights. It has also been demonstrated that, despite the predictions of an extremely high solar maximum in Cycle 22, the solar activity can be considered fairly moderate. This is consistent with the experimental data presented here.

REFERENCES

Akatov Yu. A., Dudkin V. E., Kovalev E. E., Benton E. V., Frank A. L., Watts J. W. Jr and Parnell T. A. (1990) Depth distribution of absorbed dose on the external surface of Cosmos-1887 biosatellite. *Nucl. Tracks Radiat. Meas.* **17**, 105–107.

Akopova A. B., Dudkin V. E., Karpov O. N., Melkumyan L. V., Potapov Yu. V. and Rshtuni Sh. B. (1986) Determination of cosmic radiation characteristics aboard Salyut-7 orbital station. *Nucl. Tracks Radiat. Meas.* **12**, 489–491.

Akopova A. B., Dudkin V. E., Karpov O. N., Melkumyan L. V., Potapov Yu. V. and Rshtuni Sh. B. (1988) Determination of cosmic radiation characteristics on board Salyut-7 orbital station. *Kosm. Issled.* **XXVI**, 162–165.

Akopova A. B., Dudkin V. E., Kovalev E. E., Magradze N. V. and Potapov Yu. V. (1987) Linear energy transfer spectra of cosmic radiation aboard Cosmos-1129 artificial satellite. *Radiat. Prot. Dosim.* **18**, 153–156.

Akopova A. B., Magradze N. V., Dudkin V. E., Kovalev E. E., Potapov Yu. V., Benton E. V., Frank A. L., Benton E. R., Parnell T. A. and Watts J. W. Jr (1990a) Linear energy transfer (LET) spectra of cosmic radiation in low Earth orbit. *Nucl. Tracks Radiat. Meas.* **17**, 93–97.

Akopova A. B., Magradze N. V., Moiseenko A. A., Muradyan S. H. and Ovnanyan K. M. (1983) Method of selective development of thick-layer nuclear emulsions. Preprint EFI-671 (61)-83, Yerevan Physical Institute, Yerevan, U.S.S.R.

Akopova A. B., Vikhrov A. I., Dudkin V. E., Magradze N. V., Moiseenko A. A., Muradyan A. H., Ovnanyan K. M. and Potapov Yu. V. (1985) Measuring the linear energy transfer spectra of cosmic radiation aboard the Cosmos-1129 satellite. *Kosm. Issled.* **XXIII**, 479–481.

Akopova A. B., *et al.* (1990b) Determination of radiation environments on board Cosmos-2044 by the nuclear emulsion method. *XVth Conf. Nucl. Track Detectors*, Marburg, Germany, 3–15 September.

Benton E. V. (1983) Dosimetric radiation measurements in space. *Nucl. Tracks Radiat. Meas.* **7**, 1–11.

Benton E. V. (1986) Summary of radiation dosimetry results on U.S. and Soviet manned spacecraft. *Adv. Space Res* **6**(11), 315–328.

Benton E. V., Frank A. L., Benton E. R., Dudkin V. E. and Marenny A. M. (1988) Radiation experiments on Cosmos 1887: K-6-24, K-6-25, K-6-26. University of San Francisco Report USF-TR-74.

Benton E. V. and Henke R. P. (1983) Radiation exposures during space flight and their measurements. *Adv. Space Res.* **3**, 171–185.

Dudkin V. E., Karpov O. N., Potapov Yu. V., Akopova A. B., Magradze N. V., Moiseenko A. A., Benton E. V., Frank A. L. and Watts J. W. Jr (1992) Experimental and calculated LET distributions in the Cosmos 2044 biosatellite orbit. *Nucl. Tracks Radiat. Meas.* **20**, 143–147.

Frank A. L., Benton E. V., Benton E. R., Dudkin V. E. and Marenny A. M. (1990) Radiation experiments on Cosmos 2044: K-7-41, Parts A, B, C, D, E. University of San Francisco Report USF-TR-76.

Heinrich W. (1977) Calculation of LET spectra of heavy cosmic ray nuclei at various absorbed depths. *Radiat. Effects* **34**, 143–148.

Heinrich W. and Baer J. (1984) The radiation situation in space and its modification by geomagnetic field and shieldings. *Adv. Space Res.* **4**, 133–143.

Heinrich W., *et al.* (1989) LET spectra of cosmic-ray nuclei for near-Earth orbits. *Radiat. Res.* **118**, 63–82.

ICRP-26 (1977) *Recommendations of the International Commission on Radiological Protection.* ICRP Publications, Pergamon Press, U.K.

ISSN 0208-1849 (1990) *Aerospace Technologies*, No. 8, August. Mir, Moscow.

Letaw J. R. and Clearwater S. (1986) Radiation shielding requirements on long-duration space mission. SCC Report 86–02, July.

Letaw J. R., Silberberg R. S. and Tsao C. H. (1986) Natural radiation hazards on the manned Mars mission. NASA Report M002, pp. 642–655, June.

Letaw J. R., Silberberg R. S. and Tsao C. H. (1987) Radiation hazards on space missions. *Nature* **330**, 709–710.

Silberberg R. S., Tsao C. H., Adams J. H. Jr and Letaw J. R. (1984) Radiation doses and LET distributions of cosmic rays. *Radiat. Res.* **98**, 209–226.

APPENDIX S

Cosmic Ray Particles with Different LET Values Under Various Thicknesses of Shielding In Low Altitude Orbits: Calculations and Cosmos-2044 Measurements

by

A.M. Marenny, R.A. Nymmik, A.A. Suslov, E.V. Benton, A.L. Frank and E.R. Benton

Nucl. Tracks Radiat. Meas., Vol. 20, No. 1, pp. 157–160, 1992
Int. J. Radiat. Appl. Instrum., Part D
Printed in Great Britain

0735-245X/92 $5.00 + .00
Pergamon Press plc

COSMIC RAY PARTICLES WITH DIFFERENT LET VALUES UNDER VARIOUS THICKNESSES OF SHIELDING IN LOW ALTITUDE ORBITS: CALCULATIONS AND COSMOS-2044 MEASUREMENTS

A. M. MARENNY,* R. A. NYMMIK,† A. A. SUSLOV,† E. V. BENTON,‡ A. L. FRANK‡ and E. R. BENTON‡

*Research Center for Spacecraft Radiation Safety, Moscow 123182, U.S.S.R.; †Institute of Nuclear Physics, Moscow State University, Moscow 119989, U.S.S.R.; ‡University of San Francisco, San Francisco, CA 94117, U.S.A.

(*Received* 24 *June* 1991; *in revised form* 9 *July* 1991)

Abstract—Fluxes of cosmic ray particles with different LET values were measured on board the Cosmos-2044 biosatellite under various thicknesses of shielding by stacks of CR-39 and nitrocellulose plastic nuclear track detectors (mounted outside the satellite). The component composition of the particles detected under shieldings of 0.1–2.5 g cm^{-2} is verified by comparing experimental data with the results of model simulations of the fluxes of galactic cosmic ray particles and of radiation belt protons.

1. INTRODUCTION

THE RADIATION fields in the Earth's vicinity are generated by the particles which are commonly grouped, according to some criteria (mainly their origin, composition and energy) into certain components, namely, galactic and solar cosmic rays (GCR and SCR), radiation belt (RB) particles and anomalous fluxes (AF). To date, numerous experiments have been carried out on board Soviet and U.S. spacecraft, yielding copious data on the fluxes and spectra of protons and heavy ions in the Earth's vicinity (see, for example, Benton and Parnell, 1988; Marenny *et al.*, 1987). Almost all of the data have been obtained using solid-state nuclear track detectors (SSNTD) (Marenny, 1987) which are notable for their essential characteristic of a detection threshold expressed by the smallest LET value at which detection is possible.

In the present work, an attempt is made to analyze the components of SSNTD-detected particle fluxes under various thicknesses of shielding. The experimental data are supplemented with simulations calculated by models of the radiation environment. Only GCR and RB particles are included because other heavy cosmic ray components did not penetrate to greater shielding thicknesses than 0.05 g cm^{-2} during the Cosmos-2044 flight.

2. EXPERIMENT

The Cosmos-2044 mission lasted for 13.8 days from 15 to 29 September 1989. The biosatellite orbit was elliptical, with a perigee and apogee of 216 and 294 km, respectively, and an inclination of 82.3°. Four flat, lidded containers holding a variety of dosimetric equipment were mounted outside the satellite.

The experimental results presented here were obtained by processing three SSNTD stacks, one at IBMP (Moscow) and two at USF (San Francisco). The IBMP stack of 90 × 50 × 16 mm dimensions contained 20 Soviet-made KNC-type nitrocellulose detectors of 800 μm thickness each. The detectors were etched in a 6N NaOH solution for 5 h at 50 °C. The tracks were scanned with a stereo-microscope at 80× magnification. The penetrating (a cylinder or two cones) or single-cone (of at least 100 μm length) tracks were selected by counting, and correspond with the GCR particles of $Z \geqslant 6$ and LET $\geqslant 1600$ (MeV cm^2) g^{-1} (under the given etching conditions).

The USF stacks were of 3 cm diameter and included CR-39 and Cronar polyester layers. The CR-39 SSNTDs were processed in a 6.25 N NaOH solution for 7 days at 50 °C. The bulk etch, B, was measured for each of the detectors. Pairs of detectors were reassembled in their flight orientations and the two adjacent inner surfaces were scanned with an optical microscope. This procedure permitted the particles to be separated into short-range (SR) (matching tracks appear on two inner surfaces only) and long-range (LR) (matching tracks appear on all four surfaces of the detector pairs) GCR particle tracks. The SR particles include the secondary SR particles from target nuclei within the plastic and the stopping primary GCR and trapped particles. All

‡USF portion of the work partially supported by NASA Grant Nos NCC2-521 (NASA–Ames Research Center) and NAG9-235 (NASA–Johnson Space Center).

protons were detected as SR particles because of their short registration ranges in CR-39. The GCR particles include the primary GCRs and the LR $Z \geqslant 2$ secondaries which are mainly the GCR projectile fragments. The $Z \geqslant 2$ stopping GCR particles can also contribute to the SR tracks, but with a low probability.

3. ANALYTICAL PROCEDURE

3.1. *Galactic cosmic rays*

The GCR particle fluxes outside the Earth's magnetosphere were calculated in terms of the model proposed by Suslov and Nymmik (1988) and described in detail by Suslov and Nymmik (1990). In the model, the energy spectra $F_i(E, t)$ of the $1 \leqslant Z \leqslant 28$ GCR particles are inferred from the particle rigidity spectra $\Phi_i(R, t)$:

$$F_i(E, t)\,dE = \Phi_i(R, t)\frac{A_i\beta}{|z|}dR, \qquad (1)$$

where A_i is the atomic number of a nucleus of species i; R_i is particle rigidity; t is time.

The rigidity spectra are defined by the phenomenological model

$$\Phi_i(R, t) = \frac{D_i\beta^{\alpha_i}}{R_i^{\gamma_i}}\left(\frac{R}{R + R_0(t)}\right)^{\Delta_i(t)}, \qquad (2)$$

where D_i, α_i and γ_i are the constants which characterize the spectra of particles of certain species whose values were determined through the available set of experimental data on the GCR particle fluxes during the previous solar cycles.

The data used to calculate the fluxes of all particles can be found in *Standards for Galactic Cosmic Rays* (1991); the constants used in calculating the energy spectra of the basic elements are presented in Table 1. The value of R_0 is defined by the solar activity level and by the delay of the CR particle flux variations relative to Wolf numbers. During the experiment, R_0 proved to be 0.88 GV.

The power-law exponent in (2) is determined by the formula

$$\Delta_i(t) = 5.5\left[1 + a_i\exp\left(\frac{z_i\beta R}{A_i b_i}\right)\right] + 1.0\,\mathrm{sgn}(z_i)\frac{\beta R}{R_0}\exp\left(-\frac{\beta R}{R_0}\right), \qquad (3)$$

Table 1. Values of constants used in calculating energy spectra

Element	Z_i	A_i	D_i	α_i	γ_i
H	1	1	2.0E04	3.0	2.75
He	2	4	3.5E03	3.0	2.75
C	6	12	9.6E01	3.1	2.75
O	8	16	8.4E01	3.0	2.70
Si	14	32	1.2E01	3.0	2.65
Fe	26	56	9.2E00	3.1	2.60

where the coefficients $b_i = 1.2$ and $d_i = 0.034$ describe the form of the spectrum at low energies ($R < 0.55$ GV) and were inferred from our data on the fluence of oxygen nuclei obtained in the Cosmos-2044 experiment (Marenny *et al.*, 1990).

3.2. *Function of nuclei penetrating to low orbits*

The GCR particle energy spectra on the satellite orbit were found by calculating the penetrating function on the basis of previous determinations of the boundaries for proton penetration into the magnetosphere in a Cosmos-800 experiment (Biryukov *et al.*, 1984).

Figure 1 shows the plots of the penetration function, calculated as indicated above and using the conventional techniques based on the International Reference Geomagnetic Field (IRGF) model. Our approach has yielded higher fluences of particles penetrating to low orbits as compared with conventional techniques (Nymmik, 1991).

3.3. *Radiation belt protons*

The RB proton fluxes on the Cosmos-2044 orbit were calculated using the AP-8 model (Sawyer and Vetter, 1976) for solar maximum. The calculations have shown that the orbit-integrated differential energy spectrum of the 1–100 MeV protons can be described as

$$F(E) = 8 \times 10^3 E^{-\gamma}, \qquad (4)$$

where $\gamma = 2.03$ at $E < 8$ MeV and $\gamma = 2.72$ at $E \geqslant 8$ MeV.

3.4. *Particle flux deep in matter*

The species i particle flux under shielding of thickness x is determined by the formula

$$F_{xi}(E'_x) = F_{\infty i}(L_\infty/L_x)_i\exp(-x/\lambda_i), \qquad (5)$$

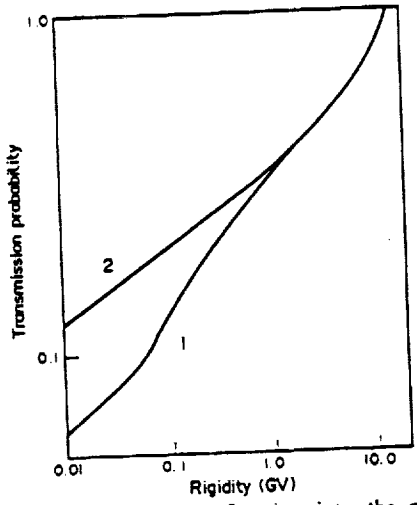

FIG. 1. Particle penetration function into the magnetosphere for the Cosmos-2044 orbit. Curve 1 is the IGRF model calculation result. Curve 2 is the Nymmik (1991) model calculation result.

where $E' = E_o - \int_0 L_i(x)\,dx$; L_o and L_x are the particle LET values above and under the shielding, respectively; λ_i is the species i particle path for nuclear interaction.

The particle energy spectra under the shielding were used to find the particle LET spectra:

$$\Phi_x(>L) = \sum_j \sum_i \int_L^\infty F_{xij}(E)\left[\frac{dL_i(E)}{dE}\right]^{-1} dL, \quad (6)$$

where $L_i(E)$ is the energy dependence of species i particle LET value; j is a given flux component (GCR or RB).

In conformity with the selection criteria for events in the USF stacks, the flux $\Phi_x(>L)$ was broken into four groups (see Fig. 2):

$$\Phi_x(>L) = \sum_{k=1}^{4} \Phi_x^k(>E). \quad (7)$$

If x_1 is the level of the upper surface of the upper detector in a pair of detectors, x_2 is the level of the lower surface of the lower detector in the pair, and x is the level between x_1 and x_2, then the pictorial pattern for breaking into four groups of events is

κ =	1 GCR	2 SR_1	3 SR_2	4 SR_3
X_1	⊗	○	○	⊗
X	⊗	⊗	⊗	⊗
X_2	⊗	Y	⊗	Y

where ⊗ means that $L > L_o$, ○ means that $L < L_o$, and Y means that a particle is not present. The particle fluxes at $L > L_o$ at the level x may be described by

$$\Phi_x^1(\text{GCR}) = \sum_{ij} \Phi_{ij}(L \geqslant L_o, x_1); (E(R) > E(x_2 - x_1)) \quad (8)$$

$$\Phi_x^4(\text{SR}) = \sum_{ij} \Phi_{ij}(L \geqslant L_o, x_1); (E(R) \leqslant E(x_2 - x_1)) \quad (9)$$

$$\Phi_x^2(\text{SR}) = \sum_{ij} \Phi_{ij}(L < L_o, x_1); (E(R) \leqslant E(x_2 - x_1)) \quad (10)$$

$$\Phi_x^3(\text{SR}) = \sum_{ij} \Phi_{ij}(L < L_o, x_1); (E(R) > E(x_2 - x_1)). \quad (11)$$

In the expressions (8)–(11), the GCR group includes the particles with LET values $L > L_o$ over a range great enough to penetrate both detector layers, from x_1 to x_2.

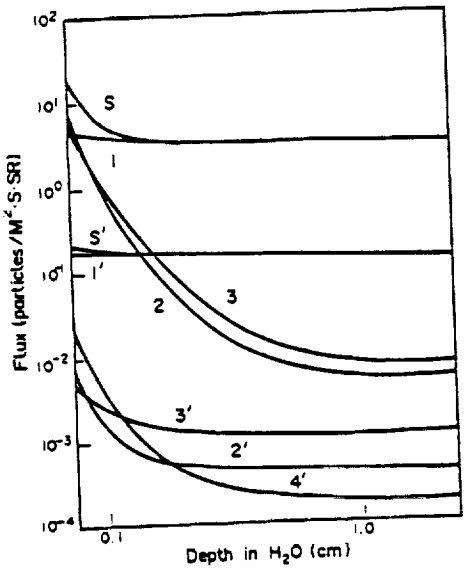

FIG. 2. The calculated flux vs detector depth. Curves 1–4 are particle fluxes calculated by formulas (8)–(11), respectively. S is the total particle flux with $L > L_o$ at depth x. The curves numbered without a prime are for $L > 40$ MeV cm g^{-1}; those with a prime are for $L > 1000$ MeV cm g^{-1}. Curve 4' is not present for the values of LET and plastic thickness used.

4. RESULTS AND DISCUSSION

Figure 2 shows the $\Phi_x^k(L > L_o)$, plots Φ_x^1(GCR), Φ_x^2(SR), Φ_x^3(SR), and Φ_x^4(SR) calculated for the experimental conditions under the shielding thicknesses ranging from 0.075 to 2.5 cm H_2O at two threshold LET values (40 and 100 MeV cm^{-2} g^{-1}). From the calculations it follows that, under the shielding exceeding 0.2 cm H_2O, the fraction of the events in groups 2–4 (SR) is less than 1% of all the detected GCR particles, while the events of group 1 include nearly the total fluence of detected CR particles within the given component. Secondary particles are not included in Fig. 2.

Figure 3 shows the experimental data (plotted points) for (a) the particle fluences detected at seven depths at $x > 0.2$ cm H_2O in the USF stacks (GCR) at $L > 100$ and $L > 500$ MeV cm g^{-1}; and (b) at two depths (0.24 and 1.53 cm) in the IMBP stack at $L > 1600$ MeV cm^2 g^{-1}. The independence of the values of GCR particle fluxes predicted by calculations for $L > L_o$ and at depths of 0.1–2.0 g cm^{-2} is confirmed by the data. The measured particle flux at $L > 100$ MeV cm^2 g^{-1} is somewhat below that predicted by the calculations, but probably within the overall accuracy expected from the comparison.

Figure 3 also presents the data on the events selected by the criteria of SR conditions (9)–(11) and shows the calculated dependence which follows from the RB proton spectrum. This data (Curve 1) has been normalized to the SR particle flux at $x = 0.25$ cm H_2O. To that end, the factor C in (4) had to be set equal to 1000, i.e. eight times less than the value given by the AP-8 model for solar maximum. The reduction in proton flux from the model prediction can be attributed to uncertainties deriving from

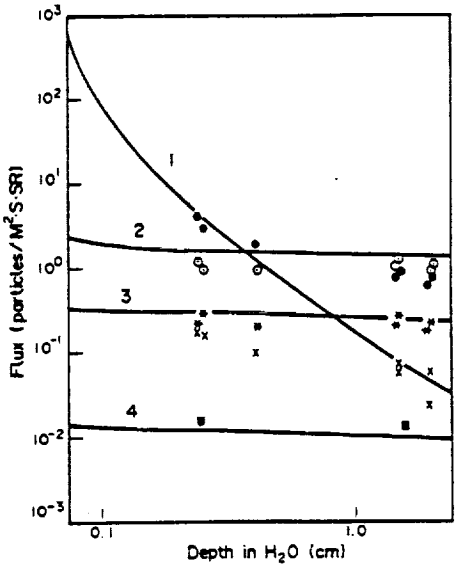

FIG. 3. Particle fluxes with $L > L_o$ vs detector depth. $L > 100$ meV cm g^{-1}: Curve 1 is the SR track density due to RB proton flux calculated by formula (4); Curve 2 is the track density due to GCR particle flux calculated by formulas (1)–(3); the black circles are experimental SR track densities; the circles with dots are experimental GCR track densities. $L > 500$ MeV cm g^{-1}: Curve 3 is the track density due to GCR particle flux calculated by formulas (1)–(3); the star-like crosses are experimental GCR track densities; the skewed crosses are the SR track densities. $L > 2 \times 10^3$ MeV cm g^{-1}: Curve 4 is the GCR track density calculated by formulas (1)–(3); the squares are the experimental GCR track densities.

two major causes. There are substantial proton flux fluctuations observed at low altitudes near the lower RB border, where the density of residual atmosphere increases. The high solar activity level during the observations may have contributed to atmospheric expansion and a decrease in proton flux. Also, the pronounced directionality of the trapped proton fluxes is not taken into account by the AP-8 model or compensated for by the SSNTDs. The assumption of isotropic proton incidence which is made in correcting the experimental measurements for detector solid angle response could therefore have introduced some error into the measured proton fluxes.

From Fig. 3 it follows that the SR particle flux at $x > 0.3$ cm H_2O is considerably greater than would be expected from the primary RB protons. For the particle flux with $L > 100$ MeV cm^2 g^{-1}, the excess equals about 1 particle (m^2 s sr)$^{-1}$. Only a small part of this can be attributed to H recoils produced by neutron collisions. The high energy (> 1 MeV) neutron flux was measured on Cosmos-2044 (Dudkin *et al.*, 1992) in the range of 275–500 n_0/m^{-2} s^{-1} sr^{-1}. The efficiency of CR-39 for high energy neutron flux detection has been reported as $\sim 10^{-4}$ proton tracks (neutron)$^{-1}$ (Durrani and Bull, 1987). This would imply a neutron-induced component of ~ 0.04 particles m^{-2} s^{-1} sr^{-1}. High energy protons also contribute through elastic scattering of target H nuclei and this would seem to be the major source of the excess tracks seen at the larger shielding depths.

The SR particles at $L > 500$ MeV cm^2 g^{-1} cannot be protons, but are mainly secondary particles of higher charges produced by inelastic interactions of RB protons and neutrons with the detector nuclei (H, C, O).

REFERENCES

Benton E. V. and Parnell T. A. (1988) Space radiation dosimetry on US and Soviet manned missions. In *Terrestrial Space Radiation and its Biological Effects*, NATO ASI Series A: Life Sciences, Vol. 154, pp. 729–794. Plenum Press, New York.

Biryukov A. S., Ivanova T. A., Kovrigina L. M., Kuznetsov S. N., Sosonovets R. N., Tverskaya L. V. and Kudela K. (1984) Boundary of solar cosmic ray penetration into the magnetosphere according to data of Intercosmos-17 and Cosmos-900. *Acta Phys. Slovaca* **34**, 153.

Dudkin V. E., Potapov Yu. V., Akapova A. B., Melkumyan L. V., Rshtuni Sh. B., Benton E. V. and Frank A. L. (1992) Neutron fluences and energy spectra in the Cosmos-2044 biosatellite orbit. *Nucl. Tracks Radiat. Meas.* **20**, 139–141.

Durrani S. A. and Bull R. K. (1987) *Solid State Nuclear Track Detection: Principles, Methods and Applications*, International Series in Natural Philosophy, Vol. 111, Pergamon Press, Oxford.

Marenny A. M. (1987) *Dielectric Nuclear Track Detectors in Space Radiation and Radiobiology Experiments*. Energoatomizdat, Moscow (in Russian).

Marenny A. M., Nymmik R. A., Hunyadi I., Csige I., Spurny F., Charvat J. and Guertzen G. R. (1990). Low-energy heavy ions of cosmic rays measured on Cosmos-2044 biosatellite. *Proc. 15th Int. Conf. Particle Tracks Solids*, Marburg, F.R.G., 3–7 September 1990.

Marenny A. M., Nymmik R. A. and Suslov A. A. (1987) Studies of the fluxes of GCR heavy nuclei using the measurements on board low-orbiting satellites in 1974–1984. *Kosmich. Issled.* **25**(4), 577–584.

Nymmik R. A. (1991) Diurnal variations of geomagnetic cutoff boundary relevant to penetration function. *Kosmich Issled.* **29**(3), 491–493.

Sawyer D. M. and Vette J. I. (1976) *AP-8 Trapped Proton Environment for Solar Maximum and Solar Minimum*. National Space Science Data Center, Goddard Space Flight Center, NSSDC/WDC-A-R&S 76-06 (June). Also see NASA TM-X-72605 (1976).

Standards for Galactic Cosmic Rays: Model for Particle Flux Variations (1991) All-Union State Standard 25645.150-190. Standartizdat, Moscow.

Suslov A. A. and Nymmik R. A. (1988) Large-scale galactic cosmic ray modulation: energy (rigidity) spectra of protons and He nuclei outside the modulation region. *Izv. Akad. Nauk U.S.S.R., Phys. Ser.* **58**(12), 2330–2334.

Suslov A. A. and Nymmik R.A. (1990) A semi-empirical model for the large-scale modulation of the galactic cosmic ray energy spectra. *Proc. 21st ICRC* **6**, 33–37.

APPENDIX T

Differential Neutron Energy Spectra Measured on Spacecraft in Low Earth Orbit

by

V.E. Dudkin, Yu.V. Potapov, A.B. Akopova, L.V. Melkumyan
E.V. Benton and A.L. Frank

Nucl. Tracks Radiat. Meas., Vol. 17, No. 2, pp. 87–91, 1990
Int. J. Radiat. Appl. Instrum., Part D
Printed in Great Britain

0735-245X/90 $3.00 + .00
Pergamon Press plc

DIFFERENTIAL NEUTRON ENERGY SPECTRA MEASURED ON SPACECRAFT IN LOW EARTH ORBIT

V. E. DUDKIN,* YU. V. POTAPOV,* A. B. AKOPOVA,† L. V. MELKUMYAN,† E. V. BENTON‡ and A. L. FRANK‡
*Institute of Biological Problems of the Ministry of Public Health of the U.S.S.R., Moscow 123007, U.S.S.R.; †Physical Institute, Yerevan, U.S.S.R. and ‡University of San Francisco,§ California, U.S.A.

(*Received* 30 *May* 1989)

Abstract—Two methods for measuring neutrons in the range from thermal energies to dozens of MeV were used. In the first method, α-particles emitted from the $^6Li(n,\alpha)T$ reaction are detected with the help of plastic nuclear track detectors, yielding results on thermal and resonance neutrons. Also, fission foils are used to detect fast neutrons. In the second method, fast neutrons are recorded by nuclear photographic emulsions (NPE). The results of measurements on board various satellites are presented. The neutron flux density does not appear to correlate clearly with orbital parameters. Up to 50% of neutrons are due to albedo neutrons from the atmosphere while the fluxes inside the satellites are 15–20% higher than those on the outside. Estimates show that the neutron contribution to the total equivalent radiation dose reaches 20–30%.

INTRODUCTION

THE RADIATION environment in low Earth orbits is studied, as a rule, using thermoluminescent dosimeters and plastic nuclear track detectors (Benton *et al.*, 1977; Akatov *et al.*, 1981, 1984). Measurements of this type yield data on absorbed dose, but cannot give information on radiation quality or on dose component composition. Also, a serious underestimation may occur because neutrons are disregarded. A few investigations were previously carried out to study the neutron component. The experimental work of Dudkin *et al.* (1968), Merker *et al.* (1970), Jenkins *et al.* (1971), Bhaff (1976), and calculational efforts of Lingenfelter (1963), Armstrong *et al.* (1973) and Merker (1973) studied the neutron fluxes and energy spectra in near-Earth orbits. These previous efforts were, at best, sporadic, so that characteristics of the neutron component in the Earth's environment have not yet been systematically studied.

The aim of the present work was to experimentally study the energy spectra and fluences of neutrons in low Earth orbit as a function of flight parameters. Two methods were used, namely, the method of fission foils with shielding screens and the NPE method. The measured values of neutron fluxes were then used to estimate the neutron dose equivalent in different energy groups and its contribution to the total equivalent dose.

MEASUREMENT TECHNIQUES

The large cross-sections for capture of thermal and resonance neutrons by ^6Li nuclei makes detection possible through the $^6Li\,(n,\alpha)T$ reaction. The fluences of α-particles emitted from ^6LiF film surfaces are recorded in plastic nuclear track detectors, for example, in a CR-39 detector. Thermal neutrons can be separated from resonance neutrons using Gd foils which shield a detector. In our experiment, 25 μm-thick foils were used. The difference between shielded and non-shielded detectors gives the value of thermal neutron flux, whereas the shielded detectors measure resonance neutron fluxes. The 4.5 mg cm^{-2} ^6LiF thickness defines the detector sensitivity to thermal neutrons which is 4.9×10^{-3} tracks/thermal neutron. The sensitivity to resonance neutrons (0.2 eV–1 MeV), where the dependence of the neutron spectrum was assumed to be $(1/E_n)$, was calculated to be 2.56×10^{-4} tracks/resonance neutron. The fluence of high-energy neutrons ($\geqslant 1.0$ MeV) was roughly estimated using thorium foils. The foils recorded the track densities produced by Th fission fragments. The disintegrations were caused by fast neutrons and by protons. Therefore, to separate neutrons and protons it was necessary to assume the forms of their energy spectra and their relative intensities.

The differential fast-neutron spectrum was determined by the NPE method using the low-sensitivity 400 μm-thick BYa-type emulsion layers whose recording power corresponds to particles whose linear energy transfer (LET) exceeds the LET of protons with kinetic energy of about 50 MeV. The background from particles with lower LET values was reduced by this method.

The fast-neutron spectrum was recovered using the recoil proton energy spectrum generated as a result

§USF work partially supported by NASA–Ames Research Center Grant No. NCC2-521, and NASA–Johnson Space Center Grant No. NAG9-235.

of the elastic (n,p)-scattering of neutrons from the hydrogen in the emulsion.

The recoil proton path in an exposed and developed emulsion was determined by measuring two orthogonal projections of a track whose ends were located within the volume of an NPE layer. Allowance was made for the fact that a fraction of the recoil protons will leave the emulsion layer and that the probability of such an event rises with increasing recoil proton energy and, hence, the energy of a neutron scattered by the recoil proton. The factor f, which depends upon proton energy and NPE layer thickness, was introduced into the recoil-proton path (energy) distribution to correct for the loss of tracks. To correctly construct the proton path (energy) distribution in NPE, the NPE shrinkage factor K_{sh} was also included.

The kinematics of elastic scattering of a non-relativistic neutron of energy, E_n, has been described elsewhere (e.g. Nemetz and Gofman, 1975). The relationship of the differential neutron energy spectrum dN/dE_n to the measured differential recoil proton spectrum dP/dE is found by graphic differentiation and can be presented as

$$\frac{dN}{dE_n} = -\frac{d}{dE}\left(\frac{dP}{dE}\cdot\frac{1}{f(E)}\right)\frac{E_n}{n_0\cdot\sigma(E_n)\cdot V} \qquad (1)$$

where n_0 is the number of hydrogen nuclei in 1 cm^3 of NPE ($n_0 = 3.05\times10^{22}$ cm^{-3} for the BYa-type emulsion; V is the volume of emulsion inspected (in cm^3); σ is the (n,p)-scattering cross-section (in cm^2).

To facilitate the graphic differentiation, we approximated the recoil proton spectrum including the correction factor f for the track extending beyond the NPE layer. The values of f as a function of proton energy, E_p, were calculated by the formulas presented in Perfilov *et al.* (1962), where the expression is of the type

$$y = \sum_i \alpha_i\cdot\exp(-\beta_i E)$$

where α_i and β_i are numerical factors.

The following three circumstances should be noted. Firstly, the measurements appear to be unreliable at neutron energies $E_n < 1.0$ MeV because of a large visual error when recording the short path-length protons (the 1 MeV proton path in NPE is $\sim 14\ \mu$m). Also, the measurements in the above-mentioned energy range are unreliable because the reactions of thermal and intermediate neutrons on nitrogen of the emulsion produce a 0.7 MeV neutron which cannot in practice be distinguished from a recoil proton in the (n,p) scattering. Secondly, the error of the given method increases at neutron energies above 10–15 MeV because the expression (1) has been obtained assuming an isotropic proton scattering in c.m.s. which is only possible at energies below 10–15 MeV. Thirdly, it should be borne in mind that, if the neutron spectrum is of a complicated non-monotone character, a differentiation error will distort the results substantially.

The reproducibility of this method in the neutron energy range above 1.0 MeV was verified by irradiating similar BYa-type emulsion packages with neutrons from sources whose spectra have been well documented in literature. For example, we irradiated the BYa-type emulsion packages with neutrons from ^{252}Cf and from Pu–Be sources, and obtained spectra which differed from published data by not more than $\pm 20\%$.

RESULTS AND DISCUSSION

Flux densities and energy spectra of neutrons in different energy ranges were measured on board several U.S. and Soviet spacecraft. The measurements were made inside the satellites and on their external surfaces. The thickness of matter screening the detector inside a satellite was different in different satellites and varied from ~ 5 to ~ 50 g cm^{-2}. Unfortunately, the exact distribution of the mass of detector-surrounding matter was not known, thereby making the analysis of the measurement results difficult.

Table 1 presents some of the results of measuring neutron flux density on board various spacecraft with ^{6}LiF detectors and fission foils (Benton and Henke, 1983 and Benton, 1986). The table also presents the neutron doses calculated on the basis of these measurements.

The doses were calculated using the flux–dose conversion factors from NCRP Proceedings of 1971, while the quality factors were taken to be 2.0, 6.4, and 10.0 for thermal, resonance and fast neutrons, respectively.

The data on the forms of the neutron and proton spectra used in calculating the doses were taken from Merker (1973) and Hewitt *et al.* (1972), respectively, while the relation between the proton and neutron fluences was taken from Fishman (1974). It should be noted that, whereas the experimental data on proton spectra in similar flights generally can be found, the fast-neutron spectral data were not available. Obviously, this circumstance can give rise to probable errors in determining the doses which are difficult to estimate. Since, as seen from Table 1, the fast neutrons make the major contribution to the neutron dose, the method of using the fission foils needs further refinement.

Table 2 presents the results of measuring the flux density of fast ($E_n \geq 1$ MeV) neutrons on board various satellites of the Cosmos series by the NPE method. In each case, the differential neutron energy spectrum was measured and then used to find the neutron flux density by energy integration. The Table 2 results also show the dose equivalent rates obtained using the differential neutron spectra and the flux density–dose rate conversion factors taken from Vikhrov *et al.* (1978).

Table 1. Radiation characteristics of neutrons in near-Earth orbits (measurements performed with solid-state detectors and fission foils)

	Satellite	Cosmos 936	Cosmos 1129	STS-3	STS-4	STS-5	STS-6
Flight parameters	Launch date	August 1977	September 1979	March 1982	June 1982	November 1982	April 1983
	Flight time (days)	18.5	18.56	8.13	7.04	5.08	5.00
	Inclination (degree)	62.8	62.8	38	28.5	28.5	28.5
	Apogee/perigee or circular orbit (km)	419/224	394/226	280	297	284	293
Thermal neutrons	Flux density (cm^{-2} day^{-1})	$(1.9 \pm 0.4) \times 10^4$	$(2.7 \pm 0.5) \times 10^4$	$(4.1 \pm 1.0) \times 10^3$	$(6.1 \pm 1.1) \times 10^3$	$(6.1 \pm 1.8) \times 10^3$	$(6.0 \pm 1.6) \times 10^3$
	Equivalent dose rate (mrem day^{-1})	0.020 ± 0.004	0.028 ± 0.006	0.004 ± 0.001	0.006 ± 0.001	0.006 ± 0.002	0.006 ± 0.002
Resonance neutrons	Flux density (cm^{-2} day^{-1})	$(6.5 \pm 3.2) \times 10^4$	$(7.5 \pm 3.8) \times 10^4$	$(4.6 \pm 2.2) \times 10^4$	$(4.7 \pm 2.3) \times 10^4$	$(3.0 \pm 1.8) \times 10^4$	$(7.6 \pm 3.8) \times 10^4$
	Equivalent dose rate (mrem day^{-1})	0.32 ± 0.16	0.40 ± 0.20	0.25 ± 0.12	0.23 ± 0.11	0.14 ± 0.08	0.38 ± 0.19
High-energy neutrons	Flux density (cm^{-2} day^{-1})	$(1.1 \pm ?) \times 10^5$	$(1.1 \pm ?) \times 10^5$	$(1.6 \pm ?) \times 10^4$	$(3.4 \pm ?) \times 10^4$	$(3.5 \pm ?) \times 10^4$	$(2.2 \pm ?) \times 10^4$
	Equivalent dose rate (mrem day^{-1})	$6.8 \pm ?$	$6.8 \pm ?$	$0.95 \pm ?$	$2.0 \pm ?$	$2.2 \pm ?$	$1.3 \pm ?$
Neutrons in total	Flux density (cm^{-2} day^{-1})	1.94×10^5	2.1×10^5	6.6×10^4	8.7×10^4	7.1×10^4	1.0×10^5
	Equivalent dose rate (mrem day^{-1})	7.1	7.2	1.2	2.2	2.3	1.7

Table 2. Radiation characteristics of fast neutrons in near-Earth orbits (measurements by the NPE method)

A Cosmos series satellite (number)	Flight parameters: Launching data	Time of flight (days)	Inclination (degrees)	Apogee/perigee (km)	NPE placed	Neutron flux density (cm^{-2} day^{-1})	Equivalent dose rate (mrem day^{-1})
936	3 August 1977	18.5	62.8	419/224	inside	$(1.1 \pm 0.5)\ 10^5$	4.5 ± 2.2
1129	25 September 1979	18.56	62.8	394/226	inside	$(1.1 \pm 0.4)\ 10^5$	4.5 ± 1.4
1129	25 September 1979	18.56	62.8	394/226	outside	$(8.6 \pm 2.6)\ 10^4$	3.5 ± 1.0
1514	14 December 1983	4.92	82.3	288/226	inside	$(7.4 \pm 2.2)\ 10^4$	3.0 ± 0.9
1514	14 December 1983	4.92	82.3	288/226	outside	$(6.2 \pm 1.7)\ 10^4$	2.5 ± 0.7
1571	11 June 1984	15.3	70	420/355	outside	$(6.9 \pm 1.7)\ 10^4$	2.8 ± 0.7
1600	27 September 1984	13.2	70	420/355	outside	$(7.8 \pm 2.6)\ 10^4$	3.1 ± 1.0
1667*	10 July 1985	7.0	82.7	297/222	outside I	$(6.7 \pm 1.7)\ 10^4$	2.7 ± 0.7
1667*	10 July 1985	7.0	82.7	297/222	outside II	$(5.6 \pm 1.7)\ 10^4$	2.2 ± 0.7
1757	11 June 1986	14.0	82.3	252/189	outside	$(5.2 \pm 1.7)\ 10^4$	2.1 ± 0.7
1781	17 September 1986	14.0	70.4	405/217	outside	$(5.2 \pm 1.7)\ 10^4$	2.1 ± 0.7
1887	29 September 1987	12.6	62.8	394/226	inside	$(5.2 \pm 1.7)\ 10^4$	2.1 ± 0.7
1887	29 September 1987	12.6	62.8	394/226	outside	$(4.5 \pm 1.7)\ 10^4$	1.8 ± 0.7

*External assembly I oriented towards the Sun; assembly II oriented towards the Earth.

Shown as an example in Fig. 1 are the neutron energy spectra measured inside and outside the Cosmos 1514 and 1887 satellites. For comparison, Fig. 1 presents also the results of a calculated albedo neutron spectra obtained in Lingenfelter (1963) for solar minimum at different orbital inclinations to the plane of the equator ($i = 40°$ and 90°).

Analyzing the experimental data has shown that most of the fast-neutron energy spectra are of the characteristic 'evaporation' form with a maximum in the 1.5–4.0 MeV neutron energy range. In any case, the form of neutron spectra presented here is realized in all the spectra measured inside the spacecraft. The external neutron spectrum is, as a rule, softer.

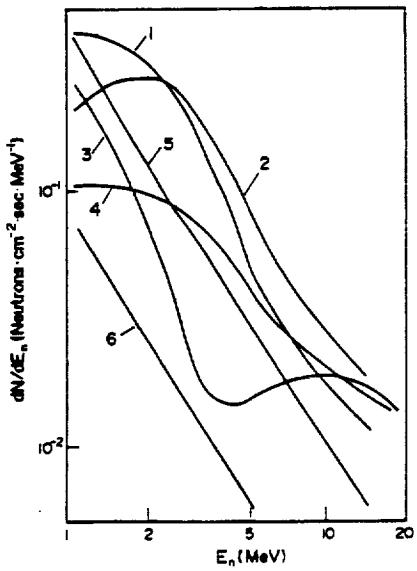

FIG. 1. Differential neutron energy spectra measured in spacecraft in low Earth orbit. Curves 1 and 2 are the Cosmos 1514 data obtained outside (1) and inside (2) the satellite. Curves 3 and 4 are the Cosmos 1887 data obtained outside (3) and inside (4) the satellite. Curves 5 and 6 are the albedo neutron spectra calculated in Lingenfelter (1963) at angle $i = 90°$ (5) and at $i = 40°$ (6) during solar minimum.

According to the present-day concepts, the detected neutrons originate from two sources, namely, the albedo neutrons produced in interactions of galactic cosmic rays with the Earth's atmosphere and the secondary neutrons produced in the spacecraft structure (the local neutrons). The form of the local neutron spectra is similar to the form of the spectra generated in inelastic proton–nuclear interactions. The local neutron spectra are obviously more rigid compared with the spectra of the albedo neutrons which undergo multiple scatterings and attenuation in the atmosphere.

The data of Table 2 show that the neutron fluences inside the spacecraft are 15–20% higher than on the outside, thereby indicating that local neutrons are accumulated in the instruments simultaneously with attenuation of albedo neutrons. This trend is observed in the neutron dose rates measured both inside and outside the satellites.

Comparing the data of Tables 1 and 2 it is seen that the fast neutron flux densities measured by the two different methods are in approximate agreement. A difference in the dose rates shown is probably due to different values of the flux–dose coefficients used.

Analyzing the measurement results has shown that the neutron flux density does not exhibit any unambiguous dependence on altitude, orbital inclination, and phase of the solar cycle. According to Jenkins *et al.* (1971), the flux density of the albedo neutrons with $E_n \geqslant 1$ MeV increases by a factor of ~ 10 as a satellite moves from the equator to the poles and is 0.03 n cm^{-2} s^{-1} at the equator and 0.2–0.5 n cm^{-2} s^{-1} at the poles. This is confirmed by our experiments (see Table 1) where the fast-neutron dose decreases by a factor of ~ 3 as the orbit inclination angle varies from 60 to 30°.

Analyzing the measurement results has also shown that the albedo neutron contribution to the total neutron flux may reach $\sim 50\%$, which is in good agreement with the estimate obtained by Yushkov

(1988) where the albedo neutron contribution to the total counting rate of the neutron detector flown on Salyut-6 was found to be 2/3.

It is of interest to estimate the neutron contribution to the total dose in low Earth orbit. This is possible since thermoluminescent detectors were used in all of the flight experiments. The rates of absorbed neutron doses are approximately a few per cent of the total absorbed dose, whereas the neutron contribution to the dose equivalent reaches 20–30% (because of a high quality factor).

In order to understand better the nature of the cosmic ray neutron component in low Earth orbit and in order to make the absolute dose measurements more accurate, it is necessary to carry out further experiments on board oriented spacecraft in different orbits and during varying phases of the solar cycle. The distribution of shielding mass about the detectors must also be taken into account. Lastly, further refinement of the measurement techniques is still necessary.

REFERENCES

Akatov Yu. A., Arkhangelsky V. V., Aleksandrov A. P., Fehér I., Deme S., Szabó B., Vagvölgyi J., Szabó P. P., Csőke A., Ránky M. and Farkas B. (1984) Thermoluminescent dose measurements on board Salyut-type orbital stations. *Adv. Space Res.* 4(10), 77.

Akatov Yu. A., Vikhrov A. I., Dudkin V. E., Marenny A. M., Nefedov N. A., Potapov Yu. V., Spurný F., Turek K. and Hashegan D. (1981) Study of cosmic radiation attenuation on board Cosmos-1129. *Third All-Union Conf. Prot. Against Ionizing Radiat. Nucl. Tech. Installation.* Tbilisi.

Armstrong T. W., Chandler K. C. and Barish J. (1973) Calculations on neutron flux spectra induced in the Earth's atmosphere by galactic cosmic rays. *J. geophys. Res.* 78, 2715.

Benton E. V. (1986) Summary of radiation dosimetry results on U.S. and Soviet manned spacecraft. XXVI COSPAR Meeting, Toulouse, 1986. COSPAR Paper No. VII. p. 7.

Benton E. V. and Henke R. P. (1985) Radiation exposures during space flight and their measurements. *Adv. Space Res.* 3(8), 171.

Benton E. V., Henke R. P. and Peterson D. D. (1977) Plastic nuclear track detector measurements of high-LET particle radiation on Apollo, Skylab and ASTP space missions. *Nucl. Track Detection* 1, 27.

Bhatt V. L. (1976). Neutron high-energy spectra at 5 mbar near the geomagnetic equator. *J. geophys. Res.* 81, 4603.

Dudkin V. E., Kovalev E. E., Novikova N. R., Ostroumov V. I., Potapov Yu. V., Skvorsov S. S. and Smirenny L. N. (1968) Measuring the proton and neutron spectra and fluxes on board satellites of the Cosmos series. *Kosm. Issled.* VI, 887.

Fishman G. J. (1974) Neutron and proton activation measurements from Skylab. AIAA Paper No. 74-1227. *AIAA/AGD Conf. scient. Experiments Skylab.* October 1974, Huntsville, Alabama.

Hewitt J. E., Schaefer H. J. and Sullivan J. J. (1972) Radiation exposure during the biosatellite III primate flight. *Hlth Phys.* 23, 461.

Jenkins R. W., Ifedili S. O., Lockwood J. A. and Razdan H. (1971) The energy dependence of cosmic-ray neutron leakage flux in the range of 0.01–10 MeV. *J. geophys. Res.* 76, 7470.

Lingenfelter R. E. (1963) Cosmic ray neutron leakage flux. *J. geophys. Res.* 68, 5633.

Merker M. B. (1973) The contribution of galactic cosmic rays to the atmospheric neutron maximum dose equivalent as a function of neutron energy and altitude. *Hlth Phys.* 25, 524.

Merker M. B., Light E. S., Mendell R. B. and Korff S. A. (1970) The flux of fast neutrons in the atmosphere. *Acta physiol. hung.* 29 (Suppl. 2), 739.

Nemetz O. F. and Gofman Yu. V. (1975) *Handbook on Nuclear Physics*, p. 386. Naukova Dumka, Kiev.

Perfilov N. A., Loszkin O. V. and Ostroumov V. I. (1962) *Nuclear Reactions Induced by High-energy Particles.* Acad. Sci. U.S.S.R. Editorial Board, Moscow.

Vikhrov A. I., Dudkin V. E., Kovalev E. E., Komochkov M. M., Lebedev V. N., Litvinova E. G., Mitrikas V. G., Potapov Yu. V., Potemkin E. L., Sichov B. S. and Frolov V. V. (1978) *Atlas of Dose Characteristics of External Ionizing Radiation* (Edited by Kovalev E. E.). Atomizdat, Moscow.

Yushkov B. Yu. (1988) Measuring neutron fluxes on board Salyut-6 orbital station. *Kosm. Issled.* 5, 793.

APPENDIX U

Radiobiological Experiments with Plant Seeds Aboard the Biosatellite Kosmos 1887

by

I.D. Anikeeva, Yu.V. Akatov, E.N. Vaulina, L.N. Kostina
A.M. Marenny, A.I. Portman, S.V. Rusin and E.V. Benton

Nucl. Tracks Radiat. Meas., Vol. 17, No. 2, pp. 167–171, 1990
Int. J. Radiat. Appl. Instrum., Part D
Printed in Great Britain

0735-245X/90 $3.00 + .00
Pergamon Press plc

RADIOBIOLOGICAL EXPERIMENTS WITH PLANT SEEDS ABOARD THE BIOSATELLITE KOSMOS 1887

I. D. ANTIKEEVA,* YU. A. AKATOV,† E. N. VAULINA,* L. N. KOSTINA,* A. M. MARENNY,† A. I. PORTMAN,† S. V. RUSIN‡ and E. V. BENTON§

*N.I. Vavilov Institute of General Genetics of the U.S.S.R., Academy of Sciences, Gubkin str.3, 117809, B-333, Moscow, U.S.S.R.; †The Institute of Medico-Biological Problems of the U.S.S.R., Ministry of Public Health, U.S.S.R.; ‡Moscow Institute of Physical Engineering, U.S.S.R. and §Physics Department, University of San Francisco, San Francisco, CA 94117, U.S.A.‖

(*Received* 30 *October* 1989)

Abstract—The effects of spaceflight factors on the seeds of *Arabidopsis thaliana* and *Crepis capillaris* were studied provided with various protective measures: the seeds were located inside the satellite and in open space, protected with aluminium foil and also exposed without the foil cover. When the seeds were in open space without any protection, their viability was found to be suppressed; the survival rate and fertility of plants grown from these seeds were also diminished. An increase in the frequency of chromosome aberrations (CA) and in the number of multiple injuries was registered in this case. Experiments with the aluminium foil shielding showed a decrease in the suppression of the seeds' viability, but mutational changes were found to be even more increased, while the survival rate and fertility of the plants decreased. An increase in the thickness of shielding resulted in a decrease in the effects up to the level of the control, except for the effects connected with CA and fertility of the plants. Analysis of the results shows that these impairments can be ascribed to the action of single heavy charged particles (HCP). The seeds can be thus regarded as an integral biological 'dosimeter' which allows estimation of the total effects of radiation, ecological and biological factors.

INTRODUCTION

EXPERIMENTS conducted aboard spacecraft have shown that biological objects can be severely damaged by HCP. There is strong evidence for the existence of direct correlations between the hitting of the object with the particles and the injuries observed (Grigoriev and Nevzgodina, 1978; Grigoriev, 1982; Nevzgodina *et al.*, 1984; Maximova, 1985). The experiments made in open space make it possible to analyze the total effect of ionizing and UV-radiations of the solar spectrum light and other spaceflight factors. At the present time, in connection with the problem of ozone holes, the studies of those electromagnetic radiations and cosmic rays which fail to reach the surface of the Earth being absorbed by the atmosphere have become increasingly important. Those experiments are to be conducted at altitudes exceeding 100–150 km. They require the employment of spacecraft to expose the studied organisms both to the conditions of spaceflight and to the factors of open space.

EXPERIMENTAL

The experiments conducted aboard the biosatellite Kosmos 1887 constitute an integral part of the programme of radiobiological research implemented by means of biosatellites of the Kosmos series. The task of the experiment was to study the effects of spaceflight on plant seeds provided with various types of protection. The experiments were carried out both inside the satellite and in open space. In the latter case, the seeds were fixed to a removable cover of a container located on the outer surface of the satellite. A monolayer of seeds fixed with PVA to the cellulose-nitrate plates was exposed to open space either without any protection or covered with aluminium foil of thickness 15 μm (1.76 mg cm^{-2}). To estimate the absorbed doses, thermoluminescent dosimeters were used. Throughout the flight a dose absorbed by the sample stored inside the spacecraft amounted to 6.7×10^{-3} Gy. A dose absorbed by the seeds exposed to open space and protected with foil ranged from 15 to 36 Gy, depending on the location of the seeds on the cover of the container. After landing, the seeds were exposed to low temperatures from -15 to -18°C. The air-dried seeds of the model plants of *Arabidopsis thaliana* and *Crepis capillaris* were employed in the experiments. Numerous tests developed for each of these plants have proved to be complementary; they allow evaluation of both the direct effect of the factors under study and future results by means of a number of indices which

‖USF work partially supported by NASA–Ames Research Center Grant No. NCC2-521, and NASA–Johnson Space Center Grant No. NAG9-235.

characterize the viability, fertility and mutability of plants. The viability was estimated by the germination energy of the *Crepis* seeds, as well as by the germination ability of both plants and also by the survival rate of the *Arabidopsis* plants. The mutability was estimated by the frequency of aberrant cells and by the multiple rearrangements which occur at first division metaphases in the root meristem cells of *Crepis*, as well as by the death of the seedlings at a cotyledon phase caused by rough chromosome aberrations. The mutability was also estimated by the frequency of recessive mutations of *Arabidopsis* (Ivanov, 1974; Anikeeva *et al.*, 1983). Taking into account the fact that differences in the doses absorbed by the seeds located at various sites of the cover outside the satellite do not exceed those detected by various dosimeters in the case of one and the same distribution, and also that the results obtained in different variants of the experiment do not differ significantly, the authors found it possible to summarize the results irrespectively of the distribution of the seeds over the cover of the container. The indices obtained in the laboratory and transport controls were also summarized, as they failed to show any statistically significant differences.

RESULTS AND DISCUSSION

The results of the action of spaceflight factors on the air-dried plant seeds are shown in Table 1. In the case of unprotected seeds located outside the satellite all the indices under study were found to deteriorate, as compared to the ground-based control, except for the frequency of recessive lethals in *Arabidopsis* (this index was found to be diminished, although these changes were statistically insignificant). This can be attributed to the selection of mutants which results from a decrease in the viability and fertility of the plants grown from the exposed seeds. Noteworthy is the fact that the germination energy of *Crepis* was found to be considerably decreased (by a factor of two) and the germination ability of both plants was found to be slightly lowered (by 10%); a 39-fold decrease was also found in the frequency of CA in *Crepis*, as compared to the ground-based control. Besides this, a great number of cells with multiple rearrangements were seen, which was not the case with the ground-based control. A thin layer of protective foil was shown to decrease the effect of open space on the viability of the seeds. The energy and ability of germination were not different from those of the control. As to all the other indices under study (except for the survival rate of *Arabidopsis*) the authors observed even greater influence of spaceflight factors, as compared to the variant without any protection. Further increase in shielding (e.g. locating the seeds inside the satellite) resulted in elimination or significant depression of these effects. As compared to the ground-based control, a statistically significant increase in the frequencies of CA and multiple rearrangements was registered in *Crepis* only. The number of unfertilized seedbuds in *Arabidopsis* was found to be increased, too.

Table 1. Effects of space on seeds of *Crepis capillaris* and *Arabidopsis thaliana* (%)

Biological characteristics of tests	Investigation tests		Control	Flight		
				Inside the satellite	Outside the satellite	
					Shielding	Without shielding
Viability	Germination energy of *C. capillaris*		88.98 ±	90.26 ± 1.18	91.11 ± 1.24	48.72 ± 2.30
	Germination ability of	*C. capillaris*	97.04 ±	97.29 ± 0.65	97.54 ± 0.677	89.61 ± 1.41
		A. thaliana	98.36 ±	97.63 ± 0.68	95.16 ± 1.03	89.44 ± 1.35
	Survival rate of *A. thaliana*		73.68 ±	69.31 ± 2.05	62.50 ± 2.33	61.04 ± 2.14
Mutability	Frequency of aberrant cells in *C. capillaris*		0.50 ±	1.52 ± 0.27	24.14 ± 0.44	19.55 ± 0.61
	Frequency of cells with multiple aberrations in *C. capillaris*		0.00	0.05 ± 0.05	3.61 ± 0.33	3.03 ± 0.28
	Death of the seedlings *A. thaliana*		17.31 ±	20.20 ± 1.84	27.36 ± 2.19	24.68 ± 1.99
	Frequency of embrional lethals in *A. thaliana*		3.00 ±	2.91 ± 0.14	4.70 ± 0.20	2.77 ± 0.11
Fertility	Unfertilized seedbuds of *A. thaliana*		39.85 ±	46.76 ± 0.32	50.43 ± 0.35	43.95 ± 0.32

A tendency to a decrease in the survival rate was shown in *Arabidopsis*. Which of the factors are responsible for the phenomena observed? In the variant without any protection the seeds were exposed to a complex of factors of open space: UV- and ionizing radiations, visual light, infrared light, vacuum, and microgravitation. As was shown in our experiments (Anikeeva *et al.*, 1983; Vaulina *et al.*, 1984) the last-mentioned factor fails to have any significant effect on the plant seeds if the duration of their exposure to microgravitation is short. Vacuum and low temperatures also failed to show any effect on the viability, mutability, and other indices. However, high temperatures may have an adverse effect on the seeds, and vacuum may enhance the effects of UV-light and ionizing radiation (Imshenetsky, 1975; Vaulina *et al.*, 1974). Unfortunately, it was not feasible to measure the radiation doses absorbed by unprotected seeds exposed to open space, since the luminescent dosimeters used for this purpose would have been ruined under those conditions. A thin foil cover protects the seeds from the UV-light and delays their drying; it creates possible additional irradiation of the seeds by means of δ-electrons formed when both high- and low-energy cosmic rays are passing through the foil (the so-called anomalous component with the maximum of the energy spectrum at 12–16 MeV nucleon^{-1}). Deceleration of the ions of the anomalous component (mainly oxygen) which occurs when they are penetrating the foil and the seed skin results in maximum losses in energy directly in the area of the seed location. In this variant the ionizing radiation dose registered was shown to be the highest. An increase in the thickness of the protective cover (the wall of the satellite) leads to a decrease in the radiation dose absorbed due to the reduction of the general flow of particles and hardening of the spectrum. In this case the radiation dose registered is rather low. And to what do the biological results testify? The whole complex of open space factors has an adverse effect on all the inherent indices. On the one hand, protection against the UV-light eliminates the effects connected with the suppression of the seeds' viability. On the other hand, an increase in the mutability and a decrease in the survival rate and fertility of plants in the experiments conducted in open space (with the foil and without it) are related to the effects of HCP. The impact of HCP is evidenced by the large number of cells with multiple chromosomal injuries. A rise in the temperature and exposure to vacuum could modify the effects observed in these variants. In the variant with the foil these effects were found to be more pronounced. Unfortunately, it was impossible to use dosimeters in open space for measuring the doses absorbed by unprotected seeds; however the biological results obtained make it possible to believe that the radiation doses in this case could be lower, as compared to the variant with the foil protection. The dose registered in the variant inside the satellite was far too small to be responsible for the effects observed. The presence of cells with multiple chromosomal injuries suggests that the impairments revealed are connected with the action of single heavy charged particles. However they are not very numerous in this case, as compared to the variants when the seeds were located inside the satellite. This is evidenced by the reading of the detectors and also by a decrease of one order of magnitude registered in the total frequency of CA, as well as by a very significant (60–70-fold) decrease in the frequencies of multiple aberrations which was lacking in the control. Multiple aberrations appear in the cell when it acquires a large amount of energy. Thus, for instance, when the cells are irradiated with gamma-rays these aberrations appear only when the doses are as high as 30 Gy. It is worth noting that the plant seeds not only exhibited all the changes in all the variants of the experiment, but also responded differently to the action of open space factors (i.e. to UV- and ionizing radiations). None of the existing dosimeters can cover such a broad spectrum of radiations either totally or quantitatively. As to the radiation-dependent effects revealed, those plants can be regarded as an integral biological dosimeter, the application of which necessitates a more detailed study to be carried out, so as to establish the dependence of the 'dosimeter readings' on the effects of the radiation and also on the ecological and biological (age, etc.) characters. The changes found are quite obvious. However, not all of these changes are statistically significant, as compared to the control and to one another. We believe that this can be attributed to the fact that at small absorbed doses the sampling of the studied materials is insufficient. Based on the analysis of the adequacy of the sampling volume, it has been shown that for obtaining statistically significant information on the radiation-induced changes in the cells by means of cytogenetic analysis it is necessary to have such a quantity of the irradiated and then analyzed biological objects which would be no less than a certain minimum volume of sampling, J_{min}. When solving the problem of prognosticating the minimum volume of sampling, J_{min}, by a number of biological objects required for the irradiation and analysis, we took into account the expected radiation dose absorbed, the fluctuations of the energy absorbed in the responsive volumes of cells, as well as the biological specificity and stochastics of the objects under study. Thus, it has been established that

$$J_{min} = \frac{t^2(P)}{\delta^2 \lambda(N,D)} \times \left[\frac{1}{N} \frac{\bar{\sigma}_n^2(D)}{\bar{n}^2(D)} + \left(1 + \frac{1}{N} \frac{\sigma_\varphi^2(D)}{\bar{\varphi}^2(D)} \right) \frac{\sigma_k^2}{\bar{k}^2} \right], \quad (1)$$

where $\bar{n}(D)$ is the expected mean number of aberrations in the cell at a dose of D which can be described by the following equation:

$$\bar{n}(D) = \bar{k}\bar{\varphi}(D). \quad (2)$$

Table 2. The volume of sampling N^* and J^*_{min} at low doses for seeds of *Crepis capillaris* (L.) Wallr. with the relative standard variance $\sigma_k/\bar{k} = 0.2$, irradiated with protons of kinetic energy 9.2 GeV

D, Gy	J^*_{min} ($N = 25$)	N^*
0.5	17.8 ± 2.6	1098 ± 164
1.0	8.9 ± 1.3	549 ± 82
2.5	3.6 ± 0.5	219 ± 33
5.0	1.8 ± 0.3	110 ± 16

The other values in formula (1) are: $t(P)$ is the solution to the equation $\Phi(t) = P$, where $\Phi(t)$ is the integral of probabilities, P is the level of confidence, δ is the pre-set maximum relative error of the center of expected empirical distribution of aberrations in the cell after its irradiation, N is the number of analyzed cells in each biological object; $\bar{k}$ and δ_k^2 are the mean value and the dispersion of the coefficient of transition from the energy absorption to the effect, $\delta_n^2(D)$ is the expected dispersion of the number of aberrations in the cell at a dose of D; $\delta_\varphi^2(D)$ is the expected dispersion of the function φ at this dose; $\lambda(N,D)$ is the probability of the fact that after the radiation exposure to a dose of D the cell of the biological object analyzed will contain not less than N of the observed (metaphase or anaphase) cell. The given probability can be found experimentally. When the doses are low this probability does not actually depend on the quality and level of the doses absorbed. The relative standard variance $\delta_k/\bar{k}$ is determined at a high dose, D, and for a large number of cells, N, when the stochastics of the absorption energy can be neglected in comparison with the biological stochastics of the objects under study. To estimate the relative standard variance $\delta_k/\bar{k}$ the empirical square variance $S_{\bar{n}(J,N)}(D)$ is used. The latter can be found from the formula given in Cocren (1976) for the independent experiment with model radiation. For this purpose the biological objects are chosen from the same assemblage as for the cytogenetic studies with planned conditions of irradiation. Practical application of formula (1) was considered with respect to the air-dried seeds of *Crepis capillaris* irradiated with protons with kinetic energy of 9.2 GeV at the stage G_0 of the cell cycle. The obtained data are given in Table 2. In spite of the particular character of these data, their analysis makes it possible to suggest that for obtaining statistically significant information on cytogenetic effects in the cells exposed to small doses of irradiation (e.g. inside the satellite Kosmos 1887) a vast volume of sampling is required as to the number of biological objects (seeds). The minimum value of this volume, J_{min}, depends considerably on the level of confidence P, the probability $\lambda(N,D)$, and the value δ. Therefore, it would be preferable to calculate the volume J^*_{min}. A correlation between the volumes of samplings J_{min} and J^*_{min} is as follows:

$$J^*_{min} = J_{min}\lambda(N,D)\delta^2/t^2(P). \quad (3)$$

Correspondingly, the volume of sampling N^* is described by the equation:

$$N^* = \frac{\sigma_\varphi^2(D)}{\bar{\varphi}^2(D)}\left[0.1\frac{\bar{\sigma}_n^2(D)}{\sigma_k^2\sigma_\varphi^2(D)} - 1\right]. \quad (4)$$

For $N \leqslant N^*$ the biological stochastics of the objects under study can be neglected. For $N^* < 1$ they should be taken into account for any N. As seen in Table 2, when the doses of irradiation and the biological stochastics are low, the ratios of the volumes of samplings J^*_{min} are inversely proportional to the dose ratios. A similar picture is observed for the objects of the samplings N^* under the indicated conditions of irradiation. Expression (1) allows more detailed planning of cytogenetic studies carried out in the radiation fields of HCP and facilitates the appropriate choice of the biological object itself. Along with this it shows that before setting the general experiment it is necessary to carry out some auxiliary calculations and experimental studies.

SUMMARY

Thus, as compared to the ground-based control, in the case with the seeds located outside the satellite without any shielding, the plants' viability, survival rate, and fertility were found to be considerably decreased. In this case there is also a significant increase in the cytogenic effect. The variant of the experiment when the seeds were located outside the satellite and covered with foil was characterized by even greater effects, as compared to the variant with unprotected seeds located outside the satellite. Comparison of these two variants (with and without the foil protection) shows even greater decrease in the viability and fertility of the plants, as well as an increase in their mutability revealed by the CA test and also by the test of embryonic lethals. The viability of the seeds in this variant corresponds to that in the control. For the seeds located inside the satellite the researchers observed a three-fold increase in the mutability, as compared to the control; this was determined by the test of CA and by the decrease in the fertility of the plants grown from exposed seeds.

REFERENCES

Anikeeva I. D., Kostina L. N. and Vaulina E. N. (1983) Experiments with air-dried seeds of *Arabidopsis thaliana* (L.) Heynh. and *Crepis capillaris* (L.) Wallr. *Adv. Space Res.* 3(8), 129–133.

Cocren W. (1976) *Metodi Vyborochnogo Issledovaniya*. Statistika, Moscow.

Grigoriev Yu. G. (1982) *Kosmicheckaya Radiobiologiya*, p. 176. Energizdat, Moscow.

Grigoriev Yu. G. and Nevzgodina L. V. (1978) *Uspekhi Kosmicheskoi Biologii*, pp. 52–57. Puschino.

Imshenetsky A. A. (1975) *Osnovy Kosmicheskoi Biologii i Meditsini*, pp. 103–107. Nauka, Moscow.

Ivanov V. I. (1974) *Problemy Kosmicheskoi Biologii*, p. 191. Nauka, Moscow.

Maximova E. H. (1985) Vliyaniye tyazheljkh zaryazhennykh chastits kosmicheskogo galakticheskogo izlucheniya na semena. *Kosm. biol. aviakosm. Med.* 3, 31–37.

Nevzgodina L. V., Maximova E. H., Miller A. T. and Marenny A. M. (1984) *Voprosy Biologicheskogo Deistviya i Dozimetrii Tyazhelykh Zaryazhennykh Chastits : Adronov Vysokikh Energii*. pp. 31–37. Puschino.

Vaulina E. N., Anikeeva I. D. and Kostina L. N. (1984) Radiosensibility of higher plant seeds after space flight. *Adv. Space Res.* 4, 103–107.

Vaulina E. N., Ioia E. L. and Kostina L. N. (1974) Vliyaniye khraneniya v vakuume i argone na radiatsionnii effekt semyan C. capillaris. *Inf. byull. Radiobiol.* 16, 55–57.

226

APPENDIX V

RADIATION EXPERIMENTS ON COSMOS 2044: K-7-41, PARTS A, B, C, D, E

A. L. Frank, E. V. Benton, E. R. Benton
Physics Research Laboratory
University of San Francisco
San Francisco, California 94117, USA

V. E. Dudkin, A. M. Marenny
Institute of Biomedical Problems
76a Khoroshevskoye shosse
Moscow 123007, USSR

FINAL REPORT
USF-TR-76
4 September 1990

Work partially supported by NASA Grants Nos. NCC2-521 (NASA-Ames Research Center) and NAG9-235 (Johnson Space Center, Houston).

TABLE OF CONTENTS

RADIATION EXPERIMENTS ON COSMOS 2044: K-7-41 PARTS A, B, C, D, E

Abstract

The Cosmos 2044 biosatellite mission offered the opportunity for radiation measurements under conditions which are seldom available (an inclination of 82.3° and altitude of 294 × 216 km). Measurements were made on the outside of the spacecraft under near-zero shielding conditions. Also, this mission was the first in which active temperature recorders (the ATR-4) were flown to record the temperature profiles of detector stacks. Measurements made on this mission provide a comparison and test for modeling of depth doses and LET spectra for orbital parameters previously unavailable. Tissue absorbed doses from 3480 rad (252 rad/d) down to 0.115 rad (8.33 mrad/d) were measured at different depths (0.0146 and 3.20 g/cm^2, respectively) with averaged TLD readings. The LET spectra yielded maximum and minimum values of integral flux of 27.3×10^{-4} and 3.05×10^{-4} cm^{-2}s^{-1}sr^{-1}, of dose rate of 7.01 and 1.20 mrad/d, and of dose equivalent rate of 53.8 and 11.6 mrem/d, for LET$_\infty$·$H_2O \geq 4$ keV/μm. Neutron measurements yielded 0.018 mrem/d in the thermal region, 0.25 mrem/d in the resonance region and 3.3 mrem/d in the high energy region. The TLD depth dose and LET spectra have been compared with calculations from the modeling codes. The agreement is good but some further refinements are in order. In comparing measurements on Cosmos 2044 with those from previous Cosmos missions (orbital inclinations of 62.8°) there is a greater spread (maximum to minimum) in depth doses and an increased contribution from GCRs, and higher LET particles, in the heavy particle fluxes.

INTRODUCTION

The Cosmos 2044 mission was the latest of five Soviet biosatellite missions in which the University of San Francisco has participated. The previous missions were Cosmos Nos. 782, 936, 1129 and 1887 /Peterson et al., 1978; Benton et al., 1978a, 1978b, 1981, 1988; Kovalev et al., 1981/. Previous work which applies to radiation measurements in space also covers a wide range of U.S. space flights, including the Gemini, Apollo, Skylab, Apollo-Soyuz and Space Shuttle missions /Benton et al., 1977a, 1977b; Benton and Henke, 1983; Benton, 1984; Benton et al, 1985; Benton, 1986; Benton and Parnell, 1987/.

The Cosmos biosatellites have been host to a wide variety of space biology and radiation experiments performed by international research groups. Radiation dosimetry and spectrometry experiments are typically included for the purpose of providing radiation measurements specific to the mission and to implement long-range goals of mapping radiation intensities in near-earth orbit and of providing measured comparisons for the radiation modeling codes. The Cosmos missions also offer the opportunity to intercompare measurements with other research groups and in this way compare measurements of certain quantities (i.e. dose, LET) using different techniques.

The Cosmos 2044 biosatellite mission took place between September 15 and 29, 1989, for a duration of 13.8 days. The orbit was elliptical, with minimum and maximum altitudes of 216 km and 294 km, respectively, and an inclination of 82.3°. The selection of international experiments on the flight included K-7-41 from the University of San Francisco. This experiment was composed of five parts (A through E) for the purpose of measuring (A) depth dose distribution in thermoluminescent detector (TLD) stacks under very low shielding, (B) LET spectra of HZE particles under low shielding, with stacks composed of plastic nuclear track detectors (PNTD) and emulsions, (C) high energy neutron and proton fluxes with ^{59}Co activation foils, (D) high energy neutron fluxes with ^{232}Th fission foils and (E) thermal and resonance neutron fluxes with ^{6}LiF foils. The measurements will be used to determine radiation levels for the special orbital parameters of this mission and will be compared with calculations from radiation modelling codes.

EXPERIMENTS

The five parts of the experiment K-7-41 are discussed individually below.

Part A

The objective of this experiment was to measure the depth dose under very thin shielding on the outside of the spacecraft and to determine what fraction of the dose was due to low energy electrons versus heavy charged particles. This required that the shielding of the outermost detectors be no more than a few mg/cm^2 and that the detectors themselves also be very thin (because of the short ranges of the particles). The maximum depth in the TLD stacks was 3.2 g/cm^2. Although computer codes exist for calculating doses encountered in LEO both from protons and electrons, there have been only a few instances where a direct comparison (under very thin shielding) has been possible between experiment and theoretical prediction. The orbit of Cosmos 2044 will allow the codes to be compared for parameters quite different from any for previous flights.

The TLD stacks were placed in cylindrical holders (Fig. 1) which were then arrayed in plates attached to the outside of the spacecraft. Three TLD stacks were placed in each of four mounting plates (B9-1, -2, -3, -4) for a total of twelve flight stacks. The TLDs and all other detectors mounted on the outside of the spacecraft were held in "clam-shell" style containers which were closed before re-entry to prevent heating of the detectors in the atmosphere. Some detectors and two containers are shown in Fig. 2.

Each stack was composed of both thin (0.02395 g/cm^2 thickness) and thick (0.2322 g/cm^2 thickness) TLD-700 extruded chips. Thin TLDs were used to a depth of 0.5175 g/cm^2 and thick TLDs at greater depths. A double window of 7.5 μm thick Kapton polyimide films, both aluminized to an optical density of 3, held the TLDs in place and shielded them from sun and space. In the depth-dose results, the mass density of the Kapton (0.00213 g/cm^2) has been converted to an equivalent mass density of ^{7}LiF (0.00266 g/cm^2) on the basis of low energy proton ranges.

Part B

The objective here was to measure the low energy, heavy particle (excluding electrons) LET spectra under very low shielding (outside the spacecraft)

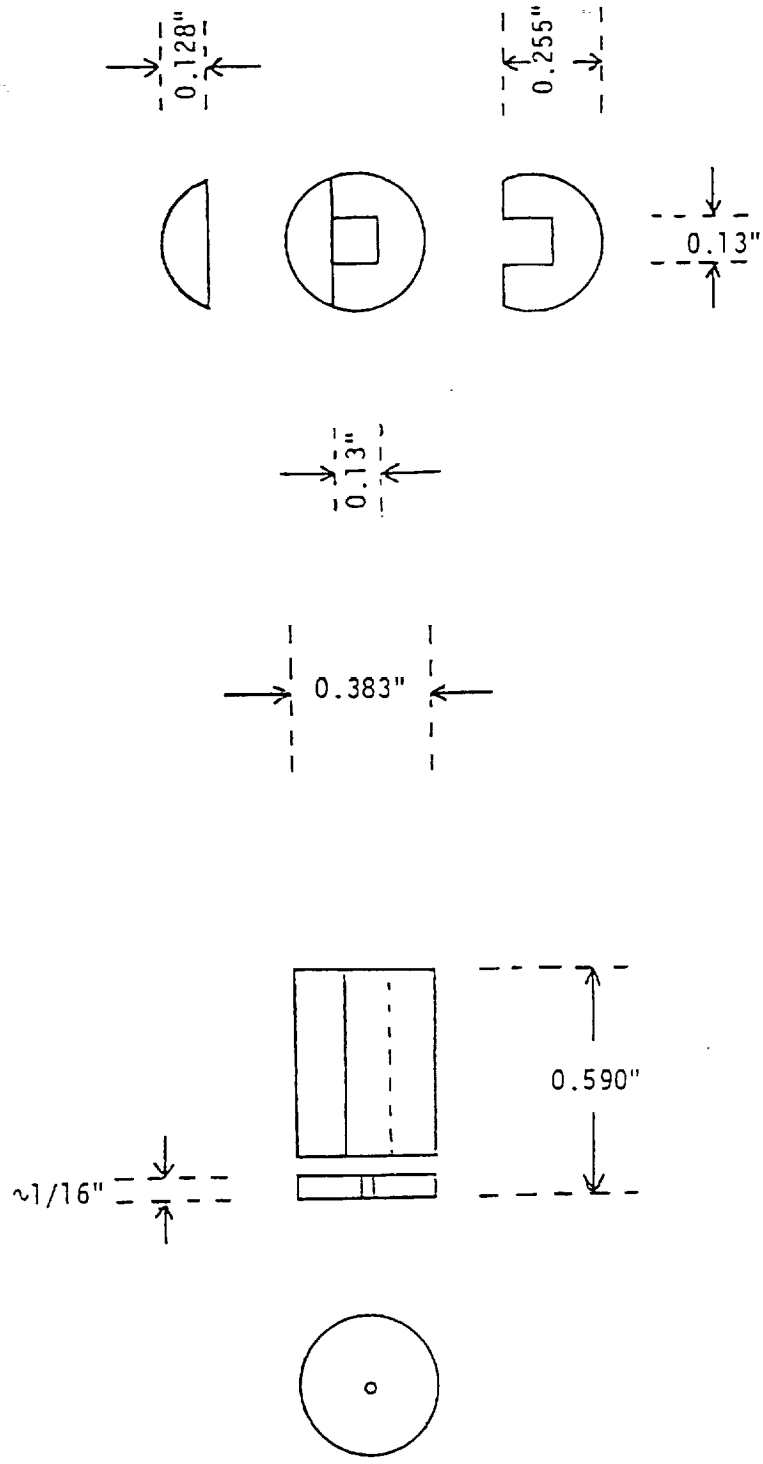

Fig. 1. Sketch of a TLD stack holder for K-7-41A, made of acrylate. Three stacks were placed in each of four plates (Plate No. B9-1, -2, -3, -4) for a total of twelve flight stacks (outside the spacecraft). A double window of aluminized Kapton polyimide (total thickness: 15 μm) separated the stacks from space.

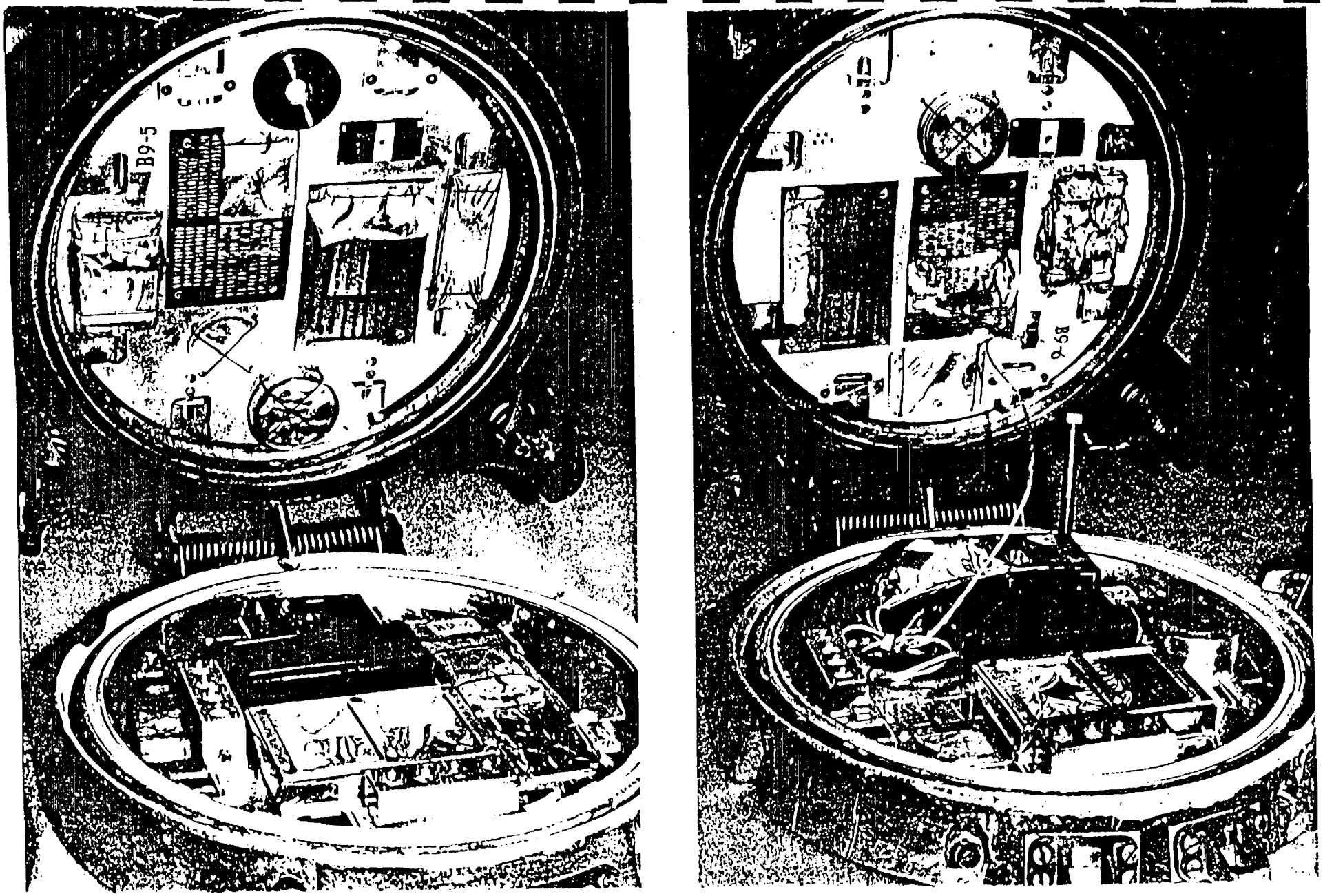

Fig. 2. Photograph of Cosmos 2044 "Clam-Shell" type containers for mission dosimeters. The containers were mounted on the outside of the spacecraft.

and as a function of depth. Although there have been some previous measurements of let spectra under such conditions, the orbital dependence and the effects of solar cycle on the low energy charged particle component are still not well understood. The very high inclination orbit of Cosmos 2044 (82.3°) will provide a test of radiation models in the polar regions, which has not been possible before.

The hardware consisted of two hermetically sealed flight units containing PNTD and nuclear emulsion stacks and with aluminized Kapton double-windows, as in Part A. The PNTD stacks were 3 cm in diameter and included sets of CR-39 and Cronar polyester detectors. The emulsion stacks were enclosed in thin stainless steel cylinders of the same diameters. The physical configurations of the units and stacks are shown in Figs. 3 and 4. The flight units were placed outside the spacecraft with F1 being in Plate B9-2 and F2 in Plate B9-1.

In addition to the radiation detector stacks, these units also held temperature sensors for the ATR-4 Ambient Temperature Recorder which has been developed by NASA for spacecraft use (NASA. 1989). This system allows a time-temperature profile to be determined for each sensor included on the mission (up to eight sensors). This is an important consideration for flight materials, such as some of the radiation detectors, which are heat sensitive.

Part C

Here the intent was to obtain some information on the neutron energy spectra. The detectors were located both on the outside and inside of the spacecraft.

The outside experiment consisted of two flight units containing ^{59}Co activation foils and PNTD films. An aluminum frame with aluminized Kapton double-windows was placed above the detectors but the sides of the units were open to vacuum. The PNTDs used were Cronar polyester. The purpose of the PNTDs in this experiment was for an intercomparison between those open to vacuum and those hermetically sealed. Due to space limitations, CR-39 was not included. The configuration of the units is shown in Fig. 5. The flight placement of the detectors was F1 in Plate B9-4 and F2 in Plate B9-3.

The inside detector consisted of a single ^{59}Co activation foil. In conjunction with the activation foil was a stack of nuclear emulsions to provide a comparison with the emulsions exposed on the outside of the spacecraft in

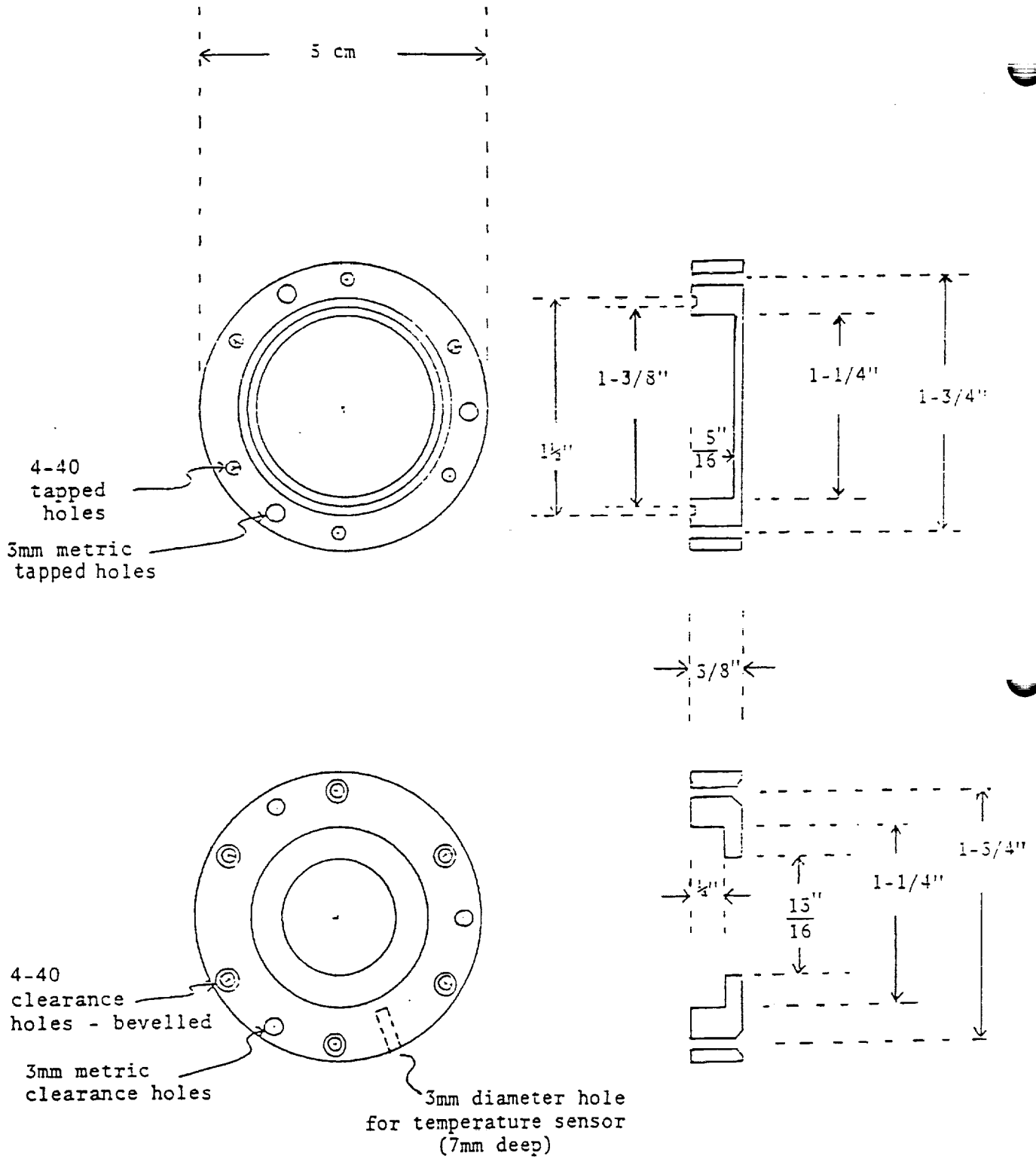

Fig. 3. Sketch of an aluminum container with O-ring seal for the plastic and emulsion stacks in K-7-41B. There were two flight units, F1 and F2 (outside the spacecraft). A double window of aluminized Kapton polyimide (total thickness: 15 μm) separated the stacks from space.

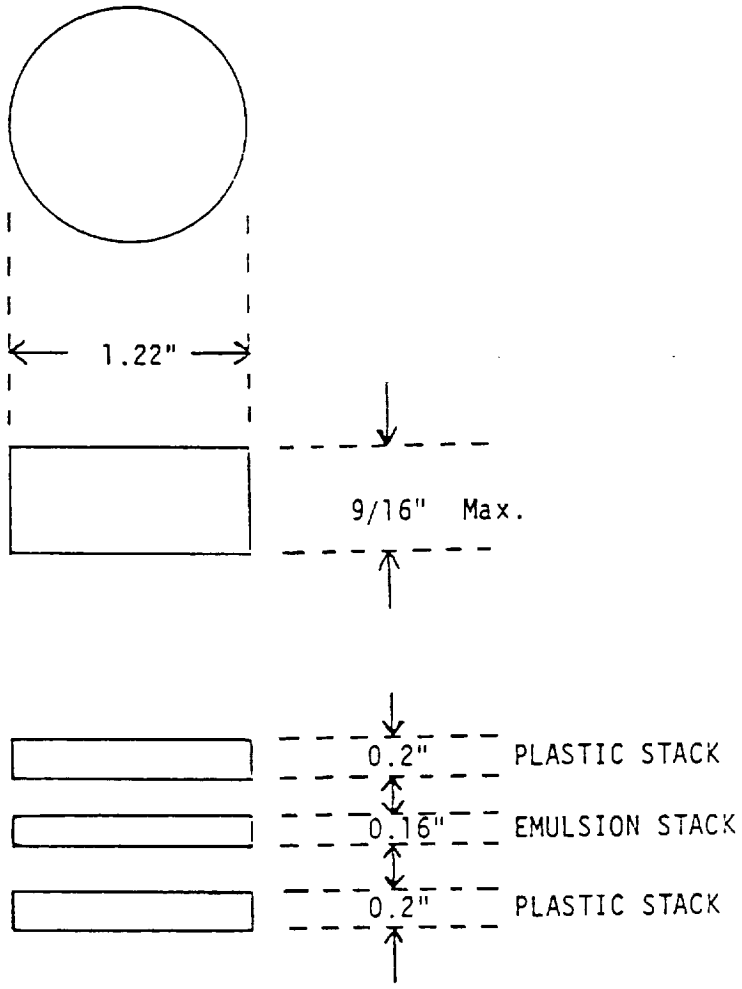

Fig. 4. Sketch of the plastic and emulsion stacks for K-7-41B

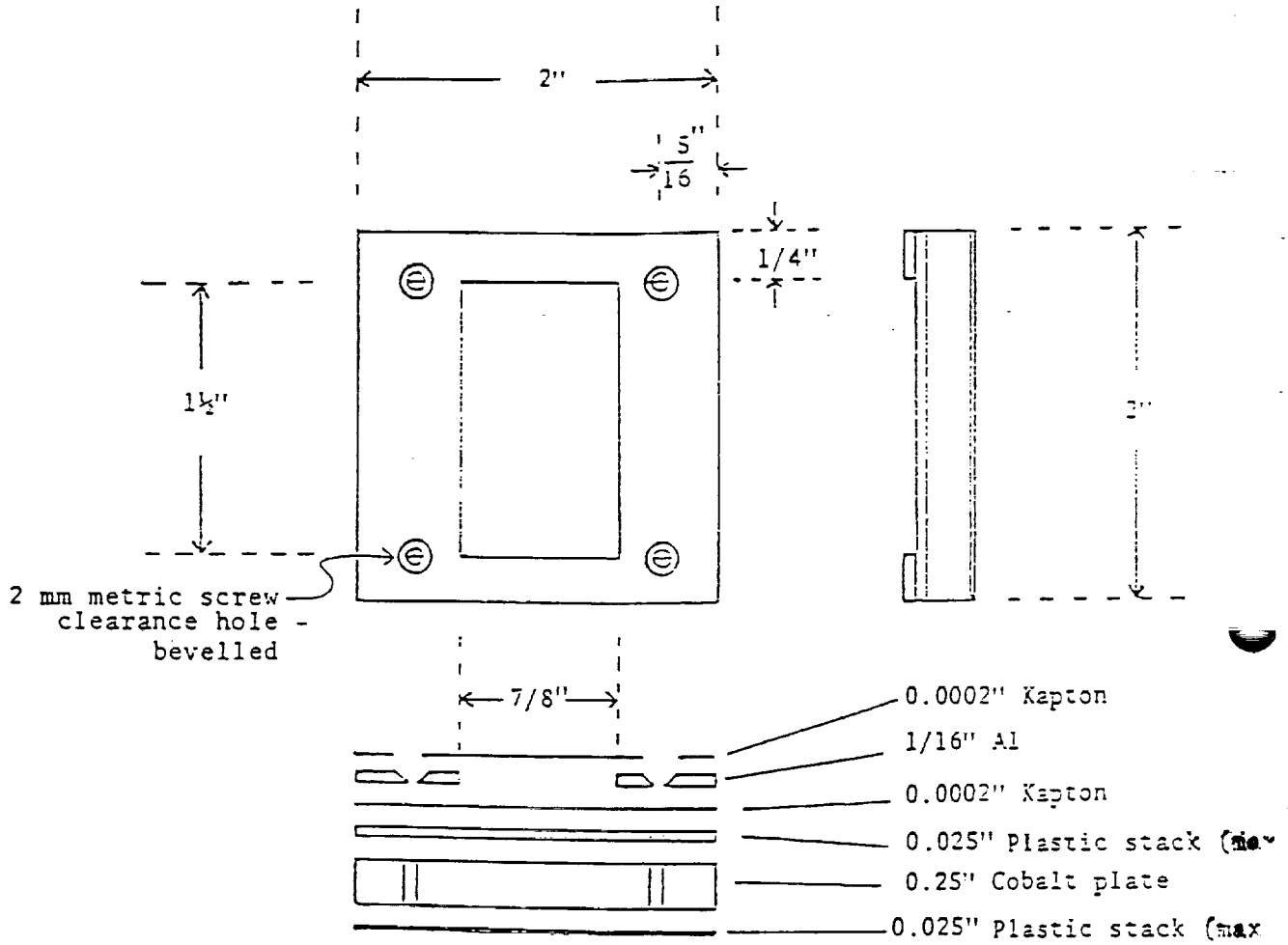

Fig. 5. Sketch of the ^{59}Co activation foil detector units for K-7-41C, two of which were placed outside the spacecraft. A third activation foil with an emulsion stack was placed inside the spacecraft.

Part B. The selection of available isotopes with suitable activation cross sections and decay product half-lives for spaceflights of a few days places severe limitations on this method. Cross sections exist for the measurement of both low energy (thermal plus resonance) and high energy (>10 MeV) neutrons, with some proton contribution, with the activations forming ^{60}Co and ^{58}Co. However, readout requires a very sensitive, low background spectrometer.

Part D

The goal of this part was to measure high energy (>1 MeV) neutron fluxes and dose equivalent rates averaged over the mission duration. The detectors were fission foils of ^{232}Th in conjunction with solid state nuclear track detectors (SSNTDs) of muscovite mica. There were two flight units (F1 and F2) and each unit was composed of four ^{232}Th foils with mica (1.27 cm in diameter) in an aluminum and Lexan polycarbonate holder (see Fig. 6). The arrangement of the foils was mica/^{232}Th/mica and lead discs of 0.5 mm thickness were placed to each side for reduction of radiation from the ^{232}Th foils. The flight units were mounted on the outside of the spacecraft, with F1 in Plate B9-8 and F2 in Plate B9-7.

Part E

The goal here was to measure the thermal ($\leq$ 0.2 eV) and resonance (0.2 eV < E_n < 1 MeV) neutron fluxes and dose equivalent rates averaged over the mission duration. The detectors were layers of ^{6}LiF (TLD-600) in conjunction with CR-39 PNTDs. There were two flight units and each unit was composed of two ^{6}LiF layers with CR-39 (1.27 $\times$ 1.27 cm) in an aluminum and Lexan polycarbonate holder (see Fig. 7). The arrangement of the components was CR-39/^{6}LiF/CR-39 with Gd foil of 0.0025 cm thickness around one of the two detectors. The Gd foil absorbs thermal neutrons and allows a separation of thermal and resonance neutrons. The flight units were mounted on the outside of the spacecraft, with F1 in Plate B9-5 and F2 in Plate B9-6.

Processing and Readout of Detectors

a) Temperature Profile and Environmental Conditions During the Cosmos 2044 Mission

The exposed Cosmos 2044 detectors were returned to this laboratory on 12 October 1989, or thirteen days after satellite re-entry. The condition

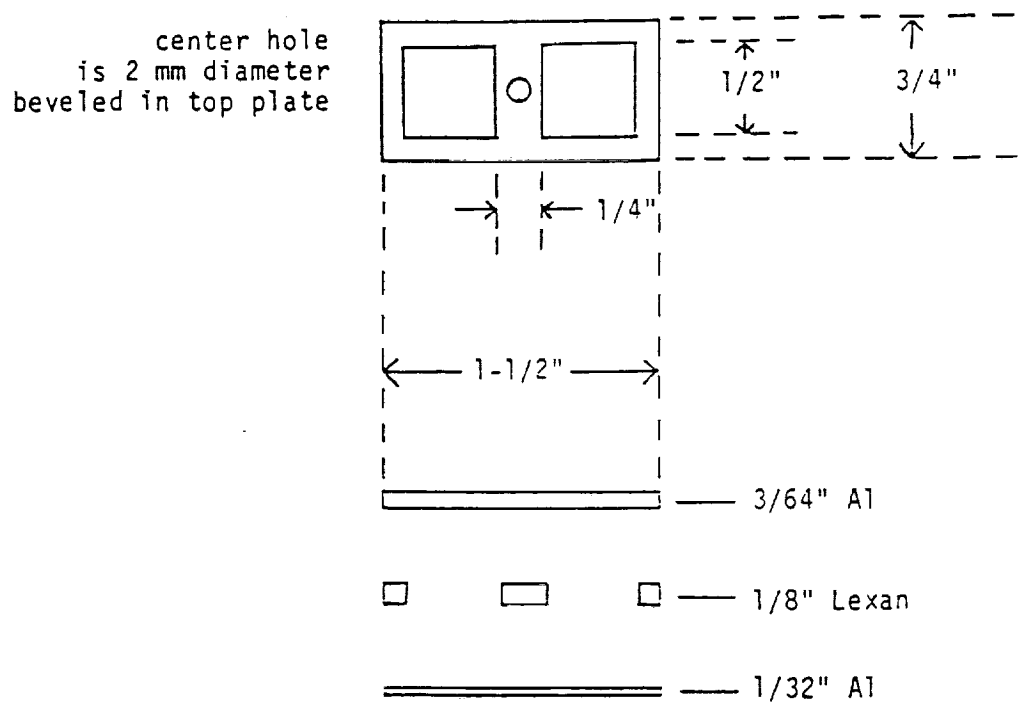

Fig. 7. Sketch of the ^{6}LiF/CR-39 neutron detector holders for K-7-41E. Each unit contained one unshielded detector and one shielded by 25 μm-thick Gd foil. Two units (F1 and F2) were placed outside the spacecraft.

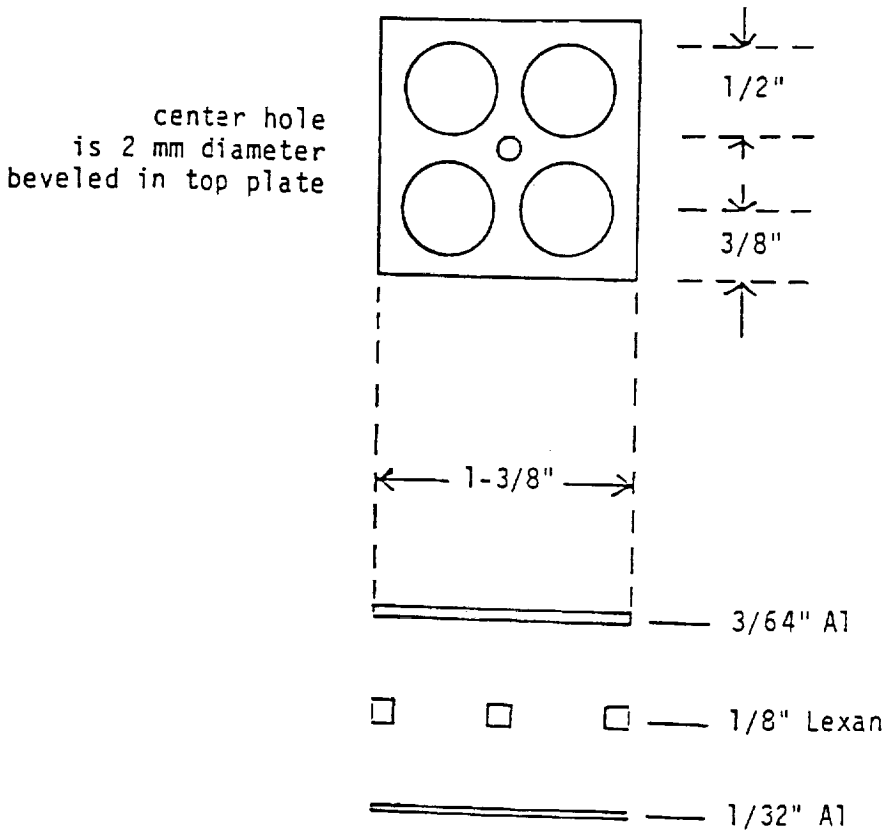

Fig. 6. Sketch of the ^{232}Th fission foil detector holders for K-7-41D. Two units, F1 and F2, were placed outside the spacecraft.

of the flight units appeared generally good, with the possible exception of the sealed PNTD/emulsion stack units (Part B) where the outer Kapton windows were found to be easily flexed. This was due to tiny perforations, apparently from micrometeorite impacts, causing the windows to lose their vacuum seals. It was subsequently determined that the inner windows were not perforated and that the flight units retained their air during the mission. This is important to the response of the PNTDs where a deficiency of oxygen results in faded or unformed latent particle tracks.

Temperature Measurement

During the mission, the temperature profiles were measured by two ATR-4 Ambient Temperature Recorders (NASA, 1989). Each of these devices had four temperature sensors which were distributed over plates containing flight dosimeters (Plates B9-2 and B9-6 in the KHA-1 clamshell container and Plates B9-1 and B9-7 in the KHA-3 container). The two aluminum canisters used in the K-7-41B experiment each had a sensor embedded in the side and sealed with a high-temperature conducting epoxy. The sensors were accurate to $\pm$ 0.5°C over the temperature range from -40° to +60°C. Temperature readings were taken from each sensor at intervals of 3.75 min.

In Fig. 8 is the temperature record of the sensor in the K-7-41B F1 canister. Aside from some brief temperature spikes the variation was between 3° and 36°C with an average of about 22°C. Based on environmental studies of the PNTDs and TLDs, no measureable effect on detector response would be expected from this temperature profile. The closure of the clamshell containers about a day before landing, as the spacecraft began moving into the outer atmosphere, is obvious from the drop in temperature.

In Fig. 9 is the temperature record of the sensor in the B F2 canister. The temperature profile is similar to, but about 5°C less than, the profile for F1 up to the last day. As the spacecraft began moving into the upper atmosphere prior to landing, the clamshell container (KHA-3) did not close. Where the F1 sensor temperature decreased, that of F2 increased to above 50°C and then spiked to above 60°C during the landing. Based on environmental studies for a more extended period of time, these temperatures could have affected the PNTD response, but because of the brevity of the conditions there was no measurable effect. The PNTDs from F1 and F2 were intercompared after the processing.

After disassembly of the flight units, the detectors were processed and

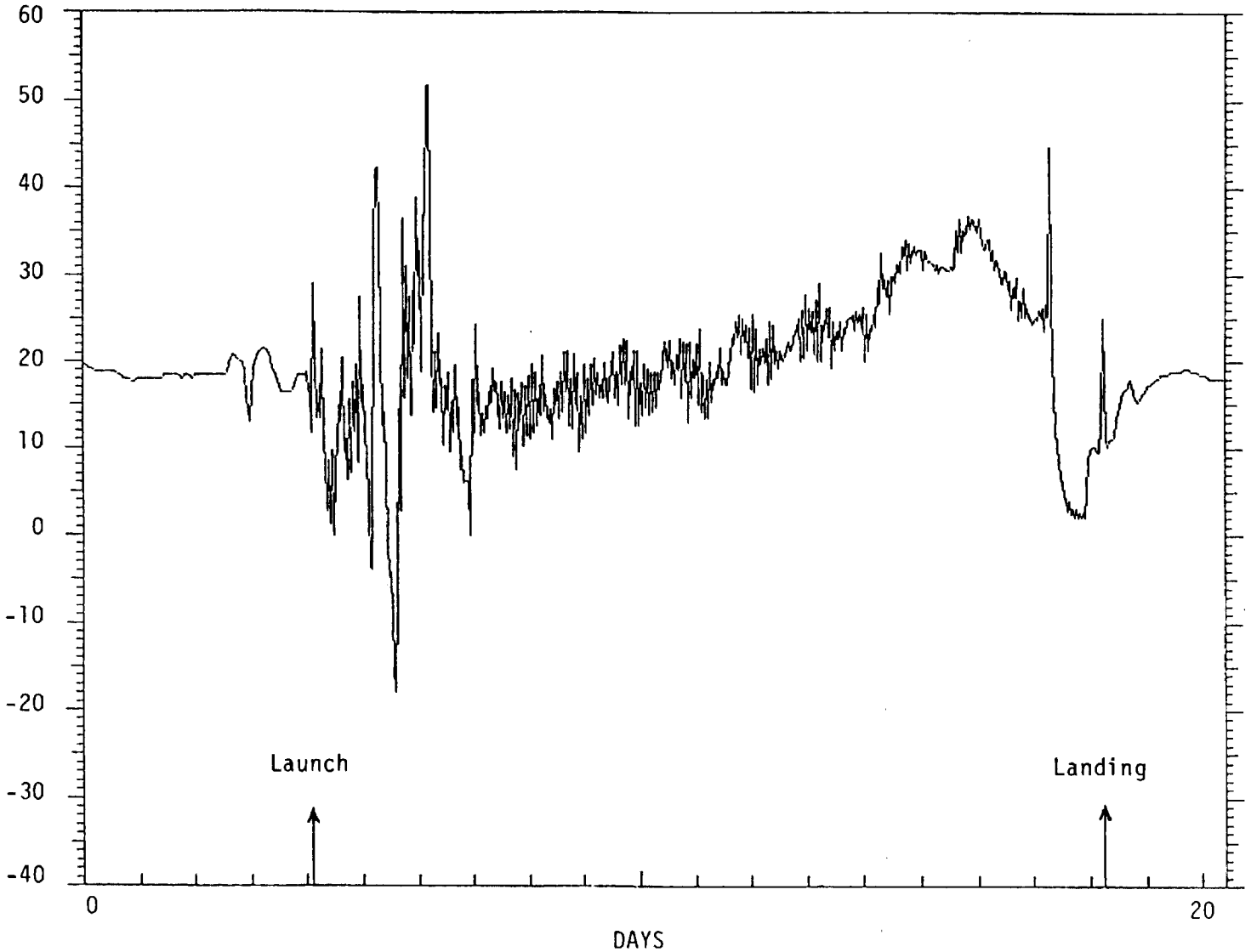

Fig. 8. Record of ATR-4 temperature probe embedded in the K-7-41B Fl canister (Plate B9-2; Container KHA-1).

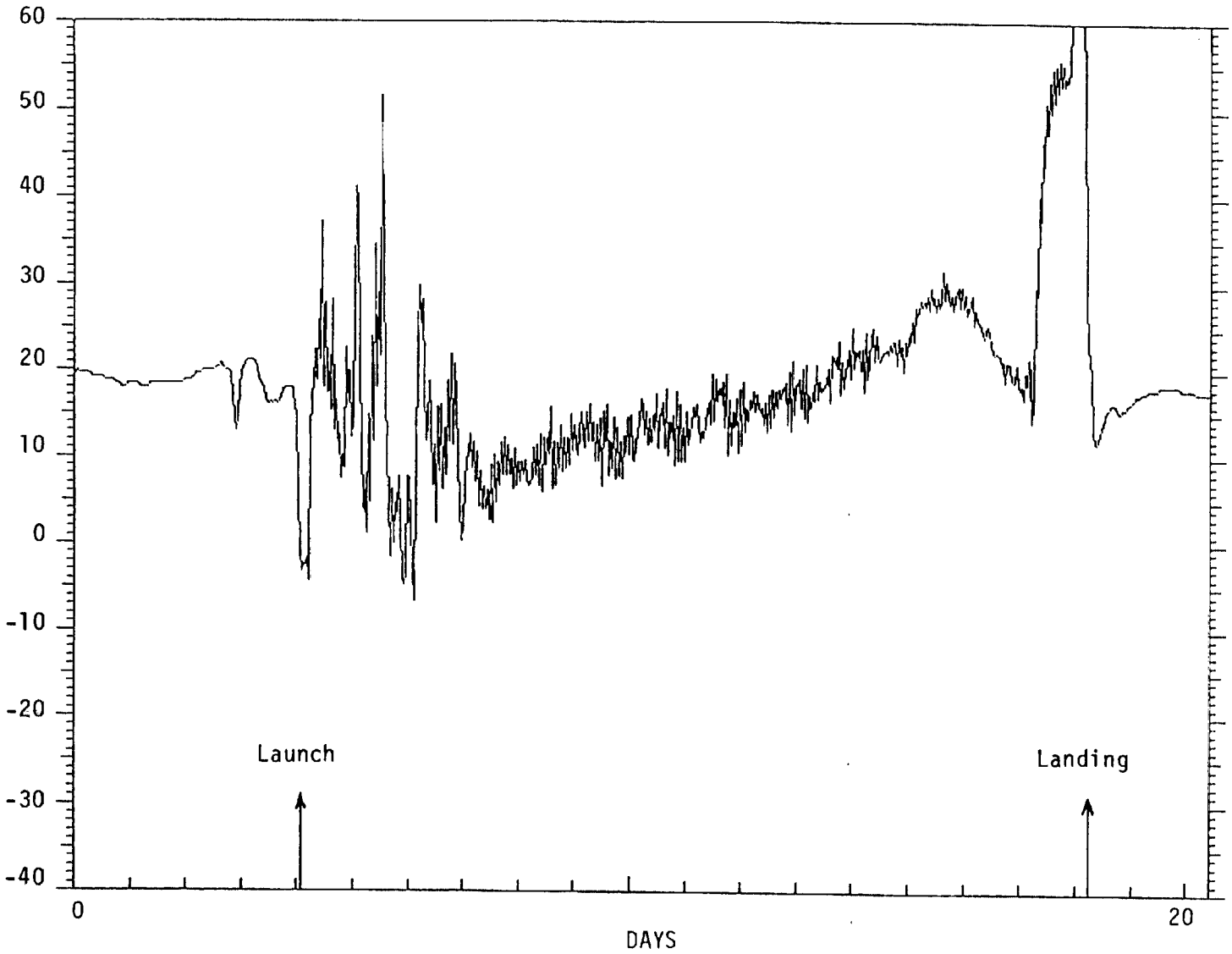

Fig. 9. Record of ATR-4 temperature probe embedded in the K-7-41B F2 canister (Plate B9-1; Container KHA-3).

read out as follows:

b) TLD Readout

The TLDs (TLD-700) were read out on Harshaw Model 2000 and 4000 Readers. In each case glow peak integrated current was measured between 120° and 250°C. In addition, the glow peak curves were recorded up to 325°C with the Model 4000 Reader. Flight, background and standard exposures were read out together for both the thin and thick TLDs. Standard exposures of 1 rad from a ^{137}Cs source were employed and TLD calibrations extending up to 10^4 rad were used to correct for the supralinear high dose response of the least shielded TLDs (Fig. 10). All flight TLD readings were then corrected for background and converted to tissue rad doses.

c) PNTD Processing and Readout

The CR-39 PNTDs were processed in 6.25 N NaOH solution at 50°C for 7 days. The bulk etch, B (thickness removed from a single surface), was measured for each film. Pairs of detectors were reassembled in their flight orientations and the two inner, adjacent surfaces were scanned under an optical microscope. This enabled the particles to be separated into short range (SR): matching tracks appearing on only the two interior surfaces, and long range, galactic cosmic rays (GCR): matching tracks appearing on all four surfaces of the pair of films. The SR particles include short-range secondary particles from target nuclei within the plastic and stopping primary galactic and trapped particles. All protons are registered as SR particles because of their short registration range in CR-39. The GCR particles include both primary GCRs and the long-range secondaries which are mainly the projectile fragments of GCRs. The major and minor axes of the elliptical surface openings of tracks were measured. The axial measurements, together with the B of the samples and the calibrated LET response function of the CR-39 material, were then used to generate particle LET spectra.

d) Nuclear Photographic Emulsions

The nuclear emulsions (Fuji types 6B and 7B) have been processed by standard techniques and are being read out at Marshall Space Flight Center, Huntsville.

e) $^{59}C0$ Activation Foils

Immediately after arrival, the ^{59}Co foils were transferred to Dr. A. Smith of Lawrence Berkeley Laboratory (LBL) to be read out at a highly shielded

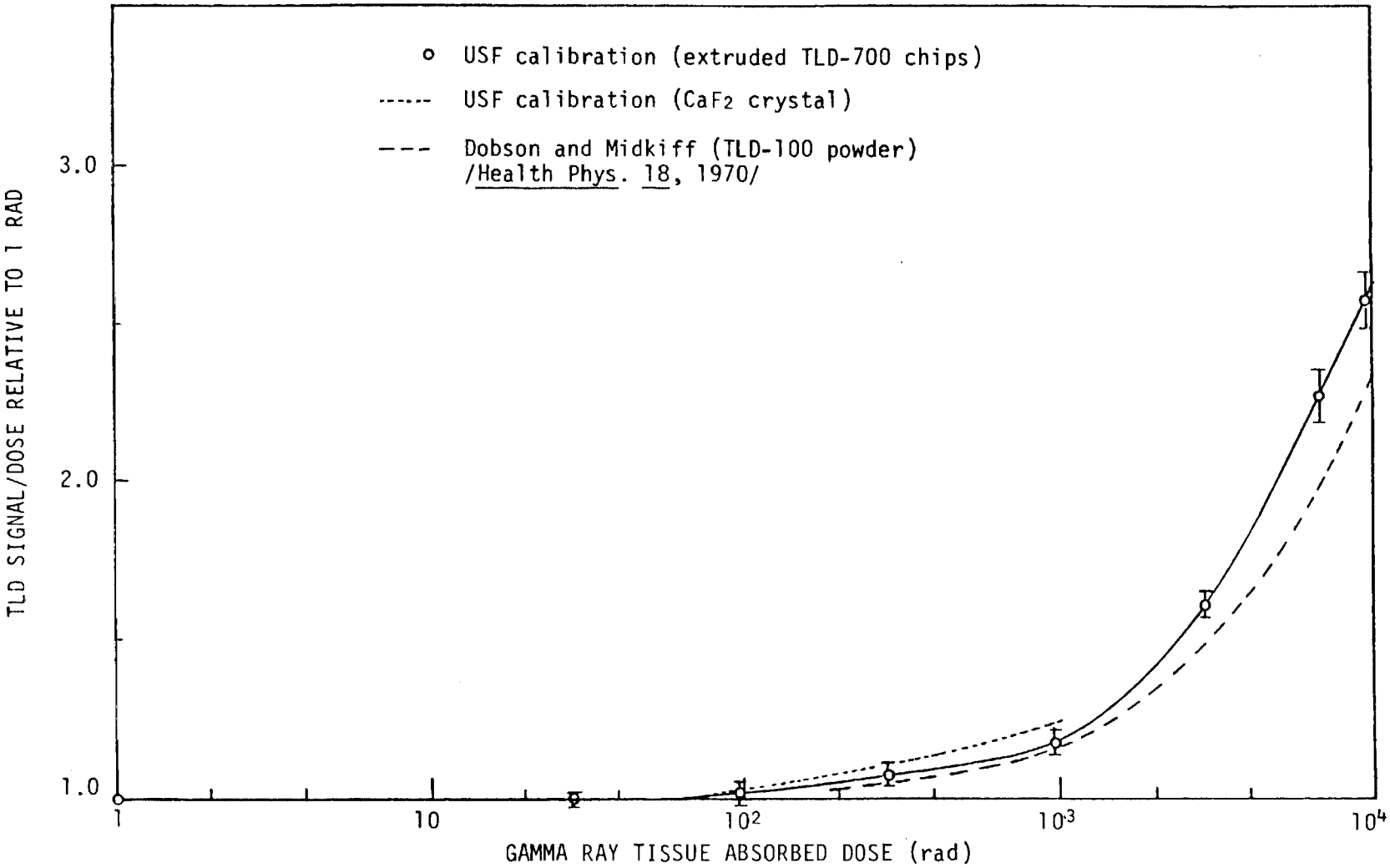

Fig. 10. TLD calibration showing the high-dose supralinearity found in TLD-700 extruded chips. The data from Dobson and Midkiff /1970/ (TLD-100 powder) was typical of LiF supralinearity reported.

site with high efficiency Ge(Li) detectors. The data analysis and background studies for these measurements are still in progress.

f) ^{232}Th/Mica Detectors

The muscovite mica discs from these detectors were processed for 2 hr at 21°C in 50% HF acid. They had been processed for 5 hr under the same conditions pre-flight to develop the fossil fission tracks to large size. The flight tracks on the discs were then counted under an optical microscope. Backgrounds were counted using the backs of the flight discs. Detector calibrations based on fission cross sections for neutrons and protons and assumed spectral distributions for neutrons and protons were used to convert track densities into neutron fluences (see Benton et al., 1978a). Dose equivalents were determined using Quality Factors (QF) of 10.

g) ^{6}LiF /CR-39 Detectors

The CR-39 films from these detectors were processed in 6.25 *N* NaOH solution at 70°C for 5 hr. Track densities were counted on the surfaces both adjacent to and opposite to the ^{6}LiF layers in order to determine net alpha particle track densities from the ^{6}Li(n,α) T reaction. The ground control detectors were used to measure the non-flight alpha particle backgrounds. Since there were CR-39 films on both the space and spacecraft sides of the ^{6}LiF layers, the average track densities on the two films yielded a measure of 4π neutron incidence.

In each flight unit, one detector was covered with 0.0025 cm-thick Gd foil and one was not. The thermal neutron absorbance of the Gd gives an effective low energy cutoff of 0.2 eV for the covered detectors. By subtraction the measured track densities were separated into those due to neutrons below and above 0.2 eV.

The flight background track densities, counted on the backs of the CR-39 detectors, were quite large and also depth dependent. Since the front and back of the detectors were at different depths, it was necessary to interpolate between only two measured points to obtain the appropriate backgrounds. Consequently, the measurement accuracy is somewhat less than implied by the associated standard deviations which were calculated from counting statistics. In addition, the neutron spectra assumed in the calibrations are the completely thermalized distribution below the Gd cutoff and a 1/E distribution above. Deviations of the flight spectra from these assumptions will also contribute to measurement error.

RESULTS

Part A

The average depth dose rates for the three TLD stacks in each of the four flight plates are plotted in Figs. 11, 12, 13 and 14. The measurements show more than a 4 order-of-magnitude decrease in dose rate down to 3 g/cm^2 depth. The average plate dose rates are given in Table 1. The total flight doses for the twelve TLD stacks are given in Tables 2a, -b, -c and -d. It can be seen that there are shielding differences for the various stacks. As an example, three individual TLD stack distributions for Plate No. B9-3 are shown in Fig. 15. Stack No. 1 dose rates are clearly less than Stacks Nos. 3 and 9. There are substantial variations at the tops of the stacks, as seen in Tables 2a–2d (2040 rad for No. 2 up to 4480 rad for No. 9) while stacks Nos. 1, 5 and 10 have smaller doses at the maximum depths than do the others.

Part B

The CR-39 PNTDs have been given the standard processing for 7 days in 6.25 N NaOH solution at 50°C. Adjacent pairs from the flight stacks were reassembled, scanned and measured with a microscope and electronic micrometer. The particle tracks were separated into galactic cosmic rays (GCR), which traversed all four surfaces of the CR-39 pair, and short range (SR), which traversed only the two inner surfaces or the two inner surfaces plus one outer surface of the pair. The GCRs are mainly galactic cosmic rays or their projectile fragments where $Z \geq 2$. Anomalous particles may also contribute to the four-surface tracks. The SR tracks are mainly short range secondary particles or primary protons near their stopping points. The short registration range of protons in CR-39 makes four-surface proton tracks very low-probability events. GCR stopping particles of $Z \geq 2$ can contribute to SR tracks, but this also has a low probability.

Five sets of integral LET spectra (Total, GCR and SR) from the PNTD stack in the F1 canister are given in Figures 16–20. Four sets of spectra from the F2 canister are given in Figures 21–24. The minimum to maximum shielding is covered in each PNTD stack. The minimum shielding is greater for F1 because the least shielded CR-39 layer was damaged on one surface by the high electron dose encountered. An extra layer of thin plastic protected the least shielded CR-39 layer in F2.

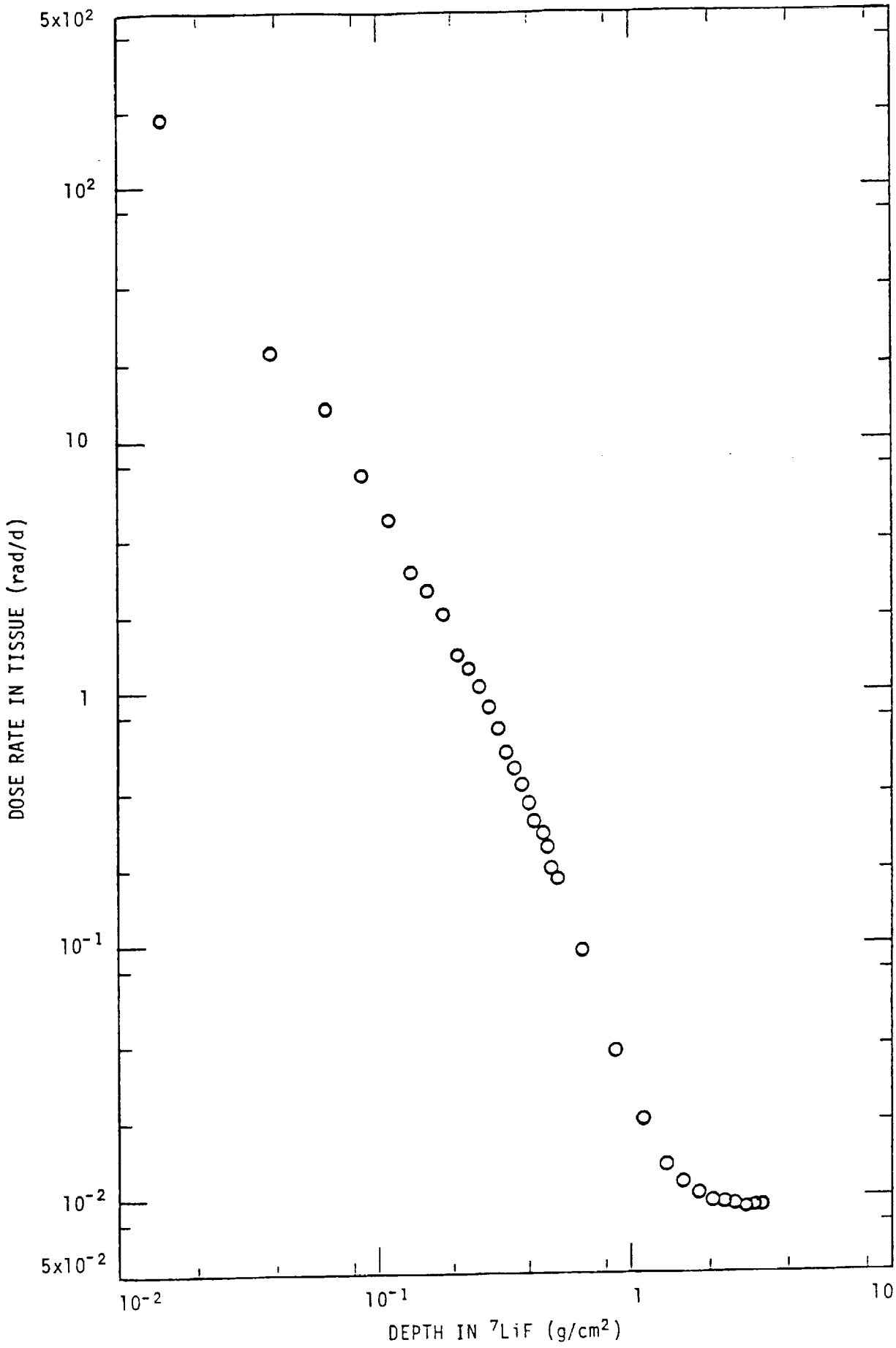

Fig. 11. Average dose rates in Plate No. B9-1 (TLD stacks Nos. 4, 8, 12)

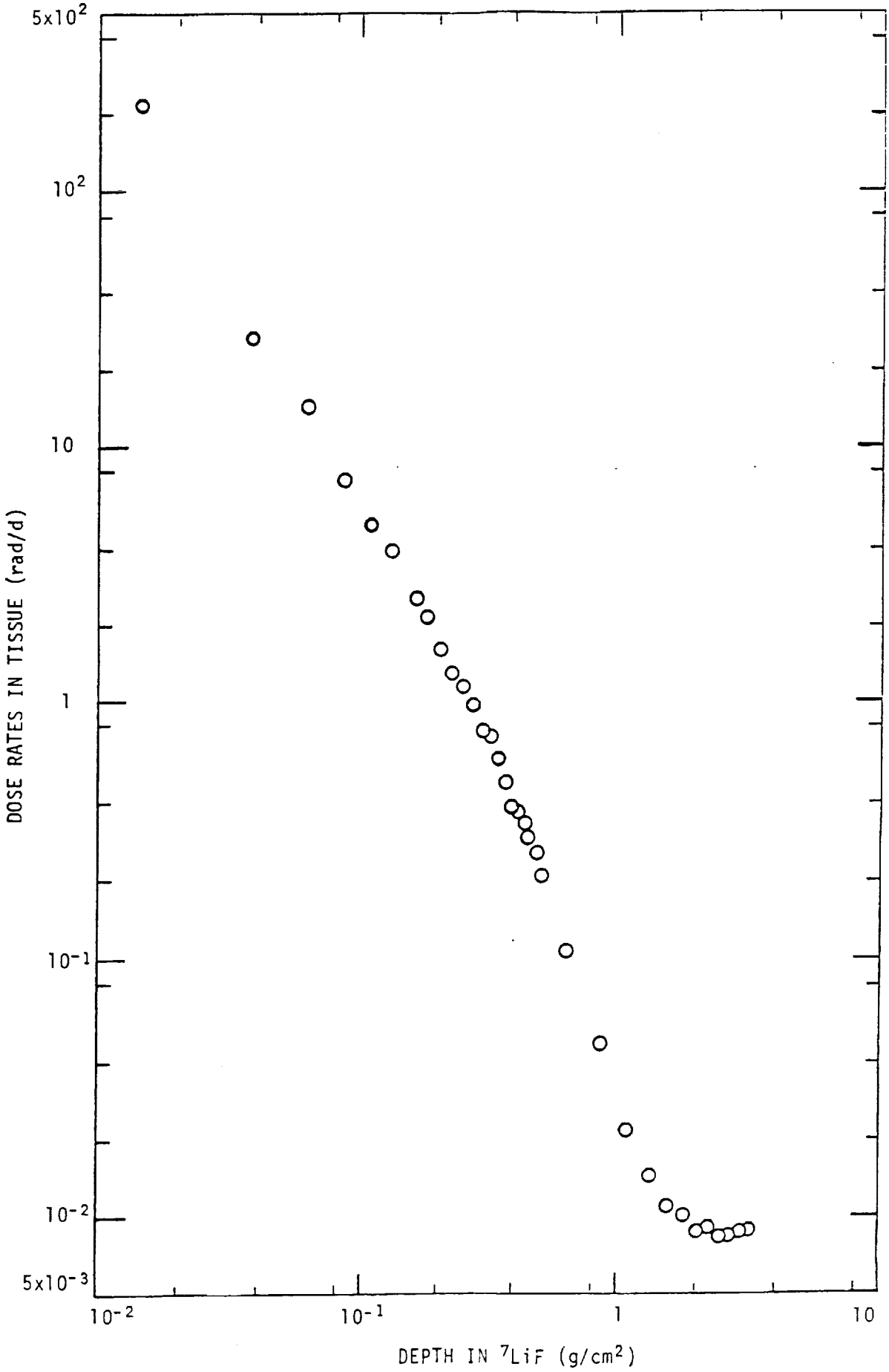

Fig. 12. Average dose rates in Plate No. B9-2 (TLD stacks Nos. 2, 6, 10)

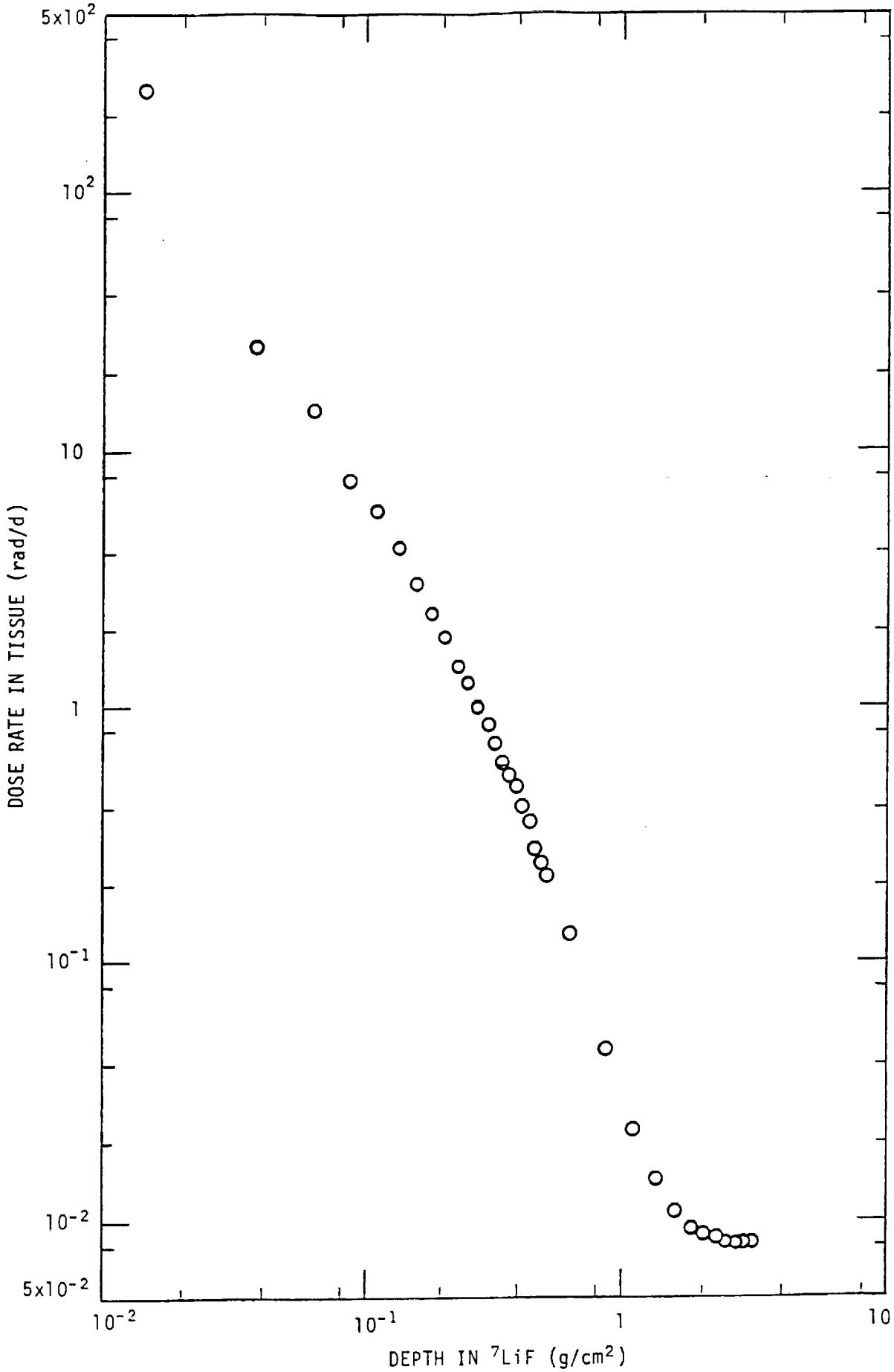

Fig. 13. Average dose rates in Plate No. B9-3 (TLD stacks Nos. 1, 3, 9)

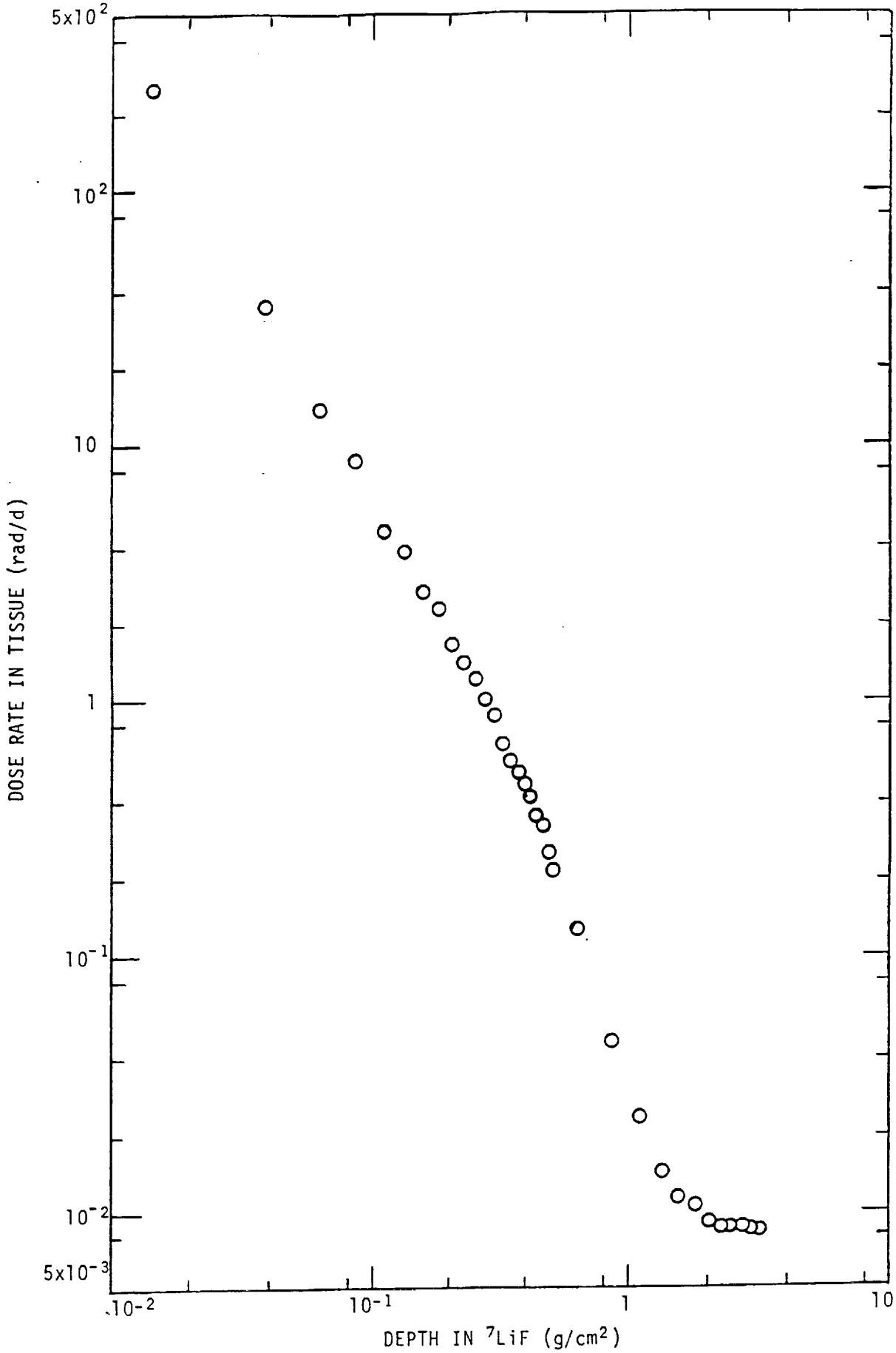

Fig. 14. Average dose rates in Plate No. B9-4 (TLD stacks Nos. 5, 7, 11)

TABLE 1 Cosmos 2044 Experiment K-7-41A TLD Stack Tissue Absorbed Dose Rates

Plate #B9-1 Ave.(rad/d)	Plate #B9-2 Ave.(rad/d)	Plate #B9-3 Ave.(rad/d)	Plate #B9-4 Ave.(rad/d)	Depth in ^{7}LiF (g/cm^2)
188	219	248	252	0.0146
22.1	27.0	24.9	35.0	0.0386
13.3	14.4	14.3	13.6	0.0625
7.32	7.39	7.54	8.55	0.0865
4.81	4.96	5.79	5.57	0.110
2.98	3.93	4.12	3.83	0.134
2.55	2.54	3.08	2.70	0.158
2.04	2.16	2.33	2.29	0.182
1.40	1.60	1.86	1.67	0.206
1.22	1.29	1.42	1.41	0.230
1.03	1.13	1.22	1.21	0.254
0.870	0.971	0.978	1.01	0.278
0.714	0.761	0.855	0.884	0.302
0.593	0.718	0.714	0.678	0.326
0.500	0.588	0.604	0.579	0.350
0.430	0.486	0.533	0.523	0.374
0.370	0.386	0.490	0.468	0.398
0.311	0.373	0.403	0.420	0.422
0.278	0.334	0.357	0.352	0.446
0.246	0.299	0.278	0.326	0.470
0.201	0.254	0.245	0.254	0.494
0.183	0.211	0.219	0.217	0.518
*				
0.0971	0.108	0.130	0.128	0.646
0.0380	0.0474	0.0457	0.0461	0.878
0.0204	0.0218	0.0225	0.0237	1.11
0.0135	0.0145	0.0145	0.0145	1.34
0.0115	0.0110	0.0108	0.0114	1.57
0.0104	0.0101	0.00928	0.0107	1.81
0.00971	0.00884	0.00899	0.00906	2.04
0.00978	0.00906	0.00862	0.00877	2.27
0.00949	0.00841	0.00841	0.00877	2.50
0.00913	0.00848	0.00826	0.00870	2.74
0.00942	0.00870	0.00833	0.00855	2.97
0.00935	0.00884	0.00848	0.00833	3.20

*Measurements from thicker TLDs below this point

TABLE 2a

COSMOS 2044 Experiment K-7-41A

TLD Stack Doses Plate No. B9-1

Stack No.4 (rad)	Stack No.8 (rad)	Stack No.12 (rad)	Plate No.B9-1 Average (rad)	Depth in ^{7}LiF (g/cm^2)
2080	2580	3130	2600	0.0146
285	362	268	305	0.0386
143	250	159	184	0.0625
95.6	112	94.3	101	0.0865
70.0	73.7	55.4	66.4	0.110
32.3	42.7	48.2	41.1	0.134
31.1	36.7	37.8	35.2	0.158
28.0	28.2	28.2	28.1	0.182
20.7	19.6	17.6	19.3	0.206
18.6	16.5	15.6	16.9	0.230
14.3	15.1	13.2	14.2	0.254
12.2	13.5	10.2	12.0	0.278
--	9.85	--	9.85	0.302
8.63	8.01	7.90	8.18	0.326
6.71	7.61	6.37	6.90	0.350
6.06	6.38	5.36	5.93	0.374
5.87	5.13	4.29	5.10	0.398
4.18	4.81	3.87	4.29	0.422
3.74	4.29	3.50	3.84	0.446
3.60	3.66	2.93	3.40	0.470
2.93	2.85	2.52	2.77	0.494
2.64	2.61	2.33	2.53	0.518
*				
1.32	1.42	1.27	1.34	0.646
0.511	0.556	0.507	0.525	0.878
0.275	0.289	0.281	0.282	1.11
0.184	0.201	0.174	0.186	1.34
0.159	0.167	0.150	0.159	1.57
0.145	0.137	0.148	0.143	1.81
0.131	0.137	0.135	0.134	2.04
0.129	0.140	0.136	0.135	2.27
0.126	0.135	0.132	0.131	2.50
0.122	0.127	0.128	0.126	2.74
0.133	0.121	0.136	0.130	2.97
--	0.134	0.124	0.129	3.20

*Measurements from thicker TLDs below this point

TABLE 2b

COSMOS 2044 Experiment K-7-41A

TLD Stack Doses Plate No. B9-2

Stack No.2 (rad)	Stack No.6 (rad)	Stack No.10 (rad)	Plate No.B9-2 Average (rad)	Depth in ^{7}LiF (g/cm^2)
2040	3410	3600	3020	0.0146
266	483	366	372	0.0386
131	232	235	199	0.0625
79.3	129	96.2	102	0.0865
62.3	79.4	63.7	68.5	0.110
44.1	73.2	45.7	54.3	0.134
27.9	46.6	30.7	35.1	0.158
31.6	33.0	24.7	29.8	0.182
19.7	27.3	19.2	22.1	0.206
15.8	21.4	16.3	17.8	0.230
14.0	21.1	11.8	15.6	0.254
11.4	18.0	10.7	13.4	0.278
9.78	13.3	8.33	10.5	0.302
9.65	11.2	8.89	9.91	0.326
8.35	9.31	6.66	8.11	0.350
6.59	8.15	5.40	6.71	0.374
5.04	6.35	4.58	5.32	0.398
5.27	5.89	4.28	5.15	0.422
4.49	5.33	4.01	4.61	0.446
4.35	4.80	3.24	4.13	0.470
3.38	4.21	2.92	3.50	0.494
2.85	3.67	2.22	2.91	0.518
*				
1.45	1.83	1.18	1.49	0.646
0.737	0.739	0.485	0.654	0.878
0.317	0.349	0.237	0.301	1.11
0.232	0.211	0.156	0.200	1.34
0.166	0.170	0.120	0.152	1.57
0.158	0.150	0.108	0.139	1.81
0.123	0.145	0.098	0.122	2.04
0.142	0.142	0.091	0.125	2.27
0.122	0.134	0.092	0.116	2.50
0.121	0.135	0.094	0.117	2.74
0.135	0.131	0.093	0.120	2.97
0.149	0.129	0.087	0.122	3.20

*Measurements from thicker TLDs below this point

TABLE 2c

COSMOS 2044 Experiment K-7-41A

TLD Stack Doses Plate No. B9-3

Stack No.1 (rad)	Stack No.3 (rad)	Stack No.9 (rad)	Plate No.B9-3 Average (rad)	Depth in ^{7}LiF (g/cm^2)
2380	3390	4480	3420	0.0146
295	343	390	343	0.0386
153	214	223	197	0.0625
89.8	113	110	104	0.0865
61.7	106	72.0	79.9	0.110
50.7	78.1	42.0	56.9	0.134
32.9	50.8	43.7	42.5	0.158
26.9	37.3	32.1	32.1	0.182
22.5	27.6	26.8	25.6	0.206
16.9	20.3	21.7	19.6	0.230
13.3	17.8	19.3	16.8	0.254
11.6	16.0	12.9	13.5	0.278
11.5	11.6	12.2	11.8	0.302
8.15	10.8	10.6	9.85	0.326
7.33	8.83	8.82	8.33	0.350
6.62	8.35	7.07	7.35	0.374
5.32	7.47	7.49	6.76	0.398
4.46	6.79	5.42	5.56	0.422
4.49	5.36	4.91	4.92	0.446
3.20	3.82	4.50	3.84	0.470
2.42	3.93	3.79	3.38	0.494
2.48	3.55	--	3.02	0.518
*				
1.56	2.01	1.82	1.80	0.646
0.479	0.729	0.683	0.630	0.878
0.237	0.346	0.349	0.311	1.11
0.144	0.227	0.228	0.200	1.34
0.105	0.174	0.167	0.149	1.57
0.097	0.152	0.134	0.128	1.81
0.085	0.140	0.147	0.124	2.04
0.089	0.135	0.133	0.119	2.27
0.086	0.133	0.128	0.116	2.50
0.079	0.128	0.134	0.114	2.74
0.084	0.129	0.133	0.115	2.97
0.091	0.127	0.133	0.117	3.20

*Measurements from thicker TLDs below this point

TABLE 2d

COSMOS 2044 Experiment K-7-41A

TLD Stack Doses Plate No. B9-4

Stack No.5 (rad)	Stack No.7 (rad)	Stack No.11 (rad)	Plate No.B9-4 Average (rad)	Depth in ^{7}LiF (g/cm^2)
2530	3750	4150	3480	0.0146
587	481	382	483	0.0386
167	196	202	188	0.0625
111	135	107	118	0.0865
64.7	83.4	82.3	76.8	0.110
48.6	52.1	58.0	52.9	0.134
34.1	40.8	37.1	37.3	0.158
28.4	34.5	32.0	31.6	0.182
20.5	23.9	24.5	23.0	0.206
18.0	18.5	21.6	19.4	0.230
14.4	15.3	20.5	16.7	0.254
12.9	13.4	15.3	13.9	0.278
10.9	12.4	13.2	12.2	0.302
9.18	9.51	--	9.35	0.326
7.96	8.01	--	7.99	0.350
6.34	7.40	7.91	7.22	0.374
5.58	6.86	6.93	6.46	0.398
4.83	6.41	6.13	5.79	0.422
4.62	5.43	4.53	4.86	0.446
4.82	4.25	4.43	4.50	0.470
3.07	3.75	3.67	3.50	0.494
2.87	2.84	3.25	2.99	0.518
*				
1.48	1.80	2.01	1.76	0.646
0.591	0.607	0.709	0.636	0.878
0.282	0.335	0.363	0.327	1.11
0.180	0.206	0.214	0.200	1.34
0.139	0.159	0.172	0.157	1.57
0.121	0.168	0.153	0.147	1.81
0.107	0.133	0.136	0.125	2.04
0.107	0.129	0.126	0.121	2.27
0.015	0.138	0.120	0.121	2.50
0.103	0.127	0.131	0.120	2.74
0.106	0.125	0.122	0.118	2.97
0.103	0.124	0.119	0.115	3.20

*Measurements from thicker TLDs below this point

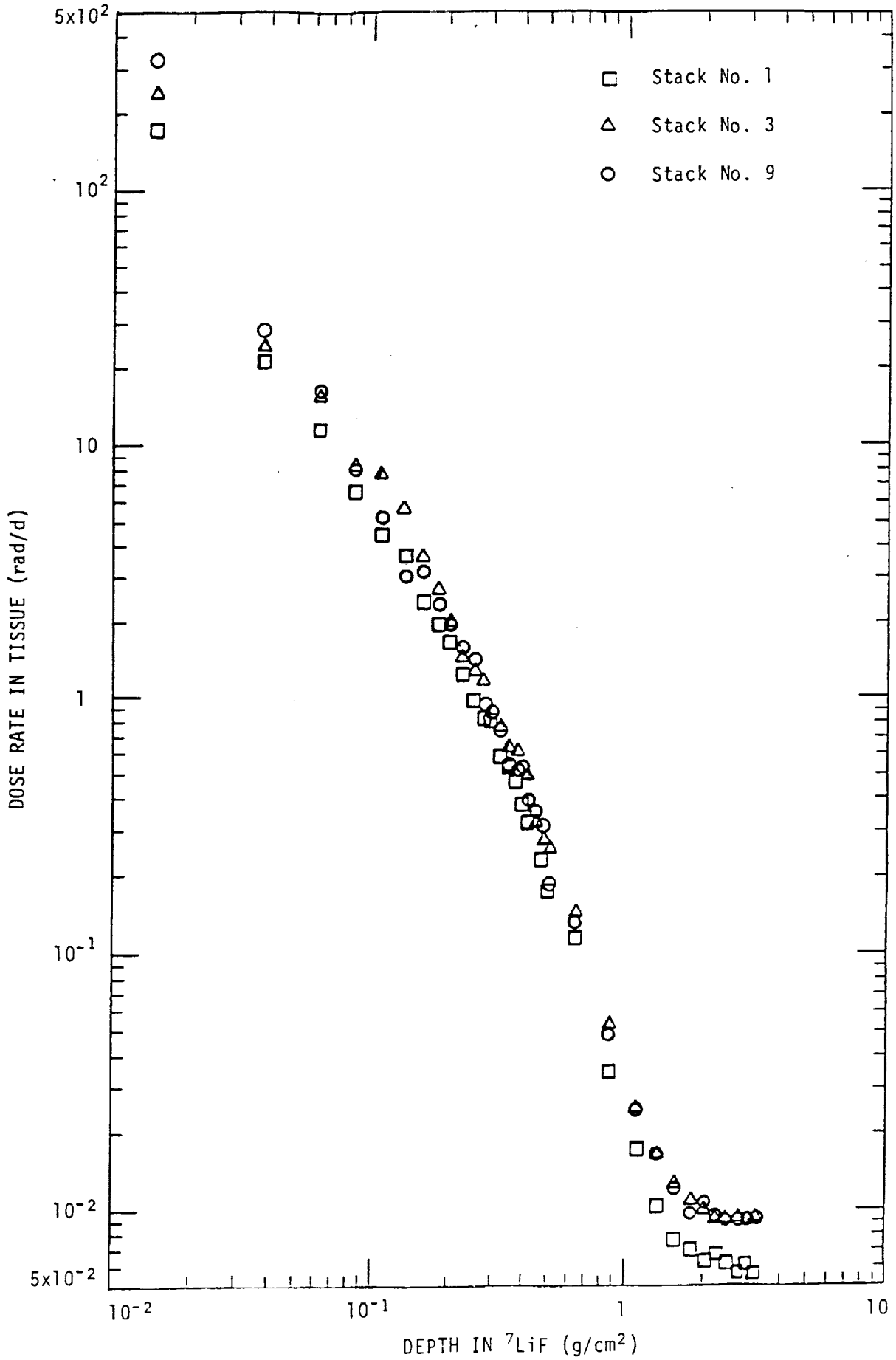

Fig. 15. Dose rates for the three TLD stacks in Plate No. B9-3

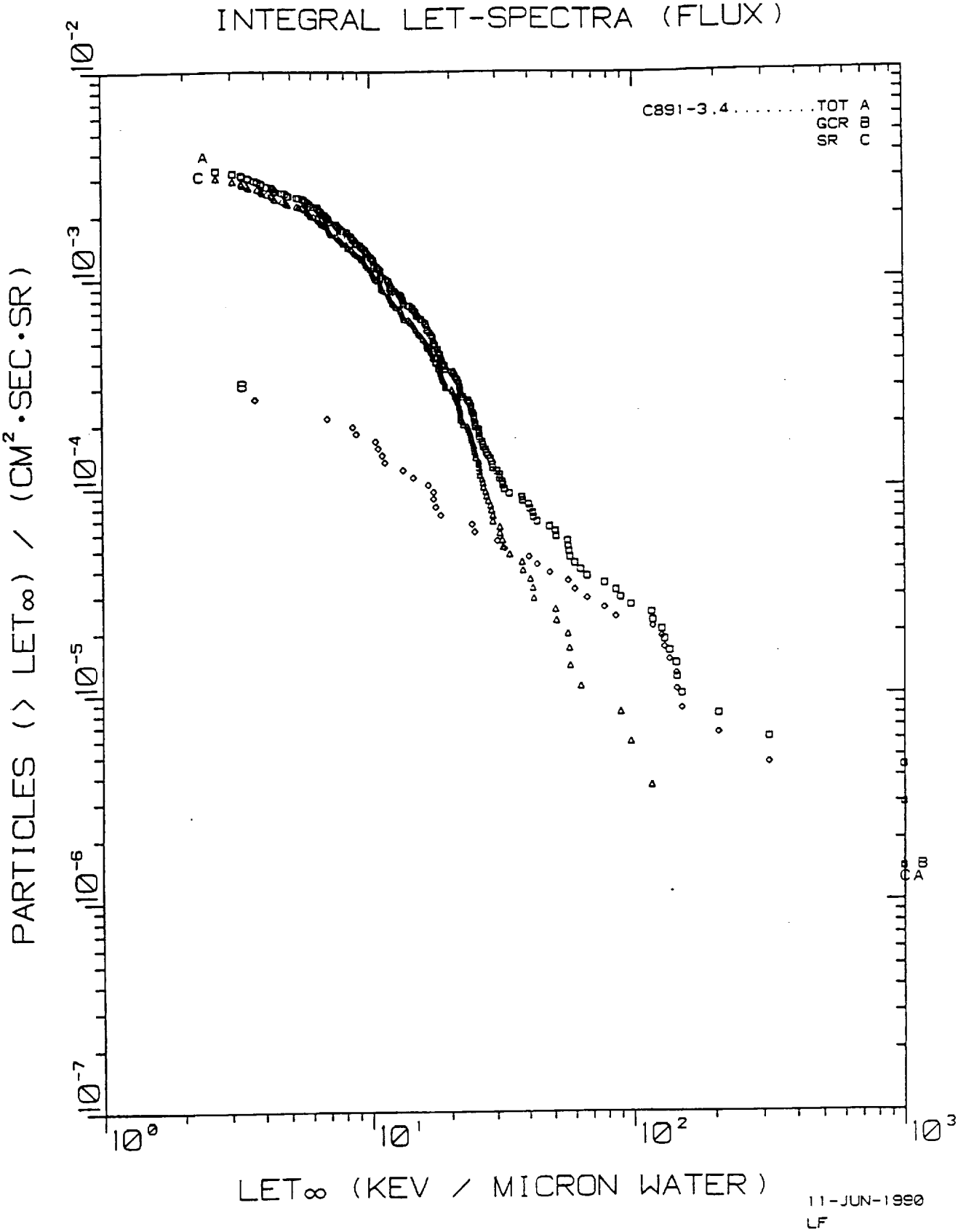

Fig. 16. Integral LET flux spectra for Experiment K-7-41B, PNTD stack F1 (outside the spacecraft). The minimum shielding was 0.164 g/cm^2 plastic.

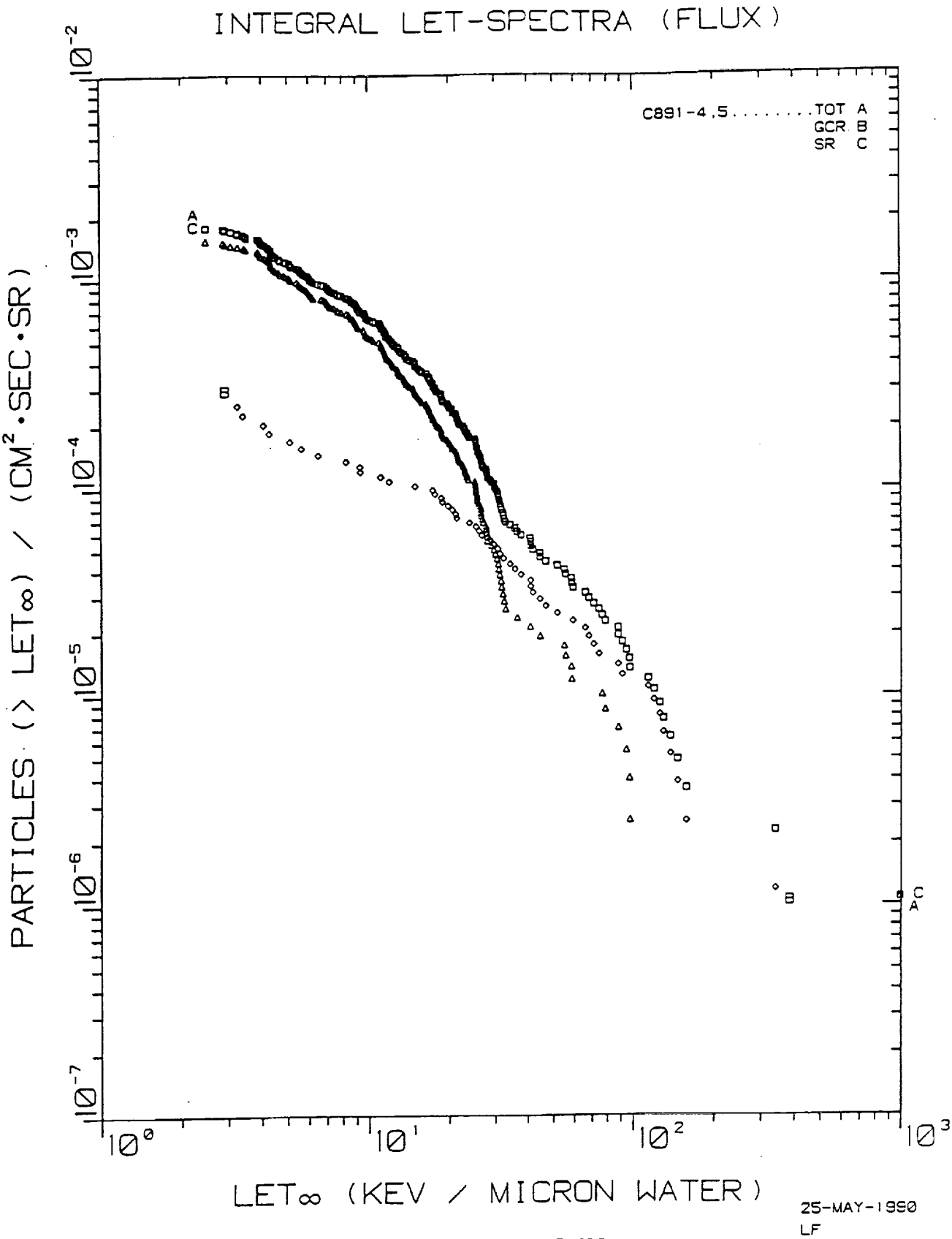

Fig. 17. Integral LET flux spectra for Exp. K-7-41B, PNTD stack F1 (outside the spacecraft). The minimum shielding was 0.239 g/cm^2 plastic.

C-4

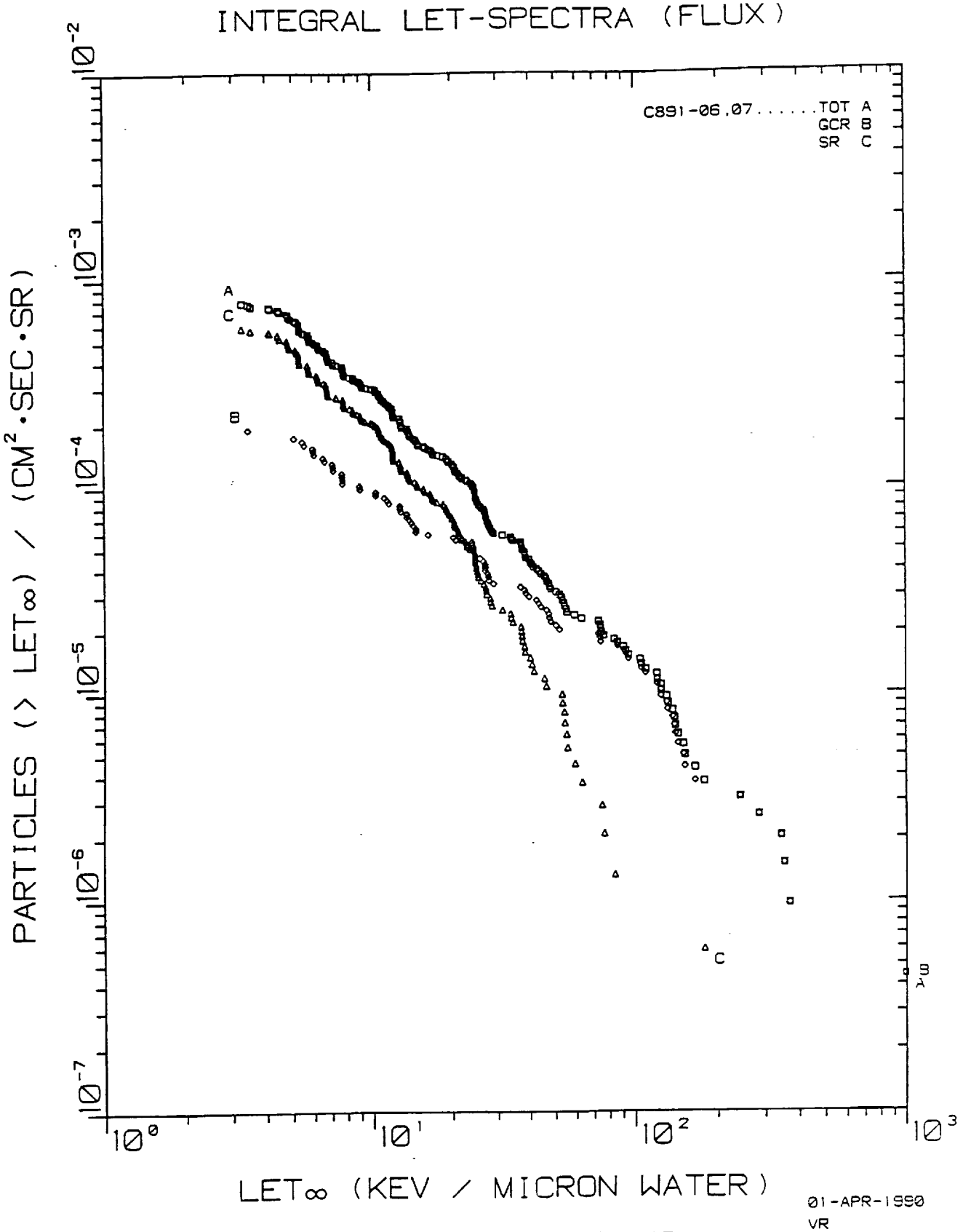

Fig. 18. Integral LET flux spectra for Exp. K-7-41B, PNTD stack F1 (outside the spacecraft). The minimum shielding was 0.397 g/cm^2 plastic.

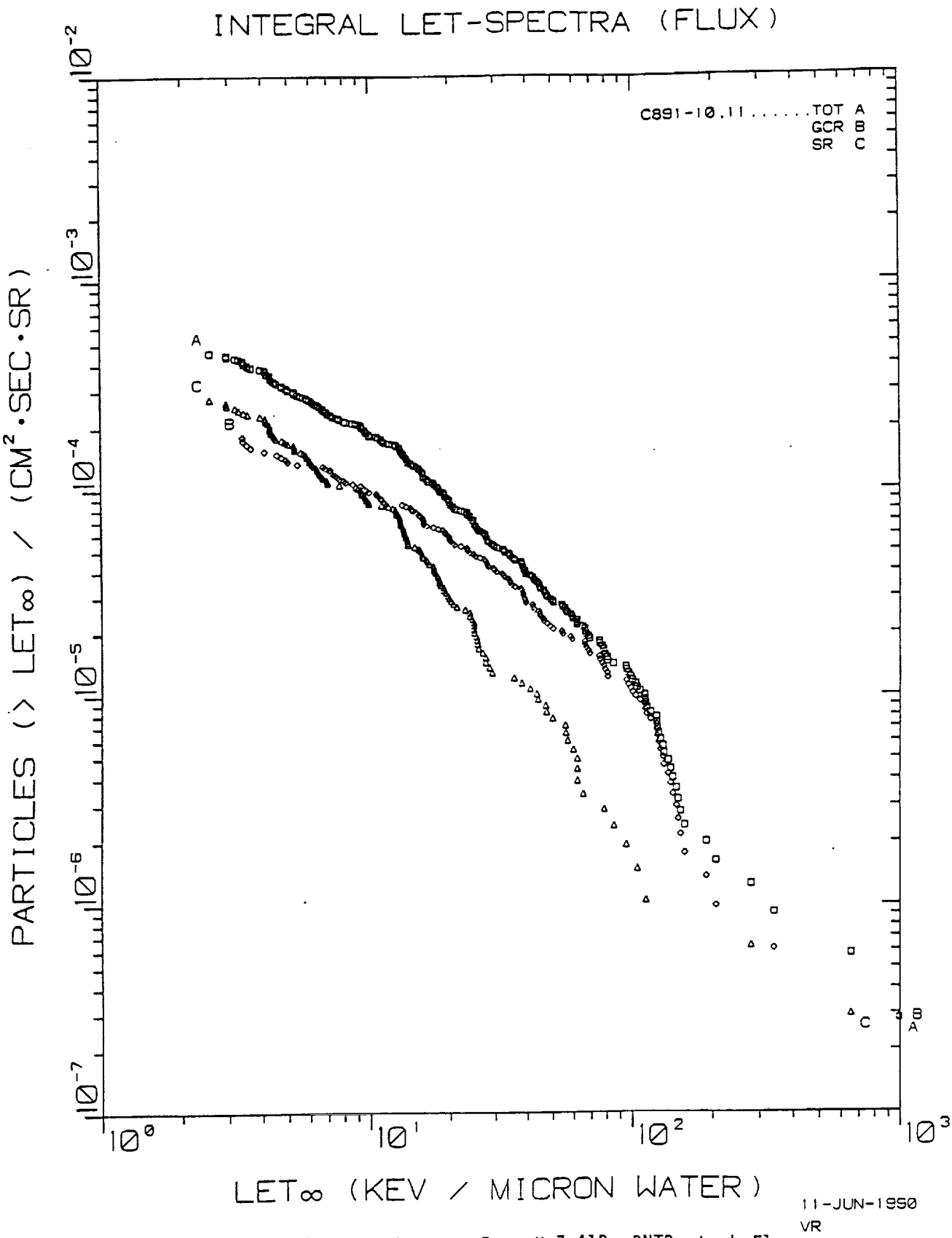

Fig. 19. Integral LET flux spectra for Exp. K-7-41B, PNTD stack F1 (outside the spacecraft). The minimum shielding was 1.47 g/cm^2 plastic, stainless steel and nuclear emulsion.

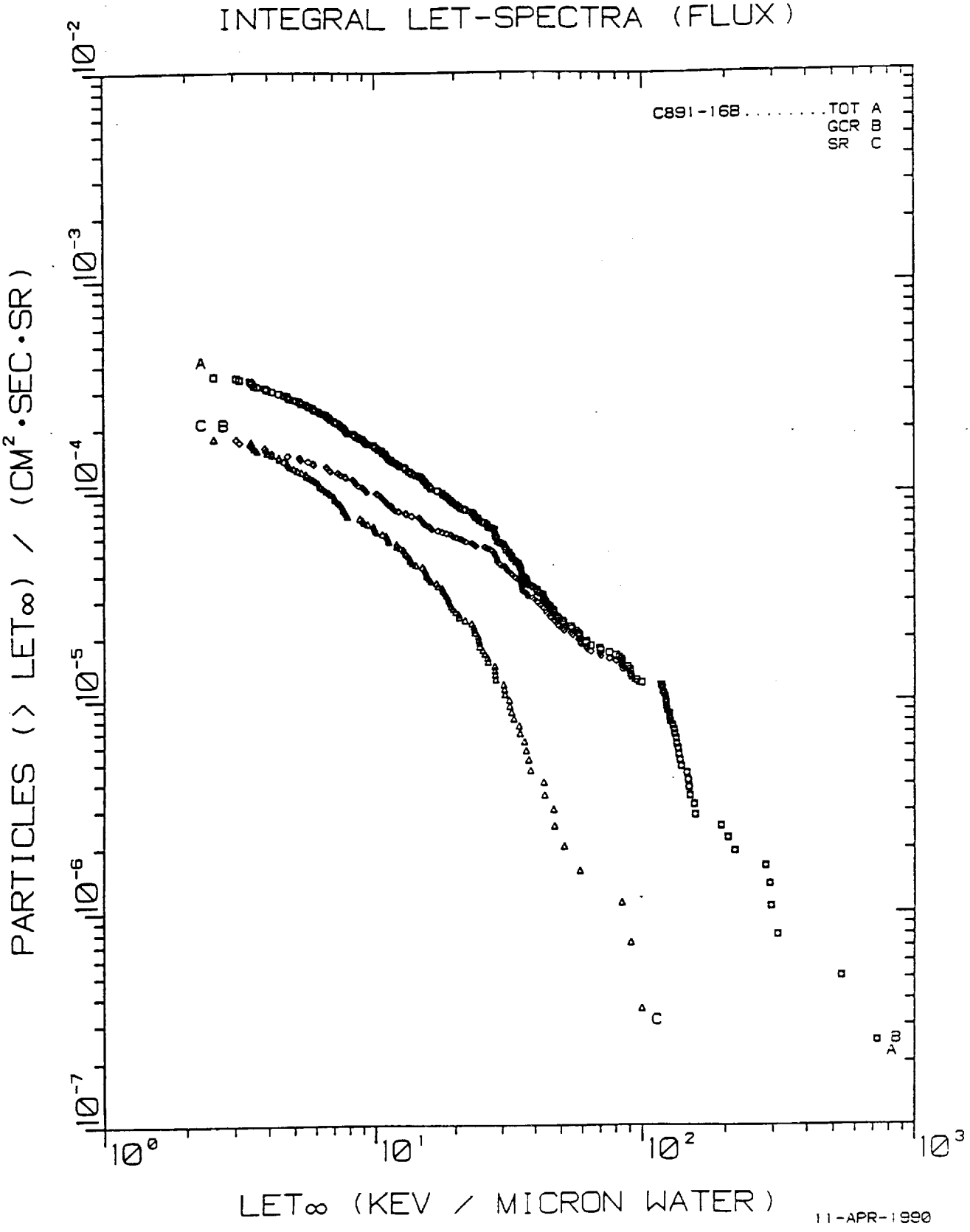

Fig. 20. Integral LET flux spectra for Exp. K-7-41B, PNTD stack F1 (outside the spacecraft). The minimum shielding was 1.95 g/cm^2 plastic, stainless steel and nuclear emulsion.

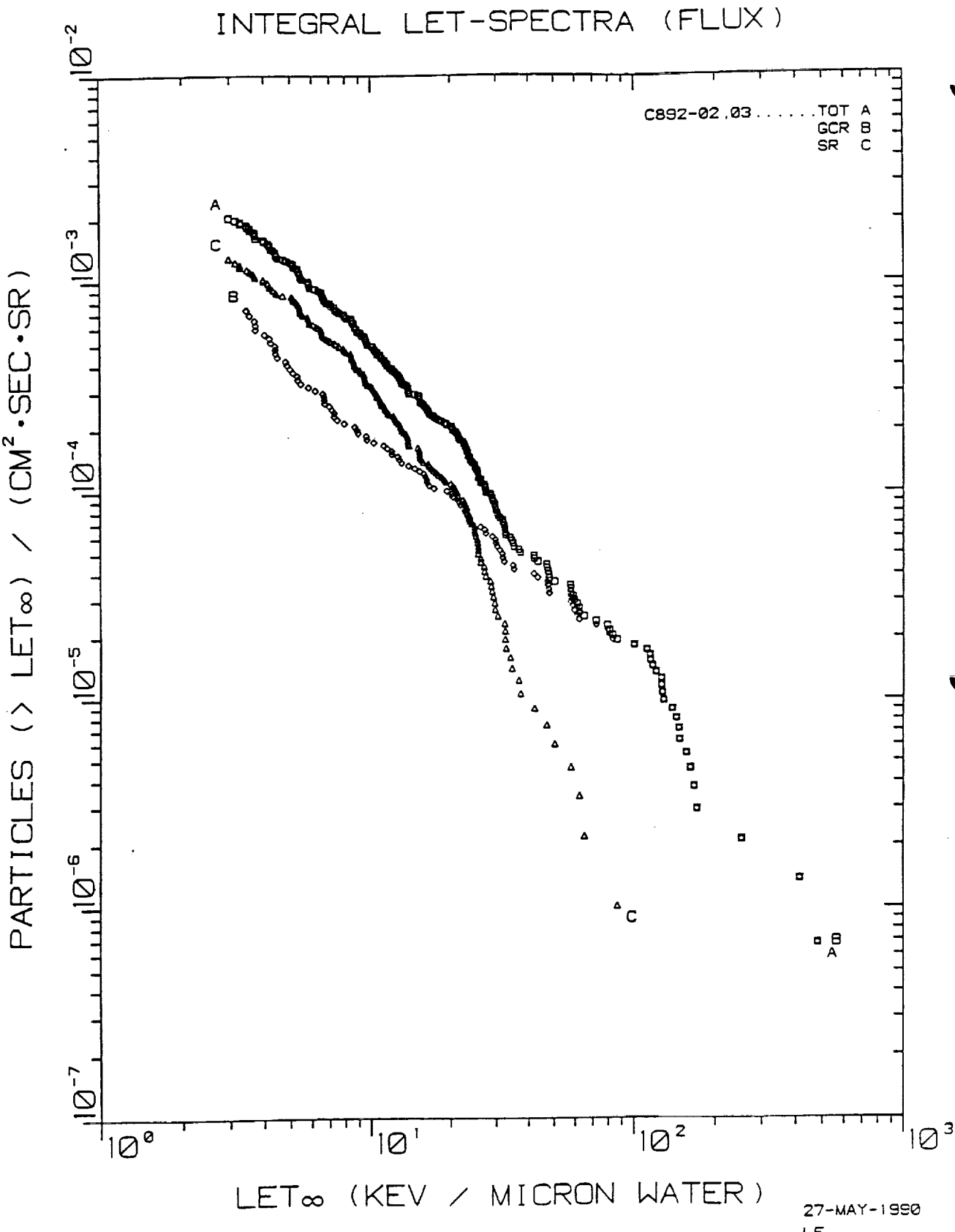

Fig. 21. Integral LET flux spectra for Exp. K-7-41B, PNTD Stack F2 (outside the spacecraft). The minimum shielding was 0.0935 g/cm^2 plastic.

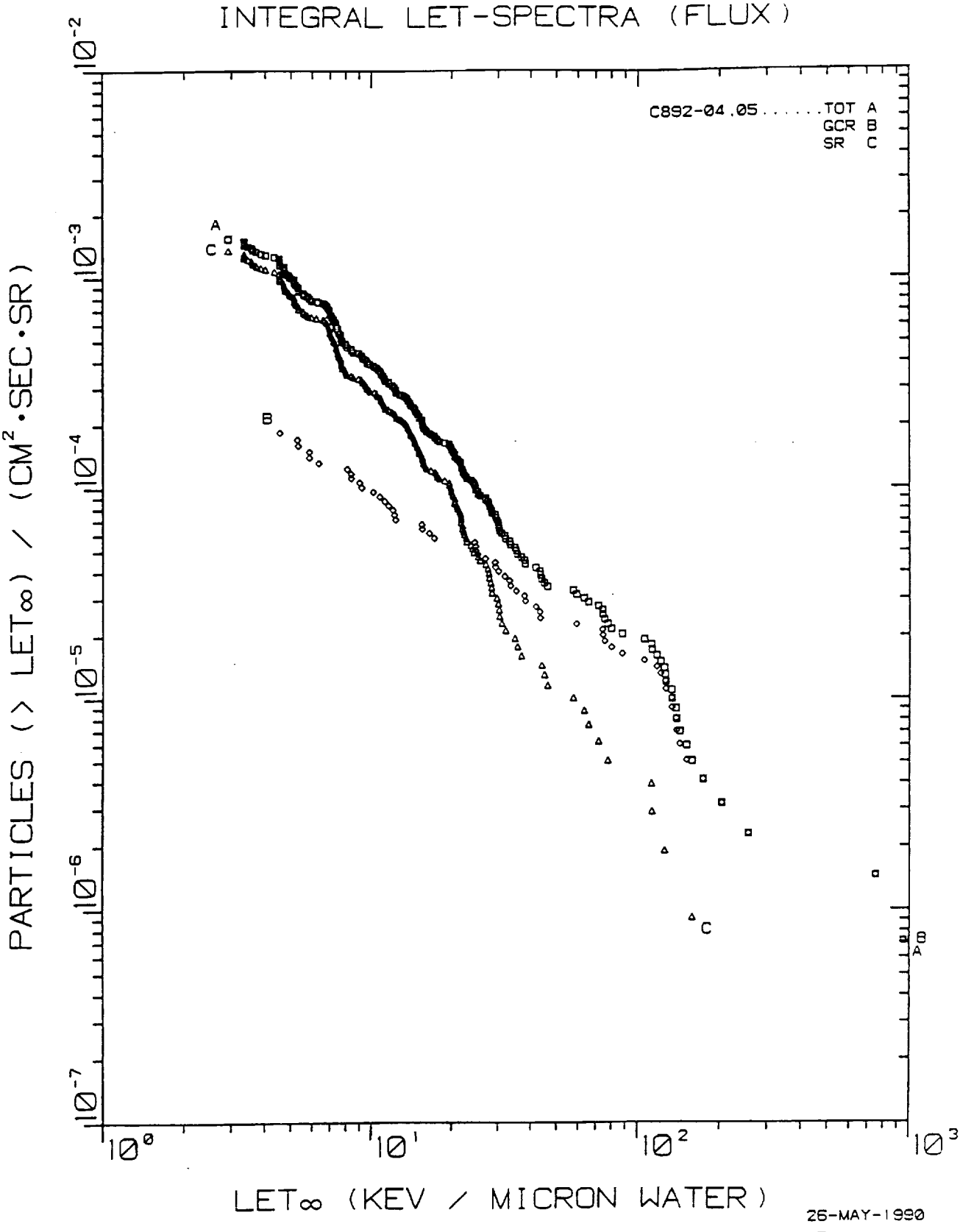

Fig. 22. Integral LET flux spectra for Exp. K-7-41B, PNTD stack F2 (outside the spacecraft). The minimum shielding was 0.250 g/cm² plastic.

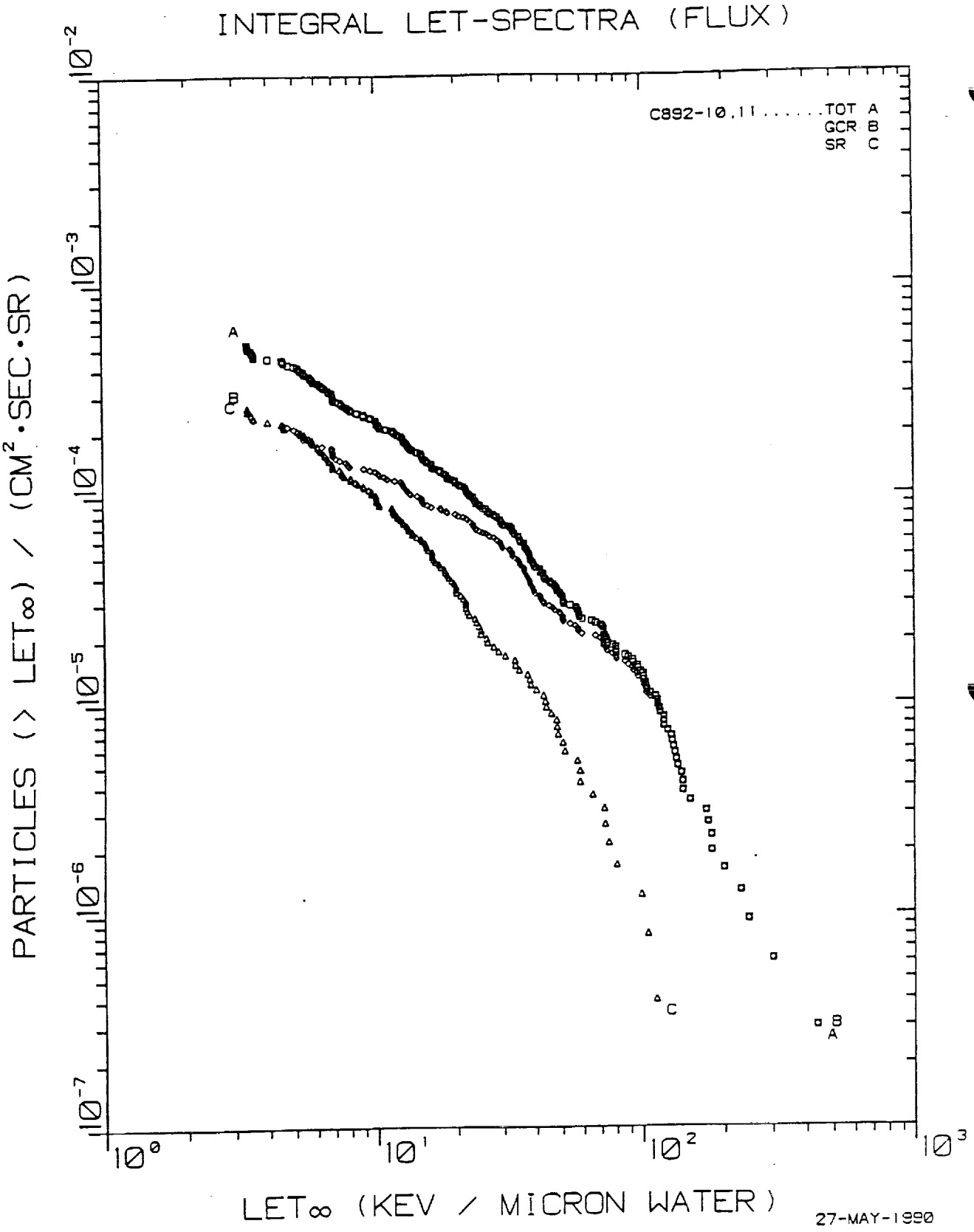

Fig. 23. Integral LET flux spectra for Exp. K-7-41B, PNTD stack F2 (outside the spacecraft). The minimum shielding was 1.49 g/cm^2 plastic, stainless steel and nuclear emulsion.

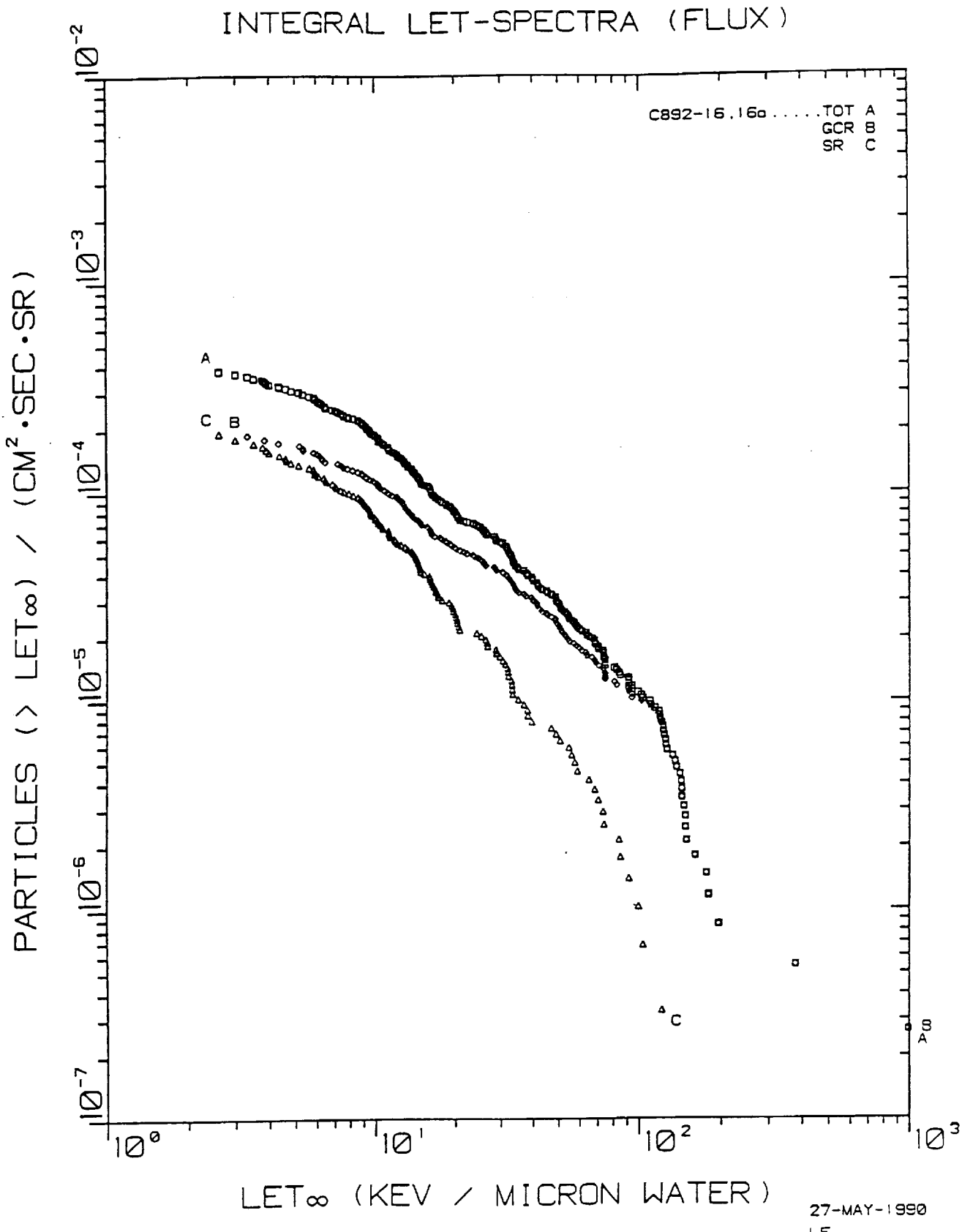

Fig. 24. Integral LET flux spectra for Exp. K-7-41B, PNTD stack F2 (outside the spacecraft). The minimum shielding was 1.97 g/cm^2 plastic, stainless steel and nuclear emulsion.

The decrease in total flux with increasing shielding thickness is obvious in both F1 and F2. However, the least shielded PNTD in F1 has a greater integral flux than that in F2 (factor of 1.7) despite being more heavily shielded. This demonstrates a directional dependence of incoming radiation with F1 (Plate B9-2 in Container KHA-1) being in better alignment with the direction of maximum flux than F2 (Plate B9-1 in Container KHA-3).

The integral measurements are given numerically in Tables 3a and 3b. The differences between F1 and F2 are seen to be greatest at small shielding thicknesses. A comparison of fluxes, dose rates and dose equivalent rates reveals that average particle LET increases with shielding thickness (dose rate/flux and dose equivalent rate/dose rate increase as average LET increases). This agrees with previous measurements on Cosmos 1887. The fraction of total flux due to SR particles decreases with shielding thickness, although this is irregular in F2. The above two observances are consistent with a more rapid filtering out of low energy protons than of higher Z particles with increasing shielding.

The nuclear emulsions which were a part of the detector stacks are still undergoing analysis and will be reported at a later time.

Part C

The ^{59}Co activation foils have been read out. Background studies and data analysis are still in progress. The results will be reported at a later time.

Part D

The measurement results from the ^{232}Th/mica fission foil detectors are given in Table 4. Each flight detector included eight mica discs (0.5 in diameter). The statistical standard deviations of the measurements were computed from the scatter of the eight counted track densities. There is a 15% difference between the neutron fluxes for the two flight units but this difference is within the limits of accuracy of the track counting statistics. The average dose equivalent rate of high energy neutrons for the mission was 3.3 mrem/d.

Part E

The results of the ^{6}LiF/CR-39 thermal and resonance neutron measurements are given in Table 5. An obvious feature is the much smaller resonance neutron dose in detector F1 as compared to F2. The CR-39 detectors both

TABLE 3a PNTD Results From K-7-41B*

Detector	Min. Shielding (g/cm^2)	Spectrum Type	Flux ($cm^{-2} \cdot s^{-1} \cdot sr^{-1}$) $\times 10^{-4}$	Dose Rate (mrad/d)	Dose Equiv.Rate (mrem/d)
F1	0.164	TOT	27.29	7.01	53.8
		GCR	2.11	1.66	23.9
		SR	25.18	5.35	29.9
	0.239	TOT	14.85	3.72	27.2
		GCR	2.02	0.94	10.1
		SR	12.83	2.78	17.1
	0.397	TOT	7.30	2.03	17.8
		GCR	1.72	0.94	12.0
		SR	5.58	1.09	5.8
	1.47	TOT	3.73	1.32	12.8
		GCR	1.52	0.79	9.0
		SR	2.21	0.53	3.8
	1.95	TOT	3.05	1.20	12.3
		GCR	1.52	0.86	10.3
		SR	1.53	0.34	2.0

*For $LET_{\infty} \cdot H_2O \geq 4$ keV/μm

Note: For the three least-shielded detectors the shielding materials were plastic. For the two detectors with greater shielding, the shielding material included 0.591 g/cm^2 of stainless steel and 0.120 g/cm^2 of nuclear emulsion.

TABLE 3b PNTD Results From K-7-41B*

Detector	Min. Shielding (g/cm^2)	Spectrum Type	Flux ($cm^{-2} \cdot s^{-1} \cdot sr^{-1}$) $\times 10^{-4}$	Dose Rate (mrad/d)	Dose Equiv.Rate (mrem/d)
F2	0.0935	TOT	15.83	3.35	23.3
		GCR	5.60	1.56	15.2
		SR	10.23	1.79	8.1
	0.250	TOT	12.74	2.89	22.9
		GCR	1.82	1.03	13.7
		SR	10.92	1.86	9.2
	1.49	TOT	4.47	1.53	13.9
		GCR	2.20	1.00	10.7
		SR	2.27	0.53	3.2
	1.97	TOT	3.27	1.22	11.6
		GCR	1.72	0.82	9.0
		SR	1.55	0.40	2.6

*For $LET_{\infty} \cdot H_2O \geq 4$ keV/μm

Note: For the two least shielded detectors the shielding materials were plastic. For the two detectors with greater shielding, the shielding material included 0.591 g/cm^2 of stainless steel and 0.120 g/cm^2 of nuclear emulsion.

TABLE 4

Experiment K-7-41D: High Energy Neutron Measurements with ^{232}Th/mica Detectors

Flight Detector	Neutron Fluence (cm^{-2})	Neutron Flux ($cm^{-2}d^{-1}$)	Dose Equiv. (mrem)	Dose Equiv. Rate (mrem d^{-1})
F1	$8.1\pm1.1\times10^{5}$	$5.9\pm0.8\times10^{4}$	48±7	3.5±0.5
F2	$7.0\pm1.1\times10^{5}$	$5.1\pm0.8\times10^{4}$	42±7	3.0±0.5

*Measurements are for neutron energies > 1 MeV

Note: The standard deviations of the measurements are those due to counting statistics only. The absolute accuracy is uncertain because of assumptions of neutron and proton spectral shapes and the ratio between neutron and proton fluxes which are used in the data reduction. The probable accuracy of the numbers is within a factor of 3.

TABLE 5

Experiment K-7-41E: Thermal and Resonance Neutron Measurements

Detector	Energy Range	Neutron / cm^2	Dose Equiv. (mrem)	Dose Equiv.Rate (mrem/d)
F1	≤0.2eV	$2.56\pm0.16\times10^{5}$	0.26±0.02	0.019±0.002
	0.2eV<E_n<1MeV	$0.99\pm1.16\times10^{5}$	0.49±0.59	0.036±0.041
F2	≤0.2eV	$2.23\pm0.16\times10^{5}$	0.23±0.02	0.017±0.002
	0.2eV<E_n<1MeV	$6.8\pm1.3\times10^{5}$	3.4 ±0.6	0.25 ±0.04
GC	≤0.2eV	$0.15\pm0.05\times10^{5}$	0.02±0.01	
	0.2eV<E_n<1MeV	$4.29\pm0.46\times10^{5}$	2.1 ±0.2	

Note: The standard deviations of the measurements are those due to counting statistics only. Probable accuracy is +/- 20% for thermal neutrons and a factor of 2 for resonance neutrons.

above (space side) and below (spacecraft side) the ^{6}LiF layer confirmed the difference. Most of the tracks measured in F2 were on the space side of the ^{6}LiF layer. The space side CR-39 yielded a track density 2.7 times higher than the spacecraft side CR-39. This could imply a large epithermal neutron flux, incident from the space side of detector F2, which was not present in detector F1. However, as mentioned in the Readout section, the background subtraction from the detectors contained an element of uncertainty. It is possible that the experimental uncertainty in the resonance neutron results is larger than expected. Because of the method of subtraction in the data reduction, the thermal neutron results are much less affected than the resonance results.

SUMMARY AND DISCUSSION

The results from Cosmos 2044 are compared with previous Cosmos measurements in Table 6. It is seen in the TLD results that in the total absorbed dose rates for tissue found outside the spacecraft there is a greater spread on Cosmos 2044 when compared to Cosmos 1887. The maximum dose rate (minimum shielding) is greater and the minimum dose rate (maximum shielding) is less. This indicates that the higher inclination, lower altitude orbit of 2044 must have encountered greater trapped electron fluxes but smaller trapped proton fluxes than 1887. The smaller trapped proton fluxes can be explained in that the lower altitude Cosmos 2044 orbit passed beneath the higher flux region in the South Atlantic Anomaly (SAA). The greater trapped electron fluxes are due to the extension of the electron belt horns to lower altitudes at the higher latitudes. The large uncertainties seen in the maximum and minimum dose rates on Cosmos 2044 are due to the spread in the three measurements of the TLD stacks in Plate No. B9-4.

The PNTD measurements on Cosmos 2044 are directly comparable with those of Cosmos 1887 outside the spacecraft. It can be seen that while the maximum flux on 2044 is 0.80 times as high as on 1887, the dose equivalent rate is 1.75 times higher. The average LET, and also particle Z, were greater on Cosmos 2044. This is consistent with the higher inclination, lower altitude orbit and the resulting greater relative contribution from GCRs.

The thermal and resonance neutron fluxes and dose equivalent rates were less than previously measured, but on Cosmos 2044 the measurements were

TABLE 6. RADIATION MEASUREMENTS ON JOINT US/USSR COSMOS FLIGHTS

FLIGHT NO.	782	936	1129	1887	2044
Launch Date	Nov. 1975	Aug. 1977	Sept. 1979	Sept. 1987	Sept. 1989
Duration (d)	19.50	18.50	18.56	12.63	13.80
Inclination (°)	62.8	62.8	62.8	62.8	82.3
Altitude (km)-- Apogee/Perigee	405/226	419/224	394/226	406/224	294/216
TLD DOSE RATE					
Outside (max) (mrad d^{-1})				$1.78\pm0.19\times10^{5}$	$2.52\pm0.50\times10^{5}$
Outside (min) (mrad d^{-1})				28.0 ± 1.4	8.3 ± 0.6
Inside (mrad d^{-1})		25.6 ± 1.3	$18.0\pm3.6^{\dagger\dagger}$	24.8 ± 1.0	
HEAVY PARTICLES					
Flux Inside ($cm^{-2}s^{-1}sr^{-1}$)	$8.7\pm1.4\times10^{-6}$*	$5.1\pm1.0\times10^{-6}$$^{\Delta}$	$6.1\pm0.1\times10^{-7}$$^{\nabla}$	$4.25\pm0.24\times10^{-4}$†	
Flux Outside ($cm^{-2}s^{-1}sr^{-1}$)			$1.21\pm0.02\times10^{-6}$$^{\nabla}$	$3.43\pm0.22\times10^{-3}$†	$2.73\pm0.17\times10^{-3}$
Dose Equivalent Rate Inside (mrem d^{-1})				11.4 ± 0.7	
Outside (mrem d^{-1})				30.8 ± 2.0	53.8 ± 3.6
NEUTRONS					
Thermal Flux (cm^{-2} d^{-1})		$1.9\pm0.4\times10^{4}$	$2.7\pm0.5\times10^{4}$		$1.7\pm0.4\times10^{4}$
Resonance Flux (cm^{-2} d^{-1})		$6.5\pm3.2\times10^{4}$	$7.5\pm3.8\times10^{4}$		$5.0\pm2.5\times10^{4}$
High Energy Flux (cm^{-2} d^{-1})		$1.1\pm---\times10^{5}$	$1.1\pm---\times10^{5}$		$5.5\pm---\times10^{4}$
Thermal Dose (mrem d^{-1})		0.020 ± 0.004	0.028 ± 0.006		0.018 ± 0.004
Resonance Dose (mrem d^{-1})		0.32 ± 0.16	0.40 ± 0.20		0.25 ± 0.13
High Energy Dose (mrem d^{-1})		$6.8\pm?$	$6.8\pm?$		$3.3\pm?$

*$LET_{\infty}\cdot H_2O \geq 105$ keV μm^{-1}; >100 μm range. $^{\Delta}LET_{\infty}\cdot H_2O \geq 106$ keV μm^{-1}; >180 μm range.
$^{\nabla}$Different processing; results not comparable to other flights.
$^{\dagger}LET_{\infty}\cdot H_2O \geq 4$ keV μm^{-1}; >100 μm range. ††Detectors irradiated during return transportation

on the outside of the spacecraft, while previous measurements were inside. Their comparability is therefore questionable.

The high energy neutrons have about half the flux and dose rate measured on Cosmos 936 and 1129; however, this comparison is also between detectors outside and inside the spacecraft.

In Figure 25, a measured depth dose profile in TLD-700 is compared with calculated depth doses for trapped electrons and protons behind plane aluminum shields for the Cosmos 2044 orbit at solar maximum /Watts, 1990/. This demonstrates that for shielding thicknesses up to 1 g/cm^2 trapped electrons contribute most of the dose. The model electron spectrum appears deficient at very low energies and somewhat harder than that measured. The trapped proton dose rate drops to about 0.001 rad/d at 3 g/cm^2, where the electron dose is a very small fraction of the total. This is a factor of 8 lower than the measurements. GCRs dominate total doses under thicker shielding for the Cosmos 2044 orbit, so this general result is expected.

In Figures 26 and 27, measured LET spectra under 0.0935 g/cm^2 are plotted with some recent calculations made with the NRL CREME code. In Figure 26, an SR spectrum is compared with calculations which omit GCRs with Z > 2. Most of the contributions to short-range tracks are included in these calculations. The fit below 100 MeV-cm^2/g (10 keV/μm) begins to diverge, but, as discussed above, the experimental measurements can also diverge in this LET region due to directional effects. The calculations are averaged over angle of incidence.

In Figure 27, the total flux spectrum is compared with calculations which include the GCRs through Z=28 (the contribution from particles with Z > 28 is insignificant). The measured spectrum falls somewhat below the spectrum for the nearest calculated shielding (0.1 g/cm^2). It should be noted that there is some loss from the measured spectrum due to loss of very short tracks in etching of the PNTDs. However, the agreement between measurements and calculations may be off by a factor of 2 because of basic difficulties in modeling the orbital radiation environment.

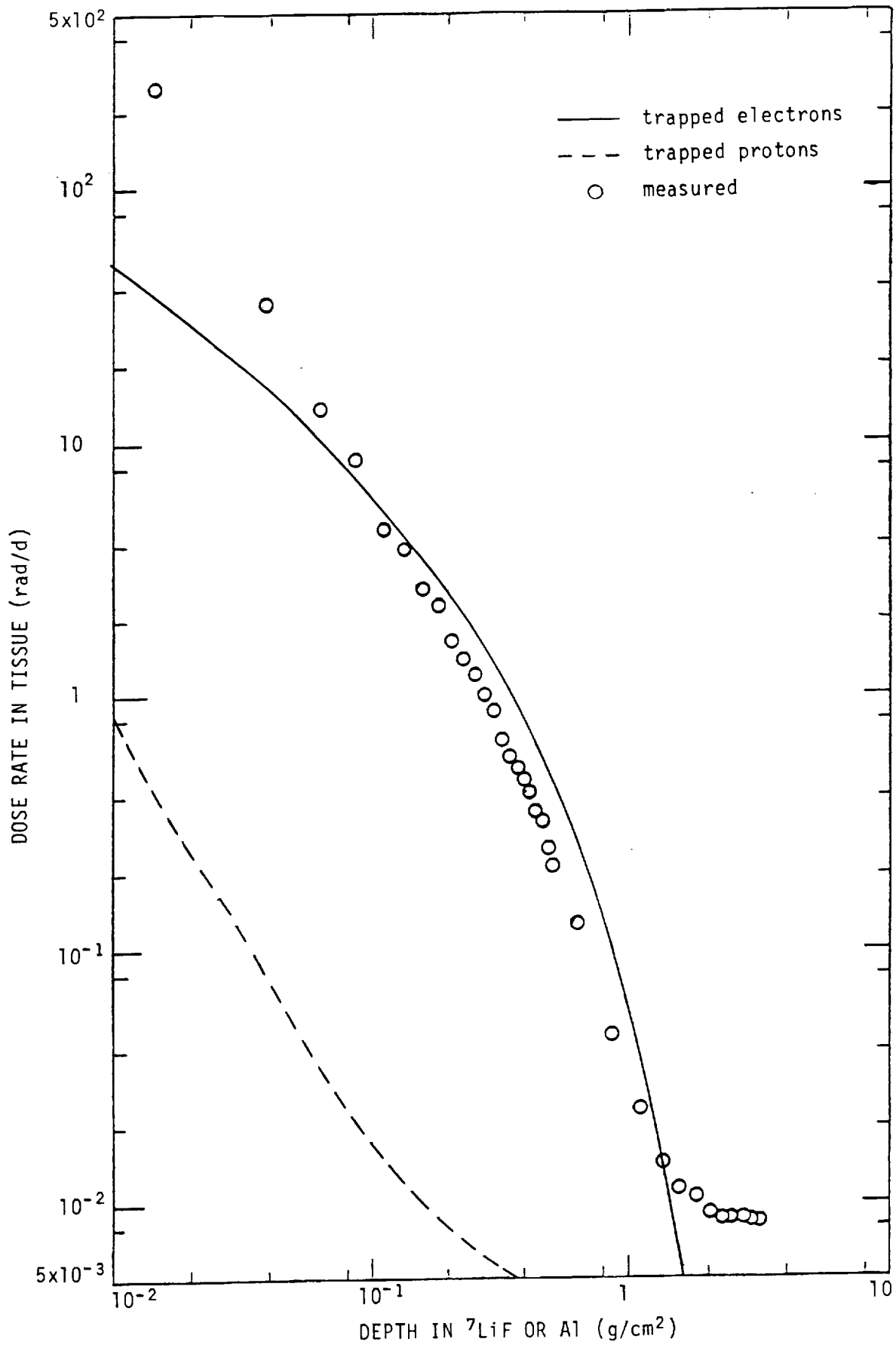

Fig. 25. Comparison of the average TLD dose rates in Plate No. B9-4 with the calculated depth dose rates of trapped electrons and protons for tissue behind aluminum plane shields /Watts, 1990/. The calculations were for the Cosmos 2044 orbit at solar maximum.

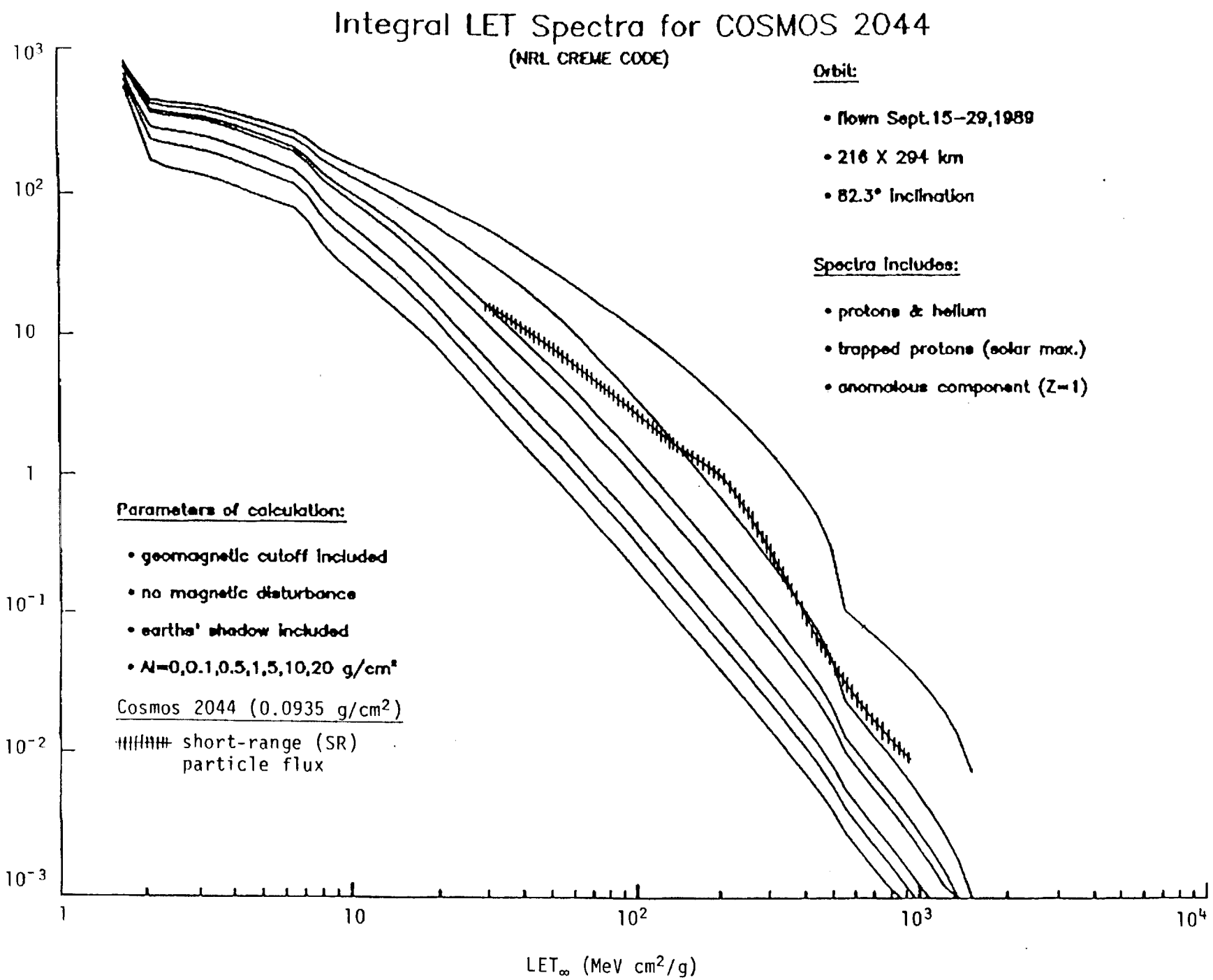

Fig. 26. Comparison of a measured Cosmos 2044 SR flux spectrum (in H_2O) with the calculated spectra (in Si) of John Watts /1990/ for Al shielding of 0–20 g/cm² and for the Cosmos 2044 orbit.

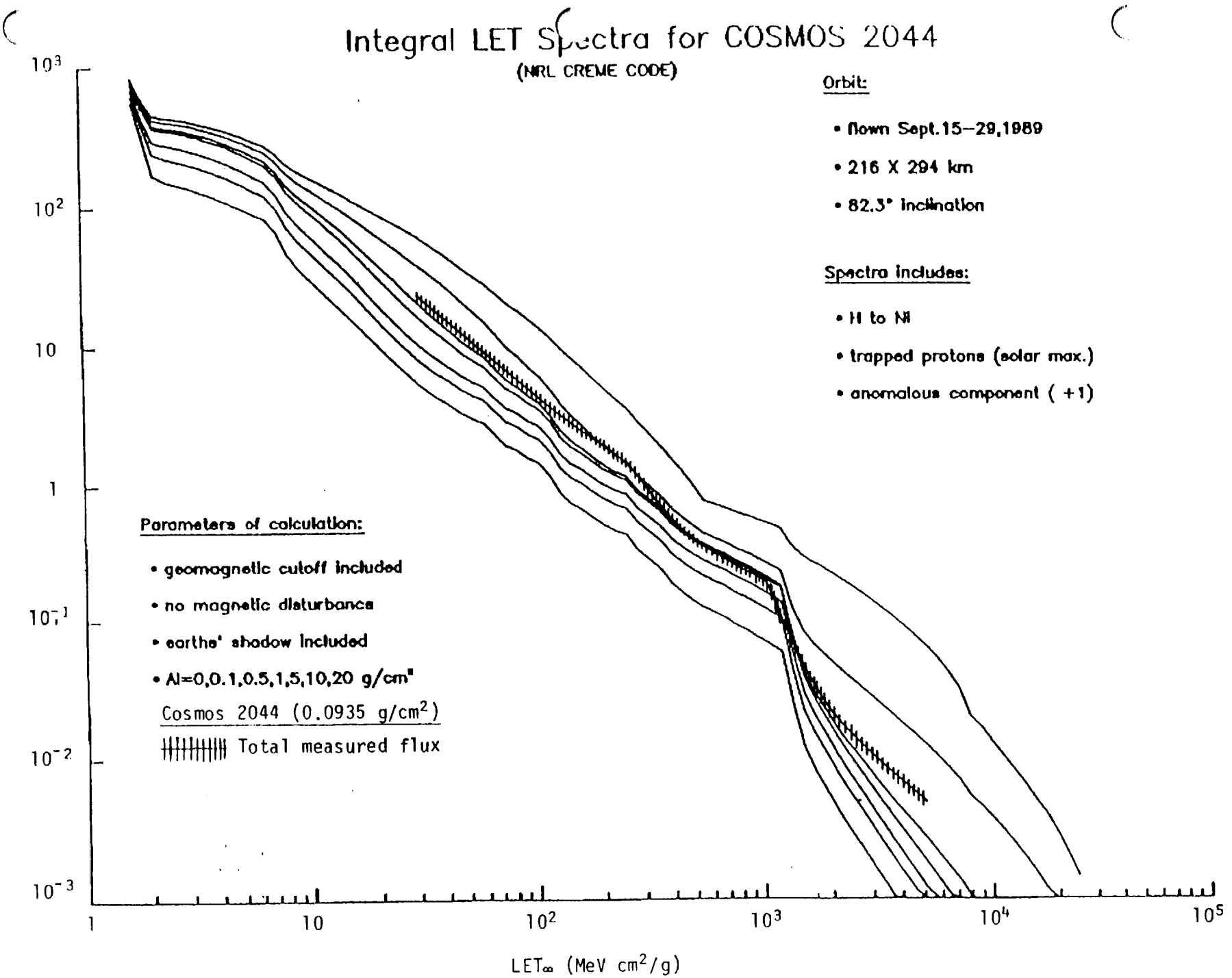

Fig. 27. Comparison of a measured Cosmos 2044 Total flux spectrum (in H_2O) with the calculated spectra (in Si) of John Watts /1990/ for Al shielding of 0–20 g/cm² and for the Cosmos 2044 orbit.

REFERENCES

Benton, E.V., Peterson, D.D., Bailey, J.V. and Parnell, T.A. (1977a), High-LET exposure of Skylab astronauts, *Hlth. Phys.* **32**, 15-20.

Benton, E.V., Henke, R.P. and Peterson, D.D. (1977b), Plastic nuclear track detector measurements of high-LET particle radiation on Apollo, Skylab, and ASTP space missions, *Nucl. Track Det.* **1**, 27-32.

Benton, E.V., Cassou, R.M., Frank, A.L., Henke R.P. and Peterson, D.D. (1978a), Experiment K206: Space radiation dosimetry on board Cosmos 936–U.S. portion of Experiment K206, in: Final Reports of U.S. Experiments Flown on the Soviet Satellite Cosmos 936 (Rosenzweig, S.N. and Souza, K.A., eds.) NASA TM 78526.

Benton, E.V., Peterson, D.D., Marenny, A.M. and Popov, V.I. (1978b), HZE particle radiation studies aboard Cosmos 782, *Hlth. Phys.* **35**, 643-648.

Benton, E.V., Henke, R.P., Frank, A.L., Johnson, C.S., Cassou, R.M., Tran, M.T. and Etter, E. (1981), Experiment K309: Space radiation dosimetry aboard Cosmos 1129: U.S. portion of experiment, in: Final Reports of U.S. Plant and Radiation experiments flown on the Soviet satellite Cosmos 1129 (Heinrich, M.R. and Souza, K.A., eds.), NASA TM 81288.

Benton, E.V. and Henke, R.P. (1983), Radiation exposures during spaceflight and their measurement, *Adv. Space Res.* **3**, No. 8, 171-185.

Benton, E.V. (1984), Summary of current radiation dosimetry results on manned spacecraft, *Adv. Space Res.* **4**, 153-160.

Benton, E.V., Frank, A.L., Parnell, T.A., Watts, J.W., Jr. and Gregory, J.C. (1985), Radiation environment of Spacelab-1, American Inst. of Aeronautics and Astronautics conference, *AIAA Shuttle Environment and Operations II*, Houston, TX, Nov. 13–15.

Benton, E.V. (1986), Summary of radiation dosimetry results on U.S. and Soviet manned spacecraft, *Adv. Space Res.*, **6**, No. 11, 315-328.

Benton, E.V. and Parnell, T.A. (1988), Space radiation dosimetry on U.S. and Soviet manned missions, in: *Terrestrial Space Radiation and its Biological Effects*, P.E. McCormack, C.E. Swenberg and H. Buecker, eds., NATO ASI Series A, Life Sciences 154, N.Y.: Plenum Press, pp. 729-794.

Benton, E.V., Frank, A.L., Benton, E.R., Dudkin, V.E. and Marenny, A.M. (1988), Radiation Experiments on Cosmos 1887, University of San Francisco, USF-TR-74.

Dobson, P.N., Jr. and Midkiff, A.A. (1970), Explanation of supralinearity in thermoluminescence of LiF in terms of the interacting track model, *Hlth. Phys.* **18**, 571-573.

Gorbics, S.G., Attix, F.H. and Kerris, K. (1973), Thermoluminescent dosimeters for high-dose applications, *Hlth. Phys.* **25**, 499-506.

Kovalev, E.E., Benton, E.V. and Marenny, A.M. (1981), Measurement of LET spectra aboard Cosmos 936 biological satellite, *Rad. Prot. J.* **1**, 169-173.

NASA-Space Life Sciences Payloads Office (1989), ATR-4 Ambient Temperature Recorder, Doc. No. A7SP-8801-D1, Ames Research Center, Moffet Field, California.

Peterson, D.D., Benton, E.V. and Tran, M. (1978), K103: HZE particle dosimetry, in: Final Reports of U.S. Experiments Flown on the Soviet Satellite Cosmos 782,(Rosenzweig, S.N. and Souza, K.A., eds.), NASA TM 78525.

Watts, J.W., Jr. (1988, 1990), Marshall Space Flight Center, Huntsville, Alabama, private communication.

APPENDIX W

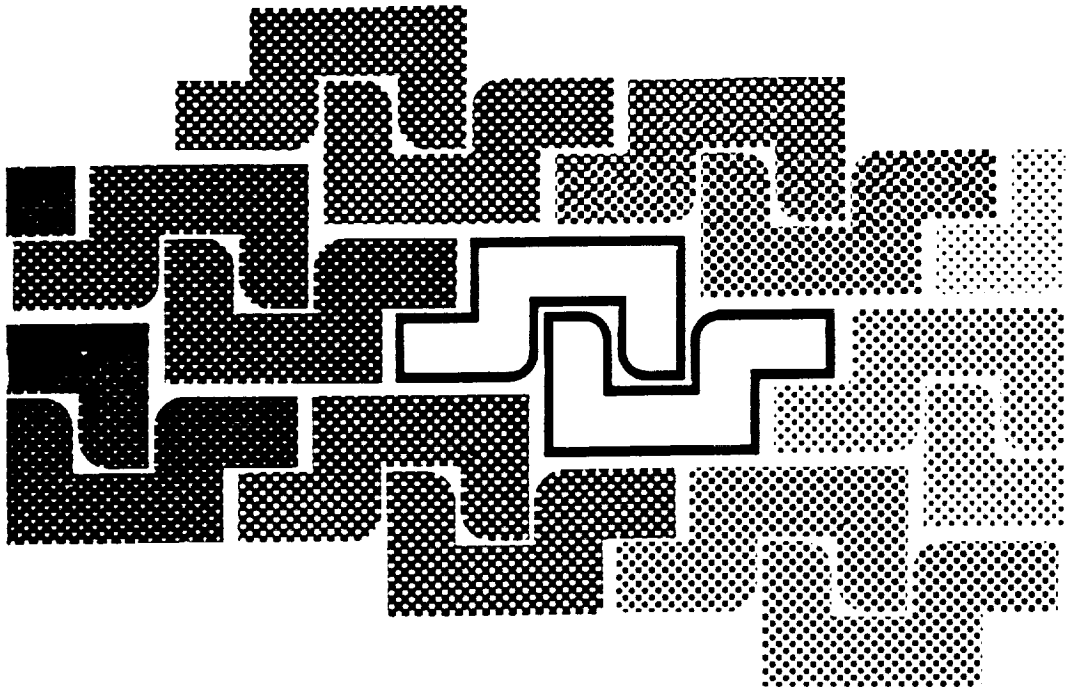

Terrestrial Space Radiation and Its Biological Effects

Edited by
Percival D. McCormack
Charles E. Swenberg and
Horst Bücker

NATO ASI Series

1988

SPACE RADIATION DOSIMETRY ON U.S. AND SOVIET MANNED MISSIONS

E. V. Benton
University of San Francisco

T. A. Parnell
NASA-Marshall Space Flight Center

NATO Advanced Study Institute
Corfu, Greece: 11-25 October 1987

Published in: NATO ASI Series A, Life Sciences, v.154
"Terrestrial Space Radiation and its Biological Effects,"
P. D. McCormack, C. E. Swenberg and H. Bücker, eds.,
Plenum Press, New York (1988), pp. 729-794

SPACE RADIATION DOSIMETRY ON U.S. AND SOVIET MANNED MISSIONS[1]

E. V. Benton* and T. A. Parnell**

*Department of Physics, University of San Francisco Ignatian Heights, San Francisco, CA 94117, U.S.A.
**NASA Marshall Space Flight Center, Huntsville, AL 35812, U.S.A.

ABSTRACT

Radiation measurements obtained on board U.S. and Soviet spacecraft are presented and discussed. A considerable amount of data has now been collected and analyzed from measurements with a variety of detector types in low-Earth orbit. The objectives of these measurements have been to investigate the dose and LET spectra within the complex shielding of large spacecraft. The shielding modifies the external radiation (trapped protons, electrons, cosmic ray nuclei) which, in turn, is quite dependent on orbital parameters (altitude, inclination). For manned flights, these measurements provide a crew exposure record and a data base for future spacecraft design and flight planning. For the scientific community they provide useful information for planning and analyzing data from experiments with high sensitivity to radiation. In this paper, results of measurements by both passive and active detectors are described. High-LET spectra measurements were obtained by means of plastic nuclear track detectors (PNTDs) while thermoluminescent dosimeters (TLDs) measured the dose. A few flights carried active detectors--tissue equivalent ion chambers (TEICs), particle spectrometers (generally to measure the LET distribution), and particle rate counters. On some flights, thermal and epithermal neutrons were measured with the use of fission foils, and metal samples analyzed by gamma ray spectroscopy measured low levels of several activation lines. PNTDs consisting of different combinations of CR-39, polycarbonate, and cellulose-nitrate sheets have proved to be an effective means of measuring the high-LET spectra. To date, they have been used on all the Space Shuttle flights including Spacelabs 1 and 2,

[1]Work partially supported by NASA Contract NAS9-17389 and NASA Grants NAG8-071 and NAG9-235.

and the earlier missions of the Gemini, Apollo and Skylab series. The assembly of various types of detectors, especially the large numbers deployed in the crew compartments, modules, access tunnels, and pallets of Spacelabs 1 and 2, have provided the most comprehensive mapping yet available of the radiation environment of a large spacecraft in low Earth orbit. They demonstrate the efficiency and advantages of coordinated measurements with passive and active detectors. The dosimetric results accumulated for over twenty-five years indicate the difficulty of accurately predicting the total picture of radiation phenomena as it will be encountered by space station crews and other future missions. Understanding the effects of different types and configurations of shielding is also of particular importance. Detailed results of the measurements and comparison with calculated values are described.

Keywords: Space radiation / U.S. and Soviet measurements / radiation dose / LET spectra / shielding / detectors / dosimetry /

1.0 INTRODUCTION

Exposure to ionizing radiation of space crews engaged in long-term space missions such as space stations, moon bases and trips to Mars, poses a set of complex scientific and technological problems which need to be resolved before adequate radiation protection can be achieved. Areas of immediate interest include providing adequate radiation measurements (i.e., dosimetry) and understanding the complex radiation environment and the effects of shielding on the different components of the incoming radiations. This paper summarizes the results of radiation dosimetry measurements which have been performed in the last twenty-five years in the U.S. and Soviet space flight programs.

The complex radiation environment and special conditions involved in space flight pose unique problems in the dosimetry of high energy radiation. First of all, there are a number of primary sources of radiation including galactic cosmic rays, radiation trapped by the Earth's geomagnetic field, rare but sometimes intense solar flares and, potentially, that from nuclear on-board sources. These radiations have broad energy spectra and may contain a variety of charged particle types such as protons, electrons, alpha particles and photons, as well as heavier nuclei including those of the entire periodic table. A gamut of secondary radiations includes mesons, neutrons, recoiling nuclei; also bremsstrahlung, π^0 decay, and activation photons. These radiations have a spatial and temporal variation which can result in orders of magnitude changes of radiation levels inside spacecraft. For low-Earth orbit the fluxes and energy spectra are dependent on altitude,

orbit inclination, solar conditions, position, and spacecraft orientation in orbit, and the amount, type and placement of shielding materials in the spacecraft. Since the equipment and supplies are usually unevenly distributed throughout the spacecraft, different radiation levels are found in the different portions of the spacecraft, as well as uneven radiation of various parts of the astronauts' bodies. The degree of non-uniformity depends upon the penetrating ability of radiation and can result in steep gradients of absorbed dose within the body. Finally, while some secondary radiation is less penetrating, in certain circumstances secondary radiations may have even greater penetrability than the primary; for example, in the situation involving the attenuation of low-energy electrons by the skin of the spacecraft and subsequent production of penetrating bremsstrahlung radiations /Parnell et al., 1986; Benton, 1986/.

2.0 DOSE AND DOSE-RATE (Mostly Passive Detectors)

For the past twenty-five years, a variety of spacecraft have been developed and used by the U.S. and U.S.S.R. In order to present an idea of the shielding involved, Fig. 1 shows (roughly to scale) the three earliest Soviet spacecraft, namely Vostok, Voskhod and Soyuz, and one of the latest space-station types of spacecraft, the Salyut-7, which is shown not to scale.

The weight and dimensions of the early spacecraft (not including antennas, solar cell banks, or panels) are (1) Vostok: about 10,400 lbs., 8.7 feet in diameter, 23.8 feet in length; the manned capsule is 7.5 feet in diameter; (2) Voskhod: about 12,000 lbs., 9.0 feet in diameter, 34.5 feet in length; the manned capsule is 7.5 feet in diameter; (3) Soyuz: 11.4 feet in diameter; the aft interstage is 14.8 feet in diameter; the length is 40.2 feet with a manned capsule 10.3 feet in diameter/Janni, 1969a/. The Salyut-7 section shown is about 15 meters in length, excluding the transport ships and a new module which was added later. With the addition of the new module and a Soyuz P-14 manned transport, the Salyut complex stretches for some 115 feet and has a mass of approximately 103,000 lbs.; it also includes a Gemini spacecraft-sized re-entry vehicle. Clearly, the size, mass and therefore the effective shielding within the different spacecraft vary greatly. While knowledge of the exact shielding is always somewhat poor, for the pre-Salyut flights the shielding (arithmetic average) generally exceeded 17 g/cm^2 /Petrov et al., 1975/.

2.1 Soviet Measurements

In Table 1 is shown some of the dosimetry data from Soviet spacecraft for the time period 1960-1983 /Petrov et al., 1975; Akatov et al., 1984; Markelov and Chernykh, 1982/. Most of the average dose-rate data is in the

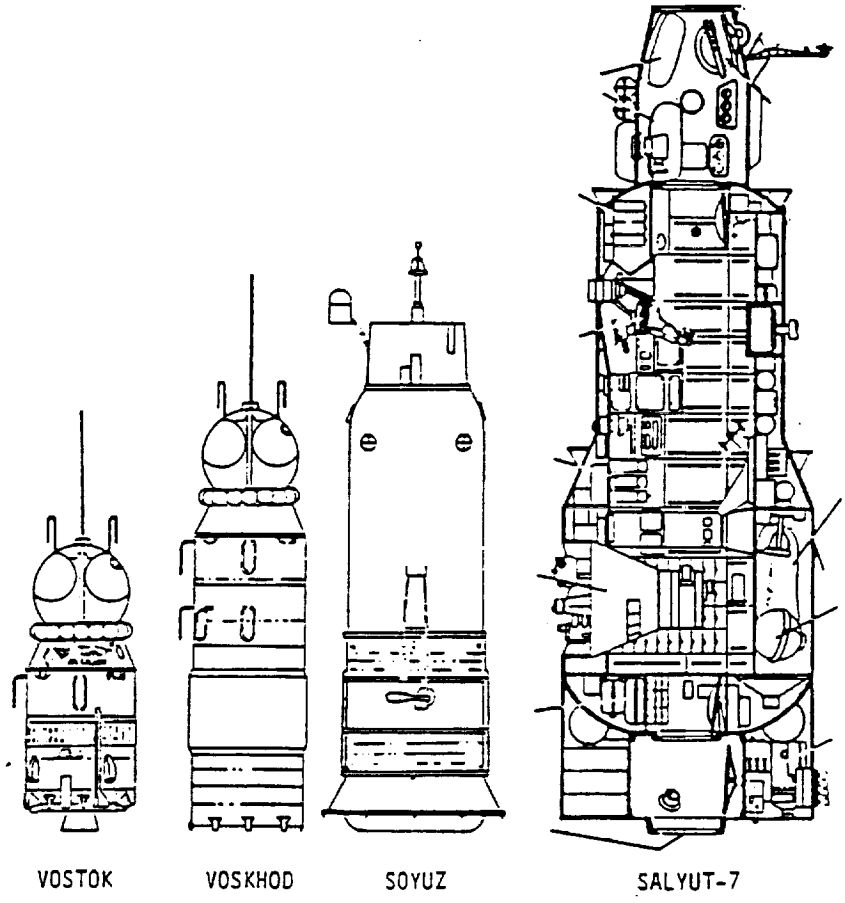

Fig. 1. Four types of Soviet manned spacecraft /Janni, 1969/. (Salyut not drawn to scale with other three.)

range of 10-30 mrad/day and reflects the fact that the Soviet manned spacecraft have consistently flown in fairly low-altitude orbits. The main exception to that was the 1965 flight with an apogee of 500 km which recorded a higher dose of 65 mrads per day, still well below that which has been recorded on a number of U.S. flights. The measurements in Table 1 were performed with a variety of active and passive types of devices, with the early measurements being accurate to about +/- 15 percent. From these early measurements, the Soviets concluded that they had observed dependence of dose-rate on the period of solar activity, noting that "during the 1964 solar minimum the dose-rates increased by roughly a factor of two." Also, "increasing the shielding from 2 to 15 g/cm^2 did not greatly decrease the dose-rate"/Petrov et al., 1975/. This again is partially a consequence of the low altitude (see Section 3.1).

Table 1. Dosimetry Data from Soviet Spacecraft

Date		Orbital Parameters			Average Dose Rate (mrad/day)
month	year	inclination	apogee (km)		
08*	1960	65°	340		12.5
04	1961	65°	330		7.2
08	1961	65°	240		8.4
05	1962	65°	330		16.0
08	1962	65°	370		45.0
08	1962	65°	240		13.5
10	1962	65°	350		30.0
11	1962	65°	380		30.0
12	1962	65°	400		35.0
04	1963	65°	340		18.0
05	1963	65°	370		15.0
05	1963	65°	400		30.0
06	1963	65°	300		12.0
06	1963	65°	220		15.5
06	1963	65°	230		15.5
10	1964	65°	410		29.0
04	1965	65°	500		65.0
09	1965	65°	360		16.0
10	1965	65°	340		15.0
11	1965	65°	350		18.0
03	1966	65°	310		11.0
04	1966	65°	330		15.5
07	1966	73°	350		21.0
07	1966	52°	360		26.0
08	1966	65°	360		29.0
11	1966	65°	340		22.0
12	1966	65°	320		14.0
11	1968	52°	∿210		21.2
01	1969	52°	∿210		20.0
01	1969	52°	∿210		24.0
10	1969	52°	∿210		14.0
10	1969	52°	∿210		13.0
10	1969	52°	∿210		14.0
06	1970	52°	∿210		13.0
12	1973	52°	∿210		12.5
07**	1974	51.6°	270	Salyut-3	15
12	1974	51.6°	270	Salyut-4	13
06	1976	51.6°	260	Salyut-5	15
09	1977	51.6°	275	Salyut-6	16
05-06†	1980	---	---	Salyut-6	10.0
03-07	1983	51.6°	340	Salyut-7	16.7
07-08	1983	51.6°	340	Salyut-7	14.8
08-09	1983	51.6°	340	Salyut-7	18.0
09-11	1983	51.6°	492	Salyut-7	16.0

*Petrov et al., 1975
**Akatov et al., 1984
†Markelov and Chernykh, 1982

In Table 2 are listed the absorbed and equivalent radiation doses for the crews of Salyut 3-6 spacecraft, while Table 3 lists the doses incurred by members of the international crews on board Salyut-6 under the Intercosmos Programme /Vorobyov and Kovalyov, 1983/. Some of the Salyut-7 data was taken using the Hungarian "Pille" TLD system and has a considerably higher accuracy /Akatov et al., 1984/. In Fig. 2 is shown the range of average dose-rates (mrad-day) measured on board Salyut-7 in various positions within the spacecraft during the three measuring sessions of 36, 28 and 49 days duration. The numbers shown in Fig. 2 represent the lowest and the highest average dose-rate measured during these three sessions in each position. The measurements, which were performed in the second half of 1983, show that for Salyut-7 as well as for Salyut-6 spacecraft, in this particular orbit, the largest ratio of dose-rates within the spacecraft was about 1.6.

The highest dose-rates were found in the passage section on the left (16-23 mrad/day), and in one of the sleeping areas on the right (17-21 mrad/day). This was only a few feet away from the position of the work station on the right which recorded the lowest dose-rate of 13-15 mrad/day.

2.2 Joint U.S./Soviet Measurements

In addition to the manned space program, the Soviets have utilized the Cosmos Biosatellite series in order to conduct radiation experiments. As of this writing, eight such missions have flown, including Cosmos Nos. 110, 605, 782, 936, 1129, 1154, 1667, and 1887.

Four sets of radiation measurements using passive detectors were carried out jointly on the Cosmos Biosatellite series including Cosmos 782, 936, 1129 and 1887. The results for two of the flights are shown in Table 4 /Benton et al., 1983/. Here are shown the TLD dose and mission dose rate as well as neutron measurements made using a set of fission foils (described later). The results from Cosmos 1887 mission are in the initial stages of readout and analysis. Since the highest inclination orbit flown to date by the Space Shuttle is 57^{0}, these joint Cosmos Biosatellite missions represent the highest inclination orbits available to the U.S. experimenters, and hence are useful in measuring the contribution to the total radiation picture of the galactic cosmic ray (GCR) component.

2.3 Measurements Under Thin Shielding

The objectives of the Cosmos missions are many and also include the development of new types of active shielding as well as dose measurements under very low shielding conditions. Fig. 3 shows a "waffle-iron" type of container which is mounted on the outside of the spacecraft and which holds various types of detectors. Once in orbit, the container is opened to the

Table 2. Absorbed and Equivalent Radiation Doses for the Crews of Salyut 3-6 Spacecraft*

Orbital Station	Transportation Spacecraft	Period and duration of flight	Astronaut	Radiation Dose Absorbed (10^{-5} Gy)	Radiation Dose Equivalent (rem)
Salyut-3	Soyuz-14	3-19 July 1974, 16 days	P. Popovich Yu. Artyukhin	265±10 295±17	0.40 0.44
Salyut-4	Soyuz-17	11 Jan–9 Feb 1975, 30 days	A. Gubarev G. Grechko	770±110 640±80	1.1 1.0
	Soyuz-18	24 May–26 Jul 1975, 63 days	P. Klimuk V. Sevastyanov	3050±300 2170±190	4.6 3.3
Salyut-5	Soyuz-21	6 Jul–24 Aug 1976, 49 days	G. Volynov V. Zholobov	830±70 820±30	1.2 1.2
	Soyuz-24	7–25 February 1977, 18 days	V. Gorbatko Yu. Gladkov	348±12 338±9	0.52 0.51
Salyut-6: Expedition I	Soyuz-26	10 Dec 1977–16 Mar 1978, 96 days	Yu. Romanenko G. Grechko	2050±100 2150±80	3.1 3.2
II	Soyuz-29 and Soyuz-31	16 Jun–2 Nov 1978, 140 days	V. Kovalyonok A. Ivanchenkov	3150±190 3350±200	4.7 5.0
III	Soyuz-32 and Soyuz-34	25 Feb–19 Aug 1979, 175 days	V. Lyakhov V. Ryumin	3670±190 3670±190	5.5 5.5
IV	Soyuz-35 and Soyuz-37	9 Apr–11 Nov 1980, 185 days	L. Popov V. Ryumin	2700±160 2700±160	4.0 4.0
V	Soyuz-T4	12 Mar–26 May 1981, 75 days	V. Kovalyonok V. Savinykh	1100±40 1060±40	1.6 1.6

*/Vorobyov and Kovalyov, 1983./

Table 3. Individual Radiation Doses Incurred by Members of International Crews on board Salyut-6 Spacecraft under the Intercosmos Programme*

Astronaut	Country	Transportation Spacecraft	Date of Launch	Radiation Dose Absorbed (10^{-5} Gy)	Radiation Dose Equivalent (rem)
A. Gubarev V. Remek	USSR Czechoslovakia	Soyuz-28	2 March 1978	250±23 260±9	0.38 0.39
P. Klimuk M. Germaszewski	USSR Poland	Soyuz-30	27 June 1978	188±18 201±16	0.28 0.30
V. Bykovsky S. Ien	USSR GDR	Soyuz-31 and Soyuz-29	26 August 1978	238±32 270±13	0.36 0.40
V. Kubasov B. Farkas	USSR Hungary	Soyuz-36 and Soyuz-35	26 May 1980	---- 135±20	---- 0.20
V. Gorbatko Fam Tuan	USSR Vietnam	Soyuz-37 and Soyuz-36	27 July 1980	190±25 216±22	0.28 0.32
Yu. Romanenko A. Mendez	USSR Cuba	Soyuz-38	18 Sept. 1980	150±15 147±15	0.22 0.22
V. Janibekov Zh. Gurragcha	USSR Mongolia	Soyuz-39	22 March 1981	165±15 182±16	0.25 0.27
L. Popov D. Prunariu	USSR Romania	Soyuz-40	14 May 1981	166±23 200±22	0.25 0.30

*/Vorobyov and Kovalyov, 1983./

Cosmos Flight No.	936	1129
Flight duration (days)	18.5	18.56
Inclination	62.8	62.8
Altitude (km, apogee/perigee)	419/224	394/226
TLD dose (mrad)	474	347 (US) 320 (USSR)
TLD dose rate (mrad/day)	25.6	18.0
Thermal Neutrons		
fluence	3.6×10^5 cm^{-2}	5.1×10^5 cm^{-2}
dose	0.37 mrem ± 20%	0.52 mrem ± 20%
Resonance neutrons		
fluence	1.3×10^6 cm^{-2}	1.4×10^6 cm^{-2}
dose	6 mrem - 30% + 50%	7.4 mrem - 30% + 50%
High energy neutrons		
fluence	2.1×10^6 cm^{-2}	2.1×10^6 cm^{-2}
dose	125 mrem ± ?	125 mrem ± ?

/Benton et al., 1983/

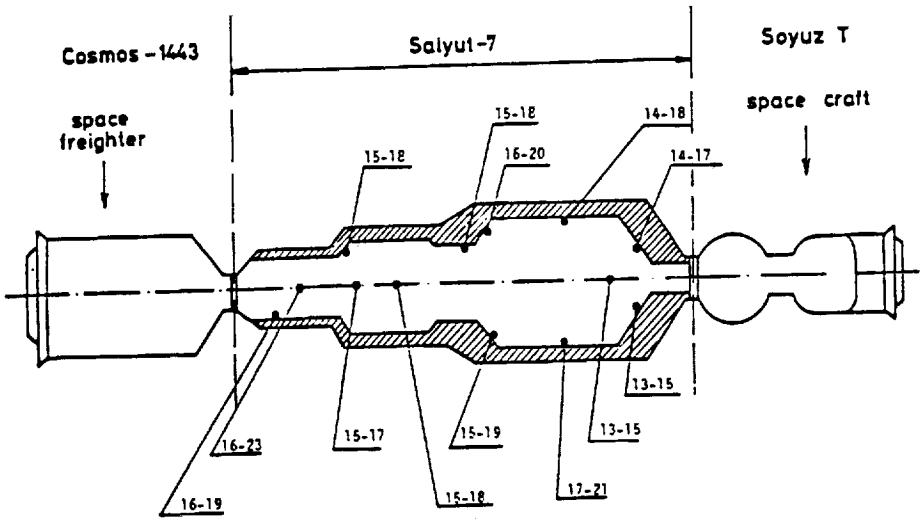

Fig. 2. Range of average dose rates (mrad/day) on board Salyut-7. /Akatov et al., 1984./

free space environment. Absorbed dose as a function of thin shielding for Cosmos 936 and 1129 is shown in Fig. 4 /Benton et al., 1981/. Here, absorbed dose decreases three to four orders of magnitude in the first ∿(1-3) g/cm^2 of material /Dudkin, 1987; Benton, 1987/. Since this means that very thinly shielded portions of the spacecraft can receive very large radiation exposures, these measurements need to be verified for the various orbits and

Fig. 3. "Waffle-iron" detector container used on Soviet Cosmos Biosatellite flights.

conditions so as to get a better picture of this environment. The rapid change in dose at these shielding depths is primarily due to absorption of low energy electrons.

2.4 U.S. Measurements

2.4.1 Early measurements. The U.S. spacecraft used in manned space exploration are shown in Fig. 5 and include the Mercury, Gemini, Apollo, Skylab, the ASTP and the Space Shuttle, all shown roughly to scale. TLD mission dose and dose-rate data measured on the early U.S. manned space missions are shown in Table 5. The data for the Gemini, Skylab and ASTP flights reflect strongly the altitude dependence of these low Earth-orbital (LEO) missions, while the Apollo series reflects the specific path through the radiation belts on the way to and from the moon. Until fairly recently, the dose-rate of some 86 +/- 9 mrad/day for the Skylab-4 mission represented the

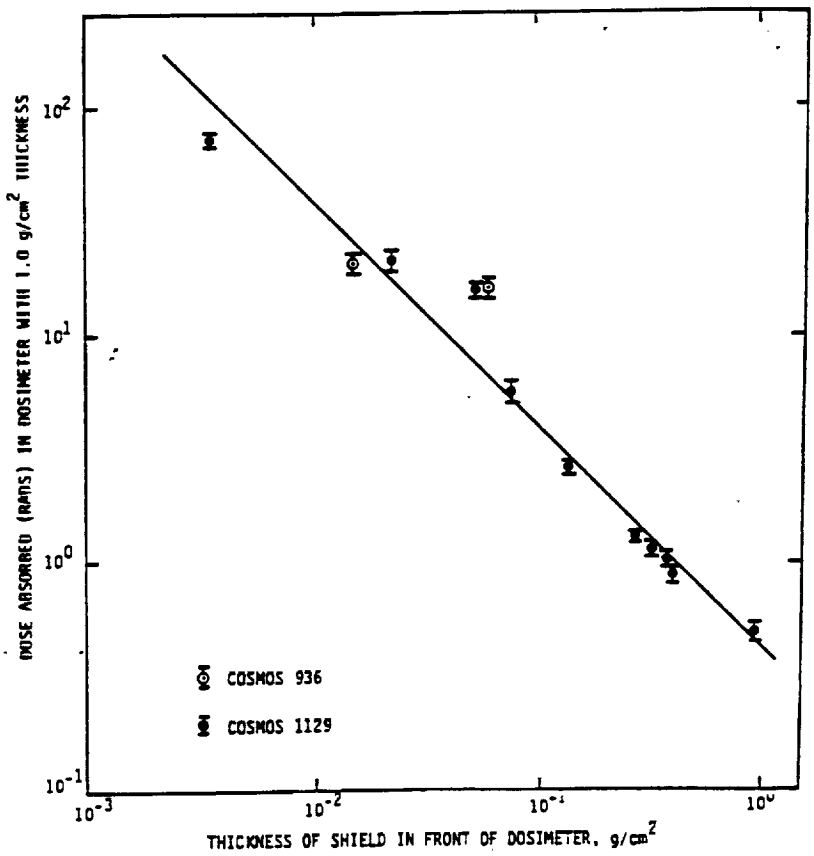

Fig. 4. Dose absorbed by dosimeter 1.0 g/cm² thick, as a function of shield thickness.

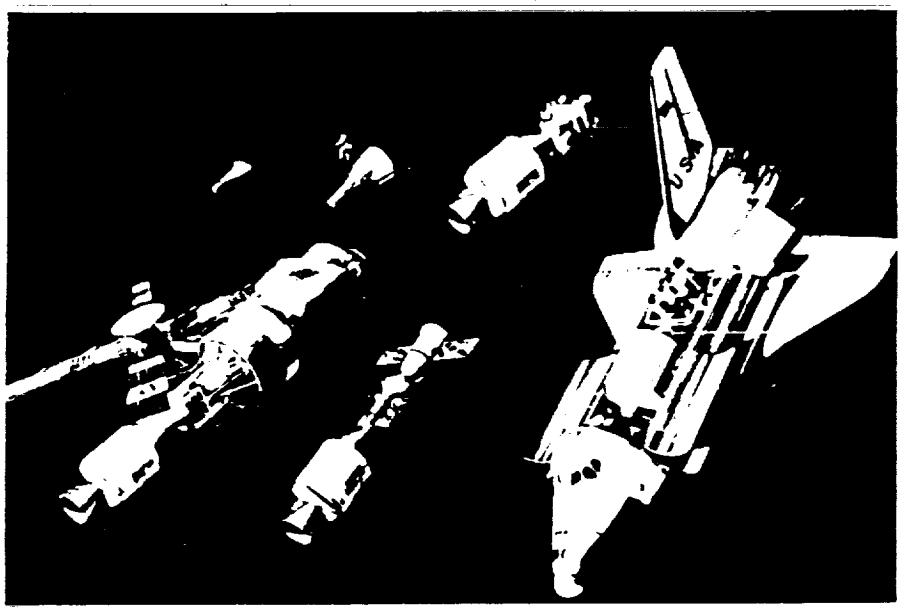

Fig. 5. Six types of U.S. manned spacecraft shown nearly to scale. (Clockwise from top left) Mercury, Gemini, Apollo, Space Shuttle, Apollo-Soyuz, Skylab.

Table 5. Crew Dose Rates from Early Manned U.S. Spaceflights

Flight	Duration (hrs/days)	Inclination (deg)	Apogee-Perigee (km)	Average Dose (mrad)	Average dose rate (mrad/day)
Gemini 4	97.3 hrs	32.5	296 - 166	46	11
Gemini 6	25.3 "	28.9	311 - 283	25	23
Apollo 7*	260.1 "			160	15
Apollo 8	147.0 "		lunar orbital flight	160	26
Apollo 9	241.0 "			200	20
Apollo 10	192.0 "		lunar orbital flight	480	60
Apollo 11	194.0 "		lunar flight	180	22
Apollo 12	244.5 "		" "	580	57
Apollo 13	142.9 "		" "	240	40
Apollo 14	216.0 "		" "	1140	127
Apollo 15	295.0 "		" "	300	24
Apollo 16	265.8 "		" "	510	46
Apollo 17	301.8 "		" "	550	44
Skylab 2**	28 days	50	alt = 435	1596	57 ± 3
Skylab 3	59 days	50	alt = 435	3835	65 ± 5
Skylab 4	90 days	50	alt = 435	7740	86 ± 9
Apollo-Soyuz Test Project	9 days	50	alt = 220	106	12

*Doses for the Apollo flights are skin TLD doses. The doses to the blood-forming organs are approximately 40% lower than the values measured at the body surface.

**Mean TLD dose-rates from crew dosimeters.

†Apollo data courtesy of J. V. Bailey /1977/.

highest dose-rate recorded by any astronaut while in low Earth-orbit /Bailey 1977/. The average crew dose-rates recorded on Apollo lunar missions ranged from 22-127 mrad/day and that recorded on Apollo 14 (127 mrad/day) is still the highest mission-average crew dose-rate recorded to date. The average dose-rates inside the heavily shielded film vault drawers B (16-30 g/cm^2) and F (30-50 g/cm^2) of Skylabs 2 and 3 were 39.5 and 33.4 mrad/day[1] respectively.

2.4.2 STS measurements. The passive dosimeters which were used on the Space Shuttle missions STS 1-61C, which include the crew passive dosimeter or CPD (which consists of the TLD module and the module containing a set of PNTDs), as well as three pencil-type, electrometer-type dosimeters, having ranges of 0-200 mrad, 0-100 rad, and 0-600 rad, are shown in Fig. 6. The plastic box at the bottom left is that of the area passive dosimeter (APD) which was flown on the first several missions and which contained, in addition to the TLDs and PNTDs, some fission-foil-type, low-energy neutron dosimeters. The APD and the electrometers are fitted into the pouch shown at the bottom right of the picture.

The TLD crew passive dosimeter data from the first twenty-four flights of the Shuttle are shown in Table 6. The doses and mission dose-rates reflect for the most part the low-LET components of the radiation. It is observed that the first eight flights of the Shuttle, which involved orbiters Columbia and Challenger and which had similar orbits of 28.5° to 40° inclination and nominal altitudes of 250-300 km, all showed very modest mission dose-rates of 5-7 mrad/day. With the first flight of the Spacelab, Spacelab-1 (STS-41A), in an orbit having about the same altitude but an inclination of 57°, the dose-rate doubled to about 12 mrad/day. From these measurements and those of Parnell et al., /1986/, we now know that, at most locations in the Shuttle or Spacelab, the bulk of the dose recorded on this type of low-altitude, 57° inclination flight is the result of GCR.

Parnell et al., /1986/, showed that on Spacelab-1, at a shielding depth of $\sim$ 8 gm/cm^2, only about 15% of the dose was attributable to the trapped protons of the South Atlantic Anomaly (SAA). This situation changed dramatically with the flight STS-41C, the Solar Max repair mission which, although at orbital inclination of 28.5°, was the first true higher altitude mission, with a maximum of $\sim$528 km and recording a mission-average crew dose-rate which was an order of magnitude greater than the nominal low-altitude flights, namely, about 74 mrad/day. In this case it is clear that the bulk of the dose comes from the SAA, with the GCR contributing something of the order of 5-6 mrad/day. Starting with flight STS-41G and continuing until the most recent flight, STS-61C, the missions showed dose-rates of 11-22

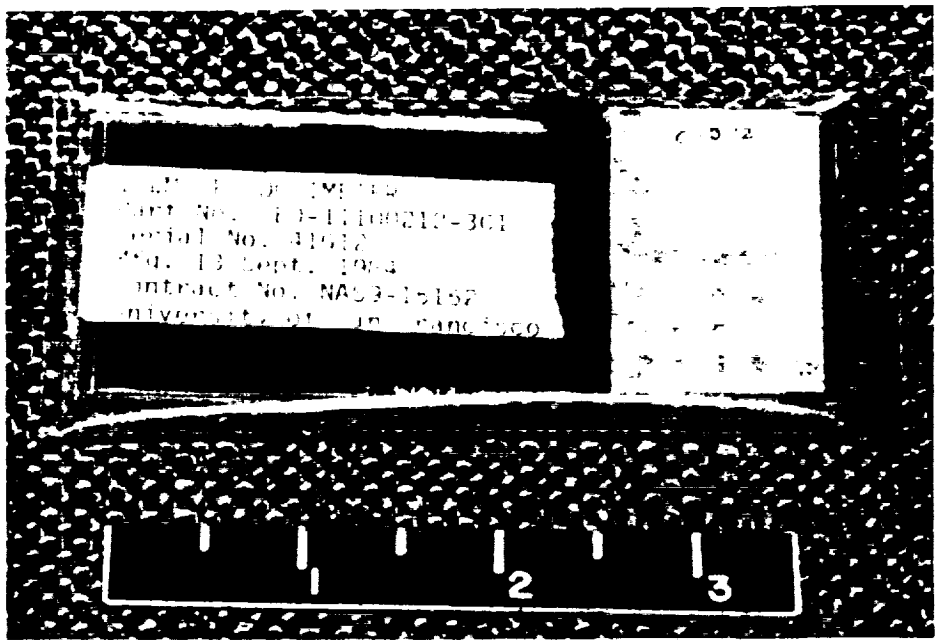

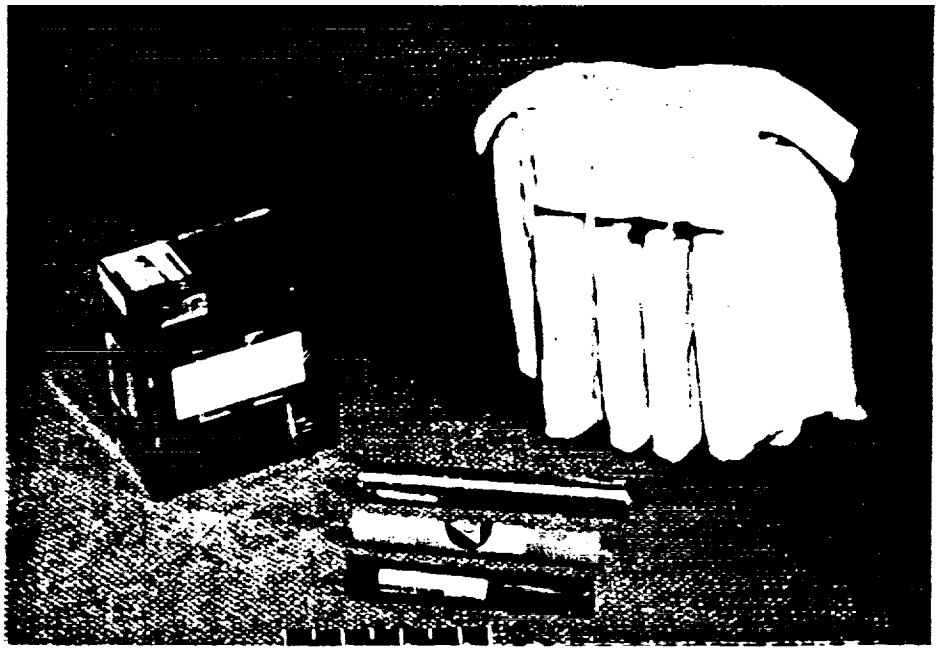

Fig. 6.

Top: STS Crew Passive Dosimeter

Bottom: Area Passive Dosimeter and three electrometer-type dosimeters with the pouch which holds the instruments.

Table 6. Crew Doses and Mission Parameters for the Space Shuttle Flights*

STS Mission Number	Spacecraft	Launch Date	Mission Duration (hr)	Alt.(km)	Inc.(°)	Number of Crew	Range of Crew Doses (mrad)	Average Crew Dose (mrad)	Ave. Crew Dose Rate (mrad/day)
1	Columbia	04-12-81	54	269	40	2	not avail.	8.9	4.0
2	Columbia	11-12-81	58	254	38	2	6-11(USF)	8.5±2.3(USF)	3.6
3	Columbia	03-22-82	195	280	38	2	50-52(USF)	50.9±0.7(USF)	6.3
4	Columbia	06-27-82	169	297	28.5	2	44-45(USF)	44.4±0.2(USF)	6.3
5	Columbia	11-11-82	122	284	28.5	4	27-29(USF)	27.8±1.2(USF)	5.6
6	Challenger	04-04-83	120	293	28.5	4	24-27	25±2	5.0
7	Challenger	06-18-83	143	297	28.5	5	43-46	44±1	7.4
8	Challenger	08-30-83	145	297(max)	28.5	5	38-41	39±1	6.5
41A	Columbia	11-28-83	248	250	57	6	119-141	125±2	12.1
41B	Challenger	02-03-84	191	297	28.5	5	45-49	48±1	6.0
41C	Challenger	04-06-84	168	528(max)	28.5	5	441-622	519±5	74.1
41D	Discovery	08-30-84	145	297	28.5	6	51-53	52±1	8.6
41G	Challenger	10-05-84	197	352(max)	57	7	84-92	88±1	10.7
51A	Discovery	11-08-84	192	297x352	28.5	5	88-159	115±2	14.4
51C	Discovery	01-24-85	74	297x334	28.5	5	35-41	39±1	12.6
51D	Discovery	04-12-85	168	297x454	28.5	7	303-472	381±5	54.4
51B	Challenger	04-29-85	166	352	57	7	127-160	148±2	21.4
51G	Discovery	06-17-85	170	380(max)	28.5	7	105-152	130±1	18.4
51F	Challenger	07-29-85	191	322x304	49.5	7	112-167	138±2	17.3
51I	Discovery	08-27-85	192	378(max)	28.5	5	99-120	106±1	13.3
51J	Atlantis	10-03-85	95	510(max)	28.5	5	329-513	426	107.8
61A	Columbia	10-30-85	169	324	57	8	112-139	121	17.2
61B	Atlantis	11-26-85	165	380	28.5	7	125-171	143	20.8
61C	Columbia	01-12-86	146	324	28.5	7	65-75	69	11.3

*Stated uncertainty represents measurement precision, 1σ of the mean, rather than absolute accuracy. Previous measurements of absolute accuracy suggest that the given values are accurate to within 6-8%. Data for missions STS-1 through STS-5 supplied by the University of San Francisco; remainder supplied by the Radiation Dosimetry Laboratory, NASA-Lyndon B. Johnson Space Center.

mrad/day; however, most of these flights involved changes in altitude. By looking at the average crew dose-rate after a mission, it is possible to ascertain whether a higher-than-300 km altitude orbit was involved. For example, mission 51J, the first flight of Atlantis, with orbital inclination of 28.5° and a maximum altitude of 510 km, recorded an average crew dose-rate of 107.8 mrad/day, which is now the highest average crew dose-rate recorded by any crew while in low Earth-orbit. There is a steep dose-rate gradient, increasing with altitude above ∿300 km. The dose does not change as dramatically with inclination between 28.5° and 57°, where the variation is about a factor of 2. At the lowest altitudes (∿250 km) the dose increases with inclination due to the increased cosmic ray flux at higher geomagnetic latitudes. At the higher altitudes (400-500 km) the dose would be maximum near 35° inclination, since the spacecraft spends more time in the peak region of the SAA. It should also be noted that in higher-inclination orbits the LET spectrum is shifted towards the higher values.

The steep dose gradient with altitude and the changing energy spectrum of trapped protons which are responsible for most of the dose (at altitudes ∿500 km) was clearly observed in the data of Atwell et al., /1987a/. The devices used were flown beginning with mission STS-6 and continuing through STS-61C with six Passive Radiation Detectors (PRDs) deployed at specific locations in the spacecraft. Each PRD, which weighs about 25 grams and contains 32 TLD chips, is attached to the same specific location each time by means of a Velcro strip. PRD Nos. 1, 2 and 3 are located on the inside of the outer periphery of the mid-deck, while PRD Nos. 4, 5 and 6 are located on the inside of the outer periphery of the flight deck (see Fig. 7). The shielding at these six locations differs significantly (see Fig. 8) /Atwell and Beever, 1987b/. Location No. 1 is the most heavily shielded of the six, while location No. 2 is the least shielded. The data for STS missions 6-24 are shown in Figs. 9 /Benton, 1986/ and 10 /Atwell et al., 1987a/. For missions 6 through 41B the dose-rate for the six locations is very similar, as seen from the clustering of the data from the six detector locations (see Fig. 9). The dose-rate points spread out considerably for the three high-altitude missions, 41C, 51D and 51J. Here, in each case, location No. 2, which is on the mid-deck on the left wall facing aft, consistently gives a substantially higher dose-rate than position No. 1 which is also on the mid-deck, just above the payload bay air-lock. The ratio of dose-rates between position No. 2, as compared to location No. 1, was as high as 2.2. In location No. 2 was recorded the highest mission dose rate measured inside the orbiter, ∿200 mrads/day, on STS-51J. The PRD data for only the 28.5° incli-

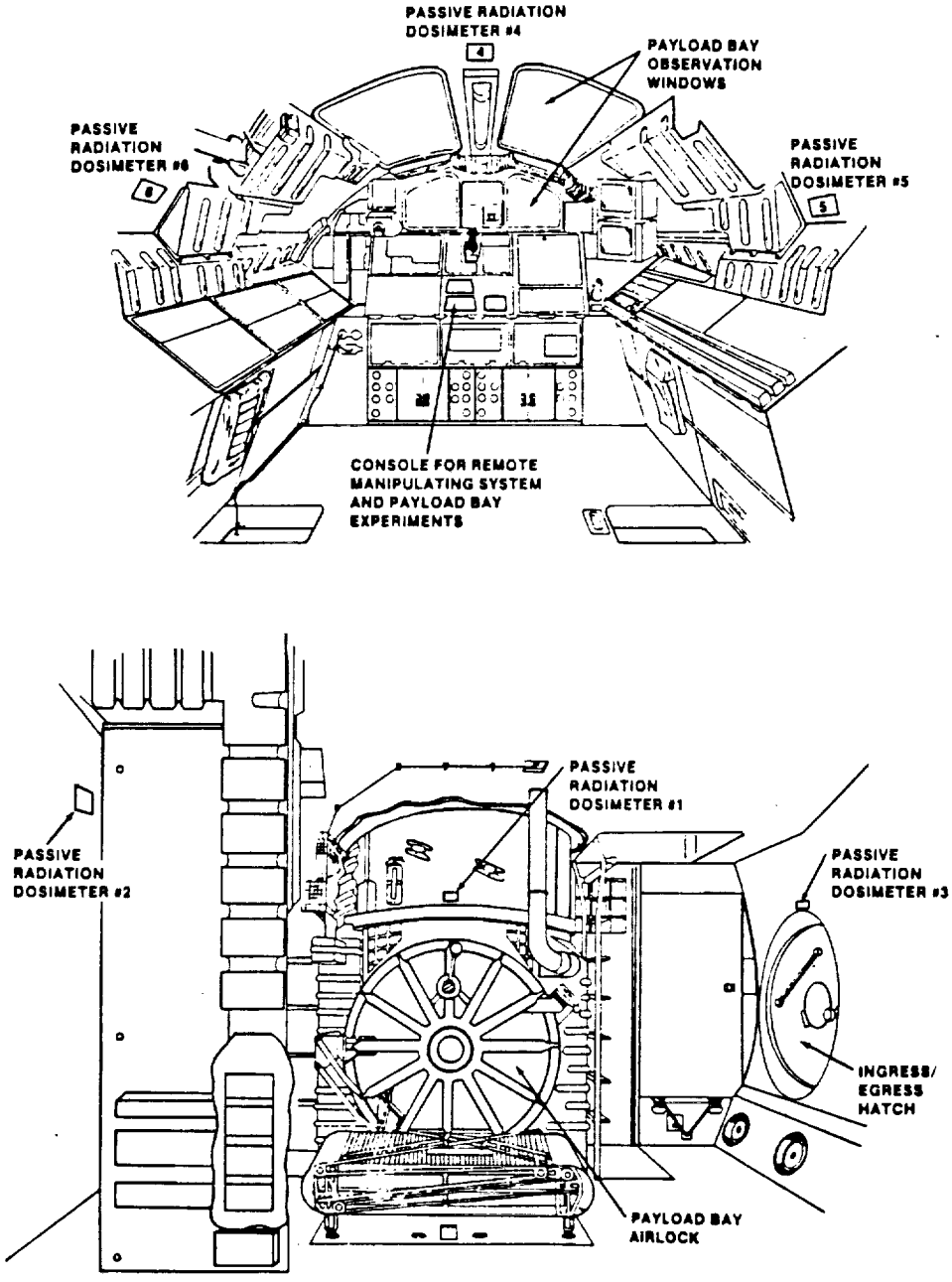

Fig. 7. Passive Radiation Detector locations on Space Shuttle.
Top: aft flight deck
Bottom: aft mid-deck
/Atwell et al., 1987a/

nation flights was plotted as a function of orbital altitude and compared with calculations for solar minimum and solar maximum (see Fig. 10) /Atwell et al., 1987a/.

Measurements performed with the APDs on STS-1 through 51C and giving the mission dose-equivalent are shown in Table 7. Here, the TLDs used were of the 700 type. The high LET portion of the LET spectrum was measured using the six orthogonally-positioned stacks of CR-39 detectors. This was needed in order to take account of the strong directionality of the plastic detectors. The neutron measurements were made using ^{6}LiF and ^{232}Th foils positioned against CR-39 and mica detectors, respectively (as discussed later).

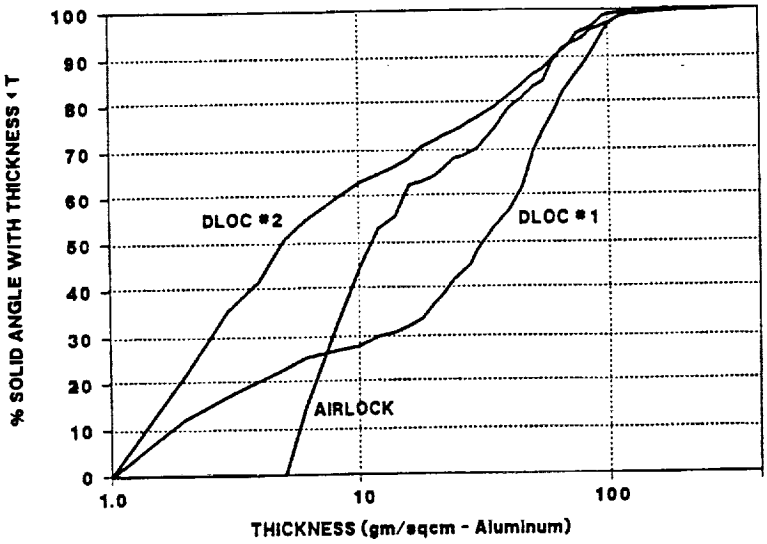

Fig. 8. STS orbiter shield distributions for PRD locations No. 1, 2, and the airlock /Atwell and Beever, 1987b/.

The dose-equivalent for the high LET ($\leq$ 20 keV/µm H_2O) particles as measured by the CR-39 detectors was obtained by integration of the integral LET spectra with the use of the appropriate quality factors as recommended by the ICRU (see Note 1). The low LET dose is obtained by taking the TLD data and subtracting from it the high LET absorbed dose as measured by plastic detectors. Then the total mission rem dose is obtained through the addition of the low LET, the high LET, and the neutron contributions (see Table 7). Because of some unusual behavior of the plastic track detectors experienced during the early flights (prior to STS-41B), the reported high LET rem doses may be somewhat (10-20%) higher than actual. LET measurements are discussed more completely in Section 5.0.

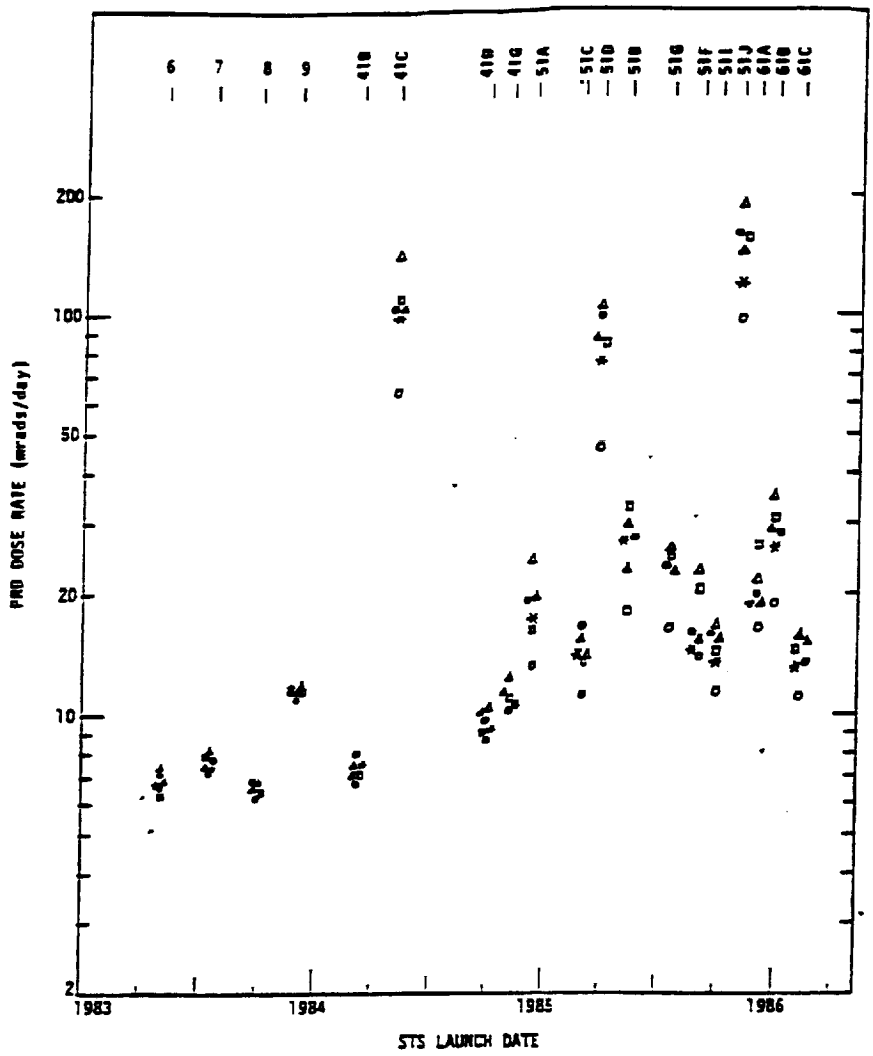

Fig. 9. The dose rate in mrad/day obtained by flying the six PRDs on missions STS-6 through 61C, as a function of launch date. Data courtesy of R. Richmond, NASA-JSC.

Key: PRD-1 (○ —on airlock, above hatch)
PRD-2 (△ —on outer wall behind and aft DFI)
PRD-3 (□ —on outer wall, above ingress/egress hatch)
PRD-4 (* —aft, toward CL of observation window)
PRD-5 (● —on closeout panel above locker L-10)
PRD-6 (▲ —on closeout panel above locker R-11)

Table 7. Space Shuttle Dosimetry Summary: Measurements from the Area Passive Dosimeters

	Whole-Body Dose Equivalents (mrem)			
	STS-1	STS-2	STS-3	STS-4
LOW-LET*		12.5 ± 1.8	52.5 ± 1.8	44.6 ± 1.1
Rate (/day)		5.2 ± 0.8	6.5 ± 0.2	6.3 ± 0.2
Neutron				
Thermal	< 0.05	< 0.03	0.03	0.04
Resonance	< 0.75	< 0.3	2.0	1.6
High Energy	----	----	7.7	14
Total	< 15	< 6	9.7	15.6
HIGH-LET**	3.6 ± 0.4	1.0 ± 0.4	6.3 ± 1.0	7.7 ± 2.9
Total Mission Dose Equivalent		< 19	68.5	67.9
Mission Parameters				
Storage Locker				
Duration (hrs)	54	57.5	194.5	169.1
Inclination (deg)	38	38	40.3	28.5
Altitude (km)	240	240	280	297

	STS-5	STS-6	STS-7	STS-8
LOW-LET*	27.8 ± 2.5	27.3 ± 0.9	34.3 ± 2.3	34.8 ± 1.3
Rate (/day)	5.6 ± 0.5	5.5 ± 0.2	5.8 ± 0.4	5.8 ± 0.2
Neutron				
Thermal	0.03	0.03	0.02	0.02
Resonance	0.7	1.9	1.4	2.6
High Energy	11	6.5	----	----
Total	11.7	8.4	1.4***	2.6***
HIGH-LET**	14.5 ± 1.6	13.8 ± 1.8	11.7 ± 1.6	19.2 ± 3.5
Total Mission Dose Equivalent	54.0	49.5	47.9***	56.6 ± 3.7***
Mission Parameters				
Storage Locker	MF14O	MF28K	MF28K	MA16F
Duration (hrs)	120	120	143	70 75
Inclination (deg)	28.5	28.5	28.5	28.5
Altitude (km)	297	284	297	297 222

	STS-9	STS-41B	STS-41C	STS-41D
LOW-LET*	101.1 ± 3.1	43.6 ± 1.8	403 ± 12	42.0 ± 2.8
Rate (/day)	10.1 ± 0.3	5.5 ± 0.2	57.6 ± 1.7	7.0 ± 0.5
Neutron				
Thermal	0.1	0.02	0.05	0.01
Resonance	2.2	0.5	3.1	1.5
Total***	2.3	0.5	3.2	1.5
HIGH-LET**	76.3 ± 9.2	13.6 ± 1.5	98 ± 3	21.3 ± 1.3
Total Mission Dose Equivalent***	179.7 ± 9.7	57.7 ± 2.3	504 ± 12	64.8 ± 3.1
Mission Parameters				
Storage Locker	MF28E	MF28O	MF28O	MF28O
Duration (hrs)	240	191	168	145
Inclination (deg)	57	28.5	28.5	28.5
Altitude (km)	241	297	519	297

	STS-41G	STS-51A	STS-51C
LOW-LET*	82.4 ± 2.4	94.3 ± 4.9	35.4 ± 2.0
Rate (/day)	10.0 ± 0.3	11.3 ± 0.6	11.5 ± 0.6
Neutron			
Thermal	0.03	0.04	---
Resonance	1.1	0.9	---
Total***	1.1	0.9	---
HIGH-LET**	71.0 ± 2.8	37.8 ± 2.3	12.2 ± 2.1
Total Mission Dose Equivalent**	154.5 ± 3.7	133.0 ± 5.3	47.6 ± 2.9
Mission Parameters			
Storage Locker	MF28O	MF28O	MF28O
Duration (hrs)	29/19/148.5	192	73.6
Inclination (deg)	57.0	28.5	28.5
Altitude (km)	352/274/224	324	297–334

*Photons and electrons of any energies. High LET at lower efficiency.
**HZE particles with LET >20 keV/um of water.
*** Does not include high-energy neutron dose.

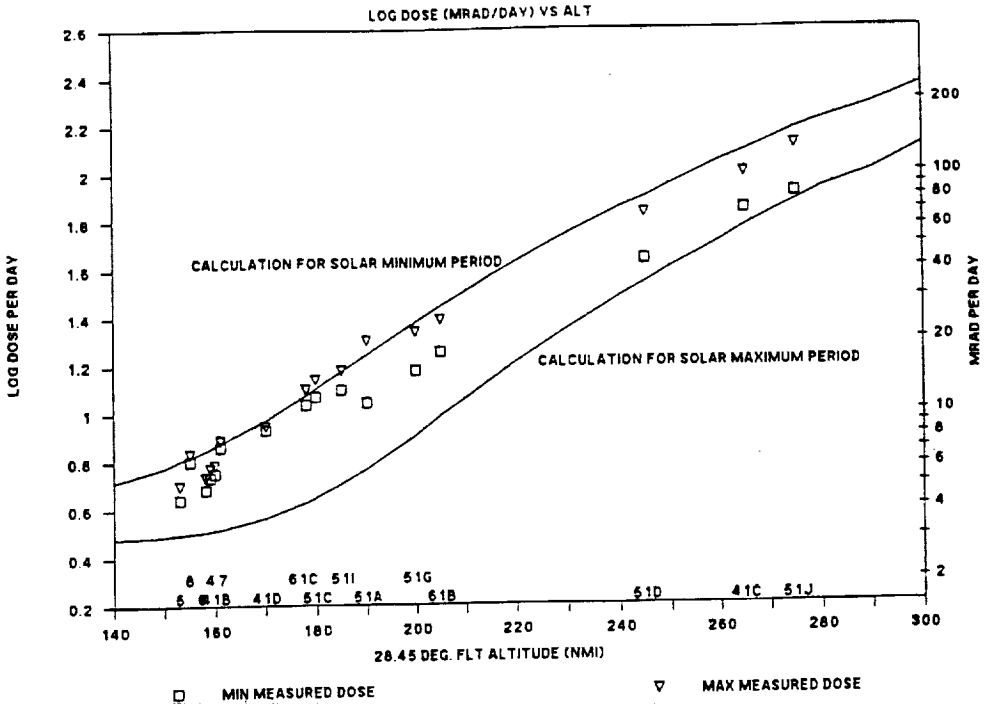

Fig. 10. STS PRD dose measurements/calculations /Atwell et al., 1987a/.

3.0 ACTIVE DETECTORS FOR DOSIMETRY

Active, real time detectors play an important role in radiation measurements in that they allow the determination of temporal changes in the radiation environment, provide information on dose and flux rates, and can allow the separation of dose contributions from the different components, i.e., GCR, trapped protons, electrons and bremsstrahlung, etc. Relatively few active dosimetry-related measurements to date have been made in the U.S. manned space program.

The Soviets have flown a number of active instruments in their manned program, but very little information is available in the literature concerning either instrumentation or results. They have, however, reported LET spectra from Cosmos 782, 986, and 1129, from a particle spectrometer. These results are discussed in Section 5.0.

3.1 Early Measurements on Gemini and Apollo

Beginning with the Gemini program, a variety of ion chamber dosimeters and solid state detector "dosimeters" were developed and carried on the Gemini and Apollo flights. The chambers were generally of the tissue-equivalent

ion chamber (TEIC) type, the principles and construction of which are described by Janni /1976/. These detectors and some of the measurements have been summarized /Janni, 1969b; Schneider and Janni, 1969; Richmond, 1969/. The data was often subject to telemetry and other limitations, so synoptic data on missions are not always available. Nevertheless, some pioneering results are still very useful for comparison with more recent data. Their usefulness is an indication of the paucity of recent measurements and also the utility of TEIC measurements. For Gemini IV (163 x 281 km, 32.5^{o}), measurements were published for orbits outside the SAA, and peak dose rates in the SAA /Schneider, 1969/. Two TEICs were carried, mounted inside each hatch, which had minimum shielding of >1 g/cm^2 of aluminum over large solid angles. One TEIC was demountable and was used to survey the effects of equipment and self-shielding around the crew members' bodies /Schneider and Janni, 1969/. At the highest geomagnetic latitudes, dose rates up to 0.18 μrads/s due to GCR were recorded. In the center of the SAA, dose rates up to 35 μrads/s were obtained, an indication of the thin shielding and the influence of the artificial electrons from the Starfish explosion three years before.

The two TEICs on Gemini IV also indicated the directionality of the SAA trapped particles by indicating doses that varied in opposite directions by a factor of >2 while the spacecraft changed attitude. Table 8 lists major features of the Gemini IV data compared with that from similar TEICs carried on Skylab and Spacelab-1, to be discussed in the next two sections.

Gemini VI (259, 328 x 161 km, 29^{o}) used the same ion chambers, one with a 2.5 g/cm^2 brass shield. This one-day mission varied in altitude, with the apogee out of the SAA. The shielded chamber showed doses lower by a factor of two, compared to the unshielded chamber in the SAA, with interesting variations due to the directionality of the trapped flux.

The Apollo program carried a complement of dosimeters similar to Gemini /Richmond, 1969/. Because of the short time the lunar missions spent in the trapped belts, the majority of these doses were from cosmic rays (see Section 2.4). However some of the Apollo flights passed near the maximum trapped proton flux region. Apollo VI TEICs recorded maximum doses of 10^3 μrads/s (3.6 rad/hr) and 720 μrads/s (2.6 rad/hr) for the "skin dose" and "depth dose," with two ion chambers in the command module.

3.2 Skylab Results

Skylab (415 km, 50^{o}) carried a rather comprehensive set of passive detectors available at the time and also active instruments /Janni, 1976/. The passive detectors were TLDs (CaF_2, LiF), nuclear track emulsions, plas-

Table 8. Dose Measurement from Gemini IV, Skylab and Spacelab-1 Measured with Tissue-Equivalent Ion Chambers (TEICs)

	Dose-rates in microrads/second		
	Max. CR†	Av. CR	Max. SAA
Gemini IV (281x161 km, 32.5°)	0.18	0.047	35*
Spacelab-1 (250 km, 57°)	0.28	0.110	1.7
Skylab II (415 km, 50°)	0.55	0.055	23

*Note shielding of Gemini IV TEIC ($\gtrsim$ 1 gm/cm^2), flown three years after Starfish
†Cosmic rays

tic nuclear track detectors, activation foils, and quartz fiber electroscopes. The active detectors were TEICs and a small two-detector solid state particle telescope to measure LET spectra. The instrumentation is completely described in Janni /1976/. The TEIC chamber was designed according to the Bragg-Gray principles (to provide accurate results in a mixed radiation field) and constructed of approximately tissue-equivalent plastic and filling gas. Results from the Skylab-2 mission TLD measurements and some TEIC results are contained in Janni /1976/, including numerous passes through the South Atlantic Anomaly. Dose rates up to 23 μrads/s were recorded in the center of the SAA. Outside the anomaly, dose rates averaged about 0.055 μrads/s due to cosmic rays, which increased to ∿0.55 μrads/s at the highest geomagnetic latitudes. At the geomagnetic equator the dose rate was as low as ∿0.014 μrads/s. These values may be compared with the average mission dose measured by the TLDs of about 0.5 μrads/s (1.2 rads for the 28-day mission).

3.3 Coordinated Active and Passive Measurements, Results from SL-1 and SL-2

An example of the usefulness of even very simple active devices when coordinated with passive detector arrays is the work by Parnell et al. on SL-1 and -2 /1986/. Two Active Radiation Detector (ARD) packages were flown on SL-1, each containing an integrating TEIC (see Refs., Note No. 2) and two xenon-filled proportional counters (see Refs., Note No. 3, and Figs. 11 and 12). These simple omnidirectional detectors were flown to measure temporal variations of radiation dose and count-rate due to cosmic ray nuclei, trapped protons and electrons, and bremsstrahlung X-rays from electrons. The ion chambers had a sensitive gas volume of 180 cm^3. Preflight calibra-

tions of the ion chambers were reproduced after the flight within 5 percent. The proportional counters (PCs) had a sensitive volume of ∿60 cm^3 and counted each ionizing event with energy deposition greater than 5.9 keV in the gas (about 85% of the charged particles and 2% of 100-keV photons). In the laboratory the PC count rate was ∿1/s. One PC in each unit was surrounded by a copper sleeve 1 g/cm^2 thick which would absorb 40% of 100-keV photons. The ARDs were placed in the top and bottom of equipment rack No. 3 in the SL-1 module. Passive detector packages containing TLDs, PNTDs, neutron fission foils, activation samples, and nuclear track emulsions were placed beside each active detector and at other locations in the Spacelab module.

The Spacelab-1 mission flew for 10 days at ∿250 km altitude and 57° inclination. Twenty-nine passive and two active detector packages were used at a variety of shielding locations in the module and tunnel, and one passive unit was on the pallet.

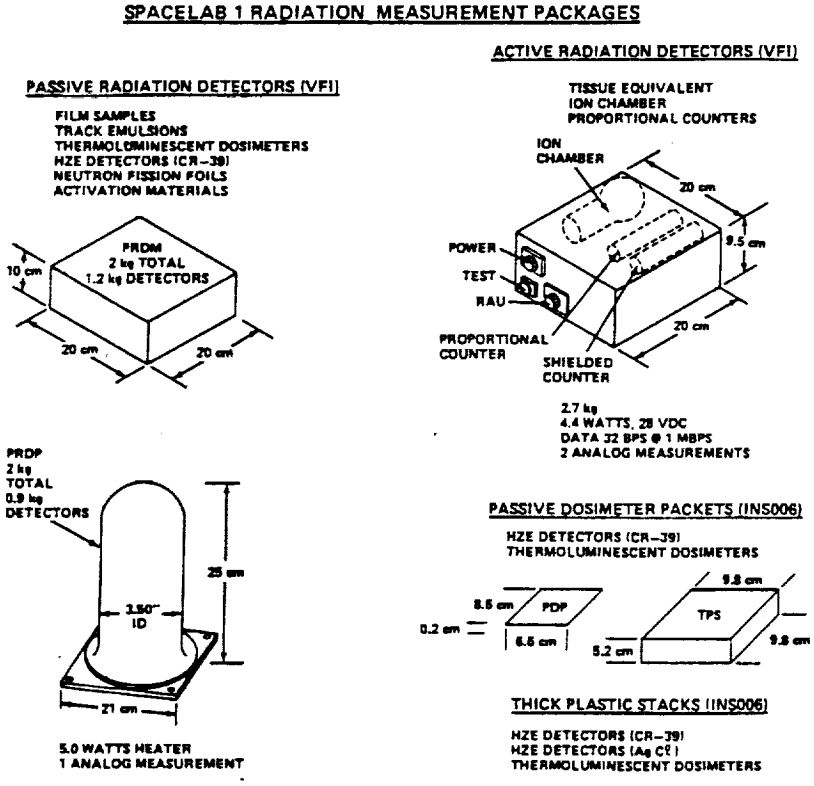

Fig. 11. Detector package configurations for Experiment INS006 and Verification Flight Instrumentation (VFI) on Spacelab-1 /Parnell et al., 1986/.

The average ion chamber dose rates were 12.5 ± 0.7 and 12.8 ± 0.7 mrads/day in the top and bottom of rack No. 3. TLD measurements in adjacent PRD-Ms registered 9.7 ± 0.3 mrad/day and 10.9 ± 0.3 mrad/day, respectively. The ion chambers thus appear to measure about 20% higher values than the TLDs. Part of this is due to the TLDs' lower sensitivity to heavy nuclei. As determined from the ion chambers and proportional counters, about 85% of the SL-1 module dose comes from cosmic rays, and the TLDs are less sensitive to very heavy nuclei than singly charged particles. Other contributions to the difference may be systematic biases in calibration and biased environment sampling due to data gaps, which existed for about 45% of the mission.

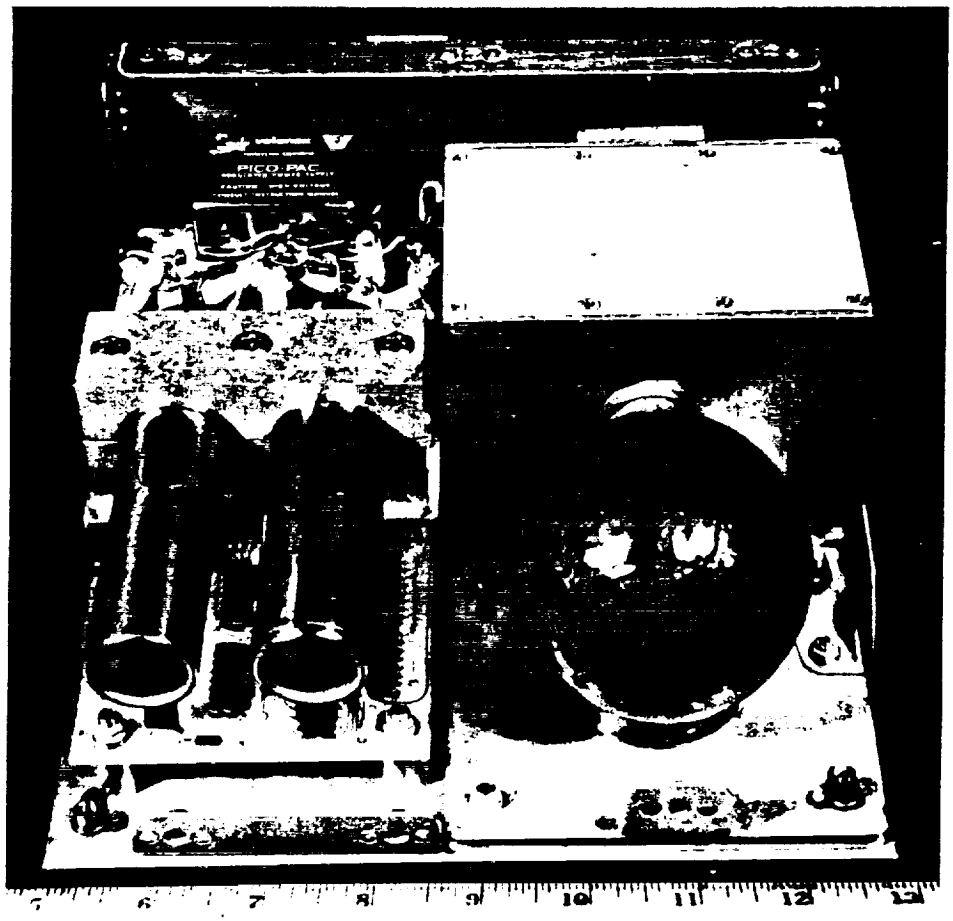

Fig. 12. Active Radiation Detector (ARD) package flown on Spacelab-1, containing an integrating tissue-equivalent ion chamber and two xenon-filled proportional counters.

The temporal information from the ion chambers and proportional counters allowed an assessment of the relative contributions of the cosmic rays and trapped belt particles. Fig. 13 is a one-hour segment of data from one ion chamber and the two PCs in the same unit. This shows variations in the integrated ion chamber dose and PC rates due to cosmic rays (with the expected geomagnetic dependence as the spacecraft travelled from north to south); this effect and the trapped particles in the SAA region and the south "horn" of the electron belt are shown in Fig. 14. The small "bump" of electrons in the middle are probably transiently trapped on those field lines. The observation that the ion chamber dose rates in the south horn region are not significantly different from rates at other high latitude portions of the orbit (see Fig. 15) shows that the high PC rates there are due to bremsstrahlung photons produced by electrons stopping in the Spacelab structure. In Fig. 15, one can see the effect of the copper shield on one PC in absorbing ∿40% of the photons. The high PC rates in the SAA are mostly due to the trapped protons that produce the increase in ion chamber (IC) dose rate in that region. The similar proportional counter rates in the SAA and electron horn regions are an artifact of the orbit and the sensitivity of the xenon-filled PC to photons.

The segments of the ion chamber data indicating the SAA (see Figs. 14 and 15) by temporal behavior of the PC count rate comprise 0.13 of the average mission dose for the top ion chamber and 0.10 for the one in the bottom of rack No. 3. These fractions may be somewhat biased by data gaps, but show clearly that the dose in the SL-1 orbit is dominated by the cosmic rays, as predicted by pre-flight calculations /Watts and Wright, 1976/. Those calculations also predict that trapped protons would dominate above ∿350-400 km for similar locations in the Spacelab module.

Occasionally at large geomagnetic latitudes, sudden increases in proportional counter rates occurred as shown in Fig. 16. Bremsstrahlung photons of ∿100 keV characteristic energy are indicated by the relative count rates of the shielded and unshielded PCs and the lack of significant ion chamber dose rate above that expected from cosmic rays. The intensity was occasionally approximately twice that observed in the undisturbed south electron horn and episodes lasted from a few to ∿500 s. Seventeen significant episodes occurred in five days of ARD data. These events resemble trapped electron "precipitation" events previously observed /Imhof et al., 1979 and 1986/. These bremsstrahlung photons are generated by electrons stopping in the atmosphere and are probably seen from large distances.

The low fraction of dose due to trapped particles in the SL-1 module makes assessment of the trapped environment and its absorption by shielding

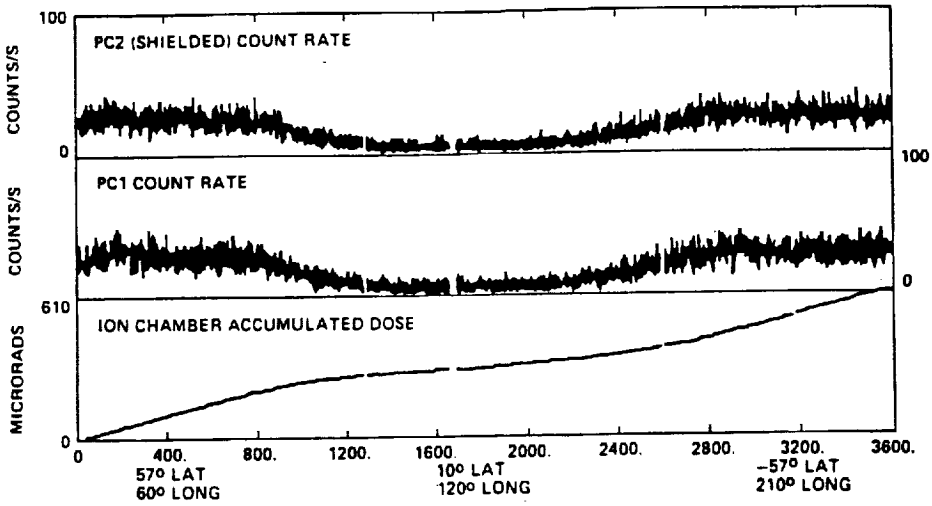

Fig. 13. One-hour segment of data from one ion chamber and two proportional counters in the same unit. Variations in ion chamber dose integration and PC rates due to cosmic rays are shown.

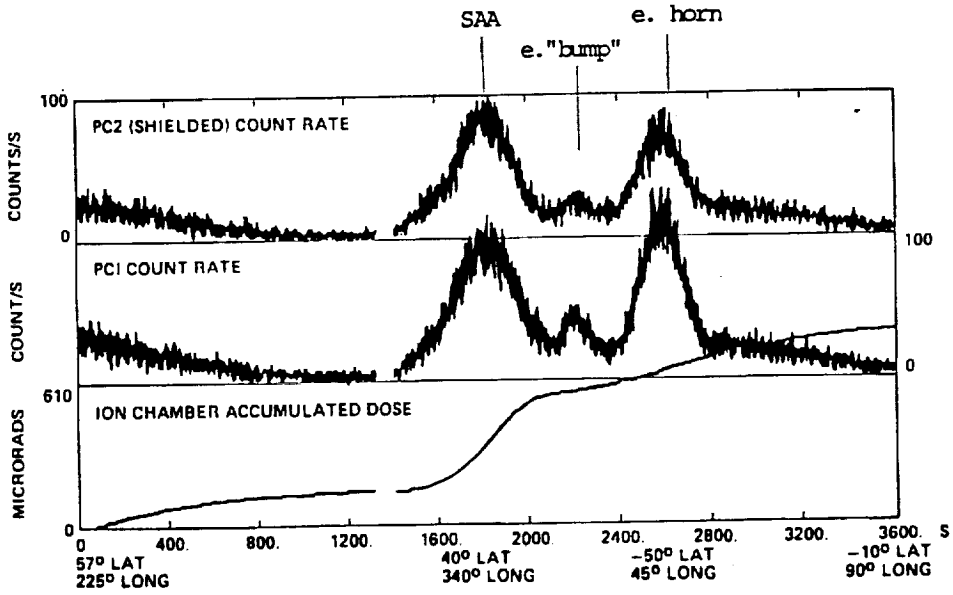

Fig. 14. Effect of geomagnetic dependence as spacecraft travels north to south and of trapped particles in the SAA region, the electron "bump", and the south horn of the electron belt. Note effect of shielding between the two counters.

somewhat uncertain. Analysis is also complicated by the short mission and variation in attitude of the Shuttle because the trapped particle angular distribution is directional, with more particles arriving nearly perpendicular to magnetic field lines in a "pancake" distribution /Heckman and Nakano, 1963; Watts et al., 1987/. To aid in assessing the SAA and south electron horn effects, contour maps of the radiation were assembled. The maps were constructed by averaging data around geographical points (e.g., within 3^{o}), and smoothing. Displayed in Fig. 17 are the rates from two ICs and one of

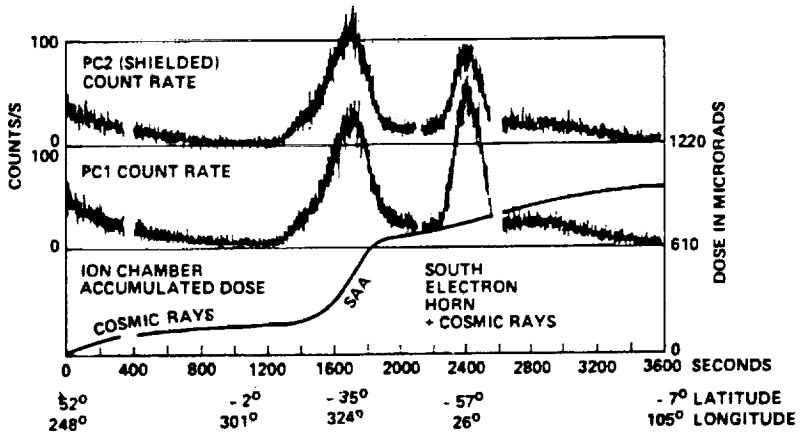

Fig. 15. Count rate of two proportional counters and ion chamber accumulation at high northern latitudes, the geomagnetic equator, the SAA, and the electron horn.

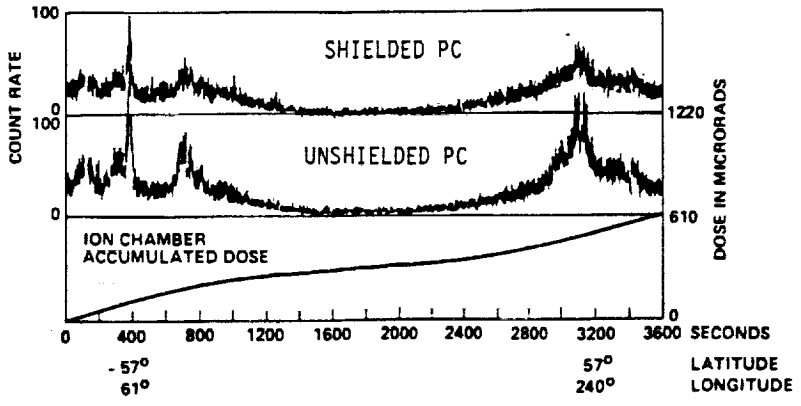

Fig. 16. One hour of ARD data in which the SAA and electron horns are not encountered. Large fluctuations in the PC count rates are likely due to electron precipitation.

the PCs in the SAA region. That the two ICs are in different shielding situations is obvious. Comparisons between the maps show high PC count-rates in the south electron horn region, but the ICs have no significant dose accumulation there. This is due to the relatively high sensitivity of the xenon-filled PCs to bremsstrahlung photons as previously noted. The averaging process reduced the maximum dose and count-rate contours displayed ~20% below the actual values.

The 29 passive packages all contained TLDs and plastic track detectors and were designed to map the low and high LET dose in the Spacelab module. Some passive packages carried fission foil detectors for neutrons, metal samples for activation analysis and nuclear track emulsions to record the entire LET spectrum. This array of passive packages at 29 locations would have been prohibitive to implement with active detectors and it provided specific information on radiation components of interest in a number of contexts including the determination of the biological dose-equivalent (neutrons, HZE particles), and activation of sample materials.

The large number of passive detectors at different locations, the measurement of the different environment constituents, and the temporal information from the active detectors presented an extensive survey of the radiation environment within SL-1. Cosmic rays produced most of the dose at all locations in the Spacelab module. Only at a few detector locations was the dose significantly above that expected from the cosmic rays alone. This was due to the large shielding depths (~14-66 g/cm^2 arithmetic average) of the Spacelab-Orbiter structure, and the low altitude. Detectors that had low shielding depths (< 1.5 g/cm^2) over significant solid angles (~8% of 4 pi sr) registered the largest doses in the module. For these detectors, the fraction of the measured dose attributable to trapped particles was about one-half the calculated values. This might indicate that the environmental model flux is too high. However, the trapped flux is directional, which is not in the model, and caution must be observed in such comparisons.

The steep trapped electron and proton spectra cause small solid angles about detectors subtended by light shielding (< 2 g/cm^2) to dominate the trapped particle dose component. Thus a "dose-weighted shield," calculated with the available trapped environment models, was found convenient to place the measured doses in order with respect to shielding. For a massive spacecraft such as this, an accurate vector shield model is necessary before accurate doses can be predicted. The directional characteristics of the ambient radiation may also need to be used. These considerations become particularly important at altitudes above 350-400 km where the trapped component is dominant and the proton energy spectrum is softer.

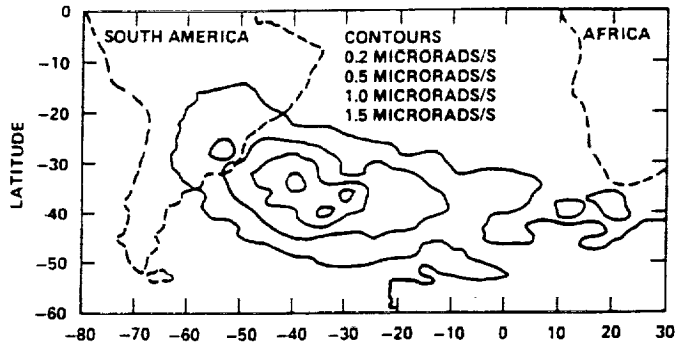

17(a) – IC-1

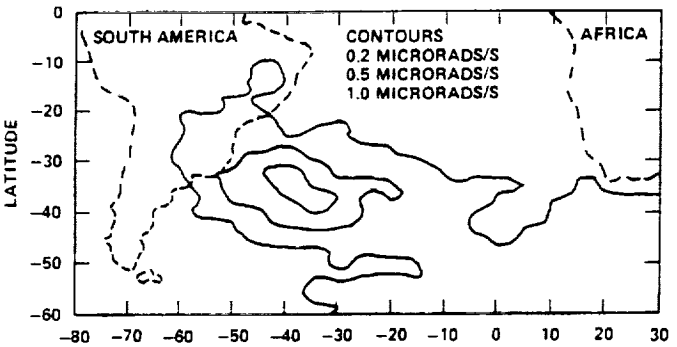

17(b) – IC-2

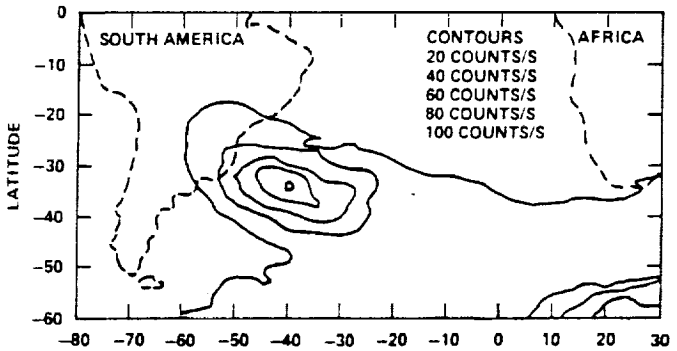

17(c) – PC-11

Fig. 17. Maps of dose isocontours in the SAA for ion chambers 1 and 2. The PC count rate for the counter in ARD 1 (unshielded) is also shown. Dose rates for the ion chamber in the top of rack 3, shown in 17(a), are higher in the center of the SAA than for the one in the bottom of rack 3, shown in 17(b). The contours of the proportional counter 17(c) show high rates in the south horn, near longitude 30°E /Parnell et al., 1986/.

3.4 Active Dosimetry Instruments on Unmanned Spacecraft

Since Explorer I discovered the Van Allen Belts, a large number of spacecraft have carried instruments of varied sophistication to directly measure the flux, spectra, spatial distribution and temporal variations of the trapped particles. Some products of these extensive data were the models of the spatial distribution, energy spectra, and major temporal features of the trapped protons and electrons. The most widely used models are those maintained by the National Space Science Data Center (NSSDC) at NASA/GSFC. The current models, AP8MIN, AP8MAX /Sawyer and Vette, 1976/, and AE8MIN, AE8MAX /Vette and Chen, 1987/, have superseded earlier versions /Vette, 1966; Singley and Vette, 1972; Teague and Vette, 1974; Chan et al., 1976, 1977/. The trapped radiation environment is discussed in Stassinopoulos /1987/.

Some unmanned missions have carried instrumentation specifically designed for measurements of dosimetric quantities. Generally these unmanned spacecraft and the instruments have considerably less shielding than the manned missions, but in most cases the shielding is more accurately known. The unmanned spacecraft have covered high altitude and polar orbits where data is not available from manned missions (except Apollo transits).

The OV spacecraft series was contemporary with Gemini and early Apollo flights. A variety of electronic radiation instruments were flown on some OV spacecraft including particle telescopes, single silicon detectors in spherical shielding, and TEICs on some flights. Considerable data from these missions are described in an issue of Aerospace Medicine/Janni, 1969c; Thede 1969/. These missions performed significant surveys of the environment and dose rates at altitudes between ~425 and 5000 km and in polar orbits. They investigated the temporal variations of the outer belt electrons and disturbances due to solar flares.

The OV1-2 (413 x 3078 km, 144°) carried three silicon solid state dosimeters and two TEICs under light shielding (up to 5 gm/cm^2) and an X-ray detector. Iso-dose and count-rate data were presented /Radke, 1969/ over the complete B-L space covered by the orbit.

OV1-4 (886 x 1012 km, 144.5°) carried three lightly shielded (1.3-2.6 gm/cm^2) TEICs. Iso-dose contours in B-L coordinates and geographic maps were presented. Dose rates of 80 rads/hr (2.2×10^4 μrads/s) from the TEICs were seen at the center of the SAA at 956 km. The inner radiation belt was still enhanced by electrons from the Starfish explosion, which had occurred about four years before the data was taken. In these data the anisotropy of the trapped radiation was noted in changes of dose-rate as the spacecraft rotated.

The OV1-12 mission (309x428 km, 102°) carried three TEICs with shielding of 0.3, 0.8 and 2.7 g/cm^2. They gave peak rates of 2.7x10^3, 1.39x10^3 and 0.83x10^3 μrads/s in the SAA and 1.6-9.7x10^3, 0.07x10^3, and a "trace" of μrads/s in the cusps of the outer belt. These data clearly showed the large temporal variability of the electron flux in the outer belt.

OV19 (470x5,677 km, 104.7°) carried a variety of active detectors including LET spectrometers and three TEICs under 0.3, 5.0 and 12.0 g/cm^2 shields /Cervini, 1971/. Data was reported from orbits during "quiet" times and following solar flares. The thinly shielded chamber gave rates from 2.8 x10^2 μrads/s at low altitudes to saturation of 1.7x10^5 μrads/s below the maximum altitude. Following solar flares at the higher altitudes, the most heavily shielded chamber gave rates up to 3.3x10^3 μrads/s.

Much of the OV radiation data was compared to environment models by Rhede /1969/ and Vette /1966/. Although there was influence from the Starfish electrons in the inner belt, these comparisons did provide valuable information on the status of the proton models.

More recently, the Defense Meteorological Satellite Program (DMSP-F7) has carried silicon detector "dosimeters" on a nearly polar orbit at 840 km /Mullen et al., 1987/. The four small silicon detectors are covered with hemispherical aluminum shields of 0.55, 1.55, 3.05, and 5.91 g/cm^2. The energy deposition thresholds on the detectors are set so that rather good separation between electrons and protons is achieved. The data is also binned so that energy depositions due to heavy cosmic ray nuclei, and evaporation or recoil nuclei from nuclear interactions in the the detector, fall in a bin called VH LET or "star events." These events are of interest in predicting "soft faults" in microcircuits and are caused by densely ionizing particles that would have a high relative biological efficiency (RBE).

The analyzed proton and electron spectral data (from 1984) was compared to calculations using the latest electron and proton models from the NSSDC. The proton data agreed with the calculations rather well and the electron results were a factor of ∿2 low compared to the models. The DMSP data displayed the temporal fluctuations of the outer zone electrons and the geographic distribution of the SAA protons and outer zone electron "cusps" at 840 km. A global "star" count map clearly showed the importance of the SAA protons in producing high LET events through recoil or interaction, and showed the geographic distribution of such events due to cosmic rays.

The above short description of some results from active dosimeters on unmanned spacecraft indicates the value of such data which covers much of the high altitude, high inclination regime not yet available from manned missions.

4.0 HZE PARTICLE INTEGRAL FLUX -- APOLLO AND SKYLAB

Over the past two decades, the research group at the University of San Francisco has been involved with measurement of high-LET particle radiation inside manned spacecraft. This work began with the observation of tracks of a few heavily ionizing particles in plastic nuclear track detectors flown aboard Gemini IV and Gemini VI in 1966 /Benton and Collver, 1967/. It became apparent from this work that a stack of a few layers of plastic films is a simple and direct means of measuring the integrated flux of heavy particles inside spacecraft. Plastic films are well-suited for such measurements; they are lightweight, rugged, and capable of recording and storing particle tracks over long periods of time with no loss of sensitivity and little latent track fading. Their inability to record lightly ionizing particles (i.e., electrons and protons with LET <6 keV/μm H_2O) permits registration of the relatively small number of heavy cosmic-ray nuclei in a high particle-radiation background situation such as exists in space.

By the start of the Apollo program, the field of dielectric nuclear particle track detectors was sufficiently developed that the first serious effort in the measurement of high-LET cosmic-ray particles could be carried out on Apollo missions. This was done on Apollo missions 8-17. Plastic nuclear track detectors recorded heavy particle radiation incident on astronauts /Benton et al., 1975a/ and several biological experiments /Benton et al., 1974/. The particle registration threshold for cellulose nitrate and Lexan detectors is approximately 80 and 225 keV/μm H_2O.

A detailed summary of results is presented in Table 9 /Benton et al., 1975a/. Dosimeters located on the astronaut's ankle consistently recorded a particle flux higher than those recorded by chest and thigh dosimeters. This is explained as due to less shielding of particles by the astronaut's body at the ankle region compared with the thigh and chest regions. An increase in particle flux was observed which correlates approximately with solar activity. The anti-correlation of the galactic cosmic ray flux below ∿5 GeV with solar activity is a well-recorded phenomenon, and the mechanism of solar modulation is still an active field of study /Marenny, 1987/. The high-LET particle flux in the last column shows that the flux on the Apollo 17 mission was ∿2.4 times that on the Apollo 8 mission.

Of this series, Apollo 17 was the most heavily monitored mission. In addition to personnel passive dosimeters, four biologically related experiments were instrumented to contain plastic nuclear track detectors. The four experiments included the HZE Dosimeter /Henke and Benton, 1974/, the Biostack /Bücker, 1975/, the ALFMED /Osborne and Pinsky, 1975/, and the Biocore /Haymaker et al., 1975/. Table 10 /Benton et al., 1975b/ summarizes

Table 9. Apollo Mission: HZE Particle Planar Fluences Derived from a Least Squares Analysis (Particles /cm^2 with LET_{350} > 150 keV/μm in Lexan)*

Apollo mission No.	Command module pilot (only in spacecraft)			Commander and lunar module pilot (also on lunar surface)				Geometric mean fluence	Geometric mean flux (cm^{-2}day^{-1})
	Chest	Thigh	Ankle	Chest	Thigh	Ankle	Film bag		
8	2.3 ± 0.4	2.6 ± 0.4	3.2 ± 0.5				8.2 ± 0.9	3.2 ± 0.5	0.58 ± 0.09
10	2.8 ± 0.3	3.2 ± 0.4	3.9 ± 0.4				6.5 ± 0.7	4.0 ± 0.3	0.61 ± 0.05
11	2.4 ± 0.3	2.8 ± 0.4	3.4 ± 0.4	3.5 ± 0.3	3.2 ± 0.3	3.9 ± 0.4	5.5 ± 0.6	3.4 ± 0.3	0.50 ± 0.04
12	3.3 ± 0.4	3.7 ± 0.4	4.5 ± 0.5	4.7 ± 0.4	5.2 ± 0.4	5.2 ± 0.4	7.4 ± 0.8	4.6 ± 0.4	0.56 ± 0.05
13	3.1 ± 0.4	3.5 ± 0.5	4.3 ± 0.5	4.4 ± 0.5	4.0 ± 0.5	4.9 ± 0.5	7.1 ± 0.9	4.3 ± 0.5	0.74 ± 0.09
14	4.4 ± 0.5	5.1 ± 0.6	6.1 ± 0.6	6.3 ± 0.5	5.8 ± 0.5	7.1 ± 0.6	10.1 ± 1.0	6.2 ± 0.5	0.83 ± 0.07
15	6.9 ± 0.7	7.9 ± 0.8	9.6 ± 1.0	9.9 ± 0.7	9.0 ± 0.6	11.1 ± 0.8	15.8 ± 1.3	9.7 ± 0.6	1.07 ± 0.07
16	8.2 ± 0.9	9.3 ± 1.1	11.3 ± 1.2	11.7 ± 0.9	10.7 ± 0.9	13.1 ± 1.0	18.7 ± 1.8	11.5 ± 0.9	1.38 ± 0.11
17	9.4 ± 0.8	10.7 ± 1.0	13.0 ± 1.0	13.4 ± 0.7	12.2 ± 0.7	15.0 ± 0.7	21.4 ± 1.3	13.2 ± 0.5	1.41 ± 0.05
Position factor	0.71 ± 0.05	0.81 ± 0.06	0.98 ± 0.06	1.02 ± 0.05	0.93 ± 0.05	1.14 ± 0.05	1.63 ± 0.05		

*LET_{350} includes only energy transfer with secondary electron energy <350 eV (equivalent to LET_{∞}^{tissue} >225 keV/μm).

Table 10. Apollo 17: HZE Particle Track Fluences[a]

Experiment	Detector layer number	Measured		Absolute planar track fluence (tr cm^{-2})		Flux[d] (tr cm^{-2} day^{-1})
		2 cones	Etched-through holes	LET_{350}^{CN} >170 keV μm^{-1}[b]	LET_{350}^{CN} >80.0 keV μm^{-1}[c]	LET_{350}^{CN} >80 keV μm^{-1}
HZE dosimeter (2 g cm^{-2})	C5	108.5	30.8	26.1 ± 3.9	153 ± 23	16.4
Biostack (10 g cm^{-2})	E2-1	60.7	19.4	16.2 ± 2.3	95 ± 14	10.2
	E13-25	55.0	18.0	13.4 ± 1.8	78 ± 11	8.4
Alfmed (~ 20 g cm^{-2})	bottom sheet	26.6	14.7	11.7 ± 1.5	69 ± 9	7.4
Biocore[e] (30–40 g cm^{-2})	implanted mouse brain dosimeters	31.0	8.7	7.0 ± 1.6	41 ± 9	4.4

[a] All measurements are from cellulose nitrate of the type USF 4b processed for 10.0 hr at 40 C in 6.25 N NaOH.
[b] Corresponds to an $LET_{350}^{Lexan} > 150$ keV μm^{-1} in Lexan or $LET_{\infty}^{Tissue} \gtrsim 225$ keV μm^{-1}.
[c] Corresponds to an $LET_{\infty}^{Tissue} \gtrsim 105$ keV μm^{-1}.
[d] Flux is in effective days in interplanetary space; mission duration 301.5 hr or 9.33 effective days.
The Biocore numbers are average for the four live mice.

the data from these experiments. The influence of shielding is observed, with the lightly shielded HZE dosimeter recording nearly four times the flux recorded by Biocore detectors. Even for the heavily shielded Biocore, there is a significant flux of high-LET particles. This underscores the point that complete shielding from the galactic cosmic rays is not practical due to spacecraft weight limitations.

The radiation environment of the Skylab missions differed significantly from that of the Apollo lunar missions. Being a near-Earth orbital mission, the Skylab was shielded both by the physical presence of the Earth and by the geomagnetic field. Measurements of high-LET particles incident on Skylab personnel, film vault /Benton et al., 1977/ and command module /Peterson and Benton, 1975/ were made using thin plastic films which for the first time included a more sensitive detector (LET $\gtrsim$ 80 keV/μm H_2O), cellulose nitrate, as well as Lexan. In the command module, five plastic nuclear track dosimeters were distributed around the interior. The results of these measurements are shown in Table 11 for the nine astronauts, the two drawers (B and F) in the film vault, and the five positions inside the command module.

Table 11. Skylab: HZE Particle Exposure

Mission (duration)	Astronaut	(1)	Observed (particles/cm²)	Planar fluence (particles/cm² 2π sr) (2)	(3)	Planar flux (particles/cm² day 2π sr) (2)	(3)
SL2 (28 days)	C. Conrad	~5–10	55	54	15	1.9	0.5
	J. Kerwin		45	65	5.4	2.3	0.2
	P. Weitz		41	52	5.4	1.9	0.2
SL3 (59.5 days)	A. Bean	~5–10	126	181	7.10	3.04	0.12
	O. Garriott		143	145	18.1	2.44	0.30
	J. Lousma		136	165	20.3	2.77	0.34
SL4 (84 days)	J. Carr	~5–10	211	274	29.6	3.26	0.35
	E. Gibson		206	315	11.2	3.75	0.13
	W. Payne		183	255	26.0	3.04	0.31
Film vault	Drawers						
SL1-2[a]	B	~16–30	19	27	2.9	0.70	0.075
SL1-3[b]	B		82	79	11	0.59	0.079
SL1-2[a]	F	~30–50	13	14	1.4	0.36	0.036
SL1-3[b]	F		31	42	4.0	0.31	0.030
Command module	Detector						
SL2 (28 days)	1	~3–14	58.2	93.8	11.5	3.35	0.41
	2	~1–24	35.1	27.5	4.3	0.98	0.15
	3	~3–20	26.1	21.1	2.6	0.75	0.093
	4	~3–22	53.4	85.9	8.7	3.07	0.31
	5	~1–20	52.8	37.0	8.6	1.32	0.31

[1] Estimated shielding (g cm^{-2} Al).
[2] $LET_{\infty} \geq 80$ keV μm^{-1} CN^{-1} (i.e. $LET_{\pi} \geq 105$ keV μm^{-1} tissue^{-1}).
[3] $LET_{\infty} \geq 170$ keV μm^{-1} CN^{-1} (i.e. $LET_{\pi} \geq 225$ keV μm^{-1} tissue^{-1}).
[a] 39-day exposure.
[b] 134.5-day exposure.

The average planar flux incident on Skylab astronauts is 2.0, 2.8 and 3.4 particles cm^{-2} day^{-1}, respectively, for the SL2, SL3 and SL4 missions. The flux increase anti-correlates well with solar activity and may also be due in part to a decrease in spacecraft shielding as expendables such as water, food and propellant were used up. The heavily shielded film vault drawers received a much lower flux of high-LET particles. Detectors in film drawer F ($\sim$50g cm^{-2}) recorded flux up to an order of magnitude lower than that recorded for the astronauts.

5.0 LET SPECTRA

The LET spectral information is needed in determining the appropriate quality factors for the radiations present /Heinrich, 1977; Curtis and Benton, 1980/. To date, a few measurements of integral LET spectra have been made during actual space flights or in orbiting satellites. The earliest measurements of LET spectra were made by the Soviets on Soyuz and Salyut flights using nuclear emulsions /Benton et al., 1974; Benton, 1983/. More recent measurements of LET spectra on Cosmos 782, 936 and 1129 involving the use of electronic spectrometers, emulsions and plastic track detectors /Akopova et al., 1985/, are shown for comparison purposes in Fig. 18. Integral LET spectra as a function of LET_∞ in water is shown for the four Soviet experiments and several spectra measured by this laboratory on various U.S. manned space flights. Soviet spectra labeled Nos. 2 and 3 (Cosmos 782 and 936 respectively) were obtained using electronic spectrometers, spectra No.1 (Cosmos 1129) using special nuclear emulsions, while spectra No. 4 measurements were made on Cosmos 936 using PNTDs. The emulsions used were of a special type which have a controlled registration threshold in six discrete steps and operate in a range of 1-1000 keV/μm. The emulsions record protons up to $\sim$50 MeV. The most recent spectra are those of Cosmos 1129, with the average shielding reported to be $\sim$20 g/cm^2. The LET spectra measured on Cosmos 936 using electronic detectors (Curve 3) and plastic track detectors (Curve 4) are in reasonably good agreement with each other /Akopova et al., 1985/. Shielding of electronic detectors on Cosmos 782 (Curve 2) was only about 1 g/cm^2. This lower shielding on Cosmos 782 as opposed to Cosmos 1129 results in a substantial contribution to absorbed dose from the trapped protons of the SAA.

The more recent LET spectra measurements (Fig. 18) include those from three selected flights of the Space Shuttle including mission 51F (320-km flights of Spacelab-2 in a 49.5° inclination), a high-altitude mission of 51J (500 km at 28.5°) and the most recent flight of Columbia (STS-61C, 324 km, 28.5°). These three missions are fairly representative of the different

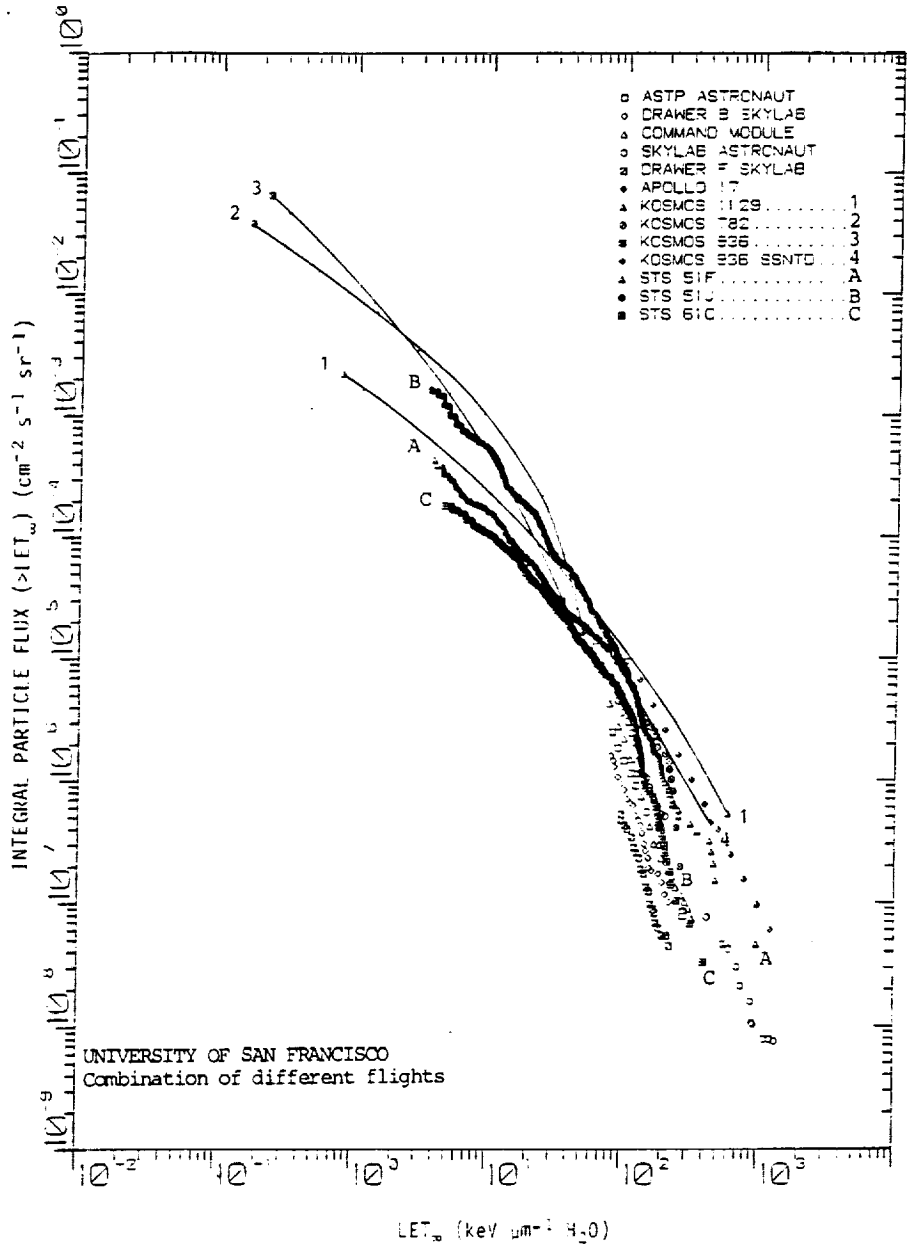

Fig. 18. Integral LET flux spectra showing number of particles as a function of LET_∞ in water for various U.S. and Soviet flights.

STS mission types flown during the first 24 flights and the corresponding LET spectra are shown as curves labelled A, B and C in Fig. 18. All three spectra represent the average obtained from the five CPDs for each flight. Here, Curve A for STS-51F differs from a similar figure published previously /Benton, 1986b/ in that the previously-published spectra represented measurements obtained from a stack of detectors located on the pallet of STS-51F (Spacelab-2). The pallet location had considerably less shielding, resulting in a much flatter spectrum at the higher LETs ($\gtrsim$ 100 keV/μm). Presumably this is the result of lower energy (predominantly Fe nuclei) particles which get shielded out at the crew locations.

Curve C, mission STS-61C (324 km, 28.5^{o}), represents the most typical low-altitude, low-inclination, 28.5^{o} mission. This can be compared with Curve B, that of mission STS-51J, at the same inclination but a considerably higher altitude. Spectra B and C are similar in slope, with spectra B being considerably higher in the lower LET portion of the spectrum since most of the tracks here come from the trapped protons. On the other hand, Spectra A from STS-51F (Spacelab-2, $\leq$ 324 km, 49.5^{o}) extends to greater LETs and is dominated by the contribution from GCR.

Measurements and/or calculations of LET spectra have also been performed by Heinrich /1977/, Letaw and Adams /1986/ and Adams et al. /1986/. Letaw /1986/ has calculated LET spectra for Skylab (Fig. 19). Here, CN and Lexan detector data include data from the crew, the command module, the two film drawers, and the calculations of Letaw and Adams /1986/. The calculated values were found to be consistently high by a factor of about two over the measured values. This disagreement also is present for their Apollo and the ASTP calculations. Work is now in progress aimed at reconciling measurements and calculations. In Fig. 20 is shown a comparison of LET spectra measured on STS-41G (352 km, 57^{o}) by Adams /1986/ and Benton /1985a/, independently, using CR-39. Both sets of detectors were exposed in separate GAS canisters located in the cargo bay of the Shuttle under similar shielding conditions. Both sets of measurements as well as the calculations of Adams appear to be in a reasonably good agreement with each other, even though the calculations did not include heavy ion fragmentation. Since the amount of shielding was low ($\gtrsim$ 2.0 g/cm^{2}), the fragmentation effect could be neglected.

6.0 NEUTRONS INSIDE SPACECRAFT

Neutrons inside spacecraft are normally produced from interactions of GCR and trapped protons with the spacecraft material. Also there are some albedo neutrons from the atmosphere. The atmospheric albedo neutrons from cosmic ray interactions are the major source of inner belt protons and their

flux and spectrum have been calculated /Armstrong, 1973/ and also measured at energies above 2 MeV /Bhatt, 1976; Lockwood, 1976/. Predictions dealing with neutron levels inside spacecraft, taking the three sources into account as well as the transport through the shielding, are not currently available. However, a few measurements have been made (see Tables 12, 13 and 14)/Frank and Benton, 1987/.

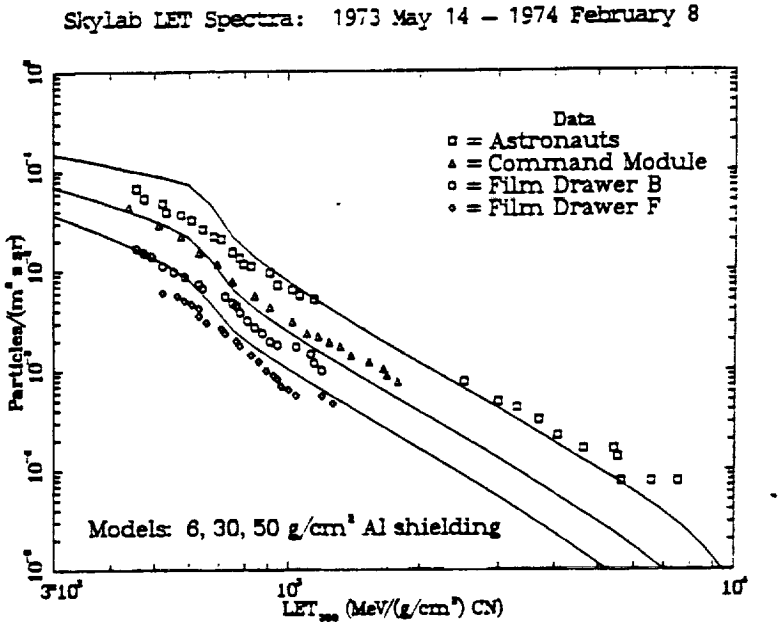

Fig. 19. Calculated and measured LET spectra for the Skylab mission. Measurements from the astronauts' dosimeters and other positions within the spacecraft are shown. All calculations have been reduced by a factor of 2 to account for heavy shielding behind the detectors /Letaw and Adams, 1986/; Benton et al., 1977/.

The high neutron capture cross-section of ^{6}Li for thermal and resonant neutrons provides a means of detection through the reaction of $^{6}Li(n,T)^{4}He$. The alpha particle fluences emitted from the surfaces of ^{6}Li TLDs are recorded with the CR-39 plastic track recorder. The thermal neutron response is separated from that of resonance neutrons by using Gd foil of 0.0025-cm thickness which shields a set of detectors. The difference between the

shielded and unshielded detectors is therefore a measure of the thermal neutron fluence, while the shielded detectors measure the resonance fluence. The thickness of the ^{6}Li TLDs was 4.5 mg/cm^2 yielding a sensitivity of 0.0049 tracks/thermal neutron. The sensitivity for resonance neutrons (0.2 eV-1 MeV), where a $1/E_n$ spectrum is assumed, has been calculated to be 2.56 x 10^{-4} tracks/neutron. The thorium/mica detectors (when used) yielded a rough estimate of the high energy neutrons (> 1 MeV). The Th/mica recorded track densities contain both proton-induced and neutron-induced components (see Tables 12, 13, 14).

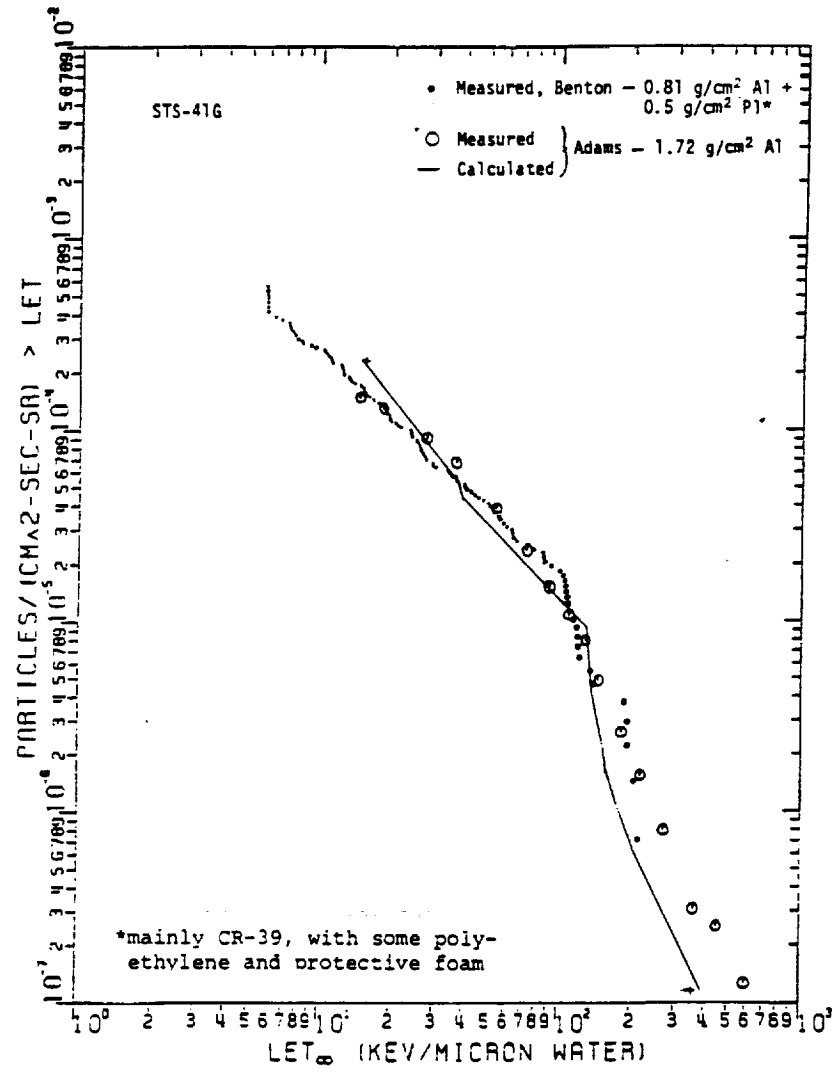

Fig. 20. Integral LET spectrum (total) for STS-41G, CRUX (experiment 3, No. 5-1, 2, batch USF3 /Adams, 1986; Benton, 1985/.

Table 12. Neutron Passive Detector Characteristics

Detector Type	Neutron Energy Range	Proton Energy Range
$^{6}LiF/CR-39$	0--1 MeV	--
$Gd/^{6}LiF/CR-39/Gd$	0.2 eV--1 MeV	--
^{238}U/mica	1.0 MeV	>15 MeV
^{232}Th/mica	1.2 MeV	>20 MeV
^{208}Bi/mica	>50.0 MeV	>50 MeV
^{181}Ta/mica	>1000.0 MeV	>1000 MeV

Detector Type	Sensitivity	Background
$^{6}LiF/CR-39$	2.04×10^{2} thermal neutrons/track	$\sim 150\ cm^{-1}$
$Gd/^{6}Lif/CR-39/Gd$	3.90×10^{3} resonance neutrons/track	$\sim 100\ cm^{-1}$
^{238}U/mica	6.70×10^{4} neutrons/track*	$\sim 0.5\ cm^{-1}$
^{232}Th/mica	1.38×10^{5} neutrons/track*	$\sim 0.5\ cm^{-1}$
^{208}Bi/mica	1.44×10^{6} neutrons/track*	$\sim 0.5\ cm^{-1}$
^{181}Ta/mica	$\sim 10^{8}$ neutrons/track*	$\sim 0.5\ cm^{-1}$

*Based on the neutron spectrum from Merker (Health Physics 25, 524-527, 1973). (for neutrons > 1 MeV).

Neutron Energy Range	QF	mrem-cm^2/neutron
<0.2 eV	2.0	1.02×10^{-6}
0.2 eV--1 MeV	6.4	4.92×10^{-6}
>1 MeV	10.0	5.95×10^{-5}

Neutron spectra have never been measured on spacecraft in orbit, while proton spectra are known only approximately for these flights. Therefore this method of measuring high-energy neutrons requires an assumption of a spectral shape in relative neutron-to-proton fluences based upon past space flight measurements and calculations of neutron production in the atmosphere. The fluence-to-dose conversion factors for thermal and resonant neutrons were from the NCRP /1971/; quality factors for thermal, epithermal and high-energy neutrons used were 2, 6.4, and 10 respectively. The accuracy of the thermal and epithermal neutron data is thought to be reasonable; however, the high energy neutron contribution which is bound to be of the most significance is fairly uncertain since the shape of the neutron energy spectra is not known.

7.0 STOPPING PARTICLES, SPALLATION PRODUCTS AND HIGH-LET RECOILS

A concern has existed for some time that short range, difficult to detect and measure, high LET tracks produced in tissue due to stopping protons, spallation products and proton-induced, high-LET recoils may have sig-

Table 13. Neutron Measurements on Selected Space Missions

Energy Range and Flux Measurements ($cm^{-2}d^{-1}$)

	< 1 MeV		> 1 MeV
Skylab	3.5×10^4		3.5×10^5
	0.02--2 eV		2 eV--2 keV
Apollo 11	$< 1.2 \times 10^6$		$< 4.0 \times 10^4$
Apollo 12	1.7×10^5		
Apollo 13	2.0×10^5		2.0×10^3
	< 0.3 eV	0.3 eV--1 MeV	> 1 MeV
Cosmos 936	2.0×10^4	6.6×10^4	1.1×10^5
Cosmos 1129	2.7×10^4	7.5×10^4	1.1×10^5
	< 0.2 eV	0.2 eV--1 MeV	> 1 MeV
STS-1	$< 2.2 \times 10^4$	$< 6.8 \times 10^4$	
STS-2	$< 7.8 \times 10^3$	$< 2.7 \times 10^4$	$< 1.6 \times 10^4$
STS-3	4.1×10^3	4.6×10^4	1.5×10^4
STS-4	6.1×10^3	4.7×10^4	3.4×10^4
STS-5	6.2×10^3	3.0×10^4	3.6×10^4
STS-6	6.0×10^3	7.6×10^4	2.2×10^4
STS-7	2.7×10^3	4.7×10^4	
STS-8	3.5×10^3	8.6×10^4	
STS-9	8.8×10^3	4.4×10^4	
STS-41B	2.4×10^3	1.4×10^4	
STS-41C	6.4×10^3	9.1×10^4	
STS-41D	1.0×10^3	5.1×10^4	
STS-41G	3.9×10^3	2.8×10^4	
STS-51A	5.0×10^3	2.4×10^4	

nificant radiobiological consequences. At least one biological phenomenon, that of light flashes observed by space crews, appears to be fluence dependent. The largest frequency of these events is observed during the passage through the SAA /Garriott, 1984; Savinykh, 1986/, as predicted by one of us /Benton and Henke, 1971/. Benton et al. /1972/ on Biosatellite III measured the high energy tail of the total recoil track distribution using plastic track detectors. Schaefer /1971, 1977, 1978/ using nuclear emulsions, measured the so-called "star" dose during the Apollo program. Space-based measurements of this component are difficult in that the measurement involves a track length distribution which ranges from the sub-micron region to a

Table 14. Summary of Neutron Dose-Rate Data

Flight	Neutron Dose Rates (mrem/day) Thermal	Resonance	High Energy
Cosmos 936	0.02	0.32	6.8
Cosmos 1129	0.03	0.40	6.8
STS-1	< 0.02	< 0.33	---
STS-2	< 0.01	< 0.13	1.0
STS-3	0.004	0.25	1.0
STS-4	0.006	0.23	2.0
STS-5	0.006	0.14	2.2
STS-6	0.006	0.38	1.3
STS-7	0.003	0.23	---
STS-8	0.003	0.43	---
STS-9	0.01	0.22	---
STS-41B	0.003	0.06	---
STS-41C	0.007	0.44	---
STS-41D	0.002	0.25	---
STS-41G	0.004	0.13	---
STS-51A	0.005	0.11	---

maximum of a few tens of microns while the detector may be in near saturation due to primary particles.

The dose and dose-equivalent fraction of this component is significant for lunar missions (see Table 15) /Schaefer, 1971/ and it is also expected to be of importance for a space station type of orbit. The Biosatellite III measurements yielded track density, ρ_R ($Z > 2$, $L_o > 10$ μm) $\tilde{\geq} 10^3$ $cm^{-3}d^{-1}$. This number is expected to increase considerably once the shorter tracks are taken into consideration.

Since the methods of measuring the charge and energy of all short-range interaction products and recoil particles have limitations, evaluation of the dose due to this component will depend more heavily on calculations. Calculations have been made of the absorbed dose and dose-equivalent for the secondary components from free space cosmic protons and for an SAA proton spectrum behind 20 g/cm^2 of aluminum /Armstrong, 1972; Santoro, 1972/. The dose contribution from secondary heavy nuclei, protons, pions, leptons and photons were individually calculated for depths up to 15 cm in tissue. In the case of the GCR protons, after ~2 cm depth, the dose-equivalents due

Table 15. Components of Mission Dose on First Lunar Landing Mission, Apollo XI

Component	Absorbed Dose, millirad	Dose Equivalent millirem
Protons	150	220
Stars	15	94
Fast neutrons	∿1	∿12
Heavy nuclei	5	46
Electrons and gamma rays	∿30	∿30
Total	201	402

/Schaefer, 1971/

to the secondary protons and secondary heavy nuclei both exceeded that due to the primary ionization of incident protons (∿4 rem/yr from the secondary heavy nuclei). On the other hand, for the trapped protons, the heavy nuclei and secondary protons both contributed a dose-equivalent of ∿10% or more of the primary ionization. These results depended heavily 1) on the QFs used (a single Q = 20 for the heavy secondaries) and 2) on the intranuclear cascade model used to obtain the distribution of the heavy target fragments/Bertini, 1969; MECC7/. More recent experimental work using heavy energetic particle beams from accelerators has improved the knowledge of the distribution of the mass and energy of the heavy target fragments. Relativistic beams of carbon and oxygen were fragmented on a series of targets ranging from hydrogen through lead /Heckman, 1975; Greiner, 1975, Lindstrom, 1975/. The momentum distribution of the multiply-charged projectile fragments were found to be related to the Fermi motion of the fragments. The average fragment energy as a function of the fragment mass was reasonably well represented by calculational models /Bertini, 1972/. However, the fragment production cross-sections were significantly different from those of the Bertini models, as shown in Table 16. As a result there is a large difference in the energy transfer cross sections (also displayed in the table). Greater differences will appear in the dose-equivalent because of the high QFs at high LET values as shown in Fig. 21 /Wilson, 1977, 1987/. The integral LET spectra are for single nuclear collisions of 2 GeV protons in water. Contributions from alpha particles derived from the Bertini model are included. Although the total event energy deposited differs by a factor of ∿35%, the highest LET

Table 16.* Comparison of Fragmentation Cross Sections (MBN) and Fragment Energy Transfer Cross Sections (MeV-MBN) of Bertini with experiments /Greiner et al., 1975/.

A_F	$\sigma_{BERTINI}$	$\sigma_{GREINER}$	$\overline{E\sigma}_{BERTINI}$	$\overline{E\sigma}_{GREINER}$
16	4.69	.02	5.04	.0006
15	103.4	61.5	60.6	56.9
14	40.0	35.4	48.8	51.7
13	18.5	22.8	37.6	48.3
12	32.2	34.1	85.8	68.2
11	8.2	26.4	37.9	99.1
10	11.0	12.7	52.8	62.0
9	1.2	5.2	6.5	25.7
8	.56	1.23	2.5	7.1
7	1.06	27.9	6.11	153.4
6	5.46	13.9	31.4	73.4
Total:	226.3	241.2	375.1	645.8

*Average integral energy transfer cross sections as a function of the LETs of heavy target products for a 2 GeV proton incident on water /Wilson, 1987/.

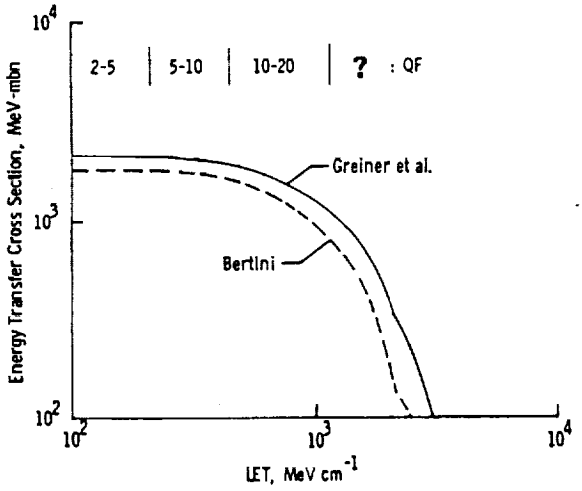

Fig. 21. Calculations from the Bertini model and derived from Greiner et al., 1975, are shown along with approximate quality factors for various LET regions /Wilson, 1987/.

components differ by a factor of three. Clearly, the assessment of risk from these components needs further work in measurement, calculation, and radiobiological studies.

8.0 INDUCED RADIOACTIVITY IN SPACECRAFT

Many materials, after exposure to high-energy space radiation, can become slightly radioactive. For gamma ray astronomers, this induced activity is of great concern since it makes a large and variable contribution to a gamma ray detector's background. This issue is of considerable interest for the Space Station since this will be a large spacecraft containing many types of materials and alloys, will spend many years in orbit, and will be bombarded by high fluxes of trapped protons (E > 30 MeV) as well as GCR, and high energy secondary neutrons (from the Earth's atmosphere or the spacecraft itself). Fishman /1974/ analyzed samples of various metals carried on Skylab 4 (400 km, 50^{0}, 84 d) at four locations with different shielding. The gamma ray activity from these samples was counted with high resolution germanium spectrometers after return to Earth. Counting began one week after sample return, and data was accumulated for $\sim 10^{6}$ s per sample. This method is not sensitive to very short half-life nuclides or those emitting short-range radiations (βs) but covers activity that significantly builds up in the spacecraft and deposits energy in the form of gamma rays in the crew areas. The data from the Skylab 4 samples, corrected to activity in orbit, and extrapolated to a very long exposure time (saturated activity) are shown in Table 17.

Following the re-entry of Skylab, some of the debris was found in Australia, returned to the U.S., and analyzed by Fishman and Meegan /1980/ (see Table 17). It should be noted that Skylab spent several months in low orbit below the SAA before re-entry so the shorter half-life nuclides in these results reflect the GCR and Earth albedo exposure only.

On the Apollo 17 mission and also on ASTP, Dyer et al. /1975/ and Trombka /19--/ flew NaI(Tl) scintillation crystals and made induced activity measurements with them immediately after return. The measurements indicated specific activation in ratio with the cosmic ray exposures of the two crystals and clearly showed activation lines due to neutrons.

Neutron measurements based on gamma ray line identification of specific nuclides with high neutron capture cross-sections have been made on a few occasions /Fishman, 1974; Keith, 1987/. They generally require long exposures to yield statistically significant results and the high energy measurements require complex corrections for proton interactions as do other passive techniques /Benton, 1985b/.

Table 17

17a). Specific Activities of Skylab-4 Activation*

Material-Interaction	Isotope	Half-Life	Specific Activity (Saturated) 1	2	3	4
$^{181}Ta + n$	^{182}Ta	115 d	17	7.9	5	3.9
$^{58}Ni + n$	^{58}Co	71 d	4.5	4.2	4.0	3.9
$^{58}Ni + p$	^{56}Co	77 d	2	2.2	3.1	4
$^{48}Ti + p$	^{48}V	16 d	0.8	1.8	1.5	3.7

*Activity is in disintegrations/kilogram-second
Location 1: in film vault
Location 2: adjacent to water tank
Location 3: on workshop wall, forward
Location 4: on workshop wall, aft
These were in descending order of shielding
Statistical errors varied from 15% to 60%

17b). Specific Activity in Skylab Debris Samples**

Material	Isotope	$T_{\frac{1}{2}}$	Specific Activity (at re-entry)
Al	^{22}Na	2.6 yr	1.1
SS	^{58}Co	71 d	0.8
SS	^{54}Mn	303 d	3.0
SS	^{56}Co	77 d	1.5

**Activity was extrapolated to re-entry time and was in dis/kg-s. /Fishman and Meegan, 1980/.

It is noted that the saturated activities from the Skylab data vary over the range ∿1-20 dis/kg-s. These are in the range of, or lower than, in some common minerals, or even ^{40}K activity in the human body. If the average saturated activity were as high as 10 dis/kg-s, the total activity in a 5×10^5 kg spacecraft would be about 150 micro-Curies, spread over a few tens of meters. An assessment of the activity and resulting contribution to dose of a spacecraft with a correct materials list and distribution would be useful, but has not been done.

9.0 COMPARISON OF DOSE MEASUREMENTS WITH CALCULATIONS

The development of methods for the accurate prediction of dose and particle flux have been long-term goals in the field of space radiation protection. Over the past two decades, a large effort has gone into the development of these methods and techniques and in applying them to many spacecraft and missions. In addition to predictions for manned flights, much of this work was motivated by a concern about radiation effects on electronic circuits, computers, solar cells, photographic material, and other radiation-sensitive components and experiments. Here, we refer only to a few selected examples and briefly discuss some of the major features and limitations of the calculations reported in the literature. The state of the art in performing such calculations was previously described by Langley /1970/. Even earlier calculation methods were described and compared with space-flight measurements for some of the Gemini, Apollo and OV1-XX flights /Case, 1969; Janni, 1969b/. The trapped proton and electron spectra as a function of McIlwain parameters (B, L) were assembled by several groups (Vette, Thede, Reagan). Sector (vector) shielding of the Gemini and Apollo spacecraft was developed from engineering drawings and by measurements using gamma ray sources. Methods were developed by which protons, electrons and bremsstrahlung photons were transported through the sector shielding and doses calculated at interior points. Initial comparisons on Gemini and the OV spacecraft showed that the trapped environmental models needed improvement, since predicted and measured doses differed by a factor of three or more for some of the models and orbit locations /Schneider, 1969; Radke, 1969; Janni, 1969b/. However, as the models were improved with new data, the differences were reduced.

By the time of the Skylab missions, the environmental models had been revised and the methods of particle transport had been improved, e.g., Watts and Burrell /1971/, Wright and Burrell /1972/, and Hill /1973/. Good agreement was found between calculated doses and measured doses at five locations in the command module on Skylab 2, with calculated values only 10% to 40% above the measured values /Janni, 1976/. Other comparisons within the Skylab Workshop were also within that range /Hill, 1976/. Dose measurements using TLDs and comparisons with calculations were also made in the Shuttle crew area /Atwell et al., 1987/ and in the Spacelab module /Parnell et al., 1986/. The measurements were within about a factor of two or better of the calculated values with the calculated doses being generally higher than the measurement values.

Methods used to transport protons, electrons and their bremsstrahlung photons, and GCR nuclei through the shielding of the Shuttle plus Spacelab-1

have been previously described / Burrell, 1964; Watts and Burrell, 1971; Wright and Burrell, 1972/. The proton transport code uses an approximation to account for interaction losses and energy deposited by secondaries, and this causes an overestimate of the actual absorbed dose. Calculated doses from this method were compared to those from a Monte Carlo calculation that included all interactions and secondaries /Alsmiller et al., 1972/. For trapped proton spectra, the Monte Carlo calculation gives absorbed doses 10-15% smaller and dose-equivalents less than 5% smaller than the approximation method. The transport method for electrons and bremsstrahlung photons /Watts and Burrell, 1971/ gives doses within a few percent of the more complex methods such as ETRAN.

The method used to transport cosmic ray nuclei also contains approximations in the treatment of interactions and cascade build-up, but the accuracy is ∿20% for prediction of absorbed dose for shielding thicknesses of up to ∿20 g/cm^2. Recently new transport methods for cosmic ray nuclei have been developed for calculating LET spectra within spacecraft /Heinrich, 1977/; Letaw and Adams, 1986; Letaw, 1986/. The Cosmic Ray Effect on Microelectronics (CREME) model /Adams, 1986/ considers loss by ionization and interaction but does not consider heavy fragments or production of other secondaries. Comparisons of measured and CREME model calculated LET spectra made with PNTDs are shown in section 5.0 of this paper.

The major limitations in the accuracy of the present methods used to calculate absorbed dose and particle fluxes inside spacecraft arise principally due to a lack of detailed knowledge of the primary environments (flux, spectra, temporal and directional properties) and of spacecraft shielding distributions. Both the trapped particles and the GCR (up to several GeV) have temporal variations due to solar activity /Webber and Lockwood, 1981; Marenny, 1987; Heckman et al., 1970, 1972/ that are only approximately accounted for through the use of the solar maximum and minimum models. In addition to the temporal variations there are directional characteristics, particularly of the trapped particles /Watts, 1987/ that have not previously been incorporated into the calculations. The currently used omnidirectional environments may be satisfactory in the case of spinning or celestial pointing spacecraft, but are not appropriate for gravity gradient or velocity vector stabilized spacecraft such as the LDEF and the Space Station. At present, the knowledge of the environments is generally considered to be accurate only to a factor of ∿2.

Accurate calculation of the dose-equivalent within orbiting spacecraft will probably require more precise calculation of the contribution from secondary charged components than has previously been included in STS-mission-

type oriented calculations. Of concern here is the contribution from the evaporation and recoil particles resulting from interactions in the tissues, the spacecraft shielding and materials. Such calculations also involve the use of quality factors that are presently uncertain for the highly-charged, low-energy, high-LET particles. Although calculations including all relevant effects have not been applied to missions and complex shielding geometries, example calculations with spherical aluminum shielding and tissue targets have clearly shown the importance of these secondaries /Armstrong, 1972; Santoro, 1972/. Those calculations also include the neutral components (neutrons, pions, etc.,) and their effects, although they are not tabulated separately in the results.

10.0 SUMMARY AND CONCLUSIONS

During the last twenty-five years, dosimetry data has been slowly accumulating in the U.S. and Soviet manned space programs. The data covers almost all manned flights, and thus a variety of low Earth orbits (from ~210 km to 500 km) and translunar flights. Data exists from flights of Vostok to Salyut 7 and Gemini to Spacelab, with their various complexities of shielding.

Passive dosimeters have yielded integral dose and mission average dose-rate information for low-Earth orbit ($\lesssim$ 500 km, and inclinations $\lesssim 65^{\circ}$). For the lowest altitudes and typical locations in the spacecraft the dose is dominated by the highly penetrating GCR contributing 5-10 mrad/day (depending on inclination), which is nearly independent of spacecraft shielding. Measurements have shown that for various locations in the Spacelab-1 module (STS-41A, 250 km, 57°) the trapped particles from the SAA contributed at most 40% and typically 15% or less of the total dose /Parnell et al., 1986/. At higher altitudes (350-500 km) the picture changes dramatically, with dose-rates increasing more than an order of magnitude and the bulk of the dose now coming from the trapped protons. Indeed, on mission STS-51J (~500 km, 28.5°), one passive dosimeter recorded an average mission dose-rate of nearly 200 mrad/day (arithmetic average shielding of ~16.4 g/cm^2).

The complex shielding of the manned spacecraft causes variations in the dose as a function of location. The arithmetic average of shielding depth can be quite high (Cosmos 1129, ~20 g/cm^2; Spacelab-1, 14-66 g/cm^2; Space Shuttle mid-deck, 16-30 g/cm^2). However, it has been shown that small solid angles (< 10% of 4π steradians) of thin shielding (< few g/cm^2) act as "radiation windows," causing dose to vary according to locations /Parnell et al., 1986; Atwell and Beever, 1987b/. These "thin windows" are not indicated in the arithmetic average of the shielding depth.

The number of locations that have been monitored limit the knowledge of the variation in dose due to shielding at different locations. Twenty-nine passive detectors showed a dose maximum/dose minimum variation of only 1.4 on Spacelab-1. On Skylab, five detectors showed a variation of 1.6, similar to the detectors on Salyut-7. The six detectors flown in the crew area of the STS at the highest orbit (51J) showed a ratio of 2.2. This indicates that the location dependency of dose rests largely on the trapped particle contribution, as expected. Most previous spacecraft have passed through the SAA in various attitudes, but the Space Station, which will have a somewhat similar attitude in the directional SAA flux, will be likely to have larger dose variations.

Only on several occasions have active detectors been used, tailored specifically to obtain data on space radiation dosimetry. Early measurements were made on Gemini and Apollo. Skylab carried a tissue-equivalent ion chamber and an LET spectrometer. On Cosmos 936 the Soviets flew an active LET spectrometer inside and outside the spacecraft /Kovalev et al., 1981/. On Spacelabs 1 and 2, Parnell et al. /1986/ and Fishman et al. 1986a/ employed active detectors which contributed significant information on the temporal variations of the radiation field inside the Spacelab module and on the pallet. These instruments allowed the separation of dose into its components of GCR, trapped protons and the bremsstrahlung from trapped electrons. Also, frequent occurrences of bremsstrahlung photon "bursts" were observed from electrons precipitating from the trapped belt. This work clearly showed the importance of detailed real-time dosimetry for the Shuttle flights, and particularly for the Space Station.

In the absence of detailed information on the flux, charge and energy spectra of charged particles, LET spectra have been measured on several missions. There is general agreement between the reported U.S. and Soviet results, even though the methods used (electronic detectors, nuclear emulsions, plastic track detectors) are different. The LET spectra clearly show differences between low and high inclination and altitude missions. However, relatively few missions, orbits, and shielding situations have been covered and much more data is needed.

While a reasonable amount of data exist for low altitude (< 500 km) and low inclination orbits, there is insufficient experimental dosimetric data for high altitude (> 500 km), polar, and geostationary orbits.

Very little data exist on the neutron component, but the measurements that have been made indicate it cannot be ignored on future missions, particularly in large spacecraft such as the Space Station. Neutron energy spec-

tral measurements need to be made as soon as possible, although this will be difficult to accomplish. There is no direct information available on the temporal variation of neutrons.

Since the LET spectra have not been measured on all missions and the neutron fluence has seldom been measured, a complete assessment of the dose-equivalent cannot be made. However we can give estimates of the fractions of dose-equivalent on a few missions. The fractions of low LET dose (from TLDs), high LET dose (from track detectors), and neutron dose (from fission foils) in the Spacelab-1 module (250 km, 57^{o}) are approximately 30%, 56%, and 14%, respectively. On STS-5 (297 km, 28.5^{o}) the fractions were ~54%, 27%, and 21%. High energy neutron measurements for higher altitude STS flights are not available for a similar comparison.

There have been some comparisons of dose and LET data with calculations that model the primary particle environments, the orbital parameters, and shielding distributions (usually simplified). Recent comparisons generally indicate that for total dose the predictions are too high. On Spacelab-1 the predictions were high by a factor of $\gtrsim 2$ /Parnell et al., 1986/. The calculations are based upon isotropic flux models, whereas the trapped environment is highly anisotropic /Heckman and Nakano, 1963/. This fact, and the effects of "thin windows" in shielding make such comparisons approximate at best. The trapped proton and electron environments have temporal changes which the models do not fully take into account, that may also affect the calculated doses and fluxes /Heckman and Lindstrom, 1972/. A comparison of LET measurements in a simple shielding situation (a GAS canister in the Space Shuttle bay) and a calculation based on GCR and geomagnetic effects agree quite well /Adams et al., 1986/. However, for situations involving greater amounts of shielding, the comparisons are not satisfactory /Letaw and Adams, 1986/. Such comparisons are also needed in more complex shielding situations and extending to low LETs where protons are important contributors of dose.

Several questions concerning temporal variations of dosimetric quantities can only be solved by long-term monitoring in various orbits. Solar activity affects both the trapped environment and the GCR flux. Higher solar activity heats and expands the Earth's atmosphere causing greater ionization loss of trapped particles and a decrease in flux in low Earth orbit. At the same time, the larger convected solar magnetic field "modulates" (reduces) the GCR flux at Earth. Very energetic, but rare, solar particle events can occasionally reach low Earth orbits. The effect of long-term secular variations in the geomagnetic field is also of concern.

It is important to determine the populations of short range tracks -- recoils and spallation products that arise as the result of irradiation of

tissue with cosmic ray nuclei and trapped energetic protons--and to assess their radiobiological consequences.

Finally, much more detailed information is needed on how the different components of the radiation field contribute to the overall dose and their spatial and temporal variations, as well as the effect of complex shielding distributions, before reasonably accurate extrapolations can be made to the case of the Space Station and other future missions of long duration.

The following is a partial summary of Soviet regulations, recently enacted, which deal with radiation safety of space crews and related issues.

APPENDIX

USSR STANDARDS FOR SPACE CREW RADIATION SAFETY IN SPACE FLIGHT

OUTLINE

	Type of Document and Effective Date	Title of Document
1.	Guiding Normative Document RD 50-25645.209-85 1 July 1987	SYSTEMATIC INSTRUCTIONS: SPACE CREW RADIATION SAFETY DURING SPACE FLIGHT (System for measuring cosmonauts' Individual dose during their career)
2.	USSR Government Standard GOST 25645.215-85 1 Jan. 1987 through 1 Jan. 1992	SPACE CREW RADIATION SAFETY DURING SPACE FLIGHT (Safety norms with flight duration up to three years)
3.	USSR Government Standard GOST 25645.202-83 1 Jan. 1986 to 1 Jan. 1992	SPACE CREW RADIATION SAFETY DURING SPACE FLIGHT (Requirements for individual and on-board dosimetric control)
4.	USSR State Committee of Standards. GOST 25645.214-85 1 Jan. 1987	SPACE CREW RADIATION SAFETY DURING SPACE FLIGHT (Model of generalized radiobiological effect)
5.	USSR Government Standard GOST 25645.203-83 1 Jan. 1985	SPACE CREW RADIATION SAFETY DURING SPACE FLIGHT (Model of human body for computation of tissue dose)
6.	Guiding Normative Document RD 50-25645.309-85 1 Jan. 1987	SYSTEMATIC INSTRUCTIONS: STANDARD METHODS OF EXPERIMENTAL DETERMINATION OF THE FUNCTION OF SHIELDING ELEMENTS AND TECHNICAL EQUIPMENT INSIDE A SPACECRAFT FROM IONIZED RADIATION
7.	USSR State Standard 25645.134-86 (no date given)	SOLAR COSMIC RAYS. A MODEL OF PROTON FLUXES

8.	USSR Government Standard GOST 25645.211-85 1 July 1987	SPACE CREW RADIATION SAFETY DURING SPACE FLIGHT (Nuclear interaction characteristics of protons)
9.	USSR Government Standard GOST 25645.212-85 1 Jan. 1987	SPACE CREW RADIATION SAFETY DURING SPACE FLIGHT (Nuclear interaction characteristics of multicharged ions)
10.	USSR Government Standard GOST 25645.116-84 1 Jan. 1986	PENETRATION OF COSMIC RAYS INTO EARTH'S MAGNETOSPHERE (Terms and definitions)

SUMMARIES OF DOCUMENTS

1. SYSTEMATIC INSTRUCTIONS
SPACE CREW RADIATION SAFETY DURING SPACE FLIGHT
(System for measuring cosmonauts' individual dose during their career)
Guiding Normative Document RD 50-25645.209-85. Effective 1 July 1987.

These instructions establish the system for measurement and control of individual radiation doses received by cosmonauts from all types of radioactive exposure during their career, and the system for determining the doses received from radiological examinations. The instructions also implement control for observance of the norms of space crew radiation safety in space flight. They apply to all authorities concerned with the selection, training and medical examination of cosmonauts and to the USSR Ministry of Health Radiation Safety Service which implements cosmonaut radiation safety measures. The document states that radiological examination of cosmonauts must be conducted on standard X-ray equipment, and that all X-ray radiation received by cosmonauts in pre-acceptance examinations, periodic examination at all stages of their careers, examination during cases of illness, and during space flight is subject to obligatory measurement and control. The procedure for examination at the first selection as cosmonaut candidates an the periods for planned radiological examination of cosmonauts' organs is outlined. The document lists the organs of the body which are subject to count, assessment and control or radiation dose absorption, and gives a for mula for this purpose. Tables show the values for specific dose strengths for various areas of the body, including organs, joints, cavities, vertebrae, etc.

Requirements for collection, registration, storage and control of information concerning individual doses of radiation of cosmonauts are given in detail. A general medical record is kept of all types of radiological examinations conducted at all stages of the cosmonauts' preparation, but individual radiation doses are recorded in a special chart which is the cos monauts' basic document throughout their career. This chart is kept where-

ever the cosmonaut underwent the last medical examination. An example of this chart and specific details of correct maintenance of the chart are given. Protection against random duplication of radiological examination by different medical personnel or in different institutions is provided by this chart, which is controlled by a representative of the USSR Ministry of Health Radiation Safety Service. The Ministry assesses the individual radiation dose of the cosmonauts at any stage of their career and gives conclusions to the medical commission upon demand.

2. SPACE CREW RADIATION SAFETY DURING SPACE FLIGHT
(Safety norms with flight duration up to three years)
USSR Government Standard GOST 25645.215-85. Effective 1 January 1987 through 1 January 1992.

Standards are established for space crew radiation safety norms during space flights of up to three years' duration and for the period of the cosmonaut's career. These standards are obligatory in all stages of development of space crew radiation safety support systems, i.e., in development of space flight programs and activities of crews; in planning of space crew radiation protection and testing its effectiveness; in planning on-board and individual dosimetric control and its implementation in space flight; in the execution of planned projects and operational measures for implementation of radiation safety; in the planning of radiological examination of cosmonauts. The radiation safety norms include: normative level of radiation risk; maximum allowed dose-equivalent of radiation in the absence of probable sources of radioactive danger; control of hourly average equivalent dose; maximum allowed dose-equivalent of a single radiation exposure during space flight; maximum allowed dose-equivalent during a cosmonaut's career (not to exceed 4 Sv). The document gives methods of calculating the above-mentioned safety norms, states the dose-equivalent of instant exposure during a space flight (not to exceed 0.5 Sv), and gives methods of determining values of dose-equivalent during a space flight and during a cosmonaut's period of preparation, selection and medical examination. A table giving the values of normalized quantities for flights of various durations is provided and explanation of terms of reference is also given.

3. SPACE CREW RADIATION SAFETY DURING SPACE FLIGHT
(Requirements for individual and on-board dosimetric control)
USSR Government Standard GOST 25645.202-83. Effective 1 January 1986 to 1 January 1992.

Standards are established for individual and on-board dosimetric control requirements for manned space flights. Various categories of radiation situations are defined by means of the ratios of the hourly dose-

equivalent to the control hourly dose-equivalent, giving the values of relative radiation risk. These ratios are given in a table showing ranges from "safe radiation" to "emergency radiation" situations. The choice of measures to ensure radiation safety of space crews is made with regard to the different radiation situation categories (RSCs) in which they may be placed, the main task of dosimetric control, therefore, being to assess the RSC and determine the generalized dose of radiation received by each crew member during flight. "Dosimetric control" is defined as a combination of individual and on-board dosimetric control (ODC); requirements for both types of control are specified as follows:

Individual dosimetric control. Methods include individual reading dosimeters, individual passive dosimeters, and ground or on-board testers to take readings from passive individual dosimeters. Must include absorption or dose-equivalent in case a radiation situation becomes non-standard, dangerous or emergency-status. (Note: a dose on the surface of a man's body is considered to be a dose at points where the depth is 7×10^{-5}m from the surface of the body.) The document states that individual passive dosimeters are intended for continuous wear by crew members throughout the flight; individual reading dosimeters need not always be worn in safe or standard RSCs but must then be placed in the compartment where crew members spend most of their time. Individual dosimeters must be capable of measuring radiation in all crews' work conditions, including extra-vehicular activity (EVA). The number and placement of individual and ODC systems must allow measurement of the generalized dose received by each crew member.

On-board dosimetric control. The ODC assesses the RSC and measures the generalized radiation dose by means of results of individual dosimetric control. To determine this dose, ODC must ensure reception of information necessary to calculate the quality of ionized radiation, space and time irregularities of the field of dose distribution, and measure the absorption and hourly dose-equivalent of radiation. To assess the RSC, the ODC must determine the generalized dose of radiation, and the correspondence of a radiation situation with its projected model, including information which establishes the source of ionized radiation which caused the degradation of the radiation situation. The ODC must also provide the crew with information concerning changes in the RSC. Information measured by the ODC must be transmitted to Earth via radio-telemetric system channel either by sampling or in complete form. The frequency and amount of information transmitted must be determined by the RSC. Technical work is performed by the dosimetric control system.

Under the heading "Volume and dosimetric control operation," the docu-

ment states that composition, volume and operation of dosimetric control is established in a technical system which ensures the radiation safety of spacecraft crews and requires expertise corresponding to the normative-technical document in force. The document enumerates further detailed requirements for dosimetric control:

a) Dosimetric control system composition and its volume must correspond to the requirements of these standards.

b) All crew members must be provided with individual dosimeters.

c) The dosimetric control system must be capable of changing its mode of operation, depending on the RSC.

d) During safe and standard radiation periods, the results of ODC must be available to the crew on demand.

e) During non-standard, dangerous or emergency radiation situations, the results of ODC must be available to the crew continuously, but for individual dosimetric control, reading dosimeters must be used.

f) During non-standard, dangerous or emergency situations, the results of individual dosimetric control must be entered into the information processing unit to determine the generalized radiation dose.

g) When a radiation situation shifts into a dangerous or emergency category, signals corresponding to the changes of the radiation situation must be given to the crew.

4. SPACE CREW RADIATION SAFETY DURING SPACEFLIGHT
(Model of generalized radiobiological effect)
USSR State Committee of Standards GOST 25645.214-85. Effective 1 Jan. 1987.

This standard establishes a mathematical model of a generalized radiobiological effect depending on the time distribution of a radiation dose-equivalent. It is intended for determination of radiation risk when evaluating and providing for the radiation safety of a spacecraft crew during space flight as required by GOST 25645.215-85. The generalized radiobiological effect (GRE) is understood as the risk faced by the crew of a space vehicle during space flight when determined sources of radiation exposure are present and probable sources are absent. The document states that:

a) The GRE characterizes quantitatively an increase in the mortality rate as a result of somatic radiobiological effects, developing as a result of radiation exposure.

b) The model of the GRE consists of a model of the dependence of the GRE on the generalized dose of radiation (GDR) and a model of the dependence of the power of the radiation dose on the time distribution of the equivalent dose of radiation.

c) In the model of the dependence of the GRE on the GDR it is accepted that the GRE changes in proportion to the mortality rate in the absence of radiation exposure.

d) The dependence of the power of the GDR on the time distribution of the equivalent dose of radiation is accepted according to the model of effective dose, which reflects the rise and fall of radiation damage to the human organism in the time following radiation exposure.

Formulae are presented to represent the dependence of GRE on GDR, taking into account such factors as time, power of the GDR, age of the cosmonaut, etc.

5. SPACE CREW RADIATION SAFETY DURING SPACE FLIGHT
(Model of human body for computation of tissue dose)
USSR Government Standard GOST 25645.203-83. Effective 1 Jan. 1985.

Standards established for the form and basic dimensions of a model of a human body and coordinates of representative points for computation of tissue dose of cosmic radiation and the development of documentation during design of such models for conducting experimental research. The standards are binding for organizations occupied with determination of the spatial distribution of an ionized radiation field in a cosmonaut's body with regard to spacecraft crew radiation protection. The model used for this purpose is an anthropomorphic, tissue-equivalent, homogeneous figure having the form and average dimensions of a human male. Simplified models, cylindrical and spherical, will also be used.

Tables and figures with accompanying text present in detail the form, basic dimensions, representative points and chemical composition of all three models: anthropomorphic, cylindrical and spherical.

An anthropomorphic figure must be used to determine the characteristics of an ionized radiation field in a cosmonaut's body and to assess the error of determining these characteristics with the aid of an average model. A cylindrical model must be used to determine the characteristics of an ionized radiation field, necessary for calculation of the generalized dose, taking into account the irregularity of space radiation. A spherical model must be used for approximate assessment of a generalized dose. Using representative points in a real human (average male) as a guide, values of the equivalent dose in similar points on the models should be used in the calculation of the generalized dose in order to evaluate the effectiveness of radiation protection for the crew of a space vehicle.

6. SYSTEMATIC INSTRUCTIONS
STANDARD METHODS OF EXPERIMENTAL DETERMINATION OF THE FUNCTION OF SHIELDING ELEMENTS AND TECHNICAL EQUIPMENT INSIDE A SPACECRAFT FROM IONIZED RADIATION
Guiding Normative Document RD 50-25645.309-85. Effective 1 Jan. 1987.

Standard methods are established for determining functional shielding of elements (including technical equipment and crew members) inside spacecraft from ionized radiation. Tests are conducted on a model which must ensure the possibility of determining the mass surface current of controlled sections. This model must also include:

a) a coordinate system for moving the gamma radiation detector on cylindrical and/or spherical surfaces;

b) a point-wise isotropic single energy source of gamma radiation;

c) a gamma radiation detector;

d) an apparatus for registering the position of the source with respect to the detector and the number of impulses acting on the detector.

The method of measuring the functional screening of a point inside the object is described in detail, as are the basic parameters which characterize a source of non-dispersed gamma radiation and the measurements in a test process. A closed isotropic source of Cs 137 (E_r = 661 keV) with isotropy not exceeding ± 10% serves as a source of gamma radiation. A scintillating spectrometer with an inorganic NaI crystal and diameter equal to height serves as a gamma radiation detector. The creation of impulses corresponding to non-dispersed gamma radiation is done by means of amplitudinal impulse discrimination levels A_1 and A_2. Level A_1 corresponds to the maximum peak of photo-absorption and level A_2 is 20% less than level A_1. Formulae for determining the mass surface density and the impulse counting speed follow.

Tests are conducted in normal climactic conditions as defined by GOST 20.57.406-81 and duration of the test is determined by the number of points being measured for screening function. Personnel participating in the tests must have a third-class rating for safe operation of electrical installations with voltage loads up to 1000 volts. The work foreman must have an engineer-physicist rating.

Detailed instructions are given for graduated measurements of radiation by the amplitude distribution of pulses within the detector. The registered number of impulses for any control section must be no less than 4×10^3.

7. SOLAR COSMIC RAYS. A MODEL OF PROTON FLUXES
USSR State Standard 25645.134-86. No effective date given.

This document establishes a model of proton fluxes of solar cosmic rays (SCR) with energy $E \geq 10$ MeV in interplanetary space beyond the magnetosphere of the Earth near the plane of the ecliptic at a distance of approximately one astronomical unit from the sun in different periods of the 11-year cycle of solar activity. The standard is intended for use in calcula-

tions of the radiation activity of SCR fluence on technical devices, biological and other objects in outer space. The duration and position of the beginning of the 11-year solar activity cycle are determined from GOST 25645.302-83. The present document gives formulae for calculating the duration of active and passive periods (characterized by different values of SCR fluxes). The document states that, during passive periods of the 11-year cycle, a total fluence of protons of solar cosmic rays with energy $E \geq 10$ MeV is assumed equal to 10^7 cm^{-2}, regardless of the duration of the spaceflight. During the active period of the cycle, the total fluence of protons of solar origin, N_E cm^{-2}, for all proton energies greater than E, is a random quantity. This randomness is a result of the occurrence, during the flight period, of a random number of solar proton events. Equations are given to determine the distribution density of the total fluence of protons. Tables show the probabilities of exceeding the total fluence of protons for flights of duration varying from ten days to three years.

8. SPACE CREW RADIATION SAFETY DURING SPACE FLIGHT
(Nuclear interaction characteristics of protons)
USSR Government Standard GOST 25645.211-85. Effective 1 July 1987.

This document establishes the nuclear interaction characteristics of cosmic ray protons, as well as protons and neutrons (nucleons) formed by them in spacecraft shielding (secondaries), for the nuclei of elements from carbon to lead in the 20-1000 MeV nucleon energy range. Among the characteristics taken into consideration are the nucleon mean path to nuclear interaction and the double differential of energy and the exit angle of distribution of secondary nucleons in an inelastic nucleon-nucleus interaction. The methods and formulae for the calculation of the nuclear mean free path are given.

9. SPACE CREW RADIATION SAFETY DURING SPACE FLIGHT
(Nuclear interaction characteristics of multicharged ions)
USSR Government Standard GOST 25645.212-85. Effective 1 January 1987.

This document establishes standards of quantitative characteristics for the nuclear interaction of cosmic ray multicharged ions where the nuclear charge is from 2 to 29 units of the absolute value of the electron charge and the range of kinetic energy on a nucleon is from 10^2 to 10^4 MeV in tissue equivalent material and shielding materials. The document states that the

mean free path to nuclear interaction is related to nuclear interaction characteristics and the GCR nuclei fragmentation parameters. The values of the interaction path and fragmentation parameters are established for representative nuclei groups of GCR nuclei. For the other nuclei of the particular group of GCR nuclei, the characteristics of the nuclear interaction are taken as being the same as for the representative nucleus of that group.

Groups of GCR nuclei are specified in accordance with GOST 25645.104.84. Representative groups of nuclei are defined as follows: helium nuclei, light nuclei, medium nuclei, heavy nuclei and very heavy nuclei groups. Nuclear fragments which form as a result of nuclear interaction are assembled in group J which is designated the same as for projectile nuclei with the addition of the group of protons with $Z = 1$, taking hydrogen ^{1}H as the representative nucleus. Composition of the tissue-equivalent material is according to GOST 18622-79. Nuclear interaction characteristics are considered independent of the GCR nuclei kinetic energy for the energy interval under consideration.

Values of interaction paths of representative nuclei from each group of GCR nuclei in a fabric-equivalent medium, graphite, aluminum and iron are presented in a table. Values of interaction paths for other safety materials are defined in accordance with the recommendations in an appendix. Values of fragmentation parameters for representative nuclei groups of GCR in tissue are presented in a second table. Values of fragmentation parameters for representative nuclei groups of GCR with mass numbers ranging from 12 to 72 are presented in a third table.

10. PENETRATION OF COSMIC RAYS INTO EARTH'S MAGNETOSPHERE
(Terms and definitions)
USSR Government Standard GOST 25645.116-84. Effective 1 January 1986.

This document establishes terms and definitions to be used in science and engineering with reference to the penetration of cosmic rays into the Earth's magnetosphere. These terms are obligatory for use in documents of all types, scientific-technical, educational and reference literature. One standardized term is established for each concept; synonyms may not be used. Short forms for distinct standardized terms are given as a reference. These may be used when there is no possibility of incorrect interpretation. In the standard, alphabetical indexes containing terms in Russian and their equivalent in English are given.

NOTES

1. Recommendations of the ICRU, 1970, ICRU Report No. 16 (II), Washington, D.C.
2. Digital Data Dosimetry, Tulsa, OK, Model 1/E-1.
3. Reuter Stokes, Cleveland, OH, Model RS-P3-0803-287.

ACKNOWLEDGEMENTS

The authors would like to thank the following persons: Dr. Stuart Nachtwey of NASA-Johnson Space Center for his support of this work; Dr. John Watts of NASA-Marshall Spaceflight Center and Dr. John Wilson of NASA-Langley Research Center for their valuable suggestions and contributions; R. Richmond, B. Cash, W. Atwell, A. Hardy and R. Beaver of NASA-JSC for contributing their data; the NATO-ASI organizing committee of Drs. P. McCormack, E. G. Stassinopoulos and C. Swenberg for the invitation to one of us (E.V.B. to give these lectures on Corfu; Profs. H. Bücker of DFVLR and W. Heinrich of Siegen University for their valuable contributions; Drs. O. Gazenko, E. Kovalev, V. Dudkin and A. Marenny of the Institute of Biomedical Studies, Moscow, for their valuable help with the Cosmos Biosatellite measurements; Drs. K. Sousa, R. Ballard, and J. Connolly of NASA-Ames Research Center and Larry Chambers of NASA Headquarters for their assistance with the Cosmos Bio satellite project; and finally, the University of San Francisco Physics Research Laboratory staff, including Allen Frank for his help, and particularly V. Rowe for her extensive work on the manuscript.

REFERENCES

Adams, J. H., Jr., Tylka, A. J., and Stiller, B., 1986, LET spectra in low Earth orbit, IEEE Trans. Nucl. Sci., NS-333: 1386.

Akopova, A. B., Vikhrov, A. I., Dudkin, V. E., Magradze, N. V., Moiseenko, A. A. and others, 1985, Measurement of the spectrum of linear energy losses of cosmic rays by the Cosmos-1129 satellite, Cosmic Res. (ISSN 0023-4206) 23:479, in Russian.

Akatov, Y. A., Arkhangelsky, V. V., Aleksandrov, A. P., Fehér, I., Deme, S., Szabó, B., Vágyölgyi, J., Szabó, P. P., Csöke, A., Ránky, M., and Farkas, B., 1984, Thermoluminescent dose measurements on board Salyut-type orbital stations, Adv. Space Res., 4 (10):77.

Alsmiller, R. G., Santoro, R. T., Barish, J., and Clayborn, H. C., 1972, Shielding of manned vehicles against protons and alpha particles, ORNL Report RSIC-35.

Armstrong, T. W., Alsmiller, R. G., and Chandler, K. C., 1972, Monte Carlo calculations of high energy nucleon-meson cascades and applications to galactic cosmic-ray transport, Proceedings of the National Symposium on Natural and Man-Made Radiation in Space, NASA TM X-2440:117.

Armstrong, T. W., Chandler, K. C., and Barish, J., 1973, Calculations of neutron flux spectra induced in the Earth's atmosphere by galactic cosmic rays, J. Geophys. Res., 78:2715.

Atwell, W., Hardy, A. C., Beever, E. R., Richmond, R. G., and Cash, B. L., 1987a, A comparison of space radiation dose calculations with onboard dosimeter measurements for space shuttle missions, Oral presentation at Lawrence Berkeley Laboratory/DOE/NASA Workshop, "High Energy Accelerator and Space Radiation," Berkeley, CA, February 17-19, 1987.

Atwell, W., and Beever, E. R., 1987b, Space radiation exposures for manned polar missions: a parametric study, Proc. NATO Advanced Study Institute, Corfu, Greece, Oct. 11-25, 1987.

Bailey, J. V., 1977, Dosimetry during space missions, IEEE Trans. Nucl. Sci., NS-23 (4):1379.

Benton, E. V., and Collver, M. M., 1967, Registration of heavy ions during the flight of Gemini VI, Hlth. Phys., 13:495-500.

Benton, E. V., and Henke, R. P., 1971, High-Z particle Apollo astronaut dosimetry with plastics, Presented at the National Symposium on Natural and Man-Made Radiation in Space, Las Vegas, Nevada, March 1971.

Benton, E. V., Curtis, S. B., Henke, R. P., and Tobias, C. A., 1972, Comparison of measured and calculated high-LET nuclear recoil particle exposure on Biosatellite III, Hlth. Phys., 23:149.

Benton, E. V., Henke, R. P., and Bailey, J. V., 1975a, Heavy cosmic ray exposure of Apollo astronauts, Science, 187:263.

Benton, E. V., Henke, R. P., Peterson, D. D., Bailey, J. V., and Tobias, C. A., 1975b, High-LET particles in manned spaceflight--preliminary report, in: "Radiation Research," Academic Press, N.Y.

Benton, E. V., Peterson, D. D., Bailey, J. V. and Parnell, T. A., 1977, High-LET particle exposure of Skylab astronauts, Hlth. Phys., 32:15.

Benton, E. V., Henke, R. P., Frank, A. L., Johnson, C. S., Tran, M. T., and Etter, E., 1981, Space Radiation Dosimetry Aboard Cosmos 1129--Experiment K-309, USF-TR-53, University of San Francisco.

Benton, E. V., 1983, Dosimetric radiation measurements in space, Nucl. Tracks Rad. Meas., 7 (1/2):1.

Benton, E. V., 1985a, Unpublished work.

Benton, E. V., Frank, A. L., Henke, R. P., Rowe, V., and Atallah, T., 1985b, STS-51C dosimetry report, University of San Francisco, USF-TR-68.

Benton, E. V., 1986, Summary of radiation dosimetry results on U.S. and Soviet manned spacecraft, Adv. Space Res., 6 (11):315.

Benton, E. V., 1987, Cosmos 1887 (work in progress).

Bertini, H. W., 1969, Phys. Rev., 88:1711.

Bertini, H. W., Guthrie, M. P., and A. H. Culkowski, 1972, Nonelastic interactions of nucleons and π-mesons with complex nuclei at energies below 3 GeV, Oak Ridge National Laboratory ORNL-TM-3148, Oak Ridge, TN.

Bertini, H. W., MECC7, a Monte Carlo intranuclear cascade and evaporation code, Oak Ridge National Laboratory, Radiation Shielding Information Center, Oak Ridge, TN.

Bhatt, V. L., 1986, Neutron high-energy spectra at 5 mbar near the geomagnetic equator, J. Geophys. Res., 81 (25):4603.

Bücker, H., 1975, Biostack--a study of the biological effects of HZE galactic cosmic radiation, in: "Biomedical Results of Apollo," R. Johnston, L. Dietlein, M.D., and C. Berry, M.D., eds., NASA SP-368, Ch. 2, NASA, Washington, D.C.

Burrell, M. O., 1964, The calculation of proton penetration and dose rates, NASA TM-X-53063.

Case, R., 1969, Techniques used for the calculation of space radiation doses, Aerosp. Med., 40:1455.

Cervini, J. T., 1971, A summary of the OV1-19 measurements, Proc. Nat. Symp. Natural and Man-Made Radiations in Space, NASA TM-X-2440: 561.

Chan, K. W., Teague, M. J., and Vette, J. I., 1976, AE-6, a model environment of trapped electrons for solar maximum, NASA/GSFC report NSSDC-76-04.

Chan, K. W., Teague, M. J., and Vette, J. I., 1977, An interim outer zone electron model AE 1-7, NASA/GSFC report WDC-A-R-S 77-05.
Curtis, S. B., and Benton, E. V., 1980, Abundances, energy, and LET spectra of HZE particles in space, LBL-TR-11220, Lawrence Berkeley Laboratory.
Dudkin, V. E., 1987, private communication.
Dyer, C. S., Trombka, J. I., Schmadeback, R. L., Eller, E., Bielefeld, M. J., O'Kelley, G., Eldridge, J., Northcutt, K., Metzger, A., Reedy, R., Schonfeld, E., Seltzer, S., Arnold, J., and Peterson, L., 1975, Space Science Instrumentation, D. Reidel Co., Dordrecht, Holland, p. 279.
Fishman, G. J., 1974, Neutron and proton activation measurements from Skylab, AIAA Paper No 74-1227, presented at the AIAA/AGU Conference on Scientific Experiments of Skylab, Huntsville, AL, Oct. 30 to Nov. 1, 1974.
Fishman, G. J., and Meegan, C. A., 1980, Induced radioactivity in recovered Skylab materials, NASA TM-78263, NASA/Marshall Space Flight Center, AL.
Fishman, G. J., Paciesas, W. S., Meegan, C. A., and Wilson, R. B., 1986a, Gamma ray and charged particle background measurements in Spacelab-2, Adv. Space Res., 6, (4):23.
Fishman, G. J., Paciesas, W. S., and Gregory, J. C., 1986b, Measurements of background gamma radiation on Spacelab-2, Proc. XXVI COSPAR Meeting, Toulouse, June 30-July 12.
Frank, A. L., and Benton, E. V., 1987, Unpublished results.
Garriott, O. K., 1984, (U.S. astronaut), private communication on Skylab and Spacelab experience.
Greiner, D. E., Lindstrom, P. J., Heckman, H. H., Cork, B., and Bieser, F. S., 1975, Momentum distributions of isotopes produced by relativistic ^{12}C and ^{16}O projectiles, Phys. Rev. Lett. 35:152.
Haymaker, W., Look, B. C., Benton, E. V., and Simmonds, R. C., 1975, The Apollo 17 pocket mouse experiment (Biocore), in: "Biomedical Results of Apollo," R. S. Johnston, L. F. Dietlein and C. A. Berry, eds., U.S. Govt. Printing Office, Washington, D.C. (NASA-SP-368).
Heckman, H. H., and Nakano, G. H., 1963, East-west asymmetry in the flux of mirroring geomagnetically trapped protons, J. Geophys. Res., 68 (3)2117.
Heckman, H. H., Lindstrom, P. J., and Nakano, G. H., 1970, Long term behavior of energetic inner belt protons, NASA SP-3024.
Heckman, H. H., and Lindstrom, P. J., 1972, Response of trapped particles to a collapsing dipole field, J. Geophys. Res., 77 (4):740.
Heckman, H. H., 1975, Heavy ion fragmentation experiment at the Bevatron, NASA CR-142589, Washington, D.C.
Heinrich, W., 1977, Calculation of LET spectra of heavy cosmic ray nuclei at various absorber depths, Rad. Eff., 34:143.
Henke, R.P., and Benton, E. V., 1974, Heavy cosmic-ray measurements on Apollo 16 and 17 missions--results of the HZE dosimeter experiment, University of San Francisco, USF-TR-34.
Hill, C. W., 1973, Methods of treating complex space vehicle geometry for charged-particle radiation transport, Science Applications Inc. Report SAI-74-549-Hu.
Hill, C. W., 1976, Skylab post-mission radiation analysis, Science Applications Inc. Report 77-681-Hu.
Imhof, W. L., Reagan, J. B., Nakano, G. H., and Gaines, E. E., 1979, J. Geo-Phys. Res., 84:6371.
Imhof, W. L., Voss, H. D., Walt, M., Gaines, E. E., Mobilia, J., Datlowe, P. T., and Reagan, J. B., 1986, Slot region electron precipitation by lightning, VLF Chorus, plasmospheric hiss, J. Geophys. Res., 91 (8): 8883.
Janni, J., 1969a, A review of Soviet manned space flight dosimetry results, Aerosp. Med., 40:1547.
Janni, J., 1969b, Spacecraft cabin radiation distributions for the fourth and sixth Gemini flights, Aerosp. Med., 40 (12):1527.

Janni, J., 1969c, Editor, Aerosp. Med., 40.
Janni, J., 1976, Skylab II--radiation dosimetry systems and flight results, Air Force Weapons Laboratory (Kirtland AFB) Report, AFWL-TR-73-222, NTIS No. AD-A032-409.
Keith, W., 1987, Private communication.
Kovalev, E. E., Benton, E. V., and Marenny, A. M., 1981, Measurement of LET spectra aboard Cosmos 936 biological satellite, Rad. Prot. Dos., 1 (3):169.
Langley, R. W., 1970, Space radiation protection, NASA SP-8054.
Letaw, J. R., and Adams, J. H., Jr., 1986, Comparison of CREME model LET spectra with spaceflight dosimetry data, SCC Report 86-01, Severn Communications Corporation.
Lindstrom, P. J., Greiner, D. E., Heckman, H. H., Cork, B., and Bieser, F. S., 1975, Isotope production cross sections from the fragmentation of ^{16}O and ^{12}C at relativistic energies, Lawrence Berkeley Laboratory, LBL-3650.
Lockwood, J. A., Chen, C., Friling, L. A., and St. Onge, R. N., 1986, Energy spectrum and flux of high energy neutrons at balloon altitudes, J. Geophys. Res., 81 (34):6711.
Marenny, A. M., Nymmik, R. A., and Saslov, A. A., 1987, Solar modulation of the galactic cosmic ray fluxes of heavy nuclei in 1974-1986, International Cosmic Ray Conference, Moscow, 1987, V. 3:328.
Markelov, V. V., and Chernykh, I. V., 1982, Direct-reading dosimeters used for monitoring radiation in Salyut stations, Kosmich. Biolog. Aviakosm. Meditsina, 16:81.
Mullen, E. G., Grussenhoven, M. S., and Hardy, D. A., 1987, The space radiation environment at 840 km, presented at NATO Advanced Study Institute, Corfu, Greece, Oct. 11-25, 1987.
Osborne, W. Z, and Pinsky, L. S., 1975, Apollo light flash investigations, in: "Biomedical Results of Apollo," R. Johnston, L. Dietlein, M.D., and C. Berry, M.D., eds., NASA SP-368, Ch. 2, NASA, Washington, D.C.
Parnell, T.A., Watts, J. W., Jr., Fishman, G. J., Benton, E. V., Frank, A. L., and Gregory, J. C., 1986, The measured radiation environment within Spacelabs 1 and 2 and comparison with predictions, Adv. Space. Res., 6 (12):125.
Peterson, D. D., and Benton, E. V., 1975, High-LET particle radiation inside Skylab (SL-2) command module, Hlth. Phys., 29:125.
Petrov, V., Akatov, Y., Kozlova, S., Markelov, V., Nesterov, V., Redko, V., Smirenny, L., Khortsev, A., and Chernykh, I., 1975, The study of the radiation environment in near-Earth space, Space Res., 13:129.
Radke, G., 1969, An evaluation of current methods of predicting space radiation doses by comparing calculations with Gemini IV OV1-2, OV1-4, and OV1-9 experimental measurements, Aerosp. Med., 40:1557.
Richmond, R. G., 1969, A review of Gemini and Apollo astronaut dosimetry data, Aerosp. Med., 40 (12):1535.
Santoro, R. T., Claiborne, H. C., and Alsmiller, R. G., Jr., 1972, Primary and secondary particle contributions to the depth dose distribution in a phantom shielded from solar-flare and Van Allen protons, Proc. Nat. Symp. Natural and Man-Made Radiation in Space, NASA TM X-2440, 117.
Savinykh, V., 1986, (Soviet cosmonaut), private communication.
Sawyer, D. M., and Vette, J. I., 1976, AP8 trapped proton environment for solar minimum and solar maximum, NASA/GSFC Report WDC-A-R&S, 76-06.
Schaefer, H. J., 1971, Apollo mission experience, Proc. Nat. Symp. Natural and Man-Made Radiation in Space, E. A. Warman, ed., NASA TM X-2440, NASA, Washington, D.C. (1972).
Schaefer, H. J., 1977, Nuclear emulsion measurements of the dose contribution from tissue-disintegration stars on the Apollo-Soyuz mission, ONR Contract No. 00014-76-C-0544, Report 2, Physics Department, Univ. of West Florida, Pensacola, FL 32504.

Schaefer, H. J., 1978, A note on the tissue star dose in personnel radiation monitoring in Space, NASA Contract No. NAS9-15417, Physics Dept., Univ. of West Florida, Pensacola, FL 32504.

Schneider, M. R., and Janni, J. F., 1965, Experiment D-8, radiation in spacecraft Gemini-4, in: "First Manned Spaceflight Symposium," Washington, D.C., p. 171.

Schneider, M. R., and Janni, J. F., 1969, A comprehensive summary of dose-rate measurements aboard the fourth and sixth Gemini flights, Aerosp. Med., 40 (12):1535.

Singley, G. W., and Vette, J. I., 1972, A model environment for outer zone electrons, NASA/GSFC Report NSSDC 72-13.

Stassinopoulis, E. G., 1987, Radiation environment in space, Presented at NATO Advanced Study Institute, Corfu, Greece, Oct. 11-25, 1987.

Teague, M. J., and Vette, J. I., 1974, A model of the electron environment for solar minimum, NASA/GSFC Report NSSDC-74-03.

Thede, A., 1969, OV3-4 dose rate and proton spectral measurements, AFWL-TR-68-128 (Kirtland AFB).

Trombka, J. I., Eller, E. L., Schmadebeck, R. L., Dyer, C. S., Reedy, R. C., Barr, D., Gilmore, J., Prestwood R., Bayhurst, B., Perry, D., Smith, A., Cordi, R., Pehl, R., Eldridge, J., Schonfeld, E., and Metzger, A., 19--, Crystal Activation Experiment MA-151, ASTP Summary Science Report, NASA-HQ report, unpublished.

Vette, J. I., 1966, Models of the trapped radiation environment, NASA-SP 3024, Vols. 1 and 2.

Vette, J. I., and Chen, C. K., 1987, Trapped electron environment models for solar minimum and solar maximum, available from NASA/GSFC-NSSDC, (private communication).

Vorobyov, Y. I., and Kovalyov, Y. Y., 1983, "Radiation Safety of Crews of Flying Vehicles," Energoatomizdat, Moscow, Ch. 7.

Watts, J. W., Jr., and Burrell, M. O., 1971, Electron and bremsstrahlung penetration and dose rates, NASA TN D-6385.

Watts, J. W., Jr., and Wright, J. J., 1976, NASA TM X-73358.

Watts, J. W., Jr., Parnell, T. A., and Heckman, H. H., 1987, An approximate angular distribution for trapped protons at low altitudes, Proceedings CHERBS, Sanibel Island, FL, Nov. 3-5, 1987.

Webber, W. R., and Lockwood, J. A., 1981, A study of the long-term variation and radial gradient of cosmic rays out to 23 AU, J. Geophys. Res., 36:11, 458.

Wilson, J. W., 1977, Analysis of the theory of high-energy ion transport, NASA TN D-8381.

Wilson, J. W., 1987, Private communication.

Wright, J. J., and Burrell, M. O., 1972, The estimation of galactic cosmic-ray penetration and dose rates, NASA TN D-6600.